AD-A019 230

MATERIALS RESEARCH FOR SUPERCONDUCTING MACHINERY-IV

Richard P. Reed, et al

National Bureau of Standards

Prepared for:

Advanced Research Projects Agency

September 1975

SEMI-ANNUAL TECHNICAL REPORTS ON MATERIALS RESEARCH IN SUPPORT OF SUPERCONDUCTING MACHINERY-IV

FOR

1 March 1975 to 1 September 1975

Edited by

Richard P. Reed and Alan F. Clark
National Bureau of Standards

and

Edward C. van Reuth
Advanced Research Projects Agency

Sponsored by

Advanced Research Projects Agency
1400 Wilson Boulevard, Arlington, VA 22209
ARPA Order No. 2569 - Program Code 5D10

Contracted for 10 August 1974

by

Cryogenics Division, Institute for Basic Standards
National Bureau of Standards, Boulder, CO 80302

Subcontracts to:

Battelle, Columbus Laboratories
General Electric Research & Development Center
Martin Marietta Aerospace, Denver Division
National Bureau of Standards, Cryogenics Division
Westinghouse Electric Research and Development Center

DISCLAIMER

The views and conclusions contained in this document are those of the authors and should not be interpreted as necessarily representing the official policies, either expressed or implied, of the Advanced Research Projects Agency or the U.S. Government.

SUMMARY

The fourth semi-annual technical reports are collected from five subcontractors of an ARPA sponsored program on the very low temperature properties of structural materials to support the development of superconducting machinery. The program is outlined and research progress is reported. Low temperature data are presented for the elastic, tensile, fatigue and fracture properties, thermal expansion, specific heat, thermal and magneto-thermal conductivity, electrical and magnetic properties of structural alloys. Effects of processing and fabrication are also reported for many of the properties; weld and braze joint properties are included. Tensile and compressive data at 4 K of selected composites are presented.

CONTENTS

NATIONAL BUREAU OF STANDARDS

Advanced Composites

Kasen, M. B.
Schramm, R. E.

Elastic Properties

Ledbetter, H. M.
Naimon, E. R.
Weston, W. F.

Fatigue Resistance and Fracture Toughness

Read, D. T.
Reed, R. P.
Tober, R. L.

Magnetothermal Conductivity

Sparks, L. L.

Thermal Conductivity

Hust, J. H.

WESTINGHOUSE ELECTRIC CORPORATION

Structural Materials for Cryogenic Applications

Wells, J. M.
Daniel, M. R.
Kossowsky, R.
Logsdon, W. A.

INTRODUCTION

This report contains results of a widespread program designed to fulfill the need for materials properties data to assist the design and development of superconducting machinery. The program was conceived and developed jointly by the staffs of the Materials Sciences - Advanced Research Projects Agency and the Cryogenics Division -National Bureau of Standards. This ARPA - sponsored program on "Low Temperature Properties of Structural Materials in Support of Superconducting Machinery" is managed by NBS, with subcontracts to four other laboratories.

PROGRAM DESCRIPTION

The program's objectives are: 1) to evaluate candidate structural materials for use in superconducting electrical machinery by determining their mechanical and physical properties between 4 and 300 K and the effects on these properties of processing and joining, 2) to explore new materials, such as composites, for potential innovative design applications by performing screening tests on their low temperature properties, and 3) to assist the information transfer of the available low temperature properties data into design use by compiling and publishing what literature data are available and assessing what properties need further study.

The second year's program plan to meet these objectives is shown in Table 1 and Table 2. These outline the efforts at the five research laboratories with a brief description of each program in Table 1. The organizational contacts for each research laboratory are shown in Table 3. It can be easily seen from the program plan that the major thrust has been fatigue and fracture measurements at low temperatures where virtually no data have previously existed.

During the first year (1973/74) research was directed toward composite review and measurement. This year (1974/75) measurements have been initiated on alloys designed to provide a structural ferromagnetic material at low temperatures and a high strength-high conductivity material. Composite research is continuing.

A major new materials conference, the International Cryogenic Materials Conference, was held at Kingston, Ontario, in July, 1975. Over 60 technical papers (14 from this program) were presented and the proceedings will appear as a bound volume.

Table 1

ARPA - Low Temperature Properties of Structural Materials

Second Year Program (FY 75)

Program Area	Organization	Program Description
Mechanical Properties		
1. Fracture and Fatigue		
a. Materials Group	NBS-Cryogenics	Fracture toughness, fatigue crack growth rate, fatigue sustained load crack growth rate tests from 4-300 K on structural alloys, and the effects of stress level and frequency.
b. Materials Group	Westinghouse	Mechanical, magnetic, electrical loss characterization of alloys proposed for use in DOD sponsored programs. Mechanical tests include tensile, fracture toughness, fatigue.
c. Materials Group	Martin-Denver	Fatigue on selected, tough alloys at 4, 76 and 300 K.
2. Effects		
a. Processing	Westirghouse	Identification of effects of fabrication and processing techniques on mechanical properties of selected alloys. Variables include industrial melting practices, powder metallurgy techniques, cold working, grain size, and inhomogeneities.
b. Joining	Westinghouse	Mechanical properties of fabricated metal joints, including welding (GTAW, EB, GMAW), brazing, and soldering from 4-300 K. Properties include tensile, notched tensile, fracture toughness, and fatigue crack growth rate in the fused and heat affected zones and the base metal.
3. Elastic Properties	NBS-Cryogenics	Tensile and dynamic elastic (Young's, shear, bulk moduli) measurements on structural alloys, electrical, and composite materials from 4-300 K.

Table 1 (continued)

Program Area	Organization	Program Description
Thermal Properties		
4. Thermal Expansion, Specific Heat	Battelle	Thermal expansion and specific heat measurements on selected insulations and structural alloys and composites.
5. Thermal-Magnetothermal Conductivity	NBS-Cryogenics	Thermal conductivity and thermal conductivity in magnetic fields up to 50 kilogauss from 4-300 K of structural alloys and composites.
Composites		
6. Evaluation of Advanced Composites	NBS-Cryogenics	Screening tests (tensile, fatigue at 4 K) on selected candidate metal and non-metal base composites, including B-epoxy, C-epoxy and polyimide, PRD 49-epoxy, borsic-Al, steel-Al.
7. Evaluation of Composite Bonds and Structures	General Electric	Measurement of low temperature bonds between various composites and aluminum and steel.
Data Compilation and Evaluation		
8. Handbook	Battelle	Publication of Handbook containing recommended best value data and complete set of references for over 40 additional materials (structural alloys, superconductors, electrical materials, and polymers). Data presented in graphical and tabular formats; mechanical, thermal, electromagnetic properties from 0-300 K.
9. Workshop Meeting	NBS-Cryogenics	Organization of meeting for mutual data sharing and interaction with service agencies and their contractors.

Table 2

PROPERTIES	MATERIAL OBJECTIVES				
	STRUCTURAL	COMPOSITES	FERROMAGNETIC	SUPERCONDUCTING MAGNET	HIGH STRENGTH HIGH CONDUCTIVITY
Fracture Toughness, Fatigue Crack Growth Rate, and Tensile	21-6-9 (NBS) Inc 718 (NBS,W) 2014 Al (NBS) Inc 750, weld (W) Inc 718, weld (W) Inc 706, parent (W) and weld Low Expan Fe-Ni,(W) parent and weld		Fe-9Ni (NBS)		PD-135 (W)
Fatigue	AlSl 304 (M) AlSl 310 (M) 21-6-9 (M) Inc 718 (M) A-286 (M)				
Tensile, Compression, Shear		B/epoxy (NBS) B/Al (NBS) C/epoxy (NBS) K-49/epoxy (NBS) S-glass/epoxy (NBS) Composite - metal joints (G.E.)			
Elastic	Inc 718 (NBS)			Cu-Ni (NBS) Cu-Sn (NBS) Nb-Ti (NBS)	OFHC (NBS) PD-135 (NBS)
Thermal Conductivity	Inc 750 (NBS)	B/Al (NBS)			
Thermal Expansion and Specific Heat		Fiber-reinforced composites (B)		Cu-Sn (B) Cu-Ni (B) Bakelite (B) Potting Compds. (B)	Cu-Al_2O_3 (B) Cu-Zr (B)
Magneto-Thermal Conductivity	Inc 750 (NBS) AlSl 310 (NBS) Ti-6Al-4V (NBS) 2024 Al (NBS)				PD-135 (NBS)
Magnetic	Inc 718 (W) Low Expan Fe-Ni (W)		AlSl 410 (W) Fe-9Ni (W) Fe-78Ni (W) Fe-3Si (W) Armco Fe (W)		PD-135 (W)

Table 3

ARPA - Low Temperature Properties of Structural Materials

Organizational Contacts

Advanced Research Projects Agency, 1400 Wilson Blvd., Arlington, Virginia 22209

Program Director	Edward C. van Reuth	202-694-4750 694-4750 (FTS)	

National Bureau of Standards, Cryogenics Division, Boulder, Colorado 80302

Program Manager	Richard P. Reed		Ext. 3870
Contract Monitor	Alan F. Clark		Ext. 3253
Fracture, Fatigue	Ralph L. Tober	303-499-1000	Ext. 4447
Elastic	Hassell M. Ledbetter	323-ext. (FTS)	Ext. 3232
Thermal Conductivity	Jerome G. Hust		Ext. 3733
Magnetothermal Conductivity	L. L. Sparks		Ext. 3612
Composites	Maurice B. Kasen		Ext. 3558

Battelle, Columbus Laboratories, 505 King Avenue, Columbus, Ohio 43201

Program Manager	Kenneth R. Hanby		Ext. 1784
Mechanical Properties Data	Kenneth R. Hanby		Ext. 1784
Thermal Properties Data	Kenneth E. Wilkes	614-424-6424	Ext. 3489
Magnetic Properties Data	J. Ken Thompson	941-8045 (FTS)	Ext. 2612
Physical Properties Meas't.	Frank Jelinek		Ext. 1735

General Electric Company, Research and Development Center, P.O. Box 8, Schenectady, N.Y. 11506

Program Manager	William B. Hillig	518-346-8771	Ext. 6139
Mechanical Properties	Richard L. Mehan	518-346-8771	Ext. 6398
Polymer Properties	Donald G. LeGrand	518-346-8771	Ext. 6396

Martin Marietta Aerospace, Denver Division, P.O. Box 179, Denver, Colorado 80201

Program Manager	Fred R. Schwartzberg	303-794-5211	Ext. 2365
Principal Investigator	Ted Kiefer	303-794-5211	Ext. 2886

Westinghouse Electric Corporation, Research & Development Center, Beulah Road, Pittsburgh, Pennsylvania 15235

Program Manager	Joseph M. Wells	412-256-7000	Ext. 3633
Joining & Processing	Joseph M. Wells	412-256-7000	Ext. 3633
Fracture Mechanics	William A. Logsdon	412-256-7000	Ext. 3652
Magnetic Measurements	Michael R. Daniels	412-256-7000	Ext. 7267
Metallurgy-Fractography	Ram Kossowsky	412-256-7000	Ext. 3684

RESULTS HIGHLIGHTS

A general overview of this large program is best obtained by reading the technical summary of each contractor report. A summary of materials included in all programs for the second year is presented in Table 2, listed by property and material category. We feel it is useful to briefly outline the major technical accomplishments.

Our data handbook, "Handbook on Materials for Superconducting Machinery" became available at the first of the year (1975). A second edition will be published in December of this year; this will include approximately 40 more materials and additional data for those materials already included in the handbook.

New notched and unnotched fatigue S-N data have been generated for the first time at 4 K for selected structural alloys (21-6-9, 304L, 310, A-286, and 718).

Adhesive joints between S-glass-epoxy composites and aluminum alloys were evaluated; bond strengths were found to improve at lower temperatures.

Thermal expansion of 23 new materials and specific heat of six materials were measured to 4 K.

Processing and joining effects on low temperature mechanical properties were continued on alloys 718, 750, Inconel LEA, and PD-135.

Fracture toughness of alloy 21-6-9 was measured at 300, 76, and 4 K and the fatigue crack growth rate behavior of austenitic steels at 4 K summarized.

New tensile data at low temperatures are reported for five epoxy and metal-base composites.

A new major materials conference, 14th International Cryogenic Materials Conference (ICMC) was held in Kingston, Ontario during July, 1975. Over 60 contributed papers were presented; these will be published in a bound volume during early 1976.

A third workshop is planned to be held in Vail, Colorado in early April, 1976. Details will be announced near the end of the year.

HANDBOOK

One of the most important outputs of this program is, of course, the handbook. It collects in one volume all the data that are available, including the new data generated by this program, on the low temperature properties of structural materials for use in superconducting machinery. This work is being handled by Battelle, Columbus Laboratories under the direction of Ken R. Hanby. The handbook presents in loose leaf format, so that it can be added to in the succeeding years, mechanical, thermal, electrical, and magnetic properties of materials for superconducting machinery. Both tabular and graphical presentations are made for best-value data along with original data and test conditions. The reference sources have been the Materials and Ceramics Information Center (MCIC), the Defense Documentation Center (DDC), and the Cryogenic Information Center (CIC).

The first volume of the handbook is available. It contains data on more than 40 metals and alloys in various conditions, and is 511 pages long, including 740 references. The handbook is available from the National Technical Information Service (NTIS), Operations Division, Springfield, Virginia 22151, under the following information:

Handbook on Materials for Superconducting
Machinery -- November 1974
MCIC - HB - 04.

8<

SEMIANNUAL TECHNICAL REPORT

on

PREPARATION OF A HANDBOOK ON MECHANICAL, THERMAL, ELECTRICAL, AND MAGNETIC PROPERTIES OF MATERIALS FOR SUPERCONDUCTING MACHINERY

Sponsored by
Advanced Research Projects Agency
ARPA Order No. 2569
Program Code 4D10
Contract No. CST-8303

Contract Monitor
Cryogenics Division
National Bureau of Standards
Boulder, Colorado 80302

October 20, 1975

METALS AND CERAMICS INFORMATION CENTER
A Department of Defense Information Analysis Center
BATTELLE
Columbus Laboratories
505 King Avenue
Columbus, Ohio 43201
Telephone (614) 424-6424

FOREWORD

This research was supported by the Advanced Research Projects Agency of the Department of Defense with Dr. Edward C. VanReuth as Project Monitor. The handbook preparation task was subcontracted to Battelle-Columbus by the Cryogenics Division, National Bureau of Standards under Contract No. CST-8303 with Dr. Richard P. Reed as Program Manager and Dr. Alan F. Clark as Contract Monitor.

The research described in this report was carried out under ARPA Order No. 2569 and Program Code 4D10 by the Metals and Ceramics Information Center (MCIC) with K. R. Hanby (614, 424-6424, Extension 1784) as the Program Coordinator, and E. A. Eldridge (614, 424-6424, Extension 2572), and J. K. Thompson (614, 424-6424, Extension 2612) as Principal Investigators. Contract No. CST-8303 includes two tasks. Task I of the current program provides for a compilation of low-temperature property data on an expanded series of selected materials for structural applications in superconducting machinery. These data compilations will be produced as the First Revision of the "Handbook on Materials for Superconducting Machinery". Task II provides for determination of thermal expansion and specific heat values at cryogenic temperatures for selected structural alloys. The Semiannual Technical Report on the latter program is presented under separate cover. Overall contract funding was $100,000 with $50,000 for the handbook program and $50,000 for the laboratory study. The effective date of the current contract was September 10, 1974, and the contract expiration date September 10, 1975.

DISCLAIMER

PREPARATION OF A HANDBOOK ON MECHANICAL, THERMAL, ELECTRICAL, AND MAGNETIC PROPERTIES OF MATERIALS FOR SUPERCONDUCTING MACHINERY

A rough draft of the First Revision of "The Handbook on Materials for Superconducting Machinery" has been completed. Copies of the tables and figures incorporating most of the data that are to be added to the existing Handbook have been submitted to Cryogenics Division, NBS, for their comments. Most of the layout decisions have been made, and the modifications required to change the First Edition into the First Revision will be in the form of about 74 replacement sheets and 112 insert sheets, for a total package of approximately 186 sheets of paper. The count is approximate because the typing of the Reference section, to be reorganized and augmented, has not been completed as yet. The modifications involved in preparation of the First Revision include (1) additions of data, (2) corrections of data, (3) additions of new features (e.g., index table and revised Reference section), and (4) changes required by format conventions.

The published version of the First Revision will be prepared and issued by Metals and Ceramics Information Center. The 186 sheets will be punched for insertion in the existing Handbook, and accompanied by directions for turning the First Edition into the First Revision.

The First Revision is best described by Tables 3.1 and 3.2 attached to this report; these were prepared for the First Revision, and the attached copies show exactly how they will appear in the Handbook. Note that the arrangements of materials in the two tables are slightly different.

Table 3.1 lists all the materials selected for inclusion in the First Revision (including those in the First Edition), and they are listed in the order in which they appear in the Handbook. The order in Table 3.1 and in the Handbook is not always what might appear to be the most logical one with respect to the alloy specification numbers. The AISI-numbered stainless steels are a good case in point. The situation with the steels occurred because Types 303, 310S, and 347 were selected for inclusion in

the First Revision after the other steels in that series already had been assigned numbers for the First Edition.

Table 3.2, on the otherhand, is arranged by the material specification numbers to the extent possible. This table provides an index to tables and figures where available properties data are given. Unlike Table 3.1, materials for which no data were found are not listed in Table 3.2. This index table, a new feature, covers all materials, forms, and conditions for the First Revision.

Features of the First Revision

General

- An index table is included, for the readers' convenience.
- Wherever they are available, Unified Numbering System (UNS) designations are included along with compositions in Table 3.1.
- The Reference section is separated into two separate sections, one containing references cited in the data sections and the other, a bibliography of literature that provides additional useful information on behavior of materials at cryogenic temperatures.
- The right-hand pages of all sheets prepared for the First Revision contain ready-reference indicators of material and form for those pages.

Mechanical Properties

- A new data category "Dynamic Moduli" has been added. Bulk modulus (B) values, included for the first time in this Revision, have been obtained by calculations from dynamic measurements of longitudinal and transverse compliances. The previous format did not lend itself to inclusion of B.
- Shear modulus has been added to the polymers format.

- J-integral data are presented in lieu of valid K_{Ic} data in cases where the latter are not obtainable (because of plastic zone behavior), and J-integral data are available. Only those values based on compact specimens are reported.
- Fatigue crack-growth rate data are included. In cases where compatible data are available from several sources, combination is accomplished by photographic superposition.

Thermal/Electrical Properties

- Revision I incorporates modification of some thermal-conductivity versus temperature curves from the First Edition. Insofar as possible, data are fitted to a straight line in the low temperature region below that where maximum thermal conductivity occurs.
- Magnetothermal conductivity data have been incorporated as available.

Magnetic Properties

- Data on magnetic moments as a function of magnetic field strength are presented for the first time.

TABLE 3.1. NOMINAL COMPOSITIONS OF ALLOYS AND CORRESPONDING SECTION NUMBERS

Section		Unified No. System	Composition in Weight Percent[a]						
			Si	Cu	Mn	Mg	Cr	Zn	Others
4.0.0	**Aluminum and Aluminum Alloys**								
4.1.0	**Unalloyed Aluminum**								
4.1.1	99.99Al	A91199							(99.45 min Al)
4.1.2	EC	A91145							(99.50 min Al), 0.40Fe
4.1.3	1050	A91050	0.25	0.05	0.05	0.05		0.05	(99.00 min Al)
4.1.4	1100	A91100	1.0(Si+Fe)	0.05-0.20	0.05			0.10	
4.2.0	**2000 Series**								
4.2.1	2014	A92014	0.5-1.2	3.9-5.0	0.4-1.2	0.2-0.8	0.10	0.25	0.7Fe, 0.15Ti
4.2.2	2219	A92219	0.20	5.8-6.8	0.2-0.4	0.02		0.10	0.3Fe, 0.02-0.10Ti
4.3.0	**5000 Series**								
4.3.1	5083	A95083	0.40	0.10	0.4-1.0	4.0-4.9	0.05-0.25	0.25	0.4Fe, 0.15Ti
4.4.0	**6000 Series**								
4.4.1	6061	A96061	0.4-0.8	0.15-0.40	0.15	0.8-1.2	0.04-0.35	0.25	0.7Fe, 0.15Ti
4.5.0	**7000 Series**								
4.5.1	7039	A97039	0.30 max	0.10 max	0.25	2.8	0.20	4.0	0.4 max Fe, 0.10 max Ti
4.5.2	7005	A97005	0.35 max	0.10 max	0.2-0.7	1.0-1.8	0.06-0.20	4.2-5.0	0.01-0.06Ti, 0.06-0.20Zr, 0.35 max Fe
4.5.3	7006	–	0.10	0.04	0.22	2.24	0.12	4.10	0.17Fe, 0.01Ti

		Unified No. System	CDA No.	Composition in Weight Percent[a]				
				Cu	Pb	Fe	Zn	Others
5.0.0	**Copper and Copper Alloys**							
5.1.0	**99.9+Cu**							
5.1.1	99.96Cu	C10100	101	99.96+				0.0003 max P, 0.001 max Pb
5.1.2	Electrolytic Tough Pitch	C11000	110	99.9+				
5.1.3	OFHC	C10200	102	99.95				
5.1.4	Phosphorized	C12200	122	99.9+				0.02P
5.2.0	**Cu-Zn Alloys**							
5.2.1	80Cu-20Zn	C24000	240	80	0.05 max	0.05 max	20	
5.2.2	70Cu-30Zn	C26000	260	70	0.07 max	0.05 max	30	
5.3.0	**Cu-Ni Alloys**							
5.3.1	90Cu-10Ni	C70600	706	Bal.	0.05 max	1.0		1.0Mn, 9.0-11.0Ni
5.3.2	80Cu-20Ni	C71000	710	Bal.	0.05 max	1.0 max	1.0 max	1.0 max Mn, 19.0-23.0Ni
5.3.3	70Cu-30Ni	C71500	715	Bal.	0.05 max	0.4-0.7	1.0 max	1.0 max Mn, 29.0-33.0Ni
5.4.0	**Cu-Be Alloys**							
5.4.1	Cu-Be(1.6-1.8)	C17000	170	Bal.				1.6-1.8Be, 0.20-0.40Co
5.4.2	Cu-Be(1.8-2.0)	C17200	172	Bal.				1.8-2.0Be, 0.20 min Ni+Co (0.60 max Ni+Co+Fe)
5.5.0	**Cu-Sn Alloys**							
5.5.1	95Cu-5Sn	C51800	518	Bal.	0.02 max			4.0-6.0Sn, 0.10-0.35P
5.5.2	92Cu-8Sn	C52100	521	Bal.	0.05 max	0.10 max	0.20 max	7.0-9.0Sn, 0.03-0.35P
5.5.3	90Cu-10Sn	C52400	524	Bal.	0.05 max	0.10 max	0.20 max	9.0-11.0Sn, 0.03-0.35P
5.6.0	**Cu-Zr Alloy**							
5.6.1	Cu-0.2Zr (Amzire)	C15000	150	99.8				0.10-0.20Zr
5.7.0	**Cu-Cr-Cd Alloy**							
5.7.1	Cu-0.4Cr-0.4Cd (PD-135)	–	–	Bal.				0.4Cr, 0.4Cd (Te deox.)
5.8.0	**Cu-Al_2O_3 Alloys**							
5.8.1	Cu+0.2Al_2O_3	(AL-10)	–	Bal.				0.2Al_2O_3 dispersion
5.8.2	Cu-0.7Al_2O_3	(AL-35)	–	Bal.				0.7Al_2O_3 dispersion
5.8.3	Cu+1.1Al_2O_3 (Glid Cop Alloys)	(AL-60)	–	Bal.				1.1Al_2O_3 dispersion

(a) max = maximum, min = minimum.

TABLE 3.1. (Continued)

Section		Unified No.	Composition in Weight Percent[a]						
			Ni	Cr	Fe	Mn	Si	C	Others
6.0.0	**Nickel and Cobalt Alloys**								
6.1.0	Ni-Cu Alloy	System							
6.1.1	K Monel (K-500)	N05500	Bal.		1.0	0.6	0.15	0.15	29.5Cu, 2.8Al, 0.5Ti
6.2.0	**Ni-Cr-Fe Alloys**								
6.2.1	Inconel 600	N06600	Bal.	15.8	7.2	0.2	0.2	0.04	0.10Cu
6.2.2	Inconel X-750	N07750	Bal.	15.0	6.75	0.7		0.04	0.8Al, 2.5Ti, 0.85Nb
6.2.3	Inconel 718	N07718	Bal.	18.6	18.5			0.04	0.4Al, 0.9Ti, 5.0Nb, 3.1Mo
6.3.0	**Controlled Expansion Alloys**								
6.3.1	Invar 36	–	36		Bal.				
6.3.2	Ni-Span C	–	42.1(Ni+Co)	5.4	48.4	0.40			2.4Ti, 0.65Al
6.3.3	Unnamed Inco LEA Alloy	–	39.6		55.4	0.22	0.12	0.01	0.22Al, 1.46Ti, 2.90Nb+Ta

		Unified No.	Composition in Weight Percent[a]						
			C max	Mn max	P max	S max	Si	Ni	Others
7.0.0	**Alloy Steels**								
7.1.0	Nickel Steels	System							
7.1.1	9-Ni Steel	–	0.13	0.80	0.035	0.04	0.15-0.30	8.5-9.5	
7.1.2	18Ni(200) Maraging	–	0.03	0.10	0.01	0.01	0.10	17-19	8.5Co, 3.25Mo, 0.20Ti, 0.10Al
7.2.0	**Fe-Si Steel**								
7.2.1	Transformer Steel								

		Unified No.	Composition in Weight Percent[a]								
			C	Mn	P max	S	Si	Cr	Ni	Mo	Others
8.0.0	**Stainless Steels**										
8.1.0	300 Series	System									
8.1.1	AISI 301	S30100	0.15 max	2.0 max	0.045	0.03 max		16-18	6-8		
8.1.2	AISI 304	S30400	0.08 max	2.0 max	0.045	0.03 max	1.0 max	18-20	8-10.5		
8.1.3	AISI 304L	S40503	0.03 max	2.0 max	0.045	0.03 max	1.0 max	18-20	8-12		
8.1.4	AISI 310	S31000	0.25 max	2.0 max	0.045	0.03 max	1.5 max	24-26	19-22		
8.1.5	AISI 316	S31600	0.08 max	2.0 max	0.045	0.03 max	1.0 max	16-18	10-14	2.0-3.0	
8.1.6	AISI 321	S32100	0.08 max	2.0 max	0.045	0.03 max	1.0 max	17-19	9-12		(5xC)Ti min
8.1.7	AISI 303	S30300	0.15 max	2.0 max	0.20	0.15 min	1.0 max	17-19	8-10	0.6 max (or Zr)	
8.1.8	AISI 310S	S31008	0.08 max	2.0 max	0.045	0.03 max	1.5 max	24-26	19-22		
8.1.9	AISI 347	S34700	0.08 max	2.0 max	0.045	0.03 max	1.0 max	17-19	9-13		(10xC)Nb+Ta
8.2.0	**Other Stainless Steels**										
8.2.1	A-286	K66286	0.05	1.4			0.4	15	26	1.25	0.2Al, 2.15Ti, 0.003B, 0.3V
8.2.2	Kromarc-58[b]	–	0.03	9.3	0.005	0.005 max	0.05	15.5	23	2.2	0.02Al, 0.008Zr, 0.016B, 0.16V, 0.17N
8.2.3	Armco 21-6-9	–	0.08 max	8.0-10.0				19.0-21.5	5.5-7.5		
8.2.4	Armco 22-13-5	–	0.06 max	4.0-6.0			1.0 max	20.5-23.5	11.5-13.5	1.5-3.0	0.1-0.3Nb, 0.1-0.3V, 0.2-0.4N

(a) max = maximum, min = minimum.

(b) Analysis of Westinghouse plate used in evaluation program.

TABLE 3.1. (Continued)

Section		Unified No.	Composition in Weight Percent[a]								
		System	Al	Sn	V	Fe max	O max	C max	N max	H max	Mn max
9.0.0	**Titanium and Titanium Alloys**										
9.1.0	**Unalloyed Ti**										
9.1.1	Ti-65A	–						0.20	0.07	0.015	
9.1.2	Ti-75A	–					0.40	0.20	0.07	0.0125	
9.2.0	**Alpha Ti Alloys**										
9.2.1	Ti-5Al-2.5Sn[c]	–	4.0-6.0	2.0-3.0		0.50	0.20	0.15	0.07	0.020	0.30
9.2.2	Ti-5Al-2.5Sn (ELI)[d]	–	4.7-5.6	2.0-3.0		0.20	0.12	0.08	0.05	0.0175	
9.3.0	**Alpha-Beta Ti Alloy**										
9.3.1	Ti-6Al-4V (ELI)[d]	–	5.5-6.5		3.5-4.5	0.15	0.13	0.08	0.05	0.015	
9.3.2	Ti-6Al-4V[c]	–	5.5-6.75		3.5-4.5						
10.0.0	**Special Metals and Alloys**										
10.1.0	**Nb and Nb Alloys**										
10.1.1	Nb	–									
10.1.2	Nb_3Sn	–									
10.1.3	Nb-Zr	–									
10.1.4	Nb-Ti	–									
10.1.5	Nb-Ti+Cu composites	–									
10.2.0	**V-Ga Alloys**										
10.2.1	V_3Ga	–									
12.0.0	**Polymers**										
12.1.1	PE	Polyethylene									
12.1.2	PCTFE	Polychlorotrifluoroethylene									
12.1.3	PTFE	Polytetrafluoroethylene									
12.2.1	PMM	Polymethylmethacrylate									
12.3.1	PS	Polystyrene									
12.4.1	PVA	Polyvinylacetate									

(a) max = maximum, min = minimum.
(c) Normal interstitial content.
(d) ELI = extra low interstitial type.

TABLE 3.2. INDEX TO MATERIALS, FORMS, CONDITIONS, AND PROPERTIES FOR DATA REPORTED IN FIRST REVISED EDITION[a]

				Mechanical Properties												Thermal-Electrical Properties						Magnetic Properties		
Material	Mat'l Code	Form[b,c]	Condition[c,d,e]	Prop. Code	Ultimate Props.	Elastic Props.	NTS	Compress. CUS, CYS, E_c	Shear SUS, G	Impact Charpy V	Fracture Toughness K_{IC}, K_{IE}, J_{IC}	Fatigue da/dN	Fatigue S-N	Dynamic Moduli[b] E, G, B, ρ	Flexure FUS, FYS E_{f_1}, E_{f_2}	Prop. Code	C Thermal Cond.	C Magneto-Thermal Cond.	E Thermal Expansion	S Specific Heat	R Electrical Resistivity	Prop. Code	Magnetic Moment	Perm. or Suscept.
Aluminum Alloys																								
Aluminum	4.1.1		Annealed	ME												TR	1,F1		1,F1	1,F1,F2,F3	1,F1	Me		1
1099-H14 Al	4.1.4	Plate	H14	ME	1,F1																			
1100-O Al	4.1.4	Bar	O	ME	2,F1																			
1100-O Al	4.1.4	Rod	O	ME										3										
1100-O Al	4.1.4		O													TR	1,F1		1,F1		1,F1			
2014-T6 Al	4.2.1	Sheet	T6	ME	1,2,5,F1	2	2						3,F2											
2014-T62 Al	4.2.1	Sheet	T62	ME	4,F1		4																	
2014-T62 Al	4.2.1	Plate	T62	ME	6						7													
2014-T651 Al	4.2.1	Plate	T651	ME	6,F1		6				9													
2014-T6 Al	4.2.1	Bar	T6	ME	10	10																		
2014-T6 Al	4.2.1	Forging	T6	ME	11																			
2014-T6 Al	4.2.1		T6													TR	1,F1		1,F1		1,F1			
2219-T87 Al	4.2.2	Sheet	T87	ME	1,6,F1,F3	6	6						7											
2219	4.2.2	Sheet	T6	ME	2,F1		2																	
2219-T62 Al	4.2.2	Sheet	T62	ME	3	3	3						4											
2219-T81 Al	4.2.2	Sheet	T81	ME	5,F1	5	5																	
2219-T81 Al	4.2.2	Plate	T81	ME	6,16,17		6		9															
2219-T87 Al	4.2.2	Plate	T87	ME	10,11,13,14,18, 19,20,F2,F3	11,13	10,11, 13,18			12	12,15,21													
2219-T852 Al	4.2.2	Forging	T852	ME	22,24																			
2219-T81 Al	4.2.2	Extrusion	T81	ME	24	24																		
2219-T81 Al	4.2.2		T81													TR	1,F1		1,F1			MA		1
Al-Mg Alloys	4.3.0	Rod	Annealed																					
5083-H38 Al	4.3.1	Sheet	H38	ME	1		1																	
5083-H113 Al	4.3.1	Plate	H113	ME	5		5						2,8											
5083-O Al	4.3.1	Plate	O	ME	3,4,8,9,F1		3					F2		5,1										
5083-H321 Al	4.3.1	Plate	H321	ME	7		7																	
5083-O Al	4.3.1		O													TR	1,F1				1,F1			
5083-H113 Al	4.3.1		H113													TR			1,F1		1,F1			
6061-T6Al	4.4.1	Sheet	T6	ME	1,2,F1	2	1,2						3											
6061-T6 Al	4.4.1	Plate	T6	ME	4,6,F1		4		5	5														
6061-T651 Al	4.4.1	Plate	T651	ME	7		7				8													
6061-T6 Al	4.4.1	Bar	T6	ME	9,F1					10			11											
6061-T6 Al	4.4.1	Forging	T6	ME	12																			
6061-T6 Al	4.4.1		T6													TR			1,F1		1,F1			
7005-T6 Al	4.5.2	Sheet	T6	ME	1		1																	
7005-O Al	4.5.2	Plate	O	ME										2										
7005-T5351 Al	4.5.2	Extrusion	T5351	ME	3		3																	
7005-T6 Al	4.5.3	Sheet	T6	ME	1		1																	
7005-T63Al	4.5.3	Sheet	T63	ME	2		2																	
7005-W Al	4.5.3	Sheet	W	ME	3		3																	
7039-T6 Al	4.5.1	Sheet	T6	ME	1,2,F1	2	1,2						3											
7039-T81 Al	4.5.1	Sheet	T81	ME	4																			
7039-T6,T61 Al	4.5.1	Plate	T6,T61	ME	5,6,7,F1		5,6,7				5													
7039-T6 Al	4.5.1	Plate	T6	ME	9,10		9,10																	
7039-T6,T61 Al	4.5.1	Extrusion	T6,T61	ME	11,12		11,12																	
7039-T61	4.5.1		T61													TR	1,F1		1,F1		1,F1			
Copper Alloys																								
Cu, 99.95	5.1.1		Annealed													TR	1,F1	1,F2	1,F1	1,F1,F2	1,F1			
Cu, 99.95+	5.1.1	Wire	Cold drawn, annealed																			MA		1
			As formed																			MA		2
Cu, 99.95+	5.1.1	Rod	Annealed																			MA		3,4
Electrolytic Tough Pitch Cu	5.1.2	Sheet	HR + annealed	ME	1,F1																			
Ditto	5.1.2	Sheet	HR, annealed, CR	ME	2																			
"	5.1.2	Plate	HR + annealed	ME	3,F1																			
"	5.1.2	Plate	HR, annealed, CR	ME	4																			
"	5.1.2		Annealed													TR	1,F1							

TABLE 3.2. (Continued)

Material	Mat'l Code	Form[b]	Condition[c,d,e]	Mechanical Properties: Prop. Code	Ultimate Props.	Elastic Props.	NTS	Compress. CUS, CYS, E_c	Shear SUS, G	Impact Charpy V	Fracture Toughness K_{IC}, K_{IE}, J_{IC}	Fatigue da/dN	Fatigue S-N	Dynamic Moduli[b] E, G, B, ρ	Flexure FUS, FYS E_{f_1}, E_{f_2}	Thermal-Electrical Properties: Prop. Code	C Thermal Cond.	C Magneto-Thermal Cond.	E Thermal Expansion	S Specific Heat	R Electrical Resistivity	Magnetic Properties: Prop. Code	Magnetic Moment	Perm. or Suscept.
OFHC Cu	5.1.3	Sheet	Annealed	ME	1,F1																			
OFHC Cu	5.1.3	Sheet	HR + annealed	ME	2																			
OFHC Cu	5.1.3	Sheet	HR, annealed, CR	ME	3																			
OFHC Cu	5.1.3	Plate	HR + annealed	ME	4																			
OFHC Cu	5.1.3	Plate	HR, annealed, CR	ME	5																			
OFHC Cu	5.1.3	Plate	Stress relieved	ME	5		6																	
OFHC Cu	5.1.3	Wire	Annealed	ME	6,1,F1																			
OFHC Cu	5.1.3	Wire	Hard drawn	ME	7	7																		
OFHC Cu	5.1.3	Bar	Annealed	ME	5,9	9																		
OFHC Cu	5.1.3	Bar	Cold drawn	ME	10,F1		10																	
OFHC Cu	5.1.3		Annealed													TR	1,F1	1,F2	1,F1	1,F1,F2	1,F1			
OFHC Cu	5.1.3	Rod	Annealed																			MA		1
Cu, phosphorized	5.1.4	Sheet	HR, annealed	ME	1,F1																			
Cu, phosphorized	5.1.4	Sheet	HR, annealed, CR	ME	2																			
Cu, phosphorized	5.1.4	Plate	HR, annealed	ME	3																			
Cu, phosphorized	5.1.4	Plate	HR, annealed, CR	ME	4																			
Cu, phosphorized	5.1.4	Bar	Annealed	ME	5,F1	5	5		5															
Cu, phosphorized	5.1.4	Bar	Cold drawn	ME	7,F1		7																	
Cu, phosphorized	5.1.4		Annealed													TR	1,F1							
90Cu-20Zn	5.2.1		Annealed													TR	1,F1			1,F1				
70Cu-30Zn	5.2.2	Sheet	Tempered + stress relieved	ME	1	1							2											
70Cu-30Zn	5.2.2	Bar	3/4 hard	ME	3,F1					4														
70Cu-30Zn	5.2.2		Annealed													TR	1,F1							
Cu-Ni Alloys	5.3.0	Strip	Annealed																			MA		1
90Cu-10Ni	5.3.1	Bar	Annealed	ME	1,F1	1	1																	
90Cu-10Ni	5.3.1		Annealed													TR	1			1,F1	1,F1			
90Cu-10Ni	5.3.1	Rod	Homogenized																			MA		1
70Cu-30Ni	5.3.3	Bar	Annealed	ME	1	1	1			2														
Cu-Be	5.4.2	Sheet	STA	ME	1,F1																			
Cu-Be	5.4.2	Sheet	1/2 hard	ME	2	2																		
Cu-Be	5.4.2	Sheet	1/2 hard, aged	ME	3	3							4											
Cu-Be	5.4.2	Bar	STA	ME	5,F1	5																		
Cu-Be	5.4.2	Bar	ST, overaged	ME	5	5																		
Cu-Be	5.4.2	Bar	1/2 hard	ME	7,F1	7																		
Cu-Be	5.4.2	Bar	Hard drawn	ME	5																			
Cu-Be	5.4.2	Bar	1/2 hard, aged	ME	9	9																		
Cu-Be	5.4.2		Aged													TR	1,F1		1,F1		1,F1			
95Cu-5Sn	5.5.1	Bar	Cold drawn	ME	1	1	1			2														
92Cu-8Sn	5.5.2	Bar	Full hard	ME	1		1																	
92Cu-8Sn	5.5.2		Annealed													TR				1,F1				
Cu-0.2Zr	5.8.1	Bar	Annealed, cold drawn, aged	ME	1		1			2														
Cu-0.4Cr-0.4Cd	5.7.1	Extrusion	Aged	ME	1		1																	
Nickel-Base Alloys																								
K-500	6.1.1	Sheet	Aged	ME	1,2		1,2						3											
K-500	6.1.1	Bar	Aged	ME	4					5			5											
K-500	6.1.1	Rod	Aged																			MA		1
Inconel 600	6.2.1	Sheet	CR	ME	1								2											
Inconel 600	6.2.1	Bar	Cold drawn	ME	3,F1	3	3			3														
Inconel X-750	6.2.2	Sheet	Annealed + aged	ME	1,3,F1	3	1,3						2,4											
Inconel X-750	6.2.2	Plate	Annealed + aged	ME	5		5		5															
Inconel X-750	6.2.2	Plate	HIP	ME	5.1		5.1					F2												
Inconel X-750	6.2.2	Plate	HIP, STDA	ME	5.2		5.2					F2												
Inconel X-750	6.2.2	Bar	Annealed + aged	ME	7,F1					5														
Inconel X-750	6.2.2	Bar	Complex	ME	10,10.1		10.1						9											
Inconel X-750	6.2.2	Bar	ST	ME	10.3		10.3																	
Inconel X-750	6.2.2	Bar	STDA	ME	10.4		10.4					F3,F4,F5												
Inconel X-750	6.2.2	Forging	Aged	ME	11				12															
Inconel X-750	6.2.2	Forging	STDA	ME	12.1						12.2													
Inconel X-750	6.2.2		STA													TR	1,F1		1,F1	1,F1	1,F1			
Inconel X-750	6.2.2	Rod	ST																			MA	1,F1	
Inconel X-750	6.2.2	Rod	STDA																			MA	2,3,F1	
Inconel 718	6.2.3	Sheet	Annealed, aged	ME	1,2,3,4,F1	3,4	1,3,4						5,F2											
Inconel 718	6.2.3	Bar	Annealed, aged	ME	7,8,F1	5	7						9											

TABLE 3.2. (Continued)

Material	Mat'l Code	Form[b]	Condition[c,d,e]	Mechanical Properties: Prop. Code	Ultimate Prop.	Elastic Prop.	NTS	Compress. CUS, CYS, E_c	Shear SUS, G	Impact Charpy V	Fracture Toughness K_{IC}, K_{IE}, J_{IC}	Fatigue da/dN	Fatigue S-N	Dynamic Modulii[b] E, G, B, ρ	Flexure FUS, FYS E_{f_1}, E_{f_2}	Thermal-Physical Properties: Prop. Code	C Thermal Cond.	C Magneto-Thermal Cond.	E Thermal Expansion	S Specific Heat	R Electrical Resistivity	Magnetic Properties: Prop. Code	Magnetic Moment	Perm. or Suscept.
Inconel 718	6.2.3	Forging	Annealed, aged	ME	10,11,12,14, 15,F1		11,12, 14,15			13,18														
Inconel 718	6.2.2		Annealed													TR	1,F1	1,F2			1,F1			
Inconel 718	6.2.3		Aged													TR			1,F1					
Inconel 718	6.2.3	Rod	STDA																			MA	1	
Invar 36	6.3.1	Bar	Cold drawn	ME	1,F1																			
Invar 36	6.3.1	Rod	Cold drawn	ME										2										
Invar 36	6.3.1		Annealed													TR			1,F1		1,F1			
Ni-Span C	6.3.2	Sheet	CR, annealed, aged	ME	1								2											
Ni-Span C	6.3.2	Bar	Aged + tempered	ME	3																			
Ni-Span C	6.3.2		Age hardened													TR			1,F1					
INCO LEA	6.3.3	Sheet	Annealed	ME	1,3,5		5			6														
INCO LEA	6.3.3	Sheet	Age hardened	ME	2,1,7,9		2,4,7,9			6,10														
INCO LEA	6.3.3	Plate	Age hardened	ME	11		11																	
INCO LEA	6.3.3	Bar	Age hardened	ME	12		12																	
INCO LEA	6.3.3		Annealed													TR	1,F1		1F,1	1,F1	1,F1			
Alloy Steels																								
9Ni Steel	7.1.1	Sheet	Q+T	ME									0.1,0.2											
9Ni Steel	7.1.1	Sheet	2n+T	ME	1								2											
9Ni Steel	7.1.1	Plate	Q+T	ME	2.01,2.03,2.07, 2.11					2.04, 2.08, 2.12		F2												
9Ni Steel	7.1.1	Plate	2N+T	ME	2.02,2.05,2.09					2.06, 2.10												MA		1
9Ni Steel	7.1.1	Bar	2N+T	ME	3,F1																			
9Ni Steel	7.1.1		2N+T													TR	1,F1		1,F1					
18Ni(200) Marag.	7.1.2	Plate	Aged	ME	1,F1	1	1				3,4,5													
18Ni(200) Marag.	7.1.2	Plate	STA	ME	2	2																		
Stainless Steels																								
Type 201	8.1.1	Sheet	CR (1/2H)	ME	1,F1																			
Type 301	8.1.1	Sheet	CR (H)	ME	2,8		2,8																	
Type 301	8.1.1	Sheet	CR (XH)	ME	3,7,F1	3,7	3,7						4,F2											
Type 301	8.1.1	Sheet	(CR (1/4H)	ME	5																			
Type 301	8.1.1	Plate	Annealed	ME	8		8			9														
Type 301	8.1.1		Annealed													TR			1,F1					
Type 303	8.1.7	Bar	Annealed	ME	1					2														
Type 304	8.1.2	Sheet	CR (H)	ME	1,F1	1	1																	
Type 304	8.1.2	Sheet	Annealed	ME	2,F1		2																	
Type 304	8.1.2	Plate	Annealed	ME	3,F1					3.1		III												
Type 304	8.1.2	Bar	Annealed	ME	4,F1		4																	
Type 304	8.1.2		Annealed													TR	1,F1		1,F1					
Type 304	8.1.2	Rod	Annealed + WQ																			MA		1
Type 304L	8.1.3	Sheet	CR	ME	0.1		0.1																	
Type 304L	8.1.3	Sheet	Annealed	ME	1,F1		1																	
Type 304L	8.1.3	Plate	Annealed	ME						1.1														
Type 304L	8.1.3	Bar	Annealed	ME	2,F1	2							F2											
Type 304L	8.1.3	Plate	STA	ME								F3												
Type 304L	8.1.3		Annealed													TR					1,F1			
Type 304L	8.1.3	Rod	Annealed, WQ																			MA		1
Type 310	8.1.4	Sheet	CR	ME	0.1		0.1																	
Type 310	8.1.4	Sheet	Annealed	ME	1,F1		1						2											
Type 310	8.1.4	Plate	Annealed	ME	3,1,F1		3			3.2		F3,F4												
Type 310	8.1.4	Bar	Annealed	ME	4,F1	4	4						F2											
Type 310	8.1.4		Annealed													TR	1,F1	1,F1	1,F1		1,F1			
Type 310	8.1.4	Rod	Annealed, WQ																			MA		1
Type 310S	8.1.8	Forging	ST, WQ	ME	1		1					F1												
Type 310S	8.1.8	Forging	ST, FC	ME	2		2					F1												
Type 310S	8.1.8		Annealed													TR				1,F1	1,F1			
Type 310S	8.1.8	Rod	ST, WQ																			MA	1,F1	
Type 310S	8.1.8	Rod	ST, FC																			MA	2,F1	
Type 316	8.1.5	Sheet	Annealed	ME	1,F1																			
Type 316	8.1.5	Plate	Annealed	ME	2,F1		2			3		III												
Type 316	8.1.5	Bar	Annealed	ME	4,F1																			
Type 316	8.1.5		Annealed													TR	1,F1		1,F1		1,F1			
Type 316	8.1.5	Rod	Annealed, WQ																			MA		
Type 321	8.1.6	Sheet	Annealed	ME	1,F1	1	1						2											
Type 321	8.1.6	Plate	Annealed	ME	3,F1		3																	
Type 321	8.1.6	Bar	Annealed	ME	4,F1																	MA		2

TABLE 3.2. (Continued)

Material	Mat'l Code	Form[k]	Condition[c,d,o]	Mechanical Properties: Prop. Code	Ultimate Props.	Elastic Props.	NTS	Compress. CUS, CYS, E_c	Shear SUS, G	Impact Charpy V	Fracture Toughness K_{IC}, K_{IE}, J_{IC}	Fatigue da/dN	Fatigue S-N	Dynamic Moduli[b] E, G, B, ρ	Flexure FUS, FYS E_{f_1}, E_{f_2}	Thermal-Electrical Properties: Prop. Code	C Thermal Cond.	C Magneto-Thermal Cond.	E Thermal Expansion	S Specific Heat	R Electrical Resistivity	Magnetic Properties: Prop. Code	Magnetic Moment	Perm. or Suscept.
Type 321	9.1.6		Annealed													TR			1,F1		1,F1			
Type 321	9.1.6	Rod	Annealed, WQ																			MA		1
Type 321	9.1.6	Balls	Annealed, WQ																			MA		3
Type 347	9.1.9	Sheet	Annealed	ME	1,3	1							2,4,F1											
Type 347	9.1.9	Plate	HR, annealed, pickled	ME	5				9															
Type 347	9.1.9	Plate	Annealed	ME	7		7			9														
Type 347	9.1.9	Bar	Annealed	ME	9		9			10														
Type 347	9.1.9		Annealed													TR			1,F1					
A-286	9.2.1	Sheet	STA	ME	1,2,3,4,F1		1,2,3,4						5											
A-286	9.2.1	Plate	STA	ME					6			F2												
A-286	9.2.1	Bar	STA	ME	7,8,10,F1	9	7,8			9	11	F3												
A-286	9.2.1		Annealed													TR	1,F1				1,F1			
A-286	9.2.1		Age hardened													TR			1,F1					
Kromarc-58	9.2.2	Sheet	Annealed	ME	1,2,3,4,5,6, 7,F1		4,5,6,7																	
Kromarc-58	9.2.2	Plate	ST, WQ	ME	9		9					F2												
Kromarc-58	9.2.2	Plate	Cold worked	ME	9		9					F2												
Kromarc-58	9.2.2		ST, Q													TR	1,F1		1,F1	1,F1	1,F1			
Kromarc-58	9.2.2	Rod	ST, Q																			MA	1	
Kromarc-58	9.2.2	Rod	Cold worked																			MA	2	
Armco 21-6-9	9.2.3	Plate	Annealed, WQ	ME	1					2														
Armco 21-6-9	9.2.3	Sheet and Rod	Various																			MA		1
Armco 22-13-5	9.2.4	Plate	Simulated braze	ME	1						1													
Titanium Alloys																								
Ti-6Al-4V	9.1.1	Bar	Annealed	ME	1,2[g]		1																	
Ti-7Al-4V	9.1.2	Sheet	Annealed	ME	1,F1		1																	
Titanium	(h)		Annealed													TR	1,F1		1,F1	1,F1,F2	1,F1			
Ti-5Al-2.5Sn	9.2.1	Sheet	Annealed	ME	1,2,F1	1	1,2						F2											
Ti-5Al-2.5Sn	9.2.1	Bar	Annealed	ME	3,5,F1					4	5.1	F6,F7		F3,F4,F5										
Ti-5Al-2.5Sn	9.2.1	Forging	Annealed	ME	5,2																			
Ti-5Al-2.5Sn	9.2.1	Forging	As forged	ME	9,7,8,F1		9,7,8																	
Ti-5Al-2.5Sn	9.2.1		Annealed													TR			1,F1		1,F1			
Ti-5Al-2.5Sn(ELI)	9.2.2	Sheet	Annealed	ME	1,2,4,F1	1,2,4	1,2				5		3											
Ti-5Al-2.5Sn(ELI)	9.2.2	Plate	Annealed	ME	9,8,F1				7															
Ti-5Al-2.5Sn(ELI)	9.2.2	Bar	Annealed	ME	9,F1	9	9						10											
Ti-5Al-2.5Sn(ELI)	9.2.2	Forging	As forged	ME	11,12,13		11,12,13				14													
Ti-5Al-2.5Sn(ELI)	9.2.2	Extrusion	As extruded	ME	10		15																	
Ti-6Al-4V	9.3.2	Plate	Annealed	ME	1							(i)												
Ti-6Al-4V	9.3.2		Annealed													TR			1,F1		1,F1			
Ti-6Al-4V(ELI)	9.3.1	Sheet	Annealed	ME	1,2,F1	1	1,2																	
Ti-6Al-4V(ELI)	9.3.1	Plate	Annealed	ME	3						4													
Ti-6Al-4V(ELI)	9.3.1	Bar	Annealed	ME	5,FI	b				6														
Ti-6Al-4V(ELI)	9.3.1	Forging	Annealed	ME							9.1	F2												
Ti-6Al-4V(ELI)	9.3.1	Forging	As forged	ME	7,F1		7																	
Special Metals																								
Niobium	10.1.1															TR	1,F1,F2		1,F1	1,F1,F2, F3,F4	1,F1			
Nb_3Sn	10.1.2															TR	1,F1,F2							
Nb-0.2Zr	10.1.3															TR	1,F1,F2							
Nb-2Zr	10.1.3															TR	2,F3,F4							
Ti-7Nb	10.1.4	Bar	Annealed	ME	1		1																	
Ti-11Nb	10.1.4	Bar	Annealed	ME	2		2																	
Nb-Ti-Zr	10.1.4			ME	3,4																			
Nb-26Ti(+Zr)	10.1.4	Wire		ME	9																			
Ti-Nb(to 4% Nb)	10.1.4			ME	F1																			
Ti-9Nb	10.1.4															TR			1,F1					
Ti-18Nb	10.1.4															TR			2,F2					
Ti-28Nb	10.1.4															TR			3,F3					
Ti-33Nb	10.1.4															TR			4,F4					
Polymers[j]			Crystallinity, %							Izod														
PE	12.1.1	Am	–													TR			1,F1	1,F1				
PCTFE	12.1.2	xt	37.6-40.0	ME	1	1			1															
PCTFE	12.1.2	xt	52.6-55.0	ME	1	2			2															

TABLE 3.2. (Continued)

Material	Mat'l Code	Form[k]	Condition[c,d,e]	Mechanical Properties: Prop. Code	Ultimate Props.	Elastic Props.	NTS	Compress. CUS, CYS, E_c	Shear SUS, G	Impact Charpy V	Fracture Toughness K_{IC}, K_{IE}, J_{IC}	Fatigue da/dN	Fatigue S-N	Dynamic Moduli[b] E, G, B, ρ	Flexure FUS, FYS E_{f_1}, E_{f_2}	Thermal-Electrical Properties: Prop. Code	C Thermal Cond.	C Magneto-Thermal Cond.	E Thermal Expansion	S Specific Heat	R Electrical Resistivity	Magnetic Properties: Prop. Code	Magnetic Moment	Perm. or Suscept.
PCTFE	12.1.2	xt	67.6-60.0	ME						3														
PCTFE	12.1.2	xt	67.6-70.0	ME	4	4			4	5						TR								
PCTFE	12.1.2	Am													1,2									
PTFE	12.1.3	xt	47.6-50.0	ME	1	1		1	2						3,4									
PTFE	12.1.3	xt	50.1-52.5	ME	3	3			4	4														
PTFE	12.1.3	xt	55.1-57.5	ME				5																
PTFE	12.1.3	xt	57.6-60.0	ME	6	6									7,8									
PTFE	12.1.3	xt	65.1-67.5	ME	7	7			8															
PTFE	12.1.3	xt	67.6-70.0	ME	9			9																
PTFE	12.1.3	xt	70.1-72.5	ME						10														
PTFE	12.1.3	Am	–													TR				1,F1				
PMM	12.2.1	Am														TR				1,F1				
PS	12.3.1	Am														TR				1,F1				

(a) Numbers containing an "F" prefix refer to figure numbers; others refer to table numbers. Each table or figure number contains the material code followed by property code and table or figure number. The figure numbers for thermal-electrical properties contain a C (thermal or magneto-thermal conductivity), E (thermal expansion), S (specific heat), or R (electrical resistivity) following the material code.

(b) Young's shear, bulk moduli and Poisson's ratio, respectively.

(c) HR = hot rolled; CR = cold rolled.

(d) STA = solution treated and aged; STDA = solution treated + double aged; HIP = hot isostatic pressed.

(e) Q+T = quenched and tempered; 2N+T = double normalized and tempered.

(f) See Figure 8.1.4 – ME 3.

(g) See Figure 9.1.2 – ME 1.

(h) Exact compositions include both Ti-85A (9.1.1) and Ti-75A (9.1.2; data in handbook are on sequence of pages designated 9.1.2.

(i) See Figure 9.2.1 – ME 6.

(j) PCTFE = polychlorotrifluoroethylene; PTFE = polytetrafluoroethylene; PE = polyethylene; PMM = polymethylmethacrylate; PS = polystyrene; PVA = polyvinylacetate.

(k) xt = crystalline; Am = amorphous.

21<

SEMIANNUAL TECHNICAL REPORT

on

LOW-TEMPERATURE THERMAL EXPANSION AND SPECIFIC HEAT PROPERTIES OF STRUCTURAL MATERIALS

Sponsored by

ADVANCED RESEARCH PROJECTS AGENCY
ARPA Order No. 2569
Program Code 4D10
Contract No. CST-8303

Contract Monitor

CRYOGENICS DIVISION
NATIONAL BUREAU OF STANDARDS
Boulder, Colorado 80302

by

F. J. Jelinek and E. W. Collings

October 20, 1975

BATTELLE
Columbus Laboratories
505 King Avenue
Columbus, Ohio 43201

SEMIANNUAL TECHNICAL REPORT

on

LOW-TEMPERATURE THERMAL EXPANSION AND SPECIFIC HEAT PROPERTIES OF STRUCTURAL MATERIALS

Sponsored by

ADVANCED RESEARCH PROJECTS AGENCY
ARPA Order No. 2569
Program Code 4D10
Contract No. CST-8303

from

BATTELLE
Columbus Laboratories

F. J. Jelinek and E. W. Collings

October 20, 1975

FOREWORD

This research was supported by the Advanced Research Projects Agency of the Department of Defense and was monitored by the Cryogenics Division, National Bureau of Standards under Contract No. CST-8303. Dr. Richard P. Reed serves as Program Manager and Contract Monitor.

The research was carried out under ARPA Order No. 2569 and Program Code 4D10 by the Materials Technology and Metal Science Sections of BCL with F. J. Jelinek (614-424-6424, Extension 1735) and E. W. Collings (614-424-6424, Extension 1664) as Principal Investigators. Contract CST-8303, under the overall coordination of K. R. Hanby, covers both the handbook program and the property measurement program. Only the property measurement program is presented here. Overall contract funding was $100,000 with $50,000 for the laboratory study. Effective date of the contract was September 10, 1974, and the contract expiration date was September 10, 1975.

23<

DISCLAIMER

The views and conclusions contained in this document are those of the authors and should not be interpreted as necessarily representing the official policies, either expressed or implied, of the Advanced Research Projects Agency or the U.S. Government.

TECHNICAL REPORT SUMMARY

The development of superconducting electrical machinery requires the suitable engineering property characterization of all candidate materials at cryogenic temperatures. This program involves the determination of thermal expansion and specific heat for several structural and insulation materials in the cryogenic temperature region (4.2 to 300 K).

Several materials selected for this study were supplied through the cooperation of Westinghouse R&D. These materials are being utilized for superconducting generator development work at Westinghouse. In addition, data on several materials, generated at BCL but funded by other government agencies, are included in this report at the request of the sponsoring agency. The primary motive for this action is to insure inclusion of these materials in the cryogenic handbook. The materials in this category are appropriately labeled in the text of the report. The contributing agencies include ERDA-BNL, ERDA-ORNL, and NASA-LRC.

Thermal expansion measurements were performed utilizing a fused silica dilatometer with a linear differential transducer as the dilatometer head. The accuracy of the measurement is 1 percent. Specific heat at low temperatures is measured to 1 percent by adiabatic calorimetry from a method developed by Nernst. In this method, small increments of heat are supplied to a thermally insulated sample, and the accompanying temperature increase is measured.

In this reporting period, thermal expansion characteristics of 23 materials were determined in the temperature range 5 to 300 K. Low temperature specific heat data on seven materials previously measured have been reevaluated and analyzed. In addition, the specific heats of six new alloys were measured. A reprint from the ICMC conference entitled "Magnetic and Thermal Properties of Stainless Steel and Inconel at Cryogenic Temperatures" is included as an Appendix to this report.

25<

EXPERIMENTAL RESULTS

PART I. SPECIFIC HEAT

Introduction

Specific heat was measured in the manner described in earlier reports in the "helium-temperature" range and again near 80 K and room temperature. Since the last report, considerable time and effort has been spent in improving the experimental technique and checking the calibration of the low-temperature equipment. The specific heats of seven samples, already measured during previous reporting periods, were remeasured using the improved techniques and over wider temperature ranges than before. The seven "old" samples for which entirely new low-temperature data are available are:

Inco Low-Expansion Alloy
Stainless Steel AISI 310S STQ
Stainless Steel AISI 310S STFC
Inconel X750(MP-1)ST
Inconel X750(MP-1)STDA
Inconel X750(MP-2)STDA
Inconel X750(MP-3)STDA

New techniques of data analysis were also employed, and the applicability of multiple linear regression fitting of the specific-heat data was fully explored. All this new information is set forth in the following tables, figures, and narrative. In addition, the specific heats of six new alloys were measured over the intermediate temperature range (80 K and room temperature). These materials are:

Inconel X750 HIP
Inconel X750 HIP STDA
Inconel X706 VIM-VAR ST
Inconel X706 VIM-VAR STDA
Inconel X706 VIM-EFM ST
Inconel X706 VIM-EFM STDA

26<

In addition, five of these alloys have been measured in the low-temperature (3 - 20 K) regime.

A reprint of the paper entitled 'Magnetic and Thermal Properties of Stainless Steel and Inconel at Cryogenic Temperatures" is included in this report as Appendix A.

Intermediate Temperature Specific Heat of Stainless Steels and Inconels

Presented in earlier reports are intermediate temperature specific heat data for the alloys:

Stainless Steel 310S STQ
Stainless Steel 310S STFC
Inconel X750(MP-1)ST
Inconel X750(MP-1)STDA
Inconel X750(MP-2)STDA
Inconel X750(MP-3)STDA

The data for temperatures near 80 K are presented in Table 1 while the room-temperature results are given in Table 2. These data have subsequently been reanalyzed in order to yield specific heat values adjusted to temperatures of 80.0 K and 300.0 K, repsectively, and standard error assignments have been made. The manner in which the analyses were carried out is discussed below.

80 K Data

Straight lines were least-squares fitted to each of the three sets of data points. These lines were then numerically extrapolated (or interpolated as the case may be) to 80.0 K and the corresponding specific heat values computed. The scatter of the specific heat values about the fitted line (temperatures being assumed free from error) was used to determine standard error. The results of this procedure are presented in Table 3.

TABLE 1. MEASURED SPECIFIC HEATS OF STAINLESS STEELS AND INCONELS AT TEMPERATURES NEAR 80 K

Sample Name	Temperature (K)	Specific Heat (J/kg-deg)	Temperature (K)	Specific Heat (J/kg-deg)	Temperature (K)	Specific Heat (J/kg-deg)
Stainless Steel 310S STQ	78.46	198.1	79.88	204.0	81.36	207.0
Stainless Steel 310S STFC	81.93	209.4	83.16	212.9	84.16	216.8
Inconel X750 (MP-1) ST	79.36	180.4	80.48	183.4	81.46	186.4
Inconel X750 (MP-1) STDA	80.66	179.9	81.46	183.4	82.18	197.4
Inconel X750 (MP-2) STDA	83.06	200.2	84.01	198.5	85.16	203.6
Inconel X750 (MP-3) STDA	79.61	179.6	80.96	181.2	81.74	183.5

TABLE 2. MEASURED SPECIFIC HEATS OF STAINLESS STEELS AND INCONELS AT TEMPERATURES NEAR 300 K

Sample Name	Temperature (K)	Specific Heat (J/kg-deg)	Temperature (K)	Specific Heat (J/kg-deg)	Temperature (K)	Specific Heat (J/kg-deg)
Stainless Steel 310S STQ	298.21	486.1	299.39	482.6	300.38	486.7
Stainless Steel 310S STFC	297.71	485.6	298.59	482.3	299.39	487.5
Inconel X750 (MP-1) ST	296.72	458.6	297.66	457.5	298.46	461.4
Inconel X750 (MP-1) STDA	296.41	444.5	297.11	446.0	298.46	448.2
Inconel X750 (MP-2) STDA	298.11	455.4	298.71	469.6	298.76	453.8
Inconel X750 (MP-3) STDA	297.01	436.0	297.66	445.4	298.41	452.4

TABLE 3. SPECIFIC HEATS OF STAINLESS STEELS AND INCONELS ADJUSTED BY LINEAR FITTING TO TEMPERATURES OF 80.0 AND 300.0 K

Sample Name	Specific Heat (J/kg-deg) 80.0 K	300.0 K
Stainless Steel 310S STQ	203 ± 8	485 ± 2
Stainless Steel 310S STFC	203 ± 3	485 ± 2
Inconel X750 (MP-1) ST	182 ± 1	460 ± 2
Inconel X750 (MP-1) STDA	183 ± 6	447 ± 2
Inconel X750 (MP-2) STDA	194 ± 2	460 ± 7
Inconel X750 (MP-3) STDA	180 ± 1	445 ± 7

30<

Room-Temperature Data

Straight lines were fitted to each set of three data points as before. In so doing it was found that the slopes of the lines were too widely scattered to be useful. Accordingly, an "average slope" was determined by calling on the Debye function at temperatures of 280 and 300 K using low-temperature-measured values of θ_D. By putting lines of this slope through the experimental points, an average extrapolated (or interpolated) 300 K specific heat value was computed, and an associated standard error derived. The results of this procedure are also summarized in Table 3.

Intermediate Temperature Specific Heat of Further Inconel Samples

During the current reporting period the intermediate-temperature specific heats of the following new Westinghouse-supplied alloys have been measured.

Inconel X750 HIP
Inconel X750 HIP STDA
Inconel X706 VIM-VAR ST
Inconel X706 VIM-VAR STDA
Inconel X706 VIM-EFM ST
Inconel X706 VIM-EFM STDA

The results of this work are presented in Tables 4 and 5. Reductions of these data to specific heats at temperatures of 80.0 and 300.0 K were carried out as before.

80 K Data

Straight lines were least-squares fitted to the triplets of data points for each alloy. It was then noted that there were no

TABLE 4. MEASURED SPECIFIC HEATS OF SIX INCONEL SAMPLES AT TEMPERATURES NEAR 80 K

Sample Name	Temperature (K)	Specific Heat (J/kg-deg)	Temperature (K)	Specific Heat (J/kg-deg)	Temperature (K)	Specific Heat (J/kg-deg)
Inconel X750 HIP	86.11	208.8	86.86	204.1	87.61	207.6
Inconel X750 HIP STDA	85.46	199.9	86.51	202.8	87.51	206.8
Inconel X706 VIM-VAR ST	88.26	226.9	89.01	229.6	89.76	230.1
Inconel X706 VIM-VAR STDA	86.66	216.8	87.56	221.2	88.36	222.7
Inconel X706 VIM-EFM ST	78.16	192.9	79.61	198.2	80.76	201.0
Inconel X706 VIM-EFM STDA	78.41	188.8	79.46	193.3	80.36	196.8

TABLE 5. MEASURED SPECIFIC HEATS OF SIX INCONEL SAMPLES AT TEMPERATURES NEAR 300 K

Sample Name	Temperature (K)	Specific Heat (J/kg-deg)	Temperature (K)	Specific Heat (J/kg-deg)	Temperature (K)	Specific Heat (J/kg-deg)
Inconel X750 HIP	294.56	446.6	295.36	449.9	296.11	450.8
Inconel X750 HIP STDA	294.91	440.1	296.51	444.8	297.96	443.9
Inconel X706 VIM-VAR ST	297.86	454.7	298.16	468.2	299.61	470.6
Inconel X706 VIM-VAR STDA	296.51	480.7	297.46	479.8	298.26	463.5
Inconel X706 VIM-EFM ST	297.16	467.6	297.91	488.3	298.56	461.3
Inconel X706 VIM-EFM STDA	298.86	456.7	299.51	445.5	300.01	464.5

significant differences between the slopes of these lines. Consequently, an average slope was taken and straight lines of this slope were numerically constructed through each data point for each alloy. This operation yielded a set of intercepts with standard deviations. The intercepts and slopes were then employed to compute heats at exactly 80.0 K for each alloy and the standard deviations were applied to this value. The results of this procedure are presented in Table 6.

Room-Temperature Data

The room-temperature data were handled in exactly the manner described above, during which it was ascertained that the average C-versus-T slope was zero over the temperature range considered. The results of the fitting, averaging, extrapolation, and error assessment analysis of the room-temperature data are also presented in Table 6.

Low-Temperature Specific Heat of Pure Copper

As a check on the accuracy of the low-temperature specific heat measurement, the specific heat of a sample of high-purity, zone-refined Cu was measured and compared with literature data. As will be demonstrated below, very satisfactory agreement was obtained.

Survey of the Literature

Table 7 summarizes the results of the more recent (since 1955) evaluations of the specific heat of copper. All the authors except one fitted their data to the linear relationship

$$C/T = \gamma + \beta T^2$$

where γ is the electronic, and β is the lattice, specific heat coefficient.

The low-temperature Debye temperature is calculated from the formula

$$\theta_D = (1.944 \times 10^6/\beta M)^{1/3} ,$$

where M is the molar weight, and β is expressed in J/kg-deg^4 .

TABLE 6. SPECIFIC HEATS OF SIX INCONEL SAMPLES CORRECTED BY LINEAR FITTING TO TEMPERATURES OF 80.0 AND 300.0 K

Sample Name	Specific Heat (J/kg-deg)*	
	80.0 K	300.0 K
Inconel X750 HIP	184.6 ± 3.1	449 ± 2
Inconel X750 HIP STDA	182.1 ± 0.3	443 ± 2
Inconel X706 VIM-VAR ST	199.6 ± 0.9	465 ± 7
Inconel X706 VIM-VAR STDA	195.8 ± 0.6	475 ± 8
Inconel X706 VIM-EFM ST	199.0 ± 0.4	472 ± 12
Inconel X706 VIM-EFM STDA	194.9 ± 0.7	456 ± 8

* The standard errors are indicated.

35<

TABLE 7. LOW-TEMPERATURE SPECIFIC HEAT OF PURE COPPER--SURVEY OF THE LITERATURE

Temp. Range (K)	Type of Fit	γ (mJ/mole-deg^2)	Θ_D (K)	Reference
1-5	Linear	0.688 ± 0.002	343.8 ± 0.5	1
1.5-4.2	Linear	0.686 ± 0.005	345.1 ± 0.9	2
1.8-4.2	Linear	0.691 ± 0.006	347 ± 2	3
0.37-4.2	Linear	0.69	342	4
1.1-4.5	Linear	0.697 ± 0.007 0.696 ± 0.007	345.1 ± 1.4 342.3 ± 1.4	5
0.4-30	Polynomial	0.6910 ± 0.0007	344.4 ± 0.4	6

References:

1. W. S. Corak, et al., Phys. Rev., 98 1699 (1955).
2. J. A. Rayne, Aust. J. Phys., 9 189 (1956).
3. M. Griffel, R. W. West, and J. F. Smith, J. Chem. Phys., 27 1267 (1957).
4. N. E. Phillips, Proc. LT5 (Univ. of Wisconsin Press, Madison, Wisc., 1958) p. 414.
5. G. D. Kneip, J. O. Betterton, and J. O. Scarbrough, Phys. Rev., 130 1687 (1963)
6. D. L. Martin, et al., Rev. Sci. Inst., 44 675 (1973).

One of the authors, Martin, fitted his specific heat data to the polynomial

$$C = \sum_{n=0}^{n=6} \alpha_n T^{2n+1} ,$$

in which $\gamma \equiv \alpha_0$, and $\beta \equiv \alpha_1$. In such a polynominal expansion, θ_D is still derived from β (or α_1) using the expression given above.

Low-Temperature Specific Heat Measurement

A specimem of high-purity, zone-refined copper obtained from Materials Research Corporation was measured in a calibration check of the apparatus. The supplier's analytical report for this material is reproduced in Table 8.

Specific heat was measured in the temperature range 3 - 28 K. Prior to analyzing the data, the calorimeter heater resistance-temperature characteristic was remeasured in the temperature range 3 - 20 K, and the specific heat of the empty calorimeter was redetermined, yielding a new so-called "addenda" correction. With the newly-acquired information, the high-purity copper data was analyzed over the temperature range 3 - 21 K,

$$C = \gamma T + \beta T^3 + \alpha_5 T^5 + \alpha_7 T^7$$

Our conclusions, expressed in terms of the principal parameters γ and θ_D (from β), were found to be in excellent agreement with literature data, as testified by the listing in Table 9 in which a comparison is made between the present results and those of Martin, et al (see Table 7, footnote).

We then proceeded to apply the new heater and addenda calibrations to the previously-acquired data for stainless steels and Inconels. The results of this, and those of the subsequent statistical analysis, are presented in the next section.

TABLE 8. MATERIALS RESEARCH CORPORATION (MRC) ZONE-REFINED COPPER--SUPPLIER'S ANALYTICAL REPORT

Impurity Element Symbol	Parts per 10^6 (ppm) by weight	Impurity Element Symbol	Parts per 10^6 (ppm) by weight	Impurity Element Symbol	Parts per 10^6 (ppm) by weight
O	< 5.0	Si	< 2.0	Zr	< 4.0
H	0.6	S	< 0.5	Cb	< 10.0
N	< 1.0	V	< 0.2	Mo	< 2.0
C	5.0	Mn	< 0.3	Ru	< 2.0
Al	1.0	Co	< 0.3	Rh	< 0.2
Ca	2.0	Ni	< 0.4	Pd	< 1.0
Cr	2.0	Ga	< 2.0	Ag	< 0.4
Fe	3.0	Ge	< 1.0	Cd	< 1.0
K	2.0	As	< 0.3	In	< 2.0
Na	4.0	Br	< 2.0	Sn	< 0.6
Pb	1.0	Rb	< 0.2	Sb	< 0.4
Zn	< 3.0	Sr	< 0.2	Te	< 3.0
Mg	< 4.0	Y	< 0.4	Ta	< 10.0
				Au	< 1.0

TABLE 9. LOW-TEMPERATURE SPECIFIC HEAT OF MRC ZONE-REFINED COPPER--COMPARISON WITH LITERATURE DATA

	Martin, et al.†**	Present Results**
Electronic Specific Heat Coefficient, γ (10^{-1} J/kg-deg^2)	0.10875 ± 0.00011	0.110 ± 0.003
Lattice Specific Heat Coefficient, β (10^{-4} J/kg-deg^4)	7.492 ± 0.023	7.44 ± 0.11
Debye Temperature, θ_D (K)	344.4 ± 0.4	345 ± 2

† D. L. Martin, et al., Rev. Sci. Inst. 44 675 (1973)

* Error limits are 95% confidence limits

** Standard errors indicated

Low-Temperature Specific Heats of Stainless Steels and Inconels-- A Re-Analysis of Earlier Data

As discussed in our contribution to the Kingston Conference (preprint attached), the low-temperature specific heats of stainless steels and Inconels yielded 1/T-type rather than linear behavior when plotted in the format C/T versus T^2. This effect is due to the existence of a temperature-independent specific heat component of magnetic origin. In treating the specific heat data we took into account not only the temperature, independent term, but also the possible existence of higher order odd-power terms in T. In particular, we examined, in turn, fits to the following equations

$$C = A + \gamma T + \beta T^3 + \alpha_5 T^5 + \alpha_7 T^7 \quad ,$$

$$C = A + \gamma T + \beta T^3 + \alpha_5 T^5 \quad ,$$

$$C = A + \gamma T + \beta T^3 \quad ,$$

over the temperature range ~ 3 - 20 K.

When fitting data to a polynomial, although the addition of more and more terms may significantly improve the goodness of fit, because of competition between the terms, the physical significance of the individual coefficients tend to become obscured. For example, four-term (to T^5) and five-term (to T^7) fits to the data for stainless steel 310S yielded negative values of β, and consequently, θ_D. Such results are physically meaningless and must be regarded with extreme caution. Since reasonably good fits to the simple three-term expression could be obtained in all cases, once outlying points had been rejected, we applied the three-term fitting procedure to all of the alloys.

The results of multiple linear regression analysis of the specific heat data for two stainless steels and four Inconel samples, in the form of a set of A, γ, β coefficient and the parameter θ_D, are presented in Table 10. In each case some 70 or 80 data points were fitted to the equation

$$C = A + \gamma T + \beta T^3 \quad .$$

Normally, a $1/C^2$ weighting factor should be applied in order to give proper consideration to the small-C (low-temperature) points. But since the point density, itself, went roughly as 1/C, a point-weighting factor of 1/C was employed.

Using the coefficients listed in Table 10, it is then possible to calculate specific heats corresponding to any temperature within the temperature range 3 - 20 K. This has been done with regard to the temperatures 4, 5, 10, 15, and 20 K, and the results are given in Table 11.

Low-Temperature Specific Heats of a Set of Five Inconel Alloys

During the current reporting period the low-temperature specific heats of five new alloys were measured. As before, these alloys were obtained through the courtesy of Dr. J. M. Wells of the Westinghouse Electric Corporation. Typically, about 100 sets of data were taken within a temperature range of 1.5 - 27 K. Curve fitting to the formula

$$C = A + \gamma T + \beta T^3 \quad ,$$

using a 1/C weighting factor, and restricting the upper temperature of analysis to 21 K was carried out as before. The sets of coefficients so obtained are listed as Table 12. Debye temperature have not yet been computed, since we are not as yet in possession of chemical analyses from which to calculate the molar weights. Finally, we list in Table 13, a set of fitted specific heat values for the temperatures 4, 5, 10, 15, and 20 K.

TABLE 10. LOW-TEMPERATURE SPECIFIC HEAT PARAMETERS FOR STAINLESS STEELS AND INCONELS

Parameter	Alloy and Parameters Value*					
	310S-STQ	310S-STFC	X750(MP-1)ST	X750(MP-1)STDA	X750(MP-2)STDA	X750(MP-3)STDA
A, 10^{-1} J/kg-deg	3.34 ± 0.02	3.03 ± 0.14	2.11 ± 0.06	1.92 ± 0.38	1.49 ± 0.01	1.86 ± 0.09
γ, 10^{-1} J/kg-deg^2	4.60 ± 0.04	4.92 ± 0.03	2.31 ± 0.02	2.32 ± 0.02	2.26 ± 0.02	2.24 ± 0.02
β, 10^{-4} J/kg-deg^4	2.68 ± 0.13	2.92 ± 0.12	3.10 ± 0.05	3.19 ± 0.06	2.83 ± 0.05	2.88 ± 0.07
θ_D, K	508 ± 8	494 ± 7	479 ± 3	474 ± 3	494 ± 3	492 ± 4

* The standard errors are indicated.

TABLE 11. LOW-TEMPERATURE SPECIFIC HEATS (FITTED VALUES) FOR STAINLESS STEELS AND INCONELS AT SPECIFIED TEMPERATURES

Temperature, (K)	Alloy and Specific Heat, C (J/kg-deg)*					
	310S-STQ	310S-STFC	X750(MP-1)ST	X750(MP-1)STDA	X750(MP-2)STDA	X750(MP-3)STDA
4.0	2.19 ± 0.02	2.29 ± 0.02	1.15 ± 0.02	1.10 ± 0.05	1.07 ± 0.01	1.10 ± 0.02
5.0	2.67 ± 0.02	2.80 ± 0.03	1.40 ± 0.02	1.35 ± 0.05	1.31 ± 0.02	1.34 ± 0.02
10.0	5.20 ± 0.06	5.52 ± 0.05	2.83 ± 0.03	2.74 ± 0.07	2.69 ± 0.03	2.71 ± 0.04
15.0	8.14 ± 0.10	8.67 ± 0.09	4.72 ± 0.05	4.61 ± 0.09	4.49 ± 0.05	4.52 ± 0.06
20.0	11.68 ± 0.18	12.48 ± 0.17	7.31 ± 0.09	7.20 ± 0.13	6.93 ± 0.08	6.97 ± 0.11

* The standard errors are indicated.

TABLE 12. LOW-TEMPERATURE SPECIFIC HEAT PARAMETERS FOR FIVE INCONEL ALLOYS

Parameter	Alloy and Parameter Value*				
	Inconel X750 (HIP) as-HIP	Inconel X750 (HIP) STDA	Inconel X706 (VIM-VAR) ST	Inconel X706 (VIM-VAR)STDA	Inconel X706 (VIM-EFM) ST
A, 10^{-1}J/kg-deg	1.88 ± 0.08	1.63 ± 0.08	2.33 ± 0.07	2.35 ± 0.08	2.21 ± 0.06
γ, 10^{-1}J/kg-deg^2	2.36 ± 0.02	2.30 ± 0.02	3.08 ± 0.02	3.13 ± 0.02	3.10 ± 0.02
β, 10^{-4}J/kg-deg^4	3.16 ± 0.07	3.17 ± 0.06	3.99 ± 0.06	3.45 ± 0.09	4.10 ± 0.05

* The standard errors are indicated.

TABLE 13. LOW-TEMPERATURE SPECIFIC HEATS (FITTED VALUES) FOR FIVE INCONEL ALLOYS AT SPECIFIC TEMPERATURES

Temperature (K)	Alloy and Specific Heat, C (J/kg-deg)*				
	Inconel X750 (HIP) as-HIP	Inconel X750 (HIP) STDA	Inconel X706 (VIM-VAR) ST	Inconel X706 (VIM-VAR)STDA	Inconel X706 (VIM-EFM) ST
4.0	1.15 ± 0.02	1.10 ± 0.02	1.49 ± 0.02	1.51 ± 0.02	1.49 ± 0.01
5.0	1.41 ± 0.02	1.35 ± 0.02	1.82 ± 0.02	1.84 ± 0.02	1.82 ± 0.02
10.0	2.86 ± 0.04	2.78 ± 0.03	3.71 ± 0.04	3.71 ± 0.04	3.72 ± 0.03
15.0	4.80 ± 0.06	4.68 ± 0.06	6.20 ± 0.06	6.09 ± 0.07	6.22 ± 0.06
20.0	7.44 ± 0.10	7.30 ± 0.10	9.59 ± 0.09	9.26 ± 0.12	9.63 ± 0.09

* The standard errors are indicated.

PART II. THERMAL EXPANSION

Introduction

Low-temperature thermal expansion results are reported for 23 materials in the temperature range 5 to 300 K. The technique used to perform the measurements was a fused silica dilatometer which has been previously described.

In addition to the nine materials furnished by Westinghouse for this study, we have included alloy materials furnished by ERDA-ORNL and NASA-LRC, as well as polymeric film wraps, for electrical and thermal insulation, furnished by ERDA-BNL. The latter was the subject of an ICMC presentation during the summer of 1975.

Table 14 lists the materials in their order of appearance in this report as well as the condition under which they were measured.

Data Presentation

The results reported in this work are shown as percent contraction versus temperature (K) with all data normalized at the ice point (273 K).

The data are reported in tabular (Tables 15 throu 31) and graphic (Figures 1 through 23) form.

TABLE 14. LIST OF MATERIALS FOR WHICH THERMAL EXPANSION DATA WAS GENERATED FOR INCLUSION IN HANDBOOK

Material	Condition	Program Source
Inconel 706	VIM-VAR-ST	NBS/ARPA
Inconel 706	VIM-VAR-STDA	NBS/ARPA
Inconel 706	VIM-EFM-STDA	NBS/ARPA
Inconel 706	VIM-EFM-ST	NBS/ARPA
Inconel X750	HIP-STDA	NBS/ARPA
Inconel X750	As Hipped	NBS/ARPA
PD-135	(Cd-Cr-Cu) Alloy	NBS/ARPA
Inconel 718	VIM-VAR-ST	NBS/ARPA
Inconel 718	VIM-VAR-STDA	NBS/ARPA
Nb-45Ti	Annealed	ERDA/ORNL
Nb-48Ti	Annealed	ERDA/ORNL
MCA 233-1	Multifilament NbTi in Cu ratio Cu/NbTi = 4	ERDA/ORNL
Incoloy 903	Annealed	NASA/LRC
Makrofol KG Polycarbonate	2.4 mil film	ERDA/BNL
Mylar WC Polyester	3.0 mil film	ERDA/BNL
Valeron Polyethylene	4.0 mil oriented high-density film	ERDA/BNL
LD #400 Polyethylene	4.0 mil low-density film	ERDA/BNL
HDPE Polyethylene	0.75 mil high-density film	ERDA/BNL
Cryovac Polyethylene	1.5 mil oriented high-density film	ERDA/BNL
Rilsan F Polyamide	1.5 mil film	ERDA/BNL
Kapton H Polyimide	5.0 mil film	ERDA/BNL
Bicor 400-S Polypropylene	1.25 mil oriented film	ERDA/BNL
Rowland Polysulfone	5.0 mil film	ERDA/BNL

ST - Solution Treated
STDA - Solution Treated, Double Aged
VIM - Vacuum Induction Melted
VAR - Vacuum Air Remelted
HIP - Hot Isotatic Pressing
EFM - Electric Furnace Melted

47<

TABLE 15. THERMAL EXPANSION BEHAVIOR OF INCONEL 706

T(K)	VIM-VAR-ST $-\Delta L/L_o$, percent	VIM-VAR-STDA $-\Delta L/L_o$, percent	VIM-EFM-ST $-\Delta L/L_o$, percent	VIM-EFM-STDA $-\Delta L/L_o$, percent
300	-0.034	-0.037	-0.035	-0.041
290	-0.021	-0.023	-0.022	-0.026
280	-0.009	-0.009	-0.009	-0.010
273	0	0	0	0
270	0.004	0.004	0.004	0.004
260	0.016	0.018	0.018	0.018
250	0.027	0.031	0.032	0.032
240	0.038	0.044	0.046	0.045
230	0.050	0.057	0.058	0.059
220	0.065	0.070	0.072	0.072
210	0.079	0.081	0.085	0.086
200	0.090	0.094	0.097	0.099
190	0.101	0.106	0.107	0.109
180	0.112	0.118	0.119	0.121
170	0.122	0.129	0.130	0.132
160	0.133	0.140	0.141	0.143
150	0.144	0.150	0.151	0.153
140	0.155	0.160	0.161	0.164
130	0.164	0.169	0.170	0.173
120	0.172	0.178	0.178	0.181
110	0.180	0.186	0.186	0.189
100	0.187	0.193	0.193	0.196
90	0.192	0.199	0.199	0.203
80	0.197	0.204	0.205	0.208
77	0.197	---	---	0.210
68	0.205	0.211	0.210	0.213
60	0.210	0.213	0.213	0.218
51	0.213	0.218	0.218	0.221
42	0.217	0.221	0.222	0.225
28	0.221	0.224	0.224	0.228
19	0.222	0.225	0.226	0.229
8	0.223	0.227	0.228	0.230

TABLE 16. THERMAL EXPANSION BEHAVIOR OF INCONEL X750 (HIP)

T(K)	As HIPPED $-\Delta L/L_o$, percent	HIP/STDA $-\Delta L/L_o$, percent
300	-0.033	-0.034
290	-0.020	-0.023
280	-0.008	-0.009
273	0	0
270	0.003	0.004
260	0.016	0.016
250	0.026	0.029
240	0.038	0.040
230	0.051	0.052
220	0.062	0.065
210	0.071	0.076
200	0.081	0.087
190	0.092	0.098
180	0.103	0.110
170	0.113	0.122
160	0.123	0.133
150	0.133	0.143
140	0.143	0.153
130	0.153	0.162
120	0.163	0.171
110	0.171	0.179
100	0.177	0.186
90	0.182	0.193
80	0.187	0.198
77	0.187	0.198
67	0.189	0.204
58	0.192	0.209
49	0.198	0.212
40	0.201	0.216
30	0.203	0.219
20	0.204	---
12	---	0.221
10	0.206	---
8	---	0.222
5	0.207	---

49<

TABLE 17. THERMAL EXPANSION BEHAVIOR OF PD-135 (Cd-Cr-Cu) ALLOY. MATERIAL EXTRUDED AND PRECIPITATION HEAT TREATED

T (K)	$-\Delta L/L_o$ (percent)
300	-0.043
290	-0.024
280	-0.011
273	0
270	0.005
260	0.021
250	0.036
240	0.052
230	0.067
220	0.083
210	0.098
200	0.113
190	0.127
180	0.142
170	0.157
160	0.172
150	0.186
140	0.200
130	0.213
120	0.226
110	0.238
100	0.249
90	0.261
80	0.270
77	0.272

50<

TABLE 18. THERMAL EXPANSION BEHAVIOR OF INCONEL 718

T(K)	VIM-VAR-ST $-\Delta L/L_o$, percent	VIM-VAR-STDA $-\Delta L/L_o$, percent
300	-0.039	-0.027
290	-0.025	-0.018
280	-0.011	-0.008
273	0	0
270	0.005	0.004
260	0.022	0.016
250	0.033	0.027
240	0.042	0.040
230	0.053	0.052
220	0.066	0.064
210	0.090	0.076
200	0.098	0.087
190	0.105	0.098
180	0.114	0.109
170	0.123	0.120
160	0.132	0.131
150	0.142	0.141
140	0.153	0.151
130	0.163	0.161
120	0.173	0.170
110	0.181	0.178
100	0.190	0.186
90	0.197	0.192
80	0.204	0.196
77	0.206	0.196
68	0.211	0.204
60	0.215	0.209
50	0.221	0.212
40	0.226	0.218
30	0.230	0.220
20	0.233	0.221
10	---	0.222
8	0.237	---

TABLE 19. THERMAL EXPANSION BEHAVIOR OF Nb-45Ti AND Nb-48Ti ALLOYS

T(K)	Nb-45Ti $-\Delta L/L_o$, percent	Nb-48Ti $-\Delta L/L_o$, percent
300	-0.026	-0.025
290	-0.017	-0.016
280	-0.007	-0.006
273	0	0
260	0.011	0.012
250	0.018	0.020
240	0.026	0.029
230	0.036	0.037
220	0.044	0.046
210	0.052	0.054
200	0.059	0.063
190	0.069	0.072
180	0.074	0.080
170	0.082	0.088
160	0.090	0.095
150	0.097	0.103
140	0.105	0.110
130	0.112	0.117
120	0.120	0.125
110	0.128	0.132
100	0.137	0.140
90	0.143	0.146
80	0.148	0.151
77	0.151	0.153
70	0.154	0.157
60	0.159	0.162
50	0.163	0.163
40	0.165	0.168
30	0.167	0.170
20	0.168	0.171
10	0.169	0.172
4	0.169	0.174

TABLE 20. THERMAL EXPANSION BEHAVIOR OF MULTIFILAMENT NbTi IN Cu (MCA 4:1) Cu TO NbTi RATIO = 4

T(K)	MCA 4:1 233-1 $-\Delta L/L_o$, percent
300	-0.040
290	-0.025
280	-0.010
273	0
260	0.018
250	0.031
240	0.043
230	0.054
220	0.067
210	0.080
200	0.093
190	0.103
180	0.114
170	0.126
160	0.138
150	0.148
140	0.157
130	0.167
120	0.176
110	0.184
100	0.192
90	0.199
80	0.206
77	0.210
70	0.212
60	0.218
50	0.220
40	0.223
30	0.225
20	0.226
10	0.227
4	0.231

TABLE 21. THERMAL EXPANSION BEHAVIOR OF INCOLOY 903 ALLOY

T(K)	Incoloy 903 $-\Delta L/L_o$, percent
300	-0.022
290	-0.013
280	-0.006
273	0
260	0.010
250	0.019
240	0.027
230	0.036
220	0.043
210	0.052
200	0.059
190	0.068
180	0.076
170	0.085
160	0.092
150	0.100
140	0.108
130	0.115
120	0.122
110	0.129
100	0.135
90	0.142
80	0.146
77	0.146
65	0 152
55	0.157
35	0.163
20	0.168

54<

TABLE 22. THERMAL EXPANSION BEHAVIOR OF MAKROFOL KG POLYCARBONATE IN THE LONGITUDINAL AND TRANSVERSE DIRECTION

Longitudinal		Transverse	
T(K)	$-\Delta L/L_o$, percent	T(K)	$-\Delta L/L_o$, percent
300	-0.044	300	-0.054
290	-0.033	273	0
280	-0.013	250	0.046
273	0	200	0.152
260	0.029	150	0.250
250	0.052	100	0.343
240	0.075	77	0.371
230	0.096	50	0.394
220	0.116	30	0.408
210	0.137	20	0.415
200	0.158	10	0.417
190	0.177	5	0.417
180	0.199		
170	0.218		
160	0.237		
150	0.256		
140	0.275		
130	0.292		
120	0.309		
110	0.327		
100	0.349		
90	0.373		
80	0.377		
77	0.377		
73	0.386		
60	0.397		
52	0.405		
44	0.412		
33	0.419		
23	0.425		
12	0.428		
5	0.430		

TABLE 23. THERMAL EXPANSION BEHAVIOR OF MYLAR WC POLYESTER IN THE LONGITUDINAL AND TRANSVERSE DIRECTION

Longitudinal		Transverse	
T(K)	$-\Delta L/L_o$, percent	T(K)	$-\Delta L/L_o$, percent
300	-0.044	300	-0.059
290	-0.027	273	0
280	-0.011	250	0.050
273	0	200	0.151
260	0.021	150	0.261
250	0.043	100	0.352
240	0.067	77	0.375
230	0.090	50	0.396
220	0.113	30	0.404
210	0.136	10	0.411
200	0.159	5	0.412
190	0.183		
180	0.206		
170	0.228		
160	0.247		
150	0.267		
140	0.287		
130	0.307		
120	0.325		
110	0.345		
100	0.362		
90	0.379		
80	0.394		
70	0.405		
60	0.414		
50	0.420		
40	0.426		
30	0.430		
20	0.432		
10	0.434		
5	0.435		

TABLE 24. THERMAL EXPANSION BEHAVIOR OF VALERON LAMINATED POLYETHYLENE IN THE LONGITUDINAL AND TRANSVERSE DIRECTION

Longitudinal		Transverse	
T(K)	$-\Delta L/L_o$, percent	T(K)	$-\Delta L/L_o$, percent
300	-0.269	300	-0.174
290	-0.164	290	-0.118
280	-0.068	280	-0.050
273	0	273	0
260	o.117	260	0.089
250	0.202	250	0.149
240	0.286	240	0.214
230	0.366	230	0.260
220	0.447	220	0.323
210	0.528	210	0.385
200	0.622	200	0.444
190	0.700	190	0.503
180	0.770	180	0.564
170	0.836	170	0.620
160	0.907	160	0.674
150	0.979	150	0.724
140	1.035	140	0.770
130	1.088	130	0.796
120	1.137	120	0.836
110	1.184	110	0.871
100	1.227	100	0.901
90	1.292	90	0.926
80	1.305	80	0.941
77	1.315	70	0.971
70	1.334	60	0.988
60	1.357	50	1.012
50	1.383	40	1.017
40	1.401	30	1.036
30	1.418	20	1.045
20	1.428	10	1.049
10	1.431	5	1.051
5	1.437		

TABLE 25. THERMAL EXPANSION BEHAVIOR OF LD #400 LOW DENSITY POLYETHYLENE IN THE LONGITUDINAL AND TRANSVERSE DIRECTION

Longitudinal		Transverse	
T(K)	$-\Delta L/L_o$, percent	T(K)	$-\Delta L/L_o$, percent
300	-0.502	300	-0.466
290	-0.301	280	-0.126
280	-0.127	273	0
273	0	250	0.412
260	0.228	230	0.729
250	0.411	200	1.174
240	0.578	180	1.419
230	0.733	150	1.698
220	0.898	130	1.874
210	1.035	100	2.034
200	1.180	77	2.144
190	1.293	50	2.209
180	1.426	25	2.217
170	1.528	10	2.224
160	1.623	5	2.224
150	1.713		
140	1.796		
130	1.869		
120	1.937		
110	2.000		
100	2.050		
90	2.118		
80	2.148		
77	2.158		
70	2.183		
60	2.208		
50	2.220		
40	2.228		
30	2.233		
20	2.237		
10	2.238		
5	2.238		

58<

TABLE 26. THERMAL EXPANSION BEHAVIOR OF HDPE HIGH DENSITY POLYETHYLENE IN THE LONGITUDINAL AND TRANSVERSE DIRECTION

Longitudinal		Transverse	
T(K)	$-\Delta L/L_o$, percent	T(K)	$-\Delta L/L_o$, percent
300	-0.630	300	-0.540
290	-0.313	273	0
280	-0.142	250	0.460
273	0	200	1.063
260	0.248	150	1.557
250	0.398	100	1.855
240	0.537	50	1.965
230	0.663	20	1.970
220	0.785	10	1.977
210	0.907	5	1.979
200	1.029		
190	1.142		
180	1.251		
170	1.349		
160	1.443		
150	1.524		
140	1.594		
130	1.655		
120	1.708		
110	1.771		
100	1.834		
90	1.857		
80	1.881		
70	1.895		
60	1.920		
50	1.930		
40	1.943		
30	1.952		
20	1.958		
10	1.963		
5	1.965		

TABLE 27. THERMAL EXPANSION BEHAVIOR OF CRYOVAC ORIENTED POLYETHYLENE IN THE LONGITUDINAL AND TRANSVERSE DIRECTION

Longitudinal		Transverse	
T(K)	$-\Delta L/L_o$, percent	T(K)	$-\Delta L/L_o$, percent
300	-0.286	300	-0.165
290	-0.170	290	-0.170
280	-0.070	280	-0.044
273	0	273	0
260	0.131	260	0.081
250	0.229	250	0.144
240	0.328	240	0.206
230	0.429	230	0.269
220	0.530	220	0.332
210	0.628	210	0.394
200	0.712	200	0.457
190	0.786	190	0.515
180	0.860	180	0.574
170	0.929	170	0.631
160	0.998	160	0.685
150	1.060	150	0.735
140	1.110	140	0.779
130	1.160	130	0.823
120	1.210	120	0.861
110	1.251	110	0.895
100	1.286	100	0.925
90	1.339	90	0.950
80	1.361	80	0.972
70	1.389	70	0.986
60	1.411	60	0.990
50	1.429	50	0.996
40	1.446	40	1.001
30	1.456	30	1.005
20	1.464	20	1.007
10	1.470	10	1.008
5	1.473	5	1.008

TABLE 28. THERMAL EXPANSION BEHAVIOR OF RILSAN F, NYLON 11 POLYAMIDE IN THE LONGITUDINAL AND TRANSVERSE DIRECTION

Longitudinal		Transverse	
T(K)	$-\Delta L/L_o$, percent	T(K)	$-\Delta L/L_o$, percent
300	-0.303	300	-0.276
290	-0.176	273	0
280	-0.072	250	0.235
273	0	200	0.722
260	0.134	150	1.133
250	0.238	100	1.419
240	0.342	50	1.561
230	0.446	20	1.574
220	0.548	10	1.576
210	0.627	5	1.576
200	0.745		
190	0.833		
180	0.921		
170	1.003		
160	1.077		
150	1.150		
140	1.213		
130	1.276		
120	1.339		
110	1.391		
100	1.436		
90	1.476		
80	1.512		
70	1.542		
60	1.563		
50	1.580		
40	1.594		
30	1.608		
20	1.615		
10	1.618		
5	1.621		

TABLE 29. THERMAL EXPANSION BEHAVIOR OF KAPTON H POLYMIDE IN THE LONGITUDINAL AND TRANSVERSE DIRECTION

Longitudinal		Transverse	
T(K)	$-\Delta L/L_o$, percent	T(K)	$-\Delta L/L_o$, percent
300	-0.053	300	-0.049
290	-0.035	273	0
280	-0.012	250	0.041
273	0	200	0.129
260	0.029	150	0.238
250	0.043	100	0.328
240	0.055	50	0.386
230	0.073	25	0.403
220	0.092	10	0.408
210	0.116	5	0.409
200	0.138		
190	0.161		
180	0.185		
170	0.210		
160	0.232		
150	0.250		
140	0.269		
130	0.288		
120	0.316		
110	0.327		
100	0.346		
90	0.365		
80	0.373		
70	0.386		
60	0.397		
50	0.403		
40	0.413		
30	0.419		
20	0.425		
10	0.429		
5	0.431		

TABLE 30. THERMAL EXPANSION BEHAVIOR OF BICOR 400-S ORIENTED POLYPROPYLENE IN THE LONGITUDINAL AND TRANSVERSE DIRECTION

Longitudinal		Transverse	
T(K)	$-\Delta L/L_o$, percent	T(K)	$-\Delta L/L_o$, percent
300	-0.261	300	-0.067
290	-0.145	290	-0.035
280	-0.060	280	-0.014
273	0	273	0
260	0.111	260	0.023
250	0.196	250	0.034
240	0.281	240	0.045
230	0.366	230	0.055
220	0.451	220	0.064
210	0.536	210	0.072
200	0.614	200	0.081
190	0.687	190	0.090
180	0.757	180	0.099
170	0.823	170	0.107
160	0.886	160	0.115
150	0.948	150	0.123
140	1.011	140	0.130
130	1.069	130	0.137
120	1.133	120	0.144
110	1.194	110	0.150
100	1.247	100	0.157
90	1.303	90	0.164
80	1.351	80	0.168
70	1.389	70	0.172
60	1.406	60	0.176
50	1.441	50	0.179
40	1.455	40	0.182
30	1.472	30	0.185
20	1.485	20	0.187
10	1.492	10	0.187
5	1.495	5	0.188

TABLE 31. THERMAL EXPANSION BEHAVIOR OF ROWLAND POLYSULFONE IN THE LONGITUDINAL AND TRANSVERSE DIRECTION

Longitudinal		Transverse	
T(K)	$-\Delta L/L_o$, percent	T(K)	$-\Delta L/L_o$, percent
300	-0.143	300	-0.131
290	-0.090	273	0
280	-0.037	250	0.111
273	0	200	0.352
260	0.069	150	0.587
250	0.122	100	0.789
240	0.175	50	0.904
230	0.228	25	0.931
220	0.281	10	0.937
210	0.335	5	0.939
200	0.387		
190	0.437		
180	0.486		
170	0.536		
160	0.584		
150	0.627		
140	0.670		
130	0.713		
120	0.756		
110	0.799		
100	0.837		
90	0.872		
80	0.907		
70	0.938		
60	0.960		
50	0.977		
40	0.993		
30	1.005		
20	1.010		
10	1.015		
5	1.017		

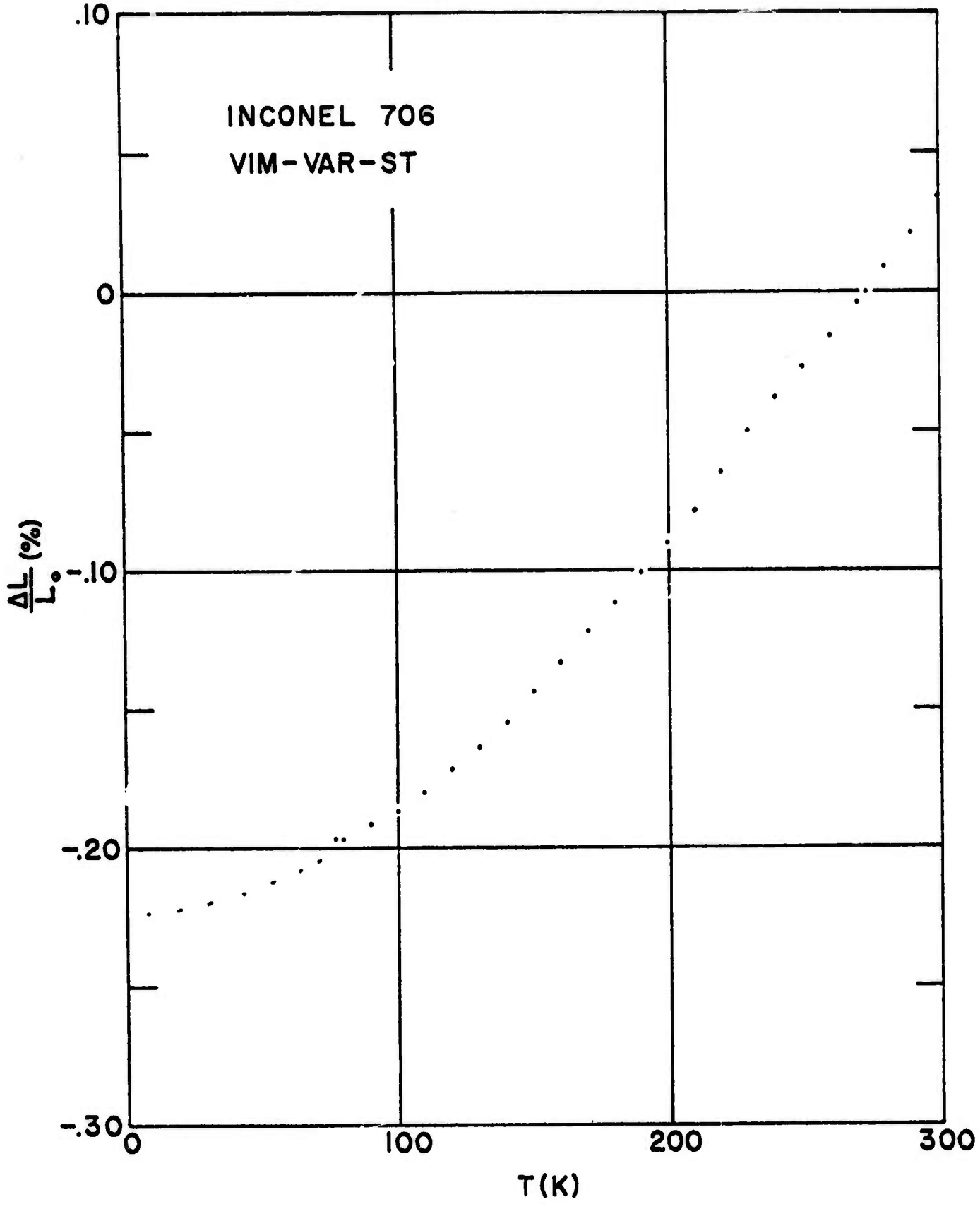

FIGURE 1. THERMAL EXPANSION BEHAVIOR OF INCONEL 706, VIM-VAR-ST

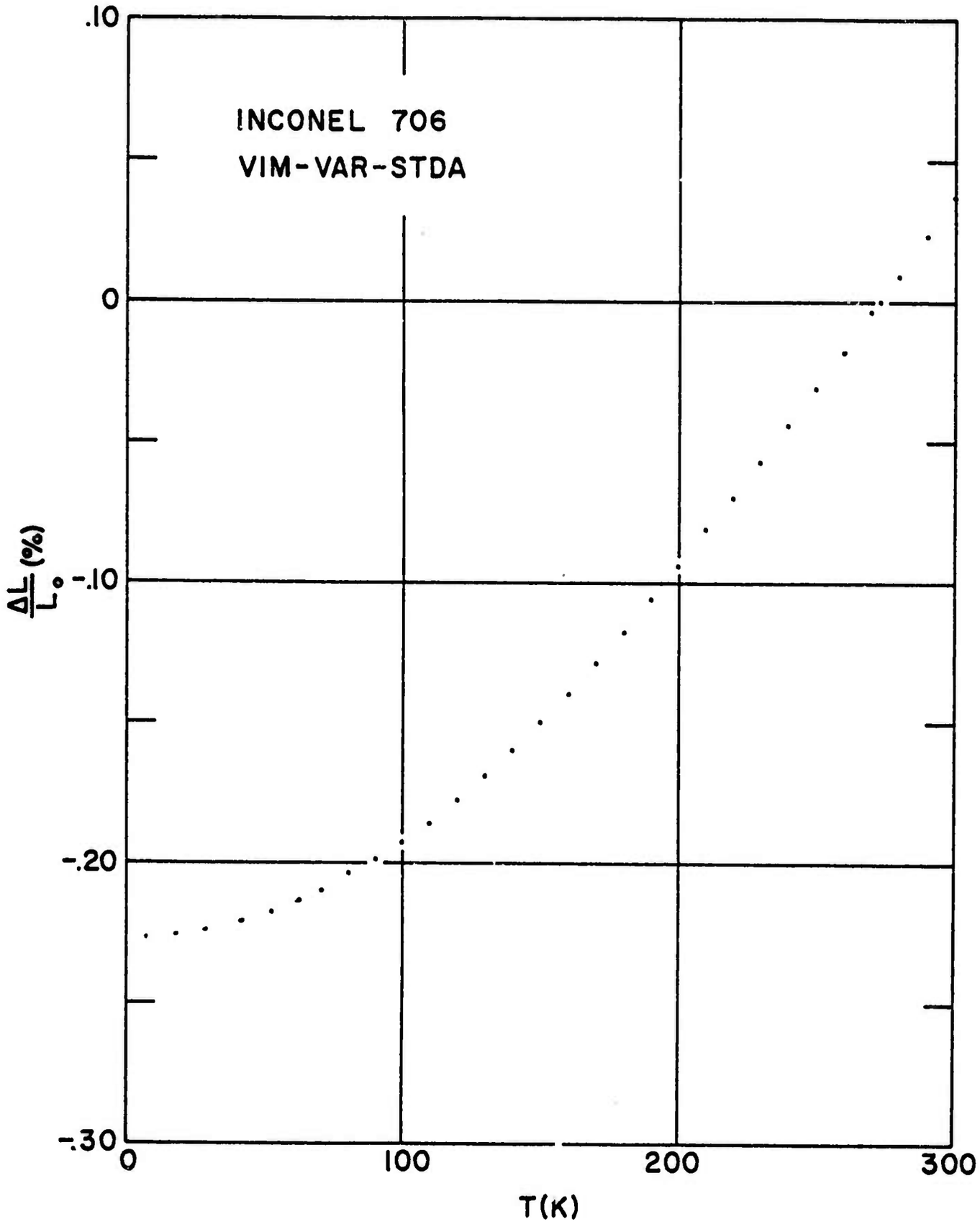

FIGURE 2. THERMAL EXPANSION BEHAVIOR OF INCONEL 706, VIM-VAR-STDA

66<

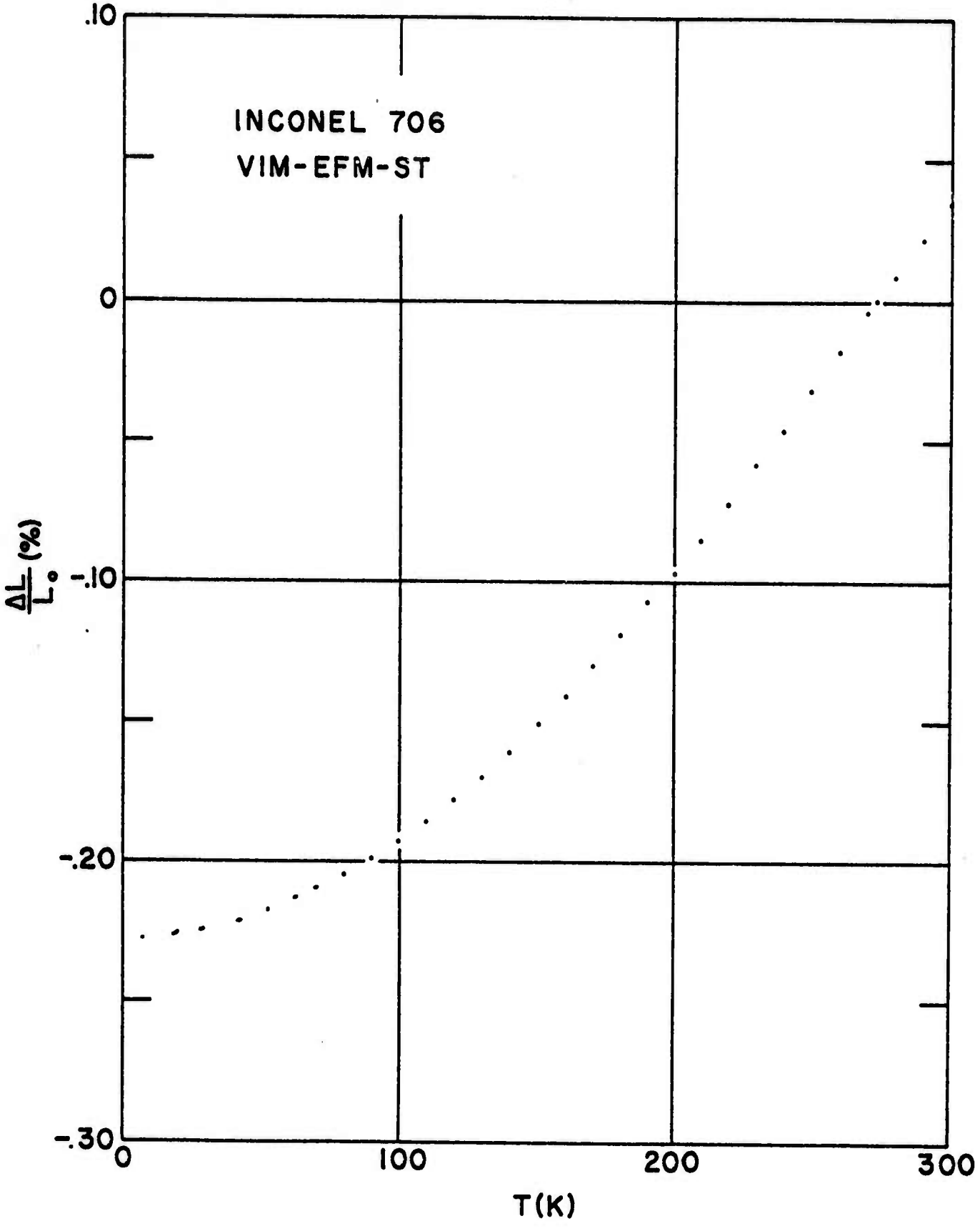

FIGURE 3. THERMAL EXPANSION BEHAVIOR OF INCONEL 706, VIM-EFM-ST

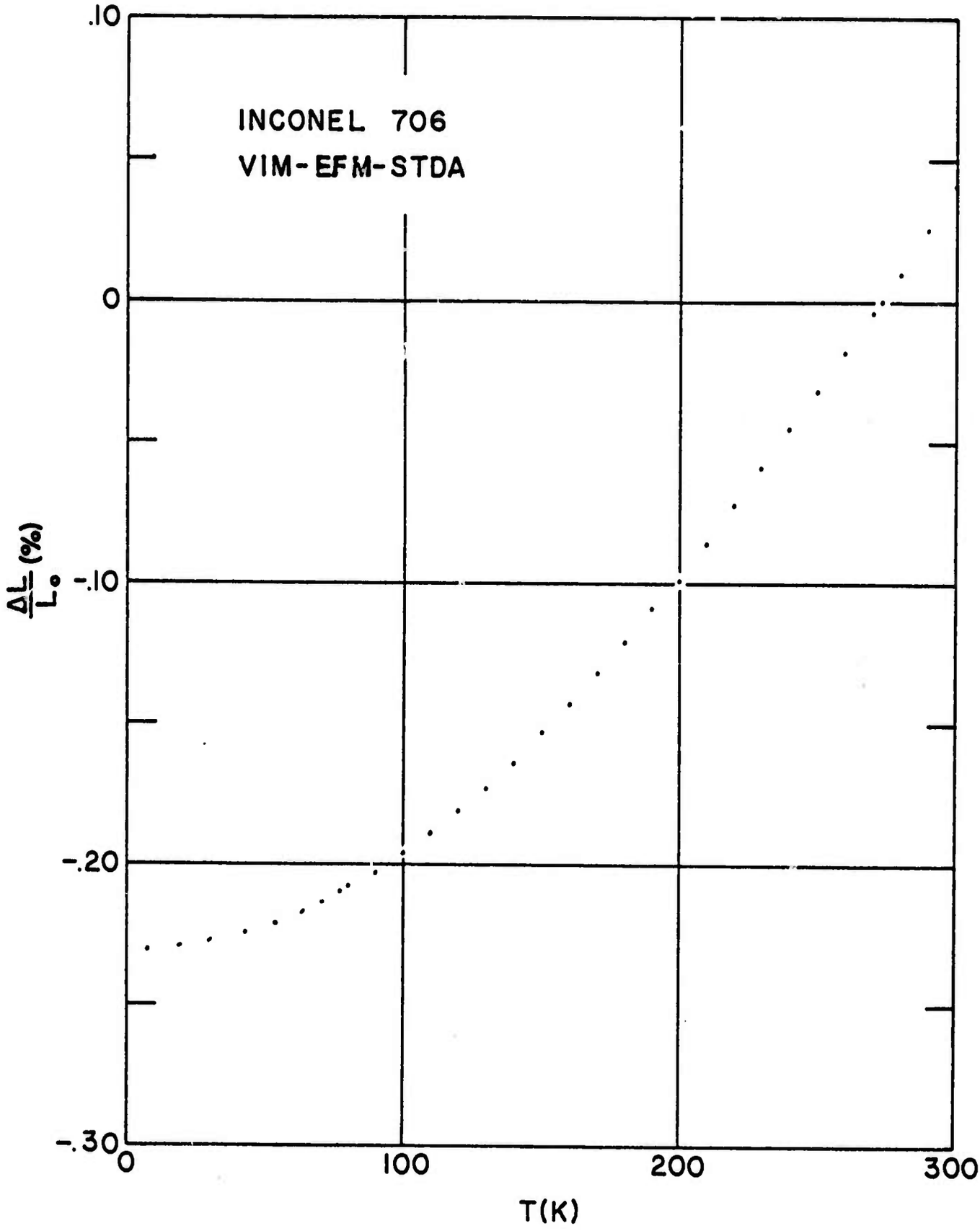

FIGURE 4. THERMAL EXPANSION BEHAVIOR OF INCONEL 706, VIM-EFM-STDA

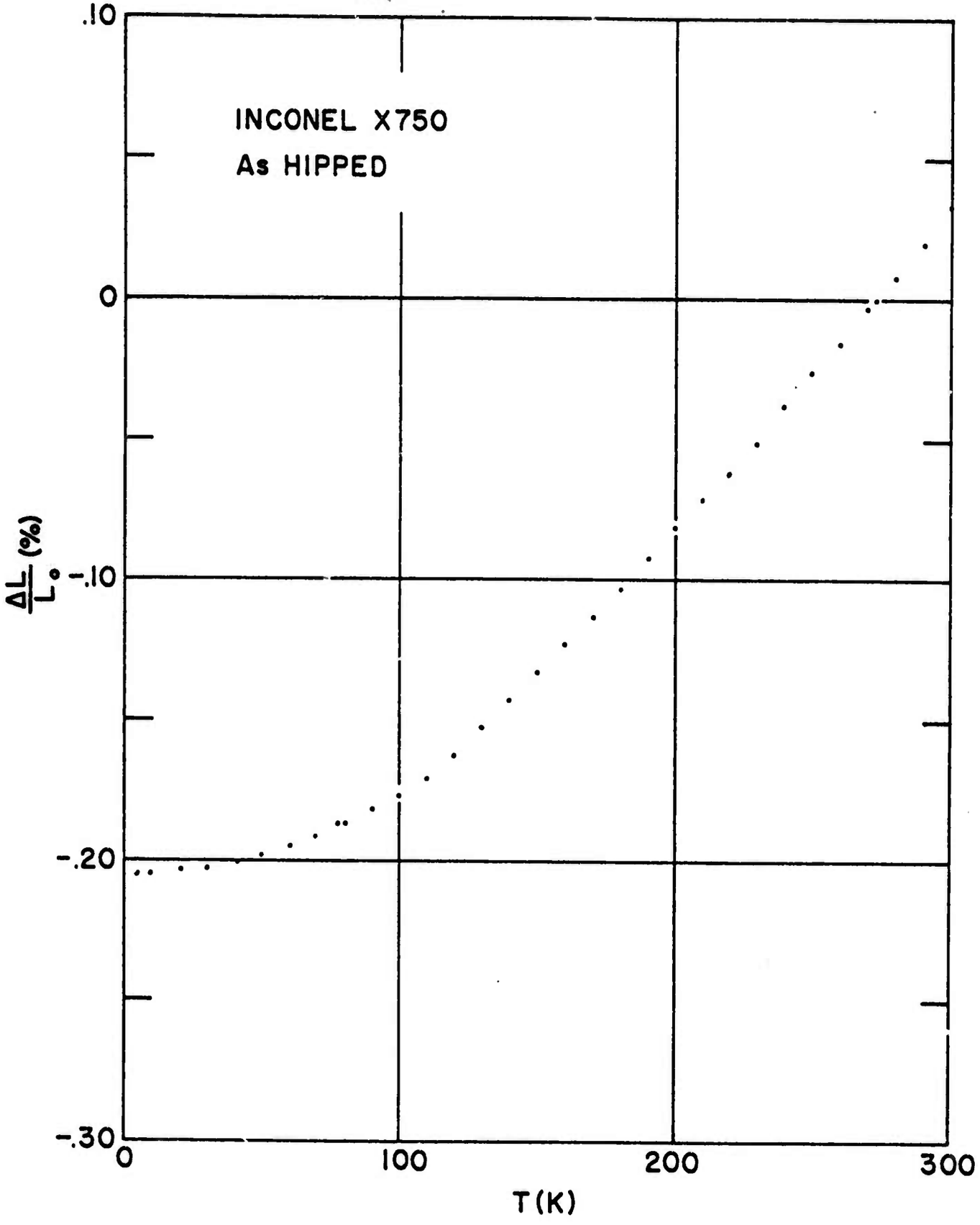

FIGURE 5. THERMAL EXPANSION BEHAVIOR OF INCONEL X750, AS HIPPED

69<

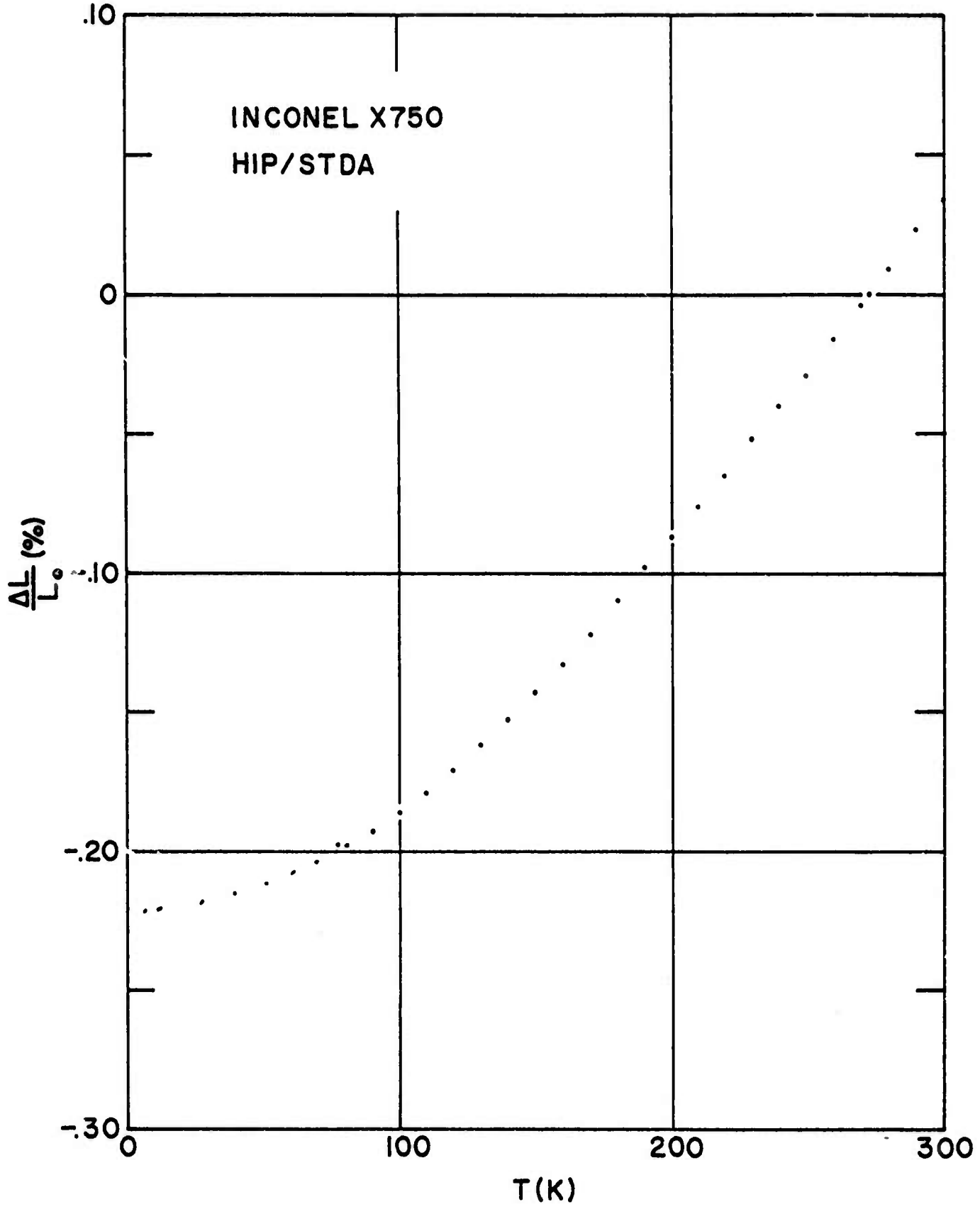

FIGURE 6. THERMAL EXPANSION BEHAVIOR OF INCONEL X750, HIP-STDA

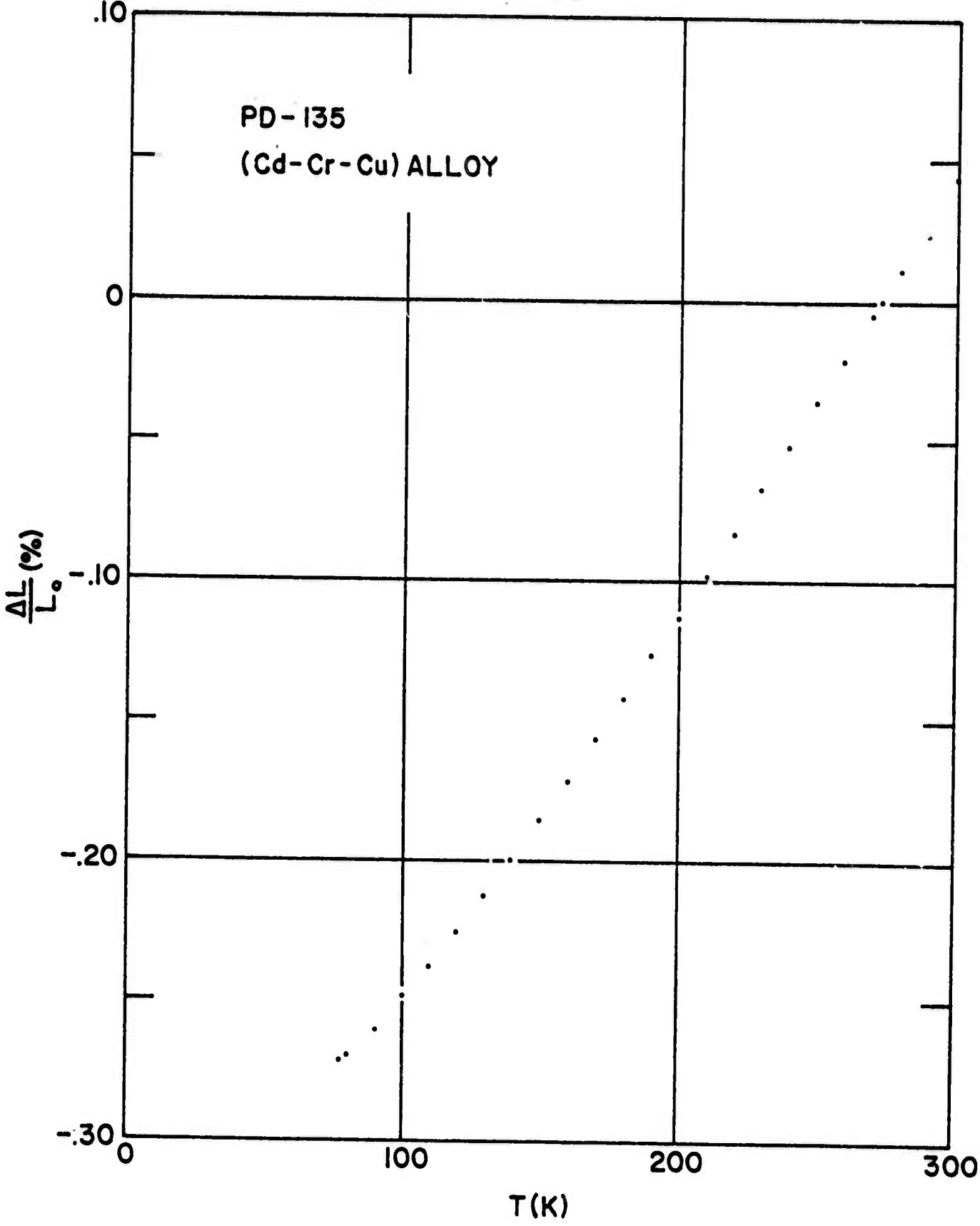

FIGURE 7. THERMAL EXPANSION BEHAVIOR OF PD-135 (Cd-Cr-Cu ALLOY)

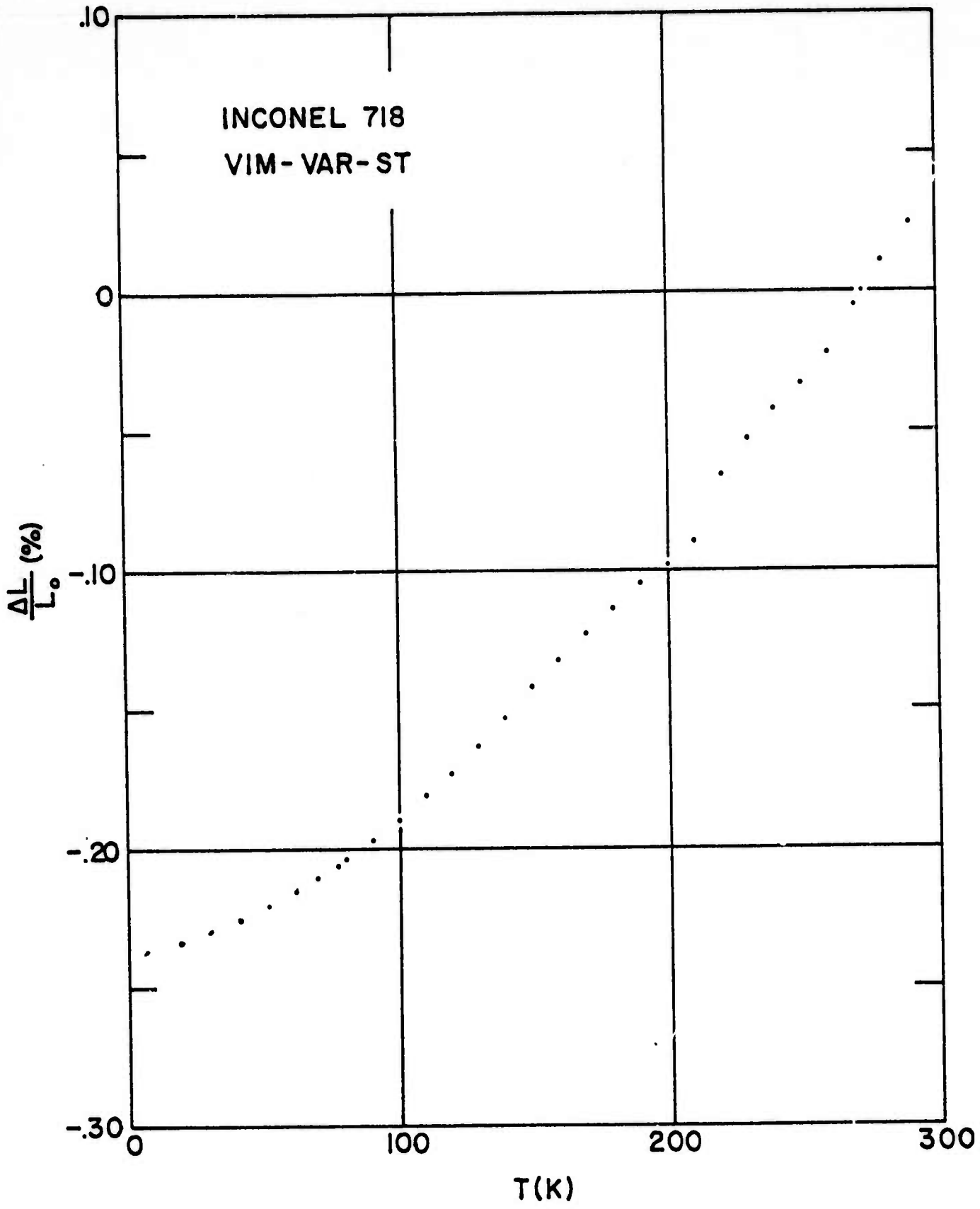

FIGURE 8. THERMAL EXPANSION BEHAVIOR OF INCONEL 718, VIM-VAR-ST

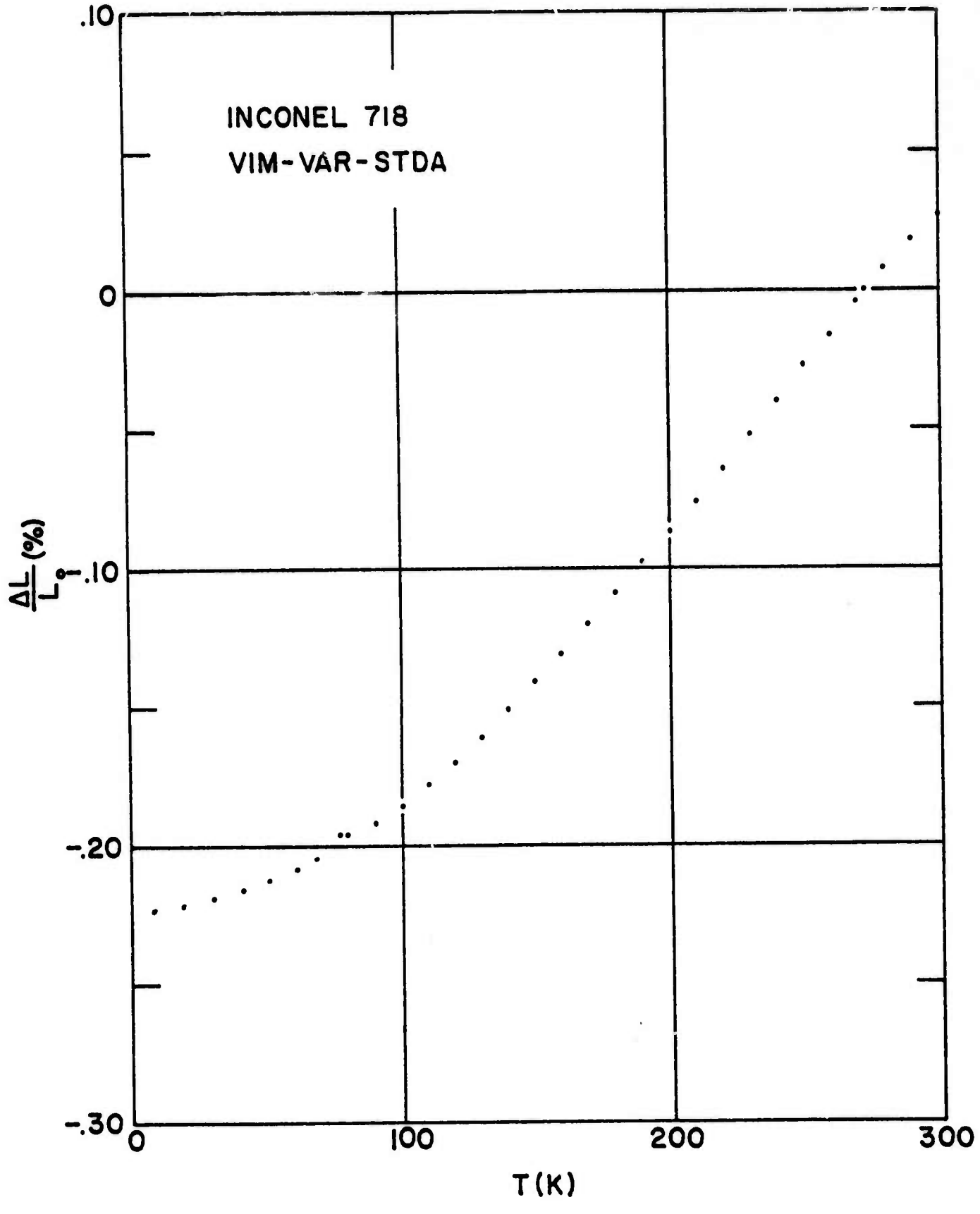

FIGURE 9. THERMAL EXPANSION BEHAVIOR OF INCONEL 718, VIM-VAR-STDA

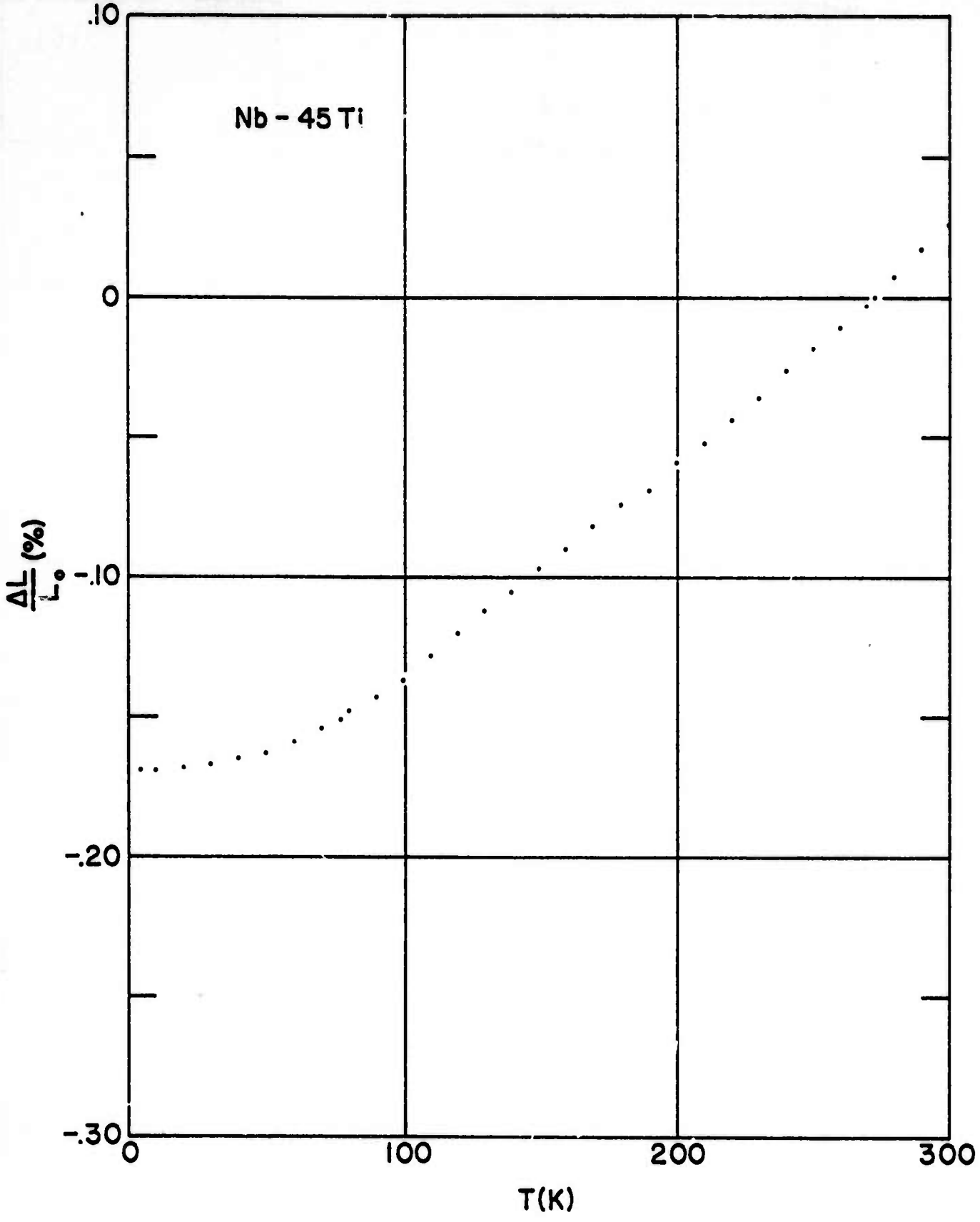

FIGURE 10. THERMAL EXPANSION BEHAVIOR OF Nb-45Ti ALLOY

74<

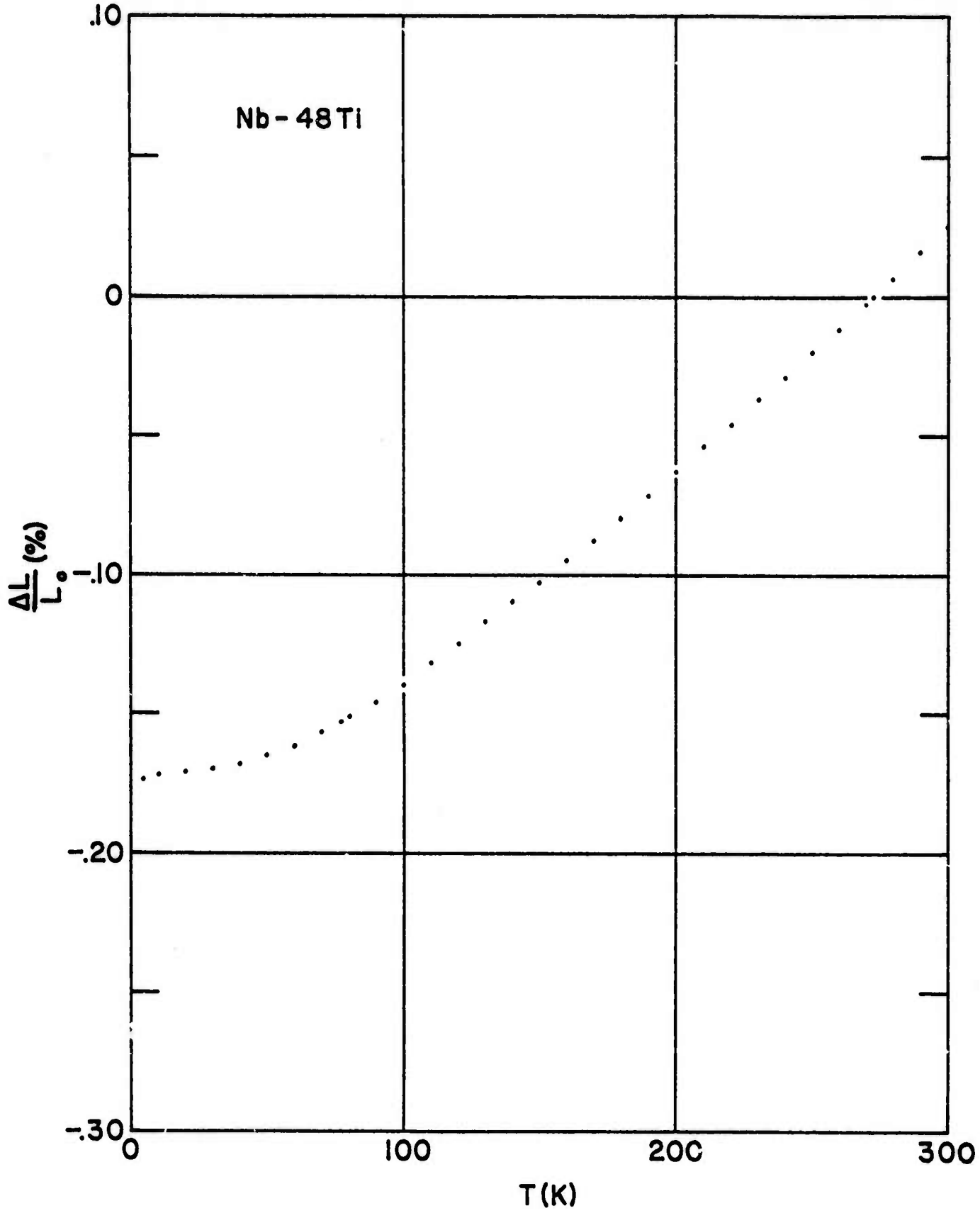

FIGURE 11. THERMAL EXPANSION BEHAVIOR OF Nb-48Ti ALLOY

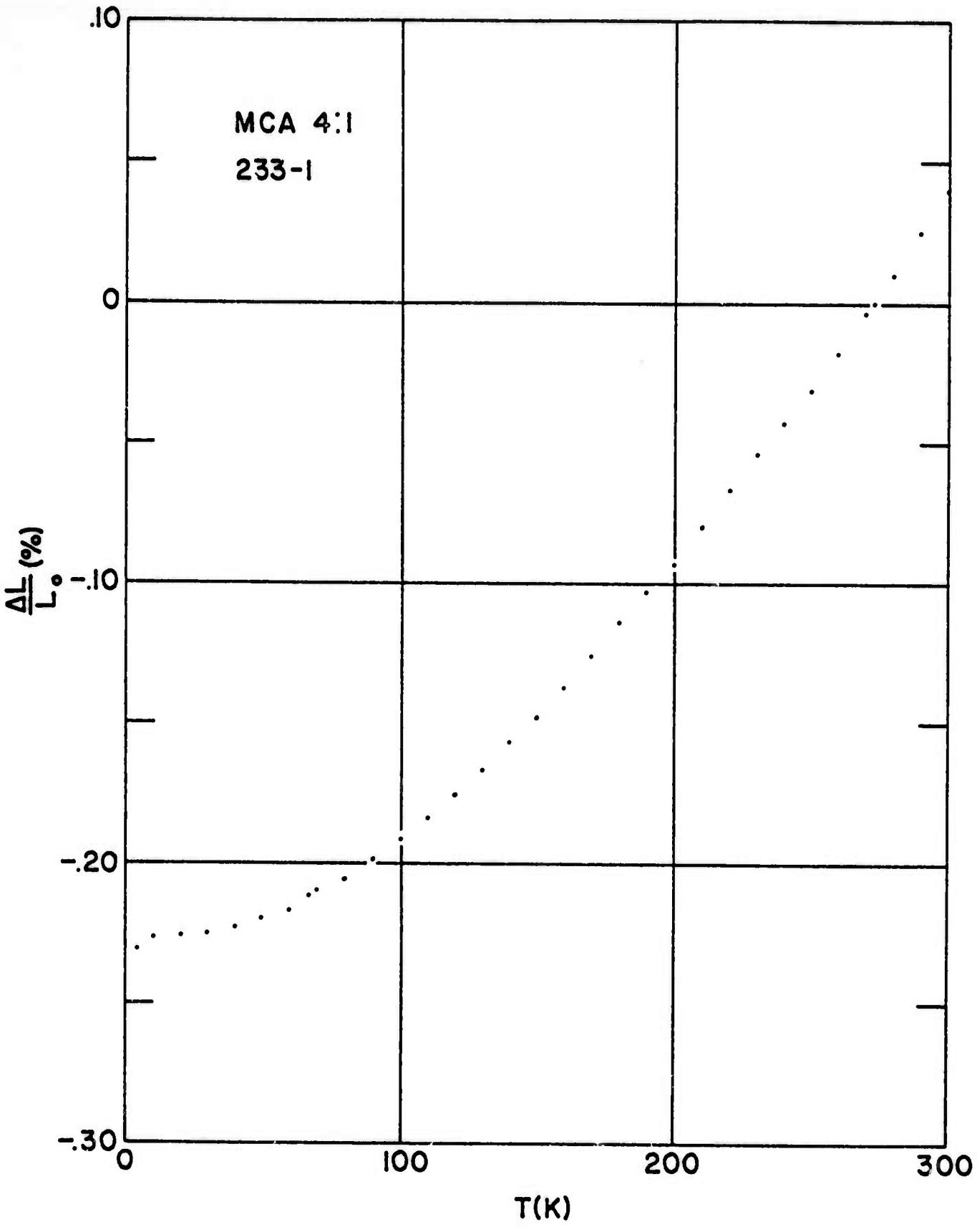

FIGURE 12. THERMAL EXPANSION BEHAVIOR OF MULTIFILAMENT NbTi IN Cu. Cu TO NbTi RATIO = 4

76<

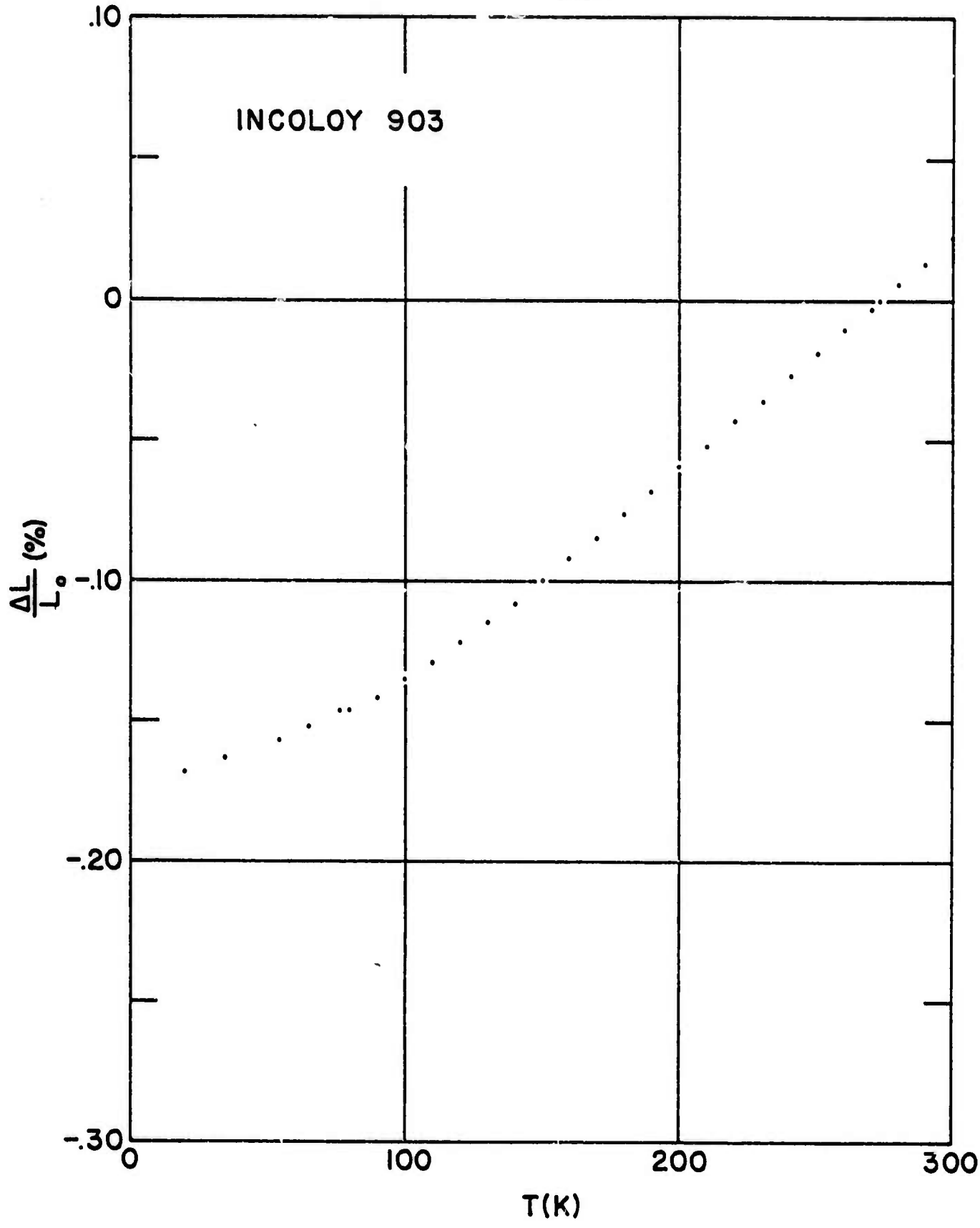

FIGURE 13. THERMAL EXPANSION BEHAVIOR OF INCOLOY 903 ALLOY

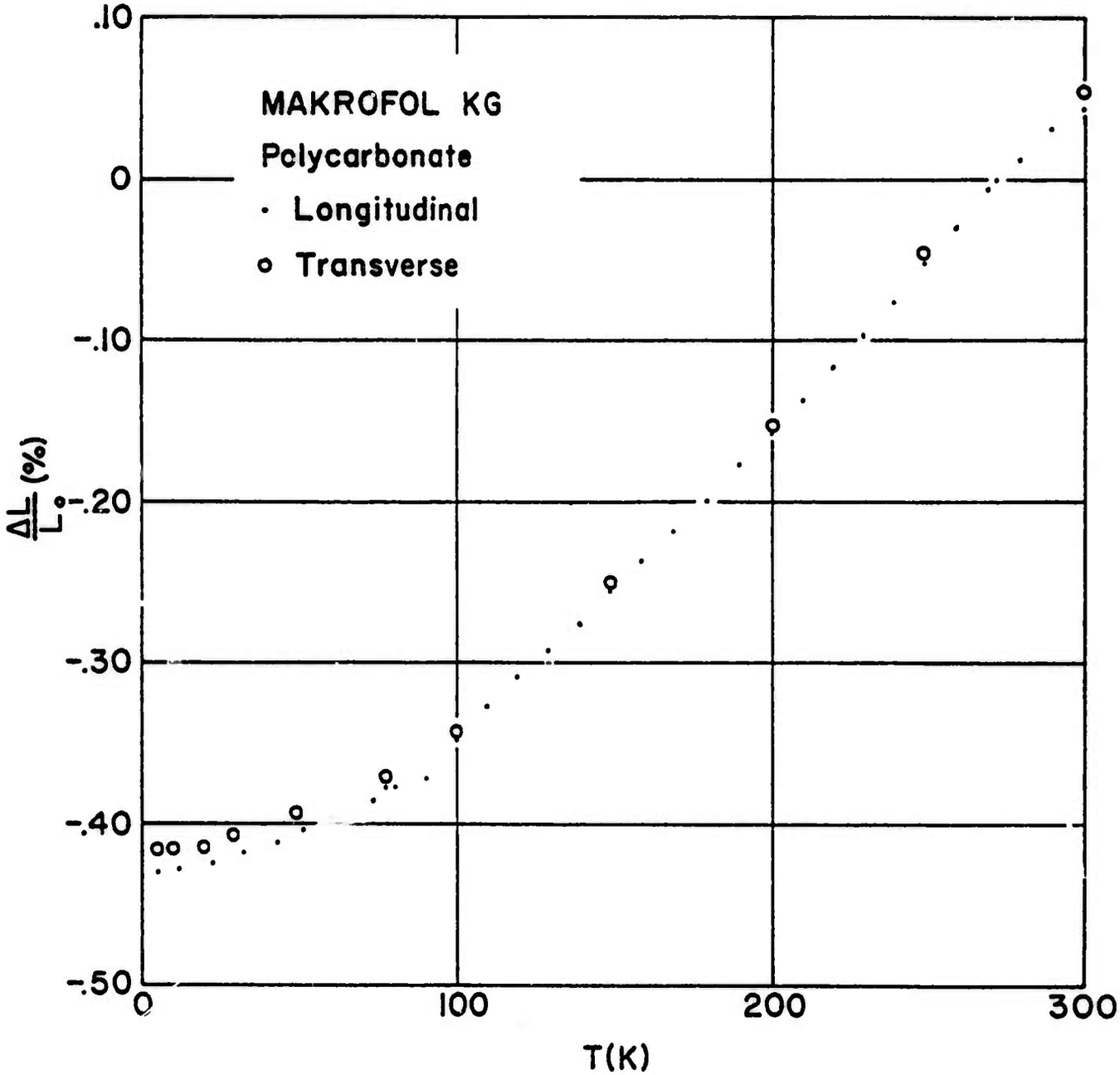

FIGURE 14. THERMAL EXPANSION BEHAVIOR OF MAKROFOL KG - POLYCARBONATE

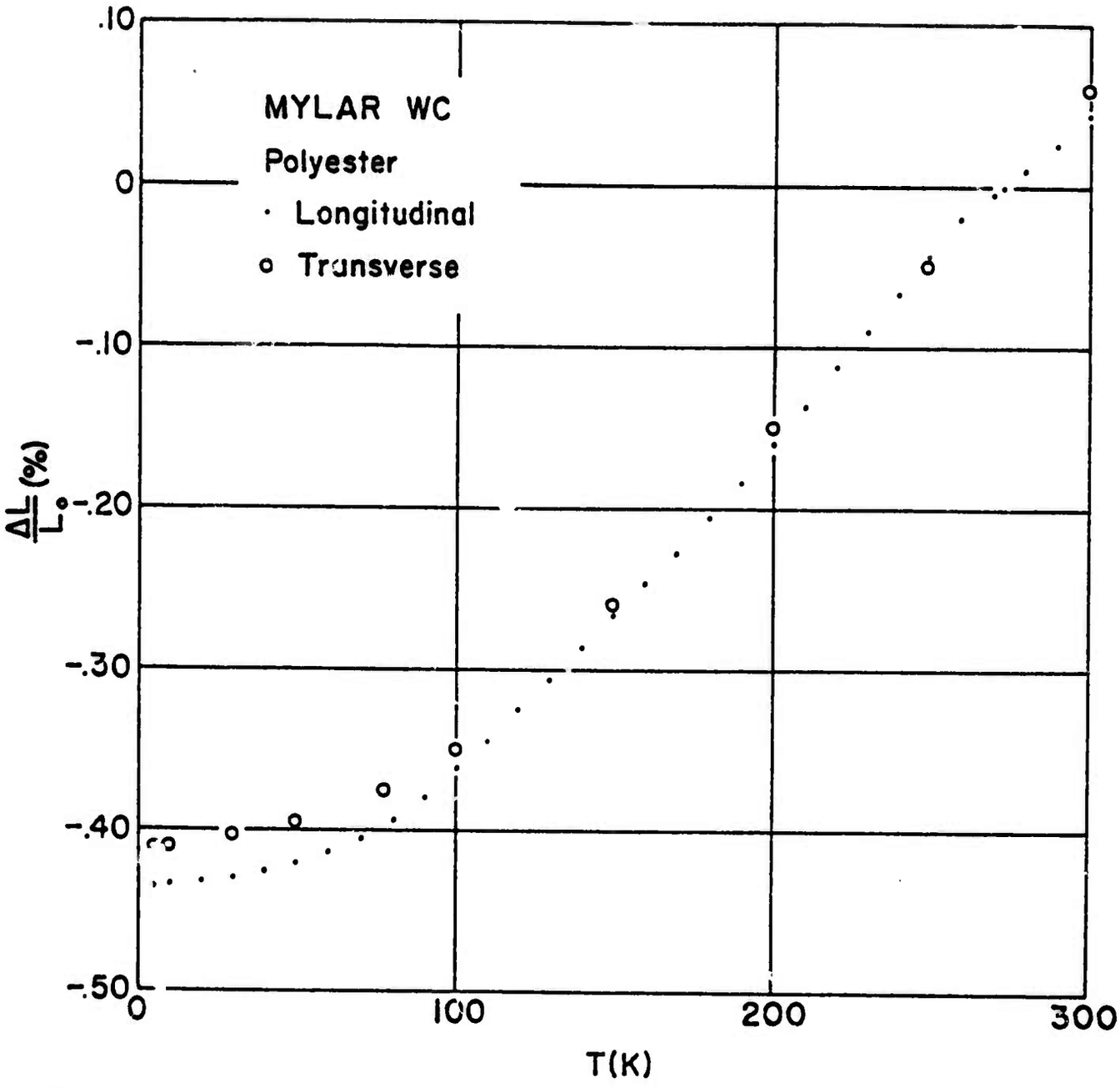

FIGURE 15. THERMAL EXPANSION BEHAVIOR OF MYLAR WC POLYESTER

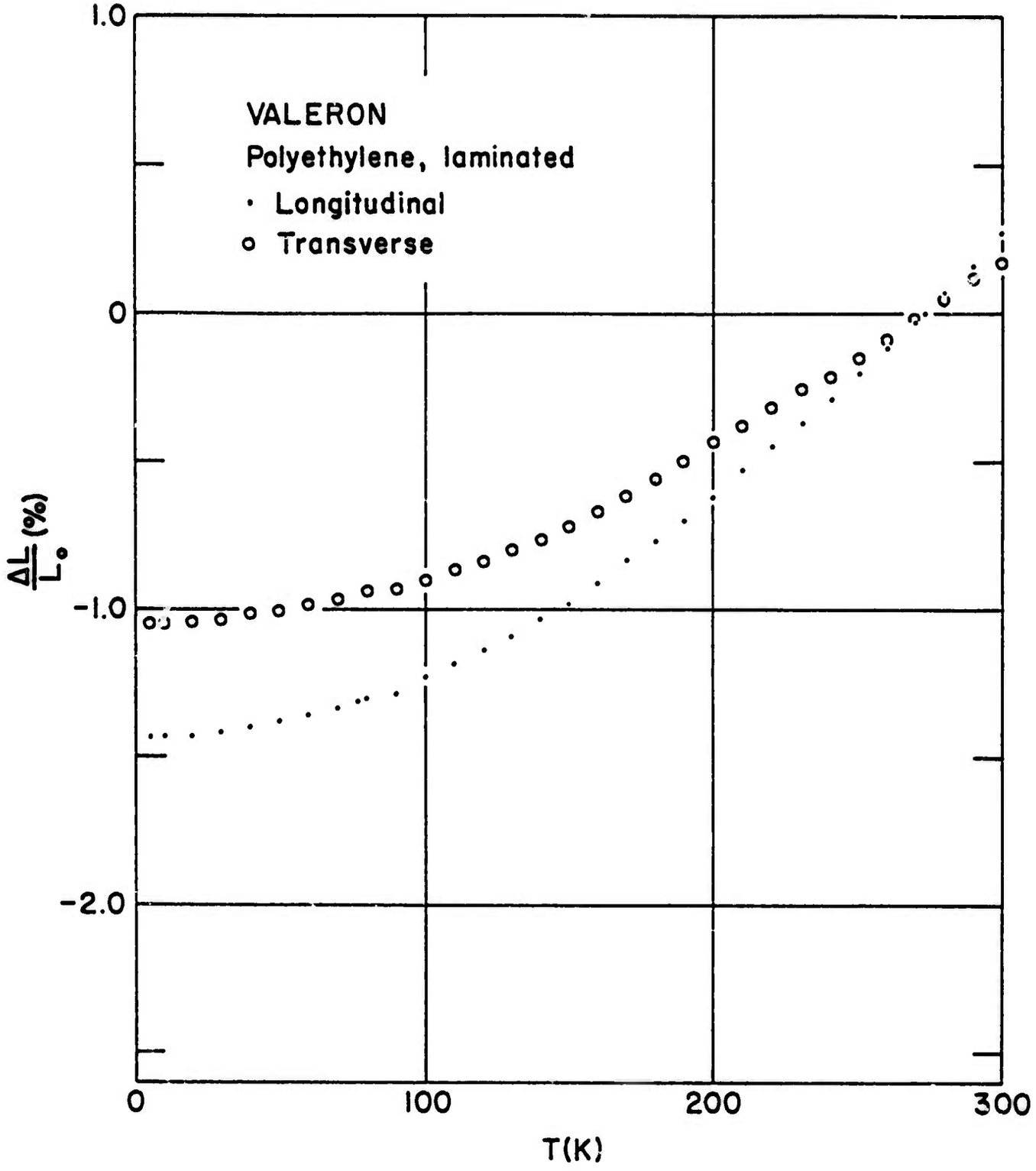

FIGURE 16. THERMAL CONTRACTION BEHAVIOR OF VALERON POLYETHYLENE, LAMINATED

80<

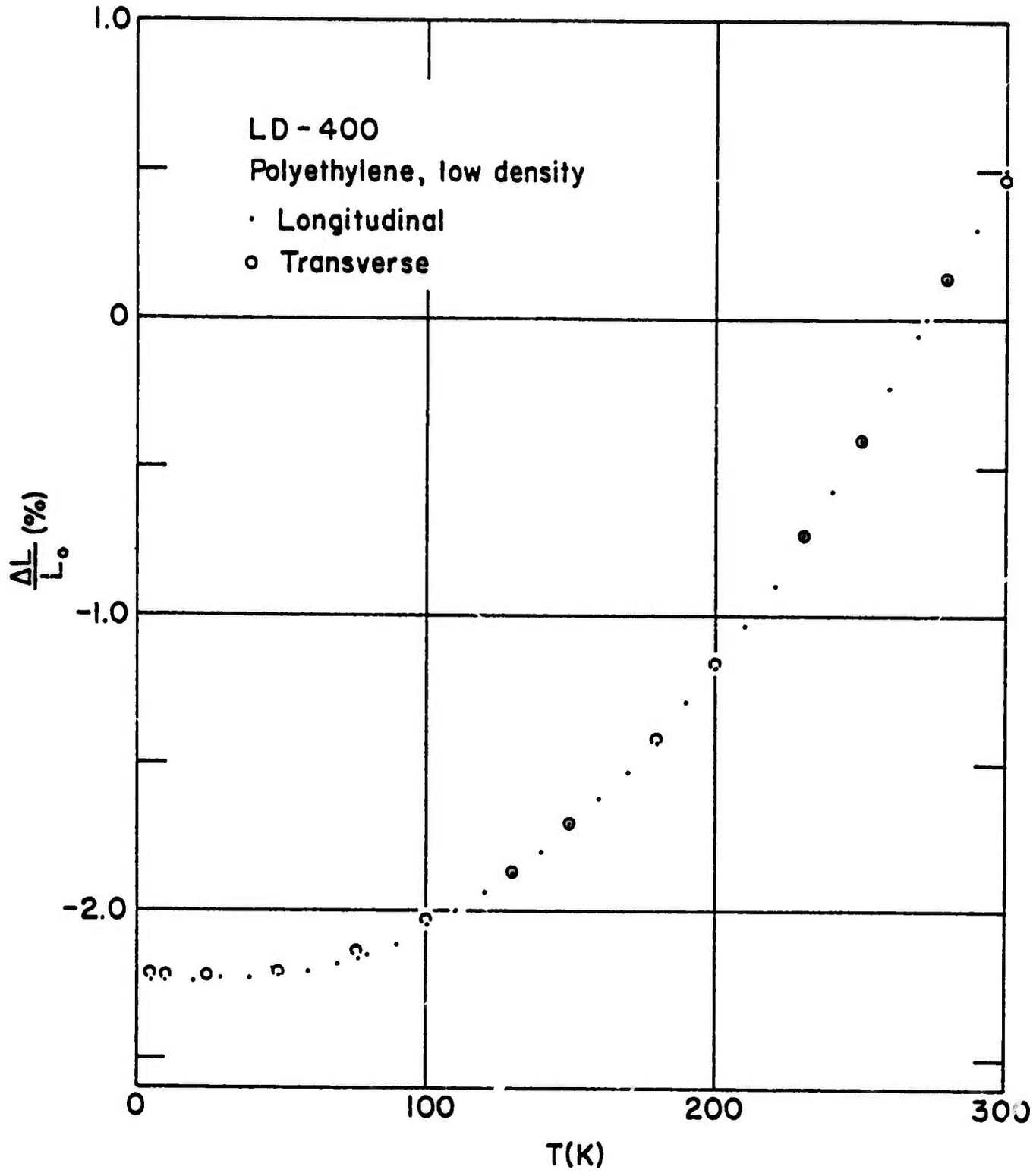

FIGURE 17. THERMAL EXPANSION BEHAVIOR OF LD-400 POLYETHYLENE, LOW DENSITY

81<

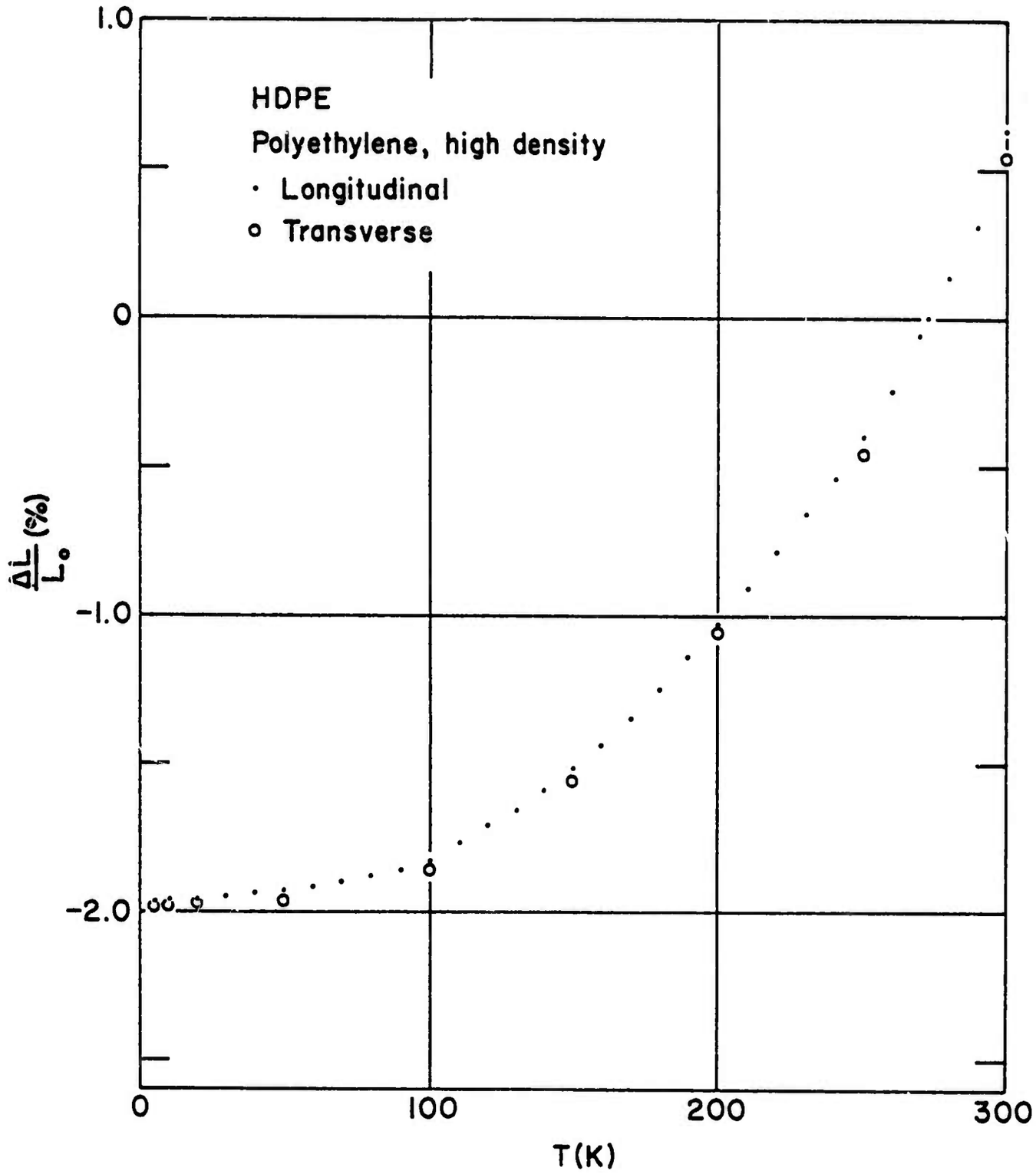

FIGURE 18. THERMAL EXPANSION BEHAVIOR OF HDPE POLYETHYLENE, HIGH DENSITY

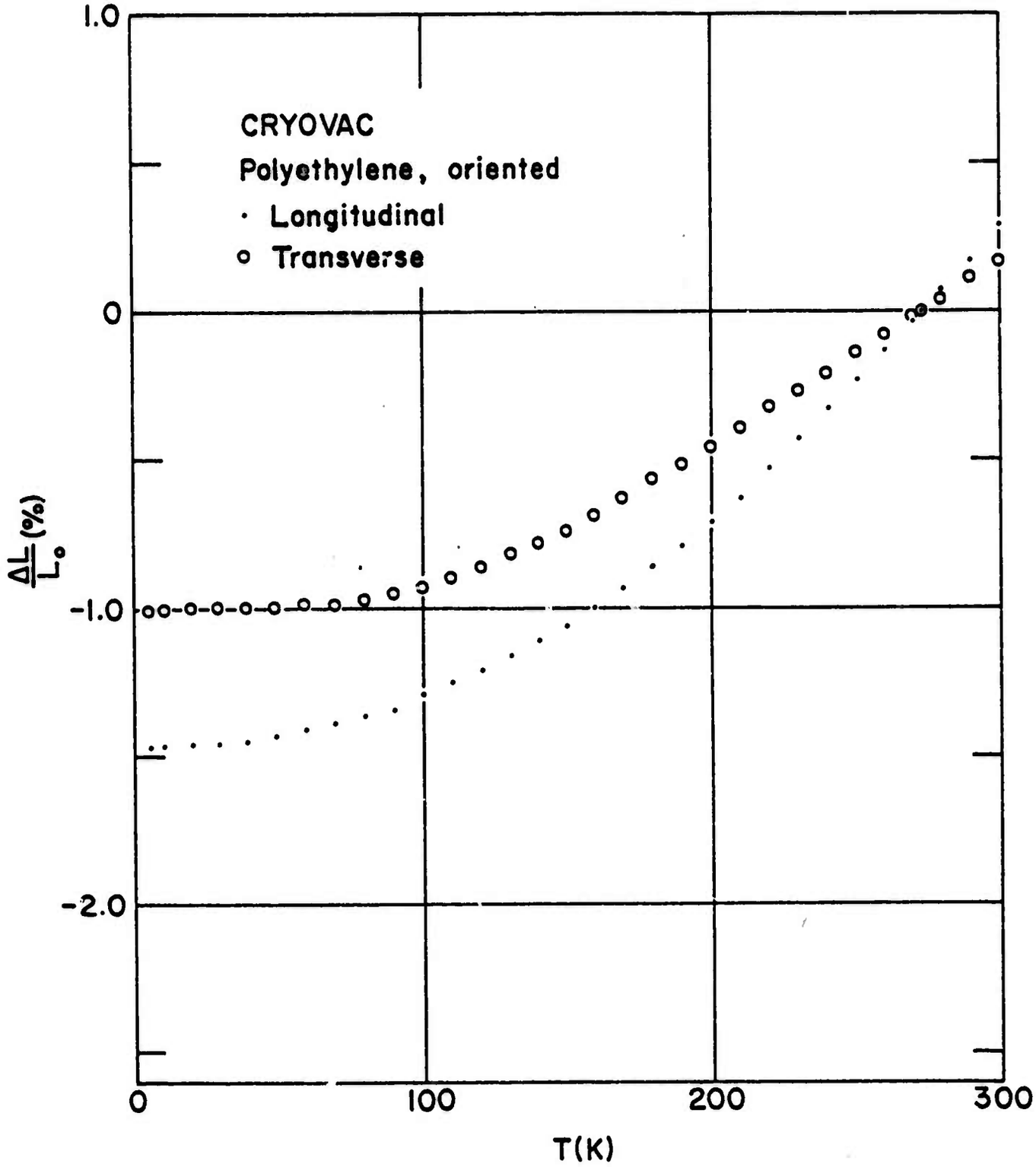

FIGURE 19. THERMAL CONTRACTION BEHAVIOR OF CRYOVAC POLYETHYLENE, ORIENTED

83<

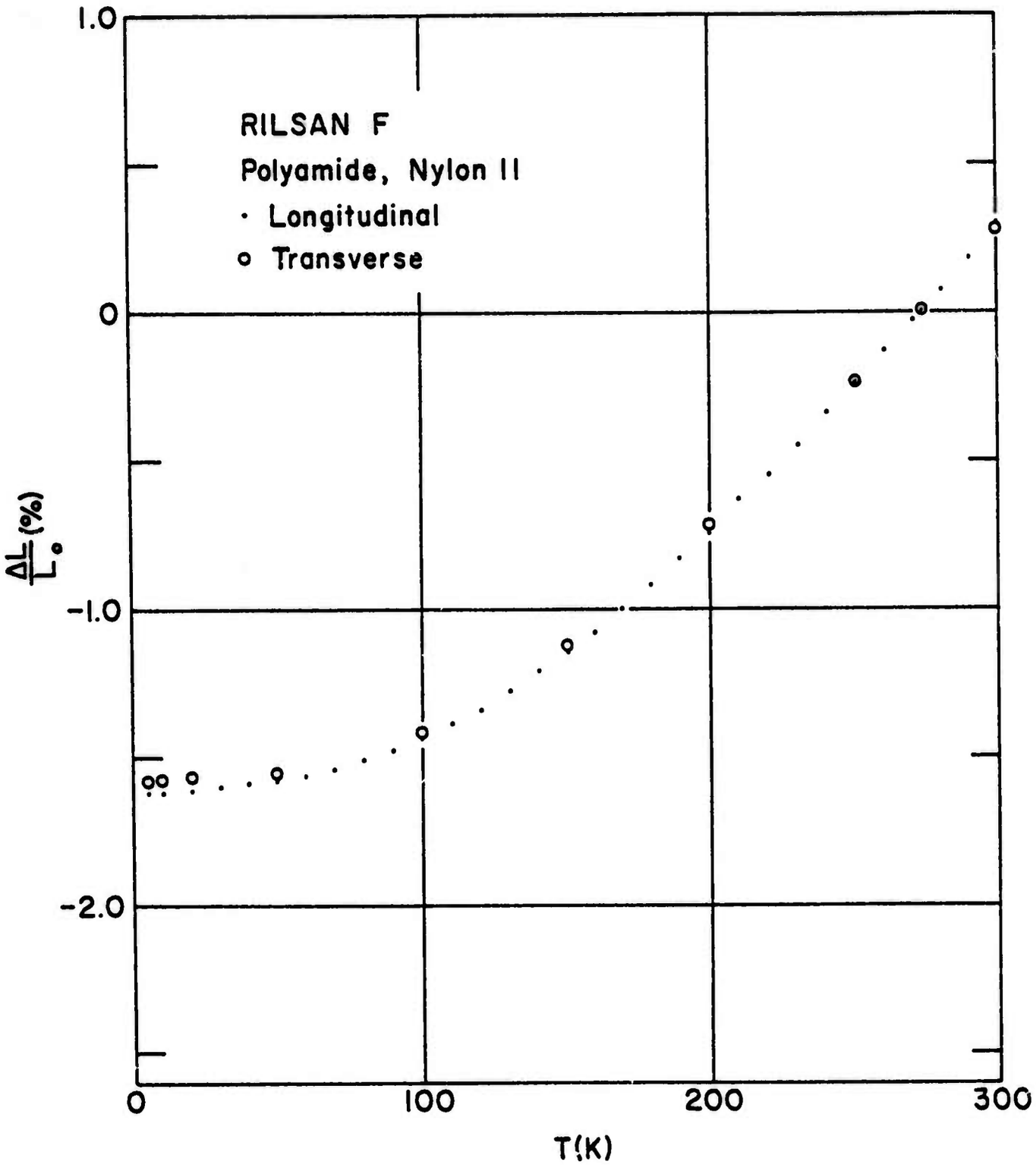

FIGURE 20. THERMAL EXPANSION BEHAVIOR OF RILSAN F POLYAMIDE, NYLON 11

84<

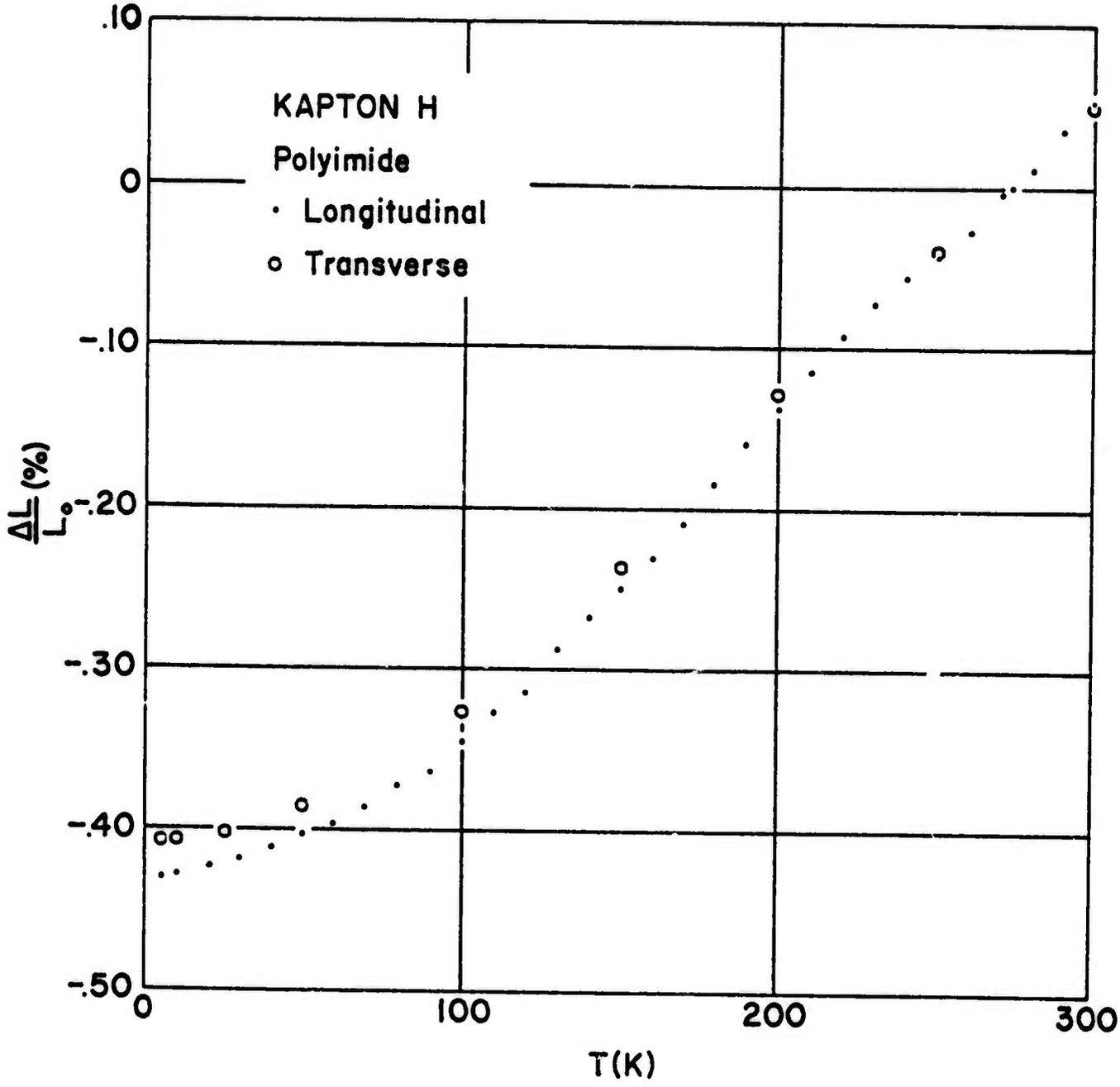

FIGURE 21. THERMAL EXPANSION BEHAVIOR OF KAPTON H POLYIMIDE

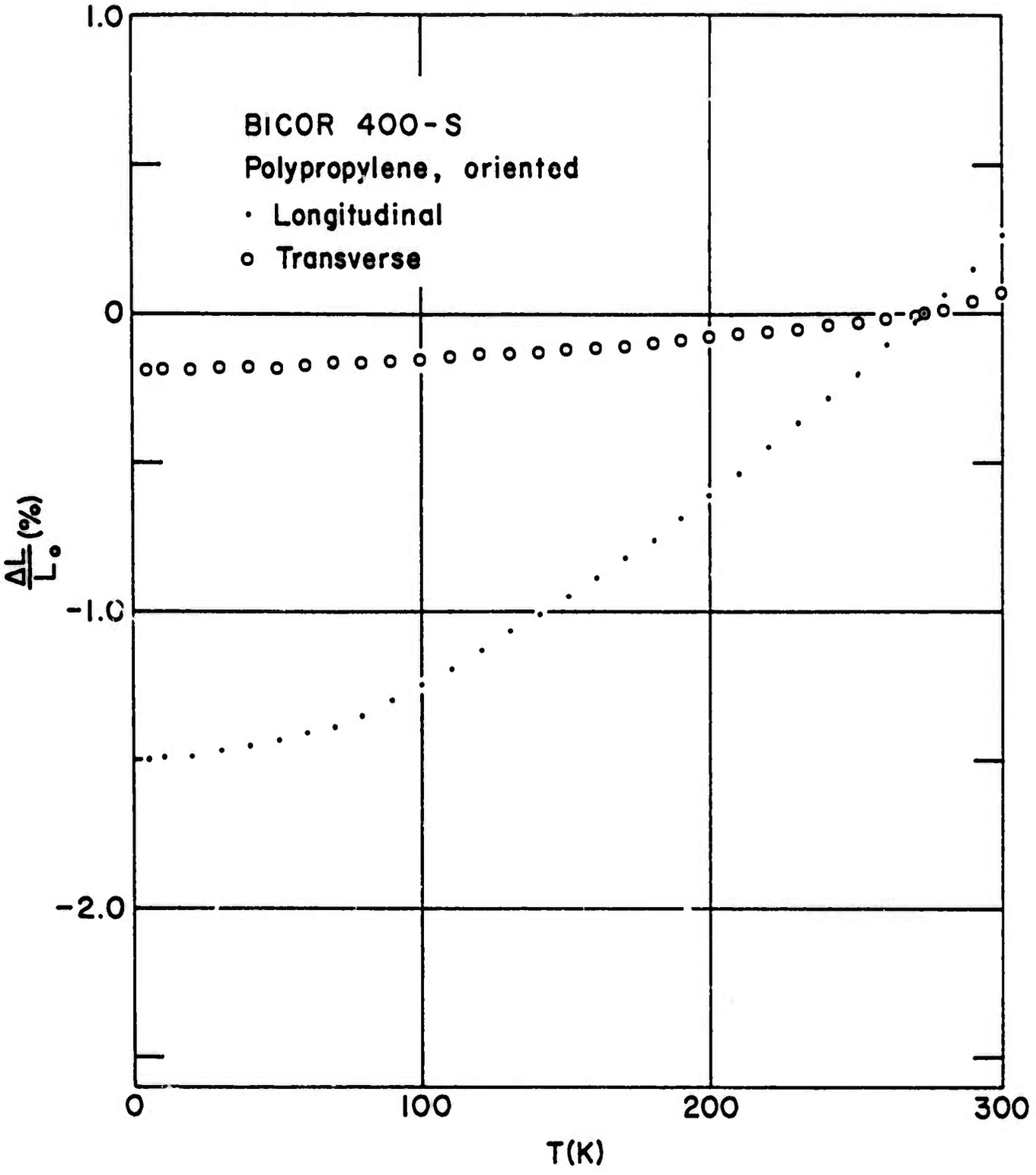

FIGURE 22. THERMAL CONTRACTION BEHAVIOR OF BICOR 400-S POLYPROPYLENE, ORIENTED

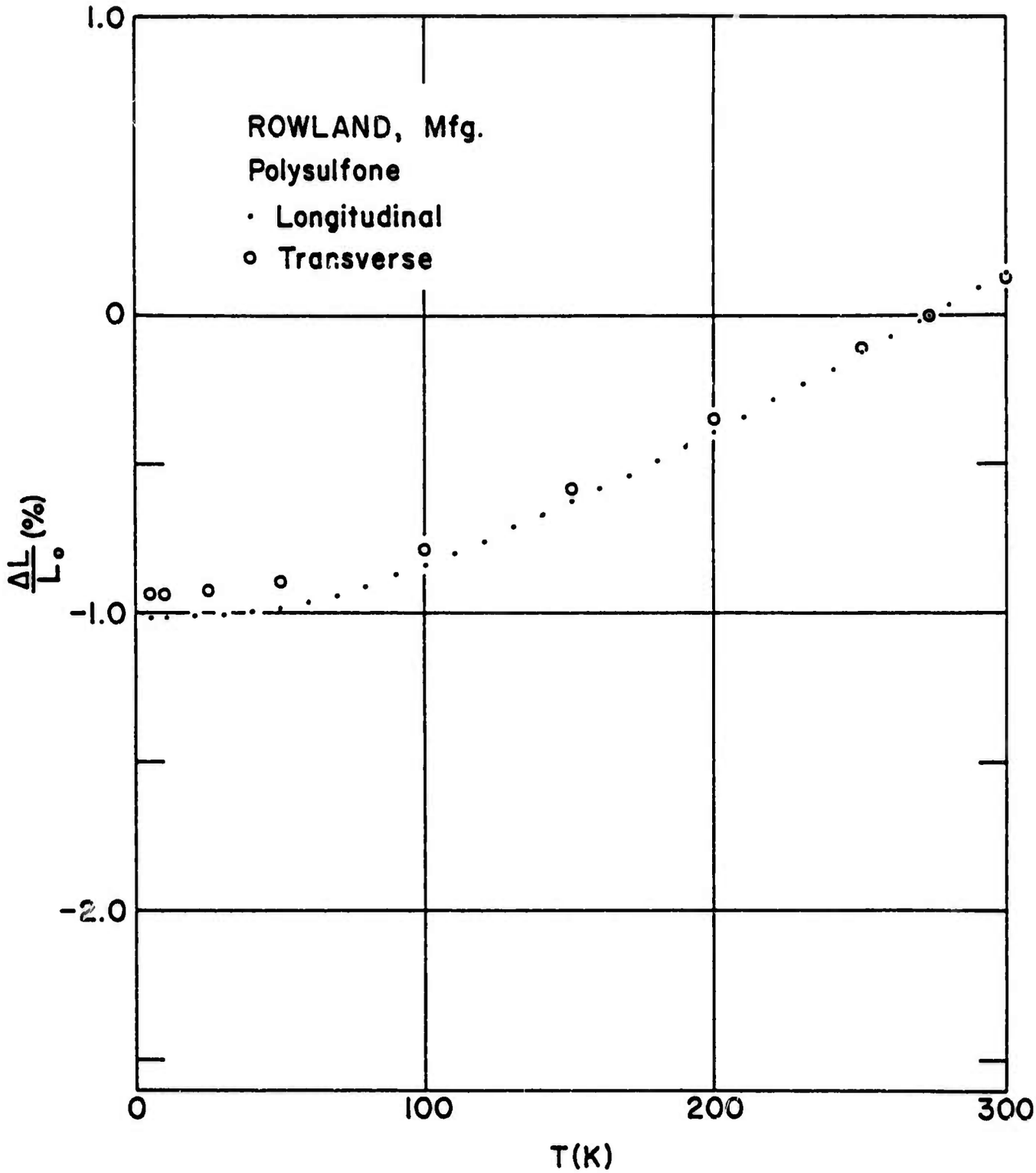

FIGURE 23. THERMAL EXPANSION BEHAVIOR OF ROWLAND, MFG. POLYSULFONE

COMPOSITE STRUCTURAL MATERIALS INVESTIGATION AT CRYOGENIC TEMPERATURES

Semi-Annual Technical Report
3/1/75 through 8/31/75

Principal Investigator
W.B. Hillig

Co-Contributors
D.G. LeGrand
P.D. deTorres
R.L. Mehan
J.W. Nehrich

Sponsored by
Advanced Research Projects Agency
ARPA Order No. 2569
Program Code 4D10

This research was supported by the Advanced Research Projects Agency of the Department of Defense and was monitored by the Cryogenics Division, National Bureau of Standards, Boulder, Colorado 80302, under Contract No. CST-8300, 9/1/73 through 8/31/75, $120,000.

General Electric Company
Corporate Research and Development
P. O. Box 8
Schenectady, New York 12301

Phone: (518) 346-8771

SRD-75-103

SUMMARY

Adhesive joints between S-glass fiber reinforced epoxy composite and 6061T-6 aluminum have been evaluated at room temperature and at 4°K. The main variables were the method of cleaning the aluminum, the type of primer (if any) used, and the processing of the metal/composite/metal sandwich plaques. The composite was cured in contact with the aluminum so that the matrix resin served as the adhesive. About 300 specimens representing 15 different treatments were tested using the lap shear and short beam shear methods. The results indicate that the bond strength improves at the lower temperature, and that the mode of failure is different for these two tests. The effect of the surface treatment is more pronounced at room temperature. A tentative assignment of the best treatments is offered.

I. INTRODUCTION

This semi-annual report describes the results and conclusions obtained from our continuing study of adhesive joints at cryogenic temperatures. Our previous work and that of others have shown glass fiber reinforced polymer (FRP) composites have attractive properties for cryogenic structural applications. Typically, cryogenic structures will require that composites be used in conjunction with metals. Thus, satisfactory, reliable joints are needed which must not only be able to carry high stress, but which often must be vacuum or hermetically tight as well. Adhesive bonds would be the simplest way to achieve such joints. However, such bonds are known to be sensitive to surface preparation and environmental conditions. This study has focused on selecting a representative composite and metal adherend system. The surface preparation and processing conditions were varied, and the effect on the bond strength was determined. The strength and reliability of the bond were evaluated using the short beam shear and lap shear methods at room temperature and at 4°K. The FRP composite selected was S-glass fiber in conjunction with the "Polaris" formulation of epoxy resin. The metal chosen was 6061T-6 aluminum. The method of preparation was to cure the FRP between surface-prepared plates of the alloy. This approach was selected as being the most convenient way to incorporate (1) the use of known standard materials, (2) the application of controlled, documented, and reproducible surface treatments, (3) the assessment of the potential level and uniformity of bond strengths that are practically attainable,

and (4) the evaluation of the effectiveness of the various surface treatments. The details of the methods of preparation along with some preliminary results can be found in our previous report.[1]

II. SPECIMEN PREPARATION

Fifteen plaques consisting of FRP sandwiched between the surface-prepared aluminum sheets were fabricated, each under a different set of conditions. The variations in the fabrication parameters are summarized in Table I. As may be noted in some cases, the surface treatments were held constant, but the lamination/curing procedure was altered. Among the variables explored was the application of an intermediate coating of the matrix resin in which some primer had been added. This was applied to the primed metal prior to bonding. The purpose of this was to explore how a graded system would affect the strength or uniformity of the adhesive.

These plaques were cut up to provide ca. 300 test coupons for the mechanical evaluation tests. Thus, each plaque provided ca. 20 nominally identical materials of which half were subjected to testing at room temperature, and the other half at 4°K. Similarly, each lot was divided to provide lap shear and short beam shear specimens.

III. MECHANICAL PROPERTIES

As discussed in the previous semi-annual technical report, the short beam shear test and single lap shear test were chosen to evaluate the effect of aluminum surface treatment on the interface between the metal and composite. The advantages and

TABLE I. PLAQUE PREPARATION CHART

Plaque	Surface Preparation	Laminate Preparation	Characterization
#9	1. Sanded with #1 emery paper. 2. Tri-sodium phosphate wash. 3. 60°C chromic/sulfuric acid for 15 min. 4. Distilled water rinse. 5. Air dried 6. Coated with uncured resin solution in MEK.	1. 3 layers 828/1031 prepreg layed up. 2. Placed in vacuum bag in oven at 100°F. 3. Vacuum applied temp raised slowly to 180°F. 4. Temp held at 180°F for 20 min, then raised to 220°F. 5. Held at 220°F for 1 hr. Temp raised to 125°C. 6. Held at 125°C for 1 hr, then 150°C for 1 hr. 7. Post cured 16 hrs at 175°C in air.	
#10	Same as #9 Except - 30 min in 60°C chromic/sulfuric acid.	1. 3 layers of 828/1031 prepreg layed up & laminate assembled. 2. Placed in vacuum oven at 75°C. Temp raised slowly to 125°C. 3. Cured at 125°C for 10 min under full vacuum. 4. Placed in press at 150°C, 500 psi, for 1 hr. 5. Post cured 16 hrs at 175°C in oven.	
#11	Same as #10	1. Coated plates degassed 15 min at 125°C in vacuum oven. 2. 3 layers 828/1031 prepreg layed up & laminate assembled. 3. Laminate placed in Carver press at 125°C. Pressure raised to 360 psi & held for 15 min. 4. Cured under pressure at 1 hr at 150°C. 5. Post cured in air oven at 175°C for 16 hrs.	

TABLE I - Cont'd.

Plaque	Surface Preparation	Laminate Preparation	Characterization
#12	Plaque was treated the same as #11 except that during assembly one of the prepreg sheets was inadvertently crossplied. The laminate was fully treated. When cut up, it had a good uniform cross section.		
#13	Same as #11	1. Same as #11. 2. Same as #11. 3. Placed in Carver press at 125°C and 60 psi for 15 min. 4. High pressure 500 psi and 150°C applied for 1 hr. 5. Post cured 16 hrs at 175°C in air oven.	This plaque was thick and had bubbles.
#14	Same as #9	1. 3 layers 828/1031 prepreg layed up & laminate assembled. 2. Placed in Carver press at 125°C. 3. Squeezed quickly to 500 psi, held for 15 min. 4. Held under pressure 1 hr at 150°C. 5. Post cured.	Very thin sample.
#15	Same as #9 5. Air dried in 50°C oven. 6. Coated with solventless uncured resin, paste-like mixture. 7. Resin melted on plate & was brushed on.	1. 3 layers 828/1031 prepreg layed up & laminate assembled. 2. Sandwich placed in Carver press at 125°C, squeezed down quickly down to 30 mil shims, held for 15 min, 500 psi. 3. Shims removed, pressure reapplied for 1 hr at 150°C. 4. Post cured.	Very hard to remove from press, because platens only slightly larger than sandwich.
#16	Same as #15 Except - a little loner in acid bath ≈ 45 min.	Same as #15 Except that it was pressed with shims in the large Pasadena press.	Good thickness.

TABLE I - Cont'd.

Plaque	Surface Preparation	Laminate Preparation	Characterization
#17	1. Sanded with #1 emery paper. 2. Tri-sodium phosphate wash. 3. Water rinse. 4. Chromic/sulfuric acid bath for 30 min. 5. Distilled water rinse. 6. Air dried in 60°C oven. 7 γ-AP triethoxy silane (F-primer) applied using foam sponge. 8. Plates heated on hot plate & uncured resin applied with brush.	1. 3 layers 828/1031 prepreg layed up on tacky resin. 2. Sandwich assembled. Put in Pasadena press at 125°C with 31 mil shims. Pressure applied quickly & held for 15 min. 3. Temp raised to 150°C, shims removed & pressure reapplied for 1 hr. 4. Post cured.	Good plaques. Good thickness. Low voids.
#18	Same as #17	Same as #17	Nice even plaques.
#19 #20	Except for primer: #18 γ-AP triethoxy silane #19 γ-AP methyl diethoxy silane #20 γ-AP trimethoxy silane	Except all three laminated at the same time in press.	
#21	Same as #17	Same as #17	
#22 #23 #24	Except for primer: #21 no primer #22 γ-AP triethoxy silane #23 γ-AP methyl diethoxy silane #24 γ-AP trimethoxy silane This next series was to see if a more uniform adhesion could be obtained by mixing some of the primer in the resin coating.	Except all four plaques pressed at the same time in Pasadena press. Bow in platen caused thickness variation.	

TABLE I - Cont'd.

Plaque	Surface Preparation	Laminate Preparation	Characterization
#26	Same as #21-24	Same as #21-24	
#27 #28	#26 coated with γ-AP triethoxy silane and then uncured resin.	Except pressing was done on Wabash four-post press.	
#29	#27 coated with γ-AP triethoxy silane and uncured resin with 1% triethoxy silane mixed into resin. #28 coated with γ-AP trimethoxy silane and uncured resin. #29 coated with γ-AP trimethoxy silane and a mixture of uncured resin with 1% pure γ-AP trimethoxy silane.		

disadvantages of these tests were examined. It was concluded that neither test yields a "true" value of the bond shear stress. The short beam shear specimen undergoes large deflections in the aluminum, which makes the values of the shear stress calculated from the following equation inaccurate:

$$\tau_{max} = \frac{3}{4} \frac{P}{bh} \qquad (1)$$

where P = load
b = specimen width
h = specimen height.

Furthermore, this equation was not derived for the case of specimens consisting of two different materials. Nevertheless, by calculating a "stress" from (1) above, considering the calculation basically a normalizing procedure to account for differing specimen dimensions, and noting the location of failure (i.e., interface or composite), one can compare different surface treatments.

On the other hand, the lap shear test also has disadvantages It is characterized by having a non-uniform shear stress, as well as a high value of normal stress due to bending of the joint. As stated in the previous semi-annual report, the maximum shear stress is about 2.5 times the average value. Furthermore, a normal stress is also present, acting transversely to the joint, and is equal to about one-half the longitudinal stress. With such a high normal stress present, a tendency toward adhesive failure should be noted, and this was indeed observed.

The data obtained at room temperature and in liquid helium are shown in Tables II and III and in Figs. 1 and 2. The plaque numbers refer to the surface treatments listed in Table I. In all cases, the failure mode for the lap shear test (Table II) was almost completely adhesive for the reasons previously discussed.

TABLE II. CALCULATED AVERAGE LAP SHEAR STRENGTH AT 300°K AND 4°K.
VALUES SHOWN REPRESENT MEAN AND STANDARD DEVIATION

Plaque No.	300°K Lap Shear Strength psi	300°K No. of Specimens	4°K Lap Shear Strength psi	4°K No. of Specimens
11	3090 ± 676	4	4310 ± 731	4
15	3270 ± 495	4	3610 ± 1330	4
16	2620 ± 388	3	3250 ± 1120	3
17	3820 ± 721	5	4860 ± 1000	5
18	3880 ± 436	5	4540 ± 582	5
19	3330 ± 876	5	5340 ± 502	5
20	3820 ± 583	5	4380 ± 954	5
21	2220 ± 918	5	5310 ± 1110	4
22	1690 ± 1480	4	2510 ± 965	3
23	2860 ± 394	5	5000 ± 224	3
24	3250 ± 743	5	4200 ± 764	3
26	2974 ± 822	5	3930 ± 1058	5
27	2410 ± 555	5	3960 ± 1190	3
28	2520 ± 1012	5	3800 ± 1930	4
29	2660 ± 251	5	3830 ± 550	5

TABLE III. CALCULATED SHORT-BEAM SHEAR STRENGTH AT 300°K AND 4°K. INDIVIDUAL RESULTS, MEAN, AND STANDARD DEVIATION ARE SHOWN

Plaque No.	300°K Shear Stress psi	300°K No. of Specimens	300°K Failure Mode[1]	4°K Shear Stress psi	4°K No. of Specimens	4°K Failure Mode[1]
2	8600		I	16750		C
	7830			7180		I
	4460			14280		M
	7910			19900		C
	7920			12930		I
	9010			16370		M
	9360			14490		M
	7870 ± 1617	7		14560 ± 3954	7	
5	8480		I		Not Obtained	
	8130					
	8350					
	8090					
	8260 ± 184	4				
6	10060		I			
	11240		I			
	10960		C			
	10610		I			
	10720 ± 508	4				
7	12050		C	18440		
	12080		I	18600		
	12070	2		18520	2	

(1) C = Composite Failure; I = Interface Failure; M = Mixed Failure.
(2) Tested at 77°K (N_2(l)).

TABLE III- Cont'd.

Plaque No.	300°K Shear Stress psi	300°K No. of Specimens	300°K Failure Mode[1]	4°K Shear Stress psi	4°K No. of Specimens	4°K Failure Mode[1]
11	11580 11400 10540		I ↓	14700[2] 14100[2] 13200[2]		C ↓
	11200 ± 556	3		14000 ± 755	3	
14	10680 10520 9760		I ↓	16800[2] 17000[2] 16100[2]		M ↓
	10300 ± 492	3		16600 ± 472	3	
15	11600 11300 11300		I ↓	13950[2] 14500[2] 16500[2]		M ↓
	11400 ± 173	3		15000 ± 1340	3	
16	11800 11500 10800 10600		I ↓	Not Obtained ↓		
	11200 ± 568	4				
17	12870 13290 11720 12760 13620		C M C M M	17490 12650 12900 12540 12660		M ↓ M C
	12850 ± 720	5		13650 ± 215	5	

TABLE III- Cont'd.

99<

Plaque No.	300°K Shear Stress psi	300°K No. of Specimens	300°K Failure Mode[1]	4°K Shear Stress psi	4°K No. of Specimens	4°K Failure Mode[1]
18	8240		I	13700		C
	11530		M	14960		C
	9650		I	14020		C
	8310		I	8340		I
	10040		M			
	9550 ± 1360	5		12750 ± 3000	4	
19	9300		I	2500		C
	10300			14400		M
	9870			15000		M
	10600			17600		M
	11000		↓	13300		C
	10200 ± 657	5		17000 ± 4710	5	
20	11390		M	11500		I
	11700		I	14700		M
	7500			14500		M
	10900			17100		C
	8080			17100		C
	10500		↓	16600		C
	10000 ± 1780	6		15200 ± 2170	6	
21	8780		I	15900		C
	9960			15200		C
	9660			16400		M
	5940			12200		C
	8660			16600		C
	10700		↓	18800		M
	8950 ± 1660	6		15800 ± 2160	6	

TABLE III - Cont'd.

Plaque No.	300°K Shear Stress psi	300°K No. of Specimens	300°K Failure Mode[1]	4°K Shear Stress psi	4°K No. of Specimens	4°K Failure Mode[1]
22	10400		I	13300		I
	11300		I	20100		M
	10200		I	17800		M
	5460		C	12800		M
	9850		I	11700		I
	9490		I	24900		M
	9450 ± 2050	6		16800 ± 5130	6	
23	9290		I	8880		M
	10300			8900		C
	5840			19600		M
	10000			17800		I
	9970		↓	8460		I
	9080 ± 1850	5		12700 ± 5490	5	
24	9170		I	20700		M
	10700		I	17400		C
	10400		I	11700		C
	9840		M	14100		I
	10600		I	19100		I
	10300		M	8930		I
	10170 ± 573	6		15300 ± 4540	6	
26	10700		C	12200		C
	13100			13000		C
	10600			15400		C
	9000			14700		M
	12500			11760		M
	11740		↓	14700		C
	11300 ± 14800	6		14600 ± 1900	6	

TABLE III- Cont'd.

Plaque No.	300°K Shear Stress psi	300°K No. of Specimens	300°K Failure Mode[1]	4°K Shear Stress psi	4°K No. of Specimens	4°K Failure Mode[1]
27	12200		I	13700		I
	13000		I	20100		C
	11900		T	8910		C
	11300		M	14400		M
	12300		I	19200		C
	11500		I	15900		M
	12000 ± 612	6		15400 ± 4070	6	
28	11600		C	12100		C
	11700		I	15400		C
	11500		"	13900		C
	10700		"	16400		M
	11300		"	14500		M
	10600		"	15000		I
	11200 ± 4720	6		14600 ± 1470	6	
29	10800		I	15400		C
	11800		"	18700		M
	11300		"	14800		C
	10800		"	13400		"
	11200		"	16100		"
	10700		"	14500		"
	11000 ± 420	6		15500 ± 1820	6	

Occasionally, small pieces of resin would adhere to the aluminum surface. In contrast, the failure modes for the short beam shear specimens differed, and the significance of this is discussed below.

Because of the mass of data involved, use was made of an available computer program to aid in the analysis. All the data were analyzed three ways, as described below. In all cases, a group of data was considered to be the results of specimens tested at a given temperature and specified surface treatment.

1. The mean, variance, standard deviation, and standard deviation of the mean were computed for each group of data (see Tables II and III).
2. A standard one-way analysis of variance was conducted for each of the four groups of data at 300°K and 4°K for both the lap shear and short beam shear tests.
3. A Student's t test was run for each set of treatments tested at 300°K and 4°K.

The results of this analysis can be summarized as follows:

A. Lap Shear Test

- At 300°K there was a difference between groups at a 89.5% confidence level.
- At 4°K there was a difference between groups at a 98.8% confidence level.
- Between 300°K and 4°K, eight groups had a significant difference above the 90% level, and seven below.

B. Short Beam Shear Test

- At 300°K there was a difference between groups at a 100% level.
- At 4°K there was a difference between groups at a 70% level.
- Between 300°K and 4°K, fourteen groups had a significant difference above 90%, and ten below.

These results confirm the general impression received when one examines Figs. 1 and 2. Although the means in both sets of tests are higher (stronger joints) at the lower temperature, the scatter in the data tends to prevent significant differences. In the case of the lap shear tests, if the results for one treatment (#22) were eliminated, a significant difference would no longer exist between groups either at 300°K or 4°K. However, we have no independent basis for discarding the data for #22.

The short beam shear tests are of more interest. It may be noted that the failure at room temperature generally occur at the interface with a relatively small spread in data, while at 4°K the failure is generally cohesive or mixed, with a larger spread in the data. Furthermore, from the analysis of variance, a highly significant difference exists between groups at room temperature, while at 4°K the difference between groups is much less significant. This is consistent with the observation that at 4°K the failure is generally governed by the composite, and thus is insensitive to surface treatment. At room temperature, however, the effect of surface treatment is more obvious because of the interfacial aspects of the failure. This also leads to the happy conclusion that, at 4°K, interface effects are less important than at 300°K. This implies that bonding at liquid helium temperatures may not be as difficult than at higher temperatures.

There appears to be little correlation between the results of the lap shear tests and the short beam shear tests. The former exhibits considerably greater variance than the latter. As discussed above, the stress conditions are quite different in these two situations and, in turn, results in differing failure modes. While this may suggest the need of a better measuring technique, such as torque shear, it also indicates that it is important to devise evaluation tests that closely simulate actual conditions in an engineering application.

On the basis of the limited results to date, plaques 11 and 17 resulted in the best overall behavior, depending on whether the emphasis is on bond strength or uniformity; the former being the more uniform, and the latter having the greater absolute average strength. These comparisons are made on the basis of the relative rankings under the four test conditions (4°K, 300°K, lap shear, and short beam shear). However, more measurements should be made before making a firm recommendation in view of the relatively small population tested. Finally, it should be noted that the merits of the various surface treatments may be expected to reveal themselves more prominently under thermal cycling conditions. Such tests were beyond the scope of the present work.

REFERENCE

1. W.B. Hillig, Principal Investigator, previous semi-annual report under Contract CST-8300 for the period 9/1/74 through 2/28/75, "Composite Structural Materials Investigation at Cryogenic Temperatures."

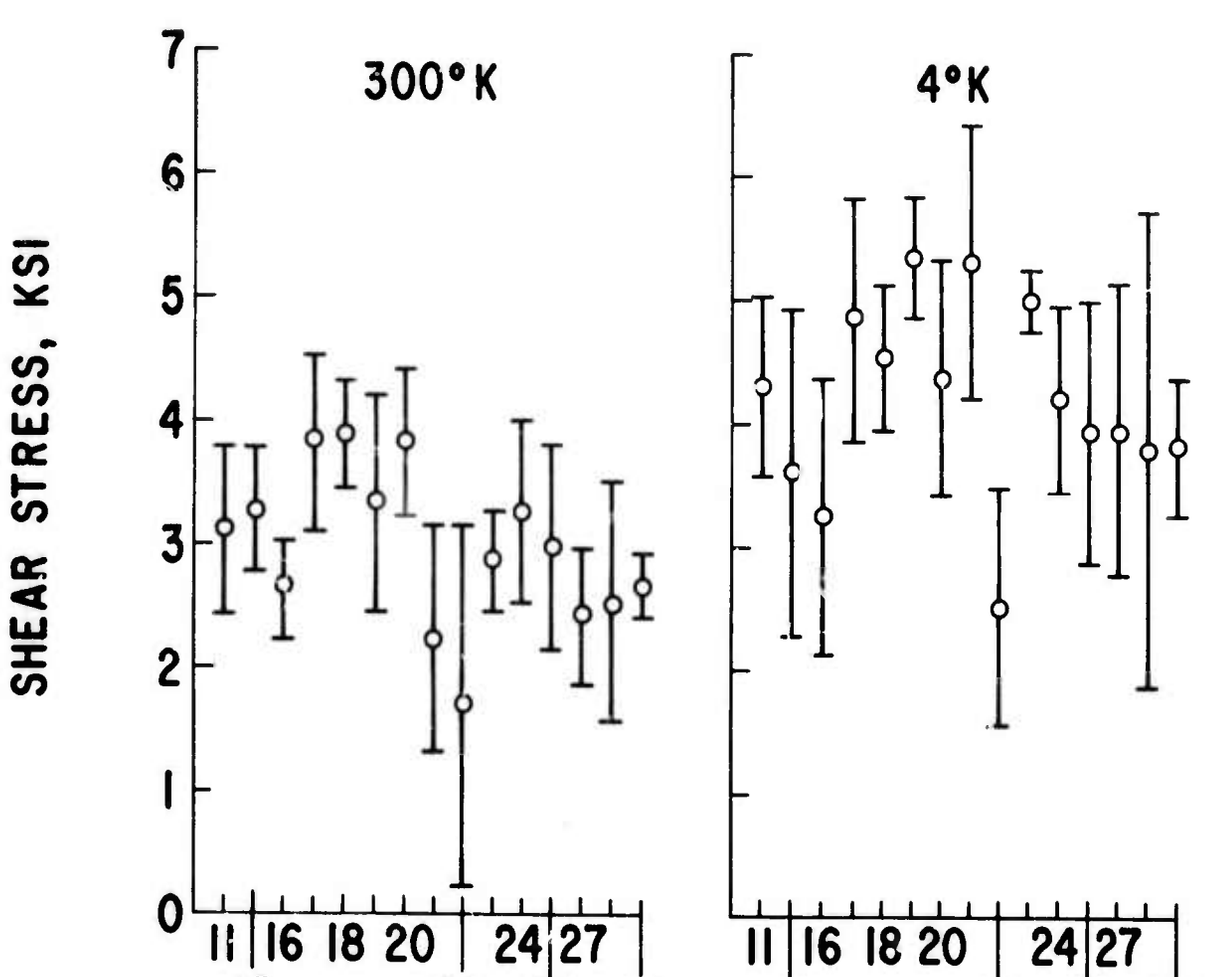

FIG. 1 LAP SHEAR STRESS AT 300°K AND 4°K FOR VARIOUS SURFACE TREATMENTS. RANGE SHOWN IS THE STANDARD DEVIATION.

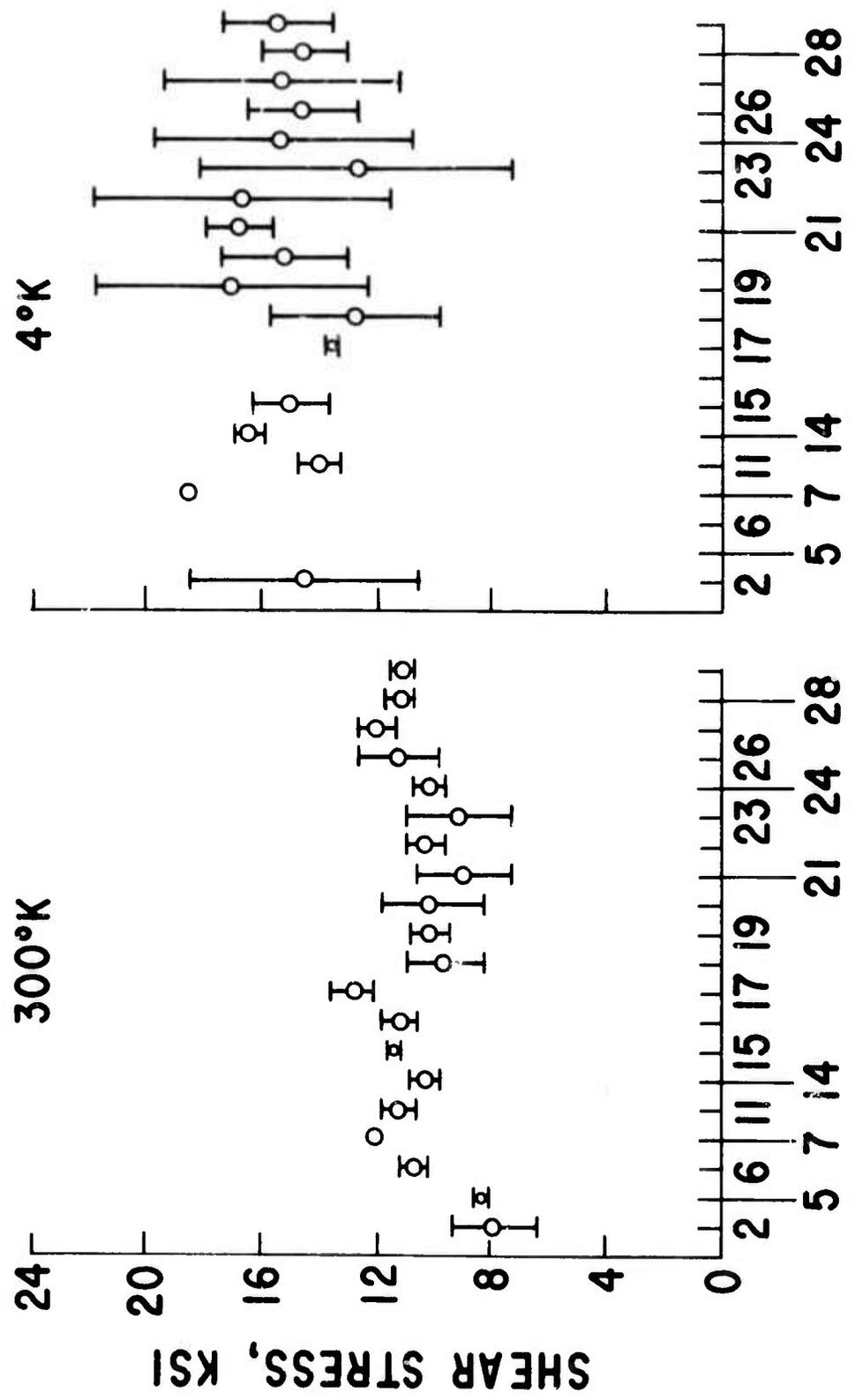

FIG. 2 SHORT-BEAM SHEAR STRESS AT 300°K AND 4°K FOR VARIOUS SURFACE TREATMENTS. RANGE SHOWN IS THE STANDARD DEVIATION.

MCR-74-89 (Issue 4)

Annual
Technical
Report

November 1975

STUDY OF FRACTURE BEHAVIOR OF METALS FOR SUPERCONDUCTING APPLICATIONS

Sponsored by Advanced Research Projects Agency
ARPA Order No. 2569, Program Code 4D10
Contract Monitor: Cryogenics Division
National Bureau of Standards, Boulder, Colo. 80[illegible]2
NBS Contract No. CST 8301
Period of Performance: 9/19/74 to 11/3/75

Fred R. Schwartzberg
Program Manager
303-979-7000, Ext 2365

Ted Kiefer
Principal Investigator
303-979-7000, Ext 2886

MARTIN MARIETTA CORPORATION
P. O. Box 179
Denver, Colorado 80201

FOREWORD

This report describes technical activities conducted by the Denver Division of Martin Marietta during the period 19 September 1974 through 3 November 1975 under National Bureau of Standards (NBS) Contract CST-8301.

The views and conclusions contained in this document are those of the authors and should not be interpreted as necessarily representing the official policies, either expressed or implied, of the Advanced Research Projects Agency or the U. S. Government.

CONTENTS

Figure

Table

I. INTRODUCTION

The information essential for optimum state-of-the-art superconductive machinery design is extensive and varied. With the goal of building this machinery as efficiently and expeditiously as possible, a number of programs were initiated to obtain physical and mechanical properties of judiciously-selected candidate materials that might prove applicable to superconductive cryogenic use. The lack of sufficient fatigue-life data on several candidate materials in the temperature range of 293 to 4°K prompted the initiation of the work being done in this program.

The purpose of this program was to obtain preliminary characterization of unnotched and notched (K_t = approximately 3.1) fatigue behavior using parent metal round bar specimens under fully reversed stressing, R = -1, if technically feasible. The five alloys evaluated follow:

1) 304L stainless steel, annealed
2) 310 stainless steel, annealed
3) 21-6-9 stainless steel, annealed
4) A-286 stainless steel, STA
5) 718 nickel alloy, STA

II. MATERIALS

Certified test data for the five alloys are given in Table II-1.

Stock of each alloy was obtained in ½-in. diameter round bar. The A-286 and 718 alloys were procured in a solution-treated condition; aging was performed by Martin Marietta. The aging schedule was as follows:

Alloy	Aging Treatment
A-286	16 hr at 1325°F/aircool
718	8 hr at 1325°F/furnace cool 2 hr to 1150°F/hold for 8 hr/aircool

Tensile test specimens were machined from the ½-in. diameter stock. The specimen configuration is shown in Figure II-1. The tensile and hardness properties for the alloys tested are given in Table II-2.

Metallographic examination was performed on 304L, 310, 21-6-9, A-286, and 718 alloys. Typical microstructures were observed for these alloys and conditions. Micrographs for each material are shown in Figures II-2 through II-6. The grain size obtained for these alloys is listed below.

Alloy	Condition	Grain Size
304L stainless steel	Annealed	6-7
310 stainless steel	Annealed	6
21-6-9 stainless steel	Annealed	8
A-286 stainless steel	STA	8
718 nickel alloy	STA	8

Table II-1 Certified Test Report Data

Material	Diameter, inch	Heat No.	Condition	Chemical Analysis	Mechanical Properties at Room Temp			
					Tensile Strength, ksi	Yield Strength, ksi	Elongation, %	R. A. %
21-6-9	½	636255	Annealed	20.20 Cr, 9.00 Mn, 7.15 Ni, 0.74 Si, 0.034 C, 0.024 P, 0.005 S, 0.20 Mo, 0.31 Cu, 0.30 N	117	95	45	73
304L	½	66599	Annealed	18.32 Cr, 9.66 Ni, 1.59 Mn, 0.53 Si, 0.29 MO, 0.23 Cu, 0.20 Co, 0.034 P, 0.018 C, 0.010 S	86.6	54.8	62.5	77
310	½	55748	Annealed	24.39 Cr, 20.82 Ni, 1.35 Mn, 0.67 Si, 0.37 Cob, 0.27 Mo, 0.24 Cu, 0.04 C, 0.030 S, 0.025 P	96.2	74	36	57
718	½	69F6E4	STA	53.96 Ni, 18.23 Cr, 17.61 Fe, 5.01 Cb + Ta, 3.01 Mo, 0.98 Ti, 0.57 Al, 0.23 Si, 0.15 Cu, 0.14 Mn, 0.05 Co, 0.03 C, 0.005 S	203	170	23	43
A-286	½	G8549K5	STA	24.79 Ni, 14.38 Cr, 2.30 Ti, 1.41 Mo, 1.27 Mn, 0.66 Si, 0.25 Va, 0.23 Al, 0.05 C, 0.019 S, 0.018 P, 0.0053 B	162.3	106.3	23.2	46

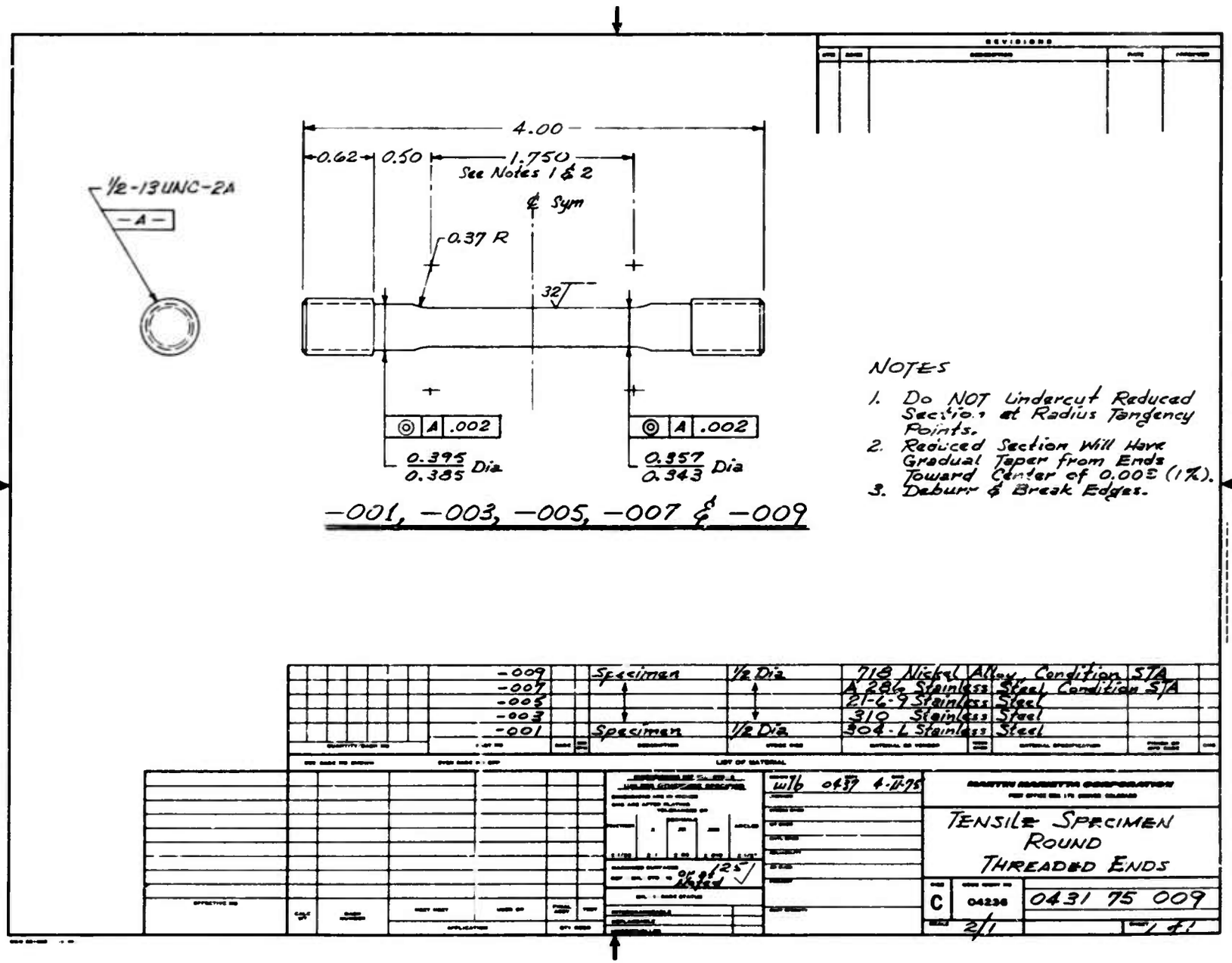

Figure II-1 Tensile Test Specimen

Table II-2 Tensile and Hardness Data at 293°K

Alloy	Ultimate Strength, ksi	Yield Strength, ksi	Elongation, %	Reduction in Area, %	Hardness, Rockwell
21-6-9	117.7	87.3	43	75	100 R_B
304L	87.7	56.6	56	81	88 R_B
310	102.1	88.6	26	69	97 R_B
A-286	161.6	126.3	22	46	35 R_C
718	197.1	158.9	22	46	42 R_C

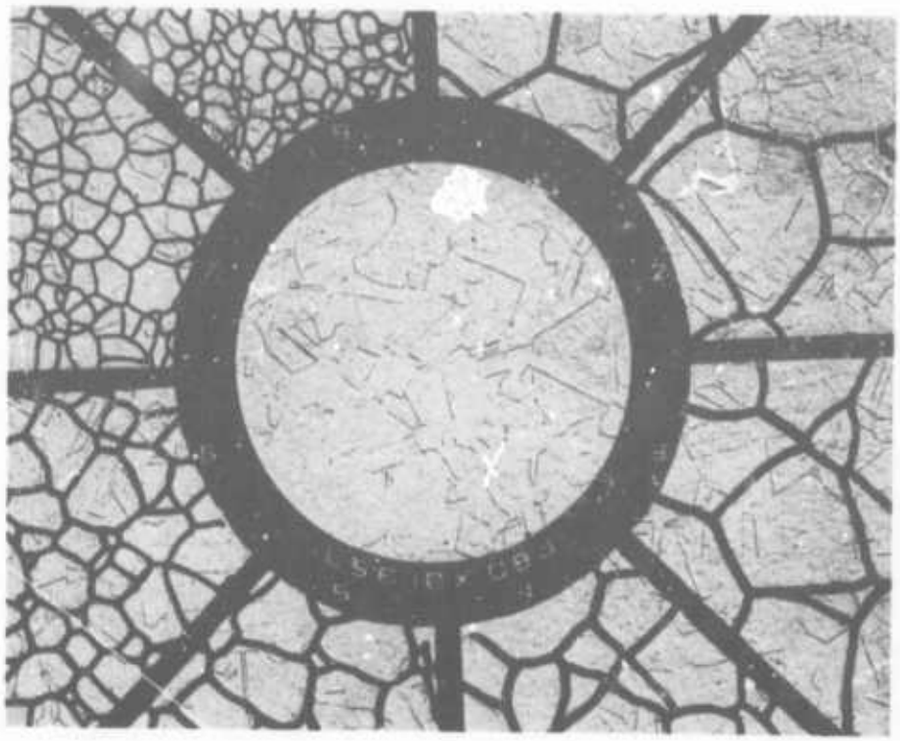

100X

400X

Figure II-2 Microstructure of 304L Annealed Stainless Steel

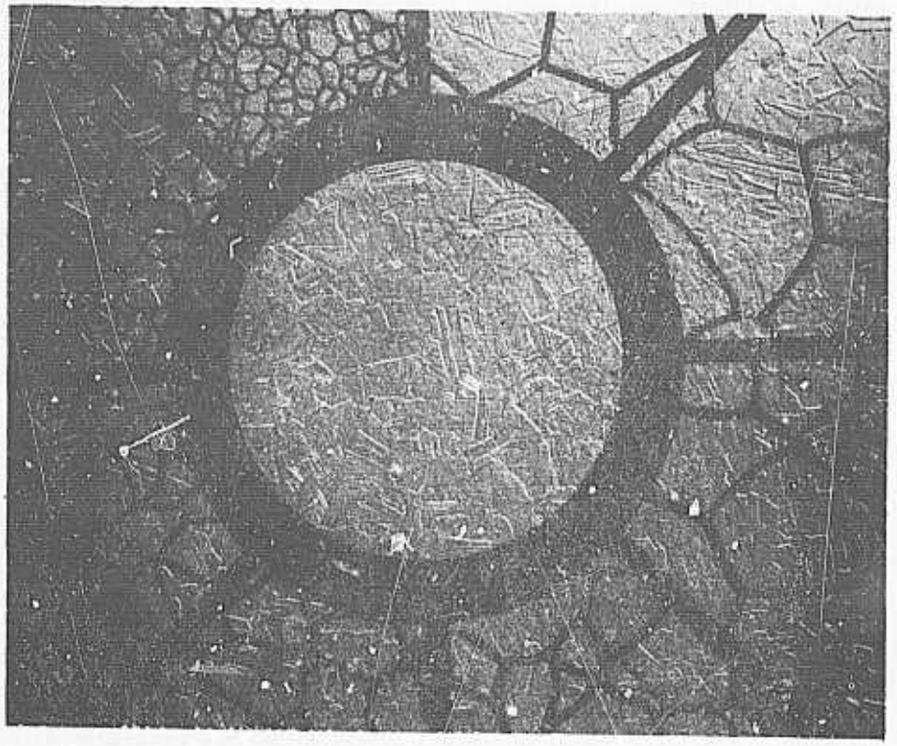

100X

400X

Figure II-3 Microstructure of 310 Annealed Stainless Steel

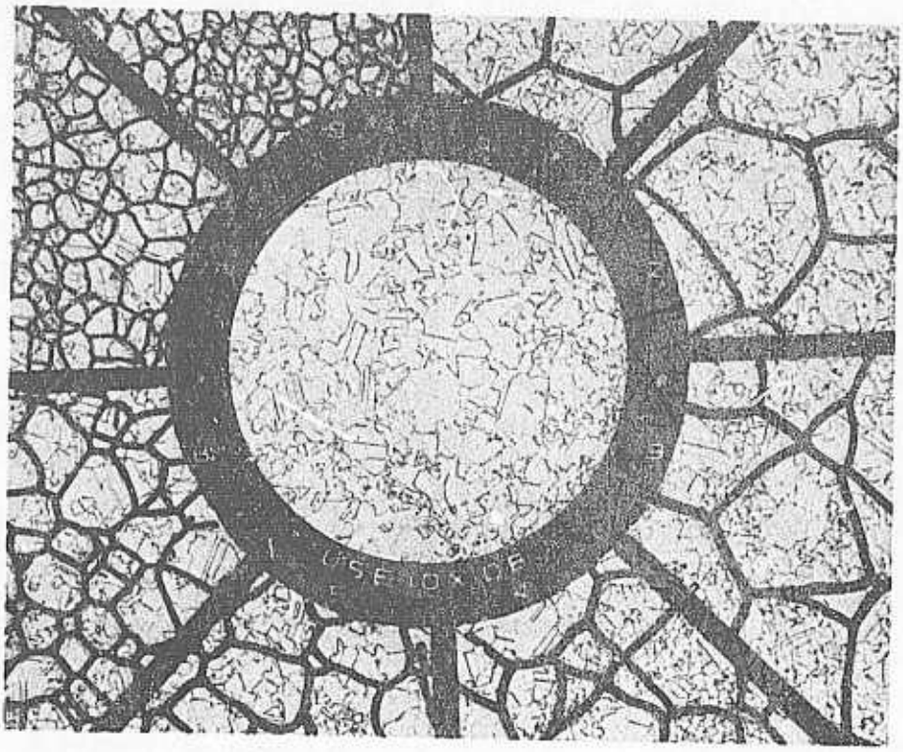

100X

400X

Figure II-4 Microstructure of 21-6-9 Annealed Stainless Steel

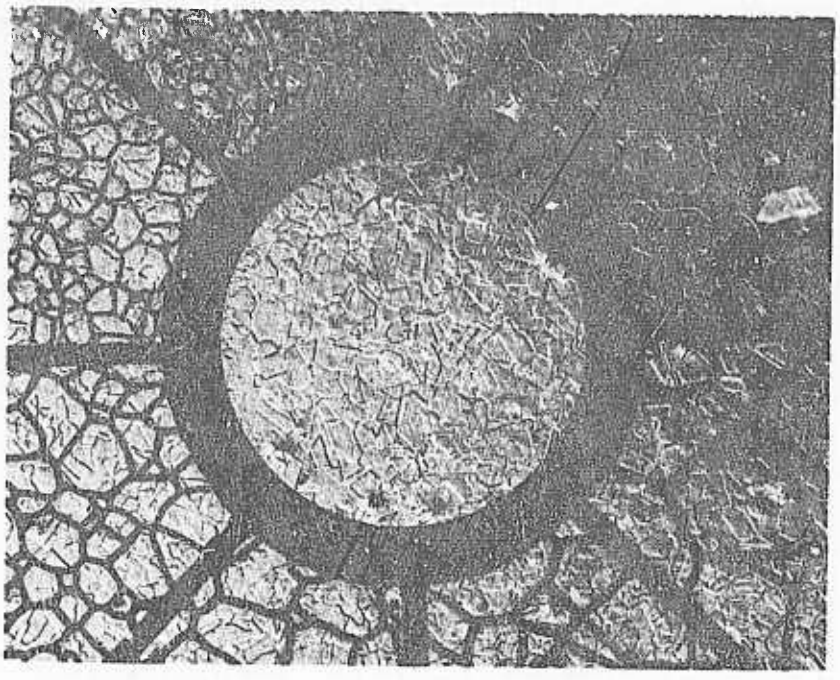

100X

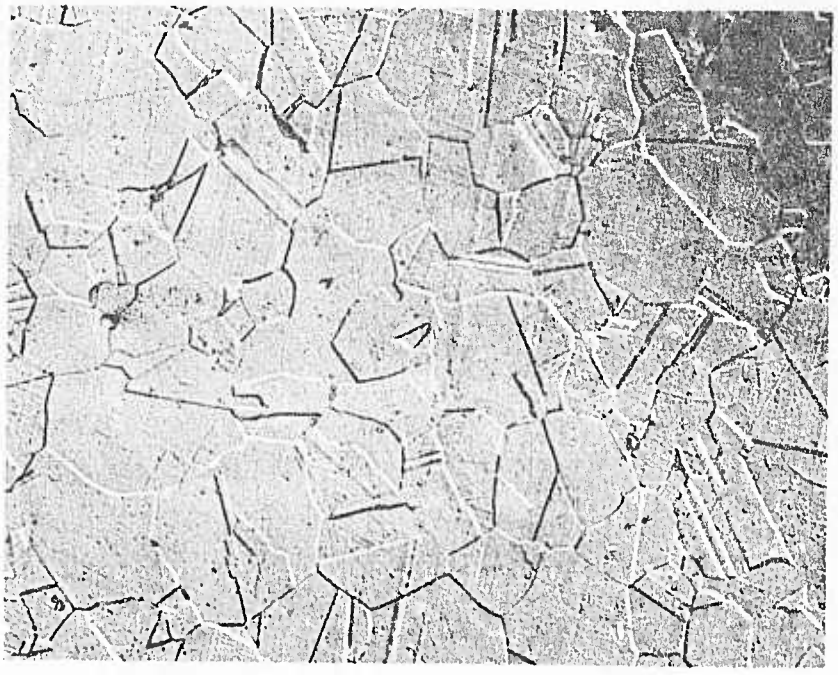

400X

Figure II-5
Microstructure of A-286 Solution Treated and Aged Stainless Steel

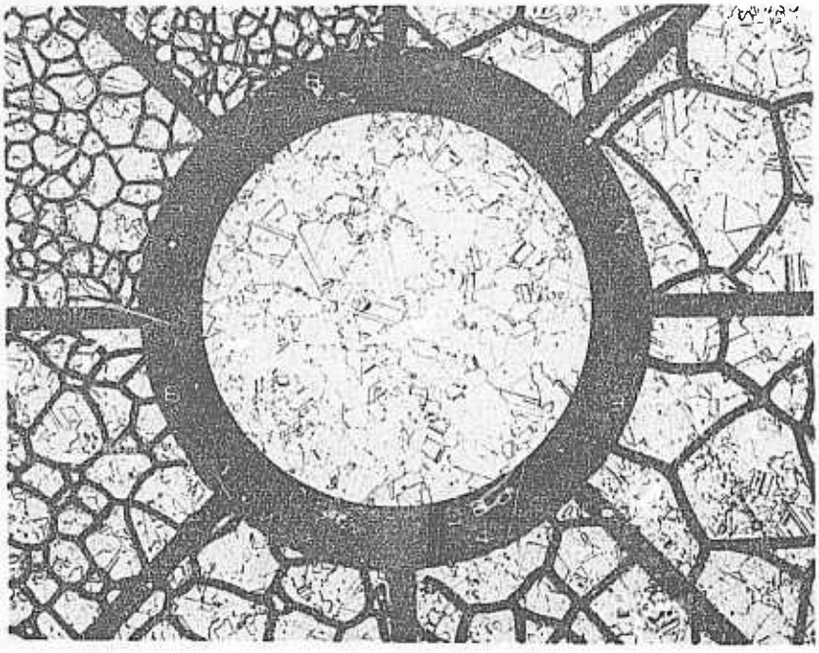

100X

400X

Figure II-6
Microstructure of Solution Treated and Aged 718 Nickel Alloy

III. TESTING TECHNIQUES AND APPARATUS

This chapter describes the specimen geometries selected and testing apparatus and techniques used to obtain the data presented in this report.

The two principal specimens used for this program are unnotched and notched fatigue types. The specimen configurations are shown in Figures III-1 and III-2 and were chosen to accomodate fully-reversed axial loading and to provide accuracy of alignment. The design incorporates a long, smooth gage with a "mild" radius and a bearing shoulder at the end of the thread section for alignment and locking, as opposed to aligning on the threads. The system is advantageous because only two close tolerance alignment surfaces are required and failure within the prescribed area of the gage is assured giving much more representative fatigue data. The specimen, when locked with a preloaded nut at each end of the threaded bar, can be subjected to a fully reversed tension compression loading cycle that is continuous through zero.

The notched specimen configuration (Figure III-2) has a theoretical stress concentration factor (K_t) equal to 3.1. The K_t of 3.1 is a moderate concentration factor and allows direct correlation with a large portion of published data. In practice, the root of each notch was dressed and polished using a 0.020-in. diameter stainless steel wire coated with 1-micron diamond paste. The coated wire was drawn through the notch

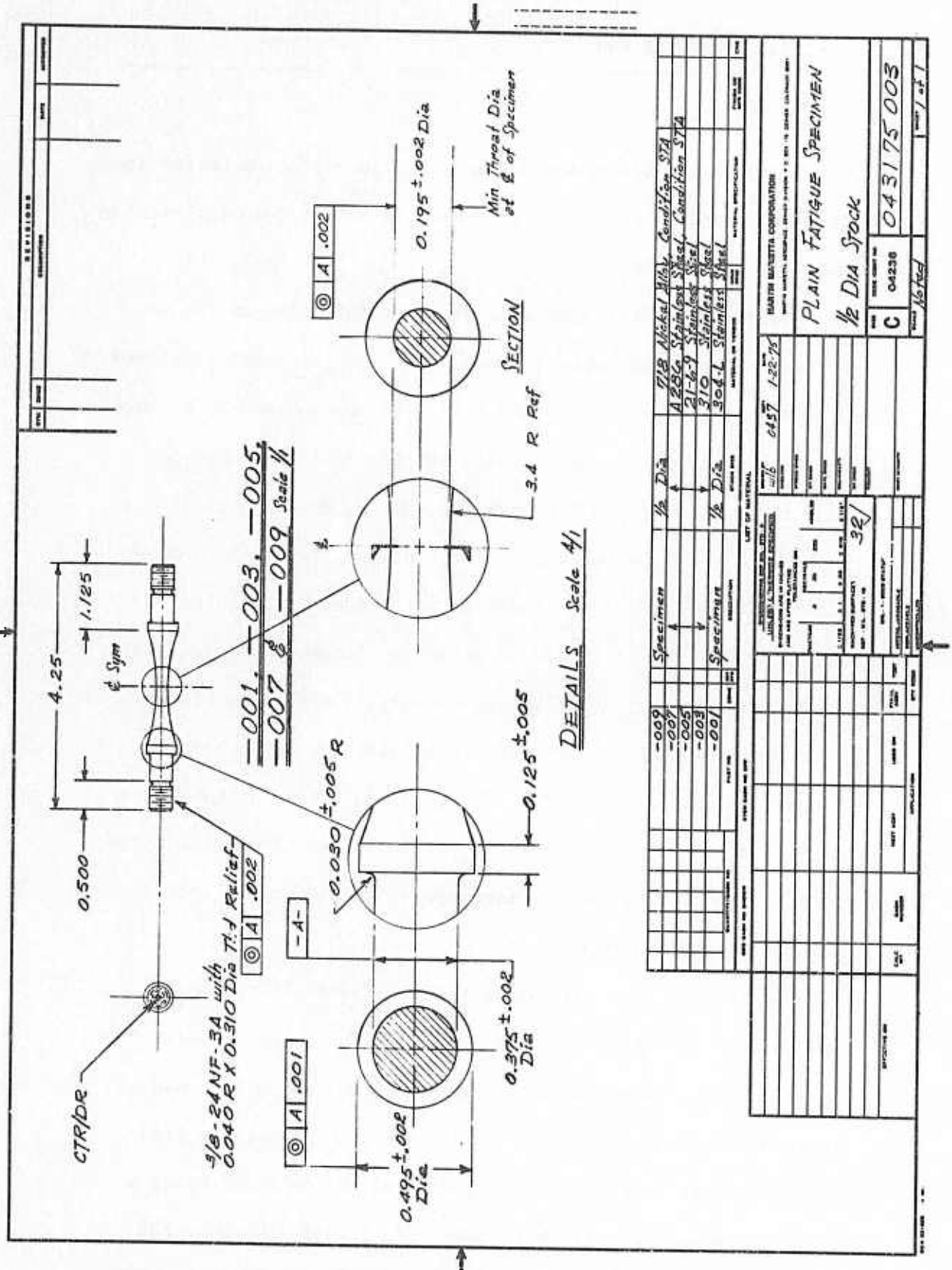

Figure III-1 Plain Fatigue Specimen

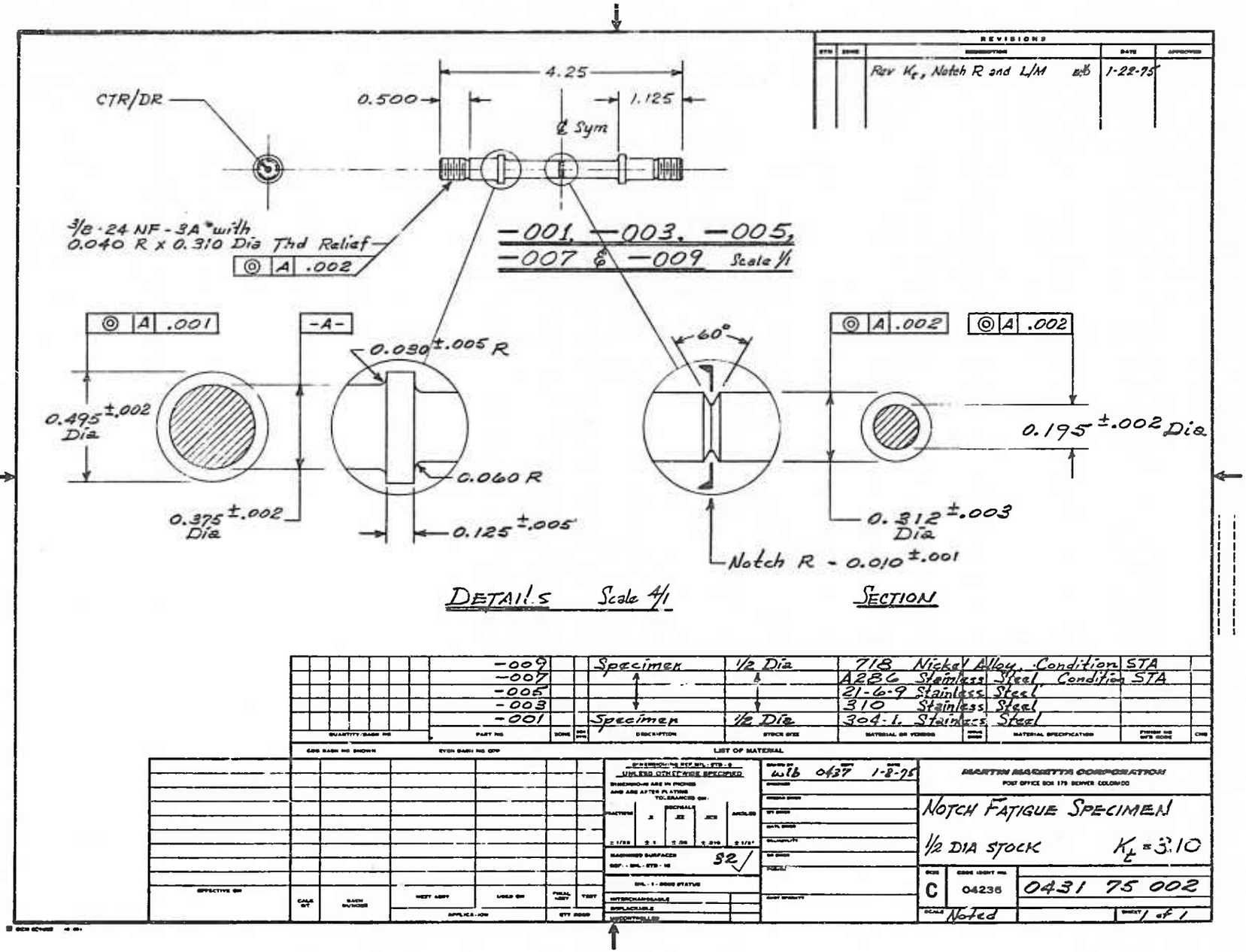

Figure III-2 Notched Fatigue Specimen

while the specimen rotated in a lathe at approximately 150 rpm. This notch dressing procedure was uniformly applied to all notched specimens and contributed to more consistent results and smaller data scatter.

The smooth, round bar fatigue specimens were polished after machining using 240 to 320 grit polishing paper (the courseness of the initial rough polishing paper depended on the alloy hardness and machined surface roughness in the gage section) and then using 320 and 600 grit paper followed by a felt wheel and 1-micron diamond paste. The polishing paper was bonded to a rubber sanding disc mounted in a small Dumore grinding tool. As the specimen is rotated at approximately 350 rpm between lathe centers, the periphery of the spinning (approximately 2000 rpm) sanding disc contacts the specimen gage section with axial strokes. The same procedure was used with all grits. The final polish used a 2-in. diameter felt wheel mounted in a Dumore grinding tool and loaded with 1-micron diamond paste. As the specimen is rotated between lathe centers at approximately 150 rpm, the spinning (approx 2000 rpm) impregnated felt wheel contacts the specimen gage section with axial strokes. This polishing technique produces a mirror finish in which any remaining polishing marks are in an axial direction that will have minimal effect on axial fatigue test results.

Fatigue testing at 293°K was performed using an axial loading rotating-eccentric mass Baldwin Sonntag SF-10 U machine (Figure III-3) while the 77°K and 4°K testing used electronically-controlled and hydraulicly actuated MTS machines. Figure III-4 shows the 77°K test setup with a cutaway in the liquid nitrogen container so that the complete load train is visible.

The critical alignment between test fixture and specimen was obtained using a strain-gage alignment cell. This alignment was maintained to within 100μ in. with periodic alignment checks.

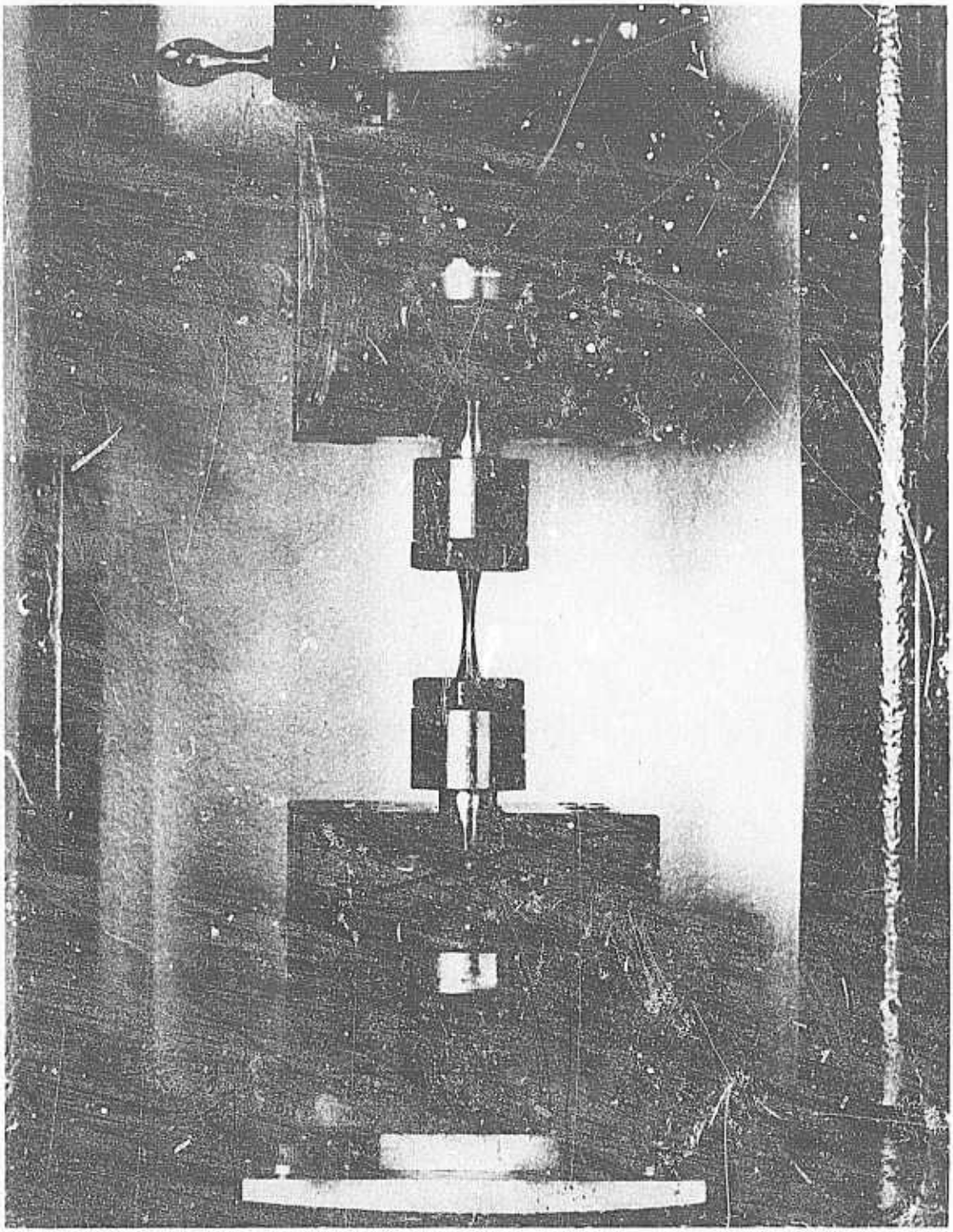

Figure III-3 293°K Fatigue Test Setup in Baldwin Sonntag SF-10U Machine

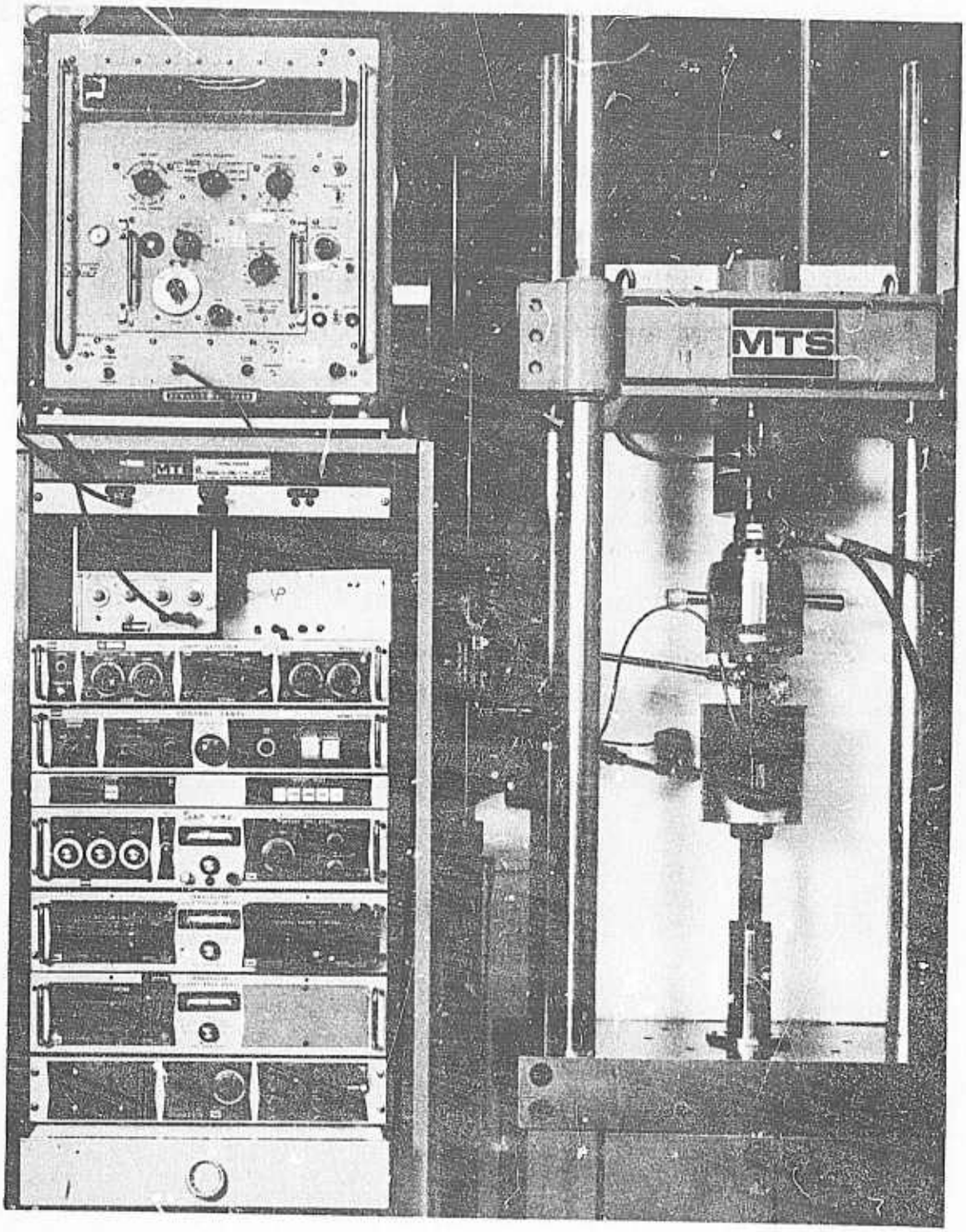

Figure III-4 77°K Fatigue Test Setup in MTS Machine (liquid container cutaway to show specimen in place)

The liquid helium test apparatus was constructed specifically for this work. A compression cage arrangement was used to avoid heat transfer losses with a design that uses a load link through the bottom of the cryostat. A long cage was used to permit long time testing with minimum refilling. The maximum stress capability of the system for the specimen diameter used was 150,000 psi. A photograph of the system is shown in Figure III-5, and a diagram of the setup is shown in Figure III-6. The diagram shows a cutaway of the cryostat and compression cage with an enlargement showing installation of the specimen. Cyclic loading was achieved using an activator removed from one of our MTS closed-loop servohydraulic testing machines and mounting it above the cryostat as shown in Figure III-5.

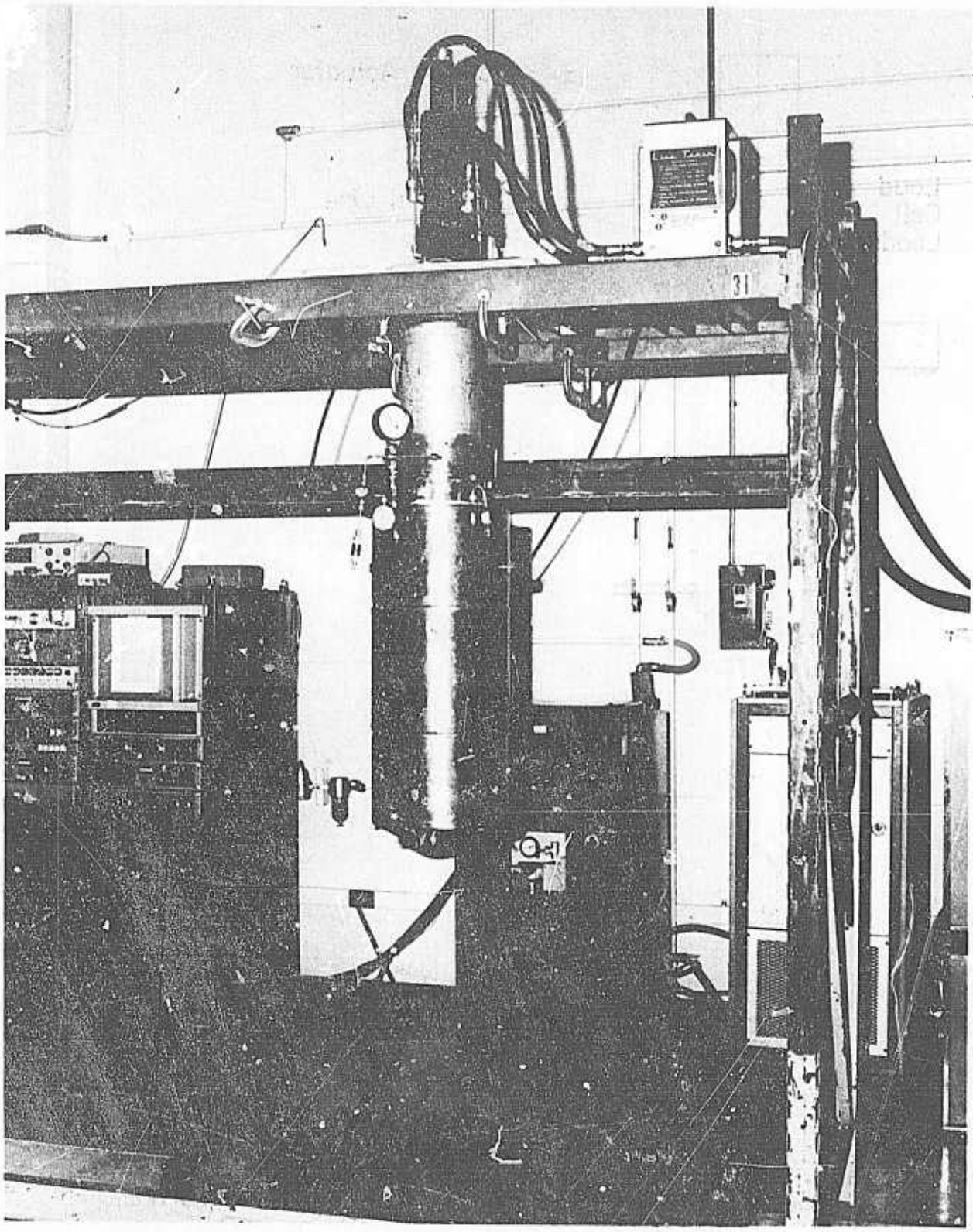

Figure III-5
4°K Fatigue Test Setup Using MTS Components in a Modified Machine

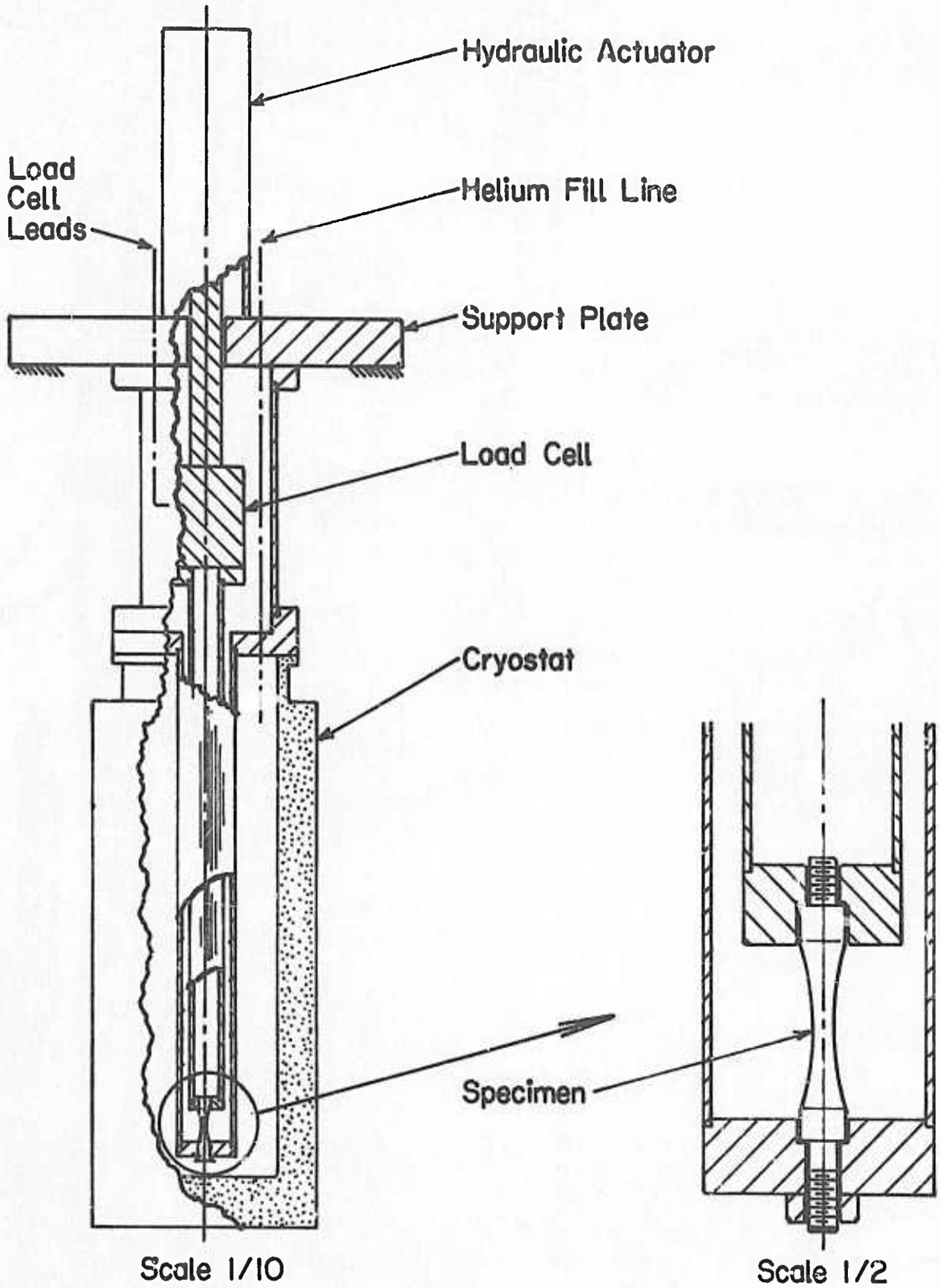

Figure III-6 Cutaway Diagram of 4°K Fatigue Test Setup

IV. EXPERIMENTAL TEST RESULTS

Fatigue behavior of each of the five alloys was characterized at 293, 77, and 4°K. Because of the extremely high cost of liquid helium and the large quantities required to obtain long time fatigue data, the number of tests at 4°K were kept to the minimum necessary to obtain characterization of behavior. Tests at 293°K and 77°K were terminated at 2 - 3 x 10^6 cycles; at 4°K, tests were discontinued if failure did not occur in 1 - 2 x 10^6 cycles.

Data is presented in tabular and graphical form as follows:

Alloy	Condition	Table	Figure
304L	Unnotched	IV-1	IV-1
	Notched	IV-6	IV-6
310	Unnotched	IV-2	IV-2
	Notched	IV-7	IV-7
21-6-9	Unnotched	IV-3	IV-3
	Notched	IV-8	IV-8
A-286	Unnotched	IV-4	IV-4
	Notched	IV-9	IV-9
718	Unnotched	IV-5	IV-5
	Notched	IV-10	IV-10

A. UNNOTCHED FATIGUE TESTS

Data for 304L (Figure IV-1, Table IV-1) show very little stress dependency of fatigue life at 293°K. Fatigue life at this temperature decreases from 40 ksi at 10^4 cycles to 36 ksi at 2 x 10^6 cycles. Fatigue strength increases appreciably between room temperature and 77°K, and additionally with a decrease in temperature from 77°K to 4°K. At the cryogenic temperatures, the curves show a moderate stress dependency of life. For the longer

cyclic lives, the fatigue strength at cryogenic temperatures is approximately twice that at room temperature.

Alloy 310 exhibits a long time fatigue strength at 293°K similar to that of 304L, but a more characteristic stress dependency to life, with a decrease in fatigue strength of almost 50% for low cycle versus high cycle life (Figure IV-2, Table IV-2). The cryogenic behavior of the 310 appears generally similar to the 304L, except that the curves are somewhat flatter. The strengthening with reduction in temperature is also similar to that of 304L.

The 21-6-9 stainless steel (Figure IV-3, Table IV-3) exhibits a rather linear loss of fatigue strength with increasing cyclic exposure at 293°K. Although the properties are similar to 310 for cyclic life up to 10^5, the strength above 10^6 cycles is superior to the 310 alloy. A significant strengthening (slightly greater than double) occurs with decreasing temperature. The properties at 4°K are slig' ·ly higher than those at 77°K.

The higher strength, solution treated and aged, A-286 stainless steel exhibits much higher strength properties than the annealed alloys previously discussed. The 293°K curve shows a knee in the curve between 10^5 and 10^6 cycles. The fatigue strength at 2×10^6 cycles is approximately 50% higher than that observed for the 300 series alloys. Fatigue strength increases with reduction in temperature (Figure IV-4, Table IV-4).

Alloy 718 (Figure IV-5, Table IV-5) exhibits a knee shaped curve at 293°K. The fatigue strength at 2 x 10^6 cycles (∿ 68 ksi) is the highest of the five alloys tested. At 77°K, significant strengthening occurs. The stress requirement at 4°K exceeded the capability of the apparatus, hence, virtually no data at this temperature was obtained.

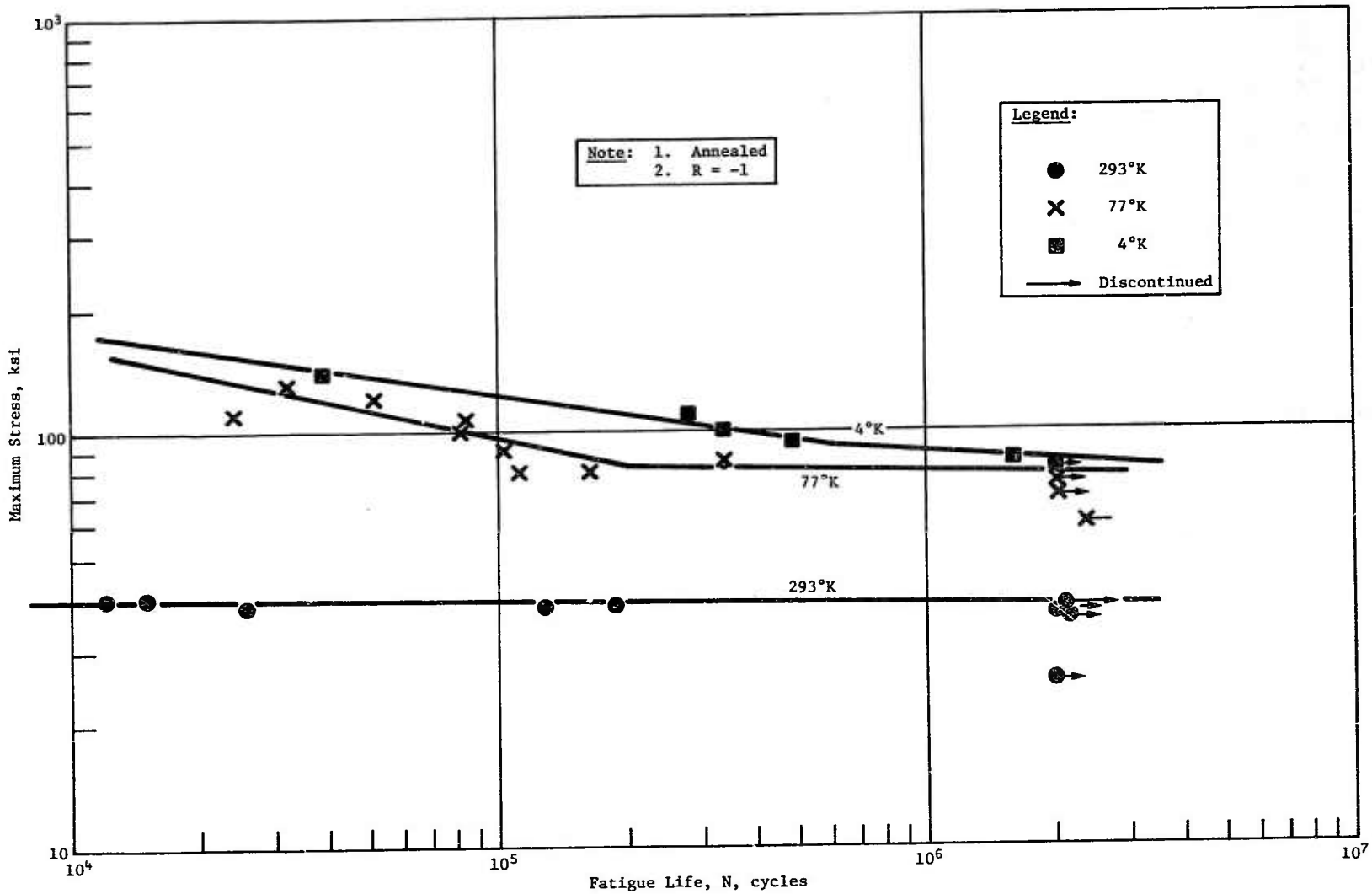

Figure IV-1 Unnotched Fatigue Life Curves for 304L Stainless Steel

Table IV-1 Unnotched Fatigue Life Data for 304L Stainless Steel

293°K		77°K		4°K	
Stress, ksi	Cycles to Failure x 10^3	Stress, ksi	Cycles to Failure x 10^3	Stress, ksi	Cycles to Failure x 10^3
42	1	130	32	140	39
40	12	120	51	110	277
40	15	110	24	100	341
38	26	107	85	93	486
		100	81		
38	127	90	103	85	1612
38	190	85	333	80	2000*
		80	111		
37	2200*	80	166		
36	2000*	75	2000*		
35	2200*	70	2000*		
25	2000*	60	599†		
		60	2300*		
		40	2000*		

Annealed
R = -1
*Discontinued
†Broke in grip section.

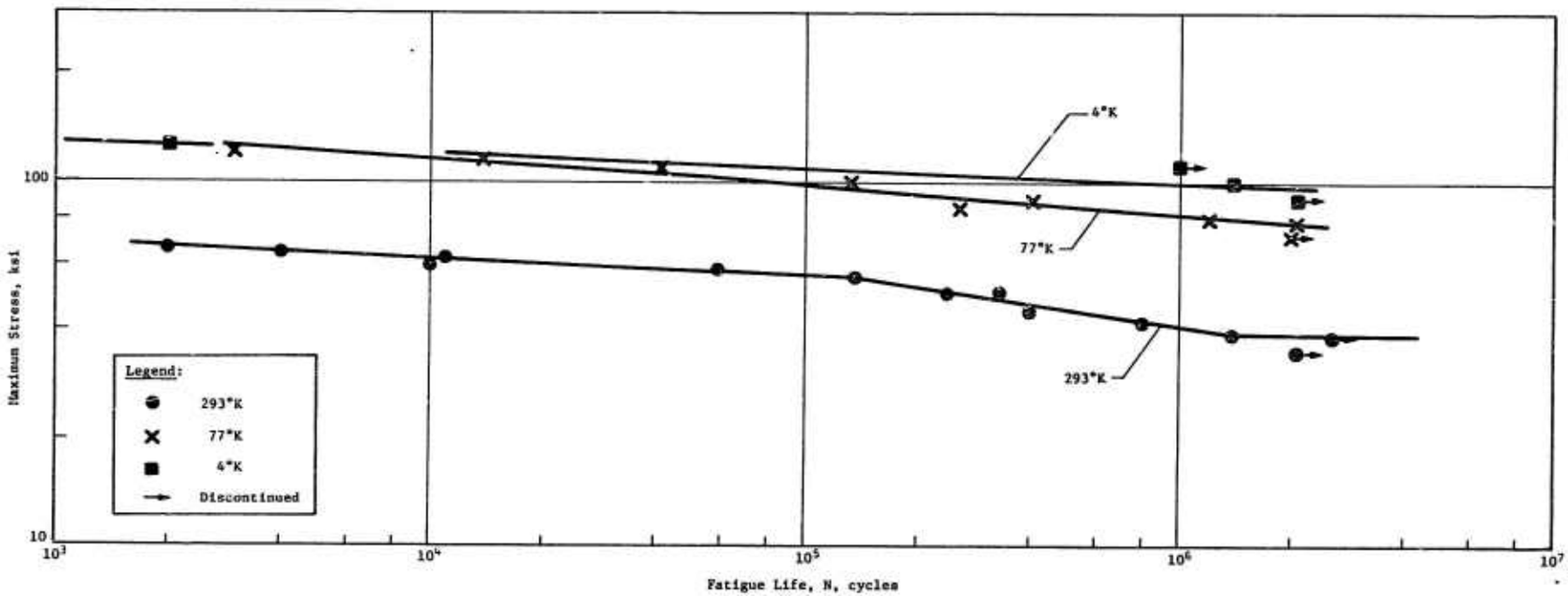

Figure IV-2 Unnotched Fatigue Life Curves for 310 Stainless Steel

Table IV-2 Unnotched Fatigue Life Data for 310 Stainless Steel

293°K		77°K		4°K	
Stress, ksi	Cycles to Failure x 10^3	Stress, ksi	Cycles to Failure x 10^3	Stress, ksi	Cycles to Failure x 10^3
67	2	120	3	130	2
65	4	114	14	120	1
62	11	110	44	110	1000*
60	10	100	134	100	1389
58	59	90	410	90	2100*
55	138	87	111†		
50	242	85	260		
50	330	80	1220		
45	399	77	2180		
42	800	72	2000*		
39	1398				
38	2600*				
35	2100*				

Annealed
R = -1
*Discontinued
†Broke in grip section.

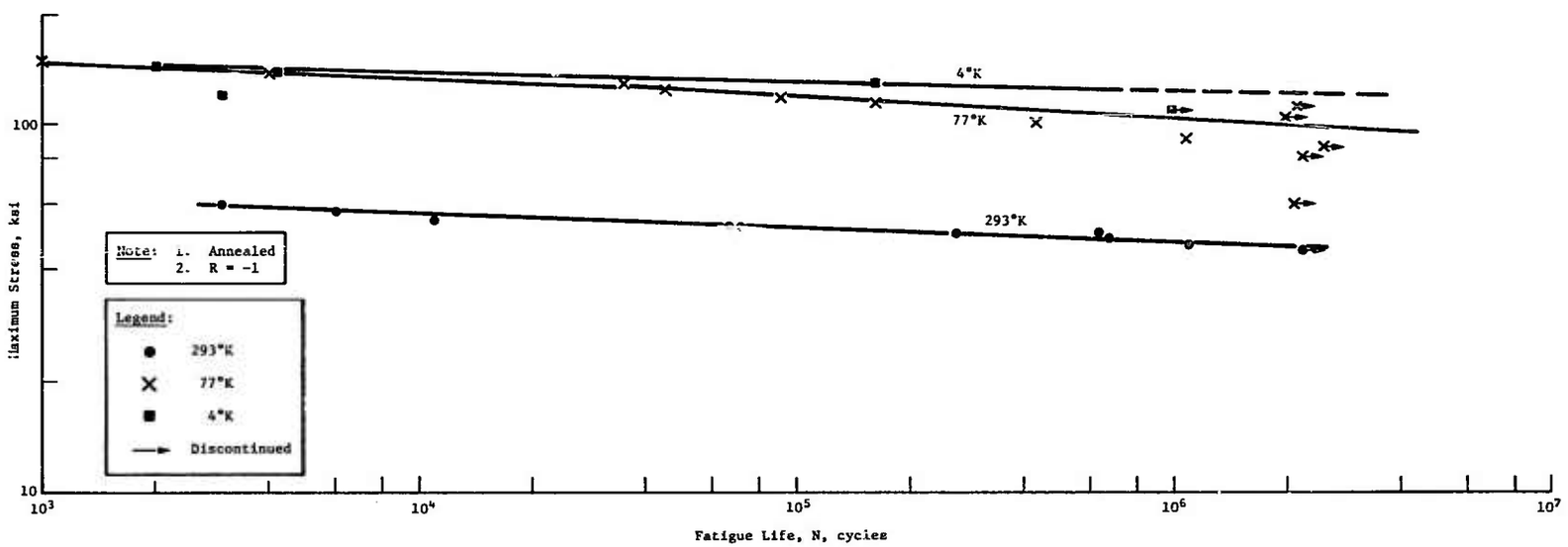

Figure IV-3 Unnotched Fatigue Life Curves for 21-6-9 Stainless Steel

Table IV-3 Unnotched Fatigue Life Data for 21-6-9 Stainless Steel

293°K		77°K		4°K	
Stress, ksi	Cycles to Failure x 10^3	Stress, ksi	Cycles to Failure x 10^3	Stress, ksi	Cycles to Failure x 10^3
60	3	150	1	145	2
57	6	150	1	140	4
54	11	140	4	130	161
52	67	130	35	120	3
52	72	125	45	110	1000*
50	264	120	91		
50	626	115	162		
48	676	110	2100*		
46	1100	105	2000*		
45	2200*	100	431		
		90	1008		
		85	2500*		
		80	2200*		
		60	2100*		

Annealed
R = -1
*Discontinued

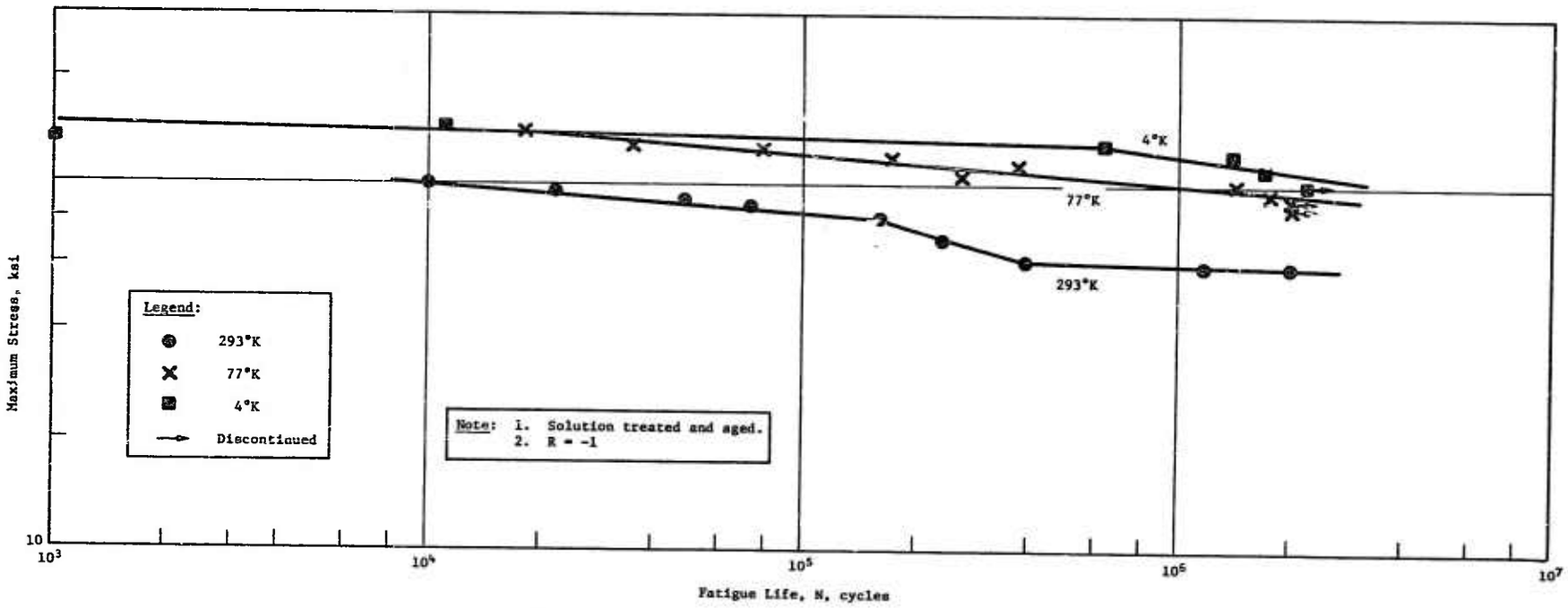

Figure IV-4 Unnotched Fatigue Life Curves for A-286 Stainless Steel

Table IV-4 Unnotched Fatigue Life Data for A-286 Stainless Steel

293°K		77°K		4°K	
Stress, ksi	Cycles to Failure x 10^3	Stress, ksi	Cycles to Failure x 10^3	Stress, ksi	Cycles to Failure x 10^3
100	10	140	18	145	11
95	22	130	35	140	1
90	48	125	78	130	643
86	72	120	172	120	1395
80	160	112	376	110	1690
75	271	105	266	100	2200*
70	237	100	1439		
65	335	95	1770		
62	392	90	2000*		
60	1087	88	2000*		
60	2000*				

Solution treated and aged.
R = -1
*Discontinued

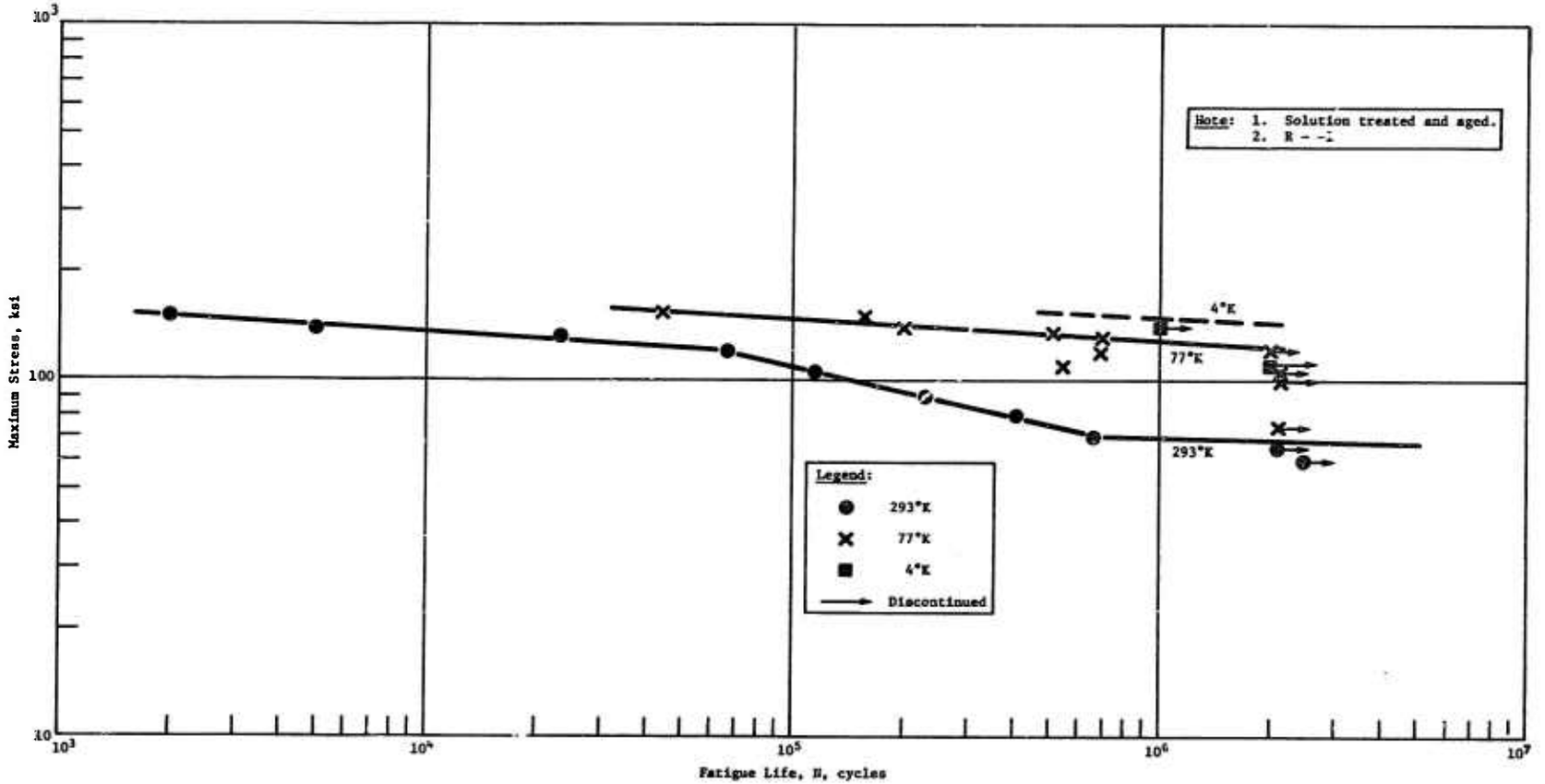

Figure IV-5 Unnotched Fatigue Life Curves for 718 Nickel Alloy

Table IV-5 Unnotched Fatigue Life Data for 718 Nickel Alloy

293°K		77°K		4°K	
Stress, ksi	Cycles to Failure x 10^3	Stress ksi	Cycles to Failure x 10^3	Stress, ksi	Cycles to Failure x 10^3
150	2	153	45	140	1100*
140	5	150	155	110	2000*
130	23	140	200		
120	67	135	513		
105	114	130	698		
90	229	120	695		
80	411	120	2000*		
70	672	110	542		
65	2100*	105	2000*		
60	2500*	100	2100*		
		75	2100*		

Solution treated and aged.
R = -1
*Discontinued

B. NOTCHED FATIGUE TESTS

Data for 304L show a uniform decrease in fatigue strength with cycling at room temperature from almost 50 ksi at 10^4 cycles to approximately 27 ksi at 2×10^6 cycles. The 77°K results are quite similar to the 293°K in the 10^4 and 10^5, but are greater than 30 ksi in the 10^6 region. At 4°K, fatigue strength is substantially greater than at the lower temperatures (Figure IV-6, Table IV-6).

Curves for the 310 stainless steel (Figure IV-7, Table IV-7) show fatigue strengths at 293°K similar to that of 304L, but at 77°K and 4°K significantly higher strengthening is observed.

The 21-6-9 stainless steel exhibits higher fatigue strength than 310 at both 293 and 77°K, but at 4°K only limited additional strengthening is observed. The fatigue strength at 4°K is below that of the 310 stainless steel (Figure IV-8, Table IV-8).

The notched fatigue curve for A-286 stainless steel at 293°K is quite steep; a decrease of strength from approximately 72 ksi at 10^4 cycles to less than 20 ksi at 2×10^6 cycles is noted. The increments of strengthening associated with reductions in temperature to 77°K and 4°K are approximately equivalent (Figure IV-9, Table IV-9).

The 718 nickel alloy exhibits the highest notch fatigue strength at all temperatures for the five alloys tested. Continuous strengthening with reduction in temperature is apparent (Figure IV-10, Table IV-10).

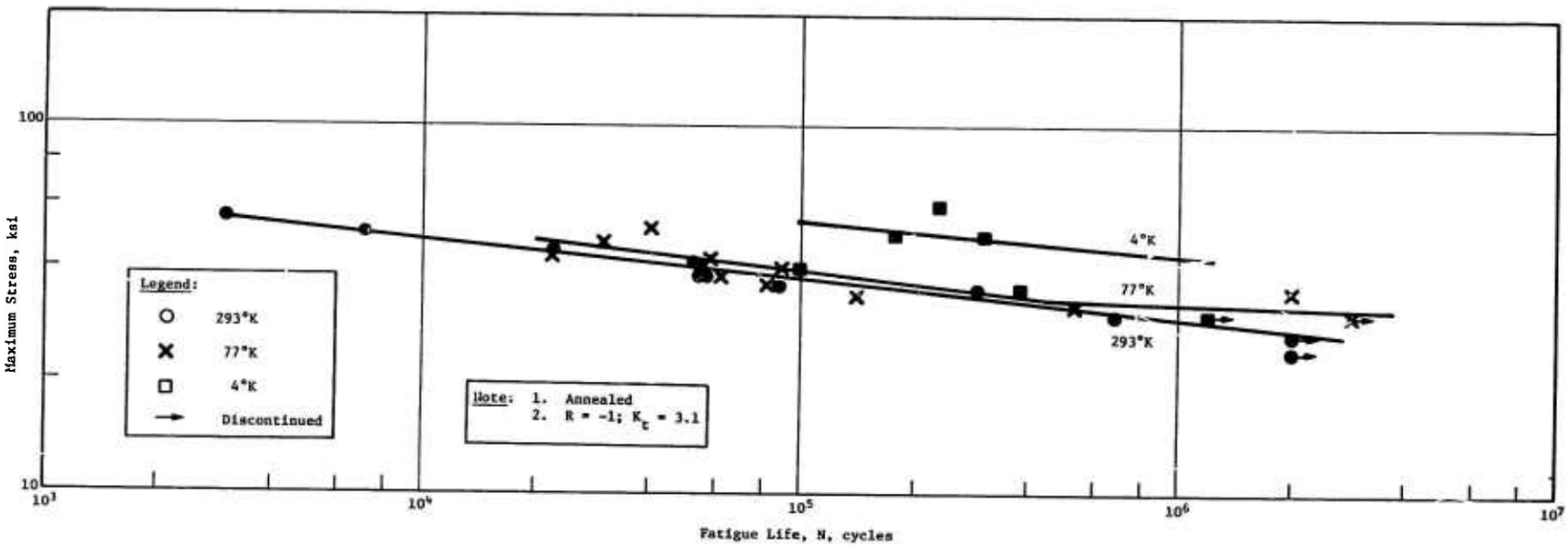

Figure IV-6 Notched Fatigue Life Curves for 3042 Stainless Steel

Table IV-6 Notched Fatigue Life Data for 304L Stainless Steel

293°K		77°K		4°K	
Stress, ksi	Cycles to Failure x 10^3	Stress, ksi	Cycles to Failure x 10^3	Stress, ksi	Cycles to Failure x 10^3
55	3	52	40	60	232
50	7	48	30	50	177
45	22	44	22	50	302
42	52	42	57	40	98
40	54	40	89	35	376
38	54	38	62	30	1200*
38	55	36	81		
36	88	35	2015		
35	293	34	140		
30	682	32	538		
27	2000*	30	2900*		
24	2000*				

Annealed
$R = -1$; $K_t = 3.1$

*Discontinued

Figure IV-7 Notched Fatigue Life Curves for 310 Stainless Steel

Figure IV-7

Table IV-7 Notched Fatigue Life Data for 310 Stainless Steel

293°K		77°K		4°K	
Stress, ksi	Cycles to Failure x 10^3	Stress, ksi	Cycles to Failure x 10^3	Stress, ksi	Cycles to Failure x 10^3
60	8	60	23	90	31
55	13	55	52	75	274
50	21	50	74	65	458
45	25	46	72	50	1300*
42	33	45	143		
38	93	42	96		
32	276	40	95		
32	416	39	170		
30	85	38	1578		
30	1793	36	1969		
28	2500*	34	2000*		

Annealed
$R = -1$; $K_t = 3.1$

*Discontinued

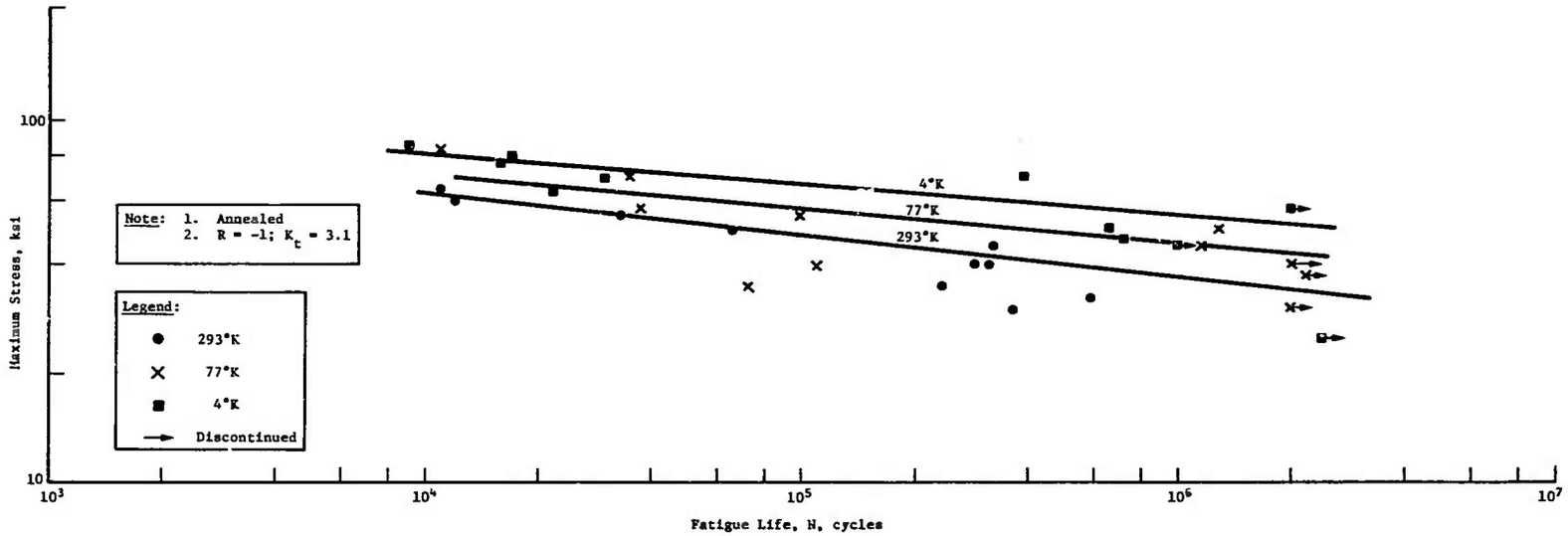

Figure IV-8 Notched Fatigue Life Curves for 21-6-9 Stainless Steel

Table IV-8 Notched Fatigue Life Data for 21-6-9 Stainless Steel

293°K		77°K		4°K	
Stress, ksi	Cycles to Failure x 10^3	Stress, ksi	Cycles to Failure x 10^3	Stress, ksi	Cycles to Failure x 10^3
65	11	85	11	85	9
60	12	70	37	80	17
55	33	57	35	77	16
50	65	55	99	70	30
45	325	50	1280	70	396
40	292	45	1140	65	22
40	306	40	109	58	2000*
35	234	40	2000*	50	660
32	590	37	2200*	47	707
30	363	35	72	40	1000*
25	2400*	30	2000*		

Annealed
R = -1; K_t = 3.1

*Discontinued

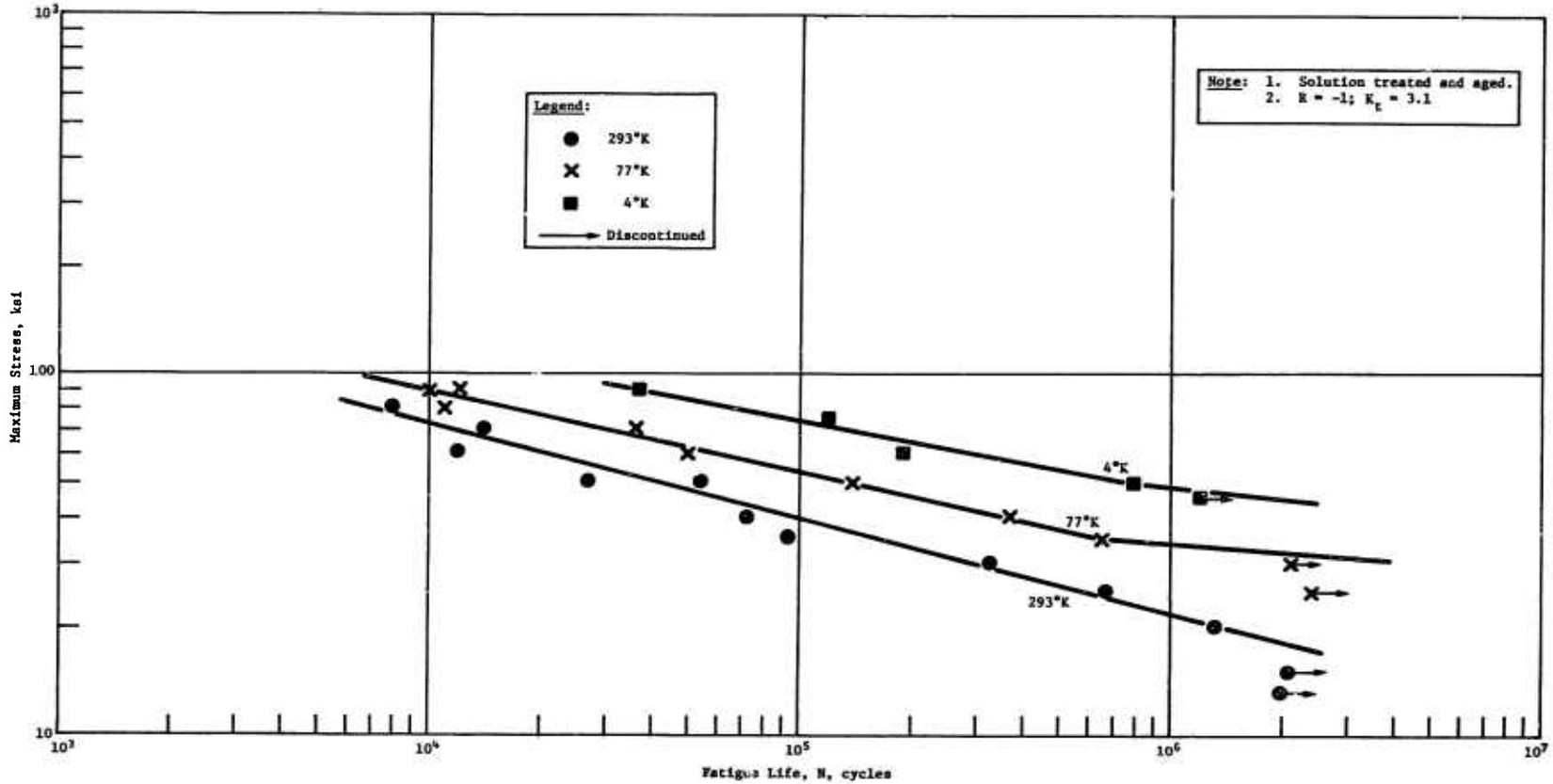

Figure IV-9 Notched Fatigue Life Curves for A-286 Stainless Steel

Table IV-9 Notched Fatigue Life Data for A-286 Stainless Steel

293°K		77°K		4°K	
Stress, ksi	Cycles to Failure x 10^3	Stress, ksi	Cycles to Failure x 10^3	Stress, ksi	Cycles to Failure x 10^3
80	8	90	10	90	37
70	14	90	12	75	119
60	12	80	11	60	192
55	27	70	36	50	790
50	54	60	50	45	1200*
40	72	50	139		
35	93	40	371		
30	325	35	648		
25	676	30	2100*		
20	1304				
15	2100*				
13	2000*				

Solution treated and aged.
$R = -1$; $K_t = 3.1$

*Discontinued

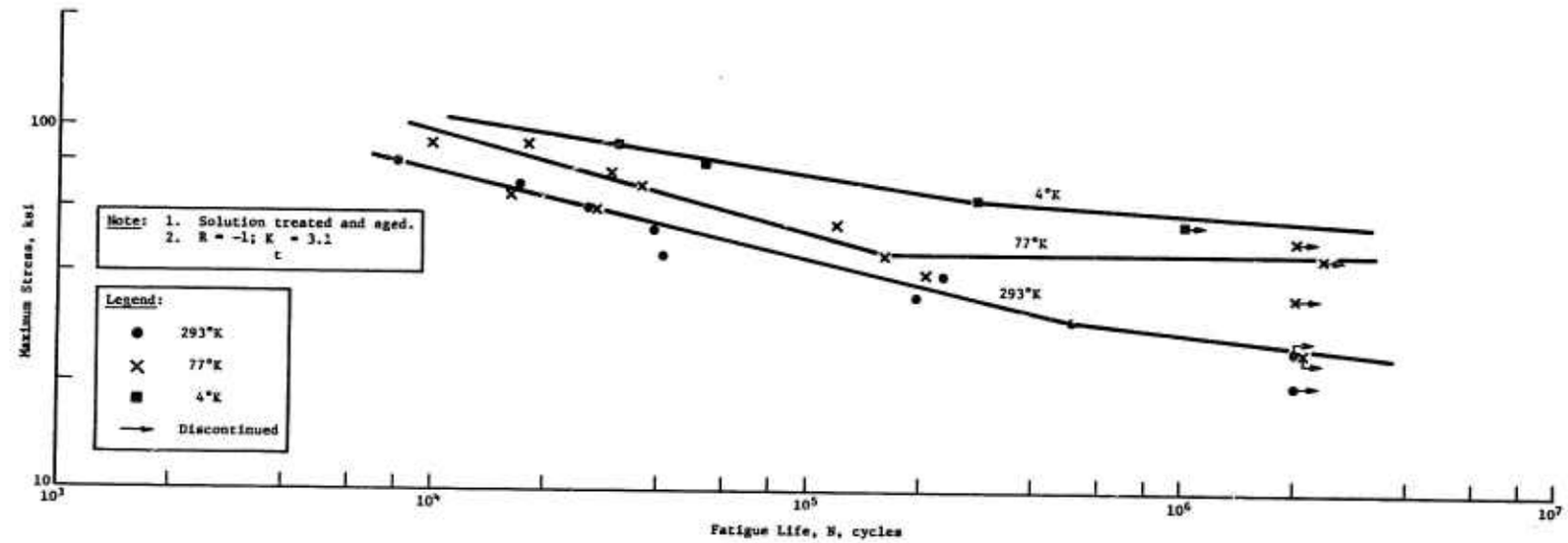

Figure IV-10 Notched Fatigue Life Curves for 718 Nickel Alloy

Table IV-10 Notched Fatigue Life Data for 718 Nickel Alloy

293°K		77°K		4°K	
Stress, ksi	Cycles to Failure x 10^3	Stress, ksi	Cycles to Failure x 10^3	Stress, ksi	Cycles to Failure x 10^3
80	8	80	18	90	31
70	17	75	30	80	54
60	26	70	36	65	284
52	39	65	16	55	1000*
45	41	60	26		
40	230	55	120		
35	195	50	2000*		
30	506	45	160		
25	2200*	45	2400*		
20	2000*	40	205		
		35	2200*		
		25	2100*		

Solution treated and aged.
$R = -1$; $K_t = 3.1$

*Discontinued

V. DISCUSSION OF RESULTS

Unnotched and notched fatigue strengths for the five alloys increased with reduction in temperature. Figure V-1 shows the nature of the increase for unnotched specimens at 10^6 cycles. The 304L and 310 alloys show similar strengths at 293°K and 77°K. However, at 4°K, 304L exhibited less strengthening than 310. The 21-6-9 stainless steel exhibits a modest increase in fatigue strength at 293°K compared to the 300 series alloys, but with reduction in temperature, the increase in fatigue strength is quite significant. The A-286 stainless steel exhibits superior fatigue strength at 293°K compared to the previously discussed alloys; however, at lower temperatures, strength is comparable to the 21-6-9. Nickel alloy 718 exhibits the highest fatigue strength of all alloys tested at all temperatures.

The ratio of fatigue strength compared to ultimate strength as a function of temperature can be used to provide semi-qualitative understanding of the effect of temperature on toughness. Another way to look at the ratio is as an efficiency factor. The data for each alloy is plotted as ratio of fatigue strength/ultimate strength for each temperature in Figures V-2 and V-3. The data show that 304L exhibits a reduction in strength ratio with decreasing temperature. This behavior is not totally surprising in light of the metastable condition of the alloy, which leads to transformation at low temperatures. The other alloys, all stable at low temperatures exhibit an increase in strength

ratio with cooling from 293°K to 77°K. However, cooling to 4°K exhibits a general decrease in fatigue strength ratio.

Replotting the data to compare the alloys at 77°K and 4°K shows that the lowest efficiency is indicated by the 304L stainless steel, with 21-6-9 the next lowest. It is interesting to note that the efficiency of the 310 alloy is greater than the A-286 steel. Figure V-4 shows the two plots.

This work was compared to results of two separate studies performed by Nachtigall†* (Figure V-5). In one study, he evaluated sheet alloys at 293°K, 77°K, and 4°K. The only alloy common to this work is the 718 composition. This data, for R = 0, is plotted in comparison to the fully revised stressing (R = -1) used in this program. The comparison shows the R = 0 data to be generally parallel and slightly higher than the R = -1 data. This is in line with anticipated results because fully reversed stressing is more deleterious to fatigue strength than tension-tension loading. In the second study, Nachtigall used strain controlled cycling, primarily in the plastic range, to obtain low cycle data.

†Nachtigall, A. J.: *Strain-Cycling Fatigue Behavior of Ten Structural Metals Tested in Liquid Helium, in Liquid Nitrogen, and in Ambient Air.* NASA TN D-7432, February 1974.

*Nachtigall, A. J., et al: *Fatigue of Liquid Rocket Engine Metals at Cryogenic Temperatures to -452°F (4°K).* NASA TN D-4274, December 1967.

A few tests were conducted using 718 at sufficiently low levels so that the strains were only elastic. Converting these elastic strains to maximum stresses permits a few additional points to be plotted. These tests were conducted using fully reversed loading and are therefore shown as a R = -1 curve. The data are, in all cases, slightly lower than the results of our tests. Nachtigall also evaluated 304L in the strain cycling studies, but strain levels were too high to permit conversion to stress cycling.

The notched fatigue data is summarized in Table V-1. Included in this summary are two measures of notch behavior. The first is the fatigue-notch factor, which is the ratio of the fatigue strength of unnotched specimens at N cycles to the fatigue ratio of notched specimens at N cycles. As shown by the table, values varied from almost unity (for 304L at 293°K) to approximately 2.5 (for the higher strength alloys). The second measure of notch behavior presented is a notch sensitivity factor, commonly called q, which is defined as follows:

$$q = \frac{K_f - 1}{K_t - 1}$$

According to this index, a material that shows no reduction in fatigue strength due to a notch would have an index value of q - 0; a material that shows as much reduction as predicted would have q = 1. Values of q varied from 0.01 to 0.85. The 304L and 310 exhibited excellent notch properties at 293°K. Alloy 310 exhibited the best overall notch fatigue behavior. The high strength A-285 and 718 alloys exhibited the poorest behavior.

Table V-1 Summary of Notched Fatigue Data

Alloy	Temperature, °K	Cycles	Notched Fatigue Strength, ksi	Notch Strength Ratio, K_f	Notch Sensitivity, q
304L	293	10^5	38	1.03	0.014
		10^6	30	1.27	0.13
	77	10^5	40	2.40	0.67
		10^6	37	2.16	0.55
	4	10^5	55	2.27	0.48
		10^6	44	2.00	0.48
310	293	10^5	39	1.44	0.21
		10^6	31	1.32	0.15
	77	10^5	45	2.22	0.58
		10^6	37	2.24	0.59
	4	10^5	80	1.38	0.18
		10^6	60	1.67	0.32
21-6-9	293	10^5	48	1.08	0.038
		10^6	37	1.27	0.13
	77	10^5	57	2.10	0.52
		10^6	46	2.28	0.61
	4	10^5	66	1.97	0.46
		10^6	54	2.30	0.62
A-286	293	10^5	40	2.10	0.52
		10^6	22	2.77	0.84
	77	10^5	53	2.28	0.61
		10^6	39	2.56	0.74
	4	10^5	74	1.82	0.39
		10^6	48	2.50	0.71
718	293	10^5	45	2.44	0.69
		10^6	28	2.46	0.70
	77	10^5	52	2.79	0.85
		10^6	46	2.78	0.85
	4	10^5	75	--	--
		10^6	59	254	0.73

$$K_f = \frac{\text{Unnotched fatigue strength at N cycles}}{\text{Notched fatigue strength at N cycles}}$$

$$q = \frac{K_f - 1}{K_t - 1}$$

The results of the unnotched and notched fatigue testing showed that all five alloys exhibit satisfactory performance for cyclic service at temperatures down to 4°K. There was no evidence of significant loss of fatigue strength due to the effect of temperature or the presence of a notch.

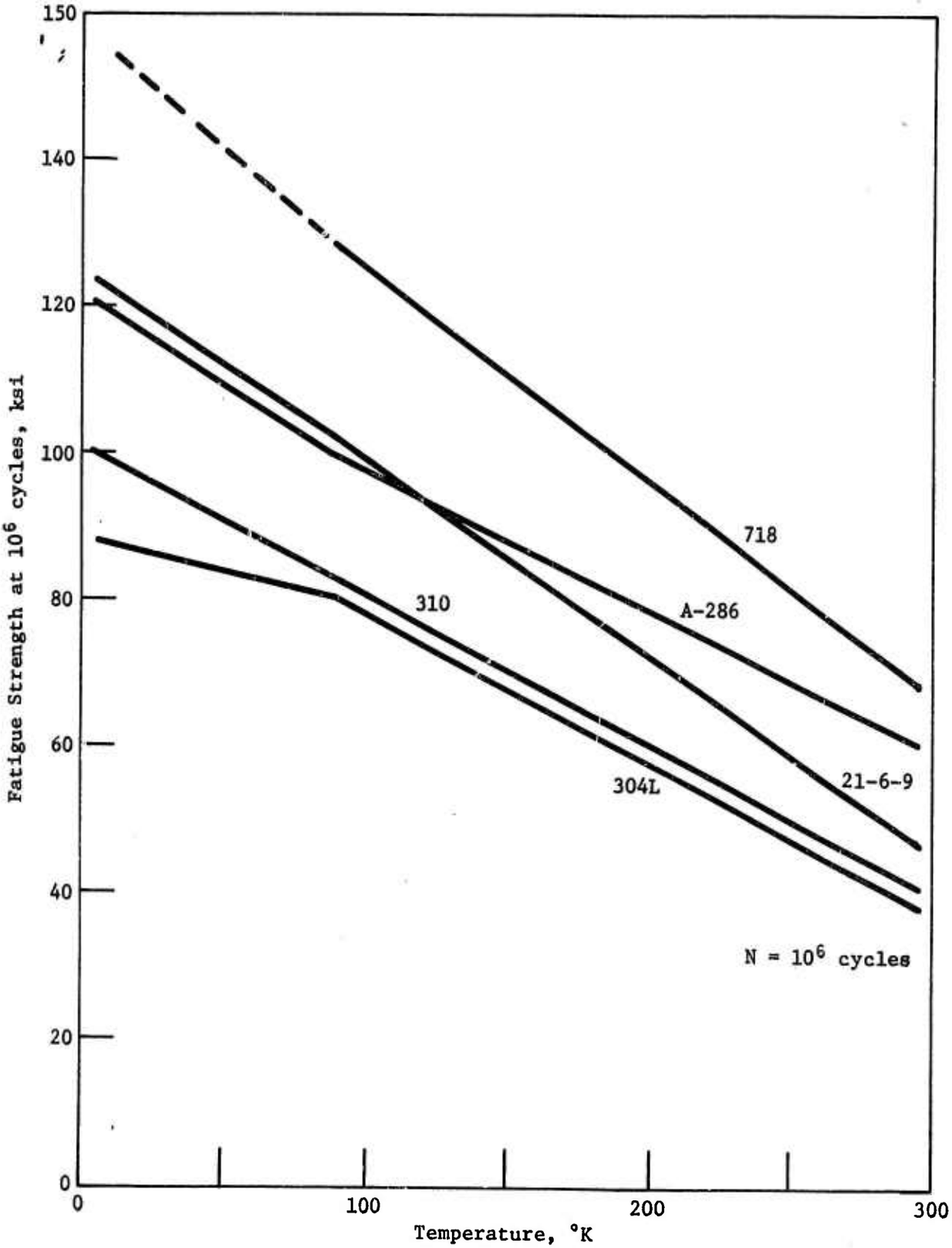

Figure V-1 Comparison of Unnotched Fatigue Data

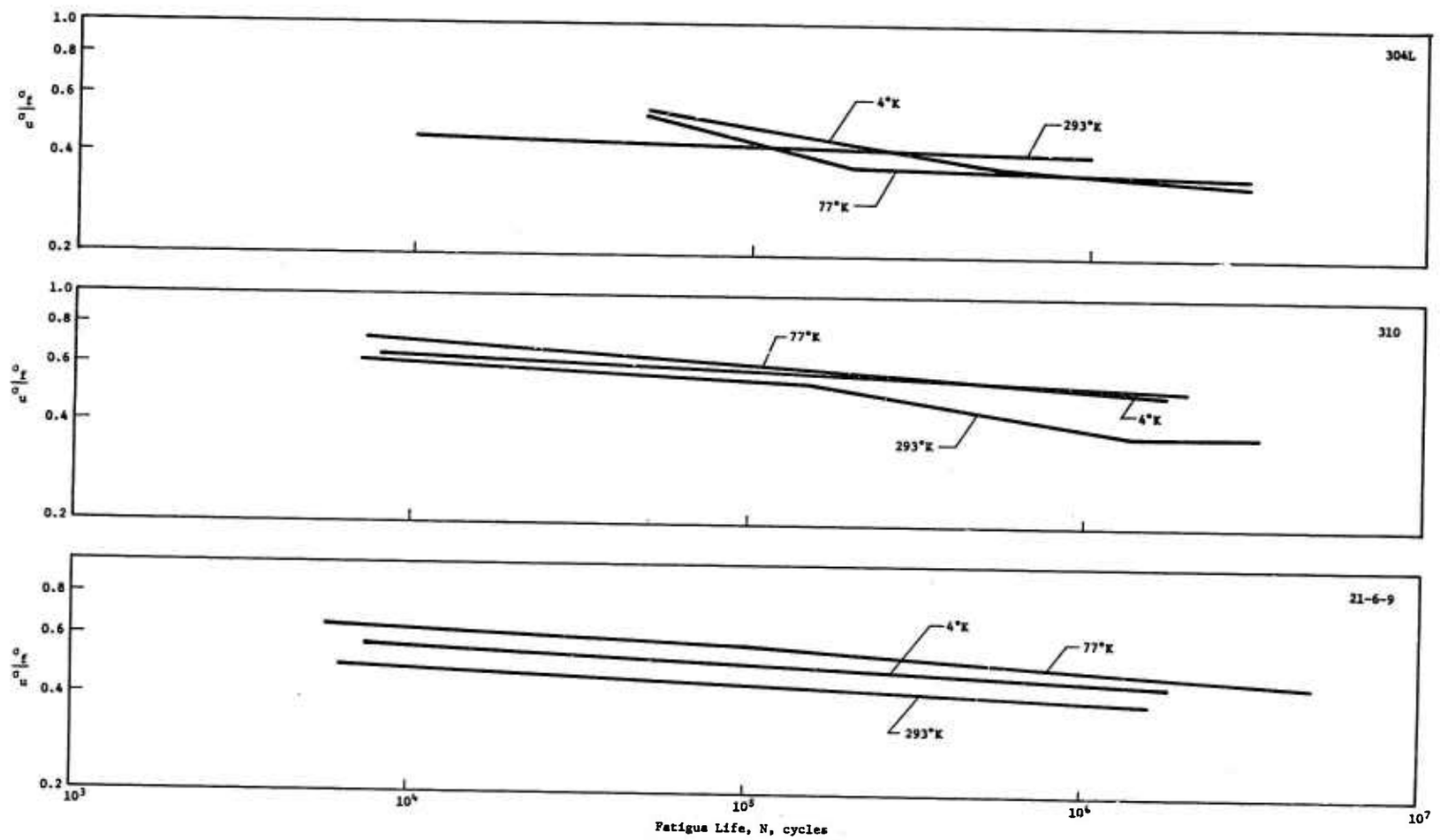

Figure V-2 Fatigue/Ultimate Strength Ratio Data for 304L, 310, and A-286 Alloys

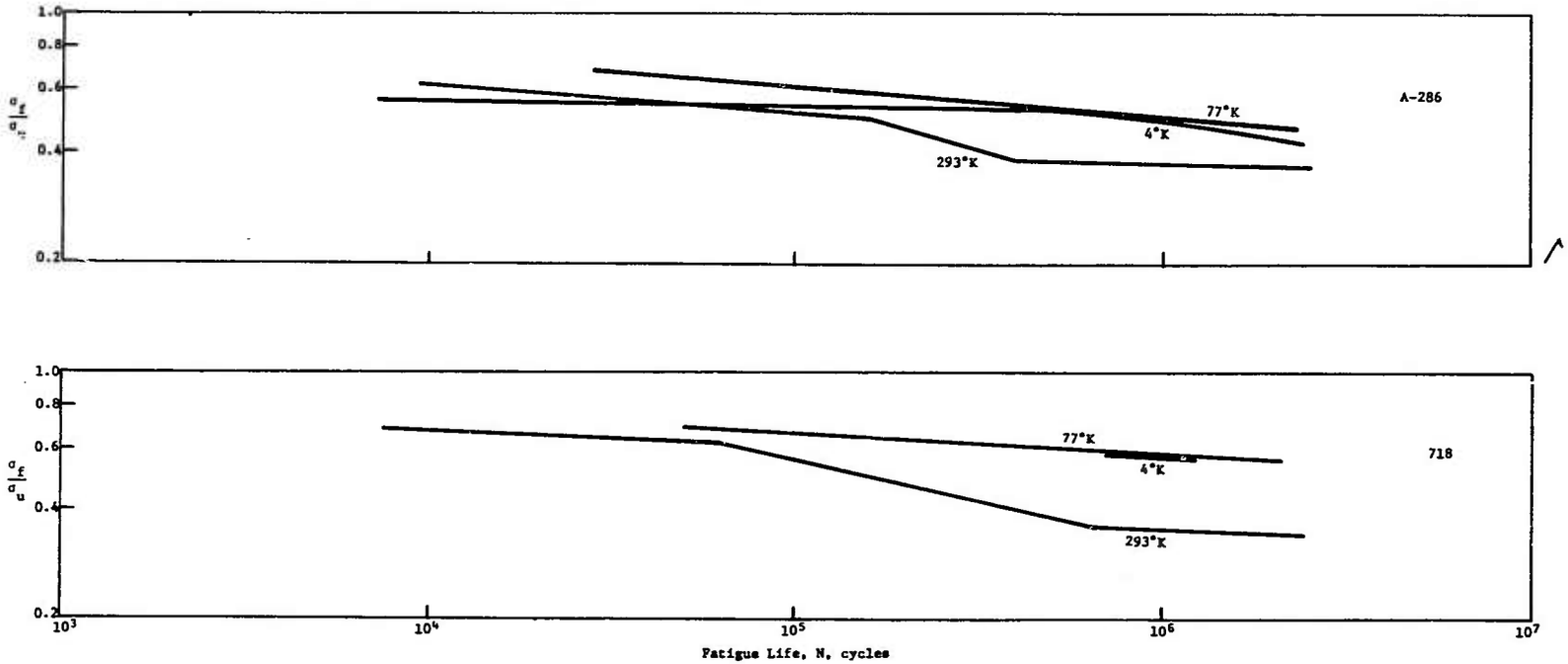

Figure V-3 Fatigue/Ultimate Strength Ratio Data for A-286 and 718 Alloys

Figure V-4

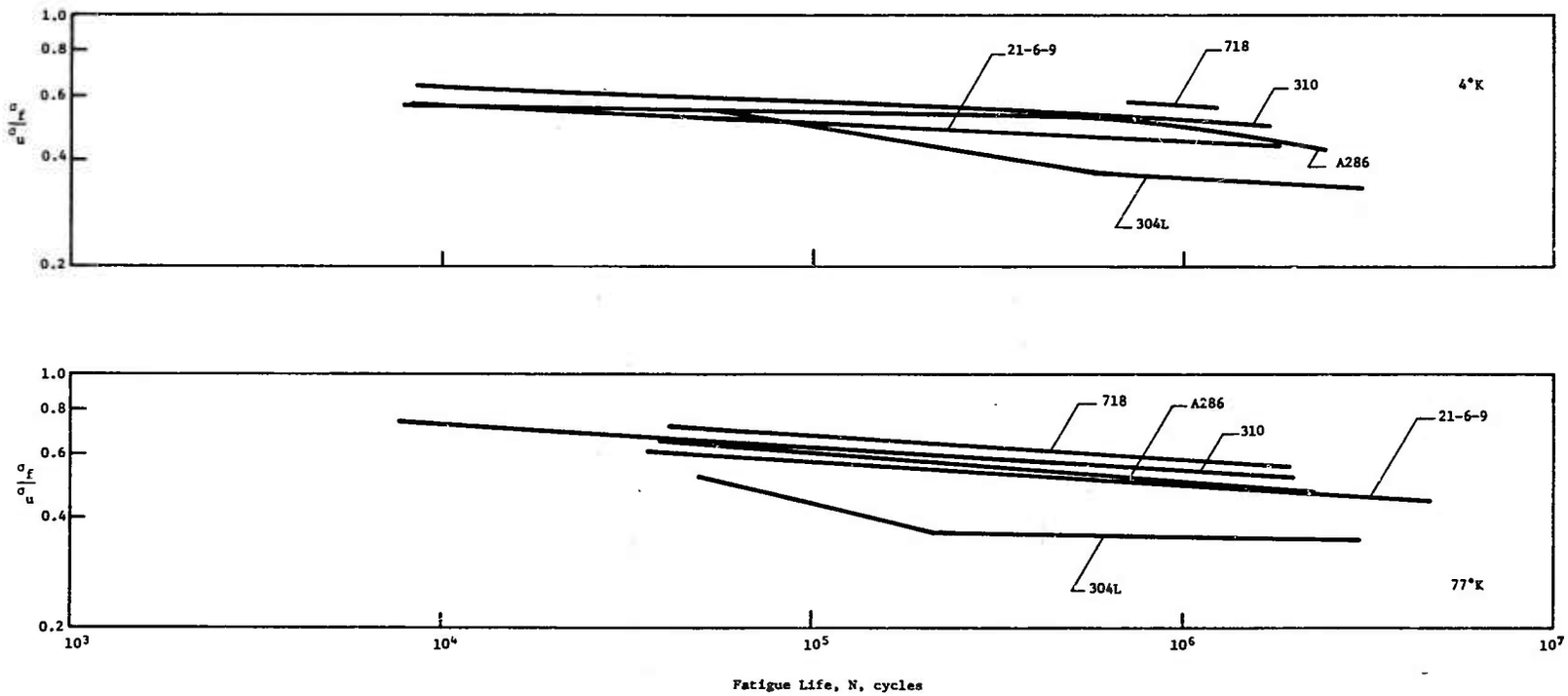

Figure V-4 Fatigue/Ultimate Ratio Data as a Function of Temperature

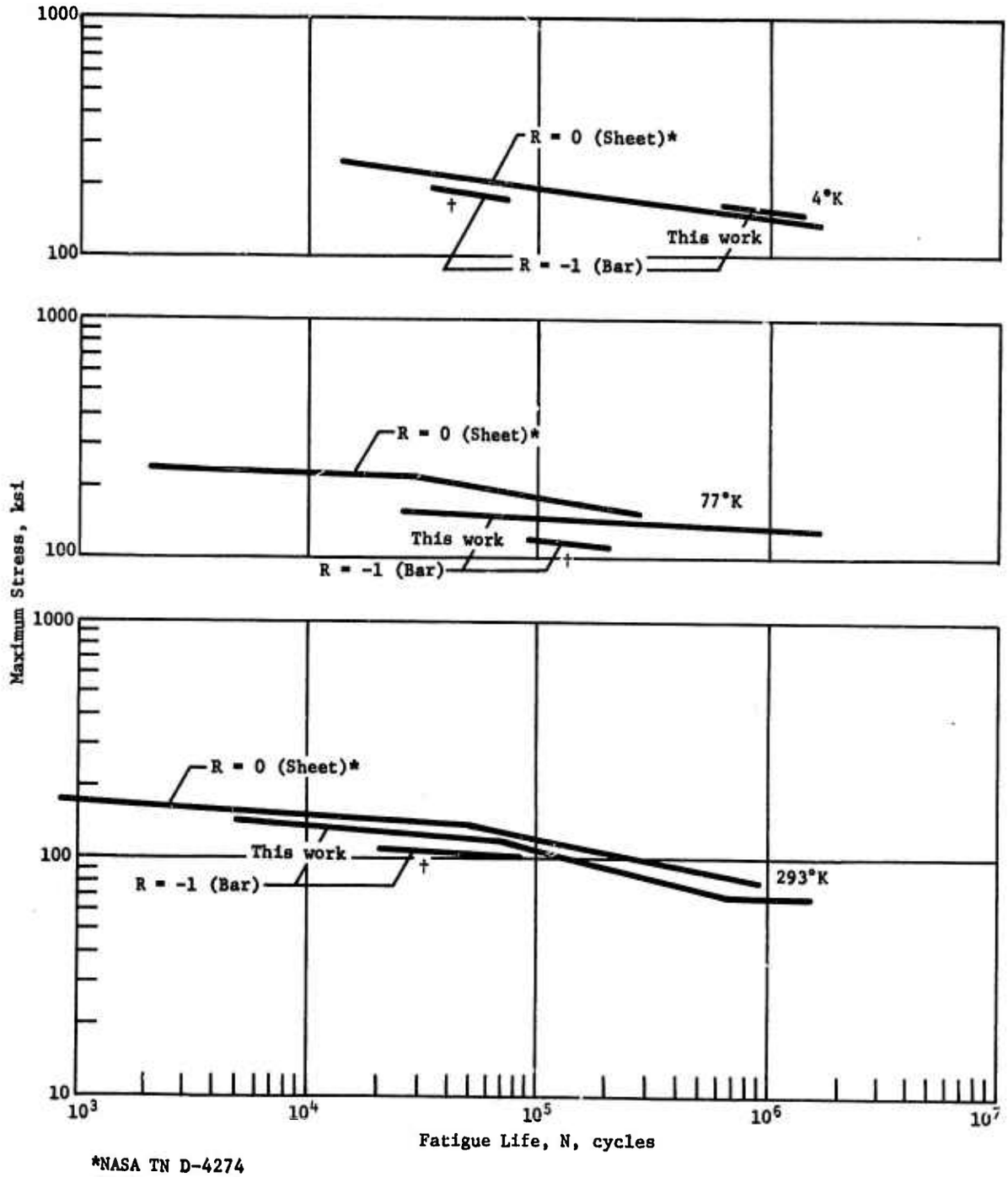

*NASA TN D-4274
†NASA TN D-7532

Figure V-5 Comparison of 718 Data with Other Work

NBSIR 75-828

SEMI-ANNUAL REPORT ON MATERIALS RESEARCH IN SUPPORT OF SUPERCONDUCTING MACHINERY

R. P. Reed, J. G. Hust, M. B. Kasen, H. M. Ledbetter, D.T. Read, E.R. Naimon, R. E. Schramm, L. L. Sparks, R. L. Tobler, and W. F. Weston

Cryogenics Division
Institute for Basic Sandards
National Bureau of Standards
Boulder, Colorado 80302

October 1975

Prepared for
Advanced Research Projects Agency
1400 Wilson Boulevard
Arlington, Virginia 22209

U.S. DEPARTMENT OF COMMERCE, Rogers C. B. Morton, Secretary
James A. Baker, III, Under Secretary
Dr. Betsy Ancker-Johnson, Assistant Secretary for Science and Technology

NATIONAL BUREAU OF STANDARDS, Ernest Ambler, Acting Director

SEMI-ANNUAL REPORT ON MATERIALS RESEARCH

IN SUPPORT OF SUPERCONDUCTING MACHINERY

Sponsored by
Advanced Research Projects Agency
ARPA Order No. 2569
Program Code 4D10
August 10, 1974 - August 9, 1975

Program Director
Dr. E. C. van Reuth
Materials Sciences
Advanced Research Projects Agency
1400 Wilson Boulevard
Arlington, Virginia 22209

Program Manager
Dr. R. P. Reed
Cryogenics Division
Institute for Basic Standards
National Bureau of Standards
Boulder, Colorado 80302

Abstract

Results are reported of a six-month study, March through August 1975, on candidate materials for superconducting machinery. The results cover five areas--advanced composites, elastic properties, fatigue resistance and fracture toughness, magnetothermal conductivity, and thermal conductivity. Material properties were studied over the temperature range 4 to 300 K. Materials studied include: oxygen-free copper; copper-nickel alloys; a precipitation-hardening copper alloy; invar; nickel-chromium-iron alloys; stainless steels; and the composite materials boron/aluminum, boron/epoxy, S-glass/epoxy, graphite/epoxy, and an organic-fiber/epoxy. Some notable results of the study are: the first 4 K fatigue data on a composite material; a ten-fold increase in the fatigue life of a uniaxial glass/epoxy composite between room temperature and liquid-hleium temperature; the first 4 K fatigue fracture toughness studies on a nitrogen-strengthened chromium-nickel-manganese steel, which show this material has higher yield strength and adequate toughness compared to conventional stainless steels; room-temperature elastic properties of a copper-cadmium-chromium precipitation-hardening alloy, which are quite different from those of unalloyed copper and show a non-parallel behavior of the shear modulus and the bulk modulus; the thermal conductivity of 304 stainless steel may be reduced one third at 4 K by a 6 MA/m (80 kOe) magnetic field; the first systematic study of the tensile properties of fiber-reinforced composite materials between room temperature and liquid-helium temperature.

This work was supported by the Advanced Research Projects Agency of the U.S. Department of Defense.

Keywords: Composites; copper alloys; elastic properties; engineering materials; fatigue; fracture; iron alloys; cryogenic temperatures; mechanical properties; nickel alloys; superconducting machinery; thermal conductivity.

Report Contents

Disclaimer

Tradenames of equipment and materials are used in this report for clarity and to conform with standard usage in the scientific and engineering literature. Selection of materials for discussion and examination with regard to application in superconducting machinery is based on properties reported in the literature, and must be regarded as preliminary and tentative. In no case does such selection imply recommendation or endorsement by the National Bureau of Standards, nor does it imply that the material or equipment is necessarily the best available for the purpose.

NBSIR

SEMI-ANNUAL REPORT ON MATERIALS RESEARCH IN SUPPORT OF SUPERCONDUCTING MACHINERY

ADVANCED COMPOSITES

R. E. Schramm and M. B. Kasen

Cryogenics Division
Institute for Basic Standards
National Bureau of Standards
Boulder, Colorado 80302

October 1975

Summary: Advanced Composites

Phase II of the experimental program is now in progress. This report contains 295 K, 76 K, and 4 K tensile measurements of elastic, plastic, and ultimate tensile properties necessary to characterize five fiber-reinforced composites selected for their potential use at 4 K: 5.6 mil boron-6061 aluminum; 5.6 mil boron-5505 epoxy; S-901 glass NASA resin 2; type A graphite-NASA resin 2; and Kevlar 49*-NASA resin 2. Compression tests are in progress.

*The use of trade names in this paper in no way implies endorsement or approval by NBS and is included only to define the material.

Contents: Advanced Composites

1.0 Review

Previous ARPA reports [1,2] included two extensive literature reviews on the cryogenic properties of glass-filament and advanced-fiber-reinforced structural composites. One has recently appeared in Cryogenics [3] and the other is now in-press for a Special Technical Publication of the American Society for Testing and Materials [4]. A reprint and preprint of these papers are Appendices II and III. This information clearly indicated the almost complete lack of 4 K data directly applicable to the design of superconducting machinery. It was possible, however, to select five candidate composites for structural use and we set out to obtain fundamental static tensile and compressive properties to make it possible to compute design values for complex, low-temperature structures by macromechanical analyses. Commercial suppliers began fabricating the following composites:

5.6 mil Boron-6061 Aluminum
5.6 mil Boron-5505 Epoxy
S-901 Glass-NASA Resin 2
Type A Graphite-NASA Resin 2
Kevlar 49-NASA Resin 2.

While awaiting material delivery, Phase I preliminary tests were begun to determine working procedures. For these tests, two commercial suppliers provided boron-epoxy and graphite-epoxy materials. With these, we developed a grip system that yielded a high fraction of satisfactory fractures and also determined that cryogenic environments changed most mechanical properties relatively little from the room temperature values for these composites. With this background, the boron-aluminum became the first material available for our Phase II characterization program. Both this preliminary data and the boron-aluminum data appeared in the last ARPA report [5]. Two previously unseen phenomena did appear among the results: a two-part elastic region in the graphite-epoxy longitudinal (0°) specimens and a serrated stress-strain curve (discontinuous yielding) in the boron-aluminum transverse (90°) and crossply (± 45°) specimens at 295 K and 4 K but not at 76 K.

The boron-aluminum measurements and those subsequently made on boron-epoxy were recently presented in a talk at the International Cryogenic Materials Conference in Kingston, Ontario, Canada (July 22-25, 1975). The paper that will appear in the proceedings of this meeting [6] is Appendix IV.

2.0 Phase II: Characterization of the Mechanical Properties of Uniaxial Composites at Cryogenic Temperatures

2.1 Introduction

This program constitutes the first attempt to characterize fiber-reinforced composites at cryogenic temperatures and obtain the basic laminar properties needed for macromechanical analysis. The present report deals with static tensile properties; compressive tests are now in progress. Other NBS investigators under ARPA contract are making plans for dynamic mechanical tests (H.M. Ledbetter) as well as thermal measurements (J.G. Hust).

While the boron-aluminum data appeared in the last report, it will be included here again to facilitate comparison and for completeness.

2.2 Materials

Each of the five composites came from the suppliers as trimmed, flat sheets that were 15.2 x 55.9 cm (6 x 22 in) for the boron-aluminum, and 27.9 cm (11 in) square for all the polymer-matrix materials. Uniaxial layups were six plies thick for the longitudinal tests and 15 plies for the transverse tests; crossply plates were ten plies thick. Table 1 gives the nominal thicknesses of the various sheets.

The suppliers stated that the void content should be < 2 volume % and that NaOH extraction on two specimens of boron-aluminum indicated an average of 47.2 volume % boron. Our own radiography of all plates revealed no visible voids. The tungsten cores of the boron filaments were visible in the radiographs, thereby permitting a spot check of their axial

alignment in the finished specimens. In all cases, the filament alignment was within 1/2° of nominal. The boron-aluminum was tested in the F temper (as fabricated). Processing procedures and a fuller characterization of all composites are forthcoming from the manufacturers.

2.3 Procedures

As noted in our last report [5], all test specimens were straight-sided coupons with no tabs. The boron-aluminum specimen length was 15.2 cm (6 in) while all other specimens were 27.9 cm (11 in) long. Specimen widths were 1.3 cm (0.5 in) for longitudinal tests and 2.5 cm (1 in) for transverse and crossply tests. Cutting was done by a diamond circular saw lubricated and cooled by a stream of water soluble oil except for the Kevlar 49 composite for which a dry slitting saw was necessary. Light hand buffing with emery paper further minimized any imperfections on the already very smooth edges. The Kevlar 49 material was again an exception since this process caused fuzzy edges.

Two commercial strain gages cemented directly to the surface monitored elongation and Poisson's ratio in the longitudinal and crossply specimens. There was only one gage on the transverse specimens since the Poisson's ratio (ν_{21}) can be calculated from the transverse elastic modulus (E_{22}) and the longitudinal values of elastic modulus (E_{11}) and Poisson's ratio (ν_{12}) by:

$$\nu_{21} = \nu_{12} E_{22}/E_{11}.$$

Curing the strain gage cement overnight at 345 K caused softening of the NASA resin 2; thus it was necessary to support these specimens on a flat plate during this process.

Following ASTM D 3039-71T, Method of Test of Tensile Properties of Oriented-Fiber Composites, pre-test conditioning of polymer-based materials was exposure for at least two days to room temperature air at 40-60% relative humidity. The grip system developed earlier [2] was attached in a separate alignment fixture just prior to the test. Gage lengths were 15.2 cm (6 in) for the long specimens and 10.2 cm (4 in) for those of boron-aluminum. Tests were conducted in air at 295 K, in liquid nitrogen at 76 K, or in liquid helium at 4 K at a strain rate of 0.01-0.02 min^{-1}.

Outputs of the load cell and strain gages were recorded continuously during the test. To check within-specimen repeatability, we cycled the load to about one third of its ultimate value (within the elastic limit) and back to no load about three times before loading to ultimate for most of the polymer-matrix specimens. In some cases, the loading was monotonic to failure: when the ultimate load was very small (e.g., graphite-NASA resin 2 transverse, and all Kevlar 49-NASA resin 2), and for the boron-aluminum which began to yield plastically early in its loading history.

As before, a "good" or acceptable fracture was one which occurred at least one specimen thickness away from the grips. The ultimate values from the unacceptable breaks (inside or too near the grips) were usually quite comparable to those of the good tests but they were not included in computing averages. This criterion of determining fracture location (at least its origin) became very difficult, usually impossible, to apply to the polymer-based longitudinal specimens due to their fracture mode (see 2.4 Results and Discussion).

The primary purpose of testing the crossply laminates here was to determine the in-plane shear modulus (G_{12}). With the Petit technique [7], the calculation requires knowledge of the uniaxial elastic properties. With the Sims and Halpin approach [8], a shear stress-shear strain curve is constructed solely from tensile data. Because of this independence from prior test data, we've chosen to calculate G_{12} with this latter method. The values calculated by the Petit technique and listed in the last report [5] for boron-aluminum agree quite well with those listed here.

2.4 Results and Discussion

Numerical results from the individual tests are presented in Tables 2-6; the average values, standard deviations, and coefficients of variation are in Tables 6-10. Table 11 gives the calculated shear moduli.

Discontinuities on the stress-strain diagram of boron-aluminum in the transverse (90°) and crossply (± 45°) orientations were graphed and discussed in our last report [5]. We still have no explanation and have found this behavior is unfamiliar to other workers.

The two-part elastic region noted in graphite-epoxy [5] was again in evidence for the graphite-NASA resin 2. With the load along the fiber direction, the initial elastic response is followed by a second of higher modulus and higher Poisson's ratio; these are noted as primary and secondary values in Tables 5 and 10. The uncertainties in Poisson's ratio make possible the argument that there is no real difference, but the change in modulus is repeatable and usually quite distinct in the load-strain curves recorded. Again, it would appear that this increase in stiffness could be due to straightening of the graphite filaments.

In almost all instances, a minimum of three tests resulting in "good" fractures were conducted at each temperature. In the case of the Kevlar 49-NASA resin 2 composite, the initial results at 295 K and 76 K were very poor and showed that it was not worth running the full series or any 4 K tests. These low strengths and the very low interlaminar shear strength, causing delamination problems in handling, are signs of severe incompatability between this particular fiber and resin. Component compatability is obviously important and, before any extensive commitment, should be checked, e.g., with short beam shear tests.

Figure 1 shows typical specimens fractured at 4 K. The longitudinal boron-aluminum specimens appear similar to most normal metals while longitudinal boron-epoxy specimens fracture into discrete pieces throughout the gage length. All of the longitudinal NASA resin 2-matrix materials tend to explode between grips and produce a fuzzy, filamentary mass. All transverse fractures are defined by fiber direction and are typically brittle. There is some necking and plastic yielding in all crossply specimens; in boron-aluminum, the specimens maintain integrity while all others fail by delamination. Figure 1 shows only 4 K fractures (except for the Kevlar 49-NASA resin 2), but tests at other temperatures produced breaks of basically the same type.

Mechanical anisotropy is an outstanding characteristic of composites and all properties must be correlated with fiber direction. The high modulus of boron marks both its composites because of their stiffnesses in the longitudinal orientation (200-235 x 10^9 N/m^2 or 29-34 x 10^6 psi). Matrix properties dominate the transverse and crossply specimens, however, and here the aluminum matrix shows a higher modulus by a factor of three or better over its polymer counterparts. The longitudinal moduli are very close to being temperature independent (< 5% change between 295 K and 4 K) while the matrix-dependent orientations show some small effects: polymer bases show some increase with lowering temperature while the boron-aluminum generally shows a small decrease.

In most metals, the Poisson's ratio is generally about 0.3; this is roughly true for boron-aluminum in all orientations and the longitudinal specimens of the other composites. For the polymer matrices, the transverse values are very low while the crossply values are much higher.

Longitudinal ultimate strengths do show some temperature dependence -- increasing at cryogenic temperatures particularly for boron-aluminum (16.4 x 10^8 N/m^2 or 238 x 10^3 psi) and glass-NASA resin 2 (19.6 x 10^8 N/m^2 or 284 x 10^3 psi). In the other two orientations the metal matrix again shows a superiority.

Those composite layups in this group which do display any yielding do not have a sharp transition between elastic and plastic zones. Consequently, the determination of a proportional limit is quite difficult and hence the rather large variation in values as seen in the standard deviations. The 0.2% yield strength is a considerably less variable measure of plastic yield.

The polymer-matrix intralaminar shear moduli in Table 11 appear to agree reasonably with other room temperature determinations [9]; the boron-aluminum values are, however, quite low. This difference is probably due to the non-linear stress-strain response in the ductile matrix invalidating assumptions necessary for the indirect $\pm$ 45° method of calculating G_{12} [10]. The boron-aluminum values listed here should serve only as lower boundaries.

Composite properties are strongly dependent on fiber volume fraction and void content but, where general comparison is possible with the data reviewed in Appendix III, there is reasonable agreement with the present data with a few exceptions. In the glass-NASA resin 2 we did not see the large increase in E_{11} at 4 K that would be indicated by earlier 20 K measurements [3]. The type A graphite-NASA resin 2 here had a very low transverse tensile strength; this may indicate low filament-resin compatability. All the Kevlar 49-NASA resin 2 properties indicate the severe compatability mentioned above.

2.5 Future Work

Compression tests are in progress. We designed and built a special fixture and have now seen it through several modifications. After working with a few specimen configurations, it now appears that the major hurdles have been cleared and good compression data are possible.

Fatigue testing will begin later this fall and, for this purpose, we now have in hand boron-aluminum and boron-epoxy materials in a ($0^\circ_2 \pm 45^\circ$) configuration.

3.0 References

1. Kasen, M. B., "Advanced Composites," Semi-Annual Technical Reports on Materials Research in Support of Superconducting Machinery, (1 Sept., 1973 to 1 March, 1974) National Bureau of Standards - Advanced Research Projects Agency.

2. Kasen, M. B. and Schramm, R. E., "Advanced Composites," Semi-Annual Technical Reports on Materials Research in Support of Superconducting Machinery - II, (1 March, 1974 to 1 Sept., 1974) National Bureau of Standards - Advanced Research Projects Agency.

3. Kasen, M. B., "Mechanical and thermal properties of filamentary-reinforced structural composites at cryogenic temperatures. 1: Glass-reinforced composites," Cryogenics 15(6), 327 (1975).

4. Kasen, M. B., "Properties of Filamentary-Reinforced Composites at Cryogenic Temperatures," Composite Reliability, ASTM STP 580, American Society for Testing and Materials, 1975 (to be published).

5. Schramm, R. E. and Kasen, M. B., "Advanced Composites," Semi-Annual Technical Reports on Materials Research in Support of Superconducting Machinery-III (1 Sept., 1974 to 1 March, 1975) National Bureau of Standards-Advanced Research Projects Agency.

6. Schramm, R. E. and Kasen, M. B., "Static Tensile Properties of Boron-Aluminum and Boron-Epoxy Composites at Cryogenic Temperatures," Paper T3, Cryogenic Engineering Conference, Kingston, Ontario, July 22-25, 1975 (to be published).

7. Petit, P. H., "A Simplified Method of Determining the In-plane Shear Stress-Strain Response of Unidirectional Composites," Composite Materials: Testing and Design, ASTM STP 460, American Society for Testing and Materials, 1969, pp. 83-93.

8. Sims, D. F. and Halpin, J. C., "Methods for Determining the Elastic and Viscoelastic Response of Composite Materials," Composite Materials: Testing and Design (Third Conference), ASTM STP 546, American Society for Testing and Materials, 1974, pp. 46-66.

9. Advanced Composite Design Guide, Third Edition, Volume IV, Materials, Air Force Materials Laboratory, Wright-Patterson Air Force Base, Ohio (1973).

10. Ramsey, J. E., Waszczak, J. P. and Klouman, F. L., "An Investigation of the Non-Linear Response of Metal-Matrix Composite Laminates," AIAA/ASME/SAE 16th Structures, Structural Dynamics and Materials Conference, Denver, Colorado (May 27, 1974).

4.0 List of Figures

1. Composite tensile specimens fractured at 4 K (except for Kevlar 49-NASA resin 2) All transverse 90° specimens broke in the same manner while all crossply (± 45°) polymer matrix specimens were similar to each other in appearance.

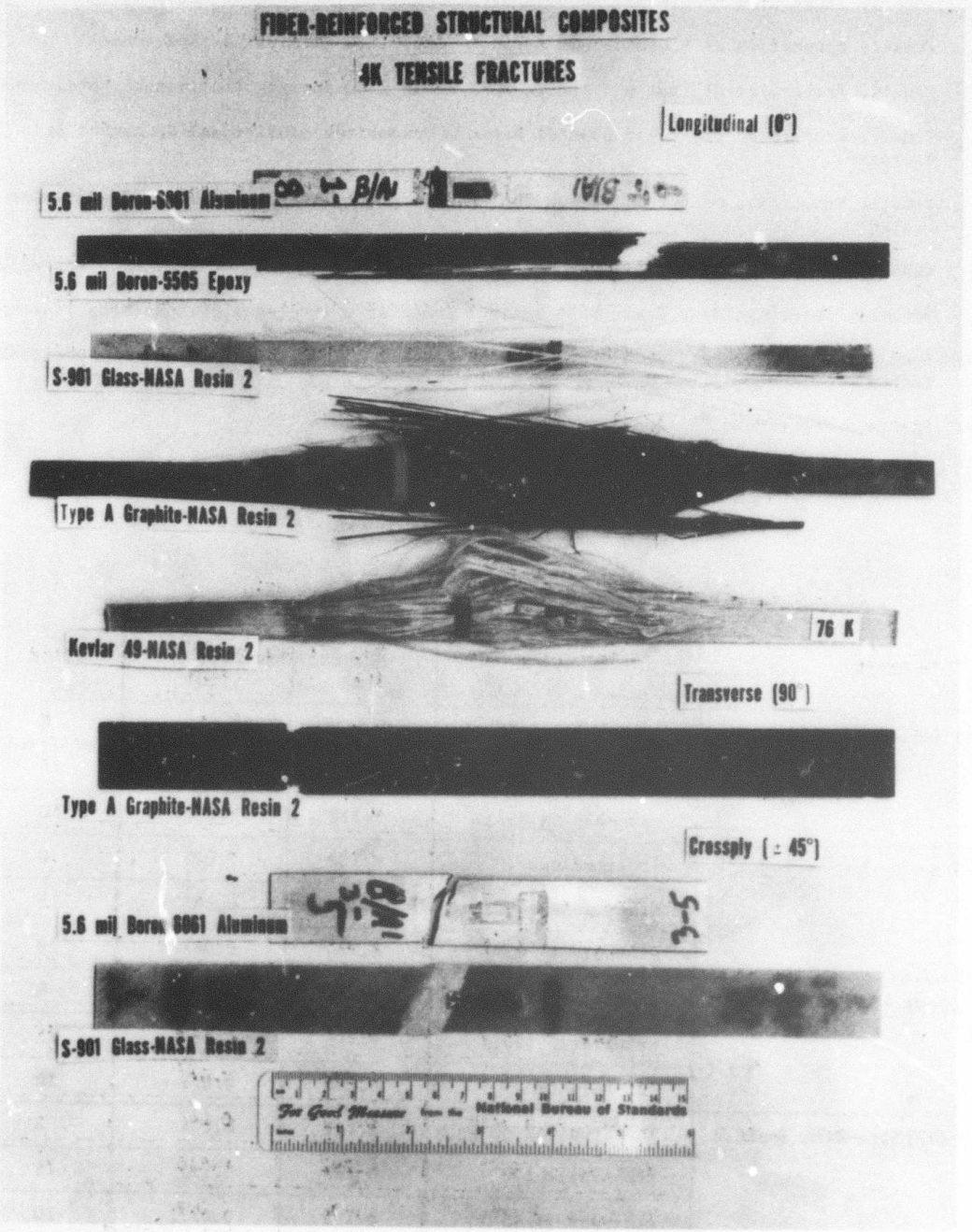

Fig. 1. Composite tensile specimens fractured at 4 K (except for Kevlar 49-NASA resin 2). All transverse (90°) specimens broke in the same manner while all crossply (±45°) polymer matrix specimens were similar to each other in appearance.

5.0 List of Tables

Table 1.

Composite Plates Used for Tensile Mechanical Tests

Composite	Orientation	Nominal Thickness (cm)	(in)	Plies
5.6 mil Boron 6061-Aluminum	longitudinal (0°)	0.109	0.043	6
	transverse (90°)	0.246	0.097	15
	crossply (± 45°)	0.178	0.070	10
5.6 mil Boron-5505 Epoxy	longitudinal (0°)	0.102	0.040	6
	transverse (90°)	0.257	0.101	15
	crossply (± 45°)	0.170	0.067	10
S-901 Glass - NASA Resin 2	longitudinal (0°)	0.124	0.049	6
	transverse (90°)	0.315	0.124	15
	crossply (± 45°)	0.196	0.077	10
Type A Graphite-NASA Resin 2	longitudinal (0°)	0.112	0.044	6
	transverse (90°)	0.292	0.115	15
	crossply (± 45°)	0.196	0.077	10
Kevlar 49 - NASA Resin 2	longitudinal (0°)	0.124	0.049	6
	transverse (90°)	0.356	0.140	15
	crossply (± 45°)	0.218	0.086	10

Table 2.

Tensile Properties of 5.6 mil Boron-6061 Aluminum Composites

(Individual Specimens)

Temperature (K)	Elastic Modulus, E (10^9 N/m^2)	Elastic Modulus, E (10^6 psi)	Poisson's Ratio[a] ν	Proportional Limit, σ^{pl} (10^8 N/m^2)	Proportional Limit, σ^{pl} (10^3 psi)	0.2% Yield Strength, σ^{ty} (10^8 N/m^2)	0.2% Yield Strength, σ^{ty} (10^3 psi)	Ultimate Strength, σ^{tu} (10^8 N/m^2)	Ultimate Strength, σ^{tu} (10^3 psi)	Ultimate Elongation, ϵ^{tu} (%)
				Longitudinal (0°)						
295	195	28.3	0.320					12.4[b]	180[b]	0.6[b]
295	194	28.1	0.280					12.7[b]	184[b]	0.6[b]
295	194	28.2	0.275					13.2[b]	191[b]	0.6[b]
295	217	31.4	0.320					12.5[b]	175[b]	0.6[b]
76	186	27.0	0.345					16.9	245	0.8
76	196	28.4	0.344					15.8	230	0.7
76	208	30.1	0.335					16.5	239	0.8
76	196	28.4	0.351					16.0[b]	233[b]	0.8[b]
4	211	30.6	0.313					14.9	217	0.7
4	207	30.0	0.358					16.9	245	0.8
4	191	27.7	0.343					16.0	231	0.8
4	206	29.9	0.360					16.4	238	0.8
				Transverse (90°)						
295	165	24.0	0.247	0.67	9.7	1.38	20.1	1.74	25.3	0.8
295	177	25.7	0.265	0.54	7.8	-	-	1.80	26.1	-
295	112	20.6	0.212	0.67	9.7	1.29	18.7	1.46	21.1	0.6
76	101	14.6	0.175	0.92	13.3	1.86	27.0	2.29[b]	33.2[b]	0.8[b]
76	155	22.5	0.268	0.75	10.9	1.67	24.3	2.57	37.3	0.8
76	138	20.1	0.239	0.65	9.4	1.94	28.2	2.47	35.9	0.8
76	116	16.8	0.201	0.72	10.5	1.66	24.1	2.42	35.1	0.9
4	180	26.2	0.304	0.50	7.3	1.97	28.6	2.79	40.5	0.9
4	152	22.1	0.256	0.80	11.6	2.05	29.7	2.73	39.6	0.8
4	118	17.1	0.199	0.86	12.5	1.87	27.1	2.76	40.0	0.9
				Crossply (±45°)						
295	112	16.2	-	0.27	3.9	0.90	13.0	3.62	52.4	13.6
295	100	14.5	0.417	0.68	9.9	1.01	14.6	3.92	56.9	-
295	120	17.3	0.375	0.17	2.4	0.92	13.3	3.32	48.2	10.6
76	61.8	9.0	0.313	0.08	1.2	1.52	22.0	4.11	59.6	4.6
76	71.8	10.5	0.361	0.20	2.8	1.44	20.9	4.64	67.2	8.8
75	99.0	14.4	0.325	0.16	2.3	1.09	15.8	3.66	53.1	-
4	109	15.9	0.405	0.48	6.9	1.40	20.3	4.25	61.7	3.2
4	111	16.0	0.378	0.26	3.7	1.20	17.4	4.06	58.9	4.1
4	84	12.1	0.337	0.18	2.7	1.41	20.5	4.02	58.4	5.2

[a] Poisson's ratios for transverse (90°) specimens (ν_{21}) were calculated from E_{22} and the average values of ν_{12} and E_{11}.

[b] These values resulted from an invalid fracture and were not included in the average value.

Table 3.

Tensile Properties of 5.6 mil Boron-Epoxy Composites

(Individual Specimens)

Temperature (K)	Elastic Modulus, E (10^9 N/m^2)	Elastic Modulus, E (10^6 psi)	Poisson's Ratio[a], ν	Proportional Limit, σ^{pl} (10^8 N/m^2)	Proportional Limit, σ^{pl} (10^3 psi)	0.2% Yield Strength, σ^{ty} (10^8 N/m^2)	0.2% Yield Strength, σ^{ty} (10^3 psi)	Ultimate Strength, σ^{tu} (10^8 N/m^2)	Ultimate Strength, σ^{tu} (10^3 psi)	Ultimate Elongation, ε^{tu} (%)
					Longitudinal (0°)					
295	235	34.1	0.261					16.3	236	0.7
295	235	34.0	0.213					16.9	245	0.8
295	228	33.1	0.227					17.1[b]	247[b]	0.8[b]
295	230	33.2	0.221					16.4[b]	238[b]	0.7[b]
295	227	32.9	0.223					15.8	229	0.7
76	240	34.9	0.243					16.6[b]	241[b]	0.7[b]
76	230	33.4	0.242					16.4	238	0.7
76	231	33.5	0.240					16.1	234	0.8
76	236	34.3	0.223					12.9[b]	187[b]	0.6[b]
76	229	33.2	0.256					17.8	258	0.9
4	244	35.4	0.227					18.5	268	0.8
4	237	34.4	0.241					18.3	265	0.8
4	234	34.0	0.262					16.2[b]	234[b]	0.7[b]
4	235	34.1	0.239					17.8[b]	258[b]	0.8[b]
4	238	34.5	0.227					17.7	257	0.8
					Transverse (90°)					
295	17.2	2.49	0.017	0.321	4.66			0.446[b]	6.47[b]	0.3[b]
295	16.3	2.36	0.016	0.348	5.04			0.472[b]	6.84[b]	0.3[b]
295	17.3	2.51	0.017	0.346	5.02			0.473	6.85	0.3
295	17.3	2.51	0.017	0.343	4.98			0.503	7.30	0.3
295	18.9	2.73	0.019	0.464	6.73			0.434	6.29	0.2
295	18.0	2.61	0.018	0.242	3.50			0.419[b]	6.08[b]	0.2[b]
76	29.6	4.29	0.031					0.502	7.23	0.2
76	28.9	4.19	0.030					0.515	7.47	0.2
76	32.5	4.71	0.034					0.420[b]	6.09[b]	0.1[b]
76	33.9	4.91	0.035					0.452	6.56	0.1
4	35.2	5.10	0.033					0.469	6.81	0.1
4	33.9	4.92	0.032					0.303	4.40	0.1
4	38.3	5.55	0.037					0.469	6.81	0.1
					Crossply (± 45°)					
295	16.8	2.43	0.856	0.421	6.11	0.939	13.6	1.28	18.5	1.8
295	18.6	2.70	0.801	0.396	5.74	0.969	14.1	1.31	19.0	1.8
295	18.8	2.73	0.794	0.402	5.82	0.961	13.9	1.30	18.9	2.0
76	31.9	4.57	0.665	0.417	6.05	0.993	14.4	1.10	15.9	0.8
76	33.0	4.79	0.624	0.388	5.63	0.940	13.6	1.13	16.4	0.9
76	33.1	4.81	0.724	0.427	6.19	0.920	13.4	1.10	15.9	0.9
4	32.1	4.66	0.677	0.328	4.75	0.849	12.3	1.02	14.8	0.8
4	35.5	5.15	0.758	0.278	4.03	0.821	11.9	0.98	14.2	0.8
4	32.2	4.67	0.664	0.282	4.09	0.821	11.9	1.03	15.0	0.9

[a] Poisson's ratios for transverse (90°) specimens (ν_{21}) were calculated from E_{22} and the average values of ν_{12} and E_{11} for each temperature.

[b] These values resulted from an invalid fracture and were not included in the average value.

Table 4.

Tensile Properties of S Glass-NASA Resin 2 Composites

(Individual Specimens)

Temperature (K)	Elastic Modulus, E		Poisson's Ratio[a],	Proportional Limit, σ^{pl}		0.2% Yield Strength, σ^{ty}		Ultimate Strength, σ^{tu}		Ultimate Elongation, ϵ^{tu} (%)
	(10^9 N/m^2)	(10^6 psi)		(10^8 N/m^2)	(10^3 psi)	(10^8 N/m^2)	(10^3 psi)	(10^8 N/m^2)	(10^3 psi)	
					Longitudinal (0°)					
295	59.3	8.59	0.238					14.9	216	3.1
295	57.2	8.31	0.261					11.9	173	2.7
295	55.4	8.05	0.305					14.1	204	2.7
76	58.0	8.40	0.257					19.1	276	3.4
76	58.6	8.50	0.278					19.3	280	3.3
76	58.2	8.44	0.272					20.3	295	3.2
4	62.8	9.10	0.310					19.1	276	3.0
4	57.4	8.35	0.299					21.6	314	3.4
4	60.2	8.74	0.261					17.5	253	2.7
					Transverse (90°)					
295	11.8	1.71	0.055	0.211	3.06	0.457	6.63	0.472	6.84	0.7
295	11.7	1.69	0.054	0.114	1.66	0.396	5.74	0.441	6.40	0.5
295	13.7	1.99	0.064	0.087	1.27	0.375	5.43	0.489	7.09	0.7
76	21.8	3.16	0.101					0.789	11.4	0.3
76	18.2	2.63	0.084					0.816[b]	11.8[b]	0.4[b]
76	22.2	3.21	0.102					0.843	12.2	0.4
76	21.5	3.12	0.099					1.13 [b]	16.4[b]	0.5[b]
76	22.4	3.25	0.105					1.10	16.0	0.5
4	19.5	2.82	0.094					0.657	9.53	0.3
4	24.8	3.60	0.120					0.921	13.4	0.4
4	21.8	3.17	0.105					0.771	11.2	0.4
					Crossply (± 45°)					
295	21.4	3.10	0.509	0.168	2.44	0.474	6.87	1.29	18.7	5.2
295	19.5	2.83	0.587	0.159	2.30	0.450	6.53	1.44	20.8	5.9
295	18.4	2.67	0.535	0.149	2.16	0.462	6.70	1.44	20.9	7.0
76	31.1	4.51	0.396	0.843	12.2	1.80	26.1	2.42	35.2	1.5
76	31.4	4.55	0.347	0.962	14.0	1.77	25.7	2.00	28.9	1.1
76	32.6	4.72	0.392	0.682	9.9	1.79	26.0	2.41	35.0	1.4
4	33.8	4.97	0.397	1.21	17.8	2.17	31.9	2.31[b]	34.0[b]	0.9[b]
4	35.1	5.09	0.419	1.06	15.3	2.19	31.7	2.35	34.1	1.0
4	33.2	4.81	0.383	1.37	19.9	2.29	33.1	2.39	34.6	0.9
4	36.0	5.21	0.349	1.10	16.0	2.10	30.4	2.31	33.5	0.9

[a] Poisson's ratios for transverse (90°) specimens (ν_{21}) were calculated from E_{22} and the average values of ν_{12} and E_{11} for each temperature.

[b] These values resulted from an invalid fracture and were not included in the average value.

Table 5.

Tensile Properties of Type A Graphite-NASA Resin 2 Composites
(Individual Specimens)

Temperature (K)	Primary Elastic Modulus, E $(10^9$ N/m^2)	Primary Elastic Modulus, E $(10^6$ psi)	Primary Poisson's Ratio[a], ν	Secondary Elastic Modulus, E $(10^9$ N/m^2)	Secondary Elastic Modulus, E $(10^6$ psi)	Secondary Poisson's Ratio, ν	Proportional Limit, σ^{pl} $(10^8$ N/m^2)	Proportional Limit, σ^{pl} $(10^3$ psi)	0.2% Yield Strength, σ^{ty} $(10^8$ N/m^2)	0.2% Yield Strength, σ^{ty} $(10^3$ psi)	Ultimate Strength, σ^{tu} $(10^8$ N/m^2)	Ultimate Strength, σ^{tu} $(10^3$ psi)	Ultimate Elongation ε^{tu} (%)
						Longitudinal (0°)							
295	115	16.7	0.314	124	18.0	0.341					12.9	187	0.9
295	113	16.3	0.316	122	17.8	0.346					14.8	214	1.0
295	126	18.2	0.341	130	18.9	0.354					11.9	173	0.9
76	112	16.3	0.272	123	17.8	0.301					12.1	176	1.1
76	97.7	14.2	0.279	116	16.7	0.285					12.6	183	0.9
76	93.8	13.6	0.288	115	16.7	0.310					12.1	176	0.9
4	111	16.1	0.263	121	17.6	0.297					12.6	183	0.9
4	132	19.1	0.377	149	21.6	0.429					13.2	191	0.9
4	107	15.5	0.253	123	17.8	0.294					13.4	194	0.9
						Transverse (90°)							
295	8.57	1.24	0.024								0.128	1.86	0.2
295	7.74	1.12	0.021								0.155	2.24	0.2
295	7.09	1.03	0.020								0.102	1.47	0.2
76	9.6	1.40	0.027								0.016	0.235	0.02
76	11.4	1.65	0.032								0.031	0.444	0.03
76	11.6	1.69	0.032								0.026	0.382	0.02
4	11.0	1.60	0.028								0.038	0.556	0.03
4	11.0	1.60	0.028								0.028	0.404	0.02
4	12.6	1.83	0.032								0.024	0.344	0.02
4	10.4	1.50	0.026								0.032	0.461	0.03
						Crossply (± 45°)							
295	12.9	1.87	0.655				0.247	3.58	0.473	6.86	0.697	10.1	1.6
295	16.7	2.42	0.706				0.200	2.90	0.511	7.42	0.678	9.8	0.7
295	17.1	2.49	0.758				0.233	3.38	0.524	7.61	0.718	10.4	0.9
76	19.4	2.82	0.903				0.212	3.08			0.451	6.54	0.2
76	16.0	2.32	0.703				0.205	2.97			0.448	6.50	0.3
76	16.6	2.41	0.794				0.225	3.27			0.423	6.13	0.3
4	19.4	2.82	0.772				0.251	3.64			0.474	6.87	0.3
4	17.5	2.53	0.602				0.264	3.82			0.470	6.81	0.3
4	17.2	2.50	0.697				0.257	3.73			0.490	7.11	0.3

[a] Poisson's ratios for transverse (90°) specimens (ν_{21}) were computed from E_{22} and the average values of ν_{12} and E_{11} for each temperature.

Table 6.

Tensile Properties of Kevlar 49 - NASA Resin 2 Composites

(Individual Specimens and Averages)

Temperature (K)	Elastic Modulus, E (10^9 Nm/^{2})	Elastic Modulus, E (10^6 psi)	Poisson's Ratio[a], ν	Ultimate Strength, σ^{tu} (10^8 N/m^2)	Ultimate Strength, σ^{tu} (10^3 psi)	Elongation, ε^{tu} (%)
			Longitudinal (0°)			
295	69.7	10.1	0.446	10.1	147	1.6
295	72.0	10.3	0.553	10.5	153	1.7
Avg 295	70.9	10.2	0.500	10.3	150	1.7
76	79.5	11.5	0.471	9.32	135	1.1
76	83.7	12.2	0.524	8.94	130	1.0
Avg 76	81.6	11.9	0.498	9.13	133	1.1
			Transverse (90°)			
295	0.638	0.093	0.004	0.002	0.032	0.02
295	0.981	0.142	0.007	0.004	0.052	0.04
Avg 295	0.810	0.118	0.006	0.003	0.042	0.03
76	0.794	0.115	0.005	0.001	0.017	0.01
76	0.597	0.087	0.004	0.001	0.017	0.01
Avg 76	0.696	0.101	0.005	0.001	0.017	0.01
			Crossply (± 45°)			
295	4.37	0.634	1.078	0.062	0.902	1.5
295	3.27	0.475	1.215	0.077	1.12	0.2
295	3.41	0.494	1.101	0.161	2.33	0.6
Avg 295	3.68	0.534	1.131	0.100	1.451	0.8
76	23.7	3.44	0.580	0.020	0.284	0.01
76	24.8	3.59	0.482	0.014	0.207	0.01
Avg 76	24.3	3.52	0.531	0.017	0.246	0.01

[a]Poisson's ratios for transverse (90°) specimens (ν_{21}) were computed from E_{22} and the average values of ν_{12} and E_{11} for each temperature.

Table 7.

Tensile Properties of 5.6 mil Boron-6061 Aluminum Composites

(Averages of Specimens Tested[a])

Temperature (K)	Elastic Modulus, E (10^9 N/m^2)	Elastic Modulus, E (10^6 psi)	CV(%)	Poisson's Ratio,[b] ν	CV(%)	Proportional Limit, σ^{pl} (10^8 N/m^2)	Proportional Limit, σ^{pl} (10^3 psi)	CV(%)	0.2% Yield Strength, σ^{ty} (10^8 N/m^2)	0.2% Yield Strength, σ^{ty} (10^3 psi)	CV(%)	Number of Specimens
					Longitudinal (0°)							
295	200(11)	29.0(1.6)	5.7	0.299(0.024)	8.2							4
76	197(11)	28.5(1.6)	5.6	0.341(0.005)	1.6							4
4	204(9)	29.6(1.3)	4.3	0.344(0.022)	6.3							4
					Transverse (90°)							
295	161(18)	23.4(2.6)	11.0	0.241(0.027)	11.2	0.63(0.08)	9.1(1.1)	11.9	1.34(0.05)	19.4(0.7)	3.6	3
76	(28)24)	18.5(3.5)	18.7	0.221(0.041)	18.6	0.76(0.11)	11.0(1.6)	15.1	1.78(0.14)	25.9(2.0)	7.8	4
4	150(31)	21.8(4.6)	20.8	0.253(0.053)	20.8	0.72(0.19)	10.5(2.8)	26.8	1.96(0.09)	28.5(1.3)	4.6	3
					Crossply (± 45°)							
295	111(10)	16.0(1.4)	9.0	0.396(0.021)	5.3	0.37(0.27)	5.4(4.0)	73.0	0.94(0.06)	13.6(0.9)	6.2	3
76	78)19)	11.3(2.8)	24.8	0.333(0.025)	7.5	0.15(0.06)	2.1(0.8)	40.7	1.35(0.23)	19.6(3.3)	16.9	3
4	101(15)	14.7(2.2)	14.9	0.373(0.034)	9.2	0.31(0.16)	4.4(2.2)	50.1	1.34(0.12)	19.4(1.7)	8.8	3

Temperature (K)	Ultimate Strength, σ^{tu} (10^8 N/m^2)	Ultimate Strength, σ^{tu} (10^3 psi)	CV(%)	Ultimate Elongation, ε^{tu} (%)	CV(%)	Number of Specimens
		Longitudinal (0°)				
295	12.7	184	-	0.6	-	1
76	16.4(0.6)	238(8)	3.4	0.8(0.0)	3.1	3
4	16.1(0.9)	233(12)	5.3	0.8(0.1)	7.7	4
		Transverse (90°)				
295	1.67(0.18)	24.2(2.7)	10.9	0.7(0.1)	14.3	3
76	2.49)0.08)	36.1(1.1)	3.1	0.8)0.1)	7.2	3
4	2.76(0.03)	40.0)0.5)	1.1	0.9)0.1)	6.4	3
		Crossply (± 45°)				
295	3.62)0.30)	52.5)4.4)	8.3	12.1)1.5)	12.4	3
76	4.(4)0.49)	60.0(7.1)	11.8	6.7(2.1)	31.3	3
4	4.11)0.12)	59.7)1.8)	3.0	4.2)1.0)	23.6	3

[a] Standard deviations are in parentheses. CV is coefficient of variation. Data from the specimens that broke at or in the grips are not included in the calculations of ultimate strength or elongation.

[b] Poisson's ratios for transverse (90°) specimens (ν_{21}) were calculated from ν_{12}, E_{11}, and E_{22}.

Table 8.

Tensile Properties of 3.6 mil Boron-Epoxy Composites
(Averages of Specimens Tested[a])

Temperature (K)	Elastic Modulus, E (10^9 N/m^2)	(10^6 psi)	CV(%)	Poisson's Ratio,[b] ν	CV(%)	Proportional Limit, σ^{pl} (10^8 N/m^2)	(10^3 psi)	CV(%)	0.2% Yield Strength, σ^{ty} (10^8 N/m^2)	(10^3 psi)	CV(%)	Number of Specimens
				Longitudinal (0°)								
295	231(4)	33.5(0.61)	1.6	0.228(0.019)	8.3							5
76	233(5)	33.9(0.7)	2.1	0.241(0.012)	4.8							5
4	238(6)	34.5(0.6)	2.3	0.239(0.014)	5.9							5
				Transverse (90°)								
295	17.5(0.9)	2.54(0.12)	5.0	0.017(0.001)	6.1	0.344(0.071)	4.99(1.02)	20.7				6
76	31.2(2.4)	4.53(0.34)	7.5	0.033(0.002)	7.3							4
4	35.8(2.3)	5.19(0.32)	6.3	0.034(0.003)	7.9							3
				Crossply (± 45°)								
295	18.1(1.1)	2.62(0.17)	6.3	0.817(0.034)	4.1	0.406(0.013)	5.89(0.19)	3.3	0.956(0.016)	13.9(0.3)	1.8	3
76	32.7(0.7)	4.72(0.13)	2.8	0.671(0.050)	7.4	0.411(0.040)	5.96(0.29)	4.9	0.951(0.038)	13.8(0.5)	3.9	3
4	33.3(1.9)	4.83(0.28)	5.8	0.700(0.051)	7.2	0.295(0.028)	4.29(0.40)	9.3	0.830(0.016)	12.0(0.2)	1.9	3

Temperature (K)	Ultimate Strength, σ^{tu} (10^8 N/m^2)	(10^3 psi)	CV(%)	Ultimate Elongation, ϵ^{tu} (%)	CV(%)	Number of Specimens
		Longitudinal (0°)				
295	16.3(0.61)	237(8)	3.3	0.73(0.04)	5.1	3
76	16.8(0.9)	243(13)	5.4	0.77(0.07)	9.3	3
4	18.2(0.41)	263(5)	2.2	0.76(0.011)	1.5	3
		Transverse (90°)				
295	0.470(0.035)	6.81(0.51)	7.4	0.27(0.06)	21.7	3
76	0.490(0.033)	7.09(0.47)	6.7	0.15(0.03)	17.6	3
4	0.414(0.096)	6.01(1.39)	23.1	0.12(0.04)	33.6	3
		Crossply (± 45°)				
295	1.30(0.02)	18.8(0.3)	1.4	1.88(0.14)	7.5	3
76	1.14(0.02)	16.1(0.3)	1.7	0.85(0.05)	5.3	3
4	1.01(0.03)	14.7(0.4)	2.8	0.83(0.05)	6.3	3

[a] Standard deviations are in parentheses. CV is coefficient of variation. Data from the specimens that broke at or in the grips are not included in the calculations of ultimate strength or elongation.

[b] Poisson's ratios for transverse (90°) specimens (ν_{21}) were calculated from ν_{12}, E_{11}, and E_{22}.

Table 9.

Tensile Properties of S Glass-NASA Resin 2 Composites
(Averages of Specimens Tested[a])

Temperature (K)	Elastic Modulus, E_{11} (10^9 N/m^2)	(10^6 psi)	CV(%)	Poisson's Ratio[b], ν_{12}	CV(%)	Proportional Limit, σ^{pl} (10^8 N/m^2)	(10^3 psi)	CV(%)	0.2% Yield Strength, σ^{ty} (10^8 N/m^2)	(10^3 psi)	CV(%)	Number of Specimens
					Longitudinal (0°)							
295	57.3(0.5)	8.32(0.27)	3.2	0.268(0.034)	12.7							3
76	58.3(0.3)	8.45(0.05)	0.6	0.272(0.011)	4.0							3
4	60.1(2.7)	8.73(0.38)	4.5	0.269(0.011)	8.9							3
					Transverse (90°)							
295	12.4(1.1)	1.80(0.17)	9.3	0.658(0.006)	9.5	0.137(0.065)	2.00(0.94)	47.6	0.409(0.043)	5.93(0.62)	10.5	3
76	21.2(2.4)	3.07(0.36)	11.7	0.098(0.008)	8.4							5
4	22.0(2.7)	3.20(0.39)	12.2	0.105(0.013)	12.3							3
					Crossply (± 45°)							
295	19.3(1.5)	2.87(0.22)	7.7	0.544(0.040)	7.3	0.16(0.01)	2.30(0.14)	6.1	0.46(0.01)	6.70(0.17)	2.6	3
76	31.7(0.8)	4.59(0.11)	2.5	0.378(0.027)	7.2	0.83(0.14)	12.0(2.1)	17.1	1.79(0.02)	25.9(0.2)	0.9	3
4	34.5(1.5)	5.02(0.21)	4.5	0.387(0.036)	9.3	1.19(0.17)	17.3(2.5)	14.6	2.15(0.10)	31.8(1.4)	4.4	4

Temperature (K)	Ultimate Strength, σ^{tu} (10^8 N/m^2)	(10^3 psi)	CV(%)	Ultimate Elongation, ε^{tu} (%)	CV(%)	Number of Specimens
			Longitudinal (0°)			
295	13.6(1.6)	198(22)	11.4	2.8(0.2)	8.2	3
76	19.6(0.6)	284(10)	3.5	3.3(0.1)	3.0	3
4	19.4(2.1)	281(31)	11.0	3.0(0.4)	11.7	3
			Transverse (90°)			
295	0.467(0.024)	6.8(0.4)	5.2	0.6(0.1)	19.2	3
76	0.936(0.234)	13.6(3.4)	25.3	0.4(0.1)	29.6	3
4	0.783(0.132)	11.4(1.9)	17.0	0.4(0.1)	15.6	3
			Crossply (± 45°)			
295	1.39(0.87)	20.1(1.2)	6.2	6.0(0.9)	15.1	3
76	2.28(0.24)	33.0(3.6)	10.9	1.3(0.2)	16.0	3
4	2.34(0.05)	34.1(0.6)	2.0	0.9(0.1)	6.6	4

[a] Standard deviations are in parentheses. CV is coefficient of variation. Data from the specimens that broke at or in the grips are not included in the calculations of ultimate strength or elongation.

[b] Poisson's ratios for transverse (90°) specimens (ν_{21}) were computed from ν_{12}, E_{11}, and E_{22}.

Table 10.

Tensile Properties of Type A Graphite - NASA Resin 2 Composites
(Averages of Specimens Tested[a])

Temperature (K)	Primary: Elastic Modulus, E (10^9 N/m^2)	(10^6 psi)	CV(%)	Poisson's Ratio[b], ν	CV(%)	Secondary: Elastic Modulus, E (10^9 N/m^2)	(10^6 psi)	CV(%)	Poisson's Ratio, ν	CV(%)	Proportional Limit, σ^{pl} (10^8 N/m^2)	(10^3 psi)	CV(%)	0.2% Yield Strength, σ^{ty} (10^8 N/m^2)	(10^3 psi)	CV(%)	Number of Specimens
									Longitudinal (0°)								
295	118(7)	17.1(1.0)	5.9	0.324(0.015)	4.6	125(4)	18.2(0.6)	3.3	0.347(0.007)	1.9							3
76	101(10)	14.7(1.4)	9.6	0.280(0.006)	2.9	118(4)	17.1(0.6)	3.7	0.299(0.013)	4.2							3
4	117(13)	16.9(1.9)	11.5	0.298(0.069)	23.1	131(16)	19.0(2.3)	11.9	0.340(0.077)	22.7							3
									Transverse (90°)								
295	7.8(0.7)	1.13(0.11)	9.5	0.022(0.002)	9.5												3
76	10.9(1.1)	1.58(0.16)	10.1	0.030(0.003)	9.8												3
4	11.3(0.9)	1.63(0.14)	8.6	0.029(0.003)	8.7												4
									Crossply (± 45°)								
295	15.6(2.3)	2.26(0.34)	15.0	0.706(0.052)	7.3						0.227(0.024)	3.29(0.35)	10.6	0.503(0.027)	7.30(0.39)	5.3	3
76	17.3(1.8)	2.52(0.27)	10.6	0.800(0.100)	12.5						0.214(0.010)	3.11(0.15)	4.9				3
4	18.0(1.2)	2.62(0.18)	6.7	0.690(0.085)	12.3						0.257(0.007)	3.73(0.09)	2.5				3

Temperature (K)	Ultimate Strength, σ^{tu} (10^8 N/m^2)	(10^3 psi)	CV(%)	Ultimate Elongation, ε^{tu} (%)	CV(%)	Number of Specimens
		Longitudinal (0°)				
295	13.2(1.5)	191(21)	11.2	0.9(0.1)	6.4	3
76	12.3(0.3)	178(4)	2.3	1.0(0.1)	11.9	3
4	13.1(0.4)	189(6)	3.2	0.9(0.0)	0.0	3
		Transverse (90°)				
295	0.128(0.027)	1.86(0.39)	20.7	0.2(0.0)	0.0	3
76	0.024(0.008)	0.35(0.11)	31.8	0.02(0.01)	28.9	3
4	0.031(0.006)	0.44(0.09)	20.5	0.03(0.01)	23.1	4
		Crossply (± 45°)				
295	0.698(0.020)	10.1(0.3)	2.9	1.1(0.5)	43.0	3
76	0.441(0.015)	6.4(0.2)	3.5	0.3(0.1)	21.4	3
4	0.478(0.011)	6.9(0.2)	2.3	0.3(0.0)	0.0	3

[a] Standard deviations are in parentheses. CV is coefficient of variation.

[b] Poisson's ratios for transverse (90°) specimens (ν_{21}) were computed from ν_{12}, E_{11}, and E_{22}.

Table 11.

In-Plane Shear Modulus[a]

(Average of Three Specimens)

Temperature (K)	Shear Modulus, G_{12} (10^9 N/m^2)	(10^6 psi)	CV(%)
	Boron-Aluminum[b]		
295	39.7(4.0)	5.75(0.58)	10.0
76	27.5(5.5)	3.92(0.80)	20.4
4	32.6(5.5)	4.73(0.80)	16.9
	Boron-Epoxy		
295	4.72(0.44)	0.68(0.06)	9.3
76	9.19(0.38)	1.33(0.06)	4.1
4	9.28(0.19)	1.35(0.03)	2.0
	Glass - NASA Resin 2		
295	6.19(0.51)	0.90(0.07)	8.3
76	11.0(0.6)	1.60(0.09)	5.8
4	12.9(0.3)	1.87(0.05)	2.8
	Graphite - NASA Resin 2		
295	4.14(0.33)	0.600(0.047)	7.9
76	4.50(0.15)	0.652(0.022)	3.3
4	5.32(0.36)	0.772(0.053)	6.8

[a]These values are calculated from the crossply ($\pm$ 45°) data using the method of Sims and Halpin. Standard deviations are in parentheses; CV is the coefficient of variation.

[b]The boron-aluminum moduli are only lower limits to the true values.

Appendix I: Symbols

E_{11}	=	longitudinal (0°) elastic modulus
E_{22}	=	transverse (90°) elastic modulus
E_x	=	crossply ($\pm$ 45°) elastic modulus
ν_{12}	=	longitudinal (0°) Poisson's ratio
ν_{21}	=	transverse (90°) Poisson's ratio
ν_x	=	crossply ($\pm$ 45°) Poisson's ratio
G_{12}	=	intralaminar (in-plane) shear modulus
σ^{pl}	=	proportional limit; stress at which a stress-strain curve deviates from elasticity, i.e., is no longer a straight line
σ^{ty}	=	0.2% tensile yield strength; stress at the intersection of the stress-strain curve with a straight line having the same slope as the elastic modulus and offset by 0.2% along the strain scale
σ^{tu}	=	ultimate strength; highest stress attained on the stress-strain curve
ε^{tu}	=	ultimate elongation; highest strain attained on the stress-strain curve

Appendix II: M. B. Kasen, "Mechanical and thermal properties of filamentary-reinforced structural composites at cryogenic temperatures. 1: Glass-reinforced composites," Cryogenics 15(6), pp. 327-349 (1975).

This article is an extensive review of the literature on the mechanical and thermal properties of glass-reinforced structural composites at cryogenic temperatures. The objective is to provide an understanding of the general magnitude of property values obtainable within the cryogenic temperature range, to provide a feel for the relative literature ranking of specific composite types with regard to a specific property, and to impart an understanding of the temperature sensitivity of the property of interest. A bibliography and bibliography-property cross-reference is included. This is Part I of a two-part series. Part II will consider advanced composites.

Mechanical and thermal properties of filamentary-reinforced structural composites at cryogenic temperatures

1: Glass-reinforced composites

M. B. Kasen

Nomenclature

σ^{tu}	tensile ultimate strength	σ^{by}	bearing yield strength
E_1^t	initial tensile modulus	σ^{I}	impact strength
E_2^t	secondary tensile modulus	λ	thermal conductivity
ϵ^{tu}	tensile ultimate strength	$\Delta L/L$	thermal contraction
n^{tu}	tensile fatigue failure stress	C_p	specific heat
σ^{fu}	flexural ultimate strength	*Units*	
E_1^f	initial flexural modulus	lb in^{-2}	pounds per square inch
E_2^f	secondary flexural modulus	lb in^{-2}	lb in^{-2} x 10^3
σ^{cu}	compressive ultimate strength	N m^{-2}	Newtons per metre squared (Pascal)
E^c	compressive modulus	J kg^{-1} K^{-1}	Joules per kilogram-Kelvin
σ^{si}	interlaminar shear strength	W m^{-1} K^{-1}	Watts per metre-Kelvin

The primary impetus for structural composite development arose from the need to obtain improved long-term mechanical properties at elevated temperatures or to reduce the cost of structures designed for ambient temperature use. Comparatively little effort has been expended on development of composites for use at cryogenic temperatures. A notable exception has been the rather extensive body of work sponsored by the USAF and NASA wherein a series of glass-reinforced plastics were characterized to 20 K. The other major field of cryogenic development has been concerned with composite reinforcement of pressure vessels for aerospace use, largely exploiting the continuous-filament method of fabrication. To a large extent, the remaining published data on composite properties at cryogenic temperatures reflects work on which the generation of cryogenic property data was peripheral to the main work objective.

This relative lack of emphasis on cryogenic structural composites is perhaps understandable, as the majority of such structural applications are presently satisfied by readily available and well-characterized metals and alloys. In view of the extensive data base available on metals, it is probable that metals will continue to constitute the main body of structural materials at low temperatures.

Why then, should one consider composites? The answer lies in the increasingly stringent demands made on materials in advancing cryogenic technology, of which superconduct-

The author is with the Cryogenics Division, National Bureau of Standards, Institute for Basic Standards, Boulder, Colorado 80302, USA. This research was supported by the Advanced Research Projects Agency of the Department of Defence under ARPA Order No 2569. Received 6 January 1975.

ing machinery may serve as an example. Undoubtedly, the first generation of superconducting motors and generators will be dependent almost entirely on metals technology. However, it is highly probable that succeeding generations of such equipment will capitalize on advanced composite technology for reasons of increased reliability, reduced weight, and increased efficiency, lecting the higher specific strengths and moduli of advanced composites coupled with a wider range of thermal and electrical properties than are obtainable with any conventional metal. In particular, the high strength of the polymeric-matrix composites combined with very low thermal conductivity will be advantageous in minimizing heat losses in critical components.

The technological problems associated with integration of composites into superconducting machinery are three-fold: (a) most designers lack a feel for the properties available with composites, (b) an adequate data base does not exist for composites at cryogenic temperatures, particularly at 4 K, and (c) most existing composites are optimized for service at room temperature and above not for for cryogenic service. The current programme at NBS is aimed at these three problem areas.

Our first effort has been to initiate an extensive review of what is known about the mechanical and thermal properties of composites at cryogenic temperatures. The objectives of the review are four-fold: (a) we wish to provide the designer with a feel for the general magnitude of property values which may reasonably be expected from a given category and class of composites within the cryogenic range. (We define a composite *category* by the general reinforcement type, for example, glass-fibre or advanced fibre (graphite, boron, etc). We subdivide the category into composite *classes* by the general matrix type, for example, glass-polyester or graphite-epoxy. We further subdivide the class by referring to a composite *type* when a specific reinforcement/matrix combination is specified, for example, HT-S graphite/X-904 epoxy.] (b) we wish to provide him with a feel for the literature ranking of specific composite classes with regard to a specific property, (c) we wish to impart a feel for whether the property of interest is likely to increase, remain unaffected, or decrease with lowering of temperature, and (d) we wish to define those areas in which further data are needed and to define the direction that future work should take in optimizing composites for cryogenic service and for implementing their use in the construction of superconducting machinery. For those with more specific interests we include an extensive Bibliography and Bibliography-property cross-reference to simplify retrieval of specific documents.

It must be emphasized that, although this survey is intended to be comprehensive, the complex nature of the subject makes it unavoidable that some works worthy of inclusion have been inadvertently omitted The author will appreciate references to any additional material which bears on the subject. It must also be emphasized that the results reported in the surveyed publications have not been experimentally confirmed by NBS and that the conclusions and evaluations presented in this paper reflect those of the cited authors and do not imply approval, endorsement, or recommendation by NBS.

The discussion of properties given below does not take into consideration the effect of variations in fibre/resin ratio of specific types of composites and test specimens, as this characteristic was not reported for all referenced works. Composite properties may be strongly influenced by this ratio. The property data discussed in this paper reflects actual values and trends reported by the cited authors for specific composites. Controlled variations in many of the properties are obtainable in practice by specific variation of the fibre content of the composite.

The literature review covers 1960 to the present time, as it is within this time span that almost all of the significant work was undertaken. We include only continuous-fibre reinforced composites, as such composites are the primary structural materials. The review excluded cryogenic insulations, superconductor composites, thin films, honeycomb strucures, composite-overwrapped metal, or fibre-only properties. Filled composites are also excluded. There remains the very large field of composites reinforced by a variety of fibres in a variety of lay-ups in a variety of matrix materials, and it is with this body of data that this review is concerned.

The wide variety of composite formulations and lay-ups are further complicated by lack of standard test procedures. Furthermore, as the field is relatively new, much of the earlier work was performed on relatively poorly characterized composites. We have attempted to cope with this complexity by dividing the review into two major sections: Part I treating glass-reinforced composites and Part II treating the so-called advanced composites, for example, boron, graphite, etc. The rationale for this separation is the distinctly different use of these two composite categories in engineering practice, that is, glass-reinforced composites are used in applications where stiffness is not a design limitation, while the advanced composites are used where a high modulus material is essential.

Within each of these categories, we present the reader with a series of graphs on which appear the *average* literature values of each property for each composite class from room temperature into the deep cryogenic range. Admittedly, presenting average data is in danger of being misleading, as each curve has associated with it a considerable scatter band. For this reason, we discuss the range of values associated with each curve, emphasizing those specific composite types for which the highest values were reported. It is of utmost importance, however, that the reader understands that the graphed data appearing in this review are class averages and are therefore not to be used for engineering design purposes. The reader interested in design values is referred to the specific literature references.

Scope of the literature survey

We initially conducted a subject search using the data bases of the NBS Cryogenic Data Center (CDC), Defense Documentation Center (DDC), and the National Technical Information Service (NTIS). Additionally, a subject search was conducted through the volumes of NASA Scientific and Technical Aerospace Reports (STAR), and the ASM-AIME Metals Review. As the search progressed, a series of contract numbers were identified as being associated with studies of the cryogenic properties of composites. The DDC and NASA data bases were then searched for all reports issued under such contracts. Finally, the DDC date base and that of the Smithsonian Science Information Exchange were searched for current work in progress.

Organization of the Bibliography

The appended Bibliography contains 148 references. As the work progressed, it became apparent that a large part of the

relevant data had been produced under a relatively few contracts sponsored either by NASA or the USAF. Eleven such contracts have been listed at the start of the Bibliography with references to the most pertinent publications issued under each contract. Only final reports are listed, as they adequately summarize the data which also appeared in numerous interim reports on each project. Journal publications are listed, as they often provide a convenient review of the subject matter contained in the comprehensive reports and are generally more readily available to the reader.

The Bibliography also contains a general section, alphabetically arranged by author, listing relevant publications sponsored by other contracts or by corporate in-house funding. A separate part of the Bibliography itemizes handbooks or reviews which will be found useful references but which do not contain original data. Finally, a miscellaneous reference section lists publications which are referenced in the text but which do not contain relevant mechanical or thermal property data.

Wherever possible, the pertinent NASA or DDC code number is included to facilitate retrieval of specific publications. Corporate reports not so identified must be obtained from the corporate source.

An extensive cross-reference relating mechanical and physical properties of specific types of composites to specific literature references is included to simplify literature retrieval by the reader. The latter includes separate references to filament-wound pressure vessels in recognition of the importance of such applications to cryogenic technology. A separate listing is also provided of reports containing information on the effect of combined cryogenic temperature and nuclear radiation.

Glass-reinforced composites

The mechanical and thermal properties of glass-polymeric composites are summarized on Figs 1–16. Where available, data are presented for 295 K, 200 K, 77 K, and 20 K (4 K data are almost non-existent). Straight lines connect average values at each temperature. Absence of a data point for a given temperature implies that no significant data was found in the literature. An asterisk adjacent to the number identifying a curve indicates that the data for that particular composite type was minimal relative to that available for the other composite types included on the figure.

When considering the mechanical property data, the reader should be aware that there exists no universally accepted method of determining these properties for composites, although committees of the ASTM are working diligently on the problem of standardization. The data discussed in the present review were for the most part obtained in the course of comprehensive research programmes by reliable investigators who were concerned with obtaining the most valid results possible. Nevertheless, it remains a possibility that some of the scatter in the data reported in the literature, particularly for compression and interlaminar shear, reflects differing test procedures. Where this has become apparent, the data have been separated by test method.

Static mechanical properties

Composite tensile strength and modulus

The reason for the widespread use of glass-reinforced composites is evident from the tensile strength data presented on Fig.1. No other type of composite can match the uniaxial tensile strengths of 250–300 k lb in^{-2} provided by the glass-epoxy formulations. Even in the 0°/90° crossply lay-up, the glass-epoxy strength is almost equal to that of the advanced composites in the uniaxial longitudinal configuration. Unfortunately, the moduli of glass-reinforced composites are quite low, as may be seen in Fig.2. It is this low modulus of glass that has given impetus for development of the advanced composites.

From Fig.1 we see that the tensile strength is reduced about 50% at all temperatures in a 0°/90° configuration as compared to uniaxial, for example, from about 300 k lb in^{-2} to about 150 k lb in^{-2} for glass-epoxies. This is expected from a 50% decrease in longitudinal fibre content, the crossply fibres contributing nothing to the overall strength when tested parallel to one fibre direction.

Approximately another 25% decrease in strength is found upon going to woven cloth reinforcement of an epoxy matrix, reflecting the decrease in load carrying capacity of fibres which are slightly bent in the weaving process.

Epoxy resins are most widely used as matrices for structural applications where maximum strength is required. This appears justified on the basis of the data of Fig.1 wherein the ultimate tensile strengths of the cloth-epoxy composites are overall higher than those of other cloth-polymeric composites at all temperatures. The polyurethane, Teflon, phenyl silane, polyimide, and silicone-matrix composites appear to have the poorest strength properties at 295 K, with phenolic, polybenzimidazole (also known as PBI or Imidite), and polyester-matrix composites being intermediate in strength. At 77 K, the polyimide, silicone, and phenyl silane-matrix composites continue their relatively poor performance, while the polyurethane, polybenzimidazole, and Teflon-matrix composites have about equalled the phenolics and polyesters.

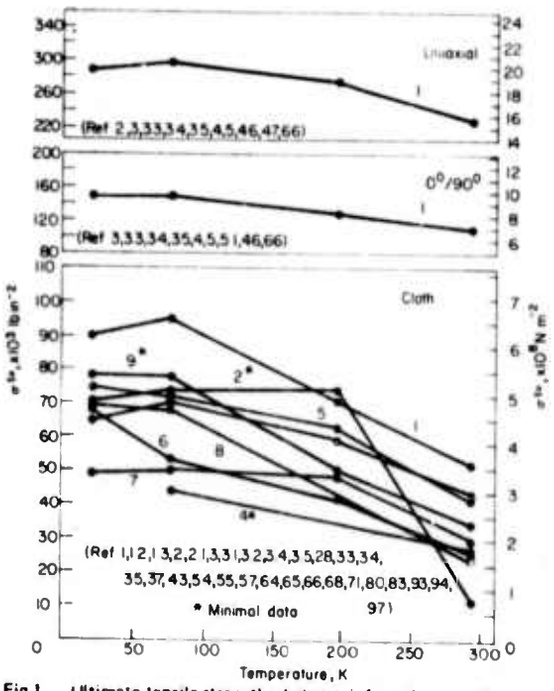

Fig.1 Ultimate tensile strength of glass-reinforced composites
1 – epoxy; 2 – polyurethane; 3 – phenolic; 4 – polyimide; 5 – polyester; 6 – silicone; 7 – phenyl silane; 8 – Teflon; 9 – polybenzimidazole

Among the uniaxial glass-epoxy composites, the highest reported strengths were about 175 k lb ln^{-2} at 77 K for NOL-ring tests with S-HTS/660 FW and S-901/ERL 2256/ZZL 0820 composites.[46,47] This work was directed toward filament-wound pressure vessels, which has been the incentive for much of the cryogenic composite development work. Other authors [3,66] have reported strengths of 315–330 k lb in^{-2} at this temperature for S-901/E-787 and S-HTS/Epon 828/Epon 1031 filament-wound composites. About the same strength was reported for Hi-Stren glass filament-wound in a NASA Resin 2 matrix.[4] The overall data range was 213–375 k lb in^{-2} at 77 K.

A comment on two of these epoxy resins is in order so as to prepare the reader for proper understanding of these and subsequent data. Resin E-787 will be referred to frequently in this paper, as it is often associated with the highest reported mechanical properties. E-787 is the US Polymeric Corporation designation for an Epon 828/Epon 1031/NMA/BDMA formulation in proportions 50/50/90/0.55 pbw. This resin is referred to as 58–68R by the Shell Chemical Company and is often referred to as the Polaris resin because of its successful use in that missile. It is a conventional type of resin, not optimized for cryogenic service. By contrast, Resin 2, consisting of Epon 828/DSA/Empol 1040/BDMA in proportions 100/115.9/20/1 pbw, is a bisphenolic. A epoxy system modified for low-temperature flexibility be means of a long-chain anhydride and a high-molecular weight tricarboxy acid. This latter resin was developed by Soffer and Molho under NASA sponsorship.[5] Soffer and Molho compared the Resin 2 formulation to that of 58–68R (E-787) in a series of burst tests on metal-lined, S-901 glass filament-wound pressure vessels, their results showing Resin 2 to develop equal strength at room temperature and higher longitudinal filament stresses at 77 K and 20 K. Additionally, Resin 2 was found to have relatively greater ductility and toughness at cryogenic temperatures and to be highly resistant to cracking when thermal cycled to 20 K. As the E-787 and Resin 2 epoxy formulations are likely candidates for cryogenic applications, the present report compares the property values obtained with each resin whenever such data are available. A further discussion of resins for cryogenic service is presented in the concluding part of this paper.

Continuing with the analysis of the data on Fig.1, it is found that among the 0°/90° data, the highest tensile strengths at cryogenic temperatures have been reported for S-901/E-787[3] and S-901/Resin 2[5] with values ranging from 170–200 k lb in^{-2}. The overall range was 115–200 k lb in^{-2}.

Among the woven-cloth composites, the highest cryogenic composite strengths were reported for the epoxy-matrix composites 181/modified Epon 828[2] and 1581/E-787,[3] having tensile strengths on the order of 125–145 k lb in^{-2} at 77 K tested parallel to the woof or warp. The phenolic-matrix composite data showed quite consistent strengths of 60–70 k lb in^{-2} at 77 K except for the work of Levin et al[71] who has reported 200 k lb in^{-2} at 77 K in a composite based on a butvar-phenolic adhesive. The polyester-matrix data scatters from 50–80 k lb in^{-2} at 77 K except for one report of 100–105 k lb in^{-2} for 181 glass in Hetron 31 or Narmco 527 resin.[2] The Teflon-matrix composites ranged from 50–80 k lb ln^{-2}, the highest value being reported for type 116 glass in TFE or FEP.[80] The silicone-matrix data showed relatively large scatter from 25–70 k lb in^{-2} at 77 K with the highest values being reported for 181/Trevarno F-131[2] and for 181/Narmco 513.[3] Few data were found for polyurethane, phenyl, silane, and polyimide-matrix composites. About 73 k lb in^{-2} was reported at 77 K for 181 glass reinforced with the flexible polyurethane Adiprene L-100 and 60 k lb in^{-2} for the same reinforcement in the phenyl silane Narmco 534.[2] Polyimides are relatively new matrix materials, having been developed primarily for elevated-temperature use, particularly for stability. Krause et al[68] reports a comparatively low value of 43 k lb in^{-2} at 77 K for a glass-polyimide composite. On the other hand, polybenzimidazole-matrix composites, which are of the same family as the polyimides, appear to develop very high strength at 77 K and at 20 K, exceeded only by the epoxies.

All of the above comparisons were made at 77 K because, as seen on Fig.1, while the tensile strength in all cases increases between 295 K and 77 K, further cooling to 20 K produces erratic results. This is more clearly illustrated by Fig.5a, which is a histogram illustrating the frequency with which the literature reports a given change in the ultimate tensile strength of glass-epoxy composites upon cooling from room temperature to 77 K and to 20 K. The data are broken down as to lay-up type. Here it is seen that cooling of glass-epoxy composites from 295 K to 77 K can produce a strength increase of from 10–140 k lb in^{-2} with a high probability of an increase on the order of 30–60 k lb in^{-2}, essentially independent of the type of lay-up. However, on cooling further to 20 K, the probability is for a slight decrease in strength for cloth and 0°/90° crossply reinforced epoxies and a reasonably high probability that uniaxial glass-epoxies will suffer a strength degradation which may be as high as 80 k lb in^{-2}. The phenolic, polyester, phenyl silane, and polyurethane-matrix composites all showed a similar erratic behaviour. An exception appeared to be the silicone-matrix composites which showed consistent moderate increases in strength at 20 K.

The behaviour at 200 K offers few surprises except for the 181/Adiprene L-100 data [2] which indicate that the strength of this flexible polyurethane composite rapidly increases as temperature is lowered.

As with the tensile strength, the initial tensile modulus (The initial slope of the stress-strain curve in crossply and cloth-reinforced glass composites), Fig.2, shows the expected dependence on fibre orientation. Values range from about 10^7 lb in^{-2} for the uniaxial longitudinal lay-ups to 5–6 x 10^6 lb ln^{-2} for the 0°/90° crossply to 2–5 x 10^6 lb in^{-2} for the woven cloth composites. The polybenzimidazole-matrix composites developed much higher moduli than any of the other cloth-reinforced materials at cryogenic temperatures. Also, the glass-cloth phenolic composites are found to have, on the average, slightly higher moduli than glass cloth-epoxies, while glass cloth-polyesters appear as good as the epoxies. The silicone, polyurethane, and Teflon-matrix composites displayed the lowest moduli with an indication that phenyl silane-matrix composites are of intermediate modulus.

Again taking 77 K as a criterion temperature, the uniaxial glass-epoxies showed a modulus range of about 8–11 x 10^6 lb in^{-2} with the higher values reflecting variants of S-HTS/Epon 828 [66] and Hi-Stren/Resin 2.[4] The 0°/90° crossply data ranged from 3–7 x 10^6 lb in^{-2} with values of 5.5–7 x 10^6 lb in^{-2} being reported for S-901 glass with a series of epoxy resin formulations.[3] The cloth-reinforced

epoxies yielded moduli from 2–5 x 10^6 lb in^{-2} with the comparatively highest values being reported for 181 glass/Epon 828 formulations.[2]

Although the average moduli of the glass cloth-phenolic composites was higher than that of the epoxies, literature values ranged from 3–4.7 x 10^6 lb in^{-2} which suggests that no significant difference in moduli should be expected for good composites made with either epoxy or phenolic matrices. A detailed look at the glass-cloth polyester data, however, shows a relatively narrow modulus range of about 3.5–4 x 10^6 lb in^{-2} suggesting that the strongest composites made with this polymeric matrix are probably weaker in modulus than the strongest epoxies or phenolics by about 10^6 lb in^{-2}. In a similar way, the glass cloth-silicone matrix composites are still weaker having moduli which vary from 2.5–2.9 x 10^6 lb in^{-2} at 77 K. Somewhat fewer moduli data are available for polybenzimidazole, Teflon, polyurethane, and phenyl silane-matrix composites, but that which is available suggests that the Teflon matrix produces moduli of only 1.6–3 x 10^6 lb in^{-2} with 3.3 x 10^6 lb in^{-2} and 3.6 x 10^6 lb in^{-2} for the polyurethane and phenyl silane matrices, respectively. The polybenzimidazole data were obtained with a 181/polybenzimidazole composite [2] and are noteworthy not only for the high average value of 4.38 x 10^6 lb in^{-2} developed at 77 K, but also for the indication of a substantial increase to 4.9 x 10^6 lb in^{-2} at 20 K.

As with the ultimate tensile strength, Fig.2 indicates that the moduli become erratic below 77 K. Reference to Fig.5b shows that, with the exception of a few crossply data, the literature indicates that cooling from 295 K to 77 K will produce a modulus increase of about 0.3–1.2 x 10^6 lb in^{-2} with about 0.7–0.8 x 10^6 lb in^{-2} being most likely. There does not appear to be a strong dependence on lay-up. Results of further cooling to 20 K are more difficult to interpret. In general, the data seem to cluster around a small increase in modulus up to 0.6 x 10^6 lb in^{-2} for cloth reinforcement and suggests that a somewhat larger increase on the order of 0.6–1.3 x 10^6 lb in^{-2} could be expected for crosspty and uniaxial composites. Nevertheless, the scatter from −0.8 x 10^6 lb in^{-2} to +3.2 x 10^6 lb in^{-2} modulus change is indicative of something erratic occurring below 77 K.

Again, the only surprises in the 200 K data of Fig.2 are the high value of the modulus of the flexible polyurethane Adiprene L-100 compared to the room temperature modulus and the almost equally large increase in the polybenzimidazole data.

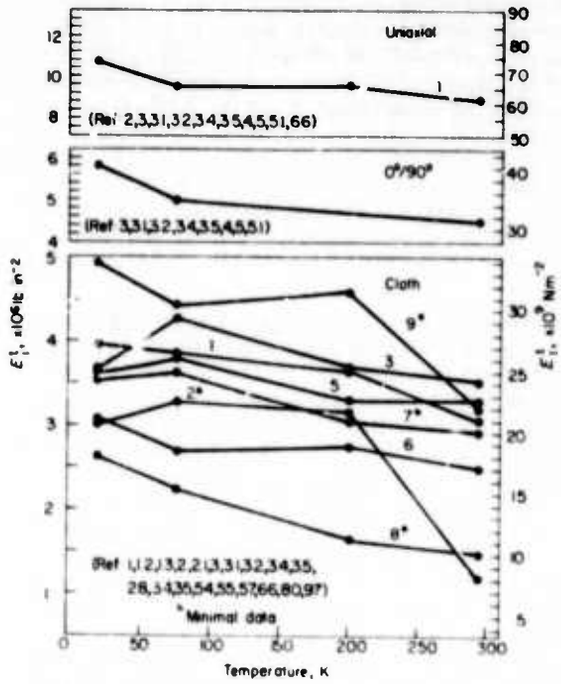

Fig.2 Initial tensile moduli of glass-reinforced composites
1 – epoxy; 2 – polyurethane, 3 – phenolic; 4 – polyimide;
5 – polyester; 6 – silicone; 7 – phenyl silane; 8 – Teflon;
9 – polybenzimidazole

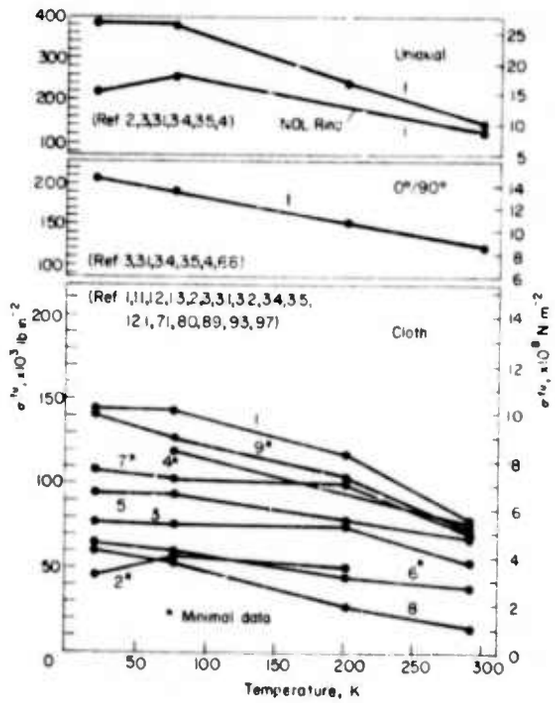

Fig.3 Ultimate flexural strength of glass-reinforced composites
1 – epoxy; 2 – polyurethane; 3 – phenolic; 4 – polyimide;
5 – polyester; 6 – silicone; 7 – phenyl silane; 8 – Teflon;
9 – polybenzimidazole

Composite flexure strength and modulus

Flexural tests are frequently used for screening a large number of composites during development studies, as such tests are simple and relatively inexpensive compared to tensile testing. In this application, flexure tests have the added advantage of testing the matrix as well as the reinforcement fibre. Unfortunately, the state of stress is continuously changing throughout the flexure specimen as the test proceeds, which makes engineering interpretation of the data difficult. Consequently, data on flexural strength and moduli are generally considered valid only for establishing relative performance ranking.

Fig.3 shows the flexural strengths of the glass-epoxies to be higher than that observed in tension by approximately

100 k lb in^{-2} k lb in^{-2} in the uniaxial specimens and by about 50 in the 0°/90° or cloth lay-ups (verified by comparison of σ^{tu} and σ^{fu} data from the same authors testing the same composites.)

As in the tensile results, the data show the epoxy-matrix composites to be superior in flexural strength at all temperatures, although the polybenzimidazole-matrix composites are almost as good. Among the other matrix types, the agreement with the tensile data is less clear. For those composites for which there are a reasonable number of data, for examples, the polyester, phenolic, and Teflon-matrix types, the strength order is the same at 77 K as it is in tension; however, the relative strength difference bear little relationship to the tensile data. The polymide and phenyl silane-matrix composites rank near the top in flexural strength, while appearing near the bottom in tension. Conversely, the polyurethane-matrix composite appears good in flexure but poor in tension. However, as the data on the former two composites are based on only one or two references and on a comparison between composites of different authors, caution is necessary in interpreting the results. The polyurethane-matrix data does reflect the same composite tested both in tension and in flexure.[2]

Within the uniaxial data, a separation has been made between data generated from flat flexural specimens and those obtained from curved segments of NOL rings because flexural properties obtained from each type of specimen are distinctly different.

Examining the available flexural strength data in more detail, we find that the flat-specimen uniaxial strength of the glass-epoxies ranged from 325–470 k lb in^{-2} at 77 K with the highest values reported for S-901/E-787.[3] A value of 375 k lb in^{-2} was reported for S-901/Resin 2.[4] The NOL specimen data were significantly lower, ranging from 200–270 lb in^{-2} at 77 K.[4] Flexural strengths varied among the 0°/90° epoxy data from 145–260 k lb in^{-2} at 77 K with the highest values again reported in S-901 glass using either E-787 or an experimental epoxy formulation.[3] Data for the cloth-reinforced epoxies showed a spread of 95–175 k lb in^{-2}. The highest values were obtained with 1581/E-787, with almost as high values reported for 181 glass in a variation of Epon 826 resin.[2] These were the same composites for which high tensile values were reported.

The glass-phenolic composites ranged from 70–110 k lb in^{-2} at 77 K. The highest values were reported for 181/CTL-91-LD.[1] Glass-polybenzimidazole data relect only the average data with 181 glass reinforcement.[2] The glass-polyesters showed a slightly higher range, 80–127 k lb in^{-2} with the highest value reported for 181/Hetron 31.[2] Reported flexural strengths of cloth-reinforced Teflon-matrix composites varied from 30–70 k lb in^{-2}, the highest values being developed with 181/FEP.[2]

Following a pattern which is found to repeat itself in all strength properties of glass-polymeric composites, the flexural strengths all initially increased upon cooling from 295 K to 77 K; however, they then changed in erratic ways upon additional cooling to 20 K. Changes in flexural strength during cooling as reported in the literature are summarized on Fig.5c, which shows that the expected strength increase from 295 K to 77 K is about 50–80 k lb in^{-2} for crossply and woven-cloth lay-ups. However, strength increases of up to 250 k lb in^{-2} have been reported for uniaxial composites, suggesting that the magnitude of the increase is lay-up dependent in flexural strength testing.

A comparison of Fig.5c with that of 5a shows a much greater scatter in the flexural data as compared to the tensile data on cooling to 77 K.

Upon cooling further to 20 K, Fig.5c indicates that one may obtain strength changes varying from −50 k lb in^{-2} to +150 k lb in^{-2} with a higher probability of a decrease than an increase. The data do not appear to be lay-up sensitive at 20 K.

The flexural modulus data, Fig.4, show a value of about 8.5 x 10^6 lb in^{-2} for uniaxial glass-epoxy. This is lower than the average moduli in tension; however, these data reflect only data for a flat specimen of S-901/E-787.[3] A check of the data shows that this specific composite had an initial tensile modulus of only about 8.8 x 10^6 lb in^{-2}, which suggests that the two methods are giving about the same answers for the uniaxial case. The same is true for the 0°/90° case, about 5 x 10^6 lb in^{-2} being obtained in both the flexural and tensile modes of testing. The cloth-reinforced polymer flexural modulus data range of 2–3 x 10^5 lb in^{-2} to about 5 x 10^6 lb in^{-2} is also similar to that of the tensile modulus.

Except for the Teflon-matrix showing the lowest modulus, the silicone-matrix showing next lowest, and the polybenzimidazole matrix showing one of the highest, in both tests there appears to be little correlation between the relative modulus ranking in flexure and in tension for the same series of composite types. This is not a condemnation of the flexural test – it may equally well indicate that average data from the literature cannot be used to predict tensile behaviour from flexural data with any degree of reliability.

Examining the flexural modulus data in more detail, we find that the reported 0°/90° crossply glass-epoxy data

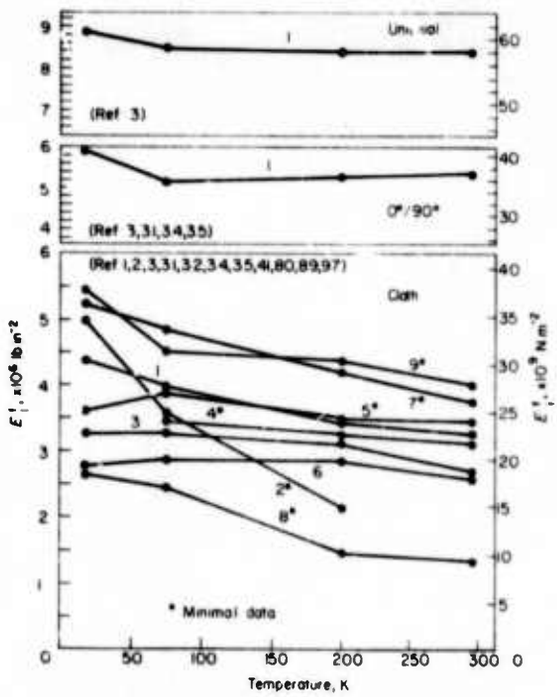

Fig.4 Initial tensile modulus of glass-reinforced composites
1 – epoxy; 2 – polyurethane; 3 – phenolic; 4 – polyimide; 5 – polyester; 6 – silicone; 7 – phenyl silane; 8 – Teflon; 9 – polybenzimidazole

ranged from 4.6–5.8 x 10^6 lb in^{-2} at 77 K with the highest values appearing for S-901/E-787.[3] Among the cloth-reinforced composites, the epoxy-matrix data varied from 2.6–5 x 10^6 lb in^{-2} with maximum values reported in 181/Epon 828 [1] and in 181 glass with modified Epon 828 resin.[2]

The phenolic-matrix data encompassed 1.2–5.3 x 10^6 lb in^{-2} at 77 K, the highest values being reported for in Conolon 516.[41,97] The silicone-matrix type composites showed a relatively small spread of 2.6–3.2 x 10^6 lb in^{-2} at 77 K, the highest value being reported for 181 glass/Trevarno F-131.[2] Among the composites for which fewer data were available, a comparatively high flexural modulus was reported by Chamberlain, et al [2] for the phenyl silane-matrix composite Narmco 534. These data again show high moduli at all temperatures for 181/polybenzimidazole composites.[2] The polyurethane and polyimide-matrix flexural modulus data reflect only one reference each.[89,2] Again, cooling below 77 K causes the data to become erratic. Fig.5d summarizes the glass-epoxy flexural modulus data and shows that, while on the average one would expect an increase of about 0.4 x 10^6 lb in^{-2} on cooling to 77 K and a like increase in further cooling to 20 K, one may find changes ranging from −0.8 to +2 x 10^6 lb in^{-2}. The data suggest that the crossply might be more adversely affected by cooling to 77 K than the cloth-reinforced specimens; however, there are not sufficient data to verify this indication.

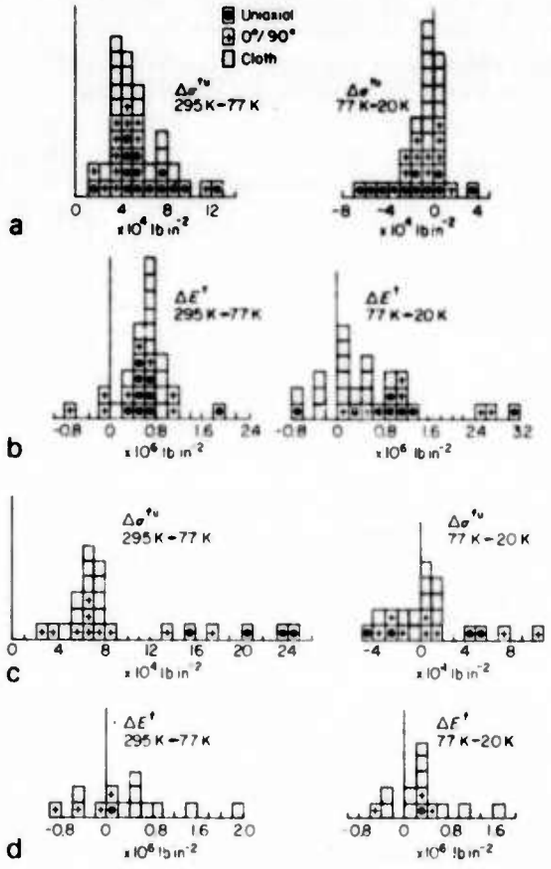

Fig.5 Histogram illustrating changes in tensile and flexural properties of glass-epoxy composites upon cooling

Composite compressive strength and modulus

The compressive strength data discussed herein were obtained by compressing in the fibre direction or, in the case of cloth-reinforced materials, in the plane of the cloth. As most composites are used in fairly thin sheet form, the major problem is one of avoiding failure by column buckling during the test. Problems are further accentuated in the uniaxial longitudinal case, where slight misorientation of the fibres can substantially reduce the compressive strength.

One observes from Fig.6 that the average of the data reported in the literature for the compressive strength of uniaxial glass-epoxy composites is less than half of the ultimate tensile strength average for the same type composites. Yet, the 0°/90° compressive strength is but slightly lower than its tensile strength, while the cloth-reinforced data span about the same range in compression and in tension. Consideration should thus be given to the possibility that the uniaxial data, and to a lesser extent the 0°/90° data, are lower than the true value due to testing problems.

Among the cloth-reinforced polymers, the epoxy-matrix composites continue to show superiority over all others. Once again, as in the tensile case, the polyurethane-matrix materials indicate a remarkable transformation from an extremely low strength at 295 K to one of the strongest of the group at 77 K. The glass-phenolics continue their reasonably good performance previously noted in the tensile results. The glass-polybenzimidazole appears to rank about average in compressive strength, similar to its performance in tension. The glass-phenyl silanes appear to rank somewhat better in compression than in tension, although few data are available. The glass-polyesters appear to have relatively low compressive strengths, although they were ranked among the top in tension. Finally, the Teflon and silicone-matrix composites display consistently the lowest compressive strengths of all materials surveyed.

Considering the uniaxial compressive strength data in more detail, we found the reported data at 77 K to vary widely from 100–240 k lb in^{-2} with about equal scatter at the other temperatures. This is almost twice the percentage variation found in the uniaxial tensile data even though the latter data were much more extensive. This large scatter very likely reflects the aforementioned problems inherent in compression testing. The highest value reported at 77 K for uniaxial compression was 237 k lb in^{-2} in S-901/E-787.[3]

The 0°/90° data showed much less scatter, ranging from 106–130 k lb in^{-2} at 77 K, the highest value reported in biaxially filament-wound S-901 glass in DER 332 epoxy.[3]

Among the glass-reinforced composites, the epoxy-matrix data varied from 90–138 k lb in^{-2} at 77 K with the highest value reported for a modified 181/Epon 828 composite.[2] Glass-phenolic properties covered a range of 60–100 k lb in^{-2} at 77 K, distinctly lower than those of the epoxies. The highest value was reported for 181/Narmco 506.[1] The polyester-matrix composites were by comparison, still another notch down in strength with a 35–68 k lb in^{-2} showing at 77 K, the highest compressive strengths being reported for 181 glass with Hetron 31 or Narmco 527 resin.[2] The 19–40 k lb in^{-2} range of the glass-silicones and the 25–40 k lb in^{-2} range of the glass-Teflons at 77 K leaves little doubt of the weakness of the latter composite types in compression. The data for polyurethane, polybenzimidazole, and phenyl silane-matrix composites reflect the work of Chamberlain et al.[2]

As with tensile and flexural properties, cooling below 77 K produces somewhat erratic results in compression. The 200 K data appear to be in line except for the glass-Teflon composite for which cooling to 200 K had no apparent effect.

No uniaxial or 0°/90° data were available at cryogenic temperatures for compressive moduli. In theory, compressive modulus of any perfectly elastic body should equal the tensile modulus. Thus, we find that the average values among the cloth-reinforced polymers which appear in Fig.7 bear a striking resemblance to the tensile modulus data. Again, the phenolic-matrix composites had highest values with the epoxy-matrix next highest. Teflon-matrices were clearly the weakest with the polyurethanes starting out equally low in modulus but again rapidly increasing its value to the middle of the group. The silicone-matrices were again on the low modulus side. The only significant change from the tensile modulus ranking is the somewhat lower value of the polyester and polybenzimidazole-matrix composites in compression.

The phenolic composites ranged from 4–8.4 x 10^6 lb in^{-2} in compression modulus at 77 K, maximum value being reported for 181/CTL-91-LD.[1] The glass-epoxy data showed much less scatter at 77 K ranging from 4–5.15 x 10^6 lb in^{-2}. The highest reported value for 181 glass/modified Epon 826 composite.[2] The phenyl silane and polyurethane data reflects only the values for Narmco 534 and 181/Adiprene L-100, respectively.[2] Somewhat more compressive moduli data were available for glass-polyester composites, values ranging from 2.5–4.3 x 10^6 lb in^{-2} at 77 K with highest values for 181/Polyester C.[66] The silicones not only averaged about like the polyesters but had about the same spread in 77 K values at 2.3–4.6 x 10^6 lb in^{-2}. The data on

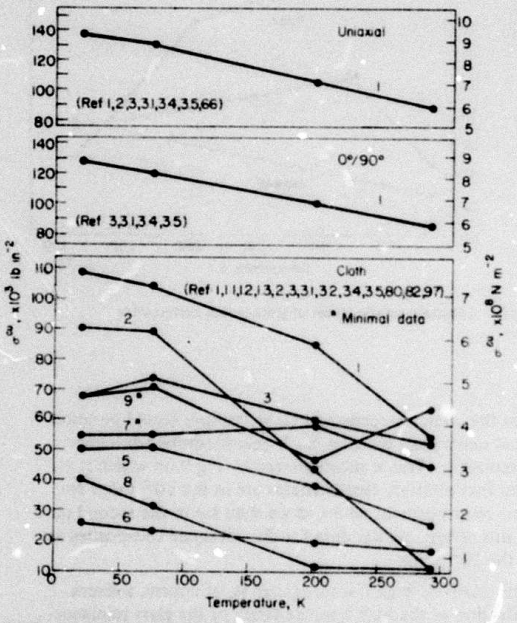

Fig.6 Ultimate compressive strength of glass-reinforced composites
1 – epoxy; 2 – polyurethane; 3 – phenolic; 4 – polyimide;
5 – polyester; 6 – silicone; 7 – phenyl silane; 8 – Teflon;
9 – polybenzimidazole

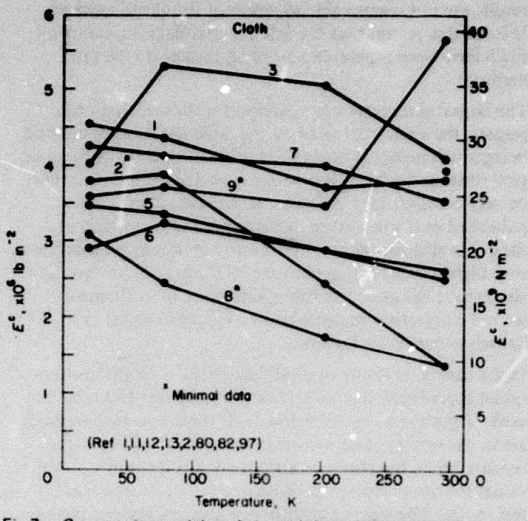

Fig.7 Compressive modulus of glass-reinforced composites
1 – epoxy; 2 – polyurethane; 3 – phenolic; 4 – polyimide;
5 – polyester; 6 – silicone; 7 – phenyl silane; 8 – Teflon;
9 – polybenzimidazole

glass-Teflon and glass-polybenzimidazole composites were provided by Chamberlain et al.[2] In contrast to its tensile modulus behaviour, the 181 glass/polybenzimidazole composite shows a sharp decline in both compressive strength and modulus on cooling from 295 K to 77 K. This is suggestive of experimental errors.

Composite interlaminar shear strength

Interlaminar shear strength is a property unique to composites; it is the resistance to shearing in the plane of the fibre reinforcement. It is believed to strongly affect structural integrity, particularly in compression loading. Like the flexural test, the results of interlaminar shear tests evaluate several composite parameters, including resin strength, resin-fibre bond strength, filament distribution, and matrix porosity. As such, interlaminar shear joins the flexure test in being a valuable indication of overall composite quality but providing little data directly useful in engineering calculations. Its most valuable application may well be in quality control during composite manufacture.

Nevertheless, it is of interest to consider the published values for interlaminar shear, if for no other reason than to compare the results obtained with the different methods. Interlaminar shear is usually measured either by the guillotine method in which interlaminar shear is forced by the imposition of opposing but offset cuts in a flat tensile specimen, or by a dimensional modification of the flat flexural specimen so as to force failure by shear on the central layers of the composite (short-beam shear). Of the two methods, the latter is most widely used. Unfortunately, the results obtained by the two methods are not comparable, the short-beam test usually yielding values higher than that of the guillotine. The overall situation is made still more complex by the understandable desire of some investigators to obtain interlaminar shear data from filament-wound composites prepared by the NOL ring method in which case the flexural method must be used with a short section of the ring. Because the specimen is not flat, the

results are not comparable to either of the above methods. It is for this reason that the interlaminar data appearing on Fig.8 have been separated according to the various test methods.

The largest discrepancy is observed for the uniaxial composites, the values obtained by the NOL short-beam method being much higher than those in conventional short-beam or guillotine methods. It is obvious from Fig.8 that one must be very cautious in comparing interlaminar shear values published in the literature. In interpreting these kind of data, it is also necessary to take into consideration that the very high values developed in the NOL short-beam test may also reflect the generally lower void content in filament-wound composites as compared to vacuum-bagged or autoclave-cured flat lay-ups.

In the case of crossply or cloth laminates, only the conventional short-beam flexure test or the guillotine test may be used. Fig.8 shows that the results of these two test methods are in reasonably close agreement for the 0°/90° crossply lay-ups, while the cloth-reinforced composites show lower values for the guillotine as compared to the short-beam test mode. The same is true for the uniaxial lay-ups tested by these two methods.

The variety of test methods used and the variety of different epoxy matrices which have been evaluated make it almost an exercise in futility to attempt to identify those composite types which have the highest values of interlaminar shear. The S-901/E-787 composite reported by Toth et al [3] at 14.7 k lb in^{-2} (77 K) in short-beam flexure has shear strength almost as high as those reported for the NOL short-beam test. The same composite also developed high values of interlaminar shear when tested by the same author in a 0°/90° biaxially-filament-wound lay-up. Other composites which appeared to have relatively high values of interlaminar shear among their group were S-901 glass in an experimental resin Epon 826/Empol 1040/Z-6077/DSA/BDMA [5] in NOL short-beam and a 0°/90° lay-up of Hi-Stren glass in Epon 828/LP-3/Cure agent D resin in conventional short-beam shear.[4] The data indicate that Resin 2 provides somewhat lower interlaminar shear strength than does E-787; for example, Soffer [5] reports a value of 9.3 k lb in^{-2} for S-901/Resin 2 in short-beam shear of flat specimens at 77 K and 14.1 k lb in^{-2} for the same composite in NOL short-beam shear.

Ignoring the NOL flexure data, one observes on Fig.8 that the interlaminar shear values are the highest for the cloth-reinforced composites and lowest for the 0°/90° crossplies with the uniaxial lay-ups in between. The relatively high values for the cloth composites probably reflect the added shear resistance provided by the convolutions in the woven glass cloth. By similar reasoning, the uniaxial composites may develop higher interlaminar strengths than the 0°/90° crossplies simply because the former provides no distinct lamella along which shear can propagate.

Again, in a repetition bordering on monotonous, the interlaminar shear strength is found to become erratic upon cooling from 77 K to 20 K, while the 200 K properties appear to be as expected.

Composite ultimate tensile strain

In view of the high strength of the glass-polymeric composites coupled with their relatively low modulus and absence of significant plastic flow at rupture, it might be expected

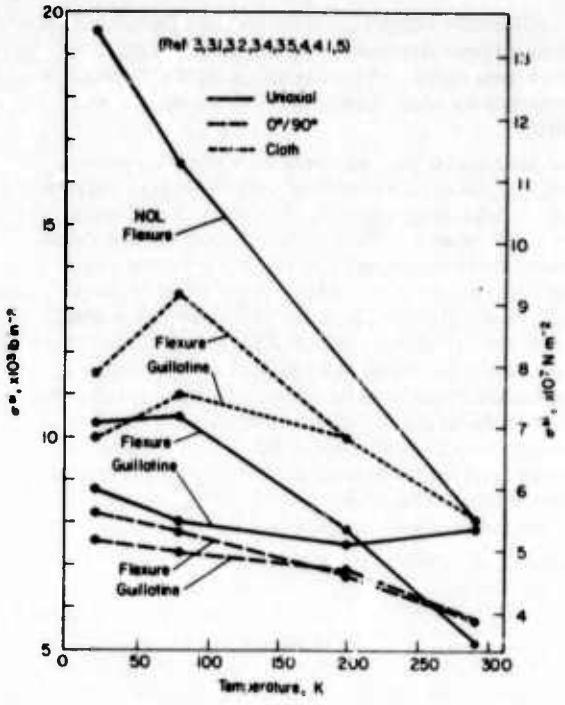

Fig.8 Interlaminar shear strength of glass-epoxy composites

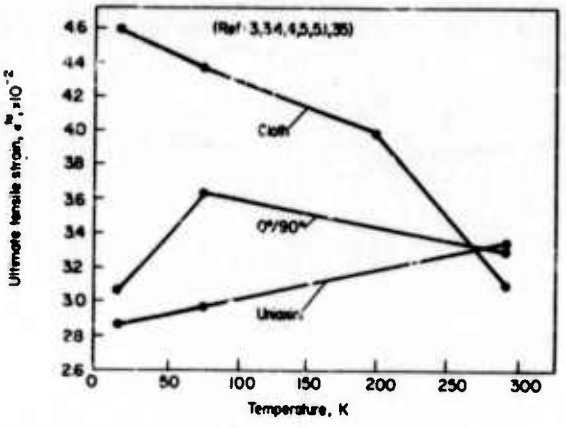

Fig.9 Ultimate tensile strain of glass-epoxy composites

that the strains accommodated at fracture would be somewhat larger than those of the higher-modulus advanced composites. This is substantiated by Fig.9 on which it is seen that ultimate tensile strains are in the 10^{-2} range for glass reinforcement while, as we shall see in the second part of this review, similar data for the advanced composites are in the 10^{-6} range.

This relatively high fracture strain is, of course, a direct reflection of the high fracture strain of the glass reinforcement. This has some interesting consequences because, while the fracture strain of some polymeric matrix materials may approach that of glass at 295 K, the ductility of almost

all polymers falls drastically upon cooling to cryogenic temperatures with the result that at low temperatures, fracturing the matrix occurs well before fracture of the glass fibres.[6] A dramatic example of this phenomenon is found during proof testing of filament-wound p essure vessels where the cracking of the polymeric matrix is very audible. It is surprising that, at least in the case of hydrostatically loaded pressure vessels, such rupturing of the matrix does not decrease the overall rupture strength of the tanks and may even produce an increase. One must emphasize, however that this does *not* imply that fracturing of the matrix is always acceptable or that it may be tolerated in other structures.

Fig.9 indicates that at 295 K, the average fracture strain will be similar for unaxial, 0°/90° and woven-cloth glass-epoxy composites, the strains being on the order of 3.2×10^{-2}. On cooling, however, marked differences develop between the lay-up types. Ultimate tensile strains in the uniaxial composites (tested in the longitudinal direction) decreased upon cooling to 77 K while cooling the 0°/90° and cloth lay-ups resulted in increased fracture strain. Detailed examination of the data shows this to be a true behaviour, as five of the six composites forming the uniaxial data showed the decline (the exception being S-901/E-787 [3]) while all eight of the 0°/90° and all three of the cloth composite types showed substantial increases upon cooling to 77 K.

Again, considering 77 K as a reference temperature, the uniaxial data were found to range from $1.9-5.3 \times 10^{-2}$, the highest being the previously noted work of Toth et al.[3] The data of Toth is somewhat suspect, as it is the only data reporting an increase in tensile strain upon cooling.

Among the 0°/90° crossply data, values showed a relatively narrow spread of $3.2-4.5 \times 10^{-2}$, the S-901/E-787 composite again showing the highest fracture strain.[3] A value of 4.3×10^{-2} was reported for Resin 2.[5] Cloth-reinforced data ranged from $3.5-5 \times 10^{-2}$, the highest ultimate tensile stain being reported for 1581/E-787.[3]

Data on strain to fracture at cryogenic temperatures are rare for other than the epoxy-matrix types. Kerlin et al [64,65] have reported a fracture strain of 2.75×10^{-2} for a Selectron 5003 glass-cloth polyester composite at the same temperature. Also, Toth et al [3] have reported 5.3×10^{-2} for a crossply glass-polyester composite Selectron 5003.

Static fatigue of composites

Under sustained room temperature loading, glass filaments have been found to deteriorate and fracture when subjected to stresses substantially below that of their normal ultimate tensile strength. As such, the failure is analogous to stress corrosion in metals. Some published data indicate that glass-filament-wound pressure vessels may undergo similar deterioration,[99] although some indication has also been obtained that static fatigue of glass-reinforced composites may pose less of a problem at cryogenic temperature than at 295 K.[66] Static fatigue will be an important factor in any composite used in superconducting motors and generators and, in view of the minimal data presently available, further studies are needed to clarify the magnitude of the problem and to select formulations providing utmost resistance to such failure at cryogenic temperatures. T.T. Chiao of the Lawrence Livermore Laboratories is currently directing an extensive static fatigue programme at room temperature on dead-weight loaded filaments coated with resin. As this latter method tests a basic structural element of the composite and permits many specimens to be run concomitantly, it should provide a useful and relatively inexpensive method of evaluating static fatigue at cryogenic temperatures.

Composite bearing yield strength

Bearing yield strength is a test designed to determine bearing stress as a function of the deformation of a hole through the composite. The load is applied by a pin inserted into the hole. The intent of the test is to provide information on the stress that may be sustained across riveted or bolted joints without loosening the joint. Bearing yield strength is defined as that stress on the stress-strain curve which corresponds to a distance of 4% of the bearing hole diameter when measured from the intersection of a line tangent to the stress-strain curve at this point and the zero load axis (see insert, Fig.10).

Bearing yield strengths for a series of epoxy-matrix composites have been reported by Toth et al [3] while Chamberlain et al [2] have provided data on silicone, polyurethane, and phenyl silane-matrix composites. These data are summarized on Fig.10.

The glass-epoxy composites developed bearing yield strengths which increased from about 50 k lb in^{-2} at 295 K to 70–75 k lb in^{-2} at 77–20 K. The uniaxial and 0°/90° data were very similar, while the cloth-reinforced epoxies were lower at 295 K and at 200 K but increased their strength to equal that of the others at 77 K.

Data on the other matrix types were only available for cloth reinforcements. The phenyl silane composite developed a bearing strength equal to that of the epoxies, while the

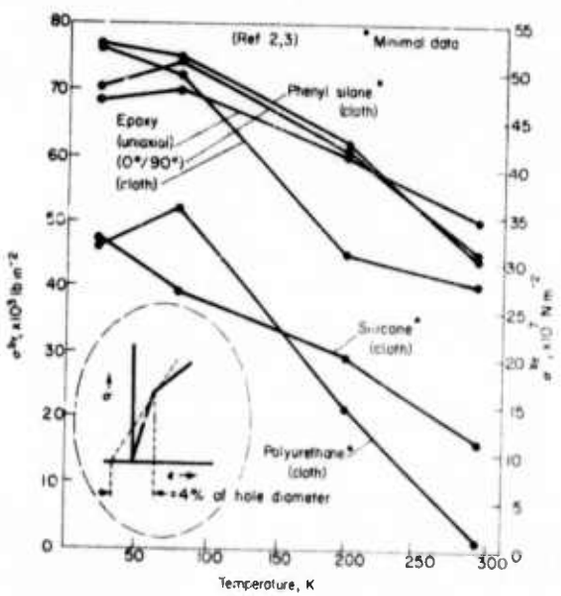

Fig.10 Bearing yield strength of glass-reinforced composites

200<

31

silicone and polyurethane-matrix materials were distinctly inferior.

Again, there is Indication of erratic behaviour on cooling from 77 K to 20 K.

Cyclic fatigue of composites

Cyclic fatigue of glass-reinforced composites at cryogenic temperatures has been studied by Brink et al [1] and by Chamberlain et al [2] in tension and by Fontana et al [34] using a reciprocating beam. Lavengood and Anderson [70] have contributed data on torsional fatigue. The data are not extensive, reflecting the very high cost of generating complete $S-N$ curves at cryogenic temperatures. Yet, such testing is mandatory to provide assurance that composite components will fulfill their life expectance in such applications as rotating cryogenic machinery. Every effort must therefore be made to restrict such testing to composites which have the best chance of developing superior fatigue properties. The data reviewed herein provide some sense of direction; however, there remains an urgent need for some type of relatively inexpensive screening test which will permit relative ranking of composite cyclic fatigue performance at cryogenic temperatures.

In comparison to that of the advanced composites or to many conventional alloys, the dynamic fatigue properties of glass-reinforced composites are relatively poor. This is primarily due to the fatigue behaviour of glass-polymeric materials being controlled by the properties of the matrix. Even at room temperature, the strain accommodation of the most epoxy resins is less than that of the glass reinforcement, and as it is the latter which controls the ultimate strength of the composite, cracking of the matrix will occur at ultimate loads far below the composite ultimate strength, allowing corrodents to attack the glass. In crossply lay-ups, such cracking may occur at stress levels as low as 20% of the ultimate composite strength.

Lavengood has pointed out that since fatigue life of a glass-reinforced composite is related to the strain capability of the matrix, embrittling of the matrix due to lowering of the temperature should lower the fatigue life. However, this is not always experimentally verified. Based on an analysis of experimental torsional fatigue data, Lavengood concluded that fatigue life at cryogenic temperatures is strongly affected by the composite interfacial stress which arises due to differential thermal contractions of the filament and the matrix. Cooling a composite increases the compressive forces at the interface and improves fatigue life. Where fatigue strains serve to increase the compressive interfacial stresses, the fatigue life may further increase, the reverse being true when strains decrease the interfacial stress.

The published tensile-fatigue data of Brink [1] and Chamberlain [2] and their co-workers were, with one exception, obtained on 181 cloth-reinforced composites. As an initial criteria, composites were screened by testing at 30% of their ultimate tensile strength developed at 295 K and 77 K. Those composites failing to achieve 10^6 cycles were dropped while those which were successful were further tested at 200 K and 20 K. The conventional polyester-matrix composites 181/Hetron 92, 181/Hetron H–31, 181/paraplex P–43, and 181/Narmco 527 were unsuccessful as was the silicone-matrix composite 181/Trevarno F–131.

It is beyond the scope of the present task to comprehensively review these data for which the reader may refer to the original references. However, in order to provided the reader with a sense of the fatigue performance of glass-polymeric composites, we have prepared Fig.11 from the data of Brink [1] and Chamberlain.[2] This figure presents the fatigue strength of the various successful materials as a function of temperature after 10^6 fatigue cycles, the maximum studied in this work. It is also instructive to know the percent of the relevant ultimate strength retained by each composite type at each temperature after 10^6 cycles; consequently, these data also appear on Fig.11.

Fig.11 shows that the absolute magnitude of the stress required to induce fatigue failure at 10^6 cycles generally increases with decreasing temperature for all materials studied, only the high-temperature polyesters (Laminac 4232 and Vibrin 135) and perhaps the silicones (Narmco 513 and Trevarno F-130) not showing an appreciable increase below 200 K. At all temperatures, these data show that the polybenzimidazole composite demonstrated comparatively superior fatigue performance both in terms of absolute retained tensile strength after 10^6 cycles and in the percentage of the original strength retained. The epoxies also looked comparatively good, but primarily because of their somewhat higher initial strength – their percentage retention of strength was among the lowest of the group. The highest values were reported for Epon 828/DDS.[2] The polyurethane, phenyl silane, and phenolic-matrix composites appeared to group into an intermediate performance class while the polyester, silicone, and Teflon-matrix composites showed distinctly lower fatigue properties. Data at 77 K only were available for a Scotchply 1002 uniaxial glass-epoxy composite,[2] which Fig.11 shows to have a much higher strength after 10^6 fatigue cycles at 77 K than any of the cloth-reinforced types; nevertheless, even this composite showed retention of only about 52% of its original strength at that temperature.

Does the data indicate the existence of a stress limit below which fatigue life is essentially infinite? In most cases, testing was not carried out to a sufficiently large number of

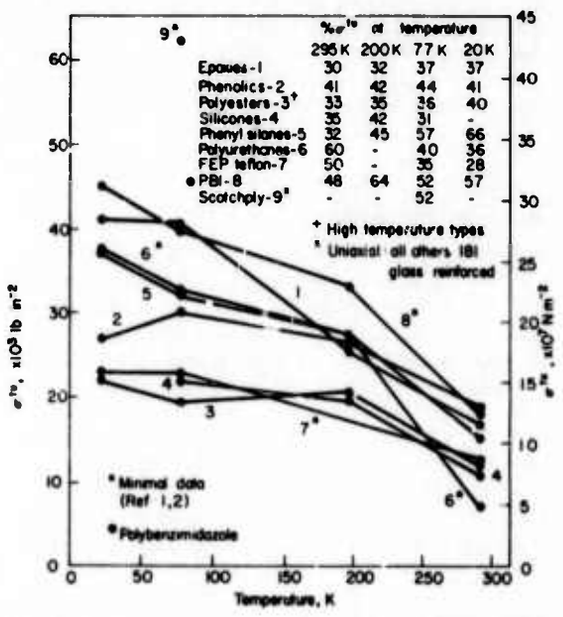

Fig.11 Cyclic tensile fatigue strength of glass-reinforced composites after 10^6 cycles

cycles to answer this question. However, judging from the shapes of the $S-N$ curves developed with 181/Epon 1001 by Brink,[1] it appears that this glass-epoxy formulation may reach such a limit at about 30 k lb in^{-2} for temperatures below 77 K (~ 30% UTS). Conversely, the $S-N$ curve for the 181/Epon 828 composite showed no indication of flattening out at 10^6 cycles. With the possible exception of the silicone-resin composites, 181/Narmco 513 and 181/Trevarno F-130, there was no evidence that cooling the composites had any effect on establishment of a fatigue limit where none was evident in the room temperature data.

Again, one notices an apparent tendency for the data to become erratic when cooling from 77 K to 20 K.

Impact strength and fracture toughness of composites

Impact strength and its more sophisticated partner, fracture toughness, are measures of the amount of energy which can be stored in a structure before the energy is released by fracture. As it is only in recent years that fracture mechanics has been put on solid theoretical grounds and exploited in homogeneous metals, it is not strange to find that application of parallel concepts to composites is still in its infancy. Furthermore, there is a major problem in applying basic principles of fracture mechanics to composites where, in most cases, multiple cracking occurs so that a unique 'crack length' cannot be defined.

Measurement of the energy required to fracture specimens, the impact test, is the most simple method of obtaining data on relative material toughness. Such tests show the glass-reinforced composites to have much greater toughness than do the advanced composites, probably reflecting the much larger strain-accommodation of glass filaments in comparison to the advanced fibre reinforcements. Unfortunately, the literature contains few low temperature data even on this simple parameter and those which are available are impossible to systematize due to differing test methods, specimen design, and filament orientation. Lewis and Bush [4] have evaluated a series of epoxies and modified epoxies reinforced with Hi-Stren glass using the Izod impact method. For unidirectional composites, they find the 295 K Impact strength to vary from 32–128 ft lb^{-1} of notch. On cooling to 77 K, the measured values ranged from 67–162 ft lb in^{-1}, some formulations showing 45% increase in impact strength, while others showed as much as a 26% decline. A 0°/90° crossply test with the same composite formulations yielded room temperature impact strengths from 49–96 ft lb in^{-1} and 77 K values of 59–76 ft lb in^{-1} with strength changes ranging from +36% to −26%, no consistent behaviour being shown by any specific composite formulation. Data published by other authors, [71,80,103,109,110] are equally confusing. Perhaps part of the answer is provided by Levin [71] who followed the change in impact strength of glass-phenolic and glass-epoxy specimens at closely spaced intervals from 295 K to 77 K and found that the impact properties peaked sharply at about −30°C followed by a rapid decline at lower temperatures. If the impact properties are indeed such a rapidly changing function of temperature, it might account for the lack of systematic change noted in data taken only at two or three temperatures. Clearly, this is an area which must be given more attention in the future if composite behaviour at cryogenic temperatures is to be understood well.

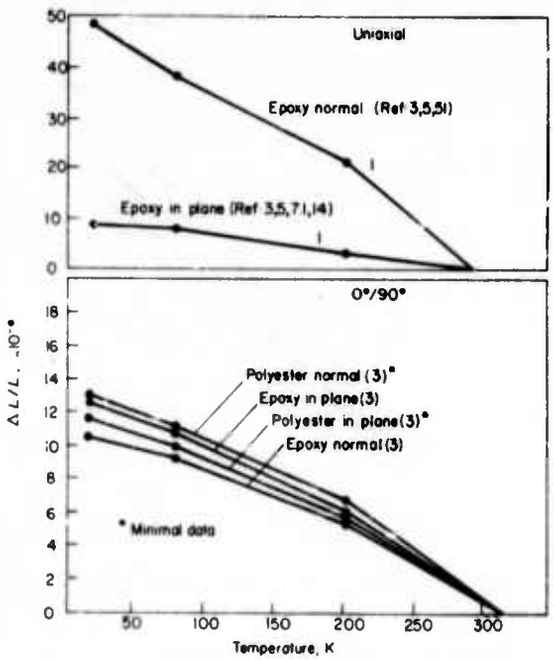

Fig.12 Thermal contraction of glass-fibre reinforced composites

Thermal properties

Thermal contraction of composites

All of the glass-reinforced polymers contract when cooled. As we wish to review the behaviour of such composites on cooling from 295 K, the data have been plotted as thermal contraction, avoiding negative values of $\Delta L/L$.

Thermal contraction is very dependent on the type of composite lay-up as well as on the orientation of the composite. Figs 12 and 13, therefore, present data on values obtained normal and parallel to the fibre reinforcement for uniaxial, 0°/90° crossply and cloth lay-ups. Other factors affecting thermal contraction are the specific resin used and the composite fibre density.

The thermal contraction is always found to be higher in a direction normal to the fibres than in the fibre plane, the difference increasing as the temperature is lowered. This reflects the much higher thermal contraction of the polymer as compared to the glass reinforcement. This is very evident in the data for uniaxial epoxy-matrix composites, where at 20 K the thermal contraction normal to the fibres varies from about 2.5 to 5 times that in the fibre direction at 20 K. An apparent anomaly appears in the 0°/90° crossply data, which shows a remarkably small difference in contraction between these two directions. This occurs because, in a filament-wound crossply composite, each layer of glass is in close proximity to the orthogonal layer next to it and thus provides resistance to dimensional change in the thickness direction. This effect is much less evident in the cloth lay-ups because the latter are prepared by methods which produce a much lower filament density than is obtained in filament winding.

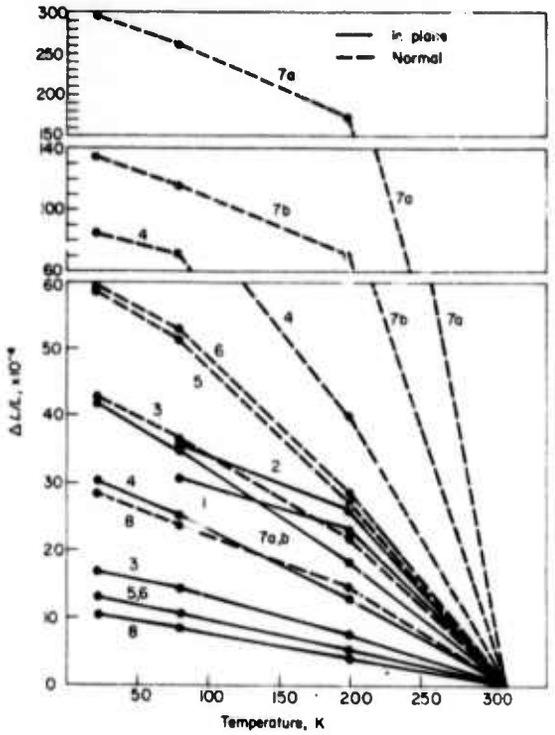

Fig.13 Thermal contraction of glass-cloth reinforced composites
1 – epoxy[85,101]; 2 – polyurethane[85]; 3 – phenolic[14]; 6 – phenyl silene[14]; 7a – Teflon TFE[14]; 7b – Teflon FEP[80]; 8 – polybenzimidazole[16]

As the thermal contraction of the composite is dominated by the properties of the polymeric matrix on cooling, one might anticipate considerable variation in contraction even within a given matrix type, reflecting, for example, the effect of additives to epoxy resins. This is found to be true; for example, the $\Delta L/L$ data for epoxy matrix composites varied from 20–75 x 10^{-4} in the thickness direction and from 4.4–11.5 x 10^{-4} in the fibre direction. In the 0°/90° lay-ups, the epoxy composites showed variations of 5.1–13.8 x 10^{-4} in thickness and 9.2–13 x 10^{-4} in the fibre direction. The polyester resins gave similar data spread in the 0°/90° lay-ups.

A much greater variation is observed in the thermal contraction among cloth-reinforced composites, reflecting both the larger variety of matrix materials for which data are available and the greater variation in fabrication method. The glass–Teflon composites have the highest thermal contractions of all the materials examined. Furthermore, the Teflon matrix may be either of the TFE or FEP type which have markedly differing thermal contraction characteristics. This difference does not appreciably affect contraction in the fibre plane due to the restraint provided by the fibres. However, the difference is marked in the direction normal to the fibres. As indicated by the dashed curves 7a and 7b on Fig.13, the TFE-matrix composites have twice the transverse thermal contraction of the FEP-matrix types.

The epoxy and the polyurethane-matrix composites also have relatively high thermal contractions. Unfortunately, no data were available in the fibre normal directions for these composites. The data indicate that the polyester-matrix composites are next in decreasing order of thermal contraction, with the fibre normal data being approximately 2.8 times greater than in the fibre plane. Showing the least thermal expansion in the fibre plane are the phenolic, silicone, phenyl silane, and polybenzimidazole-matrix composites. Of these, the phenolic composite data appear to be abnormally high for the fibre normal case, since, if all else were equal, the order in the fibre normal direction should follow that in the fibre plane.

All of the polymeric matrices create compressive stresses in the glass reinforcement upon cooling to cryogenic temperatures, such stresses being added to those already existing from cooling from the cure temperature to room temperature. This is primarily manifested as shear stress at the resin-fibre interface, so that it might be expected that an effect would be seen on those strength properties which are sensitive to debonding of the matrix-glass interface. One such property is fatigue, and from Fig.11, it is noted that the fatigue properties of the Teflon-matrix composites are poor, while that for the polybenzimidazole is good, consistent with the respectively high and low thermal expansion of these two composite types. A similar relationship holds for the flexural strength, Fig.3. Interfacial residual stress is but one of the factors influencing fibre debonding, others being the ability of the interface to sustain a shear load and the strength of the matrix itself.

Specific heat of composites

The specific heats of glass-reinforced composites show an almost linear dependence on temperature from 295 K to 77 K, and relatively small difference between matrix types. The specific heats are relatively high compared to most metals, being roughly comparable to that of aluminium but substantially above that of titanium, iron, or copper. Teflon and polyester-matrix composites have the highest specific heat. The epoxy, polybenzimidazole, silicone, and phenolic-matrix composites are bunched on the lower specific heat side of the group. The phenyl silane-matrix composite seems

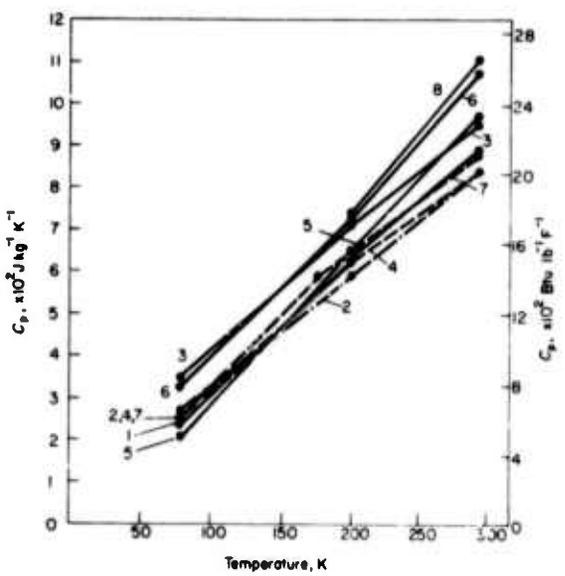

Fig.14 Specific heat of glass-reinforced composites
1 – Epoxies[15,16]; 2 – phenolics[15]; 3 – polyester[15]; 4 – silicones[15]; 5 – phenyl silenes[15]; 6 – Teflon[15]; 7 – polybenzimidazole[16]; 8 – phenyl formaldehydes[72]

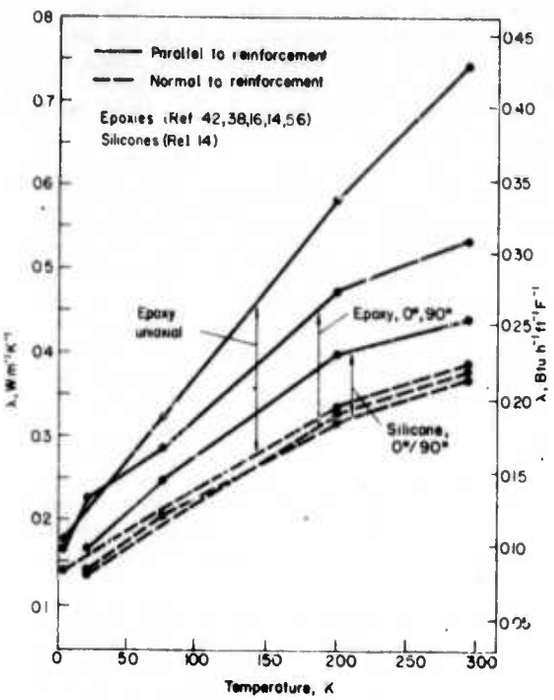

Fig.15 Thermal conductivity of glass-fibre reinforced composites

to have a slightly larger temperature dependence, starting out in the middle of the group at 295 K, but showing the lowest specific heat at 77 K.

The data reflect the work of Campbell et al [15,16] with the sole exception of the phenyl formaldehyde contribution of Luikov.[72] Except for the epoxies, the data reflect only one composite for each type of matrix. The epoxy data reflect the average of three compositions: a unidirectional and a crossply YM-31-A/DER-332 and a unidirectional S-994/E-787 composite. The spread in specific heat values for these three formulations at 295 K, 200 K, and 77 K was 8.16–9.21, 6.07–6.7, and 2.09–2.72 x 10^{-2} J $g^{-1}K^{-1}$, respectively, with the highest value associated with the S-994/E-787 composite.

Thermal conductivity of composites

Thermal conductivity is also an important parameter in cryogenic design. Unfortunately, improper experimental technique invalidates some of the data in the literature; primarily, failure to properly compensate for radiation losses, which can introduce errors approaching 100–200% in the higher temperature ranges. Figs 15 and 16 presents what the author believes to be valid data.

As with thermal contraction, conductivity is dependent on the type of lay-up and on the orientation of the composite. Figs 15 and 16 therefore present data on values obtained normal to the fibre reinforcement (thickness direction) and in the plane of the reinforcement for uniaxial, 0°/90° crossply and for woven-glass cloth lay-ups. Also, as with contraction, the thermal conductivities are affected by the type of matrix resin, necessitating a differentiation on this basis in the figures.

Unlike the other thermal properties of composites, the thermal conductivity is affected by the ambient atmosphere in which the measurement is made, that is it differs in helium, nitrogen, or in vacuum. The literature indicates that, compared to values obtained in helium, data taken in nitrogen will average 7% lower, while in a vacuum the data will, on the average, be lowered 20%. Campbell et al [16] suggests that the lower value in vacuum primarily reflects the difficulty of obtaining good contact between the composite specimen and the mating parts of the thermal conductivity apparatus when operating in a vacuum. An ambient atmosphere of nitrogen or helium increases the measured conductivity by reducing the contract resistance; however, diffusion of the gas (particularly of helium) into pores within the composite also contributes to an increase as the gas provides an overall improvement in the thermal path within the composite. This explanation is consistent with the effect of different ambient atmospheres being observed over the entire 20–295 K temperature range. The present author believes, however, that consideration should also be given to the effect of matrix cracking at very low temperatures which should act to increase the difference between values measured in the various ambient media. The data appearing in Figs 15 and 16 are averages of data taken in all three media.

The difference between the fibre normal and the in-plane conductivities for a given composite and the absolute spread of conductivity values among the various composite classes is widest at room temperature, converging as the temperature is lowered, consistent with a theoretical zero value for conductivity at absolute zero temperature. The conductivity at 20 K varies from 30–50% of that at room temper-

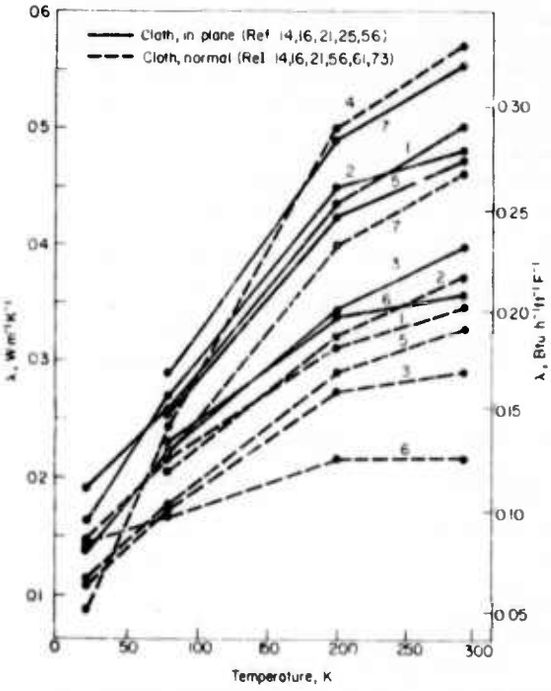

Fig.16 Thermal conductivity of glass-cloth reinforced composites
1 – epoxies, 2 – phenolics, 3 – polyesters; 4 – silicones;
5 – phenyl silanes; 6 – Teflons; 7 – polybenzimidazoles

ature for most of the composites. Exceptions are the cloth-reinforced silicones, curve 4, Fig.16, in which the 20 K value was only 15% of that at 295 K and the cloth-reinforced Teflon, curve 6, Fig.16, for which the 20 K value was reported to be 70% of the 295 K value, both of these exceptions being for the fibre normal direction.

Fig.15 contains data for uniaxial and 0°/90° epoxy lay-ups and for a 0°/90° silicone-matrix lay-up. The highest thermal conductivity was for the filament-wound uniaxial epoxy composite in the plane of the fibre. This is to be expected from the high density of continuous glass fibres in that direction. The conductivity in the fibre normal direction is 25–50% less, reflecting the lower thermal conductivity of the matrix. Thermal conductivity in the fibre plane of the 0°/90° epoxy lay-up is only about 80% of that for the uniaxial composite, reflecting the lower effective fibre density in the direction of the heat flow.

Fig.15 shows the 0°/90° silicone-matrix composite to have a substantially lower in-plane conductivity than the 0°/90° epoxy lay-up. This does not imply that the conductivity of the silicone matrix is less than that of the epoxy; indeed, the marked similarity between the fibre normal data for both polymeric matrices indicates that the matrix conductivity is very similar in both materials. The difference reflects the relatively inferior heat transfer properties of glass roving (fibre bundles) which was used for the silicone-matrix composite as compared to the continuous filament used with the epoxy.

Among the cloth-reinforced composites, the highest thermal conductivity was found for the silicone-matrix composites. Only fibre normal data were available; however, even in this least conducting orientation, the conductivity exceeded that of all the other materials in their more favourable in-plane direction. The polybenzimidazole composite was next lowest, and in decreasing order were the epoxies, phenolics, and phenyl silanes, all with approximately equal conductivities, both in-plane and plane normal. The lowest conductivities were evidenced by the polyesters and the Teflons.

The only composites for which there was more than one literature reference were the epoxies. For the latter, the data spread was found to be much greater for the in-plane conductivity than for the plane normal, as would be expected in view of the relatively high conductivity of the fibres compared to the matrix. As an example, the data which averaged 0.50 $W\,m^{-1}\,K^{-1}$ for the 295 K cloth-reinforced epoxy ranged from 0.30 to 0.65 $W\,m^{-1}\,K^{-1}$, while the plane normal data for the identical composites average 0.35 $W\,m^{-1}\,K^{-1}$ but ranged from 0.30 to 0.40 $W\,m^{-1}\,K^{-1}$. The scatter decreased significantly at lower temperatures.

Comments on glass-reinforced composites

We have reviewed the properties of filamentary-glass reinforced composites at cryogenic temperatures in order to provide the reader with an overall feel for their behaviour and the magnitude of the properties which may be expected. Having this information, for what applications should glass-reinforced composites be used? What composite formulation should be selected?

It would appear that glass-reinforced composites are most useful in applications requiring high tensile strength combined with high toughness and low thermal conductivity, but where stiffness is not required and where cyclic fatigue is not a major problem. In such applications, glass-reinforced composites have given and will continue to give excellent performance at relatively low cost. Filament-winding techniques should be used whenever possible in order to obtain the highest quality composites; in particular, the lowest void content.

Resin 2 is unique in that it was developed specifically by NASA for use in glass-reinforced composites at cryogenic temperatures. This resin was found by Soffer and Molho [5] to be the overall choice among 41 candidate resins, using the criteria of composite and fibre tensile strength, composite tensile modulus, ultimate tensile strain, thermal shock resistance, coefficient of linear thermal contraction, and interlaminar shear strength as well as favourable processing characteristics. For this reason, as well as on the basis of the successful use of this resin in the cryogenic industry, the NASA 2 formulation must be considered as a prime candidate for general cryogenic use. The reader is cautioned, however, that the plasticizers used in this resin cause the resin to become weak at the elevated temperatures required for vacuum degassing of a composite assembly. Components made with this resin must be adequately supported during this operation.

Early in their investigation of cryogenic resins, Soffer and Molho [5] rejected the Polaris (E-787, 58–68R) formulation because its glass-transition temperature of over 115°C suggested brittleness at cryogenic temperatures. However, available data show that this resin formulation is capable of producing composite mechanical properties equal to those with Resin 2 at cryogenic temperatures, at least for certain filament orientations. This suggests that low temperature ductility and thermal shock resistance may not always be of primary significance in selecting a resin for cryogenic applications. Nevertheless, the reader is cautioned that inadequate data exist on degradation of composite properties during fatigue at cryogenic temperatures, and the effects of repeated thermal cycling are not well understood. Ductility may well play an important role under the latter circumstances. In the absence of further experimental data, critical composite components subjected to dynamic loads or to cyclic thermal stresses under service conditions should be tested under simulated operational conditions, regardless of the selected matrix resin.

The present review is restricted to those composites for which cryogenic property data are available in the literature. The contemporary purchaser of composite components may find other types of polymeric matrices recommended by various fabricators for use at cryogenic temperatures. The present review should not be construed as prejudicial to any such recommendation. The purchaser should, however, ascertain that any such recommendation is supported by adequate experimental or service data at the temperature of interest.

An unexpected result of the present review is the surprisingly good overall performance of the glass-polybenzimidazole types. Available data indicate that at 77 K, such a composite ranks second only to the epoxies in ultimate tensile strength and in flexural strength, while developing tensile and flexural moduli superior to that of the epoxies. Compressive properties appear only average; however, the data indicate that the polybenzimidazole-matrix composite withstands cyclic fatigue stresses with less strength loss than is the case for the other reported matrix materials, particularly in regard to the percent of original ultimate strength retained

after fatigue cycling. A key may be the comparatively low thermal contraction of the polybenzimidazole resin as compared to the other polymer types which should reduce residual interfacial stresses between the fibre and the matrix of the composite.

A pervasive characteristic of glass-polymeric composites is the erratic behaviour of the mechanical properties on cooling from 77–20 K. With few exceptions, the strength properties increase on cooling from 295–77 K; however, on further cooling to 20 K, the data indicate that such properties may either increase, decrease, or remain unchanged. the behaviour being quite unpredictable, even among composites of the same matrix type. It is difficult to attribute this simply to the matrix becoming suddenly much more brittle between 77 K and 20 K, as cooling to 77 K has already decreased the strain capability of the matrices to a level far below that of the glass reinforcement. The present task does not permit more than a cursory consideration of the possible factors involved in this phenomena; however, the author believes it relevant to call attention to recent studies on the low temperature properties of polymers which have provided convincing evidence that, in at least the linear polymers of the polycarbonate (PC) and polyethelene terepthalate (PET) types, the media in which the low temperature test is conducted can strongly affect the fracture mode and the resultant mechanical properties measured for the polymer.[125,126] The experimental evidence indicates that the failure in such polymers in the cryogenic range is controlled by a crazing phenomena which, in turn, is related to the activity of the gas or liquid in contact with the polymer surface. Such studies have not been extended to the strongly cross-linked polymers; however, until proved otherwise, it must be considered a possibility that the mechanical properties of glass-polymeric composites may be influenced by the ambient media such that data obtained at 20 K or 77 K in liquid hydrogen or nitrogen may not be the same as those which would be obtained in a helium atmosphere.

This review suggests that the following work would be of value in implementing expanded use of glass-reinforced composites for demanding cryogenic structural applications such as would be encountered in superconducting machinery:

1. The reason for the erratic mechanical property behaviour in polymeric-matrix composites below 77 K must be ascertained. In particular, it is imperative to determine whether or not the type of cryogen in which tests are conducted has a significant effect on the mechanical properties.

2. Material research and evaluation must be directed toward obtaining the type of basic composite cryogenic property data which will be of most value to the design engineer. Contemporary composite theory requires full mechanical characterization of a uniaxial lamella of the composite of interest, that is, an experimental determination of the strength and moduli values are required for the prediction of limiting property values in complex crossply lay-ups. Accurate tensile and compression data are required in the longitudinal and transverse modes plus accurate values for intralaminar shear. Even at room temperature, tensile and compression testing in the reinforcement direction has proved difficult to perform with acceptable accuracy. Testing problems will be further complicated at cryogenic temperatures; however, these problems must be solved.

3. Having come to terms with the problems posed in 1 and 2, the static mechanical property data and the thermal property data for the best of the glass-reinforced composites must be extended down to 4 K. Available data suggest that the major characterization effort should be made on *S* glass in a NASA Resin 2 matrix. *S* glass should be characterized in the Polaris formulation as well, but with emphasis on its potential special use as uniaxial filament-wound cryogenic support members. All test materials must be fully characterized for resin/fibre density, void content, and fibre alignment before mechanical or thermal investigation.

4. Data on the performance of composites under dynamic loading conditions at cryogenic temperatures are minimal to non-existent. Yet, these type of data are mandatory if composites are to be used in cryogenic machinery. The available data are encouraging in that they suggest that fatigue performance at cryogenic temperatures is generally superior to that at room temperature. However, this will have to be more fully documented. As high-cycle fatigue testing at 4 K is very expensive, the materials included in such a testing programme must be carefully selected. For this purpose, it would be very desirable to have an efficient screening type of test capable of correlating incipient damage with expected fatigue life. Data on thermal fatigue are also required, that is, the effect of repeated cool-downs on both the static and dynamic properties of composites must be determined.

The author wishes to thank Dr R. P. Reed for his consultation and for review of the completed manuscript. The author also wishes to express appreciation to the NBS-NOAA library staff of the Boulder Laboratories for their assistance in retrieving the many documents required for this work. This research was supported by the Advanced Research Projects Agency.

Appendix

The following materials are referred to in this report. [The trade names used in this paper are those used by the cited authors. Generic names have been substituted whenever it was possible to do so without sacrificing clarity. The use of trade names in no way implies approval, endorsement or recommendation of specific commercial products by NBS.]

Glass fibres

S-HTS, S-901, 1581, 181, YM-31-A	Owens-Corning Glass Company
Hi-Stren	Aerojet General Corporation

Epoxy resins

Epon 822, 828, 1031, 58–68R	Shell Chemical Corp, Plastics & Resin Div
E-787	US Polymeric Corporation
ERL 2256	Union Carbide Plastics Company
660 FW	Stratoglas Div, Air Logistics Corp
DER 332	Dow Chemical Corporation

Phenolic resins

CTL-91-LD	Cincinnati Testing Laboratories, Div of Studebaker-Packard Corp

Conolon 506, 507	Narmco Materials Div, Telecomputing Corp
Phenyl silane resins	
Narmco 534	Narmco Materials Div, Telecomputing Corp
Polyester resins	
Narmco 527	Narmco Materials Div, Telecomputing Corp
Hetron 31, 92	Durez Plastics Div Hooker Chemical Corp
Polyester C	US Polymeric Corp
Paraplex P-43	Rohm and Haas Corp
Laminac 4232	American Cyanimid Corp
Vibrin 135	Naugatuck Chemical Co, Div of US Rubber Corp
Silicone resins	
Trevarno F-130, F-131	Coast Manufacturing Company
Narmco 513	Narmco Materials Div, Telecomputing Corp
Polyurethane resins	
Adiprene L-100	E. I. DuPont Corporation
Polybenzimidazole resins	
Imidite	Narmco Division, Whittaker Corp
Flexibilizers, coupling agents, and hardners	
Empol 1040	Emery Industries, Inc
LP-3	Thiokol Chemical Corp
Z-6077	Dow Chemical Corporation
ZZL-0870	Union Carbide Plastics Company
Miscellaneous materials	
Cure Agend D	polyamine salt
DDS	diaminodiphenyl sulphone
DSA	dodecenyl succinic anhydride
BDMA	benzyldimethylamine
NMA	nadic methyl anhydride
TFE	polytetrafluoroethylene
FEP	polytetrafluoroethylene copolymer with hexafluoro propalene

Bibliography

1. Mechanical properties

Contract AF-33 (616)–8289

Contractor: Directorate of Materials and Processes, Aeronautical Systems Division, Air Force Systems Command, Weight-Patterson Air Force Base, Ohio

Research Facility: Narmco Research and Development, San Diego, California

1 **Brink, N. O.** 'Determination of the performance of plastic laminates under cryogenic temperatures', ASD-TDR-62-794 (AD 288 944)

1.1 **Brink, N. O.** 'Mechanical behaviour of reinforced plastics at cryogenic temperatures' Technical Papers: 20th Annual Technical Conference, Society of Plastics Engineers 10 Section 15–2 (1964)

1.2 **Brink, N. O.** 'Mechanical behaviour of reinforced plastics at cryogenic temperatures' *Society of Plastics Engineers Journal* 20 (1964) 1123

1.3 **Brink, N. O.** 'Mechanical behaviour of reinforced plastics at cryogenic temperatures', Narmco Research and Development Report, Code No 105–4 (1964)

2 **Chamberlain, D. W., Lloyd, B. R., Tennant, R. L.** 'Determination of the performance of plastics laminates at cryogenic temperatures', ASD-TDR-62-794, Part 2 (1964) (N64–24212)

2.1 **Chamberlain, D. W.** 'Tensile fatigue testing at temperatures down to 20 K' *Advances in Cryogenic Engineering* 9 (1964) 131

2.2 **Chamberlain, D. W.** 'Mechanical properties testing of plastic laminate materials down to 20 K', *Advances in Cryogenic Engineering*, 10 (1965) 117

Contract NAS 8–11070

Contractor: National Aeronautics and Space Administration, George C. Marshall Space Flight Center, Huntsville, Alabama

Research Facility: Goodyear Aerospace Corporation, Akron, Ohio

3 **Toth, L. W., Boller, T. J., Butcher, I. R., Kariotis, A. H., Yoder, F. D.** 'Programme for the evaluation of structural reinforced plastic materials at cryogenic temperatures', NASA CR-80061 (Final) (1966) (N67–12051)

3.1 **Toth, L. W.** 'Properties testing of reinforced plastic laminates through the 20 degree K range', Technical Papers, 20th Annual Technical Conference, Society of the Plastics Industry, Section 7–C (1965) 1

3.2 **Toth, L. W. and Kariotis, A. H.** 'An assessment of test specimens and test techniques useful to the evaluation of structural reinforced plastic materials at cryogenic temperatures', *Advances in Cryogenic Engineering* 10 (1965) 126

3.3 **Toth, L. W.** 'Properties of glass-reinforced epoxy through the 20 K range', *Modern Plastics*, 42 (1965) 123

3.4 **Toth, L. W., Burkley, R. A.** 'Mechanical response at cryogenic temperatures of selected reinforced plastic composite systems', Goodyear Aerospace Report GER-13169, Paper No 16, 70th Annual Meeting of the American Society for Testing and Materials (1967)

3.5 **Toth, L. W., Boller, T. J., Kariotis, A. H. and Yoder, F. D.** 'Programme for the evaluation of structural reinforced plastic materials at cryogenic temperatures', NASA CR-64005, (June 1963) through June 1964 (N65–29724)

Contract NAS 3–6297

Contractor: National Aeronautics and Space Administration, Lewis Research Center, Cleveland, Ohio

Research Facility: Aerojet General Corporation, Azuza, California

4 **Lewis, A., Bush, G. E.** 'Improved cryogenic resin-glass filament wound composites', NASA CR-72163 (Final) (1967) (N67–31356)

4.1 **Lewis, A., Bush, G. E. and Creedon, J.** 'Improved cryogenic resin glass filament-wound composites', NASA Interim Report CR-54867 (1966) (N66–28040)

Contract NAS 6–6287

Contractor: National Aeronautics and Space Administration, Lewis Research Center, Cleveland, Ohio

Research Facility: Aerojet General Corporation, Azuza, California

5 **Soffer, L. M., Molho, R.** 'Cryogenic resins for glass filament-wound composites', NASA CR-72114 (Final) (1967) (N67–25076)

5.1 **Soffer, L. N., Molho, R.** 'Mechanical properties of epoxy resins and glass epoxy composites at cryogenic temperatures', Cryogenic Properties of Polymers [Koenig, J. L. (ed)] (Marcel Dekker, New York, 1968) 87 (Identical to NASA CR-84451 (1967) (N67–27217)

Contract F04701–69–C–0059

Contractor: Space and Missiles Systems Organization, Air Force Systems Command, Los Angeles Air Force Station, Los Angeles, California

Research Facility: The Aerospace Corporation, El Segundo, California

6 **Pepper, R. T., Rossi, R. E., Upp, U. W. and Riley, W. E.** 'Development of an aluminum-graphite composite', SAMSO-TR-70-301 (1970) (AD 718 409)

6.1 **Pepper, R. T., Upp, J. W., Rossi, R. C. and Kendall, E. G.** 'Aluminum-graphite composites', SAMSO-TR-70-114, April 1970 (AD 706 883). (Identical to *Metallurgical Transactions*, 2 (1971) 117

6.2 **Rossi, R. C., Pepper, R. T., Upp, J. W., Riley, W. C.** 'Development of aluminum-graphite composites', *Ceramic Bulletin* 50 (1971) 484

Contract NAS 8–11508

Contractor: National Aeronautics and Space Administration, George C. Marshall Space Flight Center, Huntsville, Alabama

Research Facility: Harvey Engineering Laboratories, Torrance, California

7 **Sumner, E. V., Davis, L. W.** 'Development of Ultrahigh strength, low density aluminum sheet and plate composites', NASA CR-85863 (Final) (1966) (N67–31181)

7.1 **Davis, L. W.** 'Composites at Low Temperature' 70th Annual Meeting of the American Society for Testing Materials (1967)

Contract NASA DPR C 10360 E

Contractor: National Aeronautics and Space Administration, Lewis Research Center, Cleveland, Ohio

Research Facility: Naval Ordnance Laboratory, Silver Springs, Maryland

8 **Simon, R. A., Alfring, R.** 'Properties of graphite fiber composites at cryogenic temperatures', NASA CR-72652 (NOLTR 69-183) (1970) Tasks I and II (AD 746 885)

9 **Larsen, J. V.** 'Properties of graphite fiber composites at cryogenic temperatures – effect of elastomeric additions to resin systems', NASA CR-72804 (NOLTR 70-195) (1971) Task III (AD 882 972)

10 **Larsen, J. V., Simon, R. A.** 'Carbon fiber composites for cryogenic filament-wound vessels', NASA CR-120899 (NOLTR 71–201) (1972) Tasks IV, V and VI, (N73–11553)

10.1 **Simon, R. A.** 'Graphite fiber composites at cryogenic temperatures', Technical Papers, 26th Annual Technical Conference, Society of the Plastics Industry, Section 10-D (197) 1

10.2 **Larsen, J. W.** 'Fracture energy of CBTN/epoxy-carbon fiber composites', Technical Papers, 26th Annual Technical Conference, Society of the Plastics Industry Section 10-D (1971) 1

Contract NAS 8–26198

Contractor: George C. Marshall Space Flight Center, Huntsville, Alabama

Research Facility: General Dynamics/Convair, San Diego, California

11 **Scheck, W. G.** 'Development of design data for graphite reinforced epoxy and polyimide composites', NASA TN-D2970, Report No GDC-DBG-70-005, final, National Aeronautics and Space Administration, Marshall Space Flight Center, Alabama (1974)

12 **Scheck, W. G.** 'Development of design data for graphite reinforced epoxy and polyimide composites', Report No GDC-DBG70-005, General Dynamics Quarterly Report No 1 (1970) [See also Maximovich, M., Scheck, W. G. Quarterley Report No 2 (1970)]

12.1 **Stuckey, J. M., Scheck, W. G.** 'Development of graphite/polyimide composites', National Technical Conference, Society of Aerospace Material and Process Engineers, Vol 3 (1971) 717

Contract F33615–70–1442

Contractor: Air Force Materials Laboratory, Wright-Patterson Air Force Base, Ohio

Research Facility: General Dynamics/Convair, San Diego, California

13 **Hertz, J., Christian, J. L., Varlas, M.** 'Advanced composite applications for spacecraft and missiles, Phase I final report, volume II: Material development', AFML-TR 71–186, Vol 2 (1972) (AD 893 715L)

13.1 **Forest, J. D., Fujimoto, A. F., Foelsch, G. F.** 'Advanced composite applications for spacecraft and missiles, Phase I Final Report, Volume I: Structural development', AFML-TR-71-186, Vol I (1972)

13.2 **Forest, J. D., Varlas, M.** 'Advanced composite applications for spacecraft and missiles, Final Report', AFML-TR-72-278 (1973)

13.3 **Christian, J. L., Campbell, M. D.** 'Mechanical and physical properties of several advanced metal-matrix composite materials', *Advances in Cryogenic Engineering* 18 (1973) 175

2. Thermophysical properties

Contract AF-33(657)–9160

Contractor: Air Force Materials Laboratory, Wright-Patterson Air Force Base, Ohio

Research Facility: General Dynamics/Astronautics, San Diego, California

The following reports are in a series entitled 'Thermophysical properties of plastic materials and composites to liquid hydrogen temperature (–423°F)'

14 **Haskins, J. F., Campbell, M. C., Hertz, J., Percy, J. L.,** ML-TDR-64-33, Part I (1964) (AD 601 337)

15 **Campbell, M. D., Hertz, J., O'Barr, H. L., Haskins, J. F.** ML-TDR-64-33, Part II (1965) (X65–18921)

15 **Campbell, M. D., O'Barr, G. L., Haskins, J. F., Hertz, J.** ML-TDR-64-33, Part III (1965) (AD 468 155)

16.1 **Hertz, J., Haskins, J. F.** 'Thermal conductivity of reinforced plastics at cryogenic temperatures', *Advances in Cryogenic Engineering* 10 (1965) 163

16.2 **Campbell, M. D.** 'Thermal expansion characteristics of some plastic materials and composites from room temperature to −253°C', *Advances in Cryogenic Engineering* 10 (1965) 154

16.3 **Campbell, M. D., Haskins, J. F., O'Barr, G. L., Hertz, J.** 'Thermophysical properties of reinforced plastics at cryogenic temperatures', *Journal of Spacecraft* 3 (1966) 596

(See also reference 13)

Contract F33615-73-C1388 (Work currently in progress)

Contractor: Air Force Materials Laboratory, Wright-Patterson Air Force Base, Ohio

Research Facility: General Dynamics/Convair, San Diego, California

17 **Forest, J. D., Schaeffer, W. H.** 'Advanced composite missile and space design data', General Dynamics Report GDCA-CHB72-001-2, Progress Report No 2 (1973)

18 **Forest, J. D.** 'Advanced composite missile and space design data', General Dynamics Report GDCA-CHB72-001-2, Progress Report No 2 (1973)

3. General bibliography

19 **Aleck, B.** 'Fiberglass-overwrapped 2219−T87 aluminum alloy low-pressure cryogenic tankage', Society of Aerospace Material and Process Engineers National Technical Conference, Space Shuttle Materials, Vol 3 (1971) 131

20 **Alfring, R. J., Morris, E. E., Landes R. E.** 'Cycle-testing of boron filament-wound tanks', NASA CR-72899, National Aeronautics and Space Administration, Lewis Research Center (1971) (N71−38023)

21 **Barber, J. R.** 'Design and fabrication of shadow shield systems for thermal protection of cryogenic propellants', NASA CR-72595, National Aeronautics and Space Administration, Lewis Research Centre, Cleveland, Ohio (1969) (N70-29098)

22 **Baucom, R. M.** 'Tensile behaviour of boron filament-reinforced epoxy rings and belts', NASA TN D-5053, Langley Research Center, Hampton, Virginia (1969) (N69−19918)

23 **Benton, W., Carr, R., Cohen, A., Gustafson, G., Lankton, C., Zeldin, B.** 'Propellant storability in space', RPL TDR-64-75 (Final), Air Force Systems Command, Edwards Air Force Base, California (1964) (AD 603 215)

24 **Brechna, H.** 'Superconducting magnets for high energy physics applications' Proc ICEC1 (Heywood Temple Industrial Publishers Ltd, London, 1968) 119-(CESCI N67-36009)

25 **Bullard, B. R.** 'Cryogenic tank support evaluation', NASA CR-72546, NASA Lewis Research Center, Cleveland, Ohio (1969) (N70−13085)

26 **Campbell, M. D.** 'Development of thermal expansion capabilities and the investigation of expansion characteristics of space vehicle materials, General Dynamics/Astronautics Report ERR-AN-251 (December 1962)

27 **Campbell, M. D.** 'Development of the thermal expansion capabilities and the investigation of the thermal expansion characteristics of space vehicle materials (II)', General Dynamics/Astronautics Report ERR-AN-450 (1963)

28 **Caren, R. P., Coston, R. M., Holmes, A. M. C., Dubus, T.** 'Low-temperature tensile, thermal contraction and gaseous hydrogen permeability data on hydrogen-vapor barrier materials', *Advances in Cryogenic Engineering* 10 (1965) 171

29 **Chiao, T. T., Moore R. L.** 'Tensile properties of PRD-49 fiber in epoxy matrix', *Journal of Composite Materials* 6 (1972) 547

30 **Cooper, G. A., Sillwood, J. M.** 'Multiple fracture in a steel reinforced epoxy resin composite', *Journal of Materials Science* 7 (1972) 325

31 **Darwish, F., Tetelman, A. S.** 'Mechanical behaviour of SiO_2-epoxy composite', Conference Proceedings No 63, Advisory Group for Aerospace Research and Development, Symposium on Composite Materials, Paper No 9, Paris (Hartford House, London, 1970)

32 **Davis, J. G., Zender, G. W.** 'Mechanical behaviour of carbon fiber reinforced-epoxy composites', 12th National Symposium, Society of Aerospace Material and Process Engineers, Vol 12 (1967) Section AC-10

33 **Dervy, A. J.** 'Reinforced plastics of high strength/weight ratio for space applications', Technical Papers, 17th Annual Technical Conference, Society of the Plastics Industry, Section 7-D (1962) 1

34 **Fontana, M. G., Bishop S. M., Spretnak, J. W.** 'Investigation of mechanical properties and physical metallurgy of aircraft alloys at very low temperatures, Part 5 − Mechanical properties of metals and a plastic laminate at low temperatures', AF Technical Report 5662, Part 5, Materials Laboratory, Wright-Patterson Air Force Base, Ohio (1953) (AD 27726)

35 **Freeman, S. M.** 'Properties of vapor barriers, adhesives and foams at cryogenic and elevated temperatures', Lockheed Aircraft Corporation Report ER-5687 (1962)

36 **Freeman, W. T., Campbell, M. D.** 'Thermal expansion characteristics of graphite reinforced composite materials', Composite Materials: Testing and Design (Second Conference) ASTM STP 497, American Society for Testing and Materials (1972) 121

37 **Funk, C. W., Dalton, C. E.** 'Cryogenic radiation damage in structural polymers', *Transactions of the American Nuclear Society* 9 (1966) 406

38 **Gille, J. P.** 'Development of advanced materials for integrated tank insulation system for the long term storage of cryogenics in space', NASA CR-102570 (Final), National Aeronautics and Space Administration, Huntsville, Alabama (1969) (N70-23348)

39 **Gleich, D.** 'Development of a filament-overwrapped cryoformed metal pressure vessel', NASA CR-72753, National Aeronautics and Space Administration, Lewis Research Center, Cleveland, Ohio (1971) (N71-22401)

40 **Gray, P. D., Cornelius, G. K., O'Donnell, J. D., Howards, W.W.** 'Rockets in space environment, Volume I: The experimental program', RTD-TDR-63-1050, Aerojet General Corporation (1963) (N63-20999)

41 **Greer, F.** 'Flexural properties of Conolon 506 at room temperature, −320°F and −423°F, Convair/Astronautics Report 55E 522 (1961) (AD 677 565)

42 **Hale, L. V.** 'Study of thermal conductivity requirements: MSFC 20-inch and 105-inch cryogenic tank analayses', NASA CR-61288, National Aeronautics and Space Administration, Marshall Space Flight Center, Alabama (1969) (N69−35811)

43 **Hall, J.** 'Cryogenics tensile tests − epoxy fiberglas', Douglas Aircraft Company Report MP 1348 (1961)

44 **Hanson, M. P.** 'Effects of temperature and creep characteristics of PRD-49 fiber-epoxy composites', NASA TN D-7120, National Aeronautics and Space Administration, Lewis Research Center, Cleveland, Ohio (1972) (N73-12607)

45 **Hanson, M. P.** 'Tensile and cyclic fatigue properties of graphite filament-wound pressure vessels at ambient and cryogenic temperatures', NASA TN D-5354, National Aeronautics and Space Administration, Lewis Research Center, Cleveland, Ohio (1969) (N69-31300) (Identical to *SAMPE* 15, 249

46 **Hanson, M. P., Richards, H. T., Hickel, R. O.** 'Preliminary investigation of filament-wound glass-reinforced plastics and liners for cryogenic pressure vessels', NASA TN D-2741, National Aeronautics and Space Administration, Lewis Research Center, Cleveland, Ohio (1965)

47 **Hanson, M. P.** 'Glass-, boron-, and graphite-filament-wound resin composites and liners for cryogenic pressure vessels', NASA TN D-4412, National Aeronautics and Space Administration, Lewis Research Center, Cleveland, Ohio (1968) [Identical to NASA TM X-52350, (1967)]

48 **Hanson, M. P.** 'Static and dynamic fatigue behavior of glass filament-wound pressure vessels at ambient and cryogenic temperatures', NASA TN D-5807, National Aeronautics and Space Administration, Lewis Research Center, Cleveland, Ohio (1970) (CFSTI-CSCL-20 K)

49 **Haskins, J. F., Hertz, J.** 'Thermal conductivity testing of coast F-224-6 phenolic-fiberglass laminate', General Dynamics Convair Report No AR-592-1-482 (1963)

50 **Haskins, J. F., Hurlich, A.** 'Measured values for the coefficients of linear expansion of Plycel 420 and Conolon 506 at low temperatures', Convair/Astronautics Report MRG-154 (1960)

51 **Haylett, J. W., Rotzmayer, E., Butcher, I.** 'Advanced composite material study for millimeter wavelength antennas',

Technical Report AFML-TR-71-205, Vol I, Air Force Materials Laboratory, Wright-Patterson Air Force Base, Ohio (1971) (AD 893 368)

52 **Haylett, C. E.** 'Advanced composite material study for millimeter wavelength antennas, Volume II: Environmental tests', AFML-TR-71-205, Vol 2, Air Force Materials Laboratory, Wright-Patterson Air Force Base, Ohio (1971) (AD 893 358 L)

53 **Herring, H. W., Baucom, R. M., Pride, R. A.** 'Research on boron filaments and boron reinforced composites', 10th National Symposium, Society of Aerospace Material and Process Engineers **10** (1966) B–21

54 **Hertz, J.** 'Tensile testing of Conolon 506 at room and subzero temperatures', Convair/Astronautics Report MRG-120 (1959)

55 **Hertz, J.** 'Tensile testing of Adlock 851, Adlock PG-LA and Adlock EG-11A-81A from −423°F to 78°F' Convair/Astronautics Report MRG 237 (1961)

56 **Hertz, J.** 'Investigation of potential low temperature insulations', General Dynamics/Astronautics Report GS/A-ERR-AN-668 (1964)

57 **Hertz, J.** 'The effect of cryogenic temperatures on the mechanical properties of reinforced plastic laminates', General Dynamics Report AR-592-1-415 (1963) (AD 405 170)

58 **Hertz, J.** 'Investigation into the high-temperature strength degradation of fiber-reinforced resin composite during ambient aging', General Dynamics/Convair Report No GDCA-DBG73-005 (Final Contract NAS 8–27435) (1973)

59 **Hoggatt, J. T** 'Development of cryogenic PRD-49-I filament-wound tanks', NASA CR-120835, National Aeronautics and Space Administration, Lewis Research CEnter, Cleveland, Ohio (1971) (N72-24941)

60 **Hoggatt, J. T.** 'High performance filament wound composites for pressure vessel applications', Society of Aerospace Material and Process Engineers, National Technical Conference, Space Shuttle Materials, Vol 3 (1971) 157

61 **Hust, J. G.** 'Thermal conductivity of an epoxy-fiberglass laminate', NBS Cryogenic Division Unpublished Laboratory Note 73–1, (1973)

62 **Johnston, H. L., Brooks, H. E.** 'Impact strength of various metals at temperatures down to 20° Absolute', Ohio State University Cryogenic Laboratory Report TR 264–17 (1952)

63 **Keller, C.W.** 'Fiberglass supports for cryogenic tanks', NASA CR-120937 (Final), National Aeronautics and Space Administration, Lewis Research Center, Cleveland, Ohio (1972) (N72-33564)

64 **Kerlin, E. E., Smith, E. T.** 'Measured effects of the various combinations of nuclear radiation vacuum and cryotemperatures on engineering materials: Biennial Report', NASA CR-77772, National Aeronautics and Space Administration, George C. Marshall Space Flight Center, Huntsville, Alabama (1966) (N66-35963)

65 **Kerlin, E. E., Smith, E. T.** 'Measured effects of the various combinations of nuclear radiation, vacuum and cryotempertures on engineering materials: Annual Report', NASA CR-58830, National Aeronautics and Space Administration, George C. Marshall Space Flight Centre, Huntsville, Alabama (1964) (N64-33043)

66 **Keys, R. D., Kieter, T. F., Schwartzberg, F. R.** 'Cryogenics properties of high-strength glass-reinforced plastics', *Advances in Cryogenic Engineering* **11** (1966) 470

67 **Krause, D. R.** 'Development of lightweight material composites to insultate cryogenic tanks for 30-day storage in outer space', NASA CR-123797, National Aeronautics and Space Administration, George C. Marshall Space Flight Center, Huntsville, Alabama (1972) (N72-30495)

68 **Krause, D. R., Fredrickson, G. O., Klevatt, P. L.** 'Effects of cyclical environments on high-performance multi-layer insulation materials', Society of Aerospace Material and Process Engineers National Technical Conference, Space Shuttle Materials, Vol 3 (1971) 639

69 **Lantz, R. B.** 'Materials for filament wound cryogenic pressure vessels', 6th National Symposium, Society of Aerospace Materials and Process Engineers, Vol 2, Engineering Paper No 1750

70 **Lavengood, R. E., Anderson, R. M.** 'Matrix properties controlling torsional fatigue life of fiber reinforced composites', Technical Papers, 24th Annual Technical Conference, Society of the Plastics Industry, Section 11–E (1969)

71 **Levin, V. A., Naumenkov, P. G., Shchitov, M. V.** 'Some properties of plastics at low temperatures', *Plasticheskia Massy* **11** (1966) 64

72 **Lukov, A. V., Vasiliev, L. L., Shashkov, A. G.** 'A method for the simultaneous determination of all thermal properties of poor heat conductors over the temperature range 80 to 500 K', Proceedings 3rd American Society of Mechanical Engineers Symposium, Purdue University (1965) 314

73 **Lyon, D. N., Parrish, W. R.** 'Low temperture thermal conductivities of two high compressive strength materials', *Cryogenics* **7** (1967)

74 **Maher, L. E.** 'Some problems arising from the use of hydrogen-fuelled propulsion systems' *Journal of the Royal Aeronautical Society* 68 (1964) 765

75 **McKannon, E. C., Gause, R. L.** 'Effects of nuclear radiation and cryogenic temperatures on non-metallic engineering materials', *Journal of Spacecraft* **2** (1965) 558

76 **Morris, E. E.** 'Glass-fiber-reinforced metallic tanks for cryogenic service', 12th National Symposium, Society of Aerospace Materials and Process Engineers, Vol 12 (1967) Section AS-4 (also NASA CR-72224)

77 **Morris, E. E.** 'The performance of glass-filament-wound pressure vessels with metal liners at cryogenic temperatures', *Journal of Materials* **4** (1969) 970

78 **Morris, E. E., Alfring, R. J.** 'Cryogenic boron-filament-wound pressure vessels', Composite Materials: Testing and Design, ASTM STP 460 (American Society for Testing and Materials, 1969) 430

79 **Morris, E. E., Landes, R. F.** 'Cryogenics glass-filament-wound tank evaluation', NASA CR-72948 (Final), National Aeronautics and Space Administration, NASA Lewis Research Center, Cleveland, Ohio, (1971) (N72-14696)

80 **Mowers, R. F., Leib, J. H., Sherman, S.** 'Program of testing nonmetallic materials at cryogenic temperatures', Rocketdyne Corporation Report R-3498, Rocket Propulsion Laboratories, Edwards, California (1962) (AD 294 772)

81 **Nadler, M. A., Yoshino, S. Y., Darms, F. J.** 'Boron/epoxy support strut for non-integral cryogenic tankage', North American Rockwell Space Division Report SD 68–99501 (1969) [See also 15th National Symposium *SAMPE* (April 1969) and North American Rockwell Report SD 995 2 (1968)]

82 **Nelson, L. F.** 'Compressive strength of Conolon 506 at +75°F and −320°F', Convair/Astronautics Report No 27E 1336 (1962)

83 **Nelson, L. R.** 'Mechanical properties of Adlock 851 at room temperature, 1000°, −320° and −423°F', Convair/Astronautics Report No 55E 812 (1961)

84 **Nelson, P. T., Archer, J. S.** 'Graphite reinforced plastic EHF antenna', TRW Systems Group, Redondo Beach, California Report No 99900–7128–RO–11 (1969)

85 **Patten, P. M.** 'Internal insulation liner alteration', Douglas Aircraft Company Report No SM 45975 (1964)

86 **Perkins-Elmer** Optical Group, Norwalk, Connecticut: Work-in-Progress on Contract No F 33615–72–C–2033, Air Force Systems Command, Wright-Patterson Air Force Base, Ohio

87 **Pink, E., Campbell, J. D.** 'The effect of strain rate and temperature on the deformation behavior of reinforced and unreinforced epoxy resin', Oxford University Department of Engineering Report No 1040/72, Oxford, England (1972) (N73–10568)

88 **Pirgon, O., Wostenholm, G. H., Yates, B.** 'Thermal expansion at elevated temperatures, IV. Carbon-fibre composites', *Journal of Physics D: Applied Physics* **6** (1973) 309

89 **Pride, R. A., Stein, B. A., Schmidt, F. W.** 'Mechanical properties of polyimide-resin glass-fibre laminates for various time, temperature and pressure exposures', Technical Papers, 23rd Annual Reinforced Plastics Technical and Mangement Conference, Washington, DC Section 17-c (1968) 1

90 **Ratcliffe, E. H.** 'Thermal conductivities of plastics with glass, asbestos and cellulosic fiber reinforcements', *Applied Material Research* **5** (1966) 200

91 **Roseland, L. M.** 'Materials for cryogenic usage', Technical Papers, 21st Annual Technical Conference, Society of the Plastics Industry Section 4-C (1966) 1

92 **Roseland, L. M.** 'Investigation of structural properties at cryogenic temperatures of filament-wound pressure vessels containing both organic and glass filaments', Douglas Aircraft Corporation Report No SM-48409, (1966)

93 **Ross, J. E.** 'Fiberglass laminate – ultimate tensile and flexural strength tests at room temperature, −100°F and 320°F', Convair Astronautics Report No 7E 1687 (1959) (AD 830 230)

94 **Sanders, R. H., Weleff, W.** 'Final report on GTR-17 effects of radiation on organic materials irradiated in liquid hydrogen', Aerojet-General Corporation Report No RN-S-0327 (1967)

95 **Sanger, M. J., Molhe, R., Howard, W. W.** 'Exploratory evaluation of filament-wound composites for tankage of rocket oxidizers and fuels', AFML-TR-65-381, Air Force Materials Laboratory, Wright-Patterson Air Force Base, Ohio (1966) (AD 477 455)

96 **Sanger, M. J., Reinhart, T. J.** 'Development of filament-wound tankage for rocket oxidizers and fuels', Technical Papers 12th National Symposium, Society of Aerospace Material and Process Engineers Section AS-7 (1967)

97 **Sewell, J. J., Kuno, J. K.** 'Aerospace use of plastic hardware and thermal insulation', Technical Papers, 17th Annual Technical Papers, 17th Annual Technical Conference, Society of the Plastics Industry, Section 7-A (1962) 1

98 **Shriver, C. B.** 'Design and fabrication of an internally insulated filament wound liquid hydrogen propellant tank', NASA CR-127, National Aeronautics and Space Administration, Washington, DC (1964) (N65–10775)

99 **Soltysiak, D. J., Toth, J. M.** 'Static fatigue of fiber glass pressure vessels from ambient to cryogenic temperatures', Technical Papers, 22nd Annual Technical Conference, Society of the Plastics Industry, Section 14–E (1967)

100 **Speare, J. C.** 'Preliminary sizing of filament-wound RNS tanks', Report No TOR-0066 (5759–07)–13, Space and Missile Systems Organization, Air Force Systems Command, Los Angeles Air Force Station, Los Angeles, California (1970) (AD 872 626)

101 **Steinhauer, R. A.** 'Linear thermal expansion of 828CL 181 cloth laminate', Douglas Aircraft Company Report No MP 11, 979 (1961)

102 **Stinnett, W. D.** 'Cryogenic tensile properties of selected materials', NASA CR-71751, AEC-NASA Space Nuclear Propulsion Office, Report No 2712 (1964) (N66-22816)

103 **Suezawa, Y., Hojo, H., Nakamura, K.** 'Impact characteristics of fiberglass reinforced plastics at low temperatures', *Kagaku Kogaku (Chemical Engineering, Japan)* 33 (1969) 1051

104 **Toth, J. M.** 'Barrier films for filament-wound fiberglass cryogenic vessels', *Advances in Cryogenic Engineering* 1 (1964) 537

105 **Toth, J. M., Soltysiak, D. J.** 'Investigation of smooth-bonded metal liners for glass fiber filament-wound pressure vessels', NASA CR-72165 (Final), National Aeronautics and Space Administration, Lewis Research Center, Cleveland, Ohio (1967) (N67–25070)

106 **Toth, J. M., Sherman, W. C., Soltysiak, D. J.** 'Investigation of smooth-bonded metal liners for glass fiber filament-wound pressure vessels', Douglas Missile and Space Systems Division Report No SM-49384, Quarterly Report No 3, Contract No NAS 3 6293, NASA Lewis Research Center, Cleveland, Ohio (1966)

107 **Toth, J. M., Sherman, W. C., Soltysiak, D. J.** 'Investigation of structural properties of fiber-glass filament-wound pressure vessels at cryogenic temperatures', NASA CR-54393, National Aeronautics and Space Administration, Lewis Research Center, Cleveland, Ohio (1965) (N65–35392)

108 **Toth, J. M., Barber, J. R.** 'Structural properties of glass-fiber filament-wound cryogenic pressure vessels', *Advances in Cryogenic Engineering* 10 (1965) 134

109 **Voloshenko-Klimovitskii, Yu. Ya., Belyaev, Yu. A., L'vof, B. S., Schpakovskaya, E. I.** 'Strength of cold-hardening GRPs based on PN-1 resin under impact tension at normal (20°C) and low (−196°C) temperatures', *Plasticheski Massy* 6 (1964) 39

110 **Voloshenko-Klimovitskii, Yu. Ya., Belyaev, Yu. A., Korenkov, Yu. A.** 'Impact tensile tests on glass-fibre reinforced plastics at normal and low temperatures', *Plasticheski Massy* 5 (1963) 51

111 **Watson, J. F., Christian, J. L., Hertz, J.** 'Selection of materials for cryogenic applications in missiles and aerospace vehicles', Convair/Astronautics Report No MRG 132–1 (1960)

112 **Weleff, W.** 'Effect of nuclear radiation and liquid hydrogen on mechanical properties of three phenolic materials', *Advances in Cryogenic Engineering* 11 (1966) 486

113 **Weleff, W.** 'Final Report, GTR-16 radiation effects test on structural materials at −423°F', Aerojet-General Corporation Report No RN-S-0290 (1966)

4. Handbooks and reviews

114 **Coston, R. M.** 'Handbook of thermal design data for multi-layer insulation systems', LMSC-A847882 Vol II (Final), George C. Marshall Space Flight Center, Huntsville, Alabama (1967) (N67–34910)

115 **Hertz, J.** 'The effect of cryogenic temperatures on the mechanical properties pof reinforced plastic laminates' *Society of Plastics Engineers Journal* 21 (1965) 181

116 **Hertz, J., Knowles, D.** 'Survey of thermal properties of selected materials', General Dynamics/Convair Report AAL-65-008 (AR-504-1-553) (1965) (N65–31775)

117 **Jurevic, W. G., Rittenhouse, J. B.** 'Structural applications handbook', AFML TR-67-332, Air Force Materials Laboratory, Wright-Patterson Air Force Base, Ohio (1968) (AD 804 585)

118 **Lackman, L. M., Arvin, G. H. et al** 'Advanced composite design guide, 3rd edn, Volume IV: Materials', Air Force Materials Laboratory, Wright-Patterson Air Force Base, Ohio (1973)

119 **Landrock, A. H.** 'Properties of plastics and related materials at cryogenic temperatures', Plastic Report No 20, Plastics Technical Evaluation Center, Picatinny Arsenal, Dover, New Jersey (1965) (AD 469 126)

120 **Maximovich, M., Scheck, W. G.** 'Data summary and reference file for graphite and boron reinforced composite materials', General Dynamics Convair Report No GDCA-DBG71-006 (1971) (Contract NAS 8–26198, George C. Marshall Space Flight Center, Huntsville, Alabama)

121 **Nored, D. L., Hennings, G., Sinclair, D. H., Smith, G. T., Smolak, G. R., Stofan, A. J.** 'Storage and handling of cryogenic fluids', NASA Special Publication SP-5053, Proceedings of Conference on Selected Technology for the Petroleum Industry, Lewis Research Center, Cleveland, Ohio, (1965) (N66-33674)

122 'Plastics for aerospace vehicles, Part 1: Reinforced plastics', MIL-HDBK-17A, Department of Defense, Washington, DC (1971)

123 **Rittenhouse, J. B., Singletary, J. B.** 'Space materials handbook', 3rd edn, NASA Special Publication SP-3051, National Aeronautics and Space Administration, Washington, DC (1969) (limited publication as AFML-TR-68-205)

124 **Schwartzberg, F. R., Hertzog, R. G., Osgood, S. H. et al** 'Cryogenic materials data handbook (Revised), Volume II, AFML-TDR-64-280-Vol II (Revised), Air Force Materials Laboratory, Wright-Patterson Air Force Base, Ohio (1970) (AD 713 620)

Miscellaneous references

125 **Kastelic, J. R., Hiltner, A., Baer, E.** 'Crazing, yielding and fracture in polycarbonate and polyethelene terephthalate at low temperatures', *Journal of Macromolecular Science-Physics* B7(4) (1973) 679

126 Relationships Between Structure and Mechanical Behavior in Polymeric Solids, ASM Materials Science Seminar, Chicago, 111, 1973 (in preparation)

Bibliography -- Property Cross Reference

Property	Glass – Epoxy	Glass – Polyester	Glass – Phenolic	Glass – Teflon	Glass – Silicone	Glass – Polyurethane	Glass – Phenyl Silane	Glass – PBI**
σ^{tu}	1–1.3, 2–2.2, 3–3.5, 4, 5, 5.1, 22, 24, 28, 33, 35 40, 43, 46, 47, 52, 54, 55, 57, 66, 71, 87	1–1.3, 2–2.2, 3–3.2, 3.4, 3.5, 34, 40, 55, 57, 63, 64, 66, 75, 109	1–1.3, 2–2.2, 40, 54, 55, 57 64–66, 71, 75, 83, 93, 97, 111, 112	2–2.2, 37, 67, 68, 80, 94, 102, 113	1–1.3, 2–2.2, 24, 40, 57 64, 66, 68, 97	2–2.2, 85	2–2.2, 57, 67	2–2.2
E_1^t	1–1.3, 2–2.2, 3–3.5, 4.5, 5, 5.1, 24 28, 35, 55, 56, 57, 66, 87	1–1.3, 2–2.2, 3, 34, 55, 57	1–1.3, 2–2.2, 54, 55, 57, 97, 111	2–2.2, 80	1–1.3, 2–2.2, 24, 57	2–2.2	2–2.2, 57, 66	2–2.2, 24
E_2^t	1–1.3, 2, 3–3.5, 28, 55, 56, 57	1–1.3, 2, 55, 57	1.1.3, 55, 57		1–1.3, 2, 57	2	2, 57	2
ϵ^t	3–3.5, 4, 5, 5.1, 35, 64 85	3–3.5, 64	64, 65, 112	80, 89, 102	64	85		
σ^{fu}	1–1.3, 2–2.2, 3–3.5, 4, 40, 57, 66, 71	1–1.3, 2–2.2, 3–3.3, 3.5, 40, 57, 66	1–1.3, 2–2.2, 40, 41, 57, 71, 83, 93, 97	2–2.2, 80	1–1.3, 2–2.2, 40, 57, 97	2–2.2	2.2.2	2–2.2
E_1^f	1–1.3, 2, 3–3.2, 3.4, 3.5, 57	1–1.3, 2, 2.2, 57	1–1.3, 2–2.2, 57, 83, 93, 97	2–2.2, 80	1–1.3, 2–2.2, 57	2–2.2	2–2.2	2–2.2
E_2^f	1–1.3, 2	1–1.3, 2	1–1.3, 2		1–1.3, 2	2	2	
σ^{cu}	1–1.3, 2, 2.2, 3–3.2, 3.4, 3.5, 24, 57, 66	1–1.3, 2, 2.2, 3–3.5, 34, 57	1–1.3, 2–2.2, 57, 82, 97	2–2.2, 80	1–1.3, 2–2.2, 24, 57	2–2.2	2–2.2, 57	2–2.2, 24
E^c	1, 1.2, 1.3, 2, 2.2, 57	1–1.3, 2, 2.2 57, 66	1–1.3, 2–2.2, 57, 82, 97	2–2.2, 80	1–1.3, 2–2.2, 57	2–2.2	2–2.2	2–2.2
σ^{si}	3–3.2, 3.4, 3.5, 4, 4.1, 5, 5.1, 22, 47, 71	3–3.5						
η^t	1, 1.3, 2, 2.1, 2.2, 66, 70, 99	1–1.3, 2–2.2, 34, 70	1–1.3, 2–2.2		1–1.3, 2	2	2	2
σ^{by}	2–2.2, 3, 3.2, 3.4, 3.5				2	2	2	2
σ^{1*}	4, 71, 103	62, 109	71, 97	80				
λ	3, 4.1, 14, 16–16.3, 21, 23–25, 38, 42, 56 61, 63, 90, 114	3, 14, 16–16.3 90	14, 16–16.3, 49	14, 16–16.3	14, 16–16.3, 24, 73, 90		14, 16–16.3	16, 24
$\Delta L/L$	3, 5, 14, 16, 16.2, 16.3, 28, 69, 85, 91, 100, 101, 104, 114	3, 14, 16–16.3	14, 16–16.3, 26, 27, 50 111	14, 16–16.3,	14, 16–16.3, 67	5, 85, 91	14, 16–16.3	16, 16.2
C_p	15, 16, 16.2 16.3, 24, 114	15, 16–16.3	15, 16–16.3, 64	15, 16–16.3	15, 16–16.3, 24		15, 16–16.3,	16–16.3, 24

* includes fracture toughness
** polybenzimidazole

Biblopgraphy – Property Cross Reference (Cont'd)

Property	Graphite – Epoxy	Boron – Epoxy	Boron – Aluminum	PRD–49 Epoxy
σ^{tu}	8,9,10,10.2, 13,13.2, 32, 47, 51, 58	13, 20, 22, 47, 53, 58, 81	13, 13.3	29, 44, 59, 60
E_l^t	8,9,10,10.1, 13, 51	13, 81	13, 13.3	44, 59, 60
ϵ^t	13	20	13	
σ^{fu}	8, 10, 10.1, 11, 12, 13, 13.2, 58	58		
E^f	8, 10.1			
σ^{cu}	13		13, 13.3	
E^c	13	13, 81	13, 13.3	
σ^{si}	8,9,10,10.1, 10.2,12,13, 13.2, 47, 58	13, 22, 47, 58, 81	13, 13.3	59, 60
η^t	45	20		
σ^{ty}			13, 13.3	
σ^{I*}	9, 10.2	81		
λ	13,17, 18, 38	13,38,63, 81		
$\Delta L/L$	10,13, 13.2, 17,18,36,51, 52,84,88	13	13, 13.3	59, 60
C_p	13	13	13, 13.3	

* Includes fracture toughness

Miscellaneous Properties

Notch Tensile Strength Glass-Epoxy (3–3.2, 3.4, 3.5, 43, 46)

Vapor Permeability Glass-Epoxy (28)

Modulus of Rigidity Glass-Epoxy (53), Glass-Teflon (80), Boron-Epoxy (53)

Poissons Ratio Glass-Epoxy (53), Boron-Epoxy (53)

Proportional Limit in Tension Glass-Epoxy (55, 56), Glass-Polyester (1–1.3, 55, 56)

Static Fatigue Glass-Epoxy (66, 99), PRD 49–Epoxy (44)

Environmental Effects Glass-Epoxy (4–4.1), Graphite-Epoxy (13, 13.2, 17, 58), Boron-Epoxy (13, 58), Boron-Aluminium (13, 36) PRD 49–Epoxy (44)

Electrical Resistivity Graphite-Epoxy (13), Boron-Epoxy (13)

Thermo-Optical Effects Graphite-Epoxy (13, 84), Boron-Epoxy (13)

Density Glass-Epoxy, Polyester, Phenolic, Silicone, Phenyl Silane (14, 57), Glass-Teflon (14), Glass-Polybenzimidazole (16), Graphite-Epoxy (9, 13), Graphite-Phenolic (14), Graphite-Polyimide (12.1)

Radiation Effects (13.2, 33, 37, 40, 51, 52, 64, 65, 75, 94, 112, 113)

Cryogen Compatability (33)

Miscellaneous Composites

Glass-Polyimide σ^{tu} (24, 67, 68), σ^{fu}(89), σ^{si}(12.1, 89), $\Delta L/L$ (67)

Glass-Melamine σ^{tu}(65), ϵ^t(65), λ(90)

Glass-Viton σ^{tu}(68)

Glass-Phenyl Formaldehyde σ^I(110), λ (72), C_p (72)

SiO_2-Epoxy σ^{tu}(31), $\Delta L/L$ (28)

Graphite-Aluminium σ^{tu} (thermal cycling effects 6–6.2)

Graphite-Polyimide σ^{tu}(13), σ^{fu}(11, 12.1, 13), σ^{si} (13), $\Delta L/L$,36)

Graphite-Phenolic λ (14, 16–16.3), $\Delta L/L$ (14, 16–16.3)

Steel-Aluminium σ^{tu} (7, 7.1), ϵ^t (7.1), σ^I (7, 7.1)

Steel-Epoxy σ^{tu} (2, 30), E^t (2, 30), σ^{fu} (2), E^f (2), σ^{cu} (2), E^c (2), n^t (2)

Boron/Steel-Aluminum
Boron/Titanium-Aluminum σ^{tu}, E^t, σ^{cu}, E^c, σ^{by}, $\Delta L/L$, C_p, (13, 13.3), σ^{si}, ϵ^t, n^t (13)

Potassium Titanate–Epoxy λ (16), C_p (16)

Pressure Vessel Applications

Glass-Filament
(19, 20, 39, 42, 46–48, 53, 67, 69, 76, 77, 91, 92, 95, 96, 98–100, 104–108, 113)

Graphite–Filament
(8, 10, 10.1, 45, 47, 100)

Boron-Filament
(20, 47, 53, 78)

PRD 49–Filament
(59, 60)

Appendix III: M. B. Kasen, "Properties of Filamentary-Reinforced Composites at Cryogenic Temperatures," Composite Reliability, ASTM STP 580, American Society for Testing and Materials, 1975 (to be published).

M. B. Kasen[1]

Properties of Filamentary-Reinforced Composites at Cryogenic Temperatures

REFERENCE: Kasen, M. B., "Properties of Filamentary-Reinforced Composites at Cryogenic Temperatures," *Composite Reliability, ASTM STP 580*, American Society for Testing and Materials, 1975, pp. 586–611.

ABSTRACT: This paper presents a review of a series of significant publications on the mechanical and thermal properties of filamentary-reinforced structural composites in the cryogenic temperature range. The objective, scope of work, and significant conclusions of the selected works are discussed. The temperature dependence of the ultimate tensile strength, tensile modulus, thermal conductivity, and thermal contraction (expansion) is presented for selected composites developed in each program. Problem areas are defined and suggestions are made for future work.

KEY WORDS: composite materials, reviews, structural composites, cryogenics, glass, boron, graphite, reinforced plastics, aluminum, tensile strength, modulus of elasticity, thermal conductivity, thermal expansion

214

45

Nomenclature

NOL	Naval Ordinance Laboratory
UFW	Uniaxial filament-wound
BFW	Biaxial filament-wound
GFRP	Glass fiber reinforced plastic
CFRP	Carbon fiber reinforced plastic
BFRP	Boron fiber reinforced plastic
NMA	Nadic methyl anhydride
BDMA	Benzyldimethylamine
L-100	Polyurethane resin (Adiprene)
MOCA	4, 4'-methylenedianiline
DSA	Dodecenyl succinic anhydride

The primary impetus for structural composite development has arisen from the desire to obtain improved mechanical properties at room and elevated temperatures, to save weight, and to reduce the cost for current and future aerospace hardware applications. Comparatively little effort has been expended on development of composites for use at cryogenic temperatures. A notable exception has been a fairly extensive body of work sponsored by the National Aeronautics and Space Administration (NASA) and the U.S. Air Force (USAF) wherein a series of glass-reinforced composites was evaluated down to 20 K. Such materials were subsequently successfully used as baffles and structural support components in various aerospace applications. The other major field of cryogenic composite development has been filament-winding for fabrication of cryogenic pressure vessels. In recent years, advanced fibers have also been investigated for the latter application. To a large extent, the remaining published data reflect work in which cryogenic properties were peripheral to the main work objective.

[1]Staff scientist, Cryogenic, NBS-Institute for Basic Standards, Boulder, Colo. 80302.

The relative lack of emphasis on cryogenic structural composites is understandable, as the majority of the applications are presently satisfied by well-characterized metals and alloys. Why then should one consider composites for such applications? The answer lies in the increasingly stringent demands being made on materials in advancing cryogenic technology, of which the development of superconducting machinery may serve as an example. While the first generation of such machines will be almost entirely dependent on metals technology, it is highly probable that succeeding generations will capitalize on composite technology for reasons of increased reliability, reduced weight, and increased overall efficiency, as composites offer higher specific strengths and moduli combined with a wider range of thermal and electrical properties than are available with any metal or alloy.

A major barrier to the wider use of structural composites for cryogenic applications is the lack of broad characterization and handbook-type data describing the properties and performance of such materials under cryogenic conditions. The Cryogenic Division of the National Bureau of Standards (NBS) has therefore undertaken a comprehensive survey of the literature on the mechanical and thermal properties of structural composites from about 1960 to the present time. In the course of the survey, it became apparent that there existed several bodies of work that were particularly outstanding and which deserved more detailed analysis than was possible in the more comprehensive review. It is the intent of the present paper to consider the results of these selected studies, reviewing their objectives, the scope of the work undertaken, and the general conclusions reached by the authors. Subsequently, selected composite types developed in each program are discussed in some detail. In the interest of brevity, discussions of the properties are restricted to ultimate tensile strength, tensile modulus, tensile fatigue, thermal contraction, and

thermal conductivities, as these properties are of most interest to the potential users.

The discussion of properties given herein does not take into consideration the effect of variations in fiber/resin ratio of specific types of composites and test specimens, as this characteristic was not reported for all referenced works. Composite properties are strongly influenced by this ratio. The property data discussed in this paper reflect actual values and trends reported for specific composites. Controlled variations in many of the properties are obtainable in practice by specific variation of the fiber content of the composite.

As composites are frequently used where weight is critical, or where specific strengths are required, typical composite densities have been summarized in Table 1.

TABLE 1—*Typical composite densities.*

Composite System	Fiber/Resin Ratio	Density, $lb \cdot ft^{-3}$ ($kg \cdot m^{-3}$)
S-glass-epoxy	60–67	0.068–0.074 (1.09–1.19)
Kevlar 49/epoxy	60–65	0.047–0.050 (0.753–0.801)
Boron-epoxy	55	0.070–0.074 (1.12–1.19)
Graphite-epoxy	55–60	0.050–0.055 (0.801–0.881)
Boron-aluminum (4 mil)	50	0.10

It must be emphasized that this survey is not exhaustive, that the results reported have not been experimentally confirmed by NBS, and that the conclusions and evaluations presented in this paper reflect those of the cited authors and do not imply approval, endorsement, or recommendation of any commercial product by NBS.

The presentation is in two parts—the first considering the work on glass-reinforced materials and the second considering a variety of advanced-fiber reinforced materials.

Glass-Reinforced Composites

Overview

Brink, Chamberlain, and their associates made the initial significant contribution to understanding the cryogenic behavior of glass-fiber reinforced plastic (GFRP) materials in report ASD-TDR-62-794 to the USAF, Part I of which was published in 1962 *[1]*[a] and Part II in 1964 *[2]*. Part I of this work evaluated the mechanical properties of commercial composite products which conformed to existing military specifications.

[a]The italic numbers in brackets refer to the list of references appended to this paper.

Tensile, flexure, compressive, and fatigue properties were evaluated from 295 K to 20 K in epoxy, phenolic, polyester, and silicone matrices reinforced with 181 glass cloth. The results indicated a general increase in strength as the temperature was lowered, while the same relative fatigue resistance was observed at cryogenic temperatures as at room temperature, the cryogenic fatigue properties being equal to or above the room temperature values. Similar resin systems were found to produce similar trends on cooling, and toughness of the GFRP composites was maintained at cryogenic temperatures while the rate of cooling was not found to be important. Part II of this work investigated a series of additional resins, including Teflon,[a] polyurethane, phenyl silane and polybenzimidazole (PBI or Imidite), which were recommended by the manufacturers for use at low temperatures. Bearing yield strength, tensile fatigue, and impact properties were evaluated in addition to the properties investigated in Part I. In general, the properties of composites made with the modified resins were found to be inferior to those of the commercial materials studied in Part I. The authors concluded that epoxies were the most desirable matrix materials, with polyesters running a close second. Flexibilized matrix systems were judged useful only if flexibility was of paramount importance. The authors concluded that there existed a need for standardization of test procedures, a conclusion which is unfortunately still valid today.

Chronologically, the next major contribution was made by Toth et al in 1966 *[3]*. This report covered a three-year effort which had the following objectives: (*a*) to critically evaluate test methods for use at cryogenic temperatures, (*b*) to establish the relationship between test results and design performance, and (*c*) to apply the developed techniques to the evaluation of a variety of glass-polymeric composites. Unidirectional as well as woven cloth reinforcement of conventional and modified epoxy resins was studied. A limited test series was also run on silicon carbide whiskers combined with S-glass as reinforcement for an epoxy resin. Test temperatures ranged from 295 K to 20 K. The authors concluded that valid test procedures had been developed and proven by subsequent model testing. The test program included tensile, flexural, compressive, interlaminar, and bearing strength as well as thermal conductivity and thermal expansion. The S-glass in an epoxy of the Polaris formulation[b] was judged by Toth *[3]* to have the most optimum overall properties for cryogenic use. (Commercial designations for the Polaris resin are E-787 and 58-68R.)

[a]The use in this paper of trade names of specific products is essential to the proper understanding of the work presented. Their use in no way implies approval, endorsement, or recommendation by NBS.

[b]The Polaris resin consists of Epon 828/Epon 1031/NMA/BDMA in proportions 50/50/90/0.55 pbw. It is referred to as the Polaris resin because of its successful use in that missile.

Two major reports appeared in 1967. In January the publication of the work of Soffer and Molho *[4]* reported the results of an intensive effort to develop improved epoxy resins for use in filament-wound cryogenic pressure vessels. Forty-one candidate resins were evaluated for mechanical properties and for suitability in filament-winding operations. Composite specimens using S-901 glass were evaluated in tension, interlaminar shear, and thermal expansion. As a result of this work, Soffer and Molho selected a modified epoxy system designated Resin 2 as superior for cryogenic use.* As a final evaluation, Resin 2 was compared with 58-68R (E 787) in a series of burst tests on metal-lined, S-901 glass filament-wound pressure vessels, the results showing Resin 2 to be clearly superior in the longitudinal filament stress level developed in the vessels at 77 and 20 K.

The second significant publication in 1967 was that of Lewis and Bush *[5]*. Again oriented toward filament-wound cryogenic tankage, the objective was to determine the extent to which various fiber finishes and coupling agents could be used to improve the cryogenic properties of composites reinforced with Aerojet General Hi-Stren glass. Naval Ordinance Laboratory (NOL) rings and flat specimens were used to obtain tensile, interlaminar shear, and thermal expansion data. The study also evaluated various modified epoxy matrices in an attempt to improve impact strength, toughness, and extensibility at cryogenic temperatures. It was concluded that glass finishing treatments could be used to improve bonding of filaments to the resin, thereby improving the mechanical properties, but that coupling agents were effective only in improvement of wet strength. At 77 K and 20 K, the highest pressure vessel longitudinal and hoop-filament tensile strengths were again developed with Resin 2.

The foregoing studies encompassed 45 separate types of glass-reinforced composites which varied not only in the glass/polymer combination, but in methods of fabrication and testing. The present paper makes no effort to discuss all of the results in detail; rather, we shall confine our attention to the tensile strength, tensile modulus, thermal contraction, and thermal conductivity properties reported for the best of the composites evaluated in these works. We shall consider only uniaxial filament-wound (UFW), biaxially filament wound (BFW) of 0/90 orientation, and woven-cloth layups. Data for UFW composites are restricted to the longitudinal properties, while data for the BFW and cloth composites refer to properties parallel to one major fiber direction unless otherwise noted.

Mechanical Properties

Figure 1 shows the expected superiority of the UFW glass-epoxy

*Epon 828/DSA/EMPOL 1040/BDMA in proportions 100/115.9/20/1 pbw. As this formulation was developed under NASA sponsorship, it will henceforth be referred to as NASA Resin 2.

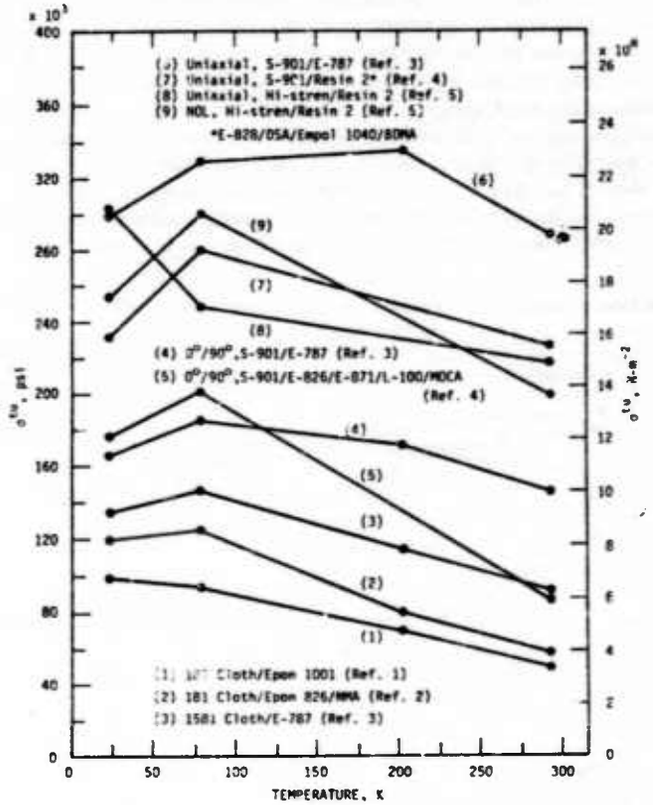

FIG. 1—*Ultimate tensile strength, σ^{tu}, of glass-epoxy composites at cryogenic temperatures.*

composites in ultimate tensile strength, with the BFW and cloth composites having sequentially lower strengths. The strength increased for all composite types upon cooling to 77 K; however, below 77 K the data appear erratic. The latter phenomenon is observed to some extent in all of the mechanical properties of filamentary-reinforced polymeric-matrix composites.

These data suggest that one can expect a maximum tensile strength on the order of 100 to 140 ksi at 77 K for cloth-reinforced epoxies, while BFW composites are capable of developing considerably higher strengths, on the order of 180 to 200 ksi at this temperature. More scatter is observed in the UFW data, which is somewhat surprising, as the tensile strength in this orientation should be essentially fiber controlled.

It may be that, within the cryogenic temperature range, the temperature-sensitive properties of the matrix are affecting the overall strength even in the UFW composites, possibly by altering the neighbor fiber interactions at fracture sites. It may also be that the difficulty in obtaining valid test data from UFW composites at cryogenic temperatures accounts for some of this scatter. Nevertheless, it appears that about 280 ksi is not an unreasonable expectation for the tensile strength of UFW composites in the fiber direction at 77 K. It is this exceptional strength coupled with comparatively low cost that has maintained the popularity of glass-fiber reinforced composites.

Curve 5 has been included on Fig. 1 to illustrate the results obtained with an epoxy polyblend designed for greater flexibility at low temperatures. The strength of this polyblend[a] is low at 295 K, but increases rapidly on cooling. On the basis of the mechanical properties at cryogenic temperatures, this particular polyblend, designated Resin 4A by Soffer and Molho, was considered by them to be the best of the resins they studied, as it was the only resin tested that did not crack during thermal shock and impact testing at cryogenic temperatures, and its notch toughness was superior to all other resins tested in the program. The authors concluded, however, that the processing characteristics of this polyblend were unfavorable, and the NASA Resin 2 formulation was selected as their overall choice of matrix material for filament-wound composites.

The UFW composite data of Fig. 1 illustrate the results reported for the epoxy formulations E-787 (58-68R) and NASA Resin 2. On the basis of these data, E-787 (58-68R) produces the higher tensile values, at least to 77 K. However, these data may not be directly comparable because of possible differences in fiber/resin ratios. Composite tensile strengths of a specific specimen are dependent on this ratio (as well as on fiber orientation), higher fiber contents yielding higher composite strengths and moduli in the direction of the reinforcement. Also, the work of Soffer and Molho has shown that the specific application may affect the choice of matrix resin. At this point it must be concluded that both of these resins should receive equal consideration for cryogenic applications.

The initial tensile moduli for the same composites appear in Fig. 2. The moduli generally tend to increase upon cooling to 77 K; however, there does not appear to be consistent behavior, even among composites of the same type and layup, possibly due to resin content variations. As with the tensile strength, the tensile modulus appears to become erratic upon further cooling to 20 K.

The cloth-reinforced composites have the lowest modulus, ranging from 4-5 × 10^6 psi at 77 K, the highest of these being reported for 1581/E-787. The S-901/E-787 BFW composite has a substantially higher modulus at

[a] Epon 826/Epon 871/L-100/MOCA (35/15/50/27.6 pbw).

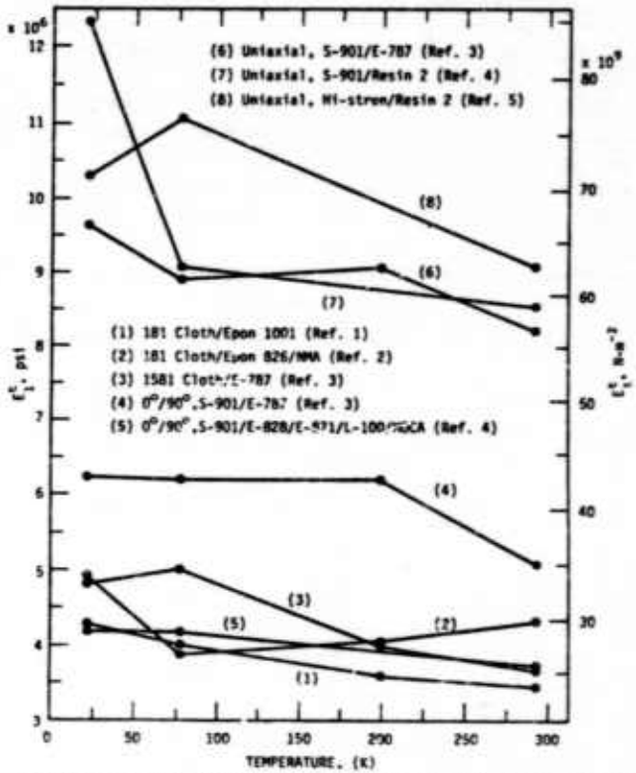

FIG. 2—*Initial tensile moduli, E_i^t, of glass-epoxy composites at cryogenic temperatures.*

slightly over 6 × 10^6 psi at this temperature. Note, however, that the polyblend BFW composite has a tensile modulus no better than that of the cloth-reinforced materials and shows very little temperature sensitivity. The UFW composites have the highest moduli, as is expected. The Hi-Stren/NASA Resin 2 composite appears to have the highest modulus; however, it should also be noted that Hi-Stren glass has a modulus 8 percent higher than S-901 glass. The latter data resulted from a series of tests investigating the effects of glass finishes on the mechanical properties, and the reported higher values of composite moduli may reflect superior bonding at the glass-matrix interface as well as higher fiber modulus. It would appear from these data that an initial tensile modulus of from 9 to 10 × 10^6 psi might reasonably be expected from UFW glass-

epoxy composites at 77 K. It is these low moduli of glass-reinforced composites that have stimulated the development of advanced-fiber composites.

It is apparent from Figs. 1 and 2 that if one wishes to speak with any degree of specificity about the temperature dependence of the tensile properties of a glass-fiber reinforced composite in the cryogenic region, one is pretty well constrained to talk about a specific composite and fiber/resin ratio, particularly for temperatures below 77 K. This is further illustrated in Fig. 3, which is a frequency histogram compiled from all available literature data on the temperature dependence of the tensile properties of glass-epoxy composites of the three considered layup types. Figure 3*a* of this diagram shows that cooling from 295 K to 77 K produces an increase in tensile strength in all cases, the extent of the increase ranging from 10 ksi to as much as 130 ksi, with the highest probability of obtaining an increase on the order of 30 to 60 ksi. However, on cooling further to 20 K these data suggest a high probability of little or no change in tensile strength, but with the distinct possibility of a strength loss of as much as 70 ksi or a strength gain of as much as

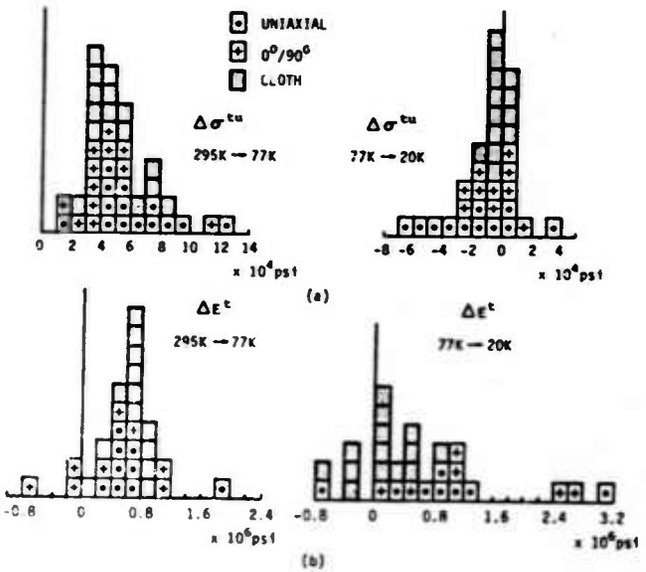

FIG. 3—*Histograms illustrating changes in tensile properties of glass-epoxy composites upon cooling into the cryogenic range. The ordinate represents the number of literature references reporting property changes of a given magnitude.*

40 ksi. The data also indicate that the probability of a strength change of a given magnitude is independent of the layup type, which, by inference, suggests that the erratic behavior below 77 K is a matrix-controlled phenomenon.

Comparable statistical data for the tensile modulus of glass-epoxy composites presented in Fig. 3*b* indicate the probability of a modest modulus increase on the order of from 0.6 to 0.8 × 10^6 psi on cooling to 77 K, but with a finite chance that the modulus may decrease by as much as 0.8 × 10^6 psi or that it may increase by as much as 2 × 10^6 psi. The results of further cooling to 20 K are more difficult to interpret. In general, the data seem to cluster around a small increase of modulus up to about 0.6 × 10^6 psi for cloth reinforcement and suggest that a somewhat larger increase on the order of from 0.6 to 1.3 × 10^6 psi could be obtained with crossply or uniaxial composites. Nevertheless, the range of scatter from −0.8 to 3.2 × 10^6 psi is again indicative of very erratic behavior upon cooling below 77 K. Microbuckling of fibers due to resin shrinkage and minimal stress relaxation at cryogenic temperatures may lead to variations in initial tensile modulus and account for some of data scatter.

This erratic behavior in strength and modulus when testing at 20 K cannot be attributed to a sudden embrittling of the epoxy matrix, as 77 K is already far below the glass-transition temperature of the matrix. Nor can it be reasonably attributed to a sudden increase in the difficulty of obtaining reliable test data, as there is no *a priori* reason for a test method giving reliable data at 77 K to become entirely unsuitable at 20 K. The author does not know the answer to this problem. However, in searching for an explanation, consideration should be given to the results of some recent studies which have shown that, at least in the linear polymers of the polycarbonate and polyethylene terepthalate types, the medium in which a low-temperature test is conducted can strongly affect the resultant mechanical properties *[6,7]*. These studies indicate that yield and fracture of such polymers in the cryogenic temperature range are controlled by a crazing phenomenon which is strongly influenced by the activity of the gas or liquid in contact with the polymer surface. As all reported data on the mechanical properties of composites at cryogenic temperatures have been obtained at liquid nitrogen or liquid hydrogen temperatures, it must be considered at least a possibility that the observed anomolous behavior is a synergistic effect of a given type of polymer in contact with a given ambient medium.

Thermal Properties

Figure 4 presents the data reported by Toth et al *[3]* for the temperature dependence of the thermal contraction of several of the E 787 matrix

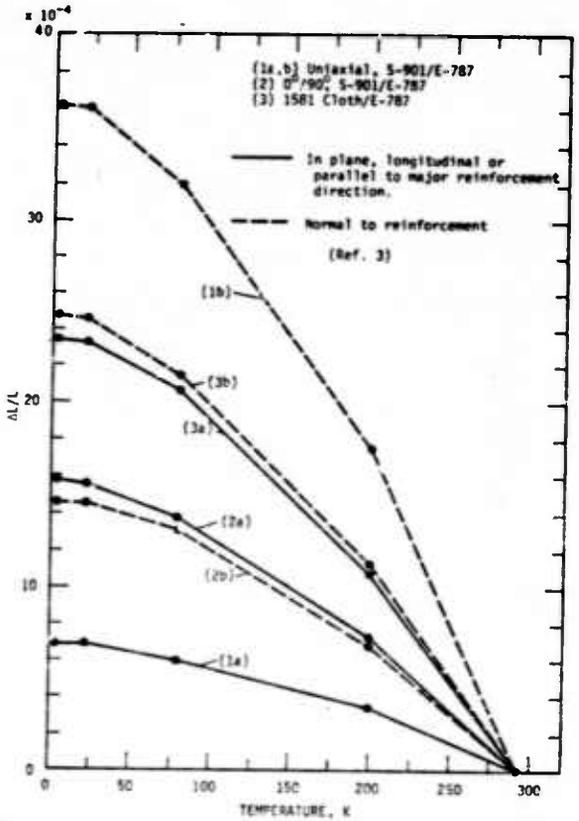

FIG. 5—*Thermal contraction, ΔL/L, of glass-epoxy composites at cryogenic temperatures.*

composites that appear in Figs. 1 and 2. As the thermal contraction of the epoxy is significantly larger than that of the glass, there will generally be a difference between the thermal contraction in the plane of reinforcement and that normal to the plane (thickness direction). Contraction in the reinforcement direction in the case of a UFW composite is held to a minimum by restraint of the glass, as shown by curve 1a, while contraction in the reinforcement-normal direction in this type of composite is very large, curve 1b, the glass providing negligible restraint in the latter case. In the BFW case, the contraction parallel to a major fiber direction is about twice that of the UFW composite, about proportional to the decrease in

fiber density. However, contraction in the reinforcement-normal direction in this type of layup is also quite low, curve 2b, reflecting the effective restraint provided by the crossplied glass fibers, which are in close proximity. The in-plane contraction of the cloth composite is the highest of the group as shown by curve 3a, reflecting the lower glass content of such composites and the lesser restraint provided by the convoluted fibers, which, in general, do not lie parallel to the reinforcement plane. The reinforcement-normal contraction is also high for composites of this type, due both to the lesser total glass content and to the lesser restraint provided by the layered cloth.

It should be noted that, in general, the literature reports a reinforcement-normal contraction about twice that of the in-plane contraction for balanced-weave cloth-reinforced glass-polymeric composites in contrast to the similar values reported by Toth for 1581/E-787.

Thermal conductivity is also an important parameter in cryogenic design. Unfortunately, improper experimental technique invalidates some of the data in the literature—primarily, failure to properly compensate for radiation losses, which can introduce errors on the order of 100 to 200 percent in the higher temperature ranges. Figure 5 presents what the author believes to be the best available data for glass-epoxy composites, based on the work of Campbell et al *[8]* and of Hertz *[10]*.

Thermal conductivity differs from the other thermal properties of composites in that it is significantly affected by the ambient atmosphere in which the test is conducted. The literature data suggest that, compared with the values obtained in helium, data taken in nitrogen will average about 7 percent lower, while data taken in vacuum will average about 20 percent lower. Campbell *[8]* suggests that the low value in vacuum primarily reflects the difficulty of obtaining good contact between the composite specimen and the mating parts of the thermal conductivity apparatus. An ambient atmosphere of nitrogen or helium increases the measured conductivity by reducing this contact resistance; however, diffusion of the gas (particularly of helium) into pores within the composite was also found to contribute to an increase in conductivity, as the gas provides an overall improvement in the thermal path within the composite. This explanation appears plausible, as it is consistent with the effect of the ambient atmosphere being observed over the entire 20 K to 295 K temperature range. The present author believes, however, that consideration should also be given to the effect on thermal conductivity of a matrix which has cracked due to thermal contraction at very low temperatures. The effect of the latter would be to increase the spread between conductivities measured in the various ambient media.

As the data taken in vacuum appear to be subject to the largest error, the data appearing on Fig. 5 are averages reported for tests in nitrogen and helium.

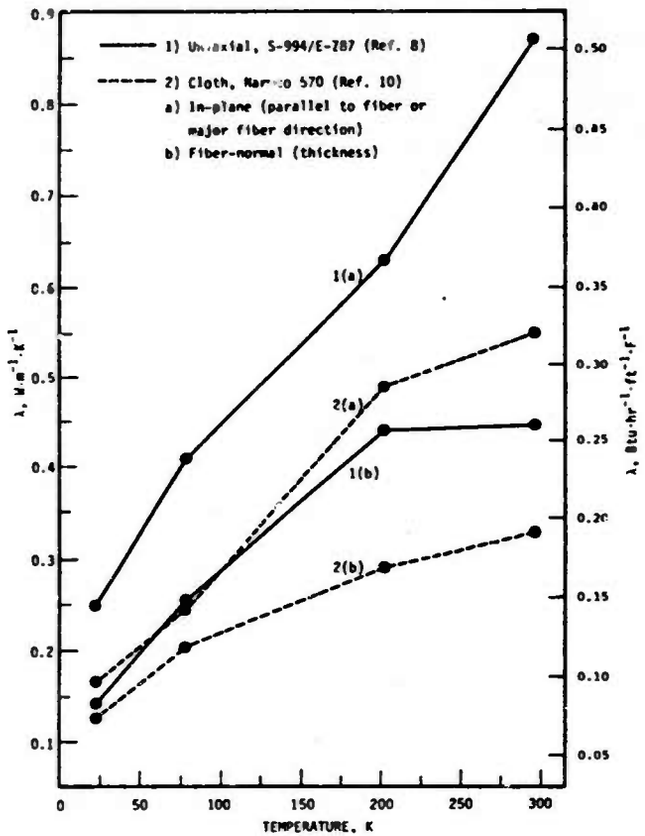

FIG. 5—*Thermal conductivities, λ, of glass-epoxy composites at cryogenic temperatures.*

Thermal conductivity at 20 K is 30 to 40 percent of that at 295 K. The difference between both the fiber-normal and the in-plane conductivities and the absolute spread of values is widest at room temperature, converging as the temperature is lowered. Conductivity is the highest for the UFW composite in the fiber direction, reflecting both the high density of fibers and the higher conductivity of glass as compared with the epoxy matrix. Fiber normal conductivity in the UFW composite is much lower than the in-plane value. Lower conductivity in both directions is observed for the cloth-reinforced composite, reflecting the lower fiber density of such composites. No reliable data were available for a 0/90

crossply; however, such a composite layup would be expected to develop intermediate conductivities in both directions, the in-plane conductivity being lower than the UFW due to lower fiber density in the direction of heat flow, while the plane-normal value should be higher than that for cloth due to the overall higher fiber density.

Other Matrices

For the sake of brevity, the author has had to confine the discussion thus far to epoxy matrix composites, although the referenced works contain data on many other matrix materials. Concentration on the epoxies is somewhat justified in that such materials are today the almost universal choice for demanding cryogenic service, based on their generally superior performance qualities. For example, if the tensile strength of cloth-epoxy specimens is taken at 100 ksi at 77 K, the next strongest composites consisting of the polyurethanes, polyesters, phenolics, Teflons, and polybenzimidazoles would form a group at about 70 to 80 ksi. The silicones, phenyl silanes, and polyimides form a third and lower strength group at about 40 to 50 ksi. The epoxies also excel in flexural and compressive strength. Only in modulus are the epoxies equaled (and often exceeded) by the phenolics, polybenzimidazoles, and phenyl silanes.

Fatigue

The author wishes to conclude this section on glass-reinforced composites with a brief discussion of the tensile fatigue studies of Brink *[1]* and of Chamberlain et al *[2]*, as these data constitute almost the entire body of research on the dynamic properties of glass-reinforced composites at cryogenic temperatures. The only other work known to the author is the study by Fontana *[11]* using a reciprocating-beam method and by Lavengood and Anderson *[12]* in torsion.

The work of Brink and Chamberlain was, with one exception, conducted with 181-cloth reinforced composites and included the variety of matrix material listed in Fig. 6, which is a plot of the failure stress of each material after 10^4 cycles at the various temperatures. Figure 6 also records the percent of the original single-cycle ultimate tensile strength retained by each composite type after 10^4 cycles. Glass-reinforced polymers have reduced fatigue performance when compared with many alloys or with the advanced composites. However, these data show that the absolute magnitude of the stress required to induce failure after 10^4 cycles generally increases with decreasing temperature. At 200 K and 20 K, the polybenzimidazoles showed superior performance, while equaling the best at 77 K. Furthermore, the percentage of original strength retained by the polybenzimidazoles was consistently among the highest of the group. The better fatigue performance of this material may be accounted for by the

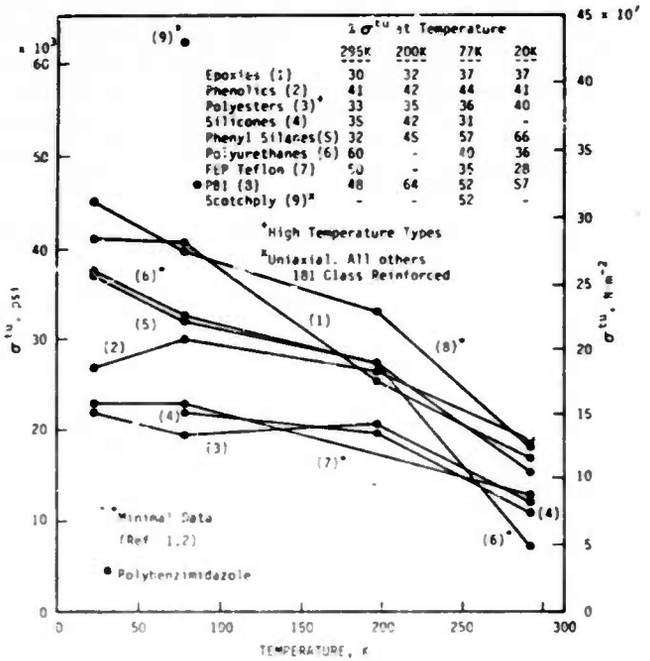

FIG. 6—*Failure stress of glass-reinforced composites, σ^{tu}, as a function of temperature after 10^6 fatigue cycles*

very low in-plane thermal contraction of polybenzimidazole composites—about one-third that of the epoxies—which decreases the residual stress at the glass-matrix interface at cryogenic temperatures. As the polybenzimidazole composites also compare well with the epoxies in static strength properties, another look at the polybenzimidazole types may be warranted for cryogenic applications requiring good dynamic performance.

The epoxies also look comparatively good, but primarily because of their high initial strength—their percentage of retained strength was among the lowest of the group. In general, the polyurethanes, phenyl silanes, and phenolics grouped into intermediate performance, while the polyesters, silicones, and Teflons had distinctly lower fatigue properties. Figure 6 contains only one data point for a UFW glass-epoxy composite at 77 K. This material had a much higher absolute strength after 10^6 cycles than any of the cloth-reinforced materials; however, it retained only about 52 percent of its original strength.

The available data are insufficient to either prove or disprove the existence of a fatigue limit at cryogenic temperatures, although the S-N curve reported by Brink *[1]* for 181/Epon 1001 did appear to be reaching a limit at about 30 percent of the original strength at temperatures below 77 K.

Advanced Composites

Overview

The application of carbon fiber reinforced epoxy composites to filament-wound cryogenic tankage was investigated by Simon, Larsen, and Alfring, their results appearing in a series of reports in 1970, 1971, and 1972 *[13-15]*. Their initial task was to evaluate the tensile, flexural, interlaminar shear, bending fatigue, and thermal expansion properties of several fibers and resins in the form of strands, bars, and NOL rings from 295 K to 20 K. The tensile modulus of these CFRP composites was observed to increase up to 20 percent on cooling to 77 K, concomitant with a decrease in ultimate tensile strength by as much as 30 percent. Bending fatigue at 50 percent of the tensile ultimate was found to cause less deterioration after 1000 cycles at cryogenic temperatures than at room temperature. The thermal contraction tests revealed a slight negative coefficient, indicating that the resin matrix might see up to 1.5 percent strain when cooled. The second task was the design and testing of filament-wound tanks using Morganite (Modmor) II and Thornel 50 fibers in a NASA Resin 2 matrix. Results indicated that these CFRP overwrapped tanks would be competitive with boron-reinforced tanks and possibly competitive with glass reinforcement in terms of strength/weight ratio.[a]

A third task undertook to study the effect of elastomeric additions on the strength and fracture toughness of epoxy resins and of CFRP composites. Results were generally unimpressive except for a CBTN-modified ERLB 4617 resin composite which demonstrated significantly improved tensile and short-beam shear strength at cryogenic temperatures at the expense of a decrease in room temperature shear strength. The remaining tasks in this program were directed at a continued study of the effect of elastomer additions to the epoxy matrix. Simon and Larsen concluded that, based on their data, Courtaulds HT-S fiber in a NASA Resin 2 matrix was a satisfactory combination for general cryogenic use for both UFW and BFW composites.

In 1972, Hertz, Christian, Varlas, et al published the results of a com-

[a]More recent work with improved graphite fibers indicates 295 K pressure vessel strength/weight ratios higher than for glass and slightly lower than for PRD 49-III (Kevlar 49).

prehensive study on the materials development portion of a larger program investigating advanced composites for specific uses in spacecraft and missiles *[16]*. The associated studies on the structural development part of this program may be found in Ref *17*, while the development of hardware is reported in Ref *18*. The objective of the study was to select advanced composites systems capable of operating for relatively short times over a 77 to 450 K temperature range. Work was directed toward the selection of two types of CRFP composites, one of high modulus and one of high strength. Boron-fiber reinforced aluminum (6061) was also studied to relate variations in mechanical properties to variables in production method or in fiber diameter. Boron-fiber reinforced plastic (BFRP) composites in the form of the commercial SP-272 material were also investigated. The mechanical and thermal properties of these materials were characterized from 77 to 450 K, including thermal expansion, thermal conductivity, specific heat, electrical resistivity, and thermo-optical properties. Three materials—5.7-mil Borsic/6061 aluminum, HT-S/X-904 epoxy, and a hybrid CFRP system utilizing both GY-70 and HM-S fibers in an X-904 epoxy matrix—were selected for determination of design allowable data. Some data on the effects of various environments on the mechanical and thermal properties of the selected composites were also reported.

Hoggatt in 1971 *[19]* and Hanson *[20]* in 1972 published the initial data on the cryogenic properties of PRD-49/epoxy composites. Hoggatt first investigated the suitability of PRD-49[a] for filament-winding applications and subsequently determined the basic property data (tensile, interlaminar shear, and thermal expansion) down to 20 K. These data were then used in the design, fabrication, and testing of a series of cryogenic pressure vessels. Results indicated that the specific strength of vessels made with PRD-49-I fiber was about the same as that for S-glass; however, the specific modulus of the PRD-49 tanks was almost three times higher. These data were obtained with epoxy matrices of both the NASA Resin 2 and ERLA 4617/CL type. Hoggatt concluded that the results justified further investigation of PRD-49 for cryogenic applications. Some recent work by Chiao et al *[20]* supports this conclusion, showing that pressure vessels reinforced with PRD 49-III fiber may develop specific strengths 30 to 50 percent higher than that of comparable glass-reinforced vessels at both room and cryogenic temperatures.

The studies of Hanson *[21]* considered both the strength and creep behavior of PRD-49-I and PRD-49-III composites from 20 to 477 K, using an ERLA 4617 epoxy matrix. At 20 K, the ultimate tensile strength of the PRD-49-III composite was found to be about 90 percent of that at room temperature, while an increase in tensile modulus by about 40 percent was noted. The creep tests, all conducted at or above room temperature, showed the presence of an initial accelerated stage, followed by a much lower secondary creep rate.

[a] Product of the E. I. DuPont Company now called Kevlar 49.

Mechanical and Thermal Properties

Figures 7-12 illustrate the temperature dependence of the ultimate tensile strength, tensile modulus, thermal contraction (expansion), and thermal conductivities of a series of advanced composites selected by the authors of the aforementioned studies as being most useful in cryogenic applications. These data show the commercial BFRP and Borsic-aluminum composites to be almost in a class by themselves, having the highest

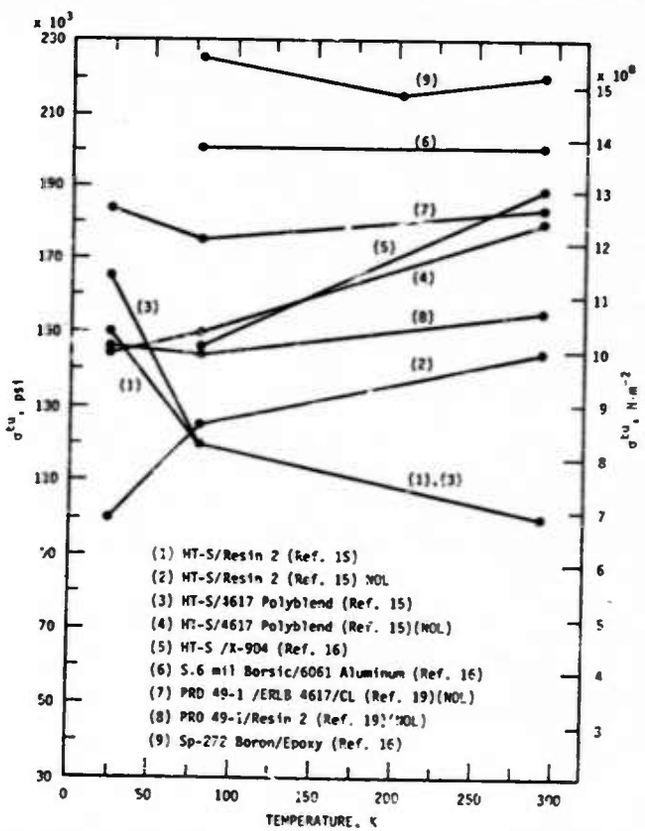

FIG. 7—*Uniaxial longitudinal ultimate tensile strengths, σ^{tu}, of advanced composites at cryogenic temperatures.*

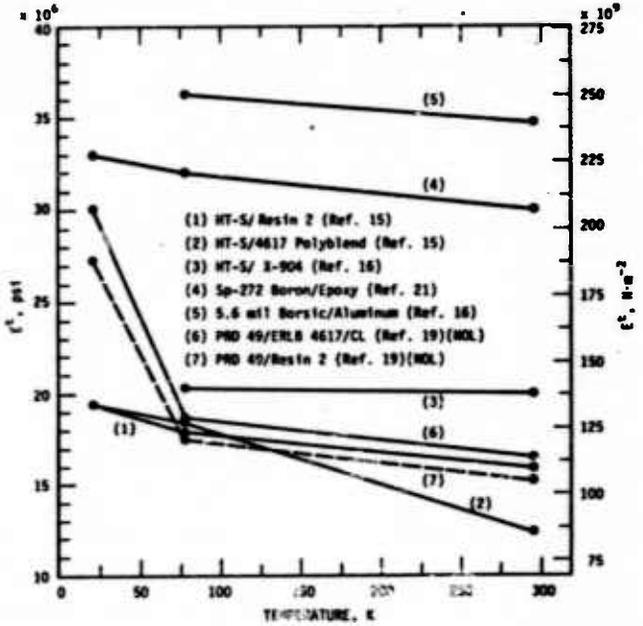

FIG. 8—*Uniaxial longitudinal tensile moduli, E¹, of advanced composites at cryogenic temperatures.*

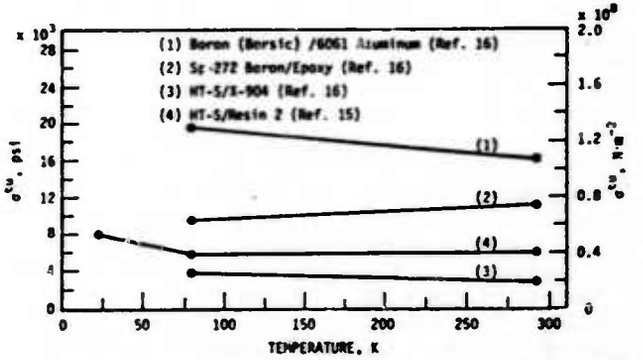

FIG. 9—*Uniaxial transverse ultimate tensile strengths, σ¹ᵘ, of advanced composites at cryogenic temperatures.*

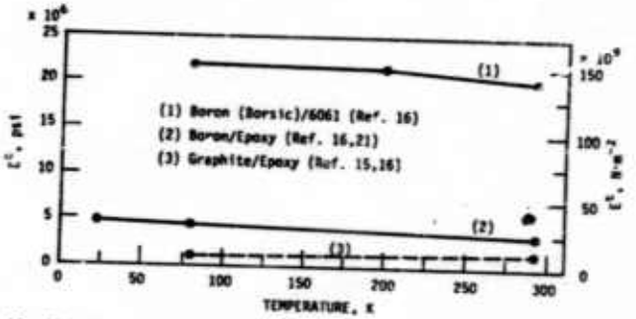

FIG. 10—*Uniaxial transverse tensile moduli, E¹, of advanced composites at cryogenic temperatures.*

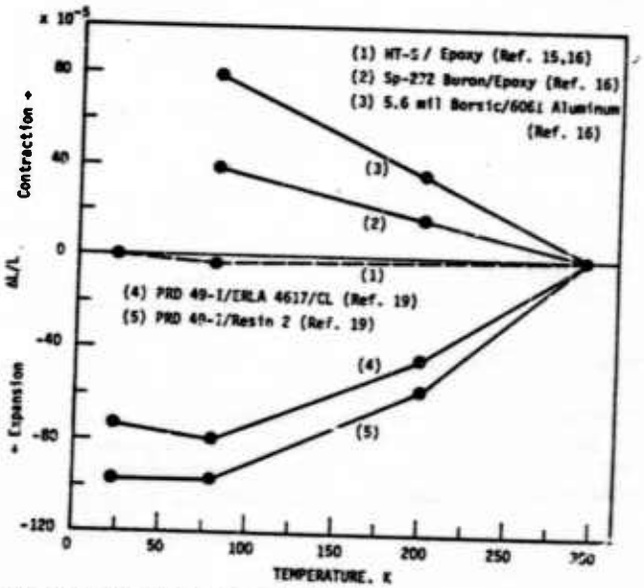

FIG. 11—*Uniaxial longitudinal thermal expansion and contraction, ΔL/L, of advanced composites at cryogenic temperatures.*

223 < 54

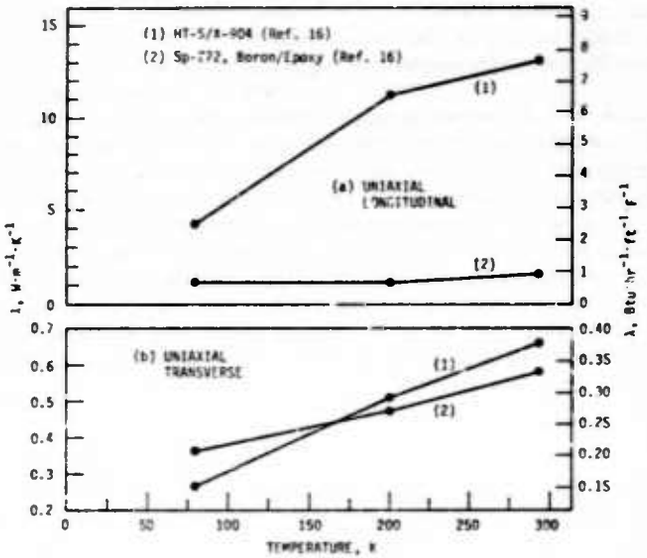

FIG. 12—*Thermal conductivities, λ, of advanced composites at cryogenic temperatures.*

strengths, highest moduli, and undergoing thermal contraction during cooling. Conversely, the CFRP and PRD-49 materials have somewhat lower strengths, considerably lower moduli, and undergo varying degrees of expansion upon cooling.

The strongest of these materials is the boron-epoxy, which develops about 225 ksi at 77 K and for which the tensile strength shows a relatively small temperature dependence. The modulus of this material is also very high, about 32 × 10^6 psi at 77 K, with the modulus appearing to slightly increase on cooling. Boron-epoxy contracts a relatively modest amount in the fiber direction, with the transverse contraction being about half of that in the fiber direction. The data shown on Fig. 7 are for the commercial SP-272 product reinforced with 4.2-mil boron fiber. Nadler et al *[22]* have also evaluated this product as well as an equivalent material, Narmco 5505, reporting strength data very close to that of Hertz. The tensile modulus data plotted in Fig. 8 reflect the work of Nadler, as Hertz did not evaluate this parameter. The 4.2-mil fiber is currently being replaced by 5.6-mil fiber in many applications, as the latter produces a less costly composite with slightly higher tensile properties. The cryogenic properties of the 5.6-mil composites have not been reported.

The uniaxial transverse tensile strength of the BFRP material is lower than

that of boron-aluminum but is higher than that of the CFRP material. The uniaxial transverse modulus is about 5 × 10^6 psi, distinctly lower than the boron-aluminum, but again higher than that of the CFRP material. The thermal conductivity is very low, particularly in the fiber-normal direction, which is an attribute in many cryogenic applications.

The plotted data illustrate the results reported by Hertz for the 5.6-mil boron fiber in its Borsic variant as a reinforcement for 6061 aluminum. Conventional 5.6-mil and 4.2-mil boron-reinforced 6061 alloys were also investigated; however, the ultimate tensile strengths of the latter were reported to be about 20 ksi lower than that for the Borsic reinforcement. Borsic (or boron) reinforced aluminum alloy appears to be an excellent choice for cryogenic applications where the high thermal contraction and high thermal conductivity can be tolerated. Hertz reports an ultimate tensile strength of 200 ksi at 77 K for uniaxial longitudinal Borsic/6061 combined with a very high tensile modulus of about 35 × 10^6 psi. The 20-ksi transverse tensile strength and a transverse tensile modulus in excess of 20 × 10^6 psi at 77 K are also impressive compared with the values for the other types of composites. These properties appear to have very little temperature sensitivity. No data were available on the thermal conductivity of boron-aluminum composites at cryogenic temperatures; however, it is certain to be matrix-dominated and very high.

Hoggatt's data for PRD 49 gives some evidence of why this new fiber is considered important. The present data suggest that the PRD 49/ERLB 4617/CL composite ranks next to the boron-aluminum in strength with a respectable 180 ksi, although the same fiber in a Resin 2 matrix comes in considerably lower at just over 140 ksi. Being NOL ring data, these values may be conservative, as the latter test is not strictly uniaxial. The moduli values of 18 to 19 × 10^6 psi at 77 K do not appear at first to be outstanding; however, they are in the same range as the HT-S CFRP composites, and, furthermore, this value would be compared with the 10 × 10^6 psi maximum modulus available for glass-reinforced composites for which PRD 49 is seen as a substitute. PRD 49 looks even better in modulus at 20 K, if the extremely large increase observed by Hoggatt in his NOL ring tests proves to be a real effect.

The data show PRD 49 composites to have a very high negative coefficient of thermal contraction—much higher than that of the CFRP composites. Normally, this would produce a sufficiently high interfacial strain at cryogenic temperatures to cause significant degrading of the mechanical properties. This does not appear to be the case with PRD 49 fiber.

Finally, a look at the CFRP data for the HT-S fiber in a series of epoxy matrices illustrates some of the problems encountered in attempting to characterize CFRP material for cryogenic use. While Simon and Larsen have shown that HT-S fiber can be put to good practical use in filament-

wound cryogenic vessels, the tensile strength data appearing in Fig. 7 would hardly justify optimism in this respect. As may be seen by comparing Curve 1 with Curve 2 and Curve 3 with Curve 4, the same composites show widely varying strengths and widely varying temperature sensitivities of strength depending on whether the test was conducted on flat uniaxial tension coupons or with NOL rings. This is, at the very least, good evidence of the need for more reliable test methods for use at cryogenic temperatures.

The moduli of the HT-S CFRP composites (all flat uniaxial coupons) show much less scatter and a tendency to converge to about 19 to 20 $\times$ 10^6 psi at the lower temperatures. As regards the uniaxial transverse properties, the strength of the CFRP composites appears to be no more than half that of the BFRP composite at best, while the transverse moduli are extremely low, on the order of 10^6 psi. Curve 3 of Fig. 10 is dashed to indicate an approximate value, the actual data showing a spread from 0.5 to 1.2 $\times$ 10^6 psi at 77 K.

The HT-S fiber composites have a very small negative coefficient of thermal contraction to 77 K. Curve 1 of Fig. 11 is also dashed to indicate approximate values. The slight reversal in contraction indicated below 77 K for this material (seen also in the PRD 49 composite in Curve 4) is apparently a real effect. Finally, from Fig. 12 we observe that the thermal conductivity of the CFRP composites is much higher in the fiber direction than is the case for the BFRP material, reflecting the relatively high thermal conductivity of the graphite itself. This difference largely disappears in the transverse direction.

Summary

Glass-reinforced polymers will continue to be used in cryogenic applications requiring high tensile strength combined with high toughness but where stiffness is not required and where cyclic fatigue is not a major problem. The data reviewed in this paper suggest that, at this time, glass filament-wound with either Resin 2 or the Polaris formulation is satisfactory for cryogenic applications. When considering the use of NASA Resin 2, the reader should be aware that this resin formulation has been optimized for cryogenic service and therefore has relatively poor elevated temperature properties. Care must be taken to properly support components made with this resin whenever elevated temperature vacuum degassing of an assembly is required.

The commercial boron-epoxy and boron-aluminum materials appear to perform very well at cryogenic temperatures and should be among the first materials considered for applications requiring very good strength combined with exceptional stiffness.

The carbon fiber reinforced epoxies seem less advantageous, as their mechanical properties appear to become substantially degraded upon cooling; however, some of this adverse behavior may reflect problems in obtaining valid test data on CFRP materials at cryogenic temperatures, as examples do exist of successful practical applications of CFRP structural materials in the cryogenic range.

The data on the cryogenic properties of composites made with PRD 49 fiber, although not very extensive, suggest that this relatively new material may be superior to carbon fibers for cryogenic use, although the large negative coefficient of thermal contraction may pose problems in some applications. In general, it appears that the epoxy resins most successful with glass-reinforcement are also very suitable for use with the advanced fibers.

This review suggests that the following work would be of value in implementing expanded use of structural composites for demanding cryogenic structural applications such as would be encountered in superconducting machinery:

1. The reason for the erratic mechanical property behavior in polymeric-matrix composites below 77 K must be ascertained. In particular, it is imperative to determine whether or not the type of cryogen in which tests are conducted has a significant effect on the mechanical properties.
2. Material research and evaluation must be directed toward obtaining the type of basic composite cryogenic property data which will be of most value to the design engineer. Contemporary composite theory requires full characterization of a uniaxial lamella of the composite of interest, that is, an experimental determination of the strength and moduli values is required for the prediction of limiting property values in complex crossply layups. Accurate tensile and compression data are required in the longitudinal and transverse modes plus accurate values for intralaminar (in-plane) shear. Even at room temperature, tension and compression testing in the reinforcement direction has proven difficult to perform with acceptable accuracy. Testing problems will be further complicated at cryogenic temperatures; however, these problems must be solved.
3. Having come to terms with the problems posed in (1) and (2), the static mechanical property data for the best of the glass-reinforced composites and of the state-of-the-art commercial boron-epoxy and boron (Borsic)-aluminum materials should be extended down to 4 K. Subsequently, PRD 49/epoxy composites should be evaluated over the entire cryogenic range and another look should be given to the CFRP materials, as the presently available data have an unacceptably large scatter which may well reflect difficulties in the testing procedures rather than inherent scatter in the material itself. All materials must be thoroughly characterized for resin/fiber density, void content, and fiber alignment.
4. Data on the performance of composites under dynamic loading conditions at cryogenic temperatures are minimal to nonexistent. Yet, these

types of data are mandatory if composites are to be used in cryogenic machinery. The available data are encouraging in that they suggest that fatigue performance at cryogenic temperatures is generally superior to that at room temperature. However, this will have to be more fully documented. As high-cycle fatigue testing at 4 K is very expensive, the materials included in such a testing program must be carefully selected. For this purpose, it would be very desirable to have an efficient screening type of test capable of correlating incipient damage with expected fatigue life. Data on thermal fatigue are also required, that is, the effect of repeated cooldowns on both the static and dynamic properties of composites must be determined.

Acknowledgments

The author wishes to thank Dr. R. P. Reed for his consultation and for review of the completed manuscript. This research was supported by the Advanced Research Projects Agency.

References

[1] Brink, N. O., "Determination of the Performance of Plastic Laminates Under Cryogenic Temperatures," ASD-TDR-62-794, (AD 2[illegible] 944), Air Force Systems Command, Wright-Patterson Air Force Base, Ohio, Aug. 1962.

[2] Chamberlain, D. W., Lloyd, B. R., and Tennant, R. L., "Determination of the Performance of Plastic Laminates at Cryogenic Temperatures," ASD-TDR-62-794, Part II, (N64-24212), Air Force Systems Command, Wright-Patterson Air Force Base, Ohio, March 1964.

[3] Toth, L. W., Boller, T. J., Butcher, I. R., Kariotis, A. H., and Yoder, F. D., "Program for the Evaluation of Structural Reinforced Plastic Materials at Cryogenic Temperatures," NASA CR-80061 (Final), (N67-[illegible]951), National Aeronautics and Space Administration, Marshall Space Flight Center, Ala., Aug. 1966.

[4] Seffer, L. M. and Molho, R., "Cryogenic Resins for Glass Filament-Wound Composites," NASA CR-72114 (Final), (N67-25076), National Aeronautics and Space Administration, Lewis Research Center, Cleveland, Ohio, Jan. 1967.

[5] Lewis, A. and Bush, G. E., "Improved Cryogenic Resin-Glass Filament Wound Composites," NASA CR-72163 (Final), (N67-31856), National Aeronautics and Space Administration, Lewis Research Center, Cleveland, Ohio, March 1967.

[6] Kastelic, J. R., Hiltner, A., and Baer, E., *Journal of Macromolecular Science-Physics*, Vol. B7, No. 4, 1973, pp. 679-703.

[7] *Relationships Between Structure and Mechanical Behavior in Polymeric Solids*, ASM Materials Science Seminar, Chicago, Ill., 1973 (to be published by American Society for Metals).

[8] Campbell, M. D., O'Barr, G. L., Haskins, J. F., and Hertz, J., "Thermophysical Properties of Plastic Materials and Composites to Liquid Hydrogen Temperature (−423°F)," ML-TDR-64-33, Part III, (AD 468 155), Air Force Materials Laboratory, Wright-Patterson Air Force Base, Ohio, Aug. 1965.

[9] Haskins, J. F., Campbell, M. C., Hertz, J., Percy, J. L., "Thermophysical Properties of Plastic Materials and Composites to Liquid Hydrogen Temperature (−423°F)," ML-TDR-64-33, Part I, (AD 601 337), Air Force Materials Laboratory, Wright-Patterson Air Force Base, Ohio, June 1964.

[10] Hertz, J., "Investigation of Potential Low Temperature Insulations," General Dynamics/Astronautics Report GS/A-ERR-AN-688, Dec. 1964.

[11] Fontana, M. B., Bishop, S. M. and Spretnak, J. W., "Investigation of Mechanical Properties and Physical Metallurgy of Aircraft Alloys at Very Low Temperatures, Part 5—Mechanical Properties of Metals and a Plastic Laminate at Low Temperatures," AF Technical Report 5662, Part 5, (AD 27726), Air Force Materials Laboratory, Wright-Patterson Air Force Base, Ohio, Dec. 1953.

[12] Lavengood, R. E. and Anderson, R. M., *Technical Papers*, 24th Annual Technical Conference, Society of the Plastics Industry, Section 11-E, 1969, pp. 107.

[13] Simon, R. A. and Alfring, R., "Properties of Graphite Fiber Composites at Cryogenic Temperatures," NASA CR-72642, (AD 746 885), National Aeronautics and Space Administration, Lewis Research Center, Cleveland, Ohio, May 1970.

[14] Larsen, J. V., "Properties of Graphite Fiber Composites at Cryogenic Temperatures—Effect of Elastomeric Additions to Resin Systems," NASA CR-72804, (AD 882 972), National Aeronautics and Space Administration, Lewis Research Center, Cleveland, Ohio, March 1971.

[15] Larsen, J. V. and Simon, R. A., "Carbon Fiber Composites for Cryogenic Filament-Wound Vessels," NASA CR-120889, (N73-11553), National Aeronautics and Space Administration, Lewis Research Center, Cleveland, Ohio, May 1972.

[16] Hertz, J., Christian, J. L., and Varlas, M., "Advanced Composites Applications for for Spacecraft and Missiles, Phase I Final Report, Volume II: Material Development," AFML-TR 71-186, Vol. 2, (AD 893 715L), Air Force Materials Laboratory, Wright Patterson Air Force Base, Ohio, March 1972.

[17] Forest, J. D., Fujimoto, A. F., and Foelsch, G. F., "Advanced Composite Applications for Spacecraft and Missiles, Phase I Final Report, Volume I: Structural Development," AFML-TR 71-186, Vol. 1, Air Force Materials Laboratory, Wright-Patterson Air Force Base, Ohio, March 1972.

[18] Forest, J. D. and Varlas, M., "Advanced Composites Applications for Spacecraft and Missiles, Final Report," AFML-TR 72-278, Air Force Materials Laboratory, Wright-Patterson Air Force Base, Ohio, March 1973.

[19] Hoggatt, J. T., "Development of Cryogenic PRD 49-I Filament-Wound Tanks," NASA CR-120835, (N72-24941), National Aeronautics and Space Administration, Lewis Research Center, Cleveland, Ohio, Dec. 1971 (also in *SAMPE*, Vol. 3, 1971, pp. 157-167).

[20] Chiao, T. T., Hamstead, M. A., Marcon, M. A., and Hanasee, J. E., "Filament-Wound Kevlar 49/Epoxy Pressure Vessels," NASA CR-134506, National Aeronautics and Space Administration, Lewis Research Center, Cleveland, Ohio, Nov. 1973.

[21] Hanson, M. P., "Effects of Temperature and Creep Characteristics of PRD-49 Fiber/Epoxy Composites," NASA TN D-7120, (N73-12607), National Aeronautics and Space Administration, Lewis Research Center, Cleveland, Ohio, Nov. 1972.

[22] Nadler, M. A., Yoshino, S. Y., and Darms, F. J., "Boron/Epoxy Support Strut for Non-Integral Cryogenic Tankage," North American Rockwell Space Division Report SD-68-99501, Feb. 25, 1969 (see also 15th National Symposium, SAMPE, April 1969).

Appendix IV: R. E. Schramm and M. B. Kasen, "Static Tensile Properties of Boron-Aluminum and Boron-Epoxy Composites at Cryogenic Temperatures," Paper T3, Cryogenic Engineering Conference, Kingston, Ontario, July 22-25, 1975 (to be published).

STATIC TENSILE PROPERTIES OF BORON-ALUMINUM AND BORON-EPOXY COMPOSITES AT CRYOGENIC TEMPERATURES

R. E. Schramm and M. B. Kasen

Cryogenics Division
Institute for Basic Standards
National Bureau of Standards
Boulder, Colorado

Paper T-3
Preprinted for the
Cryogenic Engineering Conference
Kingston, Ontario, Canada
July 22-25, 1975

STATIC TENSILE PROPERTIES OF BORON-ALUMINUM AND BORON-EPOXY COMPOSITES AT CRYOGENIC TEMPERATURES*

R. E. Schramm and M. B. Kasen

Cryogenics Division
Institute for Basic Standards
National Bureau of Standards
Boulder, Colorado 80302

ABSTRACT

State-of-the-art boron-aluminum and boron-epoxy composites have been mechanically characterized at 295, 76, and 4 K. Static tensile properties include elastic and shear moduli, Poisson's ratio, yield and ultimate strengths, and elongation. The data are in a form useful in strength or stiffness limiting predictions of complex crossply components using macromechanical composite theory. Both composite types performed well at cryogenic temperatures.

Key Words: Advanced fiber composites; boron-aluminum; boron-epoxy; cryogenics; static mechanical properties.

* This research was supported by the Advanced Research Projects Agency of the Department of Defense under ARPA Order No. 2569; it is a contribution of the National Bureau of Standards, not subject to copyright.

STATIC TENSILE PROPERTIES OF BORON-ALUMINUM AND BORON-EPOXY COMPOSITES AT CRYOGENIC TEMPERATURES

R. E. Schramm and M. B. Kasen

INTRODUCTION

The Advanced Research Projects Agency is currently supporting research to characterize the properties of various structural materials at liquid helium temperature. The objective is to obtain design data for superconducting motors and generators. Fiber-reinforced polymer-matrix composites are included in this program because their low λ/E and λ/σ ratios suggest the possibility of substantial savings in refrigeration cost compared to metal construction. An aluminum-matrix composite is also included because the very high σ/ρ and E/ρ ratios of this electrically-conductive material suggests potential applications in components such as the eddy-current damper shield.

A comprehensive survey [1,2] suggested that the boron-reinforced composites require the least optimization for cryogenic service, as their room temperature mechanical properties are relatively unaffected by cooling to 76 K. We therefore selected boron-epoxy and boron-aluminum composites as the initial materials to be characterized. The static tensile mechanical properties at 295, 76 and 4 K of these materials are reported in this paper.

Macromechanical composite theories use key mechanical properties obtained from tensile, compressive, and shear tests on uniaxial laminates to predict strength and stiffness-limiting properties of complex crossply composites [3,4]. The key properties are the elastic constants, E_{11}, E_{22}, ν_{12}, G_{12}, and the associated strength parameters, σ_{11} and σ_{22}. Some analyses require additional parameters, ε_{11}, ε_{22}, and τ_{12}. This notation refers to the composite axes defined in Fig. 1. A complete characterization requires evaluation of compressive as well as tensile properties.

MATERIALS AND TEST METHODS

Table 1 lists the materials studied in this program. All panels were obtained from commercial sources. Composite void content has not yet been determined; however, radiography failed to reveal any voids. The average ply

thickness was 0.017 cm (0.0067 in) for each material. The composite panels contained nominally 48% by volume 5.6 mil boron fiber. The 6061 aluminum alloy matrix was in the F temper (as diffusion bonded). The epoxy-matrix composite was fabricated from commercial prepreg tape. Uniaxial longitudinal (0°) tensile properties were determined from the 6-ply material, while the 15-ply material was used for evaluation of the uniaxial transverse (90°) tensile properties. The $\pm$ 45° panels were used to evaluate in-plane shear properties. Ideally, shear properties would also be determined directly from uniaxial laminates; however, the required specimens are expensive and require special test fixtures. The $\pm$ 45° tensile coupon method of calculating shear moduli is a simplified test procedure [5,6].

All testing was performed in air (295 K), liquid nitrogen (76 K), or liquid helium (4 K) on a universal testing machine at a strain rate of 0.01 min^{-1} using a tensile cryostat of conventional design [7]. Load cell calibration was confirmed by dead weights. Resistance strain gages, parallel and normal to the stress axis, were mounted on the uniaxial longitudinal and $\pm$ 45° specimens. The uniaxial transverse specimens were gaged only along the tensile axis. Strain values were calculated from manufacturer's gage factors and comparison with signal levels from precision shunt resistors in the commercial bridges. The strain gages failed at about 1% strain at cryogenic temperatures; however, larger strains were measured from crosshead displacement (corrected for load train strain) and from displacement of gage marks lightly scribed on the boron-aluminum specimens. Load and strain were recorded simultaneously with a two-pen recorder.

Test specimens were straight-sided coupons, 2.5 cm (1 in) wide for transverse and $\pm$ 45° orientations, and 1.3 cm (0.5 in) wide for the longitudinal fiber orientation. The boron-aluminum specimens were 15 cm (6 in) long with a 5 cm (2 in) gage length between grips; the boron-epoxy specimens were 28 cm (11 in) long with a 15 cm (6 in) gage length. Specimens were cut with a diamond saw. Before testing, the edges were lightly buffed with emery paper.

Grips were attached to the specimens in an alignment fixture. Specimen ends, wrapped with 100 mesh stainless steel screen, were sandwiched between serrated titanium plates attached to the load train by pins and clevises. Heavy

stainless steel pressure plates, each containing six pairs of screws, backed the titanium plates and provided compressive force on the grip. The torque on the screws was systematically increased toward the outer end of the grip to uniformly transfer the tensile load into the composite specimen. When finally assembled in the cryostat, the specimen alignment was within the limits prescribed in ASTM specification D 3039-71T [8].

The boron-epoxy specimens were conditioned for at least two days in 45 - 55% relative humidity at room temperature before testing. The boron-aluminum did not require preconditioning. At least three specimens were tested for each material, orientation, and temperature. The boron-epoxy was initially cycled three times within the elastic region (to about 25% of the tensile strength) to establish the repeatability of the modulus, before increasing the load to initiate fracture. The boron-aluminum was not cycled because of the low yield strength of the aluminum matrix.

Tensile fractures in composite materials commonly occur at the specimen grips, where a stress concentration inevitably exists. The gripping system described here reduced the frequency of grip failures to about 20%. Tensile strength data from specimens which failed close to the grips (within one specimen thickness) were rejected, even though there was no clear evidence that such failures affected the strength.

In-plane shear properties were calculated from analyses of the tensile stress-strain curves of the $\pm$ 45° specimens [5,6]. Poisson's ratio for the transverse specimens, ν_{21}, was calculated from the reciprocity relation [5]:

$$\nu_{21} = \nu_{12} \frac{E_{22}}{E_{11}}$$

where E_{22} is from uniaxial transverse specimens and ν_{12} and E_{11} is from uniaxial longitudinal tests.

RESULTS AND DISCUSSION

The static tensile properties and elastic constants for the boron-aluminum and boron-epoxy composites are presented in Table 2 and 3. In-plane shear moduli appear in Table 4. In accord with ASTM D 3039-71T, the number of specimens, standard deviation, and coefficient of variation (standard deviation

expressed as a percentage of the average value) are included. For only three or four tests, the calculated standard deviation is nearly equal to the data spread. Figures 2 and 3 illustrate the temperature dependence of the elastic moduli and tensile strengths of both composites.

Stress-strain curves for the uniaxial longitudinal test mode were essentially linear to fracture for both materials at all test temperatures. The uniaxial transverse boron-epoxy also failed with negligible yielding at 76 K and 4 K; however, some plastic deformation was observed at 295 K. All $\pm$ 45° and the boron-aluminum uniaxial transverse specimens yielded significantly prior to fracture at all test temperatures. The boron-aluminum uniaxial transverse and $\pm$ 45° specimens displayed discontinuous yielding at 295 and 4 K, but not at 76 K.

Cryogenic temperatures had relatively little effect on the measured mechanical properties. At 76 K, the averaged data indicate a minimum in the elastic modulus of boron-aluminum for the transverse and $\pm$ 45° orientations, as well as a decrease in the calculated in-plane shear modulus. However, the data scatter was such that this could be a statistical effect, rather than a true temperature effect. Significant temperature effects were noted in the orientations where the matrix contributes to the properties. Thus, the proportional limit of the $\pm$ 45° boron-aluminum slightly increased on cooling, while that of the boron-epoxy declined. Also, the elongation of the $\pm$ 45° boron-aluminum decreased sharply on cooling, while there was a relatively small change for boron-epoxy.

The aluminum-matrix composite exhibited less anisotropy than the epoxy-matrix composite, reflecting the higher strength and greater ductility of the aluminum. The boron-aluminum has a transverse modulus approximately 75% of that in the longitudinal direction, and about twice as high as that of the unreinforced 6061 aluminum alloy.

The in-plane shear modulus values calculated for the boron-epoxy appear to be in reasonable agreement with published room-temperature values [9]. However, the shear moduli calculated for the boron-aluminum are inordinately low. It has been shown that shear moduli calculated from analyses of $\pm$ 45° tensile stress-strain curves agree with moduli determined by more rigorous methods in

the case of graphite-epoxy and glass-epoxy composites [6]. However, Ramsey, Waszczak, and Klouman [10] report that the nonlinear stress-strain response of 5.6 mil boron-6061 aluminum in the F condition may invalidate the simplified $\pm$ 45° test method used here and lead to low shear moduli calculations for this material. The boron-aluminum values here serve only as lower boundaries and display the limits of this method.

ACKNOWLEDGMENT

The authors wish to thank Dr. Ralph Tobler of this laboratory for his careful reading of this manuscript.

NOTATION

E = Engineering Elastic Modulus

G = Engineering shear modulus

ε = Engineering strain

λ = Thermal conductivity

ν = Poisson's ratio

ρ = Mass density

σ = Engineering stress

τ = In-plane shear stress

REFERENCES

1. M. B. Kasen, "Properties of Filamentary-Reinforced Composites at Cryogenic Temperatures," to be published in ASTM STP 580, Composite Reliability.

2. M. B. Kasen, Cryogenics, 15(6): 327 (1975). (Also "Part II: Advanced Composites" to be published in Cryogenics).

3. Advanced Composites Design Guide, Third Edition, Volume II, Analysis, Air Force Materials Laboratory, Wright-Patterson Air Force Base, Ohio (1973).

4. M. E. Waddoups, in: Composite Materials Workshop, S. W. Tsai, J. C. Halpin, and N. J. Pagano, Eds., Technomic Publishing Co., Inc., Stanford, Ct. (1968), p. 254.

5. P. H. Pettit, in: ASTM STP 460, Composite Materials, Testing and Design, American Society for Testing and Materials, Philadelphia (1969), p. 83.

6. D. F. Sims and J. C. Halpin, in: ASTM STP 546, Composite Materials, Testing and Design, American Society for Testing and Materials, Philadelphia (1974), p. 46.

7. R. P. Reed and R. L. Durcholz, in: Advances in Cryogenic Engineering, Vol. 15, Plenum Press, New York (1970), p. 109.

8. 1973 Annual Book of ASTM Standards, Part 25, American Society for Testing and Materials, Philadelphia (1973), p. 608.

9. Advanced Composite Design Guide, Third Edition, Volume IV, Materials, Air Force Materials Laboratory, Wright-Patterson Air Force Base, Ohio (1973).

10. J. E. Ramsey, J. P. Waszczak, and F. L. Klouman, "An Investigation of the Non-Linear Response of Metal-Matrix Composite Laminates," AIAA/ASME/SAE 16th Structures, Structural Dynamics and Materials Conference, Denver, Colorado (May 27, 1974).

LIST OF TABLES

LIST OF FIGURES

Table 1. 5.6-mil Boron-Epoxy and Boron-Aluminum Composites.

Fiber Orientation	Number of Plies
Uniaxial	6
Uniaxial	15
± 45°	10

Table 2

Tensile Properties of Boron-Aluminum Composites

(Averages of Specimens Tested[a])

Temperature (K)	Elastic Modulus, E (10^9 N/m^2)	(10^6 psi)	CV(%)	Poisson's Ratio, ν	CV(%)	Proportional Limit, σ^{pl} (10^8 N/m^2)	(10^3 psi)	CV(%)	0.2% Yield Strength, σ^{ty} (10^8 N/m^2)	(10^3 psi)	CV(%)	Number of Specimens
					Longitudinal (0°)							
295	200(11)	29.0(1.6)	5.7	0.299(0.024)	8.2							4
76	197(11)	28.5(1.6)	5.6	0.341(0.009)	1.6							4
4	204(9)	29.6(1.3)	4.3	0.344(0.022)	6.3							4
					Transverse (90°)							
295	161(18)	23.4(2.6)	11.0	0.241(0.027)	11.2[b]	0.63(0.08)	9.1(1.1)	11.9	1.34(0.05)	19.4(0.7)	3.6	3
76	128(24)	18.5(3.5)	18.7	0.221(0.041)	18.6[b]	0.76(0.11)	11.0(1.6)	15.1	1.78(0.14)	25.9(2.0)	7.8	4
4	150(31)	21.8(4.6)	20.8	0.253(0.053)	20.8[b]	0.72(0.19)	10.5(2.8)	26.3	1.96(0.09)	28.5(1.3)	4.6	3
					Crossply (± 45°)							
295	111(10)	16.0(1.4)	9.0	0.396(0.021)	5.3	0.37(0.27)	5.4(4.0)	73.0	0.94(0.06)	13.6(0.9)	6.2	3
76	78(19)	11.3(2.8)	24.8	0.333(0.025)	7.5	0.15(0.06)	2.1(0.8)	40.7	1.35(0.23)	19.5(3.3)	16.9	3
4	101(15)	14.7(2.2)	14.9	0.373(0.033)	9.2	0.31(0.16)	4.4(2.2)	50.1	1.34(0.12)	19.4(1.7)	8.8	3

Temperature (K)	Ultimate Strength, σ^{tu} (10^8 N/m^2)	(10^3 psi)	CV(%)	Ultimate Elongation, ϵ^{tu} (%)	CV(%)	Number of Specimens
			Longitudinal (0°)			
295	12.7	184	-	0.6	-	1
76	16.4(0.6)	238(8)	3.4	0.8(0.0)	3.1	3
4	16.1(0.9)	233(12)	5.3	0.8(0.1)	7.7	4
			Transverse (90°)			
295	1.67(0.18)	24.2(2.7)	10.9	0.7(0.1)	14.3	3
76	2.49(0.08)	36.1(1.1)	3.1	0.8(0.1)	7.2	3
4	2.76(0.03)	40.0(0.5)	1.1	0.9(0.1)	6.4	3
			Crossply (± 45°)			
295	3.62(0.30)	52.5(4.4)	8.3	12.1(1.5)	12.4	3
76	4.14(0.49)	60.0(7.1)	11.8	6.7(2.1)	31.3	3
4	4.11(0.12)	59.7(1.8)	3.0	4.2(1.0)	23.8	3

[a] Standard deviations are in parentheses. CV is coefficient of variation. Data from the specimens that broke at or in the grips are not included in the calculations of ultimate strength or elongation.

[b] Computed from ν_{12}, E_{11}, and E_{22}.

Table 3

Tensile Properties of Boron-Epoxy Composites

(Averages of Specimens Tested[a])

Temperature (K)	Elastic Modulus, E (10^9 N/m^2)	(10^6 psi)	CV(%)	Poisson's Ratio, ν	CV(%)	Proportional Limit, σ^{pl} (10^8 N/m^2)	(10^3 psi)	CV(%)	0.2% Yield Strength, σ^{ty} (10^8 N/m^2)	(10^3 psi)	CV(%)	Number of Specimens
					Longitudinal (0°)							
295	231(4)	33.5(0.6)	1.6	0.228(0.019)	8.3							5
76	233(5)	33.9(0.7)	2.1	0.241(0.012)	4.8							5
4	238(6)	34.5(0.6)	2.3	0.239(0.014)	5.9							5
					Transverse (90°)							
295	17.5(0.9)	2.54(0.12)	5.0	0.017(0.001)	6.1[b]	0.344(0.071)	4.99(1.02)	20.7				6
76	31.2(2.4)	4.53(0.34)	7.5	0.033(0.002)	7.3[b]							4
4	35.8(2.3)	5.19(0.32)	6.3	0.034(0.003)	7.8[b]							3
					Crossply (± 45°)							
295	18.1(1.1)	2.62(0.17)	6.3	0.817(0.034)	4.1	0.406(0.013)	5.89(0.19)	3.3	0.956(0.016)	13.9(0.3)	1.8	3
76	32.7(0.7)	4.72(0.13)	2.8	0.671(0.050)	7.4	0.411(0.020)	5.96(0.29)	4.9	0.951(0.038)	13.8(0.5)	3.9	3
4	33.3(1.9)	4.83(0.28)	5.8	0.700(0.051)	7.2	0.296(0.028)	4.29(0.40)	9.3	0.830(0.016)	12.0(0.2)	1.9	3

Temperature (K)	Ultimate Strength, σ^{tu} (10^8 N/m^2)	(10^3 psi)	CV(%)	Ultimate Elongation, ε^{tu} (%)	CV(%)	Number of Specimens
		Longitudinal (0°)				
295	16.3(0.6)	237(8)	3.3	0.73(0.04)	5.1	3
76	16.8(0.9)	243(13)	5.4	0.77(0.07)	9.3	3
4	18.2(0.4)	263(6)	2.2	0.76(0.01)	1.5	3
		Transverse (90°)				
295	0.470(0.035)	6.81(0.51)	7.4	0.27(0.06)	21.7	3
76	0.490(0.033)	7.09(0.47)	6.7	0.15(0.03)	17.6	3
4	0.414(0.096)	6.01(1.39)	23.1	0.12(0.04)	33.6	3
		Crossply (± 45°)				
295	1.30(0.02)	18.8(0.3)	1.4	1.88(0.14)	7.5	3
76	1.11(0.02)	16.1(0.3)	1.7	0.85(0.05)	5.3	3
4	1.01(0.03)	14.7(0.4)	2.8	0.83(0.05)	6.3	3

[a]Standard deviations are in parentheses. CV is coefficient of variation. Data from the specimens that broke at or in the grips are not included in the calculations of ultimate strength or elongation.

[b]Computed from ν_{12}, E_{11}, and E_{22}.

Table 4. In-Plane Shear Modulus[a]
(Averages of Specimens Tested)

Temperature	Shear Modulus, G_{12} 10^9 N/m^2	10^6 psi	CV(%)
	Boron-Aluminum[b]		
295	39.7(4.0)	5.75(0.58)	10.0
76	27.0(5.5)	3.92(0.80)	20.4
4	32.6(5.5)	4.73(0.80)	16.9
	Boron-Epoxy		
295	4.72(0.44)	0.684(0.064)	9.3
76	9.19(0.38)	1.33(0.06)	4.1
4	9.28(0.19)	1.35(0.03)	2.0

[a]These values are calculated from cross-ply (± 45°) data using the method of Sims and Halpin [6]. Standard deviations are in parenthesis; CV is the coefficient of variation.

[b]The boron-aluminum moduli are only lower limits to the true values.

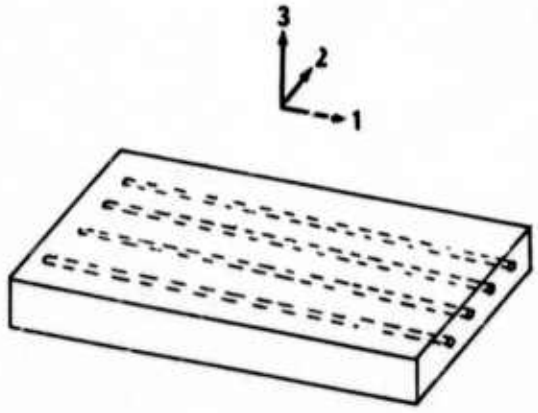

Fig. 1. Identification of composite axes.

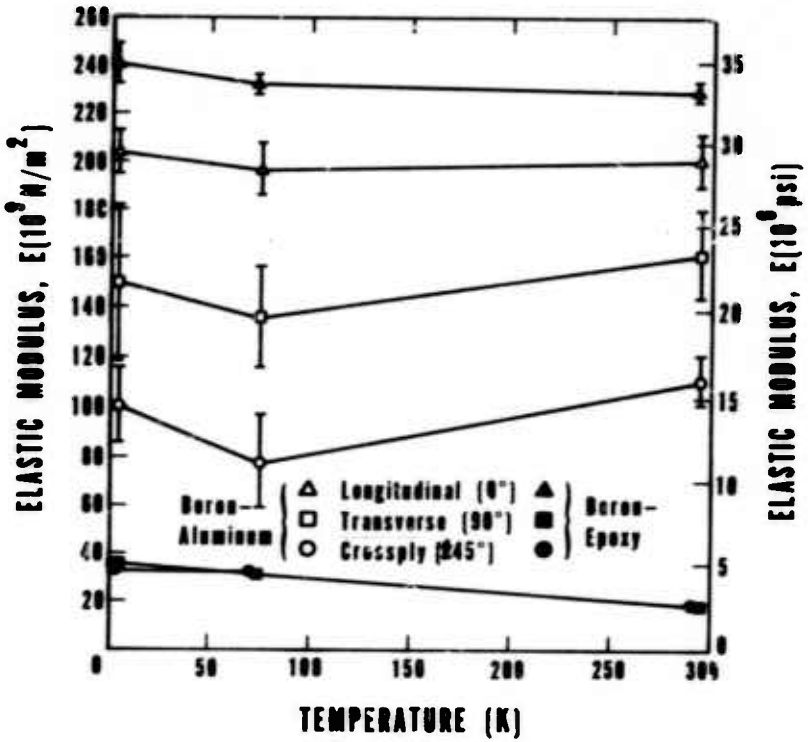

Figure 2. Temperature dependence of the elastic modulus of boron-epoxy and boron-aluminum of various orientations. Error bars reflect ± one standard deviation; in several instances, the error bars are smaller than the datum symbol.

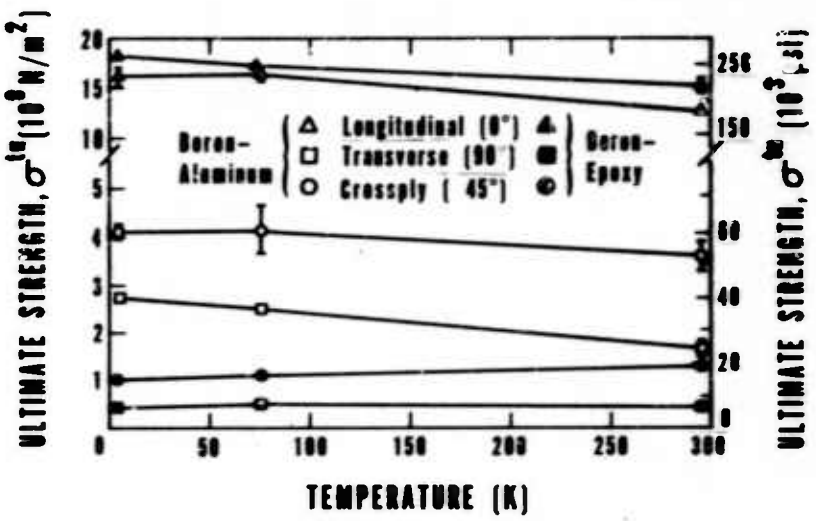

Figure 3. Temperature dependence of the ultimate tensile strength of boron-epoxy and boron-aluminum of various orientations. Error bars reflect ± one standard deviation; in several instances, the error bars are smaller than the datum symbol.

NBSIR

SEMI-ANNUAL REPORT ON MATERIALS RESEARCH IN SUPPORT OF SUPERCONDUCTING MACHINERY

ELASTIC PROPERTIES OF ENGINEERING MATERIALS AT CRYOGENIC TEMPERATURES

H. M. Ledbetter, E. R. Naimon, and W. F. Weston

Cryogenics Division
Institute for Basic Standards
National Bureau of Standards
Boulder, Colorado 80302

October 1975

Summary: Elastic Properties

During the six months preceding October, 1975, the following studies were completed:

(1) Oxygen-free copper. Room-temperature elastic constants of this material were determined by a pulse-echo method. Low-temperature Young's and shear moduli were determined by a resonance method. Results of this study are included in the accompanying manuscript describing copper-nickel alloys (See p. 73).

(2) Copper-nickel alloys. Two alloys, Cu-10 Ni and Cu-30 Ni, were studied as described above for copper. Also, the longitudinal modulus of Cu-30 Ni was determined by a pulse-echo method at low temperatures. Advantages of combining resonance and pulse-echo data for these materials are described along with results in the accompanying manuscript "Low-temperature elastic properties of some copper-nickel alloys" by H. M. Ledbetter and W. F. Weston. This study was presented at the 1975 IEEE Ultrasonics Symposium in Los Angeles, and it will be published in the proceedings of that symposium (see p. 73).

(3) Copper alloy PD135. This material, supplied and characterized by J. M. Wells of Westinghouse, was studied at room temperature by a pulse-echo method to determine its elastic constants. They are surprisingly different from those of unalloyed copper, and they are described in an accompanying manuscript "Elastic properties of a copper-cadmium-chromium precipitation-hardened alloy" by H. M. Ledbetter (See p. 77).

(4) Invar. Low-temperature elastic properties of an iron 36 nickel invar-type alloy were determined by both resonance and pulse-echo methods. This study is described in an accompanying manuscript "Low-temperature elastic properties of invar" by H. M. Ledbetter, E. R. Naimon, and W. F. Weston. This study was presented at the 1975 ICMC-CEC in Kingston, Ontario, and it will be published in the proceedings of that conference (See p. 81).

(5) Nickel-chromium-iron-alloys (Inconels). There is an accompanying reprint "Dynamic low-temperature elastic properties of two austenitic nickel-chromium-iron alloys," Mater. Sci. Engg. 20 (1975) 185-94 (See p. 95).

(6) Austenitic stainless steels. There is an accompanying reprint "Low-temperature elastic properties of four asutenitic stainless steels," J. Appl. Phys. 46 (1975) 3855-60 (See p. 105).

LOW-TEMPERATURE ELASTIC PROPERTIES OF SOME COPPER-NICKEL ALLOYS*

H. M. Ledbetter and W. F. Weston†
Cryogenics Division, National Bureau of Standards
Boulder, Colorado 80302

ABSTRACT. The polycrystalline elastic properties of Cu, Cu-10 Ni, and Cu-30 Ni were determined between room temperature and liquid-helium temperature using both pulse-echo (10 MHz) and resonance (60 kHz) methods. The temperature dependence of all three materials is regular. The composition dependence of the elastic constants is reviewed and new composition dependences are proposed.

INTRODUCTION

The study reported here was undertaken to elucidate the composition dependence and, especially, the temperature dependence of the elastic properties of copper-nickel alloys. Despite many previous studies, these properties are not known satisfactorily.

Copper-nickel alloys are well known for their resistances to corrosion and to stress-corrosion cracking. They are used in condensers and in heat exchangers. Recently, these alloys have become candidates for applications in superconducting machinery[1]. The elastic properties (Young's modulus, shear modulus, etc.) of these alloys have been studied extensively at room temperature, and one high-temperature elastic-property study has been reported. At cryogenic temperatures only the Young's modulus has been studied, and only at liquid-nitrogen and liquid-hellum temperatures. The complete set of polycrystalline elastic properties is reported here for Cu, Cu-10 Ni, and Cu-30 Ni semi-continuously between room temperature and liquid-helium temperature. The elastic constants are essential engineering design parameters, and they are related simply to interatomic forces. Copper-nickel alloys are especially interesting elastically because nickel increases copper's elastic stiffness, contrary to usual alloying effects.

Materials

Materials were obtained from commercial sources in the form of 1.9-cm (3/4-in) rods. Their chemical analyses by weight are: 9.98 Ni, 1.16 Fe, 0.07 Zn, 0.02 Pb for the Cu-10 alloy; 30.05 Ni, 0.72 Mn, 0.59 Fe, 0.04 Zn, <0.01 Pb, <0.01 Sn, <0.01 Al, <0.01 As. The copper was an oxygen-free high-conductivity grade. Their physical and metallurgical characterizations are given in Table I.

Table I. Physical and metallurgical characterization of the materials studied

	Cu	Cu-10 Ni	Cu-30 Ni
Mass density (g/cm^3)	8.952	8.303	8.914
Hardness (DPH No., 1 kg load)	45	87	124
Average grain size (mm) by linear intercept method	1.0	0.05	0.03
Condition	Cold drawn 60%, annealed	Annealed 677°C, 40 min	Commercially annealed

Experimental

Two methods, resonance (60 kHz) and pulse-echo (10 MHz), were used to determine sound velocities in the alloys. Both methods were described previously[2,3]. Low-temperature pulse-echo data were determined by a superposition method. The resonance specimens were right circular cylinders 0.48 cm (3/16 in) in diameter and about 3 cm and 2 cm long for the longitudinal and transverse cases, respectively. The pulse-echo specimens were 1 cm cubes. Temperatures were monitored with chromel-constantan thermocouples.

The problem of the effect of texture on the elastic constants was studied by measuring the sound velocities both parallel and perpendicular to the rolling axis and also measuring the shear-wave birefringence for the latter case. The shear and longitudinal wave velocities were found to vary with direction by an average of 0.6 and 0.3 percent, respectively. The birefringence in the shear velocity was found to have a maximum value of 1.5 percent. Thus, the specimens had negligible texture, and the velocities were simply averaged over direction.

Results

Some of the low-temperature elastic constants are shown in Figs. 1-3, and room-temperature values are given in Table II. Young's modulus E was determined by a resonance method, the shear modulus G by resonance (shown in Fig. 2) and by pulse method, and C_ℓ by pulse method.

Table II. Elastic constants of Cu-Ni alloys at room temperature, units of 10^{11} N/m^2 except ν (dimensionless)

	C_ℓ	B	E	G	ν
Cu	2.013	1.376	1.286	0.478	0.345
Cu-10Ni	2.092	1.424	1.345	0.501	0.343
Cu-30Ni	2.250	1.517	1.472	0.550	0.339

While there are only two independent elastic constants for an isotropic material, several are useful for various applications. Besides E, G, and C_ℓ already mentioned, the bulk modulus B (reciprocal compressibility) and Poisson's ratio ν are often required. Relationships among these elastic constants and their relationship to the sound velocities are well known:

$$G = \rho v_t^2, \tag{1}$$

$$C_\ell = \rho v_\ell^2, \tag{2}$$

$$B = C_\ell - \frac{4}{3} G, \tag{3}$$

$$E = \frac{9BG}{3B + G}, \tag{4}$$

and

$$\nu = \frac{E}{2G} - 1. \tag{5}$$

Since three elastic constants were measured -- E, G, and C_ℓ -- the problem is, in principle, overdetermined. However, as can be inferred from Table III, this is effectively not the case. It is to be recalled that in a pulse-echo experiment v_ℓ and v_t are measured with typical errors of ± 1/2 percent. In a resonance experiment, E and G are measured with typical errors of ± 1 percent.

* Contribution of NBS, not subject to copyright.
† Present address: Rocky Flats Plant Rockwell International, Golden, Colorado, 80401.

Table III. Maximum percent propagation errors involved in elastic-constant determinations, assuming $\nu = 1/3$. Boxed parameters are those measured, others are calculated.

	v_ℓ	v_t	C_ℓ	E	G	ν	B
Pulse-echo	1/2	1/2	1	1	1	2/3	1
Resonance	5-1/2	1/2	11	1	1	8	17

Thus, when E and G are determined (as in a resonance experiment), derived values of C_ℓ, ν, and B are quite inaccurate compared to pulse-echo results. Usual resonance methods are useful for determining E and G, but much less useful for determining the other elastic constants. The superiority of the pulse-echo method is apparent. However, in many cases, including copper-nickel alloys longitudinal ultrasonic velocities can be determined accurately while transverse ultrasonic velocities cannot, because of higher attenuation. Thus, it becomes advantageous to combine pulse-echo data (C_ℓ) with resonance data (E or G). In the present work, it was found that the resonance value of E was slightly more accurate than the resonance value of G. Thus, the C_ℓ (pulse-echo) - E (resonance) pair is the best choice. Then it is necessary to solve a quadratic equation for G:

$$G = \frac{(E + 3C_\ell) - [(E + 3C_\ell)^2 - 16EC_\ell]^{1/2}}{8}, \qquad (6)$$

discarding the non-physical root.

The data in Figs 1-3 were fitted to a theoretical relationship suggested by Varshni[4]:

$$C = C^o - \frac{s}{e^{t/T} - 1} \qquad (7)$$

where C^o, s, and t are adjustable parameters, and T is the temperature.

The composition dependence of the elastic constants is shown in Figs 4-9, where the present results are compared with results of sixteen previous studies.[5-20] Two of these previous studies were made on single crystals rather than on polycrystalline aggregates. These single-crystal results were averaged by a Voigt-Reuss-Hill method.[21] The lines in Figs 4-8 are linear least-squares fits to the averaged single-crystal results and to the present results.

Temperature coefficients of the elastic constants are given in Table IV.

Table IV. Temperature derivatives of elastic constants at room temperature ($10^{-4}K^{-1}$)

Alloy	$\frac{1}{B}\frac{dB}{dT}$	$\frac{1}{E}\frac{dE}{dT}$	$\frac{1}{G}\frac{dG}{dT}$	$\frac{1}{\nu}\frac{d\nu}{dT}$
Cu	-1.64	-3.64	-4.01	4.65
Cu-10Ni	--	-3.78	-3.61	--
Cu-30Ni	-1.29	-2.30	-3.20	8.22

Discussion and Conclusions

1. The low-temperature elastic properties of Cu-Ni alloys resemble those of copper, except for scaling factors. Like Cu, their behavior is quite regular--monotonically decreasing, linear at high temperature, lower slope at lower temperatures, and zero slope at zero temperature.

2. The composition dependence of the elastic constants is approximately linear over the composition range studied. The Young's-modulus/composition curve goes through the value for copper (1.27×10^{11} N/m^2) and not through the fictitious value of E for Cu (1.30×10^{11} N/m^2), as suggested by Köster.[22] The parameters proposed here for the change of E and G with composition ($\Delta C/\Delta x = 0.690$ and 0.259, respectively, where C denotes elastic constant and x denotes atomic fraction) differ from those proposed by Subrahmanyan[20] (0.798 and 0.319, respectively).

3. In some cases, there is considerable advantage in studying elastic properties of solids by both pulse and resonance methods. In the present case, the specimens transmitted longitudinal waves thus permitting the determination of C_ℓ. But they damped shear waves, precluding determination of G by a pulse method. G, or alternatively E, could be determined by a resonance method. The C_ℓ-E data gave better values of B and ν than could be obtained from resonance experiments alone.

Acknowledgment

This work was supported by the Advanced Research Projects Agency of the U.S. Department of Defense.

References

1. Handbook on Materials for Superconducting Machinery, Battelle Metals and Ceramics Information Center, Columbus, Ohio, 1974.

2. E. R. Nalmon, W. F. Weston and H. M. Ledbetter, Cryogenics 14 (1974) 246-9.

3. W. F. Weston, J. Appl. Phys., forthcoming.

4. Y. P. Varshni, Phys. Rev. B 2 (1970) 3952-8.

5. E. Grüneisen, Ann. Phys. Leipz. [IV] 22 (1907) 801.

6. Z. Nishiyama, Sci. Rep. Tohoku Univ. Sendai 18 (1929) 359-400.

7. S. Aoyama and T. Fukuroi, Bull. Sci. Res. Inst. Tokyo 20 (1941) 809-11. In Japanese.

8. H. Masumoto and H. Saito, Nippon Kingoku Gakkai-Shi 8 (1944) 49-55. In Japanese.

9. T. Fukuroi and Y. Shibuya, Sci. Rep. Tohoku Univ. A 2 (1950) 748.

10. W. F. Simmons, B. J. Sirois, D. N. Williams and R. I. Jaffee, ASTM Proc. 59 (1959) 1035-45.

11. R. E. Schmunk and C. S. Smith, Acta Metall. 8 (1960) 396-401.

12. B. Subrahmanyam and Bh. Krishramurty, Indian J. Pure Appl. Phys. 1 (1963) 185-7.

13. J. B. Greer and E. H. Bucknall, Trans. ASM 57 (1964) 555-60.

14. A. F. Orlov and S. G. Fedotov, Fiz. Metal. Metalloved. 22 (1966) 137-8.

15. R. P. Reed and R. P. Mikesell, J. Mater. ASTM 2 (1967) 370-92.

16. G. Faninger, Z. Metallk. 60 (1969) 601-5.

17. K. Salama and G. A. Alers, IEEE Trans. Sonics Ultrasonics (Jan. 1969) 28. Abstract.

18. L. M. T. Hopkin, H. Pursey and M. F. Markham, Z. Metallk. 61 (1970) 535-40.

19. H. Masumoto, H. Saito and S. Sawaya, Trans. Japan Inst. Met. 11 (1970) 88-90.

20. B. Subrahmanyam, Mater. Sci. Eng. 15 (1974) 177-9.

21. R. Hill, Proc. Phys. Soc. Lond. A65 (1952) 349-54.

22. W. Köster, Mater. Sci. Eng. 18 (1975) 289.

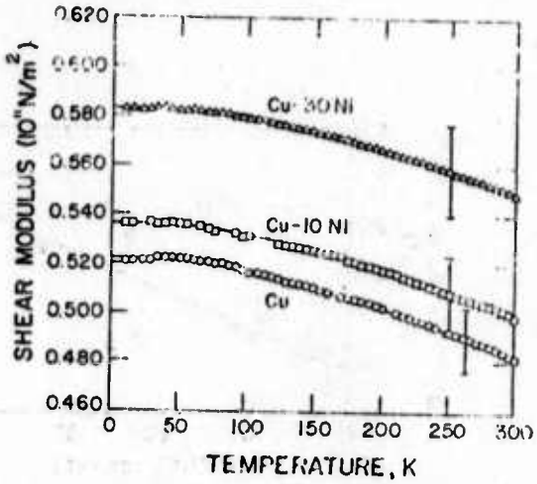

Fig. 2. Shear modulus of some Cu-Ni alloys versus temperature. Resonance results.

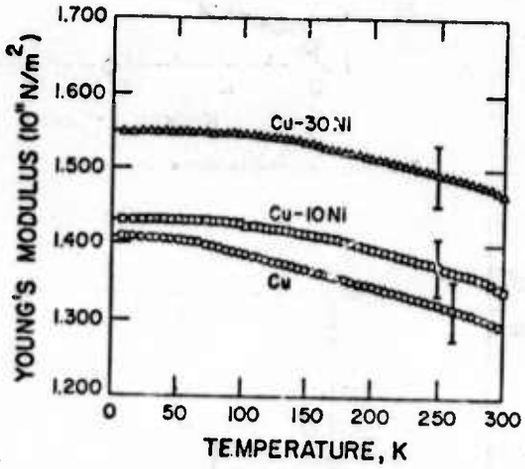

Fig. 1. Young's modulus of some Cu-Ni alloys versus temperature. Error bars are $\pm 2\sigma$ where σ is the standard deviation of nine measurements, and they reflect both experimental errors and material variability; 2σ represents, approximately, the 95% confidence interval. Resonance results.

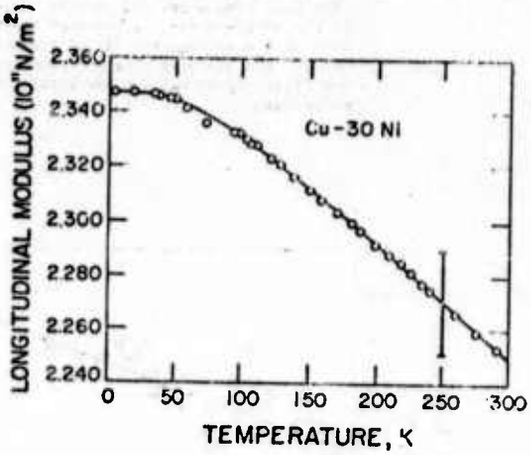

Fig. 3. Longitudinal modulus versus temperature for a Cu-30 Ni alloy. Pulse-echo results.

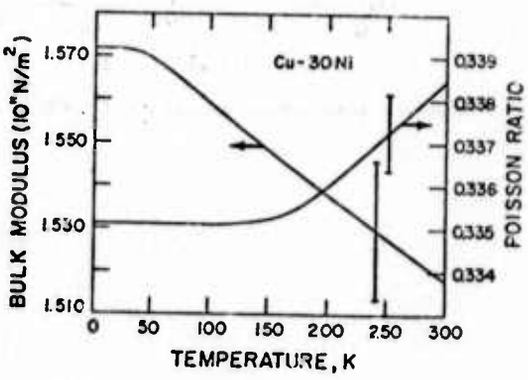

Fig. 4. Bulk modulus and Poisson ratio of Cu-30 Ni, calculated from C_ℓ (pulse-echo) and G (resonance).

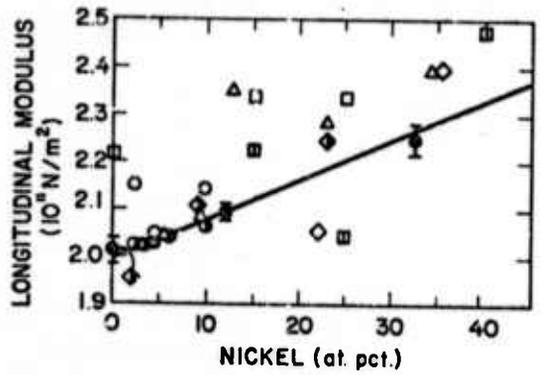

Fig. 5. Compositional variation of C_L for Cu-Ni alloys. Half-filled diamonds and circles represent single-crystal results averaged by the Voigt-Reuss-Hill arithmetic method. Line is a least-squares fit of present results and averaged single-crystal results. See first figure caption for meaning of error bars.

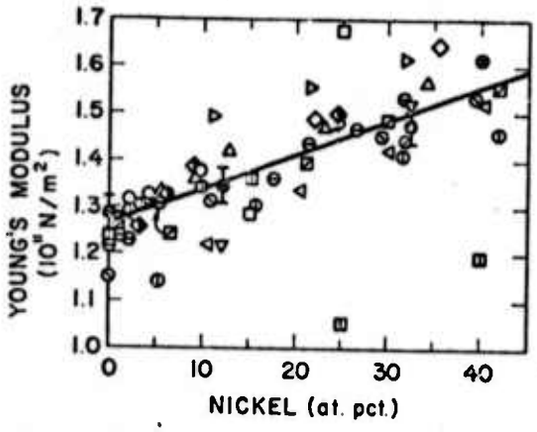

Fig. 6. Compositional variation of E for Cu-Ni alloys.

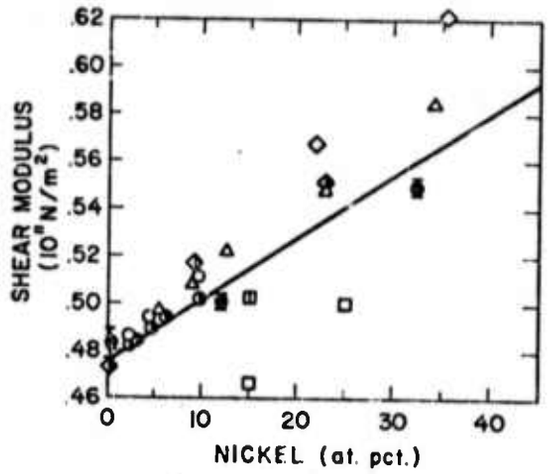

Fig. 7. Compositional variation of G for Cu-Ni alloy.

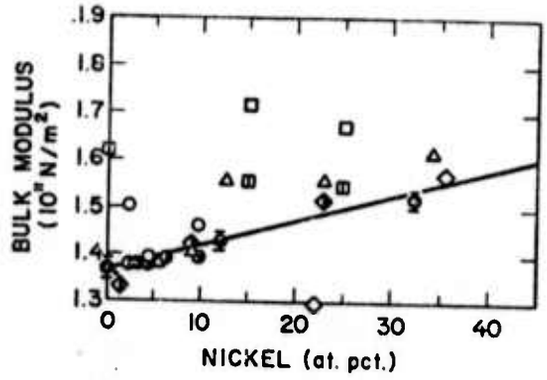

Fig. 8. Compositional variation of B for Cu-Ni alloys.

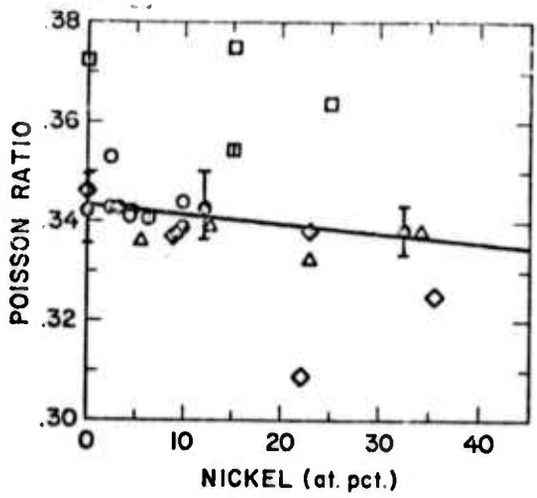

Fig. 9. Compositional variation of ν for Cu-Ni alloys.

ELASTIC PROPERTIES OF A COPPER-CADMIUM-CHROMIUM PRECIPITATION-HARDENED ALLOY*

H. M. Ledbetter

Cryogenics Division
National Bureau of Standards
Boulder, Colorado 80302

Abstract

The room-temperature elastic constants of a polycrystalline precipitation-hardened copper-cadmium-chromium alloy were determined by a 10 MHz pulse-echo method. With respect to copper the alloy has a fifteen-percent-lower bulk modulus, a fifteen-percent-higher shear modulus, and a fourteen-percent-lower Poisson ratio. These changes, especially in the Poisson ratio, are much larger than those observed in the more familiar copper-beryllium precipitation-hardened alloy and compare to those usually obtained only by mechanical deformation or by phase transformation.

Key words: Bulk modulus; compressibility; copper alloy; elastic constant; Poisson ratio; precipitation hardening; shear modulus; sound velocity; Young's modulus.

The elastic constants of a material are essential in engineering design for predicting load-deflection behavior. They are also essential for understanding material behavior related to interatomic bonding forces. Effects of many metallurgical variables on elastic constants have been studied extensively;[1-3] these variables include alloying, annealing, magnetic field, mechanical deformation, phase transformation, pressure, stress, and temperature. This subject was reviewed recently for copper by Ledbetter and Naimon.[4]

Some experimental results on the elastic constants of a precipitation-hardened copper alloy are described here. Compared to previous studies, the observed elastic-constant changes are large.

The studied material† is characterized as follows: Chemical composition by weight is 0.31 Cd, 0.33 Cr, < 0.01 Pb, < 0.01 Fe, < 0.01 Ni, < 0.01 Mn, balance Cu. Mass density determined by hydrostatic weighing is 8.94 g/cm^3. Hardness is 57.5 on a Rockwell 30-T scale. ASTM grain size number is five. The material was produced by extruding a 20.3-cm diameter, 40.6-cm long billet at 1227 K and following with an 866-K,1-hour precipitation heat treatment.

The elastic constants were determined by measuring the ultrasonic longitudinal-wave and shear-wave velocities, v_ℓ and v_t, using a McSkimin[5] pulse-echo method near 10 MHz. The usual engineering elastic constants are related to these velocities by:[6]

$$\text{Shear modulus} = G = \rho v_t^2, \tag{1}$$

$$\text{Longitudinal modulus} = C_\ell = \rho v_\ell^2, \tag{2}$$

$$\text{Bulk modulus} = B = C_\ell - \frac{4}{3} G, \tag{3}$$

$$\text{Young's modulus} = E = 3GB/(C_\ell - G), \tag{4}$$

and

$$\text{Poisson ratio} = \nu = (E/2G) - 1 = \frac{1}{2} (C_\ell - 2G)/(C_\ell - G), \tag{5}$$

where ρ is the mass density.

---

* Contribution of NBS, not subject to copyright.

† This material was obtained from the Phelps-Dodge Corporation, denoted as their alloy PD135. This trade name is used here to characterize the material; it is not an NBS endorsement of this material.

The specimen consisted of a 0.95 x 1.35 x 1.35 cm "cube" whose opposite sides were flat and parallel within 2.5 μm. For each of the three cube directions, longitudinal-wave and shear-wave sound velocities were measured. Shear-wave birefringence was found to be negligible. Both longitudinal and shear velocities varied less than one percent with direction. Thus, velocities were simply averaged over the three directions.

Results of the present study are given in Table I. For comparison, similar data are shown for unalloyed copper and for a copper -1.85 beryllium precipitation-hardening alloy. Copper data are from the single-crystal results of Overton and Gaffney[7] averaged by a Voigt-Reuss-Hill-arithmetic method.[8] Such data agree with data obtained by measuring polycrystalline specimens, and they are believed to be more reliable.[4] Cu-Be data are due to Frederick and were reported by Richards.[9] They were obtained from sound-velocity measurements on a 1.4-cm diameter specimen obtained from material that was cold drawn and then precipitation hardened.

Table I. Room-temperature elastic constants of copper, precipitation-hardened Cu-1.85 Be, and precipitation-hardened Cu-0.3 Cd-0.3 Cr. Velocities have units of 10^6 cm/sec; elastic constants have units of 10^{11} N/m^2; ν is dimensionless. Quantities in parentheses were calculated from reported results. Error limits represent one standard deviation; they reflect both experimental errors and elastic anisotropies.

	Cu	Cu-Be	Cu-Cd-Cr
ρ	8.93	8.232	8.936
v_ℓ	0.4733	(0.4848)	0.4582 ± 0.0053
v_t	0.2295	(0.2414)	0.2459 ± 0.0021
C_ℓ	2.000	(1.958)	1.876 ± 0.043
G	0.473	0.485	0.540 ± 0.009
B	1.371	(1.311)	1.156 ± 0.016
E	1.271	1.296	1.402 ± 0.012
ν	0.346	0.335	0.298 ± 0.003

Results in Table I show for the copper alloys considered that the effect of precipitation hardening is to decrease C_ℓ, B, and ν and to increase G and E. Since there are only two independent elastic constants for a polycrystalline (isotropic) aggregate, these changes in the elastic constants are not independent; and it is useful to consider their interrelationships. The most fundamental choice of an elastic-constant pair is the pair B and G because these constants characterize the two extreme types of mechanical deformation -- volume change without shape change and shape change without volume change, respectively. From Eqs. (1)-(4) it follows that:

$$\frac{dC_\ell}{C_\ell} = \frac{B}{B + \frac{4}{3}G}\,\frac{dB}{B} + \frac{4G}{3(B + \frac{4}{3}G)}\,\frac{dG}{G}\,, \tag{6}$$

$$\frac{dE}{E} = \frac{G}{G + 3B}\,\frac{dB}{B} + \frac{3B}{G + 3B}\,\frac{dG}{G}\,, \tag{7}$$

and

$$\frac{d\nu}{\nu} = \frac{9GB}{(G + 3B)(3B - 2G)}\left(\frac{dB}{B} - \frac{dG}{G}\right). \tag{8}$$

For a typical value of ν, near 1/3, these relationships become:

$$\frac{dC_\ell}{C_\ell} \approx \frac{2}{3}\,\frac{dB}{B} + \frac{1}{3}\,\frac{dG}{G}\,, \tag{6a}$$

$$\frac{dE}{E} \approx \frac{1}{9}\frac{dB}{B} + \frac{8}{9}\frac{dG}{G}, \tag{7a}$$

and

$$\frac{d\nu}{\nu} \approx \frac{4}{9}\left(\frac{dB}{B} - \frac{dG}{G}\right) \quad \frac{4}{9}\left(\frac{dE}{E} - \frac{dG}{G}\right). \tag{8a}$$

Thus, it is clear that E and G will change similarly with respect to most metallurgical variables, that C_ℓ depends more on B than on G, and that ν is expected to be relatively invariant.

There are three principal unexpected results of the present study. First, the elastic constants are changed significantly -- G is increased fourteen percent and B is decreased fifteen percent with respect to unalloyed copper. Second, Poisson's ratio is changed significantly. Köster and Franz[3] showed that ν is relatively insensitive to most metallurgical variables except mechanical deformation and phase transformation. Both these variables introduce strong elastic anisotropies, and it is not clear that these anisotropies have been carefully considered with respect to changes in ν. In the present case, however, no elastic anisotropy due to precipitation is expected and none was detected experimentally. Thus, present results demonstrate a large change in the elastic constants of copper due to precipitation. As shown by Eq. (8a), the unusually large change in ν is due to B and G being oppositely affected by precipitation. Third, the opposite behavior of B and G is unexpected; usually G and B are roughly proportional, typically $G \approx 3/8\ B$.[10] As shown by the data in table I, G/B is 0.35, 0.37, and 0.47 for copper, copper-beryllium, and copper-cadmium-chromium, respectively.

Understanding the non-parallel behavior of B and G due to precipitation hardening emerges as the principal problem of the present study. Very few experimental studies on the elastic properties of precipitation-hardening alloys have been reported. The usual elastic theories of precipitation[11] cannot explain the anomaly, either by precipitate-matrix, precipitate-precipitate, or combined elastic-interaction energies. Also, the problem remains to assure that this anomaly is not an artifact, an effective slowing of the longitudinal ultrasonic wave due to its interactions with the precipitates. If the apparent longitudinal velocity is real, then it may be necessary to invoke two mechanisms to explain the elastic-constant changes due to precipitation hardening. One mechanism would increase (decrease) both B and G while the other would decrease B (increase G), leaving G(B) unaffected.

Acknowledgment

This work was supported by the Advanced Research Projects Agency of the U.S. Department of Defense. Dr. J. M. Wells of Westinghouse supplied the material and its characterization.

References

1. R. F. S. Hearmon, Rev. Mod. Phys. 18 (1946) 409, Adv. Phys. 5 (1956) 323.

2. H. B. Huntington, in Solid State Physics, vol. 7 (F. Seitz and D. Turnbull, Eds.), Academic, New York, 1958.

3. W. Köster and H. Franz, Metall. Rev. 6 (1961) 1.

4. H. M. Ledbetter and E. R. Naimon, J. Phys. Chem. Ref. Data 3 (1974) 897.

5. H. J. McSkimin, J. Acoust. Soc. Amer. 33 (1961) 12.

6. G. Bradfield, in Physical Examination of Metals (B. Chalmers and A. G. Quarrell, Eds.), Arnold, London, 1960, p. 565.

7. W. C. Overton, Jr. and J. Gaffney, Phys. Rev. 98 (1955) 969.

8. R. Hill, Proc. Phys. Soc. Lond. A65 (1952) 349.

9. J. T. Richards, in Symposium on Determination of Elastic Constants, Spec. Tech. Publ. No. 129, ASTM, Philadelphia, 1952, p. 71.

10. C. Zwikker, Physical Properties of Solid Materials, Pergamon, London, 1954, p. 90.

11. G. Sauthoff, Z. Metallkde. 66 (1975) 106.

LOW-TEMPERATURE ELASTIC PROPERTIES OF INVAR††

H. M. Ledbetter, E. R. Naimon,*† and W. F. Weston*

Cryogenics Division
Institute for Basic Standards
National Bureau of Standards
Boulder, Colorado 80302

ABSTRACT

The elastic properties of a polycrystalline invar alloy were determined between room temperature and liquid-helium temperature by two methods: measurement of ultrasonic (10 MHz) wave velocities with a pulse-echo technique, and measurement of resonance frequencies (50 kHz) of cylindrical specimens with a composite piezoelectric-oscillator technique. The shear moduli obtained by the two methods are essentially the same. However, the other elastic constants (all of which have a dilatational component) differ both in magnitude and in temperature dependence. Present pulse-echo results agree closely with previous results obtained for both polycrystals and single crystals in a saturating magnetic field. The following elastic constants are reported: longitudinal modulus, Young's modulus, the shear modulus, the bulk modulus (reciprocal compressibility), and Poisson's ratio. The role of magnetic effects on invar's elastic properties is discussed briefly.

Key words: Bulk modulus; compressibility; Debye temperature; elastic constant; invar; iron alloy; nickel alloy; Poisson's ratio; shear modulus; sound velocity; Young's modulus.

---

* NRC-NBS Postdoctoral Research Associate, 1973-4.

† Present address: Dow Chemical, Rocky Flats Division, Golden, Colorado 80401.

LOW-TEMPERATURE ELASTIC PROPERTIES OF INVAR††

H. M. Ledbetter, E. R. Naimon,*† and W. F. Weston*

Cryogenics Division
Institute for Basic Standards
National Bureau of Standards
Boulder, Colorado 80302

INTRODUCTION

Because invar has nearly temperature-invariant dimensions, it is studied scientifically and used technologically [1-5]. It is a face-centered-cubic iron-base alloy containing about thirty-six percent nickel. Invar's unusually low thermal expansivity is related to its magnetic properties [3]. The usual thermal expansion is canceled approximately by magnetostriction, the coupling between magnetization and strain.

Other physical properties of invar are also anomalous. It has *positive* thermoelastic coefficients over a large temperature range. This anomaly is useful in developing alloys with nearly temperature-invariant elastic constants.

Knowledge of invar's elastic constants is important. First, elastic constants are related simply to interatomic potentials, and they reflect the nature of the interatomic bonding. Second, they are essential design parameters for predicting deflections in stressed components; they become particularly important in cases of large stresses, large deflections, or acute tolerances. The elastic constants of invar are of interest at low temperatures because invar is a candidate low-temperature material [6], and (as discussed below) its elastic behavior is especially anomalous below about 50 K.

The elastic properties of invar between room temperature and liquid-helium temperature are reported in the present paper. Elastic constants were determined by two dynamic methods. Longitudinal and transverse ultrasonic wave velocities were measured at 10 MHz using a pulse-echo technique. And the resonance frequencies of both longitudinal and transverse 60 kHz

---

* NRC-NBS Postdoctoral Research Associate, 1973-4.

† Present address: Dow Chemical, Rocky Flats Division, Golden, Colorado 80401.

standing waves were determined by a three-component piezoelectric composite-oscillator technique. The following elastic constants are reported: Young's modulus E, the shear modulus G, the bulk modulus B (which is the reciprocal compressibility), Poisson's ratio ν, and the longitudinal modulus C_ℓ.

PREVIOUS STUDIES

Five experimental studies on the low-temperature elastic properties of invar have been reported [7-11], and these studies are summarized in Table I. Despite considerable experimental study on them, the low-temperature elastic properties of invar are not well characterized. The curves of Durham et al. [7] are based on a few fixed-temperature measurements, the lowest of these being at 20 K. The extrapolation of these data to lower temperatures is questionable. The Meincke and Litva [8] data are limited to temperatures below 160 K. Fletcher [9] reported only relative values and limited his measurements to temperatures below 77 K. Maeda's [10] values are about twenty percent lower than other reported results for E and G. Hausch and Warlimont [11,12] measured single-crystal elastic constants; the averaging process for obtaining polycrystalline elastic constants from single-crystal elastic constants is uncertain; in particular, averaging has not been discussed for magnetic materials that may have a magnetostrictive strain component. Also, the Hausch and Warlimont data do not extend below 77 K. Thus, further experimental studies are required to better characterize the low-temperature elastic properties of invar.

High-temperature elastic-property studies were reported by: Chevenard [13]; Köster [14]; Fine and Ellis [15]; Hill, Shimmin, and Wilcox [16]; and Tino and Maeda [17].

Besides dependence on variables such as temperature, mechanical deformation, and magnetic field, the elastic properties of invar are sensitive to nickel content. This variable must be considered carefully in comparing results from specimens of different materials, particularly near thirty-six percent nickel where properties such as E and G have sharp minima [18].

EXPERIMENTAL

For brevity, most experimental details are omitted here. Both the pulse-echo technique [19] and the resonance technique [20] are described elsewhere.

Samples of invar were obtained from a commercial source in the form of 3/4-in (1.9-cm) diameter rods. The room-temperature mass density of the sample was found to be 8.084 g/cm^3 by an Archimedean method. The diamond-pyramid hardness number was 226 for a 1 kg load. Grain size was found by a linear intercept method to be approximately 0.02 mm. The composition of the sample, obtained from a mill analysis, was: 0.08 C, 0.01 P, 0.01 S, 35.99 Ni, 0.81 Mn, 0.35 Si, 0.17 Se, and the balance Fe. Materials were tested in the as-received condition, about fifteen-percent cold drawn. Annealing the specimens increased their attenuations, reducing considerably the quality of their pulse-echo patterns. (Magnetic domain walls attenuate more in the annealed state than in the mechanically deformed state.)

The possible existence of preferred orientations (textures) in the specimen was investigated by measuring the longitudinal sound-wave velocity v_ℓ in three orthogonal directions at room temperature. The longitudinal modulus is given by:

$$C_\ell = \rho v_\ell^2 = B + \frac{4}{3} G, \qquad (1)$$

where ρ is the mass density. Thus, both dilatational and shear deformation modes are sampled simultaneously. The results for the three directions are: 0.4821, 0.4825, and 0.4929 $\times 10^6$ cm/sec for the two transverse and for the longitudinal axes, respectively (longitudinal axis = rolling direction). These results were interpreted to indicate that the specimen had a slight preferred orientation, but that practically it could be ignored. The rolling direction of the bar was chosen as the wave-propagation direction for the pulse-echo experiments, and it was the specimen axis for the resonance experiments.

RESULTS

Results of the present study are shown in Figs. 1-5, together with the low-temperature elastic constants of invar reported by others. Values of the elastic constants at selected temperatures are given in Table II. Based on previous measurements on standard materials, errors in E, G, B, and C_ℓ determined by a pulse-echo method are estimated to be ± 1%. Errors in E and G by a resonance method are also estimated to be ± 1%. Errors in the pulse-echo value of ν are larger. In particular, values of B, C_ℓ, and ν obtained from resonance data tend to be inaccurate because of the propagation of measurement errors; these derived resonance values are not reported here. For the pulse-echo case, the elastic constants were obtained from the following formulas:

$$G = \rho v_t^2 , \tag{2}$$

$$B = C_\ell - \frac{4}{3} G , \tag{3}$$

$$E = \frac{9GB}{G + 3B} , \tag{4}$$

and

$$\nu = \frac{E}{2G} - 1 , \tag{5}$$

where v_t is the transverse wave velocity.

DISCUSSION

Pulse-echo Results

The present pulse-echo results agree within a few percent with results reported by Meincke and Litva [8] for polycrystalline specimens, and also with the results obtained by averaging the single-crystal results of Hausch and Warlimont [11] by a Voigt-Reuss-Hill method. Both these experiments were done in a saturating magnetic field; the present experiments were done in zero applied magnetic field.

The agreement between the zero-field and the saturated-field results can be understood as follows. At a high frequency (10 MHz in this case),

domain-wall motion is suppressed since the domain walls cannot follow the high-frequency applied stress. In nickel, it was reported that the decrement is a maximum at 150 kHz [21]; thus, domain-wall motion can contribute significantly to the strain at this frequency. At higher frequencies the domain-wall motion contributes a smaller strain. Therefore, the elastic stiffresses determined at high frequencies for unmagnetized materials are nearly as large as the elastic stiffnesses determined for magnetically saturated materials. Thus, present pulse-echo results are consistent with the previous three pulse-echo experiments [8,9,11], independent of magnetic field.

The present pulse-echo experiments were precluded below 40 K because of the high attenuation of elastic waves in invar at these temperatures. This attenuation phenomenon was detected first by Meincke and Litva [8], and it was studied in detail by Fletcher [9] who described it by a general relaxation-mechanism.

Resonance Results

The present resonance results disagree with the results reported by Maeda [10], both in magnitude and in temperature dependence. Present results are about twenty percent larger for both E and G, and the present temperature coefficients are higher. It is difficult to understand this discrepancy. It may be a frequency-dependent effect. If so, it is a large effect and deserves further study.

Pulse-echo and Resonance Results Compared

For the shear modulus, present resonance and pulse-echo results are identical within experimental error. The unusual behavior of the shear modulus of invar is shown in Fig. 1. A regularly behaved material has a shear modulus that *decreases* monotonically with increasing temperature. The two temperature coefficients are approximately the same, although the slope in the resonance case is slightly higher than in the pulse-echo case. The resonance data for G also show a minimum near 50 K and a slight upturn at lower temperatures, similar to the previously reported pulse-echo data [8-9].

For Young's modulus, the resonance and pulse-echo values differ by a few percent in magnitude, but considerably in their temperature dependence. These differences are shown in Fig. 2. The resonance value of E reaches a minimum near 150 K and then increases steadily with lower temperatures. If this is related to the minimum of E near 50 K shown by the pulse-echo data, then a frequency-dependent attenuation mechanism is indicated. Fletcher [9] found no appreciable frequency dependence of the damping in his experiments between 10 and 35 MHz, but these frequencies may be so high that the attenuation mechanism associated with the minimum is immeasurably small. It is interesting that the resonance values of E are higher at all temperatures than the pulse-echo values. From the usual ΔE_λ effect, an elastic softening would be expected in going from pulse-echo to resonance values [5]. Maeda [10] did find an elastic stiffening due to the ΔE_λ effect, as evidenced by increased values of E in a saturating magnetic field.

From the results shown for G and E, the disparity between resonance values and pulse-echo values of the elastic constants would be expected for any elastic constant that contained a dilatational component. Besides Young's modulus, these include: the longitudinal modulus, the bulk modulus (reciprocal compressibility), and Poisson's ratio. While the results of the present study confirm this disparity, resonance-derived values of C_ℓ, B and ν are not reported here because of the large errors propagated in computing them from E and G data. The basic reason for this disparity between dilatational-type and shear-type elastic constants is unclear.

However, a more fundamental problem is also unresolved -- how can the anomalous elastic behavior of invar be understood, independent of the resonance/pulse-echo disparity? Despite many attempts, no consensus of thinking on the theory of invar exists. The ΔF_λ effect due to linear magnetostriction due to domain walls accounts only for anomalies in shear-type elastic constants. The ΔE_ω effect due to volume magnetostriction accounts only for anomalies in dilatation-type elastic constants. As described above, both types of elastic constants are anomalous in invar. Thus, a combined $\Delta E_\lambda - \Delta E_\omega$ effect would have to be invoked. Hausch [5] disputed this approach and proposed that the Heisenberg magnetic exchange energy must be considered for invar. Before these questions can be resolved, additional low-temperature elastic measurements must be made on invar-type materials to permit quantitative checks on proposed theories.

REFERENCES

1. W. S. McCain and R. E. Maringer, DMIC Memorandum 207 (1965).
2. S. J. Rosenberg, NBS Monograph 106, U.S. Govt. Print. Off. (1968).
3. G. Hausch and H. Warlimont, Z. Metallk. 64:152 (1973).
4. W. F. Schlosser, J. Phys. Chem. Solids 32:939 (1971).
5. G. Hausch, Phys. Status Solidi (a) 15:501 (1973).
6. Handbook on Materials for Superconducting Machinery, Metals and Ceramics Information Center, Battelle Columbus Laboratories, Columbus, Ohio (1974).
7. T. F. Durham, R. M. McClintock, R. P. Reed, C. J. Guntner, and K. A. Warren, Cryogenic Materials Data Handbook, U.S. Dept. of Commerce (1961).
8. P. P. M. Meincke and J. Litva, Phys. Lett. 29A:390 (1969).
9. R. Fletcher, J. Phys. C 2:2107 (1969).
10. T. Maeda, J. Phys. Soc. Japan 30:375 (1971).
11. G. Hausch and H. Warlimont, Acta Met. 21:401 (1973).
12. G. Hausch and H. Warlimont, Z. Metallk. 63:547 (1972).
13. P. Chevenard, Trav. Mem. Bur. Int. Poids Mes. 27:142 (1927).
14. W. Köster, Z. Metallk. 35:194 (1943).
15. M. E. Fine and W. C. Ellis, Trans. AIME 188:1120 (1950).
16. W. H. Hill, K. D. Shimmin, and B. A. Wilcox, Amer. Soc. Test. Mater. Proc. 61:890 (1961).
17. Y. Tino and T. Maeda, J. Phys. Soc. Japan 18:955 (1963).
18. H. M. Ledbetter and R. P. Reed, J. Phys. Chem. Ref. Data 2:531 (1973).
19. E. R. Naimon, W. F. Weston, and H. M. Ledbetter, Cryogenics 14:246 (1974).
20. W. F. Weston, J. Appl. Phys., forthcoming.
21. R. M. Bozorth, W. P. Mason, and H. J. McSkimin, Bell System Tech. J. 30:970 (1951).

LIST OF TABLES

LIST OF FIGURES

Table I. Summary of low-temperature elastic studies on invar

Reference	Alloy (wt.pct.Ni)	Temperature Range (K)	Magnetic Field (kG)	Frequency of Measurement	Elastic Constants Measured	Comments
Durham et al. [7]	36.0	19-300	0	Static	E, G	
Meincke and Litva [8]	35.0	2-160	15	10 MHz	v_l, v_t	Annealing effect
Fletcher [9]	35.0	2-77	0	10-30 MHz	v_l, v_t	Relative values only; four alloys, 36-48 nickel; attenuation measurements
Maeda [10]	35.0	100-800	0-1.9	kHz region	E, G	Magnetic-field dependence
Hausch and Warlimont [11]	35.3	77-700	6	10 MHz	v_l, v_t	Single crystals; nine alloys, 32-53 nickel
Present	36.0	4-300	0	10 MHz	v_l, v_t	
				60 kHz	E, G	

Table II. Elastic constants of invar at selected temperatures, all units 10^{11} N/m^2 except ν (which is dimensionless)

	Pulse-echo Results					Resonance Results	
T(K)	E	G	B	C_ℓ	ν	E	G
300	1.433	0.558	1.109	1.853	0.285	1.523	0.565
250	1.408	0.547	1.107	1.835	0.288	1.475	0.551
200	1.379	0.533	1.112	1.823	0.293	1.427	0.535
150	1.353	0.521	1.125	1.819	0.300	1.399	0.522
100	1.334	0.511	1.139	1.821	0.305	1.398	0.509
77	1.328	0.508	1.146	1.823	0.307	1.403	0.506
4	-	-	-	-	-	1.417	0.505

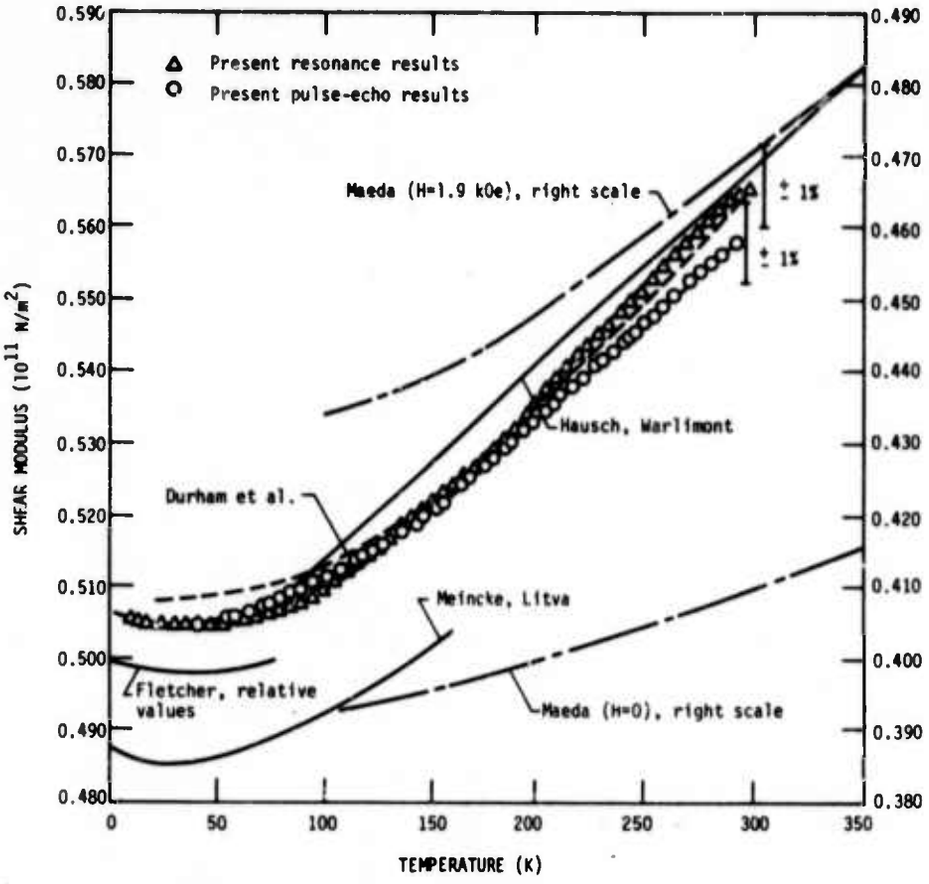

Figure 1. Temperature variation of the shear modulus of invar.

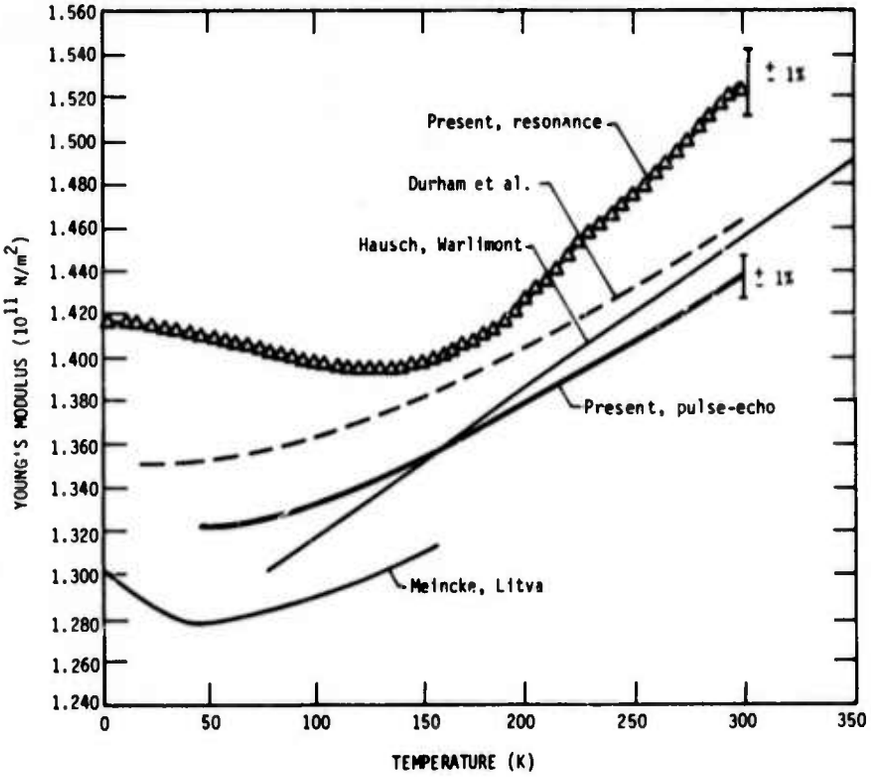

Figure 2. Temperature variation of the Young's modulus of invar.

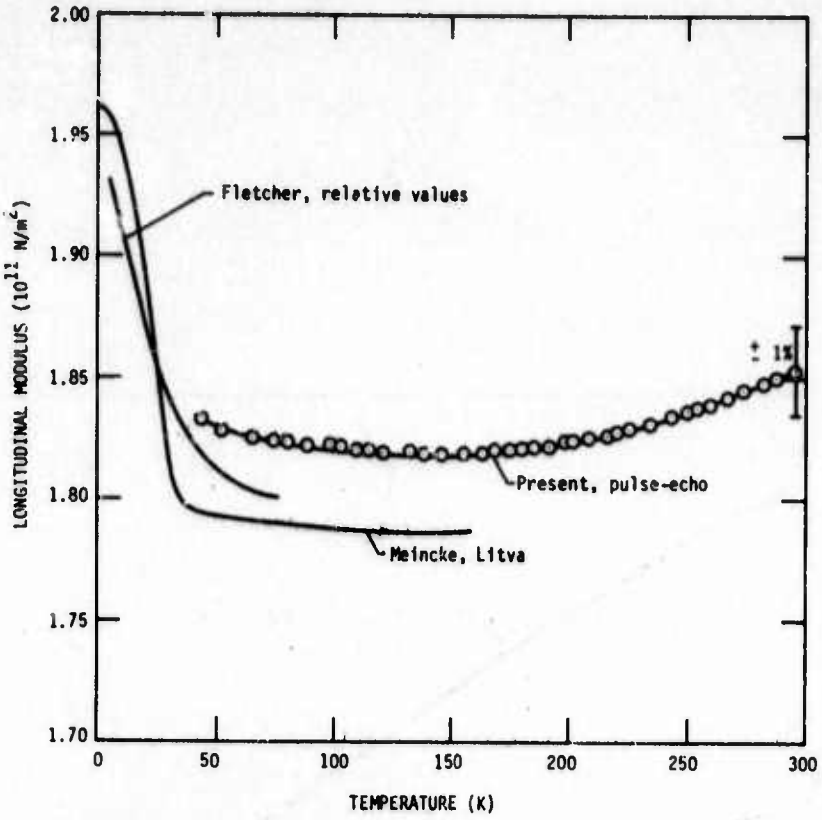

Figure 3. Temperature variation of the longitudinal modulus of invar.

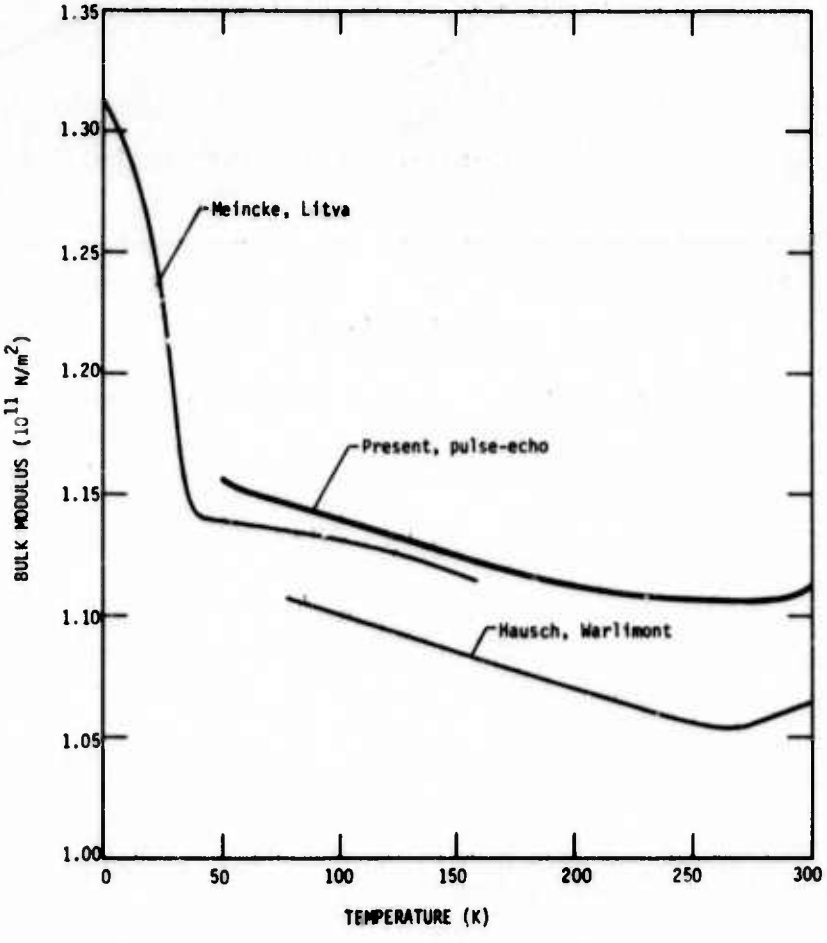

Figure 4. Temperature variation of the bulk modulus of invar.

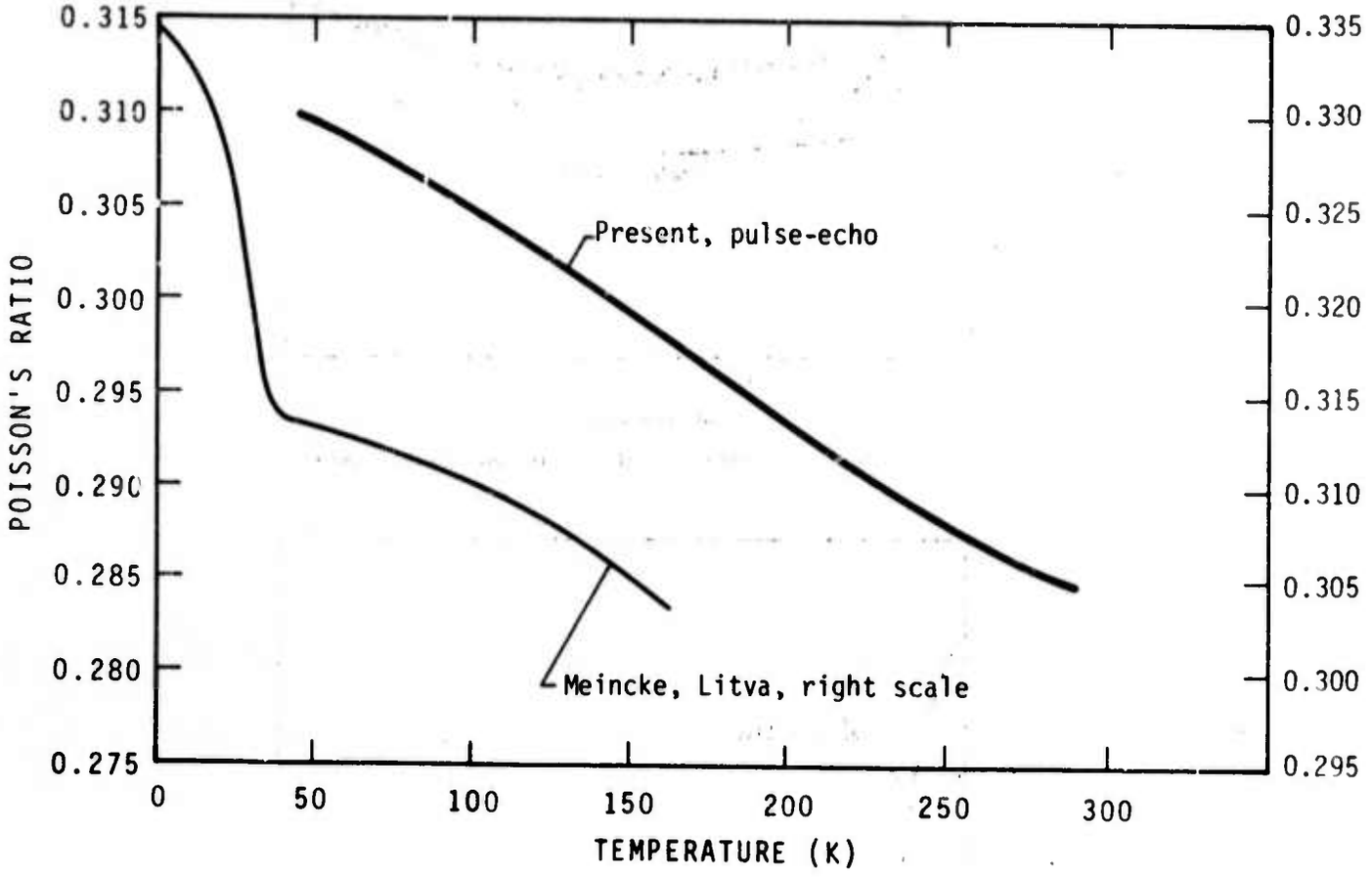

Figure 5. Temperature variation of Poisson's ratio of invar.

Materials Science and Engineering, 20 (1975) 185—194

Dynamic Low-Temperature Elastic Properties of Two Austenitic Nickel—Chromium—Iron Alloys*

W.F. WESTON†, H.M. LEDBETTER and E.R. NAIMON†‡

Cryogenics Division, Institute for Basic Standards, National Bureau of Standards, Boulder, Colorado 80302 (U.S.A.)

(Received in revised form March 3, 1975)

SUMMARY

The zero-magnetic-field low-temperature elastic properties of two polycrystalline nickel - chromium - iron alloys were determined ultrasonically between 4 and 300 K. Results are given for: longitudinal and transverse sound velocities, Young's modulus, shear modulus, bulk modulus, Poisson's ratio and elastic Debye temperature. Effects of alloying are discussed. The elastic property changes due to additions of chromium and iron to nickel are reviewed comprehensively.

INTRODUCTION

Elastic properties of metals at low temperatures have twofold interest. First, such information is essential for understanding the basic aspects of mechanical deformation, which are often described by dislocation models that contain the elastic constants explicitly. Second, low-temperature elastic properties are essential design parameters for cryogenic structures, for predicting deflections due to any combination of stress and temperature.

Austenitic nickel-base alloys containing chromium and iron are standard engineering materials. They have high heat resistance, high corrosion resistance, good high-temperature strength, and can be readily fabricated into structures. Many of these materials also have low-temperature applications. In particular, because of its mechanical properties, Inconel* 600 is used extensively at cryogenic temperatures. Its strength increases with decreasing temperature, while its ductility and toughness are preserved. Inconel X-750 (formerly Inconel X) is similar to Inconel 600, but it contains small amounts of aluminum, titanium and niobium. Aluminum and titanium make precipitation hardening possible by forming $Ni_3(Al, Ti)$ by suitable thermal treatment. (Inconel 600 is usually hardened by low-temperature mechanical deformation.) Niobium further stiffens the matrix through solid-solution hardening and stabilizes the carbides.

The zero-magnetic-field dynamic low-temperature elastic properties of Inconel 600 and Inconel X-750 are reported here. A pulse-superposition method was used to determine ultrasonic wave velocities in specimens prepared from as-received commercial bar stock.

EXPERIMENTAL

Inconel 600 and X-750 alloys were obtained from commercial sources in the form of about 3-in. (7.6-cm) and 4-in. (10.2-cm) diameter rods, respectively. Cylindrical specimens $\frac{3}{8}$-in. (1-cm) long and $\frac{5}{8}$-in. (1.6-cm) diam. were prepared by grinding. Opposite faces were flat and parallel within 100×10^{-6} in. (2.5 μm). Chemical compositions (obtained from mill analyses), hardness numbers and mass densities are given in Table 1. Hardnesses were determined by a standard method, and mass densities were determined by hydrostatic

* Contribution of NBS, not subject to copyright.
† NRC-NBS Postdoctoral Research Associate, 1973-4.
‡ Present address: Dow Chemical USA, Golden, Colorado 80401.

* Tradenames are used to characterize materials; they are not NBS endorsements of particular products.

TABLE 1

Compositions and properties of alloys

Alloy	Chemical composition, mill analyses (wt.%)										
	Ni	Cr	Mn	Fe	S	Si	Cu	C	Al	Ti	Nb + Ta
Inconel 600	Bal	15.8	0.20	7.20	0.007	0.20	0.10	0.04	—	—	
Inconel X-750	73.52	15.2	0.20	6.58	0.007	0.25	0.04	0.04	0.78	2.51	0.89

Alloy	Hardness (DPH No., 1 kg load)	Mass density at 294 K (g/cm^3)	Condition
Inconel 600	179	8.415	As received; hot rolled annealed
Inconel X-750	330	8.238	As received; hot rolled 1625°F (1158 K) and aged

weighing using distilled water as a standard.

A pulse-superposition method [1] was used to determine all ultrasonic velocities except the shear mode in Inconel X-750. This particular mode was highly attenuated, and for its measurement a standard pulse - echo technique was used. All velocities were measured along the rolling direction of the rod.

Quartz transducers (10 MHz) were bonded to the specimens with phenyl salicylate for room-temperature measurements and with a stopcock grease for lower temperatures. When these bonds failed occasionally at very low temperatures, a silicone fluid (viscosity = 200,000 cP at 25°C) was used for bonding.

The specimen holder is shown schematically in Fig 1. The holder was placed in the ullage of a helium dewar and lowered stepwise to achieve cooling. Temperatures were monitored with a chromel - constantan thermocouple contacting the specimen.

Velocity measurements were made over the range of 4 - 300 K for Inconel 600. For Inconel X-750, however, measurements were made over the range of 40 - 300 K. Below 40 K, the ultrasonic attenuation for both longitudinal and transverse waves was too high to permit accurate velocity determinations to be made. However, if a material is well behaved, little change is expected in its sound velocities from 40 to 0 K, and semi-theoretical curves fitted to the data points (as explained in the next section) should give accurate low-temperature values.

The experimental quantity of interest is the transit time t for an ultrasonic wave to propagate from one end of the specimen to the other and back. The ultrasonic wave velocity v is then given by

$$v = 2l/t, \tag{1}$$

where l is the specimen length. Elastic moduli C are related to ultrasonic velocities by

$$C = \rho v^2, \tag{2}$$

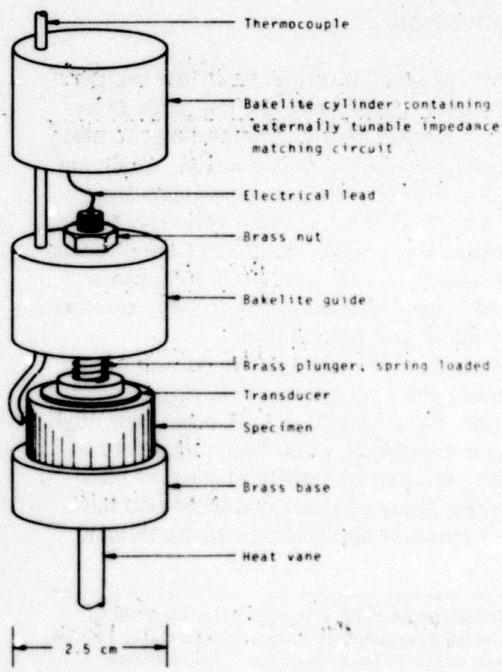

Fig. 1. Specimen holder.

where ρ is the mass density.

Denoting room-temperature values by the subscript r, it follows that

$$\rho/\rho_r = (l_r/l)^3. \tag{3}$$

Then eqn. (2) can be rewritten as

$$C = C_r(l_r/l)(t_r/t)^2. \tag{4}$$

Thus, the temperature dependence of an elastic modulus is determined from the change in transit time and from the length change due to thermal expansion or contraction. However, the relative length change for Inconel over the temperature range from 300 K to 4 K is only about 0.23% [2]. These small thermal-contraction corrections are neglected here; their omission introduces a maximum error also of 0.23% in the low-temperature values of velocity and modulus. Such small errors are insignificant for the purposes of the present study. Based on previous work in our laboratory, maximum uncertainties in the velocity measurements are estimated to be about 1%.

A quantity of some interest is the temperature coefficient $(1/C)(dC/dT)$, which is a measure of the relative modulus change due to temperature changes. From eqn. (4), it follows that

$$(1/C)(dC/dT) = -2(1/t)(dt/dT) - \alpha \tag{5}$$

where $\alpha = (1/l)(dl/dT)$ is the coefficient of linear thermal expansion. For Inconel, α is 0.13×10^{-4} K^{-1} at room temperature [2].

RESULTS

Temperature dependences of the longitudinal and transverse moduli are shown in Figs. 2 and 3. These moduli are given by

$$C_l = \rho v_l^2 = B + \tfrac{4}{3}G, \tag{6}$$

and

$$C_t = \rho v_t^2 = G. \tag{7}$$

Here v_l and v_t are the longitudinal and transverse sound-wave velocities, ρ is the mass density, B is the bulk modulus, and G is the shear modulus.

Temperature dependences of both C_l and C_t were least-squares fitted to a theoretical relationship suggested by Varshni [3]:

$$C = C^0 - s/(e^{t/T} - 1), \tag{8}$$

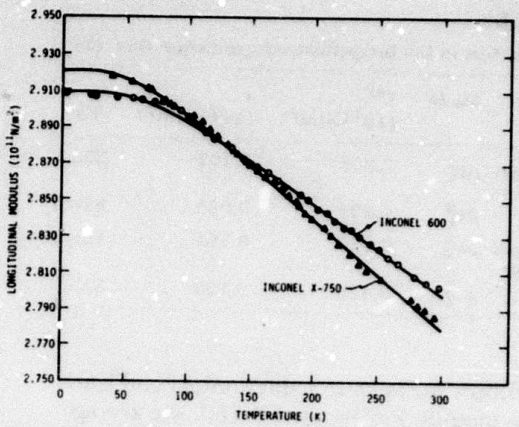

Fig. 2. Temperature dependence of longitudinal modulus $C_l = \rho v_l^2$ of two nickel - chromium - iron alloys.

where C^0, s, and t are adjustable parameters and T is temperature. The value of C at $T = 0$ K is C^0, and $-s/t$ is the high-temperature limit of dC/dT. By invoking an Einstein oscillator model of solids, it can be shown (in the absence of electronic effects) that t is the Einstein characteristic temperature. Parameters C^0, s and t for Inconels 600 and X-750 are given in Table 2. Room-temperature values of the temperature coefficients of the elastic moduli are given in Table 3.

Curves in Figs. 2 and 3 are plots of eqn. (8) determined by an unweighted least-squares fit of the data. For Inconel 600, average percentage differences between measured and curve values

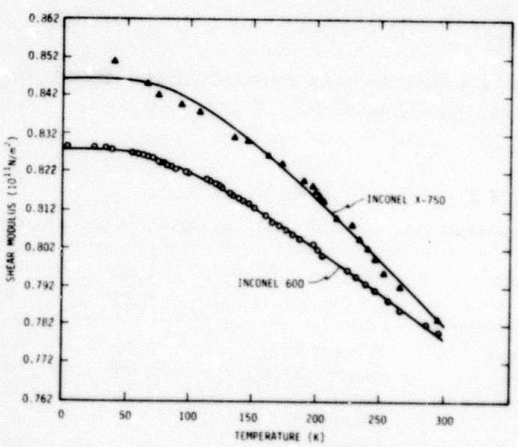

Fig. 3. Temperature dependence of transverse or shear modulus $C_t = \rho v_t^2 = G$ of two nickel - chromium - iron alloys.

TABLE 2

Parameters in the temperature-dependence eqn. (8)

Alloy	Mode	C^0 (10^{11}N/m^2)	s (10^{11}N/m^2)	t (K)
Inconel 600	ρv_ℓ^2	2.909	0.107	203.1
	ρv_t^2	0.828	0.063	246.0
Inconel X-750	ρv_ℓ^2	2.920	0.105	165.9
	ρv_t^2	0.846	0.120	315.8

are 0.05% for both the longitudinal and transverse moduli. For Inconel X-750, the average percentage differences between measured and curve values are 0.04% and 0.18% for the longitudinal and transverse moduli, respectively. The comparatively large error for the transverse modulus of Inconel X-750 was due to a relatively poor echo pattern resulting from ultrasonic-wave scattering. There are many possible sources of this scattering — for example lattice inhomogeneities and crystalline anisotropy.

While polycrystalline aggregates (quasi-isotropic solids) have only two independent elastic constants, several constants are commonly used for various applications. The four most common are the bulk modulus B, Young's modulus E, the shear modulus G and Poisson's ratio ν. The relationships among these are:

$$\frac{1}{E} = \frac{1}{3G} + \frac{1}{9B} \tag{9}$$

and

$$\nu = \frac{E}{2G} - 1. \tag{10}$$

These elastic constants were calculated from the moduli shown in Figs. 2 and 3 by the relationships:

$$E = 3C_t(C_\ell - \tfrac{4}{3}C_t)/(C_\ell - C_t), \tag{11}$$

$$B = C_\ell - \tfrac{4}{3}C_t, \tag{12}$$

and

$$\nu = \tfrac{1}{2}(C_\ell - 2C_t)/(C_\ell - C_t) \tag{13}$$

where C_ℓ and C_t are the least-squares values obtained from fitting the experimental data with eqn. (8). The constants E, B and ν are shown in Figs. 4 - 6.

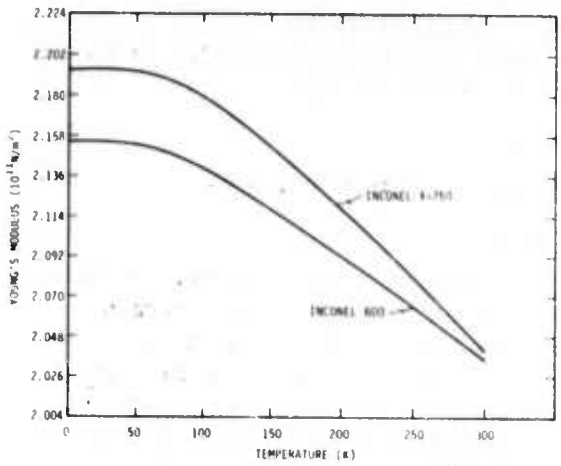

Fig. 4. Temperature dependence of Young's modulus of two nickel - chromium - iron alloys.

It is of interest to calculate the elastic Debye temperature θ for the two alloys. This fundamental parameter is important in the lattice properties of solids and is related to the average elastic wave velocity by [7]

$$\theta = K\langle v \rangle, \tag{14}$$

TABLE 3

Temperature derivatives of elastic constants at room temperature (10^{-4} K^{-1})

Source	Material	$\frac{1}{B}\frac{dB}{dT}$	$\frac{1}{E}\frac{dE}{dT}$	$\frac{1}{G}\frac{dG}{dT}$	$\frac{1}{\nu}\frac{d\nu}{dT}$
Present	Inconel 600	−1.20	−2.95	−3.21	1.10
Present	Inconel X-750	−1.02	−4.07	−4.53	1.97
Ref. 4	Nickel*	−1.56	−4.16	−4.53	1.72
Ref. 5	Inconel X			−3.09	
Ref. 6	Inconel X		−2.67		
Ref. 12	Inconel X			−3.16	

* Based on single-crystal data averaged by the Voigt - Reuss - Hill method.

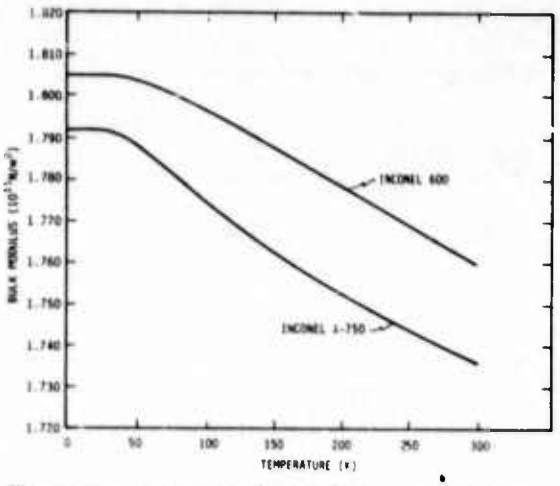

Fig. 5. Temperature dependence of bulk modulus (reciprocal compressibility) of two nickel - chromium - iron alloys.

where

$$K = \frac{h}{k}\left(\frac{3N\rho}{4\pi A}\right)^{1/3}. \qquad (15)$$

Here h is Planck's constant, k is Boltzmann's constant, N is Avogadro's constant, ρ is the mass density, and A is the effective atomic weight. The average velocity is given by

$$\langle v \rangle = \left(\frac{v_\ell^{-3} + 2v_t^{-3}}{3}\right)^{-1/3}. \qquad (16)$$

The Debye temperature of each alloy at $T = 0$ K, and also of nickel, is given in Table 4.

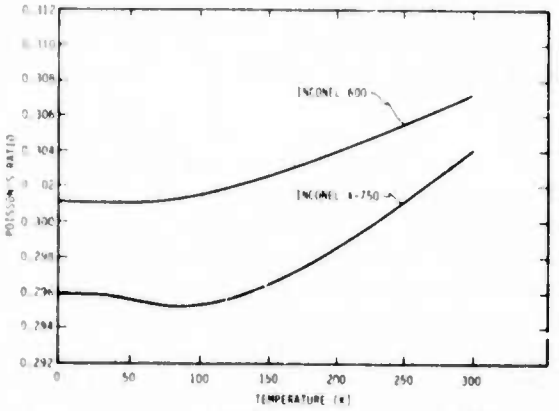

Fig. 6. Temperature dependence of Poisson's ratio of two nickel - chromium - iron alloys.

TABLE 4

Elastic Debye temperatures at $T = 0$ K

Source	Material	θ(°K)
Present	Inconel 600	464.9
Present	Inconel X-750	473.5
Ref. 8	Nickel	476.0

DISCUSSION

The elastic properties of both Inconel 600 and Inconel X-750 behave regularly with respect to temperature. The elastic moduli (C_ℓ, $C_t = G$, B, E) decrease with increasing temperature, show a relative flatness at low temperatures, achieve zero slope at $T = 0$ K, and approach linear behavior at high temperatures. Poisson's ratio also behaves regularly, having a positive temperature coefficient. For both the bulk modulus and Poisson's ratio, Inconel X-750 shows unusual curvatures in the modulus - temperature curves. The reason for this is not understood; atomic ordering based on the $Ni_3(Cr, Fe)$ composition is a possible explanation. Ordering often occurs on cooling and usually causes an increase in the elastic stiffnesses. Magnetic ordering might also affect the elastic stiffnesses.

Assuming that the specimens studied are representative of the two alloys, then conclusions concerning their relative elastic behavior can be drawn. Not surprisingly, as shown in Figs. 2 - 6 and in Tables 2 and 3, for most practical purposes the two alloys are elastically identical. Thus, additions of small amounts of aluminum, titanium and niobium have little effect on the elastic properties of nickel alloys containing about 15% chromium and about 7% iron.

Very few elastic data exist for these alloys [5,6,9 - 13], especially Inconel 600. Most information has appeared in engineering reports and is summarized in refs. 9 - 13. For comparison the room-temperature values of E, G, B and ν are given in Table 5. Good agreement is observed between previous and present results. The polycrystalline elastic constants of nickel are also given in Table 5, both those determined from experiments on polycrystalline aggregates [4] and those obtained from single-crystal data [15,16] using a Voigt - Reuss - Hill average. The elastic Debye temperatures of

TABLE 5

Room-temperature elastic constants of Inconel 600 and Inconel X-750; units of 10^{11} N/m^2 except ν (dimensionless)

Source	Inconel 600				Inconel X-750			
	E	G	B	ν	E	G	B	ν
Present	2.036	0.780	1.760	0.307	2.040	0.734	1.736	0.304
Ref. 5	—	—	—	—	—	0.789	—	—
Ref. 6	—	—	—	—	2.144	—	—	—
Refs. 9,10	2.11	0.75	—	—	2.11	0.75	—	0.29
Ref. 11	—	—	—	—	2.075	0.714	—	0.29
Ref. 12	—	—	—	—	2.041	0.824	—	—
Ref. 13	2.109	—	—	—	2.109	0.749	—	—
	Nickel - 26 iron							
Ref. 14	2.059	0.792	1.731	0.302				
	Nickel (polycrystal, zero magnetic field)							
Ref. 4	1.97	0.785	1.903	0.296				
	Nickel (VRH-averaged single crystal, zero magnetic field)							
Ref. 4	2.10	0.799	1.863	0.312				

the alloys are also within 2% of the value calculated from the single-crystal elastic data of nickel.

Low-temperature elastic data have been reported only once previously for either of these alloys; based on static measurements, Young's modulus and the shear modulus of Inconel X-750 were reported between room temperature and liquid-hydrogen temperature (20 K) [12]. The reported Young's modulus agrees closely with present results while the reported shear modulus is about 4% higher than the present results and has a lower room-temperature temperature derivative.

It is emphasized that the data reported here are dynamic (adiabatic) rather than static (isothermal) and apply to rapid, rather than slow, loading. In most cases the differences between adiabatic and isothermal elastic constants are small. The conversion formulas can be written as [17]

$$E_s = E_T(1 + E_T T\alpha^2/C_p\rho), \tag{17}$$

$$B_s = B_T(1 + 9B_T T\alpha^2/C_p\rho), \tag{18}$$

$$\nu_s = \nu_T + (1 + \nu_T)E_T T\alpha^2/C_p\rho, \tag{19}$$

and

$$G_s = G_T, \tag{20}$$

where subscripts S and T denote adiabatic and isothermal, respectively. In the above equations T is the absolute temperature, α is the linear thermal expansion coefficient, C_p is the heat capacity per unit mass at constant pressure, and ρ is the mass density. For the Inconel alloys at room temperature it is found that

$$(E_S - E_T)/E_S = 0.003,\ (B_S - B_T)/B_S = 0.022,$$

$$(\nu_S - \nu_T)/\nu_S = 0.012 \text{ and } (G_S - G_T) \equiv 0. \tag{21}$$

At lower temperatures the differences are smaller; they vanish at $T = 0$ K.

Alloying effects on material properties can be analyzed many ways. The simplest approach is a linear mixture model:

$$C = \sum_{i=1,N} x_i C_i, \tag{22}$$

where, in present context, C represents a general elastic constant of the alloy, which has N components of species i; x_i are the weight fractions, and C_i are the elastic constants of the unalloyed species. This model works best for mixtures of similar metals where effects of atomic ordering, phase transformations, etc. are absent. It can be shown simply that this model fails for transition-metal alloys, even for simpler, binary systems such as iron - nickel.

A better model proceeds on the basis of

alloy data rather than component data:

$$\frac{C}{C_0} = \text{ } + \frac{1}{C_0} \sum_{i=1,N} \left(\frac{\partial C}{\partial x_i}\right) \Delta x_i, \qquad (23)$$

where C_0 is the elastic constant of the reference material, usually (but not necessarily) a pure component, $(\partial C/\partial x_i)$ are slopes of the C - x_i curves, and x_i are the weight fractions. Expressions like eqn. (23) have been used previously to describe the elastic properties of ternary alloys [18]; it assumes that alloying effects $(\Delta C/\Delta x)$ are composition independent in the range of interest and are linearly additive. Considering Inconel alloys to be, in a first approximation, alloys of iron and chromium in nickel, then three data are required (besides composition) to solve eqn. (23) — the elastic constants of nickel and the changes of these constants with iron and with chromium additions. Nickel's elastic constants are well known [4].

Effects of iron additions on the elastic properties of nickel have been studied extensively [19 - 32], although the subject has apparently not been reviewed. A summary of the results is given in Table 6, which gives the logarithmic composition derivatives $(1/C)(\Delta C/\Delta x)$, where C represents an elastic constant such as E, G, B or ν, and x denotes weight percent iron alloyed into nickel. The effects of alloying iron into nickel are best defined for the Young's modulus and the bulk modulus; the change of the bulk modulus is quite large.

Effects of chromium additions on the elastic properties of nickel have been reported only by Chevenard [21] and are shown in Table 7. If the value of $(1/G)(\Delta G/\Delta x)_{Fe}$ from Table 6 is substituted into eqn. (23) along with the other input data, a value of $(1/G)(\Delta G/\Delta x)_{Cr} = -6.6$ is calculated. Since this disagrees with Chevenard's value of 2.9, the model represented by eqn. (23) also fails for the alloys of interest here.

The necessity of invoking higher-order terms in the Taylor expansion is indicated:

$$\frac{C}{C_0} = 1 + \frac{1}{C_0} \sum_{i=1,N} \left(\frac{\partial C}{\partial x_i}\right) \Delta x_i + \frac{1}{6C_0} \left(\frac{\partial^2 C}{\partial x_i \partial x_j}\right) \Delta x_i \Delta x_j + \ldots \qquad (24)$$

In particular, the interaction term in this case:

$$\frac{1}{C_0} \left(\frac{\partial^2 C}{\partial x_{Cr} \partial x_{Fe}}\right) x_{Cr} x_{Fe} \qquad (25)$$

may be quite important since alloying alters 3d-shell electronic structure, which in turn affects cohesion and elastic properties. At

TABLE 6

Effects of iron on the elastic properties of nickel at room temperature (evaluated from 0 - 7% iron)

Source	$\frac{1}{C}\left(\frac{\Delta C}{\Delta x}\right) \times 10^3$			
	E	G	B	ν
Honda (1919)	2.4	1.4		
Honda, Tanaka (1926)	0.3	0.7		1.7
Chevenard (1927)		0.0		
Nishiyama (1929)	4.1			
Ebert, Kussmann (1937)			−15.0	
Forster, Koster (1937)	1.7			
Engler (1938)	1.0			
Koster (1940)	1.9			
Chevenard, Crussard (1943)	0.0			
Koster (1943)	1.7			
Yamamoto (1959)	7.8			
Sakurai *et al.* (1964)*		−0.4		
Shirakawa *et al.* (1969)*	5.3	9.8	−17.5	−17.3
Tanji *et al.* (1970)	0.8	2.3	−16.8	−10.7
Average observed values	2.4	2.3	−16.4	−8.8
Linear mixture model	−0.6	−0.5	−1.1	−0.3

* Single-crystal data were averaged by the method of Voigt.

TABLE 7

Effects of chromium on the elastic properties of nickel

Source	$\frac{1}{E}\left(\frac{\Delta E}{\Delta x}\right)\times10^3$	$\frac{1}{G}\left(\frac{\Delta G}{\Delta x}\right)\times10^3$	$\frac{1}{B}\left(\frac{\Delta B}{\Delta x}\right)\times10^3$	$\frac{1}{\nu}\left(\frac{\Delta \nu}{\Delta x}\right)\times10^3$
Linear mixture model	2.2	3.1	−1.1	−3.2
Chevenard (1927)		2.9		

present, data are insufficient for evaluating this interaction term. Chevenard's [21] data on Ni - Cr - Fe alloys indicate that for the shear modulus the interaction term might be as large as $40 \times 10^{-3} x_{Fe} x_{Cr}$, which is large relative to the first-order coefficients in Tables 6 and 7. It is difficult to make any quantitative estimate of the second-order mutual interaction terms (Fe - Fe, Cr - Cr). But from the existing data they seem to be smaller than the cross-term (Fe - Cr). Additional evidence for a large interaction term results from the following reasoning. Since the elastic properties of the two Inconel alloys are so similar, additional alloying elements beyond chromium and iron seem to have negligible effects or to cancel. In either case, considering Inconels to be ternary alloys of nickel, chromium and iron seems justified from the viewpoint of their elastic properties. However, both alloys behave elastically very much like a nickel - iron alloy with the same nickel content; chromium behaves as if it were iron. This is shown in Table 5, which includes the elastic properties of a nickel-26 iron alloy, which were obtained from single-crystal data by using a Voigt - Reuss - Hill-arithmetic average. Why chromium should behave like iron is not understood.

Another anomaly of the Ni - Cr - Fe system is that the elastic stiffnesses of nickel are increased by either chromium or iron additions. Usually the elastic stiffness of a host metal is reduced by alloying. The reverse effect in this case could be magnetic in origin, as discussed below.

Magnetic interactions contribute to the energy of a material and therefore also to its elastic constants, which are related to the second spatial derivative of the total energy. However, extra energies due to magnetism take many forms, and several models have been suggested to account for the anomalous elastic behaviour of magnetic materials. At least two of these models are relevant here.

Khomenko and Tseytlin [33] showed for alloys in the invar region (Fe ~ 35 Ni) that chromium additions increased Young's modulus with $(1/E)(\Delta E/\Delta x)$ having a value near 30×10^{-3}, a very large effect compared with the coefficients in Tables 6 and 7. These authors showed that chromium increases E because it suppresses the usual ΔE effect ΔE_λ, owing to linear magnetostriction, which reduces E. Since ΔE_λ is proportional to a magnetostriction constant λ that is quite large for nickel, this is a possible model for the anomalous elastic behaviour of nickel - chromium - iron alloys.

Hausch [34] used a molecular-field approximation to evaluate the Heisenberg exchange-energy $J(r)$ contribution to the elastic constants of magnetic materials. For nickel it was shown that $\partial^2 J(r)/\partial r^2$ is negative (therefore the elastic constant contribution is negative), while for face-centered cubic iron the derivative is positive. The derivative has not been evaluated for chromium; it is probably positive as deduced from its approximate position on a Bethe - Slater curve. Thus, it is clear qualitatively that Hausch's model might also be able to explain the anomalous elastic behaviour of these alloys.

The two models could be tested by low-frequency elastic measurements on appropriate alloys, with and without a saturating magnetic field. The ΔE_λ variation with alloying disappears in a saturating magnetic field since the magnetic domain walls are immobilized.

Finally, a speculative suggestion is made concerning the source of the very high acoustic attenuation in Inconel X-750 below 40 K. Iron and nickel have Curie temperatures of 1040 K and 630 K, respectively. Alloying with chromium reduces both of these drastically; about 50% chromium in iron suppresses completely the paramagnetic - ferromagnetic

transition; for nickel, fewer data exist, but only about 12% chromium may be required to suppress the Curie transition in nickel. No studies seem to have been reported on the Curie temperatures of Ni - Cr - Fe alloys [35]. Thus, a paramagnetic - ferromagnetic transition in Inconel X-750 at low temperatures is possible. If it occurs, the exact transition temperature should depend strongly on chromium content. Such a transition would explain the attenuation increase as due to acoustic-wave scattering from ferromagnetic domain walls. The attenuation would not be associated with the Curie transition itself, but with a change in the magnetic state, a state produced by the Curie transition. Simple dip tests using a small permanent magnet indicated that both Inconels 600 and X-750 are ferromagnetic at liquid-nitrogen temperatures. Tests for ferromagnetism between room and nitrogen temperatures were not made. Further studies on this problem are planned. Studies that would be valuable include low-temperature acoustic wave-velocity and attenuation measurements in a saturating magnetic field. If a ferromagnetic transition occurs, then lower-frequency elastic measurements would be useful for determining the so-called ΔE effect. No ΔE effect is seen in the MHz region because ferromagnetic domain walls cannot respond to a high-frequency mechanical stress [36]. Measurements of Curie temperatures and saturation magnetic moments would also be useful.

CONCLUSIONS

From the results of this study the following conclusions are drawn:

1. The elastic properties of Inconel 600 and Inconel X-750 are quite similar.

2. At lower temperatures, Inconel X-750 has a slightly higher shear modulus and Young's modulus than has Inconel 600, but a slightly lower bulk modulus.

3. At low temperatures, Poisson's ratio is slightly lower for Inconel X-750 than for Inconel 600.

4. Inconel 600 shows a regular temperature dependence in all its elastic properties.

5. The temperature dependence of the elastic properties of Inconel X-750 is regular except for the bulk modulus, which has a region of positive curvature, and Poisson's ratio, which has a minimum near 80 K.

6. Inconel X-750 highly attenuates 10 MHz sound waves, both longitudinal and transverse, below about 40 K. This is speculated to result from a change in the magnetic state, which results from a paramagnetic-to-ferromagnetic transition that occurs above 77 K. Why Inconel 600, which also undergoes a magnetic transition, has lower attenuation is not understood.

7. The composition dependence of the elastic properties of these alloys cannot be described by a simple model, probably because of d-shell and magnetic interactions.

ACKNOWLEDGEMENTS

This work was supported in part by the Advanced Research Projects Agency of the U.S. Department of Defense. Dr. R.L. Moment of Dow Chemical contributed a critical reading of the manuscript.

REFERENCES

1 H.J. McSkimin, J. Acoust. Soc. Am., 33 (1961) 12.
2 R.J. Corruccini and J.J. Gniewek, Thermal Expansion of Technical Solids at Low Temperatures, NBS Monograph 29, 1961, p. 10.
3 Y.P. Varshni, Phys. Rev., B2 (1970) 3952.
4 H.M. Ledbetter and R.P. Reed, J. Phys. Chem. Ref. Data, 2 (1973) 531.
5 H.C. Burnett, unpublished results, 1956.
6 W.H. Hill, K.O. Shimmin and B.A. Wilcox, Am. Soc. Testing Mater. Proc., 61 (1961) 890.
7 P. Debye, Ann. Phys. (Leipzig), 39 (1912) 789.
8 R. Wanner, Can. J. Phys., 48 (1970) 1270.
9 Intern. Nickel Co., Rept. on Inconel Alloy 600, 1973.
10 Intern. Nickel Co., Rept. on Inconel Alloy X-750, 1970.
11 NERVA Program Materials Properties Data Book, Vol. 1A, Nickel Base Alloys, Aerojet Nuclear Systems, Sacramento, Calif., 1970.
12 Cryogenic Materials Data Handbook, AFML Rept. No. ML-TDR-64-280, PB 171809, revised, Aug. 1964.
13 Aerospace Structural Metals Handbook, Vol. II, AFML. Rept. No. ASD-TDR-63-741, Mar. 1966.
14 N.G. Einspruch and L.T. Claiborne, J. Appl. Phys., 35 (1964) 175.
15 S.G. Epstein and O.N. Carlson, Acta Met., 13 (1965) 487.
16 G. Simmons and H. Wang, Single Crystal Elastic Constants and Calculated Aggregate Properties: A Handbook, M.I.T. Press, Cambridge, 1971, p. 223.
17 L.D. Landau and E.M. Lifshitz, Theory of Elasticity, Pergamon Press, London, 1959, p. 17.
18 J.B. Greer and E.H. Bucknall, Trans. Am. Soc. Metals, 57 (1964) 554.

19 K. Honda, Sci. Rept. Tohoku Univ., 8 (1919) 59.
20 K. Honda and T. Tanaka, Sci. Rept. Tohoku Univ., 15 (1926) 1.
21 P. Chevenard, Trav. Mem. Bur. Int. Poids Meas., 27 (1927) 116.
22 Z. Nishiyama, Sci. Rept. Tohoku Univ., 18 (1929) 539.
23 H. Ebert and A. Kussmann, Physik. Z., 38 (1937) 437.
24 F. Förster and W. Köster, Naturwiss., 25 (1937) 436.
25 O. Engler, Ann. Physik, 31 (1938) 145.
26 W. Köster, Arch. Eisenhuettenw., 6 (1949) 271.
27 P. Chevenard and Ch. Crussard, Compt. Rend., 216 (1943) 685.
28 W. Köster, Z. Metallk., 10 (1943) 194.
29 M. Yamamoto, Sci. Rept. Tohoku Univ., 11 (1959) 102.
30 J. Sakurai, M. Fujii, Y. Nakamura and H. Takaki, J. Phys. Soc. Japan, 19 (1964) 308.
31 Y. Shirakawa, Y. Tanji, H. Moriya and I. Oguma, J. Japan Inst. Metals (Sendai), 33 (1969) 1196.
32 Y. Tanji, Y. Shirakawa and H. Moriya, Rept. No. 1462, Res. Inst. for Iron, Steel and Other Metals (1970), p. 84; also in J. Japan Inst. Metals (Sendai), 34 (1970) 417.
33 O.A. Khomenko and A.M. Tseytlin, Fiz. Metal. i Metalloved., 28 (1969) 246.
34 G. Hausch, Phys. Status Solidi, 15 (1973) 501.
35 T.F. Connolly (ed.), Bibliography of Magnetic Materials and Tabulation of Magnetic Transition Temperatures, Vol. 5, Solid State Physics Literature Guides, Plenum Press, New York, 1972.
36 W.P. Mason, Phys. Rev., 83 (1951) 683.

Low-temperature elastic properties of four austenitic stainless steels

H. M. Ledbetter, W. F. Weston,*† and E. R. Naimon*†

Cryogenics Division, Institute for Basic Standards, National Bureau of Standards, Boulder, Colorado 80302
(Received 11 February 1975)

The elastic properties of four austenitic stainless steels—AISI 304, AISI 310, AISI 316, and A286—are reported over the temperature range 300–4 K. These properties include longitudinal modulus, shear modulus, Young's modulus, bulk modulus (reciprocal compressibility), Poisson's ratio, and elastic Debye temperature. Elastic constants were determined from measurements of longitudinal and transverse sound-wave velocities using an ultrasonic (10 MHz) pulse-superposition method. Measurements were made in the absence of a magnetic field; these alloys undergo paramagnetic-to-antiferromagnetic transitions at low temperatures. For all four alloys, the shear modulus behaves regularly with respect to temperature. The other elastic constants, all of which have a dilatational component, decrease anomalously at temperatures below 80 K. The largest anomaly, about 3%, is in the bulk mudulus of the 304 alloy; this modulus is lower at 0 K than at 300 K. Results are interpreted on the basis of the Döring effect, which results from a large volume magnetostriction in the magnetic phase. This may be the first report of a Döring effect in antiferromagnetic materials.

PACS numbers: 62.20.D, 65.70., 75.80.

I. INTRODUCTION

Austenitic stainless steels are attractive materials for mechanical applications at low temperatures. Primarily, this is due to their having, at room temperature, a face-centered cubic (fcc) crystal structure. Metals having this crystal structure usually do not become brittle at lower temperatures. In general, steels that remain austenitic at cryogenic temperatures show increased tensile strength, a smaller increase in yield strength, and little change in ductility. However, it is not axiomatic that fcc materials will always perform well at low temperatures. For example, lower temperatures may promote a change of the crystal structure from fcc to body-centered cubic (bcc) or to close-packed hexagonal (cph), thus probably embrittling the material. Other changes such as atomic ordering or magnetic ordering may also occur at low temperatures; these also effect mechanical behavior. Thus, the nature and the magnitude of a material's low-temperature properties cannot be predicted *a priori* from room-temperature observations, and there is no substitute for careful low-temperature experimental determinations of the important properties of each material of interest. Gilman[1] concluded that "the most important mechanical characteristic of a crystal is its elastic modulus".

The same elastic constants that are related to fundamental interatomic forces in solids are also used in engineering design. For example, Poisson's ratio is an essential design parameter in problems of plate buckling or of pressure-vessel design. Young's modulus and Poisson's ratio are required if plane-stress data and plane-strain data are to be interconverted, a technique used often in the elastic stress-strain analysis of solids.

In this paper, the dynamic zero-magnetic-field elastic properties of four austenitic stainless steels—commonly designated AISI 304, AISI 310, AISI 316, and A286[2]—are reported between 300 and 4 K. These properties include longitudinal modulus, shear modulus, Young's modulus, bulk modulus (reciprocal compressibility), and Poisson's ratio. These elastic constants were determined dynamically, by measuring the velocity of longitudinally polarized and transversely polarized ultrasonic (10 MHz) pulses propagating through polycrystalline specimens of commercial as-received alloys. At low temperatures, elastic anomalies were observed in all four materials. These are believed to be associated with transitions to antiferromagnetic states. A magnetoelastic interpretation of the anomalies is given.

II. EXPERIMENTAL

A. Specimens

Materials were obtained from commercial sources in the form of $\frac{3}{4}$-in. (1.9-cm)-diam rods. Their chemical compositions are given in Table I. Hardness and mass-density data on the alloys are given in Table II. Hardnesses were measured by standard metallurgical methods, and mass densities were measured by Archimedes's method using distilled water as a standard. Materials were tested in their as-received conditions. Samples were prepared by grinding cylinders

TABLE I. Chemical analyses of the alloys, wt%, obtained from mill analyses.

Alloy	Al	C	Cr	Cu	Mo	Mn	Ni	P	S	Si	Ti	V	Fe
304		0.02	18.4			1.4	9.7	0.02	0.01	0.6			balance
310		0.08	24.8	0.1	0.1	1.7	20.8	0.02	0.02	0.7			balance
316		0.05	16.8	0.2	2.1	1.9	11.7	0.03	0.02	0.4			balance
A286	0.2	0.04	14.8		1.2	1.4	25.4	0.01	0.01	0.6	2.1	0.3	balance

TABLE II. Densities and hardnesses of the alloys.

Alloy	Mass density (g/cm^3)	Hardness (DPHN, 1 kg load)
304	7.86	225
310	7.85	220
316	7.97	210
A286	7.95	275

$\frac{1}{2}$ in. (1.2 cm) thick with faces flat and parallel within 10^{-4} in. (2.5 μm).

B. Procedures

A pulse-superposition[3] method was used to measure the longitudinal and transverse sound-wave velocities between room temperature and liquid-helium temperature. The specimen holder, which was described previously[4], was placed in the ullage of a helium Dewar and lowered (raised) stepwise to achieve cooling (heating). Measurements were made semicontinuously on cooling, and a few points were checked on heating to verify reversibility. Temperatures were measured by a chromel-constantan thermocouple contacting the specimen. Quartz transducers (10 MHz) were bonded to the specimens with phenyl salicylate for room-temperature measurements and with stopcock grease for lower temperatures. No bond corrections were made since these are insignificant for present purposes. No thermal-contraction corrections were made; for the alloys of interest this introduces a maximum error of 0.3% over the 300 K temperature range. Maximum uncertainties in the absolute velocity measurements are estimated to be about 1%. The imprecision in the relative velocities is a few parts in 10^5.

III. RESULTS

Longitudinal and transverse moduli are shown in Figs. 1 and 2 as a function of temperature. The longitudinal modulus C_l is given by

$$C_l = \rho v_l^2, \tag{1}$$

where ρ is the mass density and v_l is the longitudinal wave velocity. The transverse modulus C_t is identically equal to the shear modulus G and is given by

$$C_t = G = \rho v_t^2, \tag{2}$$

where v_t is the transverse wave velocity. Young's modulus E is given by

$$E = 3C_t(C_l - \tfrac{4}{3}C_t)/(C_l - C_t) \tag{3}$$

and is shown in Fig. 3. The bulk modulus B, or reciprocal compressibility, is given by

$$B = C_l - \tfrac{4}{3}C_t, \tag{4}$$

and is shown in Fig. 4. Poisson's ratio ν is given by

$$\nu = \tfrac{1}{2}(C_l - 2C_t)/(C_l - C_t) \tag{5}$$

and is shown in Fig. 5.

Temperature dependences of both C_l and C_t were fitted by a least-squares method to a theoretical relationship suggested by Varshni[5]:

$$C = C^0 - s/(e^{t/T} - 1), \tag{6}$$

where C^0, s, and t are adjustable parameters and T is temperature. The value of C at $T = 0$ K is C^0, and $-s/t$ is the high-temperature limit of the temperature derivative dC/dT. By invoking an Einstein oscillator model of solids, it can be shown (in the absence of electronic effects) that t is the Einstein characteristic temperature. Parameters C^0, s, and t are given in Table III. The average differences between the Varshni-curve values and measured values were 0.04 and 0.05% for C_l and C_t respectively. Of course, the low-temperature elastic anomalies are not described by Eq. (6).

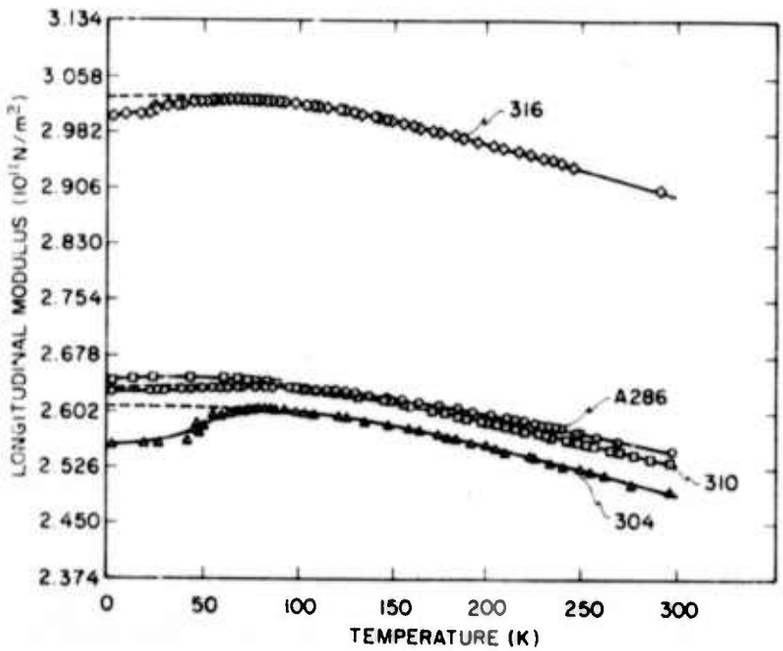

FIG. 1. Temperature dependence of the longitudinal moduli of four stainless-steel alloys.

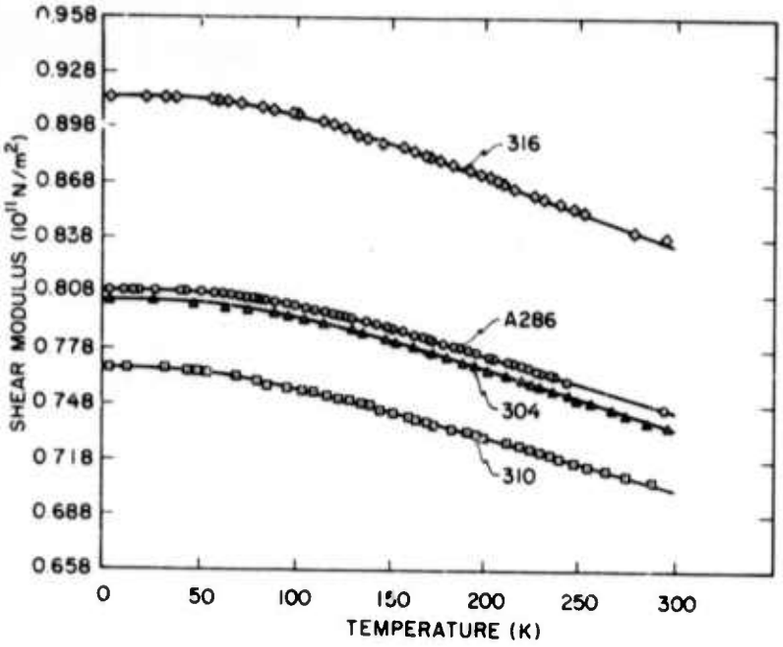

FIG. 2. Temperature dependence of the transverse (shear) moduli of four stainless-steel alloys.

which describes the extrapolated higher-temperature behavior shown as dashed lines in the figures. Temperature coefficients of the elastic constants at room temperature are given in Table IV.

Elastic Debye temperatures at $T=0$ K were calculated for both the antiferromagnetic and the extrapolated paramagnetic states, and these are given in Table V. The elastic Debye temperature Θ is related to the average sound-wave velocity according to

$$\Theta = K\langle v\rangle, \tag{7}$$

where

$$K = (h/k)(3N_0/4\pi A)^{1/3}. \tag{8}$$

Here h is Planck's constant, k is Boltzmann's constant, N is Avogadro's number, ρ is the mass density, and A is the effective atomic weight. The average velocity is given by

$$\langle v\rangle = [\tfrac{1}{3}(v_l^{-3} + 2v_t^{-3})]^{-1/3}. \tag{9}$$

For comparison, the elastic Debye temperatures at $T=0$ K of iron, chromium, and nickel are also included in Table V.

IV. DISCUSSION

The elastic constants of all four materials exhibit regular behavior from room temperature to about 80 K or lower. Below about 80 K, anomalous changes in the elastic constants occur for all four materials. These anomalies occur only in the elastic constants that have a dilatational component—the longitudinal modulus, the

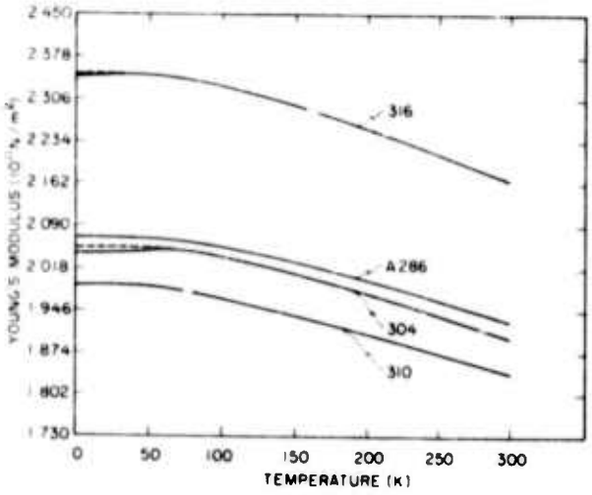

FIG. 3. Temperature dependence of the Young's moduli of four stainless-steel alloys.

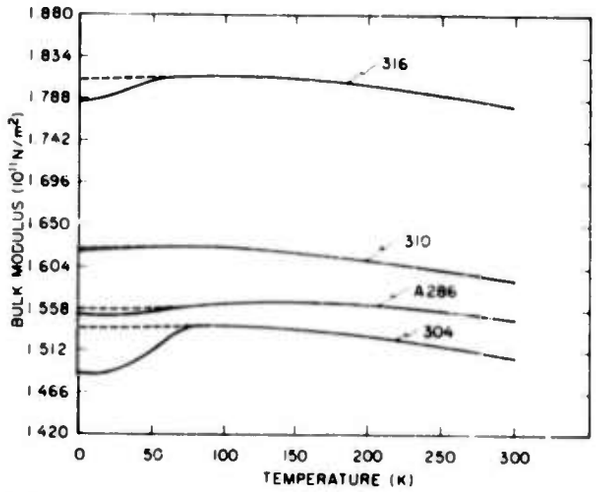

FIG. 4. Temperature dependence of the bulk moduli (reciprocal compressibilities) of four stainless-steel alloys.

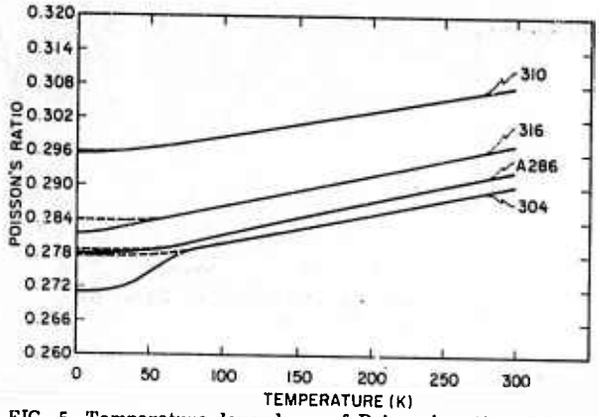

FIG. 5. Temperature dependence of Poisson's ratios of four stainless-steel alloys.

bulk modulus, Young's modulus, and Poisson's ratio. No anomalies occur for the shear modulus.

The elastic properties of some of these alloys have been studied previously at low temperatures. For example, stress-strain tests for E and G at 295, 77, and 4 K indicated anomalies somewhere below 77 K for both AISI 302 and AISI 303, but not for AISI 310.[6] Resonance tests on AISI 303 for E and G simultaneously at temperatures between 320 and 4 K showed anomalies below 80 K.[7] All these anomalous results can be interpreted in terms of the usual $\Delta E = \Delta E_\lambda$ effect (discussed below) and are not directly related to the low-temperature elastic anomalies reported in the present work.

The most likely causes of the anomalies are magnetic transitions. Stainless-steel-type alloys have been shown to be antiferromagnetic at lower temperatures; Néel temperatures near 40 K have been reported[6,8] for 304-type alloys. However, no Néel transition was detected for a 310-type alloy cooled to liquid-helium temperature.[6] This suggests that effects due to local, rather than long-range, magnetic ordering may be occurring in these alloys. This would also account for the difference in the 304 alloy between the Néel temperature (40 K) and the temperature below which anomalous elastic behavior is observed (80 K). Short-range magnetic-order effects have been discussed by Schlosser[9] for fcc iron-nickel alloys. Changes of crystal structure are probably not the cause of the anomalies since the changes were observed to be reversible within experimental error; changes of elastic constants due to crystal-structure changes are generally irreversible, showing a particularly large hysteresis in iron-base alloys. The elastic constants reported here showed a reversible behavior and indicate that the magnetic transition occurs smoothly over a range of temperatures rather than at a unique transition temperature. Thus, the transition seems to be of the second-order type.[10]

TABLE IV. Temperature coefficients of the elastic constants at room temperature (10^{-4} K^{-1}).

Alloy	$\frac{1}{B}\frac{dB}{dT}$	$\frac{1}{E}\frac{dE}{dT}$	$\frac{1}{G}\frac{dG}{dT}$	$\frac{1}{\nu}\frac{d\nu}{dT}$
304	−1.69	−4.15	−4.54	1.78
310	−1.39	−3.71	−4.05	1.45
316	−1.41	−4.17	−4.61	1.89
A286	−1.22	−3.77	−4.18	1.81

The usual so-called ΔE effect, better designated ΔE_λ, due to linear magnetostriction strains induced by an applied stress, and usually interpreted by invoking a Weiss domain model (with domain rotations and domain-wall motions), can also be excluded as a possible source of the anomalous elastic behavior. Linear magnetostriction affects Young's modulus, the shear modulus, and Poisson's ratio, but it does not affect the bulk modulus because no magnetomechanical process will respond to the application of a hydrostatic stress.[11] Also, effects due to ΔE_λ are not observed at high frequencies[12] because the domain-wall displacements cannot follow the applied stress, and therefore cannot contribute an additional strain that lowers the observed elastic stiffness. Thus, for present purposes, a high-frequency applied stress is essentially equivalent to applying a saturating magnetic field; both nullify domain-wall contributions to the strain.

In the presence of a saturating magnetic field (or its effective equivalent), the only magnetic effect that alters E, B, and ν without affecting G is the effect due to spontaneous volume magnetostriction. This effect is designated ΔE_ω, where $\omega = (V - V_p)/V_p$ is the spontaneous volume magnetostriction, V is the total volume, and V_p is the volume in the paramagnetic state. The effect was first reported by Engler[13] for an Fe-42 Ni alloy. It was explained first by Döring[14] using a thermodynamic analysis. Herein, this phenomenon will be called the Döring effect. Döring reasoned that in the paramagnetic region the elastic constant is measured at constant magnetization M, while in the ferromagnetic or antiferromagnetic

TABLE III. Parameters in the temperature-dependence equation, Eq. (6).

Alloy	Mode	C^0 (10^{11} N/m^2)	s (10^{11} N/m^2)	l (K)
304	l	2.608	0.297	371.8
	t	0.803	0.089	251.8
310	l	2.647	0.175	271.8
	t	0.767	0.051	173.7
316	l	3.028	0.332	369.7
	t	0.914	0.099	243.5
A286	l	2.636	0.334	454.4
	t	6.309	0.080	243.1

TABLE V. Elastic Debye temperature at $T = 0$ K.

Alloy	θ (K) magnetic	θ (K) extrapolated paramagnetic
304	467.8	468.1
310	459.0	459.0
316	496.7	496.8
A286	467.6	467.7
Iron (bcc)[a]	472.4	
Chromium[b]	453.0	
Nickel[a]	476.0	

[a] R. Wanner, Can. J. Phys. 48, 1270 (1970).
[b] F. H. Herbstein, Adv. Phys. 10, 313 (1961).

region the elastic constant is measured at constant magnetic field H. Döring showed that the magnitude of the anomaly in the Young's modulus is given by

$$\frac{\Delta E_\omega}{E^2} = \left(\frac{1}{E}\right)_M - \left(\frac{1}{E}\right)_H = -\frac{1}{9}\left(\frac{\partial \omega}{\partial H}\right)^2_{\sigma,T}\left(\frac{\partial M}{\partial H}\right)^{-1}_{\sigma,T}, \tag{10}$$

where $\partial\omega/\partial H$ is the forced volume magnetostriction due to the magnetization, $\partial M/\partial H$ is the high-field susceptibility χ, E^2 is $E_M E_H$ and σ is the tensile stress. An alternative derivation of Eq. (10) was given by Hausch.[15] [Wohlfarth[16] stated, without proof, that the factor of $\frac{1}{9}$ in Eq. (10) should be replaced by $(1-2\nu)^2$ where ν is Poisson's ratio. For the present materials this introduces a factor of approximately 2, which is insignificant for present purposes.] It should be noted that the Döring effect always lowers the moduli ($E_M > E_H$), whether the volume magnetostriction is positive or negative. This is related to the fact that a relaxation mechanism is involved in going to an antiferromagnetic state, and such mechanisms always soften the elastic stiffness. The Döring effect in iron-nickel alloys was discussed by Köster,[17] who denoted it as ΔE_λ rather than as ΔE_ω. The effect has been invoked by several authors to explain elastic anomalies in magnetic materials, usually of the Invar type. Hausch[15] criticized the relevance of the Döring effect in most of these cases. Schlosser[18] discussed the magnetovolume contribution to the compressibility of Invar, but Hausch[15] showed that an exchange-energy contribution is also required in this case. The present data for iron-chromium-nickel (stainless steel) alloys seem to constitute a clear case of the Döring effect.

If the Döring effect is responsible for the elastic anomalies observed in stainless-steel-type alloys, then ΔE_ω calculated from Eq. (10) should agree roughly with the magnitude of the observed anomalies. Apparently, the volume magnetostriction of these alloys has not yet been determined. Using data for Invar,[15] an iron alloy containing about 35% Ni and having the same crystal structure as the alloys considered here, it is calculated from Eq. (10) that $\Delta E_\omega/E^2 = -1.4\times10^{-14}$ cm^2/dyn. For the 304 stainless steel alloy, the present results give for the bulk modulus $\Delta E/E^2 = -0.2\times10^{-14}$ cm^2/dyn. Thus, the observed anomalies show a reasonable correspondence to the magnitude of the predicted Döring effect. A more exact correspondence could be established if the volume magnetostrictions of these alloys were known. If the Döring effect is the correct interpretation of the data, then the volume magnetostriction of these alloys must be quite large since it is large in Invar-type alloys. Besides Invar and other iron-nickel alloys, large magnetovolume effects have also been observed in iron-manganese, iron-palladium, iron-platinum, and iron-cobalt alloys.[19] A quantitative correspondence is also precluded because the alloys reported on here were studied in mechanically deformed states. Köster[17] showed that the ΔE effect depends sensitively on metallurgical variables. The usual $\Delta E = \Delta E_\lambda$ effect is generally suppressed by mechanical deformation. No studies seem to have been made on the effect of mechanical deformation on ΔE_ω. It would be expected that the ΔE_ω effect will be enhanced in annealed materials since the residual stresses due to mechanical deformation would not interfere with domain-wall motions.

Of the four alloys, the smallest elastic anomalies were observed in the 310 alloy and in the A286 alloy. These materials have a much higher nickel content. Thus, it is suggested that in stainless-steel-type alloys the effect of nickel is to reduce the volume magnetostriction but not to suppress the occurrence of the antiferromagnetic phase.

The desirability of further studies on these alloys, especially with respect to the Döring effect, is indicated. Ideally, carefully prepared alloy single crystals would be tested in magnetic fields.

Since changes in elastic constants are usually accompanied by significant changes in internal friction, it would also be interesting to study the low-temperature anelastic properties of these alloys. The magnitude of the mechanical damping determines the magnitude of stresses established in vibrating parts. And all of these alloys are candidate materials for low-temperature uses where vibrations may occur. Magnetomechanical hysteresis has already been established as an important damping mechanism in ferromagnetic materials.[20]

V. CONCLUSIONS

From the results of the present study the following conclusions are drawn:

(i) Stainless-steel alloys AISI 304, AISI 310, AISI 316, and A286 have qualitatively similar elastic-property variations with temperature.

(ii) The shear modulus behaves regularly over the entire temperature range studied.

(iii) The elastic constants with dilatational components—Young's modulus, the longitudinal modulus, the bulk modulus, and Poisson's ratio—behave regularly above about 75 K but anomalously at lower temperatures. The anomalies are largest for the bulk modulus and smallest for Young's modulus.

(iv) The anomalies are largest in the AISI 304 and AISI 316 alloys and smallest in the AISI 310 and A286 alloys. A relationship between the magnitude of the anomaly and nickel content is suggested.

(v) As suggested first by Döring, the anomalies can be interpreted thermodynamically as the difference between constant-magnetization and constant-field bulk moduli.

Noted added in proof. Subsequent studies on other samples of these materials showed that the values of E, G, and B reported here for AISI 316 are all higher than the average values by about 6%. All data reported for other materials are believed to be typical.

ACKNOWLEDGMENT

This work was supported in part by the Advanced Research Projects Agency of the Department of Defense.

*NRC-NBS Postdoctoral Research Associate, 1973-4.
†Present address: Rockwell International, Rocky Flats Plant, Golden, Colo. 80401.

[1]J. J. Gilman, Aust. J. Phys. 13, 327 (1960).
[2]This trade name is used to describe the material; its use does not imply an endorsement by NBS of a particular product.
[3]H. J. McSkimin, J. Acoust. Soc. Am. 33, 12 (1961).
[4]E. R. Naimon, W. F. Weston, and H. M. Ledbetter, Cryogenics 14, 246 (1974).
[5]Y. P. Varshni, Phys. Rev. B 2, 3952 (1970).
[6]R. P. Mikesell and R. P. Reed, J. Res. Natl. Bur. Std. (U.S.) 70C, 207 (1966).
[7]P. E. Armstrong and D. T. Eash, in *Advances in Cryogenic Engineering*, Vol. 14, edited by K. D. Timmerhaus (Plenum, New York, 1959), p. 64.
[8]E. I. Kondorsky and V. L. Sedov, Sov. Phys.-JETP 35, 1104 (1959).
[9]W. F. Schlosser, J. Phys. Chem. Solids 32, 939 (1971).
[10]J. W. Christian, *The Theory of Transformations in Metals in Metals and Alloys* (Pergamon, Oxford, 1965), p. 214.
[11]W. F. Brown, Jr., Phys. Rev. 50, 1165 (1936).
[12]R. M. Bozorth, W. P. Mason, and H. J. McSkimin, Bell Syst. Tech. J. 30, 970 (1951).
[13]O. Engler, Ann. Phys. (Leipz.) 31, 145 (1938).
[14]W. Döring, Ann. Phys. (Leipz.) 32, 465 (1938).
[15]G. Hausch, Phys. Status Solidi A 15, 501 (1973).
[16]E. P. Wohlfarth, Phys. Status Solidi A 10, K39 (1972).
[17]W. Köster, Z. Metallkde. 35, 194 (1943).
[18]W. F. Schlosser, Phys. Status Solidi A 18, 235 (1973).
[19]W. F. Schlosser, Int. J. Magn. 2, 167 (1972).
[20]A. Cochardt, Trans. Am. Soc. Mech. Eng. 75, A196 (1953).

NBSIR

SEMI-ANNUAL REPORT ON MATERIALS RESEARCH IN SUPPORT OF SUPERCONDUCTING MACHINERY

FATIGUE RESISTANCE AND FRACTURE TOUGHNESS OF ENGINEERING MATERIALS AT CRYOGENIC TEMPERATURES

R. L. Tobler, D. T. Read, and R. P. Reed

Cryogenics Division
Institute for Basic Standards
National Bureau of Standards
Boulder, Colorado 80302

October 1975

Summary: Fatigue and Fracture Toughness

This section of the report contains two manuscripts, the results of which are summarized as follows:

1) The fatigue life of a uniaxial glass-filament reinforced epoxy composite at liquid helium temperature can be an order of magnitude greater than at room temperature. Tensile and fatigue results for this material indicate that such composites can be attractive structural materials for cryogenic applications.

2) The yield strength of an Fe-21Cr-6Ni-9Mn stainless steel tripled between 295 and 4 K, reaching a value of $1.24 GNm^{-2}$ (180ksi) at 4 K. Over this temperature interval the fracture toughness was considerable, and inversely related to yield strength. This alloy should be useful at temperatures as low as 4 K, for applications requiring a balance of high strength and fracture toughness.

FATIGUE RESISTANCE OF A UNIAXIAL S-GLASS/EPOXY COMPOSITE AT ROOM AND LIQUID HELIUM TEMPERATURES

Ralph L. Tobler and David T. Read*

Cryogenics Division
Institute for Basic Standards
National Bureau of Standards
Boulder, Colorado 80302

Abstract

Tension-tension axial fatigue tests of a uniaxial glass filament-reinforced epoxy were conducted at 295 K and 4 K. The fatigue life was found to be an order of magnitude greater at 4 K than at 295 K. These results are believed to be the first 4 K fatigue data reported for a composite material.

Key words: Cryogenics; fatigue; fiber composites; liquid helium; low temperature tests; mechanical properties.

---

* NRC-NBS Postdoctoral Research Associate, 1974-75.

FATIGUE RESISTANCE OF A UNIAXIAL S-GLASS/EPOXY COMPOSITE AT ROOM AND LIQUID HELIUM TEMPERATURES

Ralph L. Tobler and David T. Read

INTRODUCTION

Glass-reinforced epoxy composites are prospective structural materials at cryogenic temperatures where high strength-to-density and strength-to-thermal-conductivity ratios are required and where relatively low elastic moduli can be tolerated. At temperatures from 295 to 4 K, these composites offer a combination of physical and mechanical properties unmatched by structural metals. Unfortunately, structural design data for composites at low temperatures are scarce, a fact which hinders the utility of these materials.

The advent of superconducting machinery prompted the need for mechanical property data for materials in a liquid helium environment at 4 K. Accordingly, programs were instituted to establish a data base [1]. Kasen's review [1,2] of the mechanical behavior of glass-reinforced composites concludes that tensile and fatigue strengths generally increase between 295 and 76 K; but, on further cooling to 20 K, there is a high probability that strengths will decrease. According to Kasen [1,2], below 20 K, tensile behavior has rarely been investigated, and fatigue data are non-existent.

In this study, fatigue tests of a filamentary-reinforced composite at room temperature and 4 K are described. Cycle life as a function of applied stress is evaluated to provide baseline fatigue data for a specific primary load carrying component of a superconducting motor. Some experimental aspects of fatigue testing at 4 K are discussed.

EXPERIMENTAL PROCEDURE

The material tested was a unidirectional composite of Owens-Corning S-901* glass roving and an epoxy resin, SCI REZ 80*. Specimens were fabricated in the form of 12.38 cm long bands, as shown in Figure 1, using a single material lot and constant fabrication procedure. The specimen is a scaled down version of 68.5 cm long support bands designed for suspension of superconducting motor components in liquid helium. All specimen dimensions, except length, are equal to those of the service component. As specified by the manufacturer, the specimen fiber content is 82% by weight, 69% by volume; the void content is less than 1% by volume, and the density is 2.1 $g \cdot cm^{-3}$ at room temperature.

Using flanged bushings, the specimens were pinned to the grips of a cryostat enabling fatigue tests in a liquid helium environment, as shown in Figure 2. The cryostat frame has a load carrying capability of 100 kN; it consists of two tubular compression members which are bridged at the bottom. The lower halves of these members are AISI 304 stainless steel having a wall thickness of 3.18 mm. The upper sections, which experience a thermal gradient during testing, were fabricated from fiberglass-reinforced plastic tubes, 6.35 mm thick. This lightweight construction provides high specific strength and low thermal conductivity, with some sacrifice of rigidity; the stiffness of the frame and load train at 4 K is approximately 23 kN/mm. Details of this cryostat design were described by Fowlkes and Tobler [3].

---

* Tradenames are used in this report for clarity; in no way does this imply recommendation or endorsement by the National Bureau of Standards, nor does it imply that the material is the best available for the purpose.

Room temperature tests were performed with the apparatus in ambient air at 295 ± 2 K, and at a relative humidity of 30 ± 5%. The tests at 4 K were accomplished using the double-dewar arrangement illustrated in Figure 2. The specimen was enclosed in a fiberglass-reinforced plastic dewar, having a volumetric capacity of 9 liters. This dewar is vacuum insulated, and is surrounded by a fiberglass-epoxy dewar containing liquid nitrogen. Tests began by cooling the specimen and apparatus to 4 K, according to the two and one-half hour cool-down procedure previously described [3]. The liquid level was maintained several inches above the specimen, and was constantly monitored with a carbon-resistor level indicator. Liquid helium was continuously transferred into the cryostat to replenish the amounts evaporated during fatigue tests.

All tests were conducted using a 100 kN closed-loop servo-hydraulic test machine. Replicate tensile tests were conducted at a loading rate of $5.7\ N \cdot s^{-1}$ to determine the nominal fracture strength and load-deflection (P-δ) characteristics of virgin specimens. Load cell and LVDT outputs were used in recording load-versus-actuator displacement curves. The nominal fracture strength, σ_f, was calculated from the maximum load, P_{max}, and the mean cross-section area, 2A, of the unloaded specimen at room temperature:

$$\sigma_f = P_{max}/2A \tag{1}$$

The specimen stiffness, P/δ_S, was obtained by deducting the load frame deflection, δ_F, from the total actuator displacement, δ_T:

$$\frac{P}{\delta_S} = \frac{P}{(\delta_T - \delta_F)} \tag{2}$$

where the load frame stiffness was measured separately by replacing the specimen with a rigid steel block. The nominal or effective value of specimen modulus was also calculated:

$$M_S = \frac{PL}{A\delta_S} \tag{3}$$

where L is the initial specimen length at room temperature, and δ_S is the specimen deflection at a 10 kN load.

The axial fatigue tests were conducted under controlled load, using a sinusoidal load cycle, at frequencies from 25 to 27 Hz. The ratio, R, of minimum/maximum load was 0.1, except as noted in the text. A digital indicator was used to measure the peak loads, which were controlled to within 2% of the specified values.

RESULTS

A representative load-displacement record obtained at 4 K is shown in Figure 3a, and static tensile results are listed in Table 1. There was no measureable change in stiffness or modulus between 295 and 4 K, but tensile strength increased by 28% above the room temperature value of 133.4 kN $\cdot$ cm^{-2}. The scatter in tensile strength at 4 K was higher than at room temperature, with one specimen at 4 K failing at a stress lower than any of the room temperature values. This anomalous result was not included in the average value of fracture strength listed in Table 1: the load-displacement record of the test of this specimen shows a noticeable increment in the displacement without a corresponding increase in the load at a low value of the load, as can be seen in Figure 3b.

The room temperature fatigue results are shown in Figure 4, where the maximum fatigue stress is plotted as a fraction of the static strength. The

data trend and scatter are similar to other results, particularly those reported by Hofer and Olsen [5] for a unidirectional S-994 glass filament-reinforced epoxy. Hofer and Olsen's data pertain to conventional hour-glass specimens having a tensile strength of about 162 kN $\cdot$ cm^{-2}. Although their material exhibited a higher cycle life capability at a given absolute stress value, the results for both composites can be normalized on the basis of differences in static strength as shown in Figure 4. It is also significant to note that these materials at room temperature do not exhibit a fatigue limit at cyclic stress levels as low as 20% of the static strength.

The effect of varying the load ratio was investigated briefly at room temperature where two specimens were fatigued to fracture at R = 0.5. As shown in Figure 4, the cycle life appeared to improve at the higher load ratio; further conclusions are not justified in view of the limited data.

The fatigue data obtained at liquid helium and room temperatures are summarized in Table 2 and Figure 5. These results clearly demonstrate a superior fatigue resistance at 4 K. Two specimens survived 10^6 stress cycles of maximum levels 29.0 and 30.0 x 10^7 N $\cdot$ m^{-2} (17.6% of tensile strength) at 4 K without failure; their tensile strength and effective modulus after cycling were only slightly less than the average values for virgin specimens, as shown in Table 2b. These high values of residual strength and residual modulus indicate that cyclic loading at these levels at 4 K does not significantly degrade the load-bearing capability of these composite specimens. A third specimen failed after 1.49 x 10^4 cycles at a stress level of 71.0 x 10^7 N $\cdot$ m^{-2}, exceeding the room temperature endurance by a factor of 30. A final specimen was cycled for specified intervals at the increasing stress levels listed in Table 2. The results show that the

cycle life at 4 K is at least ten times greater than at room temperature for maximum cyclic stresses from 38 to 82 x 10^7 N · m^{-2}.

Although a reliable S-N curve at 4 K could not be constructed without more extensive data, it appears that the stress level required for failure at a specified number of cycles may approach twice the value required at room temperature. The improvement in fatigue resistance at 4 K exceeds that which might be predicted based on scaling the fatigue stress levels to account for the increase in static strength alone.

Fatigue and tensile specimens fractured at 4 K are shown in Figure 6. Failure invariably occurred at points of tangency where the specimen contacted the bushings. Fatigue cracks initiated concurrently at all four of the points of tangency; the cracks penetrated the specimen ligaments along planes normal to the tensile axis, and delaminations subsequently emanated from the gripped regions. The delaminations propagated gradually in a direction parallel to the loading axis, along the entire length of the specimen. When fatigue damage reached critical proportions the weakest ligament splintered into filaments, which was the failure mode of tensile specimens, as shown in Figure 6. The epoxy at the four points of tangency in specimens fractured in fatigue at both 4 K and 300 K was quite dark, possibly indicating charring. Temperature had no obvious influence on the appearance of these failures.

Specimen deflection at a constant fatigue load increased progressively, as shown in Figure 7 for room temperature specimens fatigued at 25.5 x 10^7 N · m^{-2}. The rate of increase of deflection differed by an order of magnitude for these specimens, as did their fatigue lifetimes, N_f. This suggests that scatter in cycle life is due to specimen-to-specimen variability in resistance to

fatigue damage propagation, as well as initiation. The loss of stiffness was always most pronounced during the last few cycles to failure, and extreme adiabatic heating was also noted in the terminal stages of fatigue.

DISCUSSION

Relating laboratory results to service behavior is a practical problem which was minimized in this study by performing a limited number of tests under conditions nearly equivalent to those of the service application. The results must be regarded as lower bounds on the uniaxial tensile properties of the material itself, since the gripping fixture influenced the results. However, the gripping fixture is a practical one for service applications, and the data reported here are directly applicable in design.

It can be concluded from the 4 K results and known trends between 295 and 20 K [2] that the fatigue and tensile strengths of this material are lower at room temperature than at any cryogenic temperature. In the application under consideration, the component will experience temperatures ranging from 295 to 4 K. The room temperature properties are therefore limiting, and should form the basis for design. In certain applications where a component operates exclusively at cryogenic temperatures, it would also be possible to design conservatively on the basis of room temperature properties. However, a maximum level of design efficiency at cryogenic temperatures requires more extensive low temperature mechanical property data.

In many structural applications, it is essential to monitor fatigue damage and to replace critical components before catastrophic failure becomes probable. The occurrence of delaminations in this composite after

25% of total cycle life provides obvious evidence of degradation. Damage could be detected earlier by dismounting the specimen to examine the surfaces in contact with the bushing. Surface deterioration and discoloration were noted at these locations. The loss of stiffness also provides a means of detecting fatigue damage. Thus, a simple inspection of service components should provide ample evidence of degradation prior to failure.

Cyclic stressing produces specimen heating and agitation of the cryogen. This agitation increases the heat leak into the cryogen due to convection, because the cryogen is splashed into the warmer regions of the cryostat. The heat input to the cryogen from both of these sources increases strongly with displacement. In these tests the helium loss under static load was only 0.15 $\ell \cdot h^{-1}$. This increased during fatigue tests, varying from 7 to 15 $\ell \cdot h^{-1}$, over the range of stress levels investigated.

Adiabatic heating in glass-reinforced plastics results from their high internal friction and low thermal conductivities [6]. Internal temperature rises as high as 70°F were noted in room temperature fatigue tests of such materials [7]. At 4 K, adiabatic heating should be more significant since the thermal conductivity of glass reinforced epoxies is lowered by a factor of three [4]. Furthermore, the temperature in the interior of the specimen depends on the specimen thickness and cycling rate. Since the present data pertain to a specimen thickness and frequency equivalent to service conditions, the effects of adiabatic heating on fatigue resistance here are academic from an applications viewpoint. However, this effect must be accounted for in future tests if fatigue results are to be independent of specimen geometry and test variables.

CONCLUSIONS

From these tests, the following conclusions can be drawn:

1. The tensile strength and fatigue resitance exhibited by a glass roving reinforced epoxy plastic (GFRP) composite material indicate that such composites can be attractive structural materials for cryogenic applications.

2. The fatigue life of a GFRP composite material can be an order of magnitude greater at liquid helium temperature than at room temperature.

3. A measurable decrease in the stiffness of GFRP specimens may precede high cycle fatigue fracture at 300 K.

ACKNOWLEDGMENT

The cooperation of M. Calderon of Airesearch, Torrance, California in providing the specimens and reviewing the manuscript is gratefully acknowledged.

REFERENCES

1. R. P. Reed and A. F. Clark, Eds., "Materials Research for Superconducting Machinery," National Bureau of Standards, Boulder, Colorado, AD 780596 and AD/A 004 586, Nat. Tech. Inf. Serv., Springfield, Virginia (1974).
2. M. B. Kasen, "Mechanical and Thermal Properties of Filamentary-Reinforced Structural Composites at Cryogenic Temperatures-I: Glass-Reinforced Composites", Cryogenics, Vol. 15, No. 4, 230-240 (1975).
3. C. W. Fowlkes and R. L. Tobler, "Fracture Testing and Results for a Ti-6Al-4V alloy at Liquid Helium Temperature," to be published.
4. M. Segimoto, "Qualification Test Results for Glass Filament-Wound Support Bands," Report No. 7581, Structural Composites Industries, Inc., California (Jan. 1975).
5. K. E. Hofer, Jr., and E. M. Olsen, "An Investigation of Fatigue and Creep Properties of Glass Reinforced Plastics for Primary Aircraft Structures," Report M6104, Ill. Inst. Tech. Res. Inst. (Apr. 1967).
6. L. J. Broutman, "Fibre-reinforced Plastics," Chap. 13 in Modern Composite Materials, L. J. Broutman and R. H. Krock, Eds., Addison-Wesley, Massachusetts (1967).
7. R. B. Heywood, Present and Potential Fatigue and Creep Strengths of Reinforced Plastics, Tech. Note. No: Chem. 1337, Royal Aircraft Establishment, Ministry of Supply, London, W. C. 2 (Oct. 1958).

LIST OF TABLES

Table 1. Static tensile properties of S-901 glass/epoxy specimens.

Temperature (K)	Specimen (No.)	Mean X-sect. Area, 2A (cm^2)	Stiffness P/δ_S (10^5 N·m^{-1})	Effective Modulus, M_S (10^9 N·m^{-2})	Nominal Failure Strength, σ_f (10^7 N·m^{-2})
295	1[a]	.3612	N/A	N/A	134.6
	2[a]	.3604	"	"	133.8
	3[a]	.3648	"	"	131.6
	Avg.				133.4
	13	.3677	159	62.8	N/A
	14	.3652	148	61.8	"
	19	.3613	151	60.5	"
	Avg.		153	61.7	
4	4	.3664	160	66.7	158.8
	5	.3664	147	61.1	182.1
	21	.3652	145	60.6	126.7[b]
	Avg.		151	62.8	170.4

[a]Tests performed by the manufacturer [4].

[b]Not included in the average (see text).

Table 2a. Fatigue results for S-901 glass/epoxy at 295 K.

Specimen (No.)	Maximum Cyclic Stress, σ_M (10^7 N·m^{-2})	Fatigue Cycles to failure (No.)
13	25.5	7.246×10^6
19	25.5	5.76×10^5
9	29.3	6.75×10^4
16	29.3	8.36×10^4
18	29.3	7.38×10^4
7	31.0	1.96×10^5
12	31.0	1.42×10^5
20	31.0	7.46×10^5
6	37.9	8.85×10^3
10	37.9	2.22×10^4
11	37.9	2.09×10^4
24	71.0	3.93×10^2
22[a]	41.4	2.00×10^4
23[a]	55.2	5.40×10^3

[a] R = 0.50

Table 2b. Fatigue results for S-901 glass/epoxy at 4 K.

Specimen (No.)	Maximum Cyclic Stress, σ_M (10^7 N·m^{-2})	Fatigue Cycles (No.)	Residual Strength (10^7 N·m^{-2})	Residual Modulus (10^9 N·m^{-2})
8	29.0	1×10^6 (run-out)	139	58.2
17	31.0	1×10^6 "	156	65.8
14	71.0	1.49×10^4 (failure)	N/A	N/A
15[b] - 1	37.9	2.36×10^5 (run-out)	"	"
2	44.8	6.92×10^4 "	"	"
3	55.2	1×10^4 "	"	"
4	62.1	1×10^4 "	"	"
5	69.0	1×10^4 "	"	"
6	82.7	2.52×10^4 (failure)	"	"

[b]Cycled at increasing stress levels.

LIST OF FIGURES

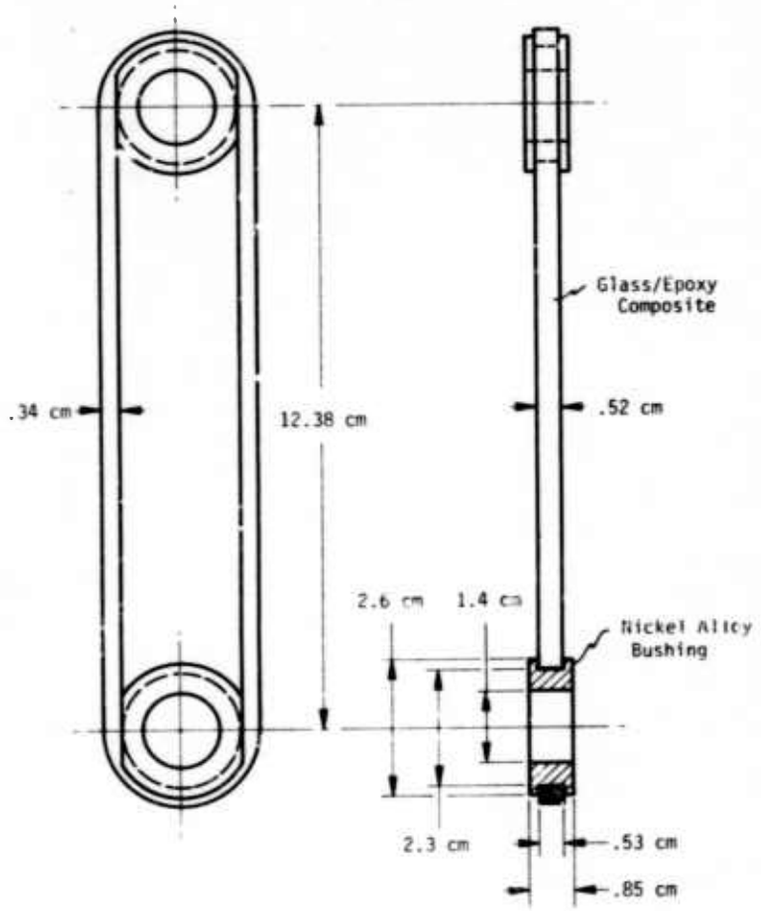

FIGURE 1 - Test specimen geometry.

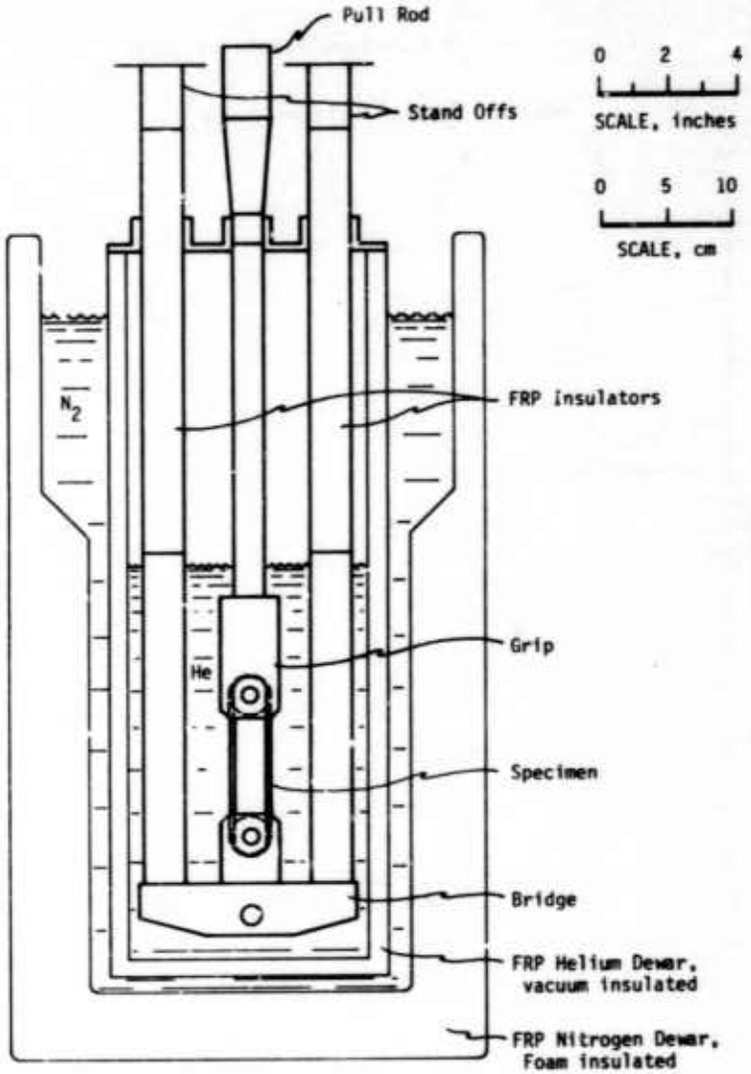

FIGURE 2 - Liquid Helium Fatigue Cryostat.

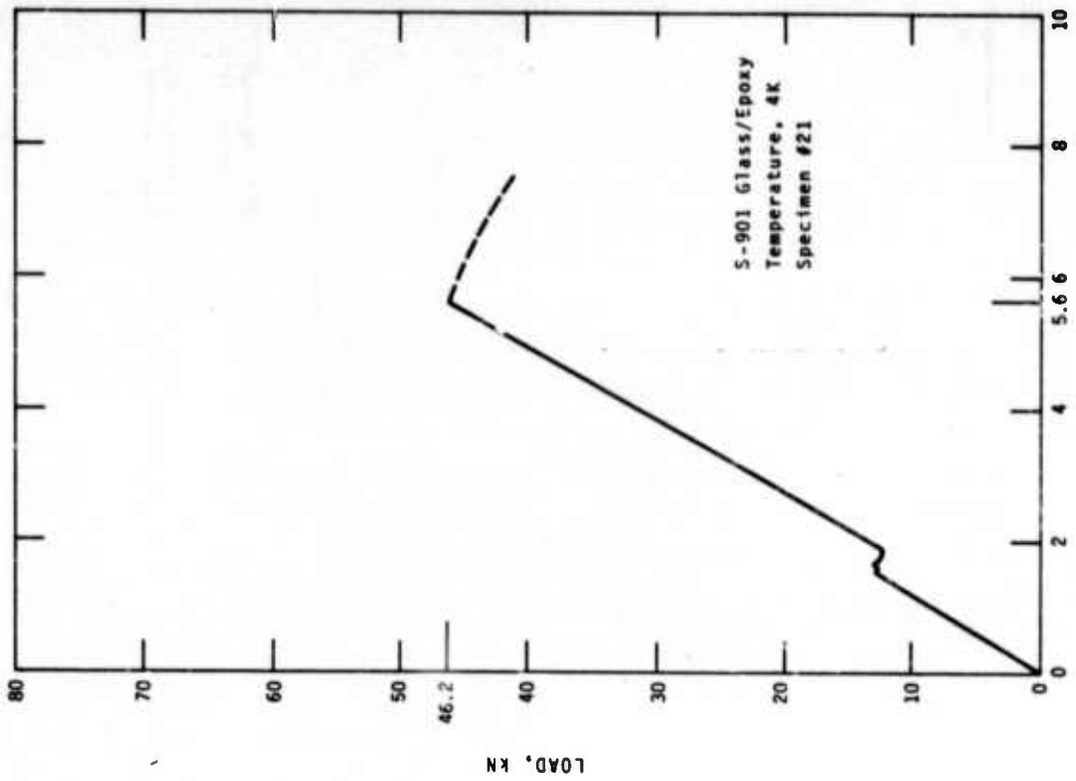

FIGURE 3b-Static test record

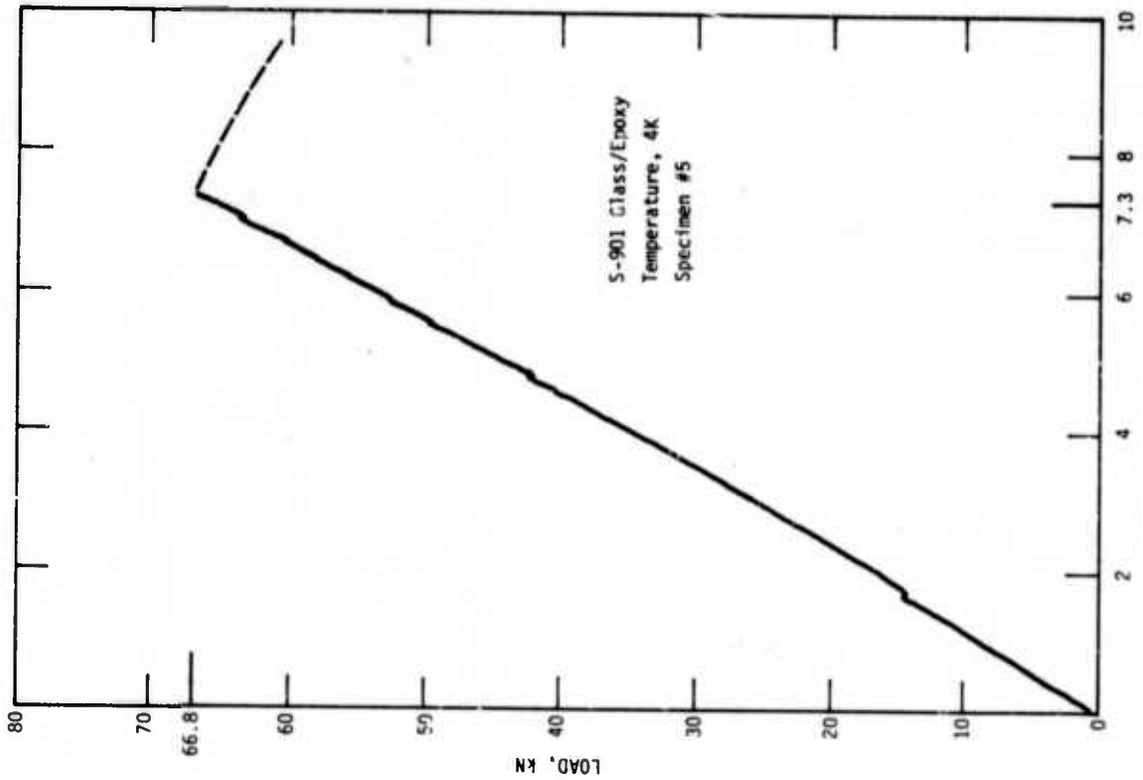

FIGURE 3a-Static test record.

297<

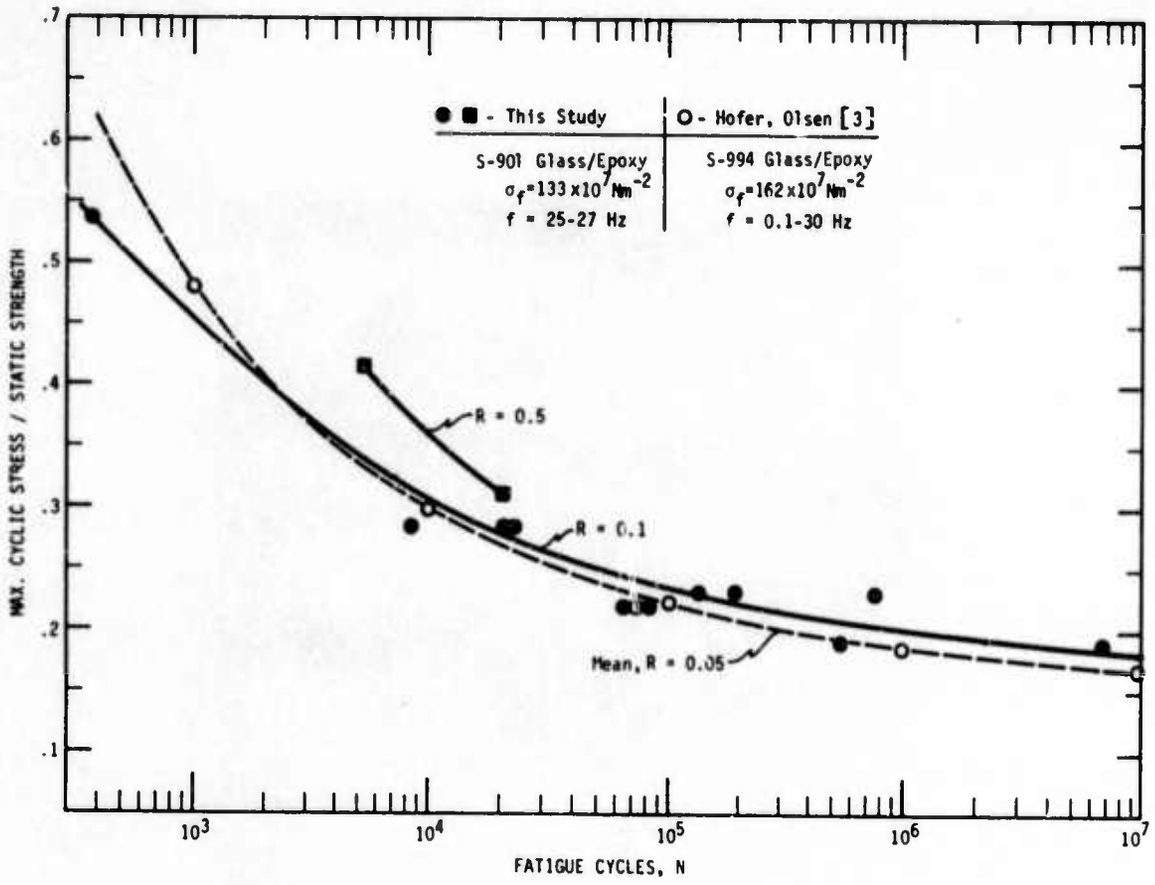

FIGURE 4 - Room temperature fatigue data.

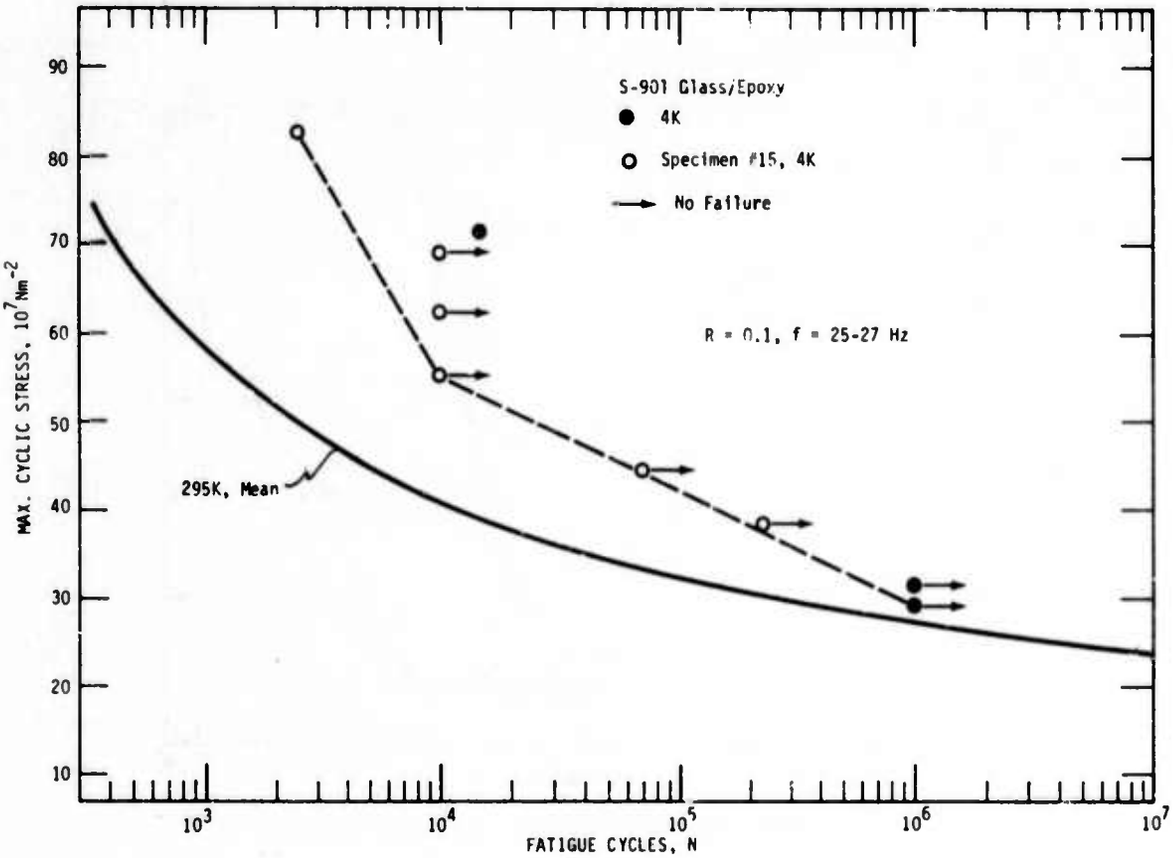

FIGURE 5 - 4K Fatigue results.

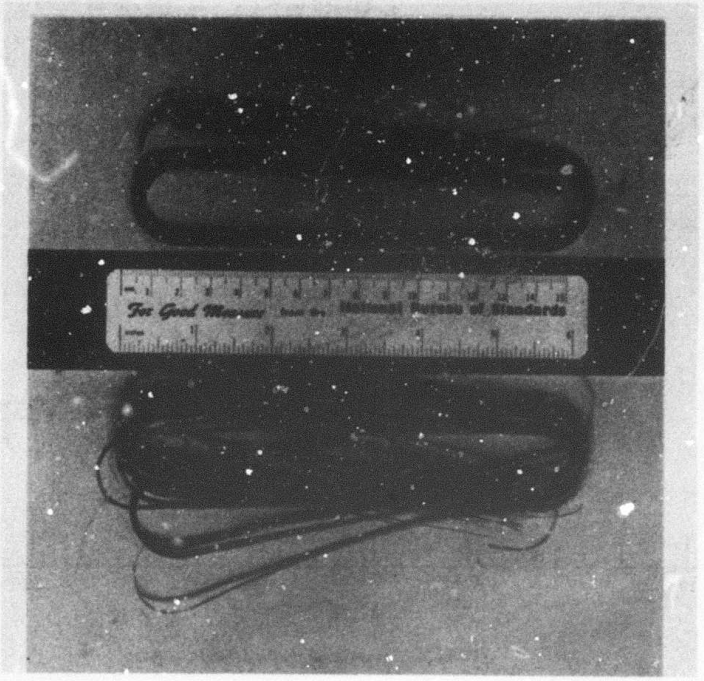

Figure 6. Tensile (lower) and fatigue (upper) failure of specimens tested at 4 K.

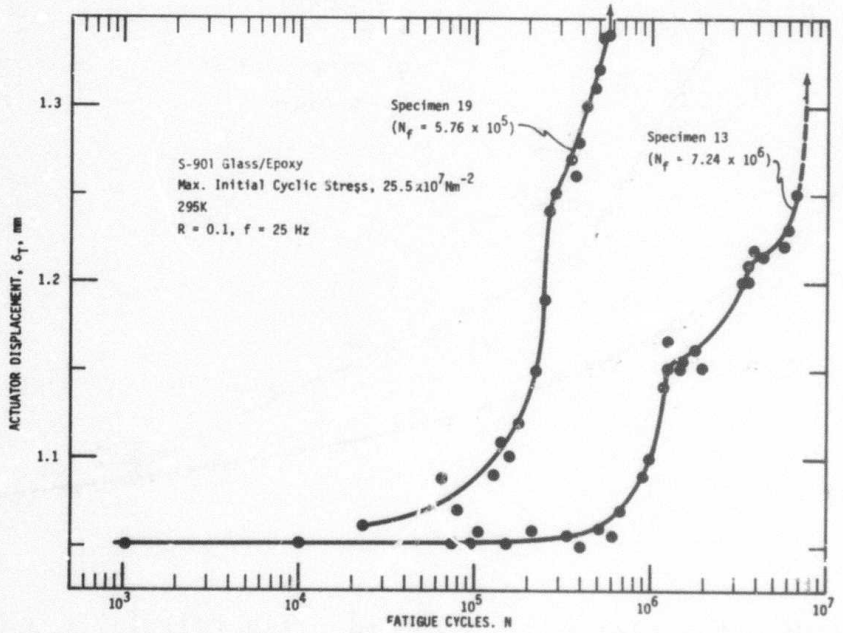

FIGURE 7 - Deflection-versus-cycles for specimens at 295K.

TENSILE AND FRACTURE BEHAVIOR OF A NITROGEN-STRENGTHENED, CHROMIUM-NICKEL-MANGANESE STAINLESS STEEL AT CRYOGENIC TEMPERATURES*

R. L. Tobler and R. P. Reed

Cryogenics Division
Institute for Basic Standards
National Bureau of Standards
Boulder, Colorado 80302

ABSTRACT

J-integral fracture and conventional tensile properties are reported for an Fe-21Cr-6Ni-9Mn austenitic stainless steel which contains 0.28 N as an interstitial strengthening element. Results at room (295 K), liquid nitrogen (76 K), and liquid helium (4 K) temperatures demonstrated that the yield strength and fracture toughness of this alloy were inversely related, exhibiting opposite temperature dependences. Over the temperature range investigated, the yield strength tripled, reaching a value of 12.4×10^8 $N \cdot m^{-2}$ (180 ksi) at 4 K. The fracture toughness, as measured using 3.8 cm thick compact specimens, decreased considerably from 295 to 4 K. During plastic deformation at 295 K the alloy undergoes little martensitic phase transformation, but at 76 and 4 K it transforms extensively to hcp and bcc martensitic products. The amount of bcc transformation product was measured as a function of elongation.

Key words: Cryogenics; fracture; low temperature tests; martensitic transformations; mechanical properties; stainless steel alloys.

Introduction

Recently, austenitic stainless steel strengths have been increased considerably by the substitution of nitrogen and manganese for nickel. In addition to the interstitial and solid solution strengthening, these elements serve to retain, and in some cases, increase the austenite stability with respect to martensitic transformations. Compared to nickel, these elements are more abundant and less expensive. The alloy studied in this report, Fe-21Cr-6Ni-9Mn-0.3N (21-6-9), has a room temperature yield strength nearly twice that of AISI 304. Available tensile and impact data[1-4] suggest that the alloy retains good toughness at low temperatures, leading to consideration of its use for applications benefiting from high strength and toughness.

Accordingly, 21-6-9 is currently being considered for such critical components as the coil for the prototype controlled thermonuclear reaction superconducting magnets and the torque tube for rotating superconducting machinery. To insure satisfactory service life and to compare with other material contenders it is necessary to evaluate the fracture resistance of the alloy. This study presents the first fracture toughness data for this alloy.

Material

The 21-6-9 austenitic stainless steel was provided by Lawrence Livermore Laboratories, Livermore, California. The chemical composition (in weight percent) of this heat is 19.75 Cr, 7.16 Ni, 9.46 Mn, 0.019 C, 0.15 Si, 0.004 P, 0.003 S, and 0.28 N.

The steel was subsequently hot rolled from 30.5 x 30.5 x 10 cm slabs to 50 x 50 x 3.6 cm plate using the following schedule:

soak for 4 hours at 1366 K;

roll from 10 cm to 9.4 cm, screw down (compress) to 9.3 cm;

roll from 9.3 cm to 8.7 cm, screw down to 8.6 cm, rotate 90°;

roll from 8.6 cm to 8.0 cm, screw down to 7.9 cm;

roll from 7.9 cm to 7.4 cm, screw down to 7.3 cm, rotate 90°;

roll from 7.3 cm to 6.9 cm, screw down to 6.7 cm;

roll from 6.7 cm to 6.3 cm, screw down to 6.2 cm, rotate 90°;

roll from 6.2 cm to 5.9 cm, screw down to 5.7 cm;

roll from 5.7 cm to 5.4 cm, screw down to 5.3 cm, rotate 90°;

roll from 5.3 cm to 5.0 cm, screw down to 4.8 cm;

roll from 4.8 cm to 4.5 cm, screw down to 4.3 cm, rotate 90°;

roll from 4.3 cm to 4.2 cm, screw down to 4.0 cm;

roll from 4.0 cm to 3.8 cm, screw down to 3.6 cm.

The final plate temperature after this hot rolling was 1089 K. Each plate was then annealed at 1283 K for 1-1/2 hours and air cooled, followed by an anneal at 1366 K for 1-1/2 hours and a water quench. The resultant hardness was Rockwell B92 and the average grain diameter was 0.16 mm.

Procedure

Tensile:

Tensile specimens were machined following ASTM specification E8-72[5]; the reduced section diameter was 0.635 cm and length was 3.8 cm.

The tensile axis was oriented transverse to the final rolling direction of the plate. Tests were performed using a 44.5 kN screw-driven machine at a cross-head rate of 0.05 cm per minute. The cryostat assembly was designed by Reed.[6]

Measurements at 76 K used liquid nitrogen and at 4 K used liquid helium. Load was monitored with a 44.5 KN commercial load cell while specimen strain was measured with a clip-on, double beam, strain gage extensometer. Yield strength was determined as the flow stress at 0.2% offset plastic strain.

Magnetic:

To detect the amount of ferromagnetic, body-centered cubic (bcc) martensitic phase in the paramagnetic, fcc austenitic matrix a simple bar-magnet, torsion balance was used.[7] Previous measurements on Fe-Cr-Ni austenitic steels established a correlation between the force required to detach the magnet from the specimen and the percent bcc martensite.[7] This same correlation was used for this study to estimate the amount of bcc martensite in the Fe-Cr-Ni-Mn alloy.

Fracture:

The J-integral specimens were 3.78 cm thick compact specimens of a geometry described in ASTM E-399-74.[8] The specimen width, W, and width-to-thickness ratio, W/B, were 7.6 cm and 2.0, respectively. Other dimensions are shown in Figure 1. The notch, machined parallel to the final rolling direction of the plate, was modified to enable clip gage attachment in the loadline.

The J-integral test specimens were precracked using a 100 kN fatigue testing machine and attached cryostat.[9] Specimens were precracked at their test temperature. All precracking operations were conducted using load control and a sinusoidal load cycle at the rate of 20 Hz. Maximum fatigue precracking loads (P_f) were, except for room temperature, well below the maximum load to fracture after precracking (P_{max}) as indicated in Table 1. The maximum stress intensity during precracking (K_f) and the approximate final average relative crack length (the ratio of the crack length, a, to the specimen width, W) are also listed in Table 1.

Subsequent to precracking, the specimens were transferred to a 267 kN (60,000 lb) hydraulic tensile machine for fracture testing. Thus, the 76 and 4 K fracture specimens were warmed to room temperature prior to testing at 76 and 4 K. This was necessary since the load limitations of the fatigue machine precluded loading this alloy to fracture at the low temperatures.

The J-integral tests followed a resistance curve technique similar to that described originally by Begley and Landes.[10,11] A series of nearly identical specimens was tested at each temperature. Each specimen was loaded to produce given amounts of crack extension. The specimens were then unloaded and heat tinted to mark the amount of crack extension associated with a particular value of J. The amount of crack extension could be identified after fracturing the specimen into halves.

Using the approximate solution for deeply cracked compact specimens,[12]

$$J = 2A/B(W-a), \tag{1}$$

the value of J for each test was calculated from the total area, A, under the load-versus-loadline deflection record. The five values of J obtained at each temperature were plotted versus the average crack extension, Δa, which was measured at five locations equidistant across the specimen thickness, and averaged.

The critical value of the J integral, J_{IC}, identified as the J value at the initiation of crack extension, is obtained by extrapolation of the best fit J-Δa curve to the point of actual material separation. Conversion to the plane-strain fracture toughness parameter, K_{IC}, is made using [10-12]

$$K_{IC}^2 = \frac{E}{1-\nu} (J_{IC}) \tag{2}$$

where E is Young's modulus and ν is Poisson ratio. Here E is taken as

the range of the ratio of the length of the crack near the specimen edges (a_e) to the length of the cracks near the specimen centers (a_c) is included in Table I. To satisfy the fracture criteria of ASTM E-399-74[8] a value of a_e/a_c = 0.90 or greater is necessary.

Table 1. Precracking Parameters for Fracture Test Specimens

Test Temperature (K)	P_f/P_{max} x 100 (percent)	K_f (10^6 N·m^2·m$^{1/2}$)	Final Average Relative Crack Length, a/W	a_e/a_c
295	40-45	48-54	0.638	0.90-0.91
76	22-27	52-63	0.640	0.87-0.90
4	30-35	52-63	0.647	0.88-0.89

Results and Discussion

Tensile:

The yield and tensile strengths, elongation, and reduction of area were obtained for the 21-6-9 alloy at 295, 76, and 4 K. These data are summarized in Table 2. The data from this study are combined in Figures 2-4 with the unpublished results of Landon[1] for the same heat, also hot rolled and annealed, and with the results of Scardigno,[2] Malin,[3], and Masteller[4] on annealed bar stock. The correlations are very good except for the ultimate strength data of Masteller. Although his alloy was described as annealed, perhaps it was tested in a worked condition. The spread of the Malin data represent specimens machined from both longitudinal and transverse directions to the rolling direction.

Typical stress-strain curves at each temperature are presented in Figure 6. The large discontinuous yield behavior at 4 K probably is associated with adiabatic specimen heating. Significant local heating is indicated, as the flow stress

drops to stress levels less than that which is sustained at 76 K. An indication of significant local heating is the rise of the reduction of area to values higher than that obtained during 76 K tests. Specimens tested at 4 K developed very local areas of increased plastic deformation, which resulted in sizable specimen necking prior to fracture. These load drops should not be attributed to martensitic phase transformations for three reasons: (1) more extensive transformation was detected in this alloy at 76 K, compared to 4 K (see later discussion) and no discontinuities in the stress-strain mode at 76 K were observed, (2) load drops have been observed in both metastable (e.g., AISI/304) and stable (e.g., AISI 310) austenitic stainless steels at 4 K and no distinction is apparent between the two alloy groups,[13] and (3) in austenitic steels the amplitude and frequency of the load drops at 4K is a function of the strain rate[13] which would be expected if local heating were responsible.

From these data it is clear that the alloy 21-6-9 has a significant decrease of ductility in the temperature range below 195 K, and that tensile elongation continues to decrease to 4 K.

A primary advantage offered by this alloy is its higher yield strength with respect to other austenitic alloys. At room temperature the yield strength of the 21-6-9 alloy is about $3.8 \times 10^8 N \cdot m^{-2}$ (55 ksi), compared to AISI 300 series steel values of 2.1 to $2.5 \times 10^8 N \cdot m^{-2}$ (30-35 ksi). The yield strength of the 21-6-9 steel approximately triples to a value of $12.4 \times 10^8 N \cdot m^{-2}$ (180 ksi) as the temperature is decreased to 4 K. The Fe-Cr-Ni austenitic alloys achieve values about double or triple their room temperature value (60-110 ksi) at 4 K. The strength advantage offered by 21-6-9 is greatest at lower temperatures.

Fracture

The load-versus-loadline deflection curves at 295, 76 and 4 K are shown in Figure 6. The curves at 295 K extended to larger deflections than indicated on the axis of the diagram. The crack remained stable and did not propagate quickly in the J-Δa tests of room temperature tests. The fracture test data are tabulated in Table 3. There are no ASTM E-399-74 valid K_{IC} data; the 5% secant offset data are denoted K_Q. Both the ASTM E-399-74 thickness and crack front curvature criteria are not satisfied at the temperatures 4, 76 and 295 K. Using $B \geq 2.5\ (K_Q/\sigma_y)^2$, a specimen thickness of 4.2 cm at 4 K is required, slightly larger than the 3.8 cm thickness. As shown in Figure 7, the crack front curvature is slightly excessive as the crack lengths of the surface are between 88 and 89% of the average of the internal crack length; 90% is suggested in E-399 as the minimum deviation.

The J versus Δa results at room temperature are plotted in Figure 8. Large extensions were observed due to plastic deformation at the crack tip; only in two specimens at the highest values of Δa was actual material separation noted. These two values fall on the same linear curve as the specimen data that did not exhibit material separation and, furthermore, the entire J versus Δa linear curve has approximately the same slope as that suggested ($J/2\sigma_f$) by Landes and Begley.[10,11] It seems that the response of this extremely ductile material to J integral tests at room temperature is inconclusive, with no well-defined break from the linear portion of the plastic deformation curve observable.

According to the tentative size criterion suggested by Landes and Begley[11], the specimen thickness for valid J_{IC} measurements should satisfy the relationship:

$$B \geq \alpha(J/\sigma_f)$$

where α is a factor greater than 25 and σ_f represents the average of the yield and tensile strengths. In the tests at 295 K, the conditional

critical J values were in the range 1350 to 1450 x 10^2 N · m/m^2. Using the flow stress value of 5.3 x 10^8 N · m^{-2} (76.5 ksi), the J-integral results at room temperature are invalid for the specimen thickness tested here. Apparently, a specimen thickness of at least 6.3 cm (2.5 inches) is needed to insure valid data.

The J-resistance curve at 76 K is also shown in Figure 8. The data fit a regular trend, with the exception of the datum point representing the largest observed crack extension. The curve drawn for the remaining specimens indicates that crack extension initiates at J values in the range $310 < J_{IC} < 350 \times 10^2$ N·m/m^2. The corresponding value of $K_{IC}(J)$, estimated using Equation 2, is 318 N · $m^{1/2}/m^2$ ± 5% (292 ksi $in^{1/2}$).

At 4 K, the alloy approached linear-elastic behavior, but the results of the first three tests failed to satisfy the ASTM validity criteria[8] for direct K_{IC} measurements. These data are listed in Table 3. Three J-Δa tests were conducted and these are included in Figure 8. Although more thorough testing is needed to confirm these, it appears that the J-Δa curve is horizontal. The resulting J_{IC} is about 150 x 10^3 N·m/m^2.

Phase Transformations

Subsequent to tensile tests at 76 and 4 K, it was noticed that the deformed specimens were magnetic. Therefore, these specimens were measured, using bar-magnet, torsion balance equipment, to correlate magnetic attraction with specimen reduction of area. The magnetic readings were converted to percent bcc martensite and the reduction of area converted to elongation, assuming constant volume. These data are plotted in Figure 9 and typical microstructures are shown in Figure 10. Several aspects deserve discussion.

Although not positively identified, it is extremely probable that hcp martensite has formed in the 21-6-9 alloy during low temperature deformation.

The microphotographs after deformation at 4 K (Figure 10) identify transformed regions which are parallel to the (111) slip band traces. These appear identical to the hcp areas identified in earlier research on AISI 304, an Fe-Cr-Ni alloy.[7,13]

The amount of bcc martensite formed is large and only slightly less than that which is formed in AISI 304 at the same temperatures[7,13]. Permeability values of the order of 10 were measured in heavily deformed specimen portions at 76 K. It is difficult to identify bcc martensite in the Figure 10 photomicrographs. Normally, in austenitic stainless steels the bcc martensitic product has an acicular, plate-like morphology with the habit plane of the plate not {111}. Examination of specimen microstructures, typified by Figure 10 indicate that only at {111} band intersections are plate-like and distinctive microstructures observed.

There is clear evidence that the amount of the transformation is suppressed, as a function of either stress or strain, at 4 K when compared to 76 K measurements. This is similar to the Fe-Cr-Ni (AISI 304) alloy martensitic transformation behavior[7,13]. Our earlier work[7,13] also indicated that the hcp martensitic phase was suppressed at 20 and 4 K. Apparently, in the complicated energy balance affecting martensitic transformation for these alloy systems at low temperatures the increase of flow stress and the decrease of dislocation mobility more than offset the gradually increasing free energy difference between the structures.

Finally, it is not clear that the observance of martensitic transformations is deleterious to material application. Normally, the material is used in service at stress levels less than the yield strength; under these conditions no martensitic transformations occur. The complexities and concern usually are discussed when one considers welds and weld techniques. Chemical

segregation and stress concentrations are both more likely, permitting particular sections to be less stable and, locally, stressed above the yield strength. In these situations martensitic products will form.

AISI 304 behaves in a similar manner; it is stable on cooling to low temperatures but transforms to hcp and bcc martensitic products during plastic deformation. But, unlike 21-6-9, the fracture toughness of AISI 304 remains extremely high at 4 K[14] This implies tnat martensitic transformations are not harmful to the fracture toughness of the Fe-Cr-Ni stainless steel. This is not clear in the case of the Fe-Cr-Ni-Mn-N alloy, however, as the toughness is rapidly decreasing at 4 K. For appropriate safety of operation at 4 K, additional research is necessary to understand the effect of martensitic transformations on fracture toughness.

Acknowledgements

The authors would like to thank Dr. P. R. Landon, Lawrence Livermore Laboratories, for kindly supplying the rolled material. Dr. R. P. Mikesell conducted the tensile tests, R. L. Durcholz contributed technical assistance to tensile, fracture, and metallographic preparation, and Dr. M. B. Kasen was responsible for the photomicrographs.

References

1. P. R. Landon, Unpublished data, Lawrence Livermore Laboratories, Livermore, CA (1975).

2. P. F. Scardigno, Masters Thesis, Naval Postgraduate School, Monterey, CA, AD/A-004555 (1974).

3. C. O. Malin, NASA SP-5921(01), Technology Utilization Office, NASA, Washington, D.C. (1970).

4. R. D. Masteller, NASA CR-72638(N70-27114), Martin Marietta Corp., Denver, CO (1970).

5. "Tension Testing of Metallic Materials", E8-72, Annual Book of ASTM Standards, Part 31 (ASTM, Philadelphia, PA, 1973).

6. R. P. Reed, Advances in Cryogenic Engineering, Vol. 7 (Plenum Press, New York, 1962) p. 448.

7. R. P. Reed and C. J. Guntner, Trans. AIME, 230, 1713 (1964).

8. ASTM Standards, E399-74, part 10 (ASTM, Philadelphia, PA 1974).

9. R. P. Reed, R. L. Tobler, and R. P. Mikesell, "Advances in Cryogenic Engineering - ICMC", Vol. 22 (Plenum Press, New York, 1976), to be published.

10. J. D. Landes and J. A. Begley, Westinghouse Research Laboratory Scientific Paper 73-1E7-FMPWR-P3, Pittsburgh, PA (1973).

11. J. D. Landes and J. A. Begley, "Fracture Analyses", ASTM STP 560, (American Society for Testing and Materials, Philadelphia, PA 1974) p. 170-186.

12. J. R. Rice, P. C. Paris, and J. G. Merkle, ASTM STP 536 (ASTM, Philadelphia, PA 1973) p. 231.

13. C. J. Guntner and R. P. Reed, ASM Trans. 55, 399 (1962).

14. R. P. Reed, A. F. Clark and E. C. van Reuth, Eds. "Materials Research for Superconducting Machinery III", AD-A012365/3WM, National Technical Information Service, Springfield, VA (1975).

15. R. R. Vandervoort, Metals Engr. Quart. 12, No. 1, 10 (1972).

List of Figures

List of Tables

Table 2. Tensile Properties of Fe-21Cr-6Ni-9Mn Alloy

Temperature (K)	Yield Strength 0.2% offset (10^8 N·m^{-2})	Tensile Strength (10^8 N·m^{-2})	Elongation 2.5 cm gage length (percent)	Reduction of Area (percent)
295 K	3.50	6.96	61	79
	3.57	7.05	61	78
Average	3.53 (51 ksi)	7.01 (102 ksi)	61	78
76 K	9.13	14.62	42	32
	8.86	14.85	43	41
Average	8.99 (130 ksi)	14.74 (214 ksi)	43	37
4 K	12.58	16.33	16	40
	12.24	16.34		
Average	12.41 (180 ksi)	16.34 (237 ksi)	16	40

Table 3.

Temperature (K)	a/W	J (10^3 N·m/m^2)	Δa (cm)	K_Q[(a)] ($MN/m^{3/2}$)
295	0.638	177	0.013*	58
	0.636	744	0.051*	61
	0.640	905	0.069*	55
	0.635	1355	0.097*	63
	0.642	1423	0.112*	50
76	0.612	261	0	134
	0.634	413	0.028	153
	0.640	499	0.053	131
	0.637	674	0.079	137
	0.645	788	0.091	130
	0.643	698	0.198	130
4	0.670	100	0	---
	0.655	147	0.020	167
	0.670	158[(b)]	0.080	158
	0.645	152[(b)]	N/A	164
	0.648	163[(b)]	N/A	162
	0.643	173[(c)]	N/A	159
	0.656	162	.076	

$$1 \frac{in \cdot lb}{in} = 1.75 \times 10^2 \frac{N \cdot m}{m^2}, \quad 1 \frac{ksi}{in} = 1.099 \times 10^6 \frac{N}{m^2} \cdot m^{-1/2}.$$

(a) from E-399-74 method; invalid due to insufficient thickness.

(b) calculated at the first load discontinuity (pop-in)

(c) calculated at the maximum load.

* refer not to crack opening distances, but to stretch zone distances.

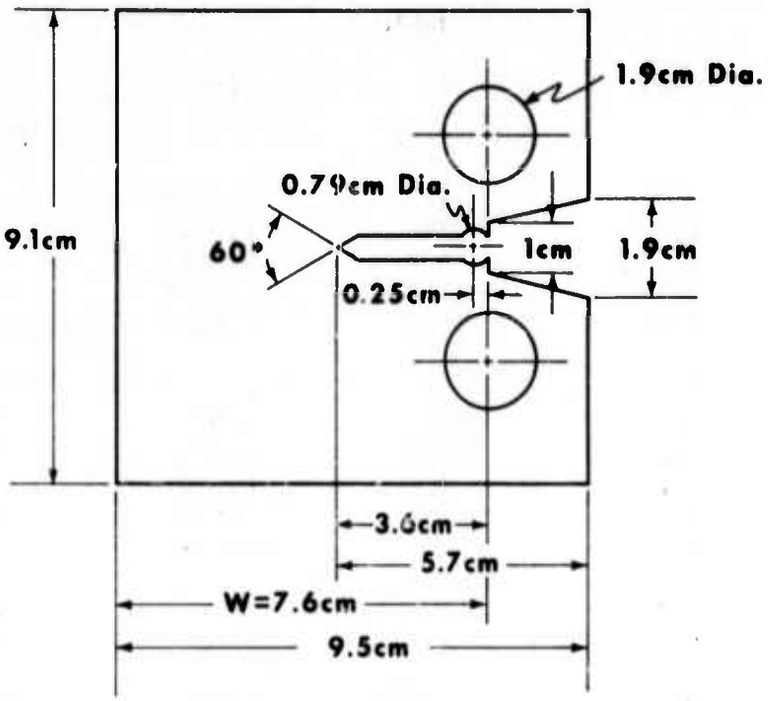

Thickness (B) = 3.8cm

Figure 1. Compact specimen for fracture testing of Fe-19Cr-6Ni-9Mn alloy.

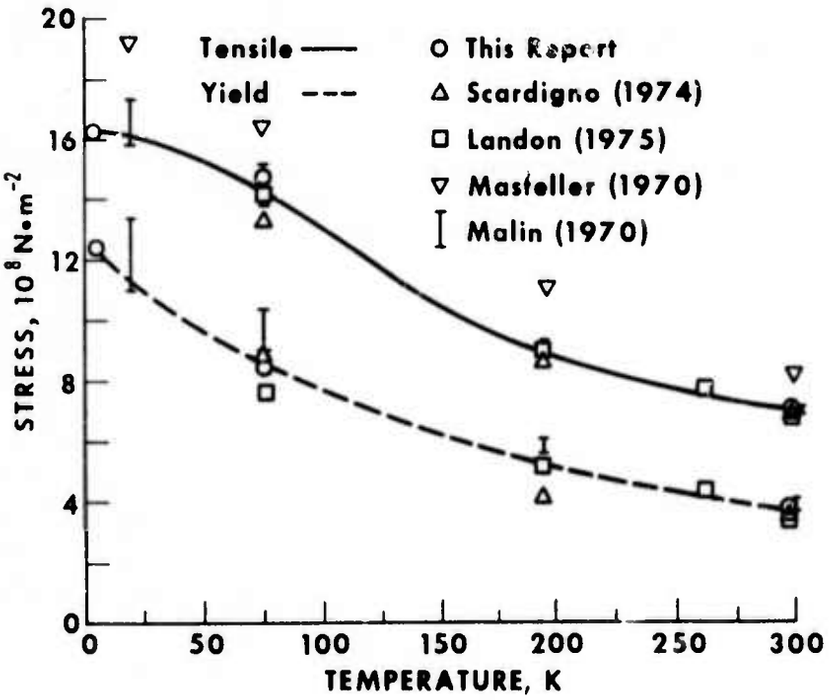

Figure 2. Summary of tensile and yield strength data as a function of temperature for the Fe-21Cr-6Ni-9Mn alloy

Figure 4. Summary of tensile reduction of area as a function of temperature for the Fe-21Cr-6Ni-9Mn alloy.

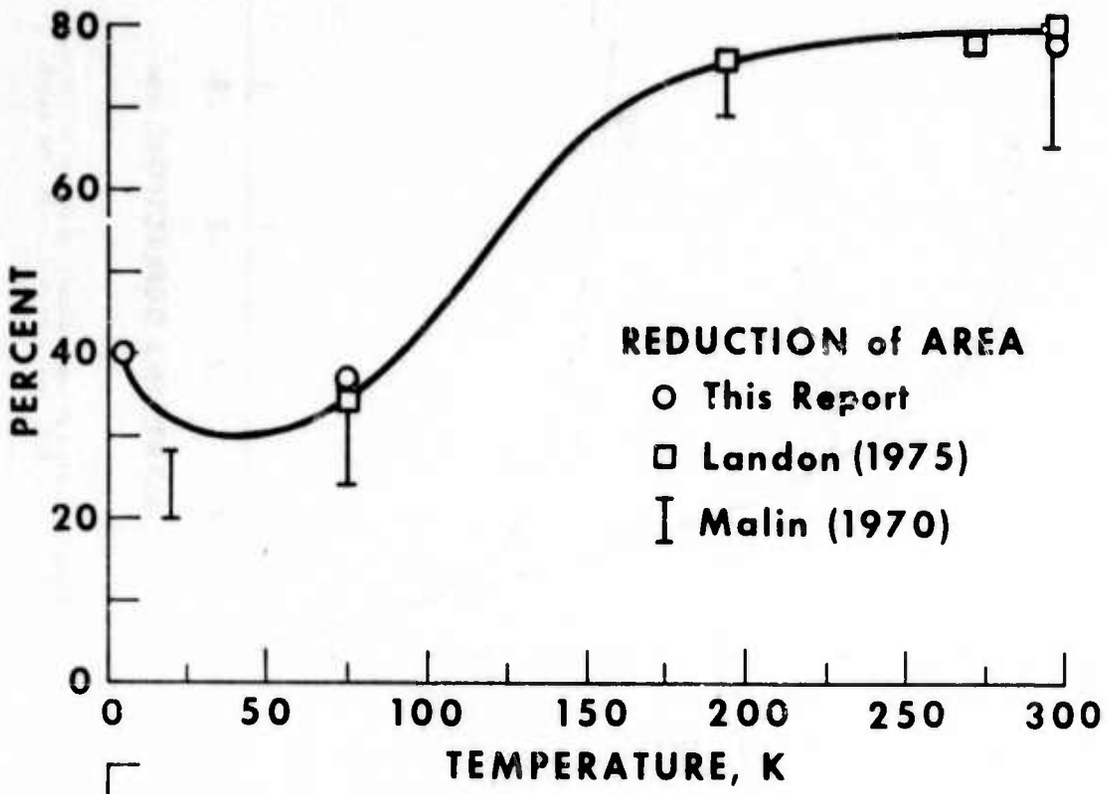

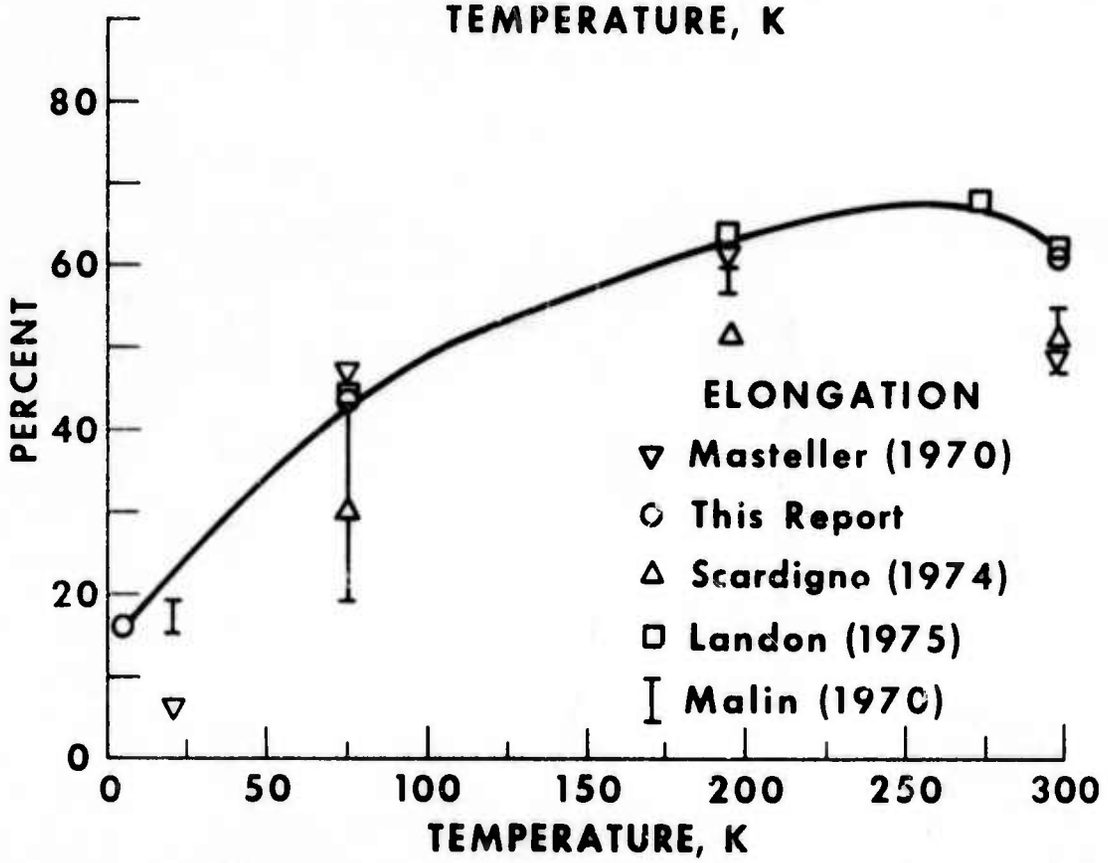

Figure 3. Summary of tensile elongation as a function of temperature for the Fe-21Cr-6Ni-9Mn alloy.

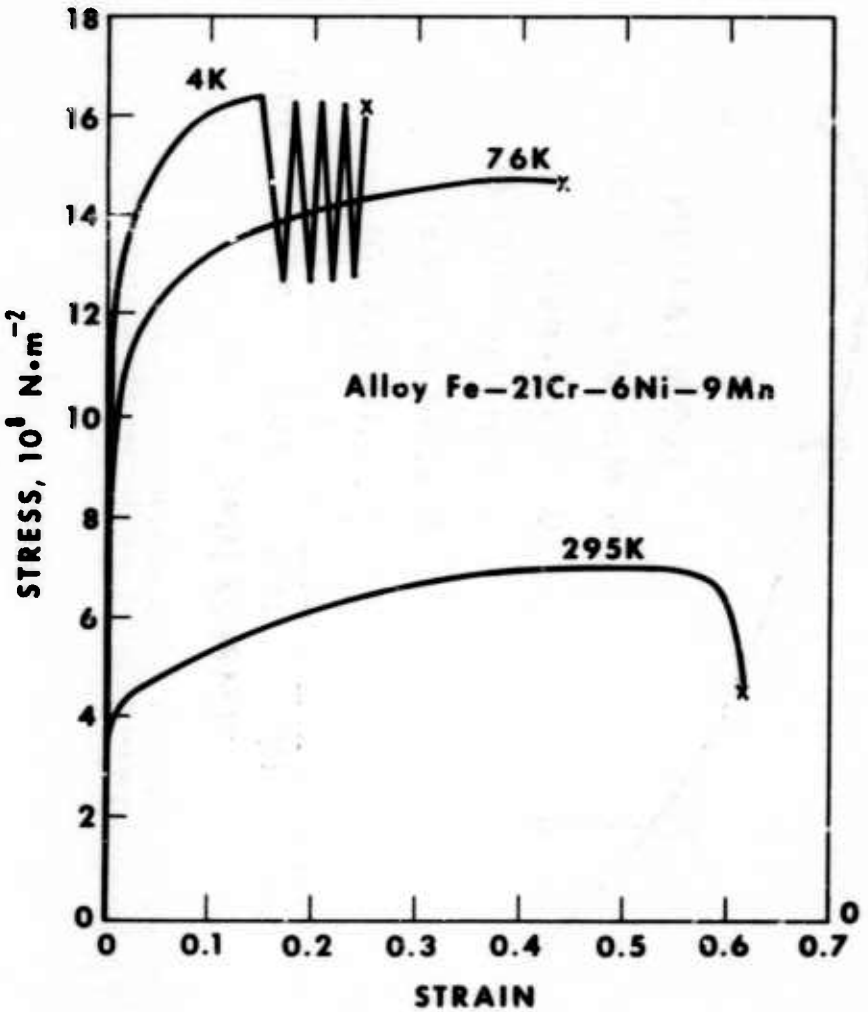

Figure 5. Stress-strain curves for the Fe-21Cr-6Ni-9Mn alloy at 295, 76, and 4 K.

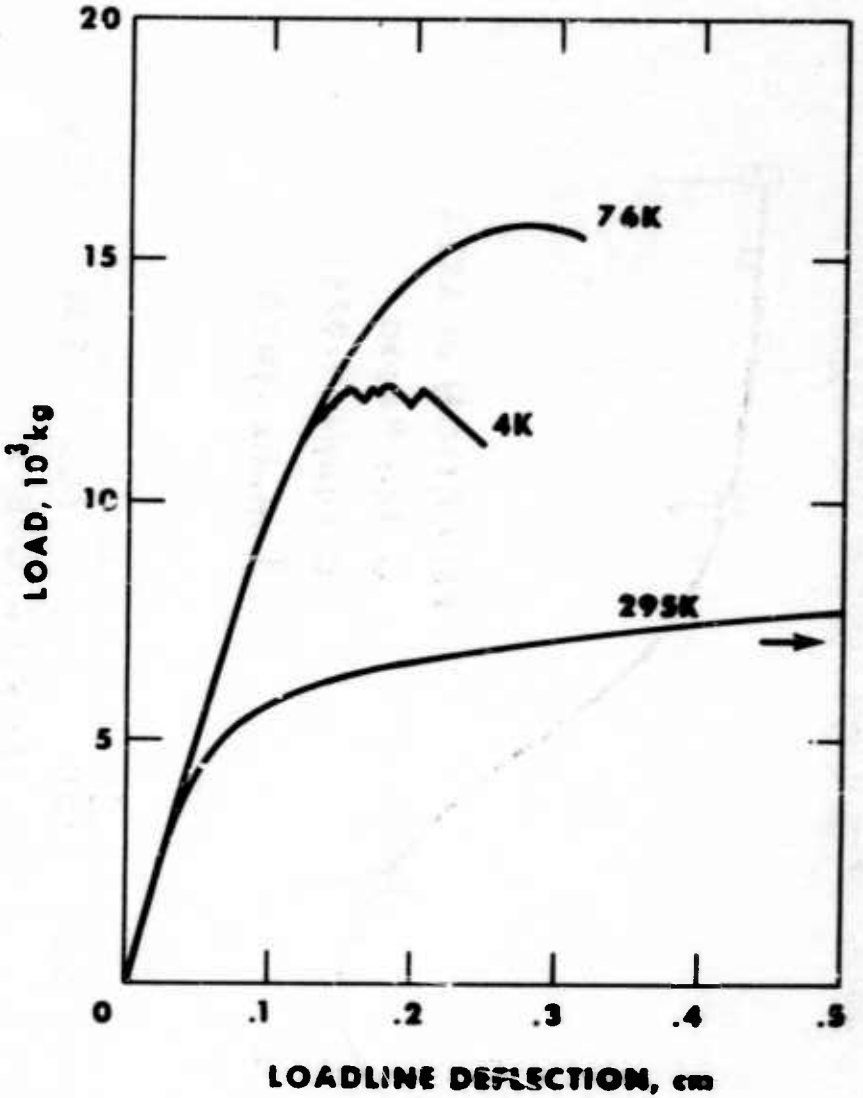

Figure 6. Typical load-deflection curves at 295, 76, and 4 K for annealed Fe-21Cr-6Ni-9Mn alloy.

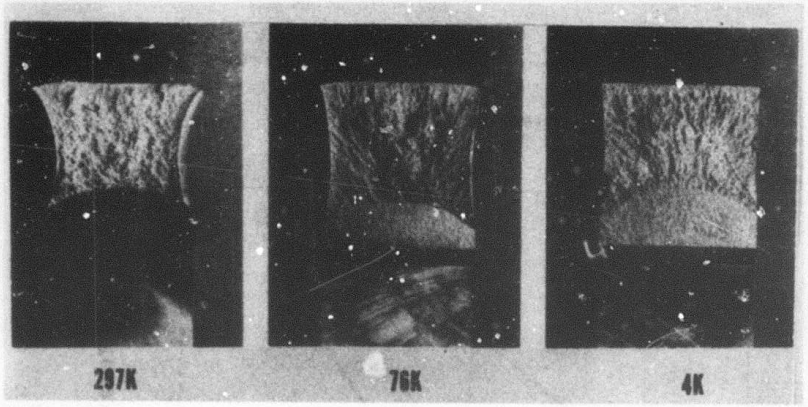

Figure 7. Fracture characteristics of Fe-21Cr-6Ni-9Mn alloy at 295, 76, and 4 K.

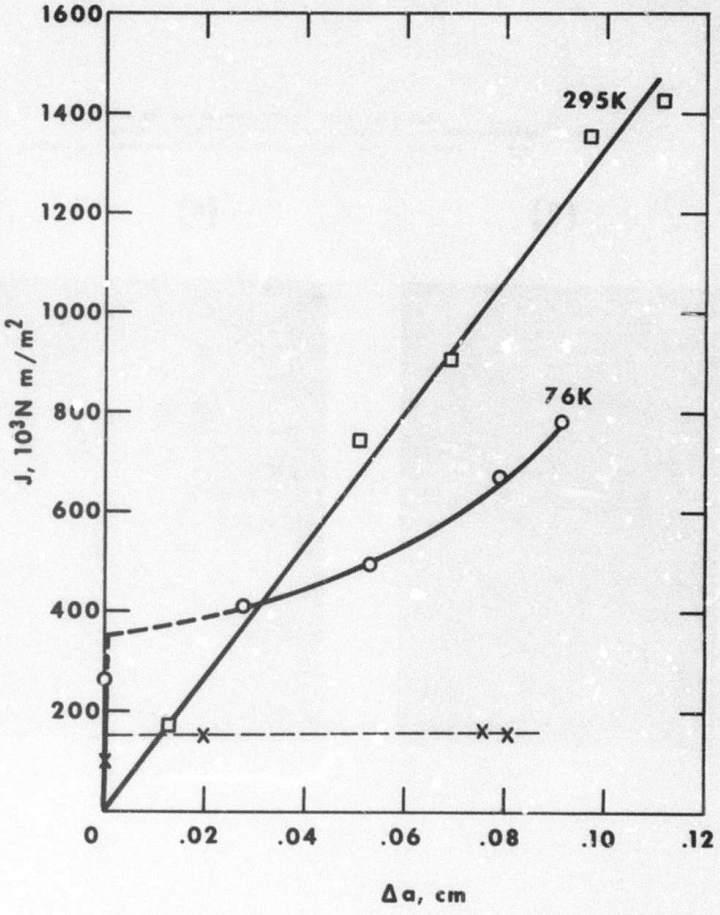

Figure 8. The J-integral as a function of crack extension at 295, 76, and 4 K for annealed alloy Fe-21Cr-6Ni-9Mn.

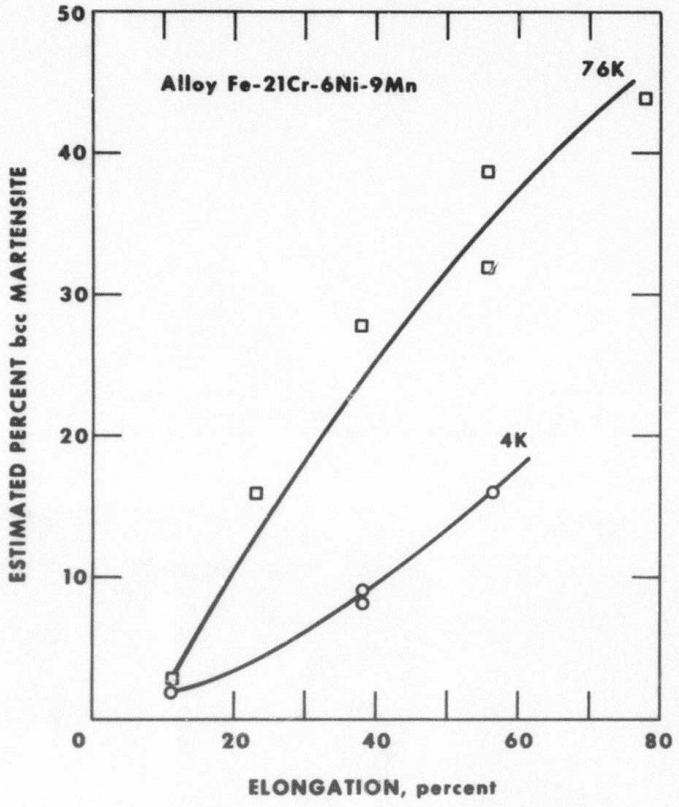

Figure 9. Estimated percent bcc martensite that forms during tensile tests as a function of tensile elongation.

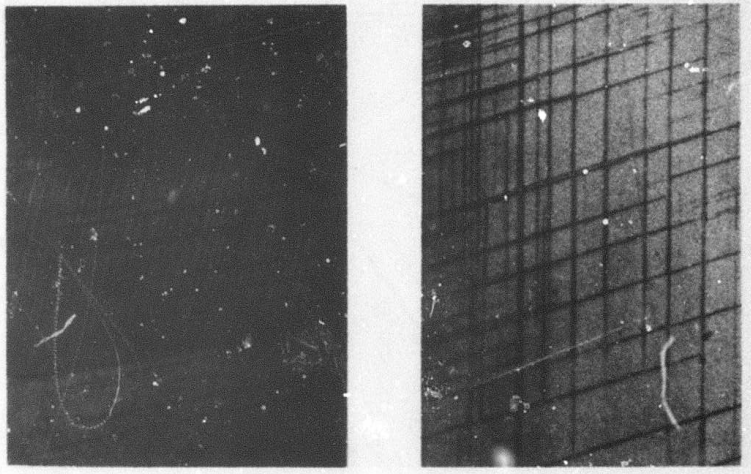

Figure 10. Microstructures of alloy 21-6-9 after deformation at 4 K. Bands lie on {111} austenite planes and probably represent hcp and bcc martensite, (a) 800X, (b) 1200X.

NBSIR

SEMI-ANNUAL REPORT ON MATERIALS RESEARCH IN SUPPORT OF SUPERCONDUCTING MACHINERY

MAGNETOTHERMAL CONDUCTIVITY

L. L. Sparks

Cryogenics Division
Institute for Basic Standards
National Bureau of Standards
Boulder, Colorado 80302

October 1975

Summary: Magnetothermal Conductivity

The thermal conductivity and effect of a magnetic field on the thermal conductivity of S30400 have been determined in the temperature range from 5 to 20 K. The results indicate that a 6366 kA/m (80 kOe) magnetic field reduces the thermal conductivity of this material by 9.2% at 5.5 K and by 6.7% at 19.75 K. The present data at H = 0 compares very well with literature data on similar materials. Several minor modifications have been incorporated primarily to provide better thermal contact between the specimen and the thermometers. Based on the S30400 tests, the precision of the measurements has been improved. The reproducibility of the results now appears to be about 5% in thermal conductivity except at the temperature extremes where it is near 8%.

Contents: Magnetothermal Conductivity

MAGNETOTHERMAL CONDUCTIVITY

L. L. Sparks

Cryogenics Division
Institute for Basic Standards
National Bureau of Standards
Boulder, Colorado 80302

1. Introduction

The objective is to determine the effect of magnetic fields on the thermal conductivity of technically important metals. The need for this information arises from the development of rotating machinery operating at cryogenic temperatures. The existing world's literature on magnetothermal conductivity, $\lambda(H)$, is concerned almost exclusively with scientific materials, e.g., very pure materials and single crystals. A complete bibliography of the subject was given by Sparks and Fickett [1].

The materials studied in this program are being used or are candidates for use in superconducting motors and generators. Optimum design of these machines, which must operate at low temperatures while in magnetic fields, requires a detailed knowledge of how the thermal properties of the constituent materials are affected by a magnetic field. The broad material categories of interest include superconductor stabilizing materials such as copper and aluminum, and structural materials such as nickel alloys, stainless steels, and metallic composites.

Results of the $\lambda(H)$ work were presented at three conferences since the last semi-annual ARPA report: American Physical Society (Denver, March), 14th International Conference on Thermal Conductivity (University of Connecticut, June), and the joint meeting of the Cryogenic Engineering Conference and the International Cryogenics Materials Conference (Kingston, Canada, July). A preprint of the paper presented at the ICMC Conference is included at the end of this report. The work was well received in each case and led to several worthwhile discussions on the effect of a magnetic field on metals.

Several changes have been made in the apparatus and instrumentation in an attempt to improve the precision of the results. The details of these changes are discussed in the procedures section of this report. Tests on S30400 (AISI 304 stainless steel) have been used to evaluate the system with the changes incorporated.

2. Procedures

2.1 Apparatus

The principle components of the $\lambda(H)$ system are shown schematically in figure 1. The basic operation of the system has been described in previous reports [1,2] and will not be repeated here except in relation to the changes.

Thermal conductivity is calculated using the equation

$$\lambda = \frac{\dot{Q}}{A/\ell\ \Delta T} \ .$$

Errors made in the measurement of the temperature difference along the specimen, ΔT, are reflected directly in λ. Perhaps the most difficult problem encountered in measuring small temperature differences is that of making good thermal contact with the temperatures of interest. Before the current changes were instituted, the carbon resistance thermometers, (CRT's), were press fit into wells in the THERMOMETER BLOCK and packed with a thermally conducting grease. The THERMOMETER BLOCKS were machined so that knife edge contacts were made when they were clamped to the specimen. This system had the following shortcomings which are eliminated or minimized by the changes made in the method of sensing the specimen temperatures: (1) It was impossible to be sure that the thermal contacts between the specimen and the THERMOMETER BLOCK and between the THERMOMETER BLOCK and the CRT's were the same

for the upper and lower THERMOMETER BLOCKS; (2) the THERMOMETER BLOCKS were comparable to the specimen in mass and heat capacity. This was the case even though the dimensions of the BLOCKS were as small as possible consistent with the CRT wells and the clamping screw; (3) it was difficult to attach the clamps to the small specimens without introducing some strain in the specimen. The new "thermometer holder", designed to alleviate the problems discussed above, is shown schematically in figure 2. Thermal contact to the specimen is achieved by soldering the 20 AWG copper wire directly to the specimen; this method assures good thermal contact and should be identical for both the upper and lower thermometer stations. Thermal contact and electrical isolation between the copper wire and the CRT is provided by the sapphire chip as shown in the figure. The thermal conductivity of sapphire is similar to that of copper at low temperatures and it is also an electrical insulator. The mass (and heat capacity) of the thermometer attachment system has been significantly reduced which allows a faster time response than was possible before.

Another change in the $\lambda(H)$ system was made to allow better null temperature control between the TEMPERING POST and the specimen. The condition T(specimen) - T(tempering post) = 0 must be maintained in order to eliminate heat flow between the specimen and the tempering post. A differential thermocouple is used as a sensor in the automatic control circuit used to maintain this zero temperature difference. It is essential that the thermocouple be electrically isolated from the system ground and yet be in very good thermal contact with both the POST and the specimen. The thermal and electrical properties of sapphire are again used to advantage as shown in figure 3. The previous method of electrically isolating the junctions was to place cigarette paper between the wires and the surfaces where the temperature was to be sensed.

The resistance of the CRT's had been measured using an a.c. lock-in amplifier as both the bridge power supply and null detector. This system has been replaced, at least for the present time, by a d.c. Wheatstone bridge. Resistance measurements made with the d.c. system are more precise; however, current reversing procedures must be followed which amounts to doubling the number of readings compared to the a.c. system.

2.2 Materials

One alloy, S30400 (AISI 304), was tested during this reporting period. The composition in weight percent of a specimen of this material taken from the same stock as the $\lambda(H)$ specimen is as follows: C = 0.07, Cr = 17.82, Mn = 1.05, Ni = 8.94, P = 0.022, Si = 0.37, S = 0.012, and the balance is Fe. The test specimen was annealed at 1000°C for 1.5 hours in a vacuum of 0.133 Pa. The residual resistance ratio (RRR) for the specimen is 1.43. The Rockwell hardness of material adjacent to the $\lambda(H)$ specimen is B93 in the unannealed condition and B71 in the annealed condition.

3. Results and Discussion

The changes in the method of mounting the thermometers and in reading the thermometer resistances appear to have increased the precision of the temperature measurements. Previously, the calibration of the CRT's by comparison to the calibrated germanium resistance thermometer yielded an analytical representation with an imprecision of 5 mK for the CRT nearest the TEMPERATURE CONTROLLED HEAT SINK and 9 mK for the CRT nearest the SPECIMEN HEATER. The initial tests on S30400 indicate that these imprecisions have been reduced to about 2 mK and 4 mK respectively.

The present data for the thermal conductivity of S30400 at H = 0 and H = 6366 kA/m (80 kOe) are shown in figure 4. Data were also taken at 796 kA/m (10 kOe), but are indistinguishable from the H = 0 data. A comparison of the present zero field thermal conductivity data with data for a similar material indicates that there are no significant systematic errors present in the H = 0 determination. Table 1 shows the compositions of the present specimen and a similar material for which there are low temperature thermal conductivity data [3].

ELEMENT	COMPOSITION (wt. %)	
	S30400	S34700
Cr	17.82	17.17
Ni	8.94	11.52
Si	0.37	0.59
C	0.07	0.057
Mn	1.05	1.34
P	0.022	0.14
S	0.012	0.007
Ni + Ta	--	1.10
Fe	bal.	bal.

Table 1. Comparative compositions of two stainless steels.

A comparison of the thermal conductivities at H = 0 for these materials is given in table 2.

TEMPERATURE	$\lambda_{S34700}/\lambda_{S30400}$
6	0.92
8	0.97
10	1.00
14	1.01
16	1.01
18	1.01

Table 2. Ratio of thermal conductivities of two stainless steels at H = 0.

Clark, et al. [4] found the RRR for their S30400 specimen to be 1.42. The RRR for the present specimen was determined to be 1.43. This excellent agreement indicates that the specimen used by Clark and the present specimen are electrically similar.

The general effect of a magnetic field is to reduce the thermal conductivity as shown in figure 4. The reduction from zero field values caused by a 6366 kA/m (80 kOe) field is 9.2% at 5.5 K and 6.7% at 19.75 K for S30400. Similar data reported earlier [5] show the corresponding reduction in conductivity for N07718 to be 8% at 5.5 K and 3% at 19.5 K; for S31000 the reduction is 20% at 5.25 K and 11% at 19.5 K. The field effect is seen to be slightly greater in the S30400 than in the N07718, as would be expected. The Lorenz numbers for the Ni-Cr alloys are typically higher than those for stainless steels. This indicates a stronger lattice component of thermal conductivity and therefore a smaller magnetic field effect. The present data exhibit a considerably smaller field dependence of thermal conductivity than was observed for the S31000 specimen. The variation in the field effect on the two stainless specimens is not understood at the present time.

4. Conclusions

The zero field thermal conductivity data for S30400 is very close to that taken for a similar steel in a high precision, zero field thermal conductivity system. The reduction in λ of S30400 caused by a 6366 kA/m magnetic field is 9.2% at 5.5 K and 6.7% at 19.75 K.

5. References

1. Sparks, L. L. and Fickett, F. R., Materials research in support of superconducting machinery, National Bureau of Standards, Boulder, Colorado, Cryogenics Division, March, 1974 NBSIR-74-359, AD-780 596/3WM.

2. Sparks, L. L. and Fickett, F. R., Materials research in support of superconducting machinery, National Bureau of Standards, Boulder, Colorado, Cryogenics Division, October, 1974 NBSIR-74-393, AD-A0004586.

3. Hust, J. G., Thermal Conductivity, Electrical Resistivity, and Thermopower of Aerospace Alloys from 4 to 300 K: II AISI 347 Stainless Steel, unpublished NBS Report.

4. Clark, A. F., Childs, G. E. and Wallace, G. H., Electrical resistivity of some engineering alloys at low temperatures, Cryogenics 10, No. 4, 295 (August, 1970).

5. Sparks, L. L., Materials research in support of superconducting machinery, National Bureau of Standards, Boulder, Colorado, Cryogenics Division, April, 1975 NBSIR-75-810, AD-A012365.

List of Figures

List of Figures

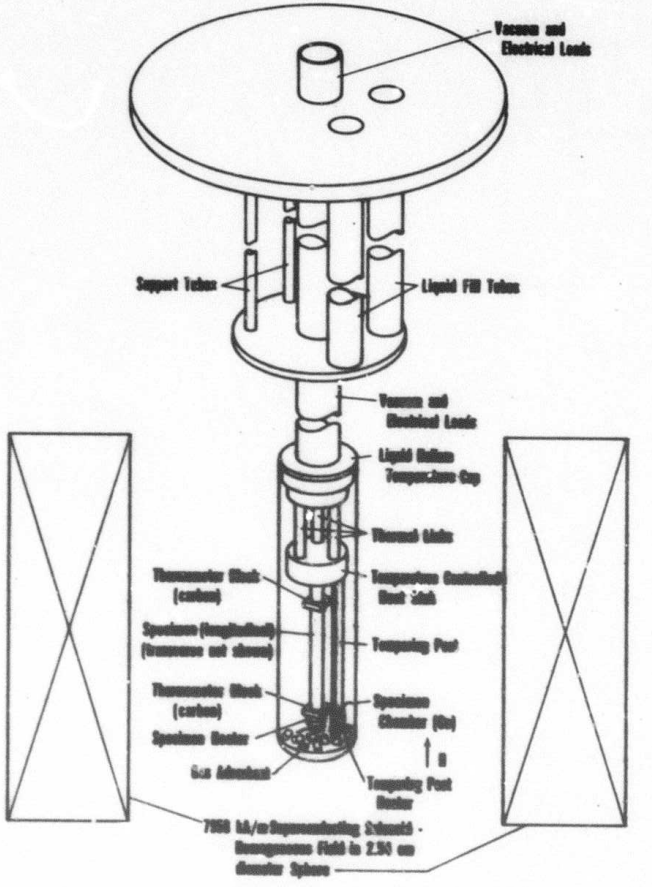

Figure 1. Magnetothermal conductivity probe and magnet.

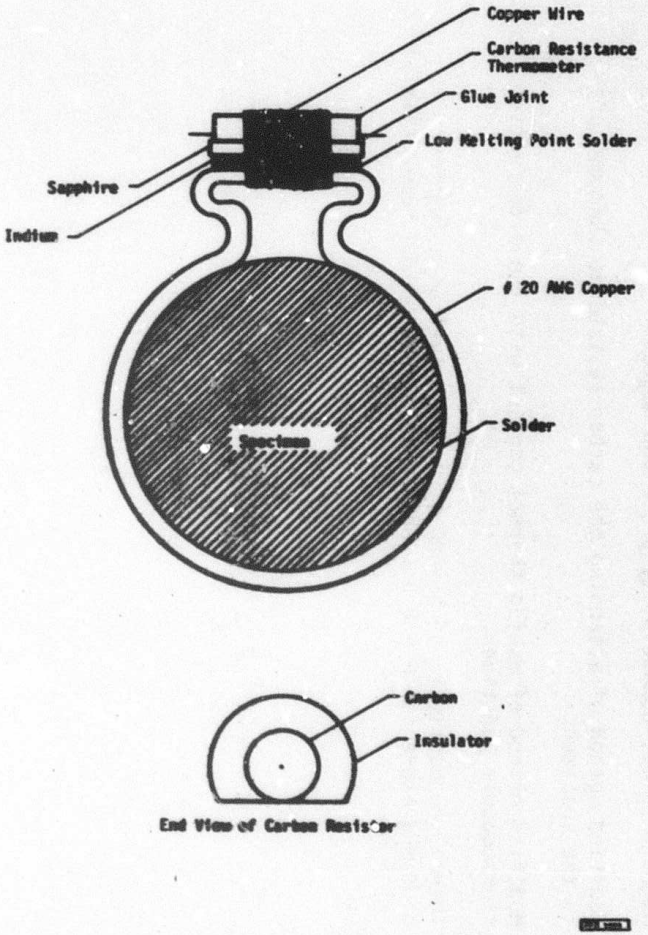

Figure 2. Modified method of attaching the carbon resistance thermometers to the specimen.

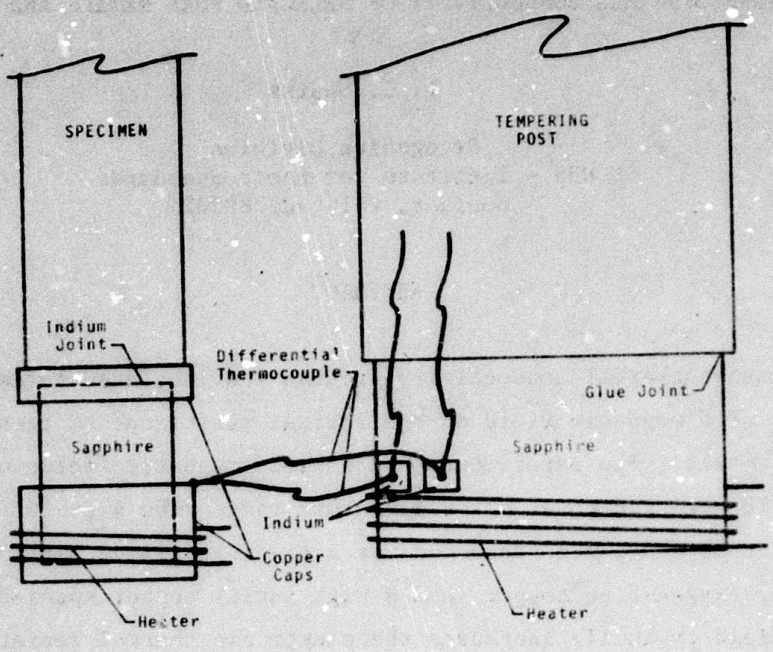

Figure 3. Modified method of making thermal contact with the differential thermocouple junctions.

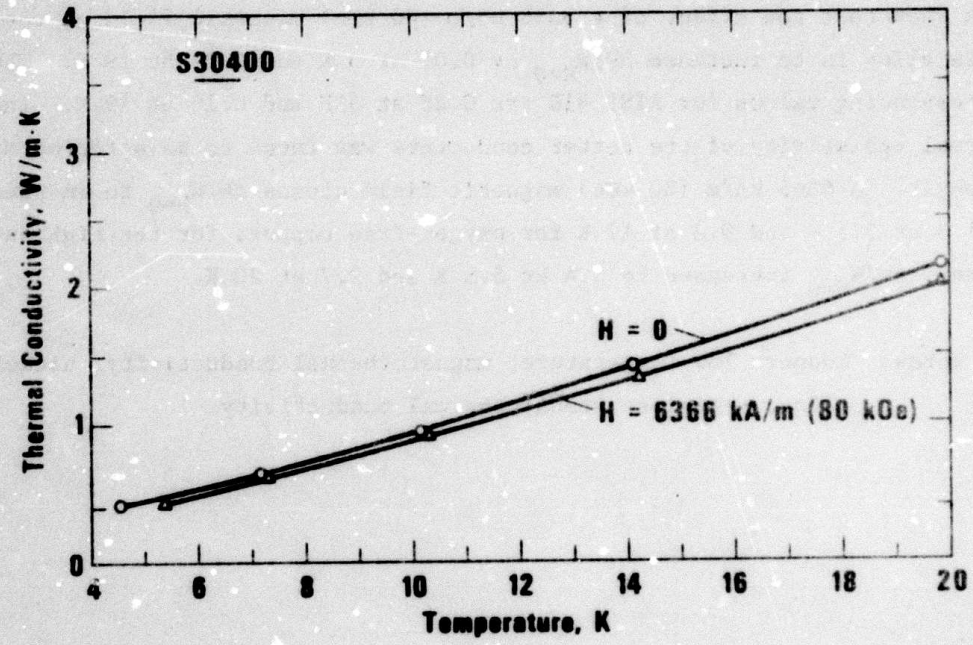

Figure 4. Thermal conductivity of S30400 stainless steel as a function of temperature for H = 0 and 6366 kA/m (0 and 80 kOe respectively).

MAGNETOTHERMAL CONDUCTIVITY OF SELECTED PURE METALS AND ALLOYS

L. L. Sparks

Cryogenics Division
NBS - Institute for Basic Standards
Boulder, Colorado 80302

ABSTRACT

The magnetothermal conductivity program was initiated to determine the effect of a magnetic field on the thermal resistance of technically important metals. The experiments are done in magnetic fields up to 6366 $\frac{kA}{m}$ (80 kOe) and cover the temperature range from 4 to 20 K. The results of this study are presented for a Ni-Cr-Fe alloy, AISI 310 stainless steel, oxygen-free copper, and a high purity copper specimen. A magnetic field typically increases the electronic thermal resistance and thus lowers the total thermal conductivity of a metal. The magnetic field effect at constant temperature is shown by the relative change in thermal resistance, $\Delta W/W_{H=0}$, where ΔW is defined as $W_{H\neq0} - W_{H=0}$. Our experimental data show that the effect of a 6366 kA/m (80 kOe) magnetic field on the Ni-Cr-Fe alloy is to increase $\Delta W/W_{H=0}$ by 0.08 at 5 K and 0.03 at 19 K. The corresponding values for AISI 310 are 0.28 at 5 K and 0.10 at 19 K. The thermal resistivity of the better conductors was found to be affected more strongly. A 6366 kA/m (80 kOe) magnetic field causes $\Delta W/W_{H=0}$ to increase to 1.3 at 5.5 K and 0.8 at 19 K for oxygen-free copper; for the high purity copper, $\Delta W/W_{H=0}$ increases to 3.4 at 5.5 K and 2.7 at 20 K.

Key words: Copper; low temperature; magnetothermal conductivity; nickel alloy; stainless steel; thermal conductivity.

MAGNETOTHERMAL CONDUCTIVITY OF SELECTED PURE METALS AND ALLOYS*

L. L. Sparks

Cryogenics Division
NBS - Institute for Basic Standards
Boulder, Colorado 80302

INTRODUCTION

The objective is to determine the effect of magnetic fields on the thermal conductivity of technically important metals. The need for this information arises from the development of rotating machinery operating at cryogenic temperatures. The existing literature on magnetothermal conductivity, $\lambda(H)$, is concerned almost exclusively with scientific materials, e.g., very pure materials and single crystals. A complete bibliography of magnetothermal conducti. ' was given by Sparks and Fickett.[1]

The materials studied in this program are being used or have potential use in superconducting motors and generators. Optimum design of these machines, which must operate at low temperatures while in magnetic fields, requires a detailed knowledge of how the thermal properties of the constituent materials are affected by a magnetic field. The broad material categories of interest include superconductor stabilizing materials such as copper and aluminum, and structural materials such as nickel alloys, stainless steels, and metallic composites.

APPARATUS AND EXPERIMENTAL PROCEDURES

The experimental determination of the $\lambda(H)$ of metals in high fields is complicated by the requirement that the specimen be contained in a region of homogeneous field. For magnets of reasonable size, this restriction necessitates small specimen lengths and resultant small temperature differences along the specimens. The $\lambda(H)$ probe employed in this study was designed to be used in a superconducting solenoid with a 3.8 cm bore and a 2.5 cm homogeneous (1%) field sphere. Specimen lengths are therefore limited to approximately 2.5 cm.

* Supported by the Advanced Research Projects Agency (ARPA); Department of Defense. ARPA Order No. 2569.

The principle components of the $\lambda(H)$ system are shown in figure 1. A specimen is shown with its axis mounted parallel to the magnetic field. This configuration is used to determine the longitudinal $\lambda(H)$. Provisions for making transverse $\lambda(H)$ measurements (heat flow perpendicular to the direction of the field) have been included in the system design.

The basic operation of the system involves balancing electrical power supplied to three heaters with the heat leak to the liquid helium bath via the THERMAL LINKS (capitalized parts refer to figure 1). The electrical heaters were wound, one each, on the TEMPERATURE CONTROLLED HEAT SINK (TCHS), the SPECIMEN, and the TEMPERING POST. The power supplied to the TCHS determines the approximate temperature of the specimen; the SPECIMEN HEATER is used to establish a temperature gradient along the specimen; and the TEMPERING POST HEATER is used to reduce the temperature difference between the specimen and the tempering post to less than $\pm$ 5 mK. The TEMPERING POST and TCHS heaters are automatically controlled during all tests while a constant current is supplied to the SPECIMEN HEATER.

The thermometers used in the probe are three 1/8 watt, 100 ohm Allen Bradley* carbon resistors (CRT's) and a single calibrated germanium resistor (GRT). The CRT's are located, one each, in the TCHS, and the two THERMOMETER BLOCKS. The GRT is located in the TCHS and is used for zero-magnetic-field calibration of the CRT resistors. The effect of the magnetic field on the resistance of the CRT's is taken to be that published by Neuringer and Shapira[2]. Resistance measurements on the two specimen CRT's are made using a lock-in amplifier as both detector and power supply for an AC bridge. Both absolute and difference resistance measurements are possible using this system.

The thermal conductivity of a specimen is computed from the specimen geometry (Area/length), the specimen heater power ($\dot{Q}$), and the measured temperature difference along the specimen (ΔT). The relationship of λ to these parameters is given by

$$\lambda = \frac{\dot{Q}}{\frac{A}{\ell}\Delta T} . \qquad (1)$$

* The use of trade names of specific products is essential to a proper understanding of the work presented. Their use in no way implies any approval, endorsement, or recommendation by the National Bureau of Standards.

A series of measurements of ΔT and $\dot{Q}$ at various fields* ($C \leq H \leq 6366$ kA/m or 80 kOe) and temperatures ($4 < T < 20$ K) result in the data presented in this report.

MATERIALS

A total of four materials have been tested--Ni-Cr-Fe alloy UNS-N07718, oxygen-free copper UNS-C10200, stainless steel UNS-S31000, and a high purity copper referred to as NBS-B stock 7. UNS-N07718 was tested in the age-hardened condition with a Rockwell hardness of C39 and an average grain diameter of 0.06 mm. The composition in weight percent for this material is: Ni = 54.57, Cr = 18.06, Fe = 17.08, Nb + Ta = 5.12, Mo = 3.18, Ti = 0.85, Al = 0.44, Mn = 0.29, Si = 0.24, Cu, C, and S < 0.1%; the residual resistance ratio ($RRR = R_{273K}/R_{4K}$) is 1.06. The UNS-S31000 stainless steel was measured in the cold worked condition; its Rockwell hardness is B77 and its RRR = 1.27. The composition in weight percent for this material is: C = 0.13, Mn = 1.72, P = 0.016, S = 0.018, Si = 0.84, Cr = 24.47, Ni = 20.44, and Fe balance. Both polycrystalline copper specimens were vacuum annealed at 850°C for one hour. RRR for the UNS-C10200 copper specimen is 107. The electrical resistivity of the NBS-B stock 7 copper specimen was too low to be measured in the $\lambda(H)$ system; however, extensive work by Fickett[3] on the electrical resistivity of this copper stock indicates that RRR = 1520 for heat treatments similar to that of our specimen.

RESULTS

The effect of a magnetic field on the thermal conductivity of UNS-N07718 is shown as a function of temperature in figure 2. Data are shown only for 0 and 6366 kA/m (80 kOe) fields; curves for H = 796, 1592, and 3183 kA/m (10, 20, and 40 kOe respectively) fall between the two curves shown. The estimated 10% uncertainty of a single data point would indicate that the data at 0 and 6366 kA/m (80 kOe) are indistinguishable. However, the curves drawn through the data points indicate a definite trend to lower thermal conductivities at 6366 kA/m (80 kOe). The zero field data for UNS-N07718 is within 10% of the zero field data by Hust, et al.[4] for a similar Ni-Cr-Fe specimen.

Preliminary data for the thermal conductivity as a function of temperature for UNS-S31000 stainless steel are shown in figure 3. Again, only the 0 and 6366 kA/m (80 kOe) curves are shown.

---

* The International System of Units (SI) designation for magnetic field strength is ampere per meter, and this unit is used throughout this paper. The more conventional unit of magnetic field strength, the oersted, is also given. Conversion of oersteds to amperes/meter is accomplished by multiplying oersteds by $1000/4\pi$.

The thermal conductivity and magnetic field effect are shown in figure 4 for UNS-C10200 copper. To my knowledge there are two other sources of zero field thermal conductivity data for similar copper in the literature. Powers, et al.[5] give no RRR for their specimen, which has a conductivity about 50% lower than these data at 20 K. Hust and Giarratano[6] find a conductivity about 90% higher than these data for a specimen whose RRR = 230. This range of results is indicative of the sensitivity of the thermal conductivity in this temperature range to trace impurities and heat treatment. Fevrier and Morize[7] measured the magnetothermal conductivity of two copper wires with RRR = 62 and 162 near 4 K. Our data fall generally between the curves for their two specimens as one would expect.

Data for NBS-B stock 7 copper are shown in figure 5. The experimental points at H = 0 represent averages while the experimental points for H ≠ 0 are single data points. The extremely high conductivity at zero field is near the limit of what can be measured in the present system. Repeat runs and data averaging were used to increase the reliability of the zero field results. The source of the curve drawn through the H = 0 data will be discussed later in this paper.

DISCUSSION

Our data indicate that a 6366 kA/m (80 kOe) magnetic field reduces the thermal conductivity of our UNS-N07718 specimen by 8% at 5.5 K and by 3% at 19.5 K. An estimate of the electronic contribution to the thermal conductivity of this alloy can be made using the Lorenz ratio ($L = \rho\lambda/T$) given by Hust and Sparks,[8] and $L_o = 2.4 \times 10^{-8}\ V^2/K^2$. This estimate indicates that the electrons carry roughly 25% of the heat flow at 5 K and 18% at 19 K. The Lorenz numbers for stainless steels are typically lower than those for Ni-Cr-Fe alloys by approximately a factor of 2. This would suggest a larger electronic component in stainless steels, and consequently a larger field effect. The effect of a 6366 kA/m (80 kOe) field on the UNS-S31000 stainless steel specimen is to reduce the conductivity by 20% at 5.25 K and 11% at 19.5 K as determined at the extremes of temperature as shown in figure 3. At intermediate temperatures the field appears to have little effect on the thermal conductivity, i.e., the H = 0 and H = 6366 kA/m (80 kOe) data are the same within the stated experimental uncertainty. This behavior was unexpected and is unexplained at the present time. Further work on similar alloys should help to determine whether the observed behavior is due to some scattering phenomenon or possible experimental error.

The zero field thermal conductivity of the present data (figure 4) for UNS-C10200 copper exhibits a nearly linear decrease with decreasing temperature. This is the behavior expected for impurity scattering of electrons. The effect of the magnetic field is to reduce the thermal conductivity of our UNS-C10200 copper specimen by 45% at 6366 kA/m (80 kOe) and 19 K and by 60% at 6366 kA/m (80 kOe) and 5 K.

The very high thermal conductivity of the NBS-B stock 7 copper specimen causes experimental difficulties that result in lower accuracy in the zero field runs than was the case for the lower conductivity materials. The solid curve shown in figure 5 for H = 0 was derived using the relationship[9]

$$1/\lambda = W = AT^n + B/T = 3.02 \times 10^{-8}\ T^{2.55} + 4.7 \times 10^{-4}/T. \qquad (2)$$

This equation represents the experimental data within the experimental accuracy; the units of W are mK/W. The effect of a magnetic field is included in figure 5. The anomalous decrease shown in this figure for λ at 1592 kA/m (20 kOe) and high temperatures is probably not real; the single data point at 21 K appears to be bad, but no reason can be found to discard it. Figure 6 presents the relative change in thermal resistivity

$$\Delta W/W_{H=0} = (\lambda_{H=0} - \lambda_H)/\lambda_H \qquad (3)$$

as a function of magnetic field. The high temperature, the 1592 kA/m (20 kOe) data have been ignored in this figure due to its anomalously low value. The result is that, although the exact placement and shape of the knee is somewhat questionable, there is no doubt a rapid decrease in slope of $\Delta W_{H=0}$ in the 796 to 3183 kA/m (10 to 40 kOe) range. A similar plot of $\Delta W/W_{H=0}$ for UNS-C10200 copper is shown in figure 7; there is no rapid change in the slope of $\Delta W/W_{H=0}$ for this material. A magnetic field should affect the electronic conductivity strongly whenever $\omega\tau \geq 1$ where ω is the angular frequency and τ is the relaxation time. ω is proportional to the magnetic field as indicated by the cyclotron relationship $\omega = eH/mc$. Further, τ (high purity copper) > τ (low purity copper), so that with increasing fields $\omega\tau$ becomes large for the high purity stock 7 copper before it does for the UNS-C10200 copper specimen; consequently, the effect of a magnetic field should be seen at lower fields for the stock 7 copper than for UNS-C10200 copper. A comparison of the data in figures 6 and 7 shows this to be the case.

In conclusion, the effect of a magnetic field on structural alloys, such as the Ni-Cr-Fe and stainless steel reported here, is relatively small. The results are not inconsistent with estimates of the possible field effects using Lorenz ratio data. Good conductors such as the two copper specimens show greater field effects which are to be expected due to the large electronic component of the thermal conductivity.

REFERENCES

1. L. L. Sparks and F. R. Fickett in: "Materials Research in Support of Superconducting Machinery," Nat. Bur. Stand. NBSIR-74-359 (March 1974). Available from NTIS, AD-780 596/3WM.

2. L. J. Neuringer and Y. Shapira, Rev. Sci. Instrum., 40(10): 1314 (1969).

3. F. R. Fickett, "A Preliminary Investigation of the Behavior of High Purity Copper in High Magnetic Fields," Annual Report to INCRA (August 1973).

4. J. G. Hust, D. H. Weitzel and R. L. Powell, J. Res. Nat. Bur. Stand. (U.S.), 75A(6): 269 (1971).

5. R. W. Powers, D. Schwartz and H. L. Johnston, "The Thermal Conductivity of Metals and Alloys at Low Temperatures I. Apparatus for Measurements between 25° and 300°K. Data on Pure Aluminum, OFHC Copper, and L Nickel," Ohio State University, TR 264-5 (1951).

6. J. G. Hust and P. J. Giarratano in "Materials Research in Support of Superconducting Machinery," Nat. Bur. Stand., NBSIR-74-393 (October 1974).

7. A. Fevrier and D. Morize, Cryogenics, 13: 603 (1973).

8. J. G. Hust and L. L. Sparks, Nat. Bur. Stand. (U.S.) Tech. Note 634, (February 1973).

9. H. M. Rosenberg, Low Temperature Solid State Physics, Oxford University Press, London (1963), p. 117.

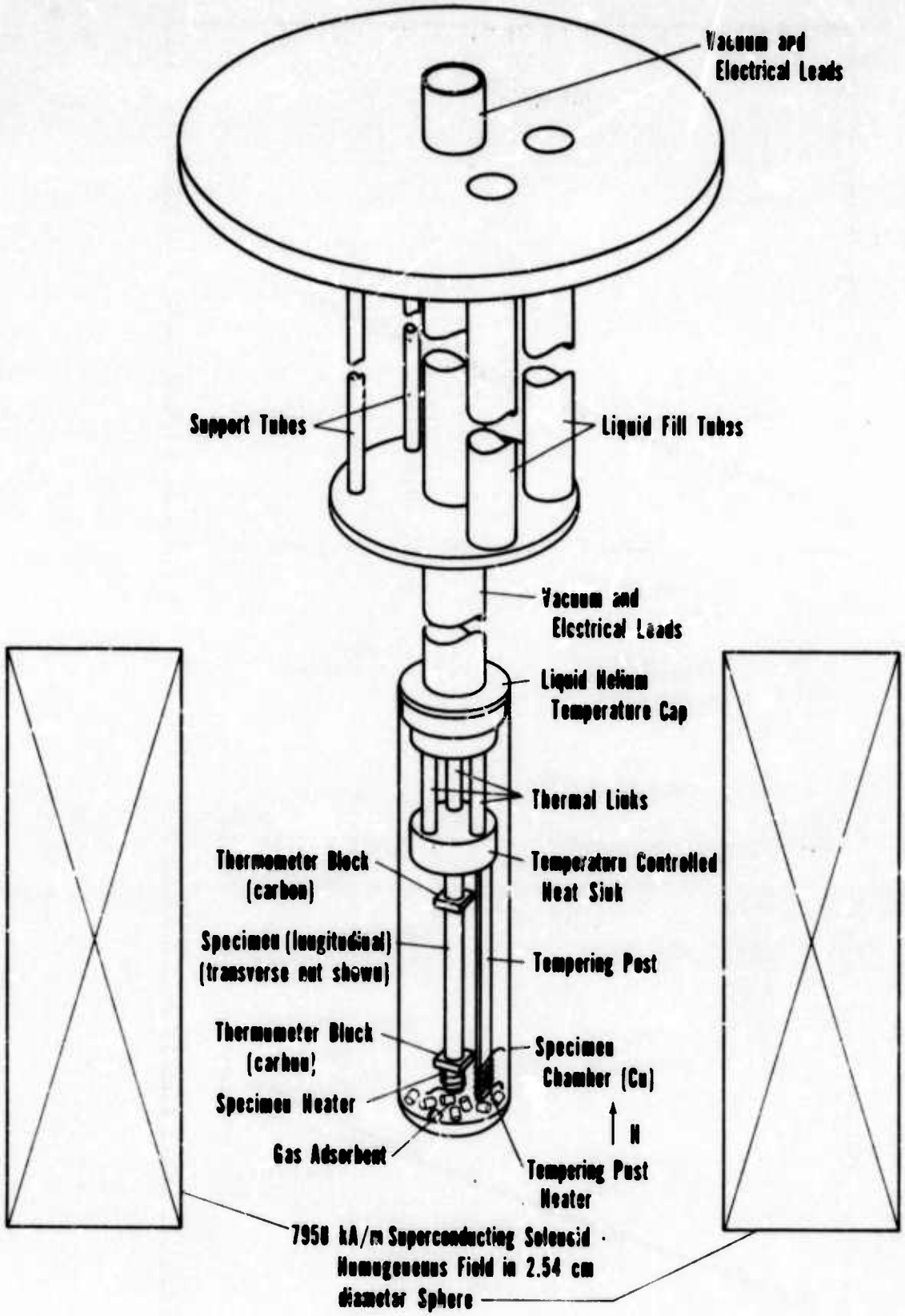

Fig. 1. Magnetothermal conductivity probe and magnet.

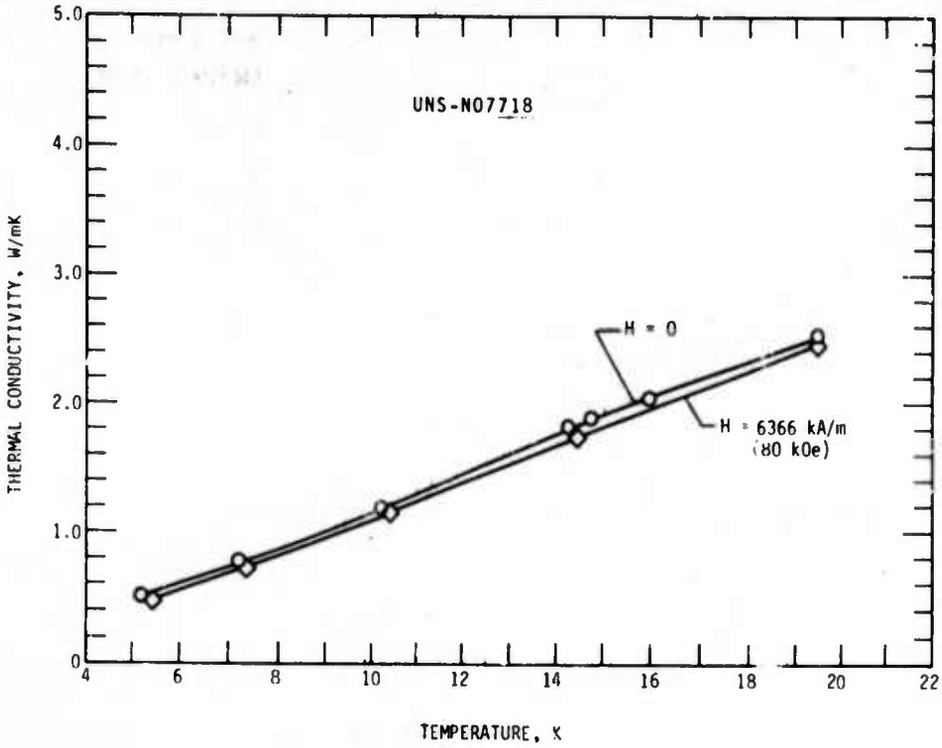

Fig. 2. Thermal conductivity of the Ni-Cr-Fe alloy UNS-N07718 as a function of temperature for H = 0 and 6366 kA/m (80 kOe).

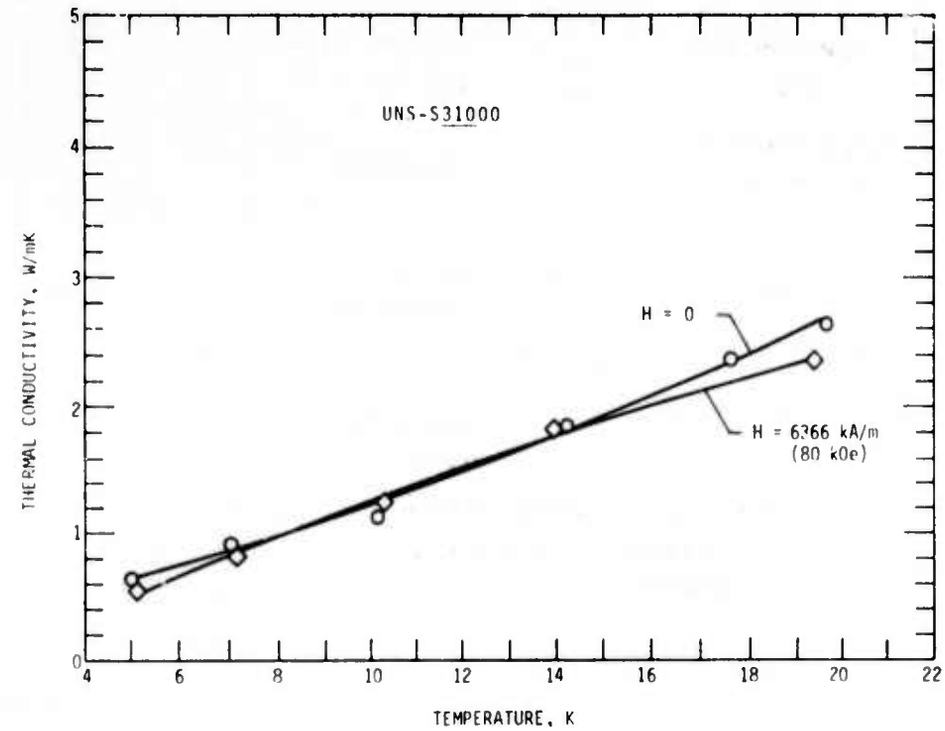

Fig. 3. Thermal conductivity of UNS-S31000 stainless steel as a function of temperature for H = 0 and 6366 kA/m (80 kOe).

337<

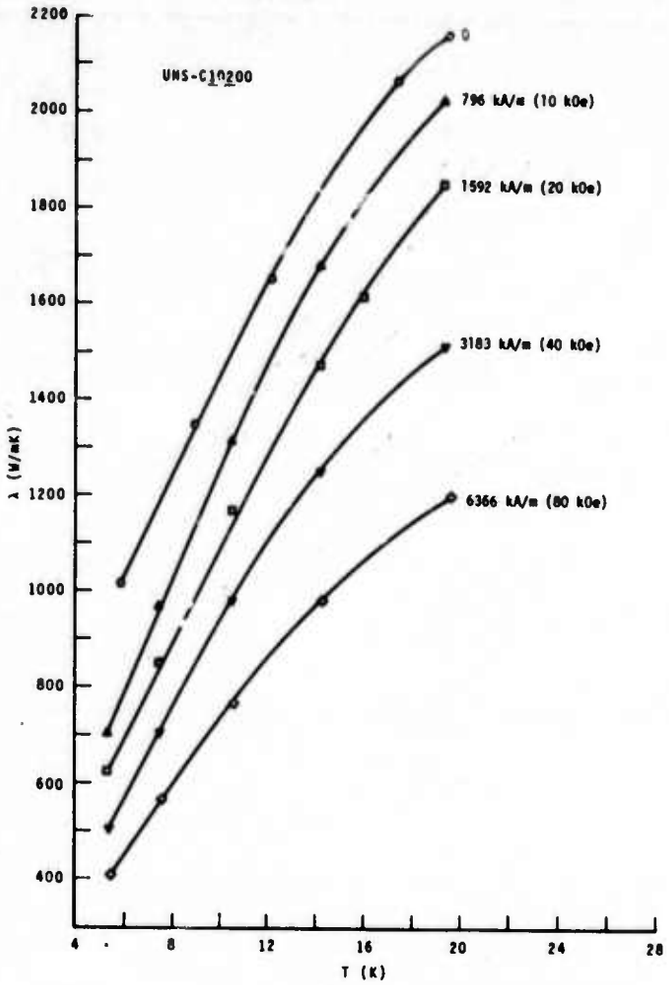

Fig. 4 Thermal conductivity of UNS-C10200 copper as a function of temperature for H = 0, 796, 1592, 3183, and 6366 kA/m (0, 10, 20, 40, and 80 kOe respectively).

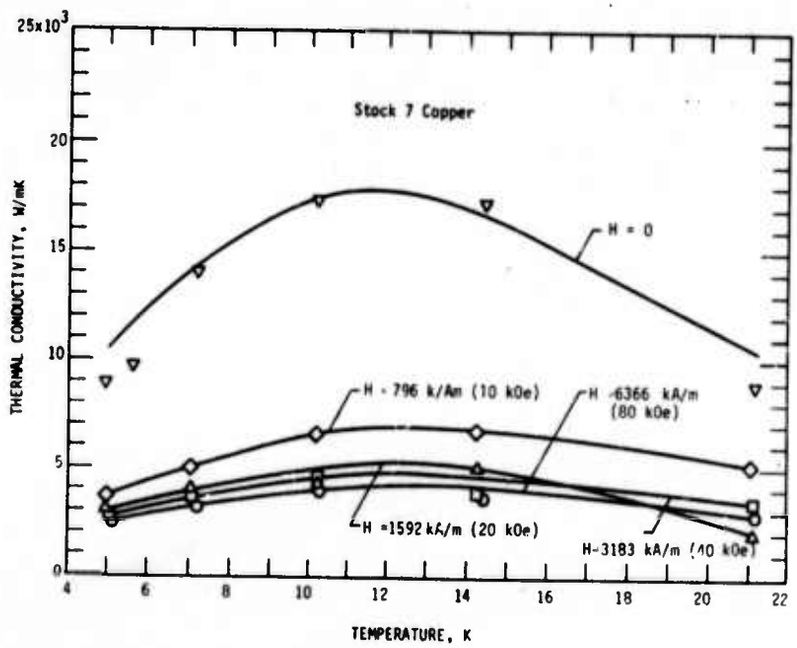

Fig. 5. Thermal conductivity of high purity copper (RRR = 1520) as a function of temperature for H = 0, 796, 1592, 3183, and 6366 kA/m (0, 10, 20, 40, and 80 kOe respectively).

338<

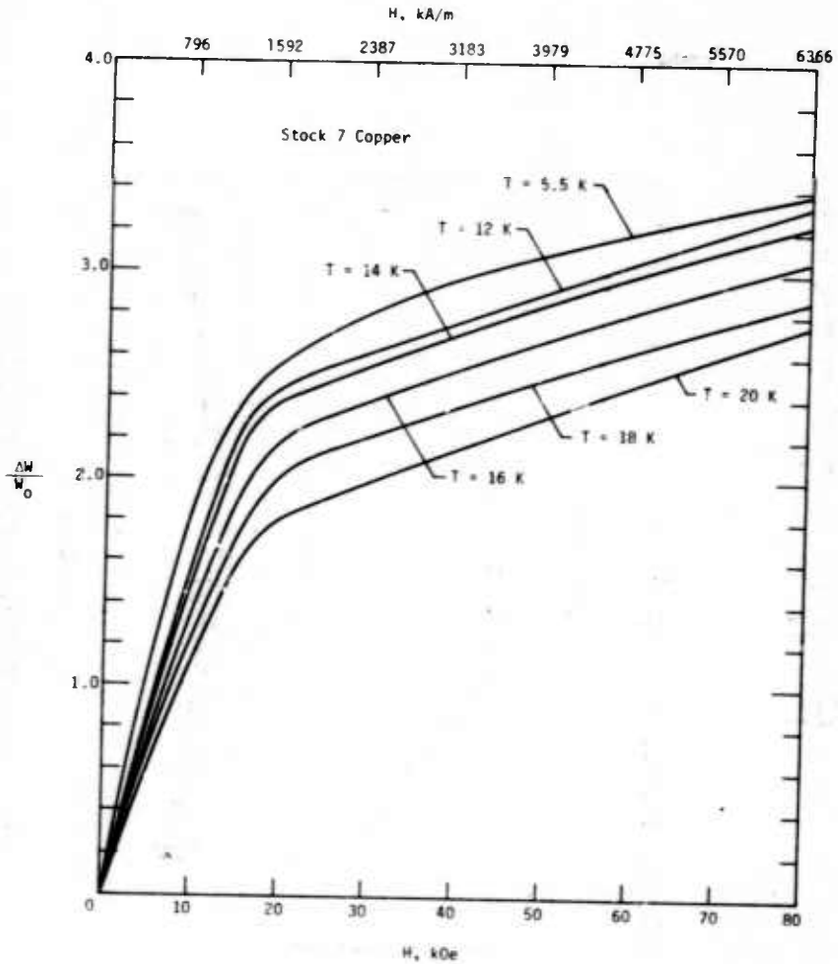

Fig. 6. Relative change in thermal resistance of high purity copper as a function of magnetic field.

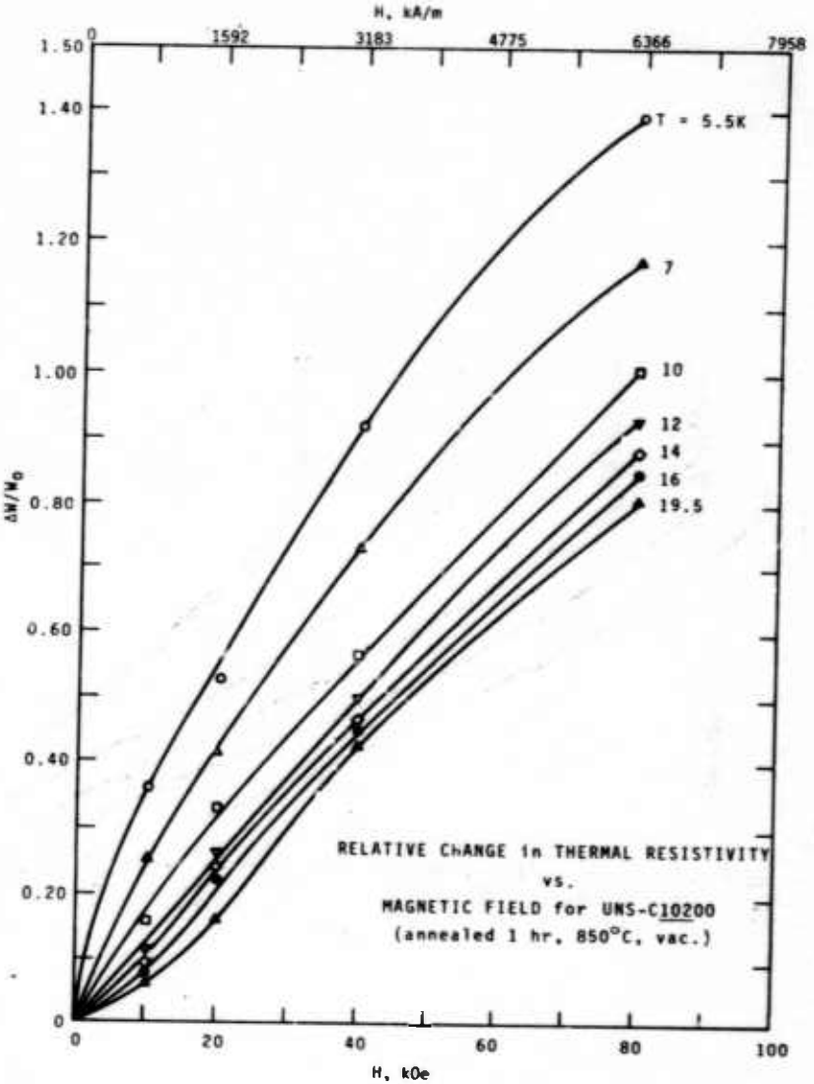

Fig. 7. Relative change in thermal resistance of UNS-C10200 copper as a function of magnetic field.

NBSIR

SEMI-ANNUAL REPORT ON MATERIALS RESEARCH IN SUPPORT OF SUPERCONDUCTING MACHINERY

THERMAL CONDUCTIVITY

J. G. Hust

Cryogenics Division
Institute for Basic Standards
National Bureau of Standards
Boulder, Colorado 80302

October 1975

Summary: Thermal Conductivity

Thermal conductivity data are reported for boron-epoxy composites. Comparisons are made with existing literature data and material variability is discussed.

THERMAL CONDUCTIVITY

J. G. Hust

Cryogenics Division
Institute for Basic Standards
National Bureau of Standards
Boulder, Colorado 80302

1. Introduction

At the request of Mike Jones for Watervliet Arsenal and in conjunction with the ARPA-NBS superconducting machinery program, the thermal conductivities of three specimens of boron-epoxy composite were measured. Both a transverse and a longitudinal specimen were measured using a fixed-point apparatus and a single longitudinal specimen was measured using a variable-temperature apparatus.

2. Apparatus and Specimen Characterization

A fixed-point thermal conductivity apparatus described by Hust [1,2] was used to measure transverse and longitudinal boron-epoxy composite specimens. The specimens were 2.54 cm in diameter and 3.56 cm in length. Thermal conductivity measurements with this apparatus are performed near the boiling point of helium (4 K) and nitrogen (76 K), the sublimation point of CO_2 (194 K), and the ice-point (273 K). The uncertainty of these measurements is estimated to be $\pm$ 10%.

The specimens were fabricated from 5.6 mil boron-epoxy pre-impregnated tape. The boron volume fraction was about 48%. The void fraction is stated to be less than 2% by the supplier. A cursory examination of the material suggests that the void fraction is appreciably less than that.

A longitudinal specimen, with the same characteristics as above, was also measured in a variable-temperature apparatus. The specimen was 23 cm long and rectangular in cross-section (1.74 cm x 2.56 cm). The variable-temperature apparatus is designed to obtain data as a function of temperature from 4 to 300 K and is more accurate than the fixed point apparatus. This apparatus is described in detail by Hust et al. [3].

3. Results

Measurements were performed on a longitudinal specimen (i.e., in the direction of the boron fibers) of boron-epoxy composite at temperatures from 4 to 300 K using the variable-temperature apparatus. The experimental data are listed in table 1 and illustrated in figure 1. The following equation was least-squares fitted to these data using orthonormal fitting techniques:

$$\ell n\lambda = \sum_{i=1}^{n} a_i [\ell nT]^{i+1} \qquad (1)$$

is thermal conductivity in $W \cdot m^{-1} \cdot K^{-1}$ and T is temperature in kelvin. The deviations of the experimental data from this representation are listed in table 2 and are illustrated in figure 2. The parameters obtained by least-squares fitting are listed in table 3. Tabular values of λ as computed from the above equation are listed in table 4 and illustrated in figure 3.

Measurements were conducted on both a longitudinal and a transverse specimen using the fixed-point apparatus. The resulting values of thermal conductivity are listed in table 5 and plotted in figure 3. The uncertainty of the smoothed data obtained with the variable-temperature apparatus is estimated at $\pm$ 4% and the uncertainty of the fixed-point apparatus data is estimated at $\pm$ 10%.

Literature data for similar composites have been compiled by Kasen [4]. These data [5,6] are included schematically in figure 3 for comparison to the data from this research. Reasonable agreement is observed between the literature data and the longitudinal specimen measured in the variable temperature apparatus and the transverse specimen. However, the longitudinal specimen measured in the fixed-point apparatus has a conductivity lower by about 50% than the other longitudinal specimen.

At ambient temperature the thermal conductivity of crystalline boron is 20 $W \cdot m^{-1} \cdot K^{-1}$ and the thermal conductivity of epoxy is typically about 0.2 $W \cdot m^{-1} \cdot K^{-1}$. Since these composites are about 50% boron one would expect a conductivity near 10 $W \cdot m^{-1} \cdot K^{-1}$ instead of 1 - 2 $W \cdot m^{-1} \cdot K^{-1}$. The observed results suggest the presence of strong phonon scattering in the boron fibers. These fibers are fabricated by vapor deposition of boron on a 0.5 mil diameter tungsten wire substrate. (See reference 7 for details). During the fabrication process compounds of tungsten and boron are formed at the center of the final filament and the major outer portion is reported to be pure amorphous or microcrystalline boron. The center portion has a lower thermal conductivity, but since it represents only a few percent of the cross section of the total filament, its effect on reducing conductivity can be neglected. If the outer boron portion of the filament is in a highly disordered or amorphous state, the thermal conductivity would be considerably reduced from that of crystalline boron. It is suggested in reference 7 that the boron is amorphous or microcrystalline structure with an effective crystal size of near 20 Å. Boundary scattering of the heat carriers (phonons) from such small crystals is sufficient to reduce the thermal conductivity considerably since the phonon-phonon scattering mean free path at ambient temperature is near 25 Å. The phonon-phonon mean free path, ℓ, is estimated from bulk boron thermal data and the classical equation $\lambda = 1/3\ Cv\ell$. It is likely that significant crystal size variations occur between different production runs of boron filaments. Thus, one would expect large batch-to-batch variations in thermal conductivity of the longitudinal specimens, which is consistent with the observed results.

In the transverse direction one can estimate the conductivity of the composite from a knowledge of the epoxy conductivity and the relative amount of epoxy present. From such considerations for this composite one obtains a value of conductivity of about 3 to 4 times greater than the conductivity of epoxy. This corresponds to 0.6 to 0.8 $W \cdot m^{-1} \cdot K^{-1}$ at ambient temperature which is in reasonable agreement with the measured value of 0.6 $W \cdot m^{-1} \cdot K^{-1}$. Similar agreement is obtained at low temperature.

References

1. J. G. Hust, Low temperature thermal conductivity measurements on longitudinal and transverse sections of a superconducting coil, Cryogenics 15, No. 1, 8-11 (1975).

2. J. G. Hust, Thermal conductivity fixed-point apparatus, NBS Laboratory Note 74-3, 9 pp. (1974).

3. J. G. Hust, R. L. Powell and D. H. Weitzel, Thermal conductivity standard reference materials from 4 to 300 K. I. Armco Iron: Including apparatus description and error analysis, J. Res. Nat. Bur. Stand. 74A, No. 5, 673-90 (1970).

4. M. B. Kasen, "Properties of filamentary-reinforced composites at cryogenic temperatures", Composite Reliability, ASTM STP 580 pp. 586-611 (1975).

5. J. Hertz, J. L. Christian and M. Varlas, "Advanced composite applications for spacecraft and missiles, Phase I final report, Volume II: Material development", AFML-TR 71-186, Vol. 2, March 1972 (AD 893 715L).

6. J. P. Gille, "Development of advanced materials for integrated tank insulation systems for long-term storage of cryogens in space", NASA CR-102 570 (Final) Sept. 1969 (N 70-23348).

7. Modern Composite Materials, edited by L. J. Broutman and R. H. Krock, Addison-Wesley Publishing Company, Reading, Mass. (1967).

NOTES RELATING TO TABLES

THE DATA LISTED ARE, IN PART, CARD IMAGES OF EXPERIMENTAL DATA AS READ INTO THE COMPUTER FOR DATA PROCESSING. THESE DATA ARE GENERALLY UNLABELLED. THE FOLLOWING IS A LINE BY LINE EXPLANATION OF THESE TABLES.

TABLE 1 (GRADIENT DATA)

LINE 1- DATA IDENTIFICATION

LINE 2- EMFS OF THERMOCOUPLES 1 THRU 8 (MICROVOLTS)

LINE 3- PLATINUM RESISTANCE THERMOMETER CURRENT (MILLIAMPS), REFERENCE PLATINUM THERMOMETER VOLTAGE (MICROVOLTS), FLOATING SINK PLATINUM THERMOMETER VOLTAGE (MICROVOLTS), GERMANIUM THERMOMETER CURRENT (MICROAMPS), REFERENCE GERMANIUM THERMOMETER VOLTAGE (MICROVOLTS), FLOATING SINK GERMANIUM THERMOMETER (MICROVOLTS)

LINE 4- SEEBECK EMF (MICROVOLTS), SPECIMEN VOLTAGE (MICROVOLTS), SPECIMEN CURRENT (MILLIAMPS), SPECIMEN HEATER VOLTAGE (VOLTS), SPECIMEN HEATER CURRENT (MILLIAMPS), CRYOGENIC BATH PRESSURE (MM OF HG), ROOM TEMPERATURE (DEGREES C), CRYOGENIC BATH CODE (1=LIQUID HELIUM, 2=LIQUID HYDROGEN, 3=LIQUID NITROGEN, 4=DRY ICE-ALCOHOL, 5=ICE WATER)

TABLE 2

THESE DATA ARE SEMI-PROCESSED COMPUTER OUTPUT. TEMPERATURE IS KELVIN, THERMAL CONDUCTIVITY IS IN WATTS PER METER PER KELVIN, ELECTRICAL RESISTANCE IS IN OHMS, AND THERMOVOLTAGE IS IN MICROVOLTS.

BORON-EPOXY (L9)

NUMBER OF CALIBRATION, ISOTHERMAL, AND GRADIENT RUNS, AND THERMOCOUPLES

66	-C	11	8

THERMOCOUPLE POSITIONS (CM)

0.0000	2.5400	5.0800	7.6200	10.1600	12.7000	15.2400	17.7800

SPECIMEN DIAMETERS BETWEEN THERMOCOUPLES (CM)

2.3815	2.3815	2.3815	2.3815	2.3815	2.3815	2.3815

TABLE 1. BASIC SEMI-PROCESSED TEMPERATURE GRADIENT DATA FOR BORON-EPOXY (L1)

THERMAL CONDUCTIVITY DATA FOR B-EPOXY(L1) 20MAY 75 1545 11

11.64	20.80	28.70	35.79	41.99	48.22	53.75	58.72
2.0005	34.80	25.78	9.9880	9657.50	7598.50		
-0.00	-0.00	-0.00	.6743	3.3280	632.7	24.0	1.0

REFERENCE TEMP		FLOATING SINK TEMP		SPECIMEN	HEATER
PRT	GRT	PRT	GRT	RESISTANCE	POWER
0.000	4.158	0.000	4.652	0.	.22431E-02

THERMAL CONDUCTIVITY DATA FOR B-EPOXY(L1) 20MAY 75 1620 12

45.03	66.97	85.00	101.14	115.12	128.43	140.57	151.52
-0.0000	-0.00	-0.00	9.9880	9505.50	4429.80		
-0.00	-0.00	-0.00	1.3560	6.6972	632.7	24.0	1.0

REFERENCE TEMP		FLOATING SINK TEMP		SPECIMEN	HEATER
PRT	GRT	PRT	GRT	RESISTANCE	POWER
0.000	4.194	0.000	6.172	0.	.9081-E-02

THERMAL CONDUCTIVITY DATA FOR B-EPOXY(L1) 20MAY 75 1715 13

127.92	167.36	204.18	230.12	256.28	280.88	303.92	324.92
2.0010	34.70	40.16	9.9880	9113.00	1529.50		
-0.00	-0.00	-0.00	2.4880	12.282J	635.0	24.0	1.0

REFERENCE TEMP		FLOATING SINK TEMP		SPECIMEN	HEATER
PRT	GRT	PRT	GRT	RESISTANCE	POWER
0.000	4.289	0.000	10.313	0.	.30554E-01

THERMAL CONDUCTIVITY DATA FOR B-EPOXY(L1) 20MAY 75 1740 14

265.04	340.28	403.64	463.67	517.90	569.72	620.56	669.33
2.0010	34.66	104.94	9.9880	8470.00	654.80		
-0.00	-0.00	-0.00	4.5140	22.2950	635.0	24.0	1.0

REFERENCE TEMP		FLOATING SINK TEMP		SPECIMEN	HEATER
PRT	GRT	PRT	GRT	RESISTANCE	POWER
0.000	4.460	16.007	15.931	0.	.1004E+00

THERMAL CONDUCTIVITY DATA FOR B-EPOXY(L1) 20MAY 75 1945 15

698.97	751.82	802.25	856.47	907.42	958.15	1010.90	1062.44
2.0000	-0.00	2743.50	9.9880	7350.00	130.18		
-0.00	-0.00	-0.00	4.6560	22.9280	635.0	24.0	1.0

REFERENCE TEMP		FLOATING SINK TEMP		SPECIMEN	HEATER
PRT	GRT	PRT	GRT	RESISTANCE	POWER
0.000	4.810	43.339	0.000	0.	.1067E+00

THERMAL CONDUCTIVITY DATA FOR B-EPOXY(L1) 17 MAY 75 2215 7

113.31	163.22	211.24	262.72	312.72	361.91	413.16	461.68
2.0020	9287.00	10280.00	-0.0000	-0.00	-0.00		
-0.00	-0.00	-0.00	4.3020	21.2100	633.5	25.0	3.0

REFERENCE TEMP		FLOATING SINK TEMP		SPECIMEN	HEATER
PRT	GRT	PRT	GRT	RESISTANCE	POWER
75.905	0.000	80.332	0.000	0.	.91245E-01

TABLE 1. (CONTINUED)

THERMAL CONDUCTIVITY DATA FOR B-EPOXY(L1) 20MAY 75 1040 10

1296.88	1464.36	1624.10	1797.40	1963.96	2124.40	2293.26	2450.64
2.0010	9318.00	23035.00	-0.0000	-0.00	-0.00		
-0.00	-0.00	-0.00	7.2740	35.7000	634.5	23.8	3.0

REFERENCE TEMP		FLOATING SINK TEMP		SPECIMEN	HEATER
PRT	GRT	PRT	GRT	RESISTANCE	POWER
76.067	0.000	138.550	0.000	0.	.25968E+00

THERMAL CONDUCTIVITY DATA FOR B-EPOXY(L1) 18 MAY 751155 8

348.66	468.54	584.84	712.57	835.65	956.94	1083.82	1203.94
2.0000	9290.20	12589.00	-0.0000	-0.00	-0.00		
-0.00	-0.00	-0.00	6.5260	32.0900	633.7	25.5	3.0

REFERENCE TEMP		FLOATING SINK TEMP		SPECIMEN	HEATER
PRT	GRT	PRT	GRT	RESISTANCE	POWER
75.962	0.000	90.790	0.000	0.	.20942E+00

THERMAL CONDUCTIVITY DATA FOR B-EPOXY(L1) 14 MAY 75 1345 3

126.50	195.80	263.20	334.80	403.80	469.70	537.00	600.20
2.0025	34565.00	35520.00	-0.0000	-0.00	-0.00		
-0.00	-0.00	-0.00	4.5540	22.3600	-0.0	23.0	4.0

REFERENCE TEMP		FLOATING SINK TEMP		SPECIMEN	HEATER
PRT	GRT	PRT	GRT	RESISTANCE	POWER
193.251	0.000	197.391	0.000	0.	.10183E+00

THERMAL CONDUCTIVITY DATA FOR B-EPOXY(L1) 15 MAY 75 2140 5

591.89	776.83	956.91	1149.69	1335.47	1511.59	1692.39	1859.22
2.0010	34720.00	39595.00	-0.0000	-0.00	-0.00		
-0.00	-0.00	-0.00	7.4000	36.3000	-0.0	23.0	4.0

REFERENCE TEMP		FLOATING SINK TEMP		SPECIMEN	HEATER
PRT	GRT	PRT	GRT	RESISTANCE	POWER
194.118	0.000	217.087	0.000	0.	.26862E+00

THERMAL CONDUCTIVITY DATA FOR B-EPOXY(L1) 7 MAY 75 835 1

48.78	102.73	153.90	208.29	260.50	310.31	360.70	407.00
2.0000	51010.00	51420.00	-0.0000	-0.00	-0.00		
-0.00	-0.00	-0.00	3.9068	18.9450	-0.0	-0.0	5.0

REFERENCE TEMP		FLOATING SINK TEMP		SPECIMEN	HEATER
PRT	GRT	PRT	GRT	RESISTANCE	POWER
273.474	0.000	274.735	0.000	0.	.74014E-01

TABLE 2 THERMAL CONDUCTIVITY DEVIATIONS FOR BORON-EXY (L1)

THERMAL CONDUCTIVITY DATA FOR B-EPOXY(L1) 20MAY 75 1545 11

MEAN TEMPERATURE	TEMPERATURE DIFFERENCE	OBSERVED THERMAL CONDUCTIVITY	CALCULATED THERMAL CONDUCTIVITY	PERCENT DEVIATION
5.922	.678	.189E+00	.191E+00	-1.1
6.133	.546	.234E+00	.230E+00	1.9
6.654	.495	.258E+00	.265E+00	-2.7
7.112	.421	.304E+00	.297E+00	2.3
7.518	.390	.328E+00	.325E+00	.9
7.898	.370	.345E+00	.352E+00	-1.9
8.243	.320	.400E+00	.376E+00	6.0

THERMAL CONDUCTIVITY DATA FOR B-EPOXY(L1) 20MAY 75 1620 12

MEAN TEMPERATURE	TEMPERATURE DIFFERENCE	OBSERVED THERMAL CONDUCTIVITY	CALCULATED THERMAL CONDUCTIVITY	PERCENT DEVIATION
8.240	1.417	.385E+00	.376E+00	-2.9
9.510	1.122	.461E+00	.466E+00	-1.0
10.576	1.009	.513E+00	.541E+00	-5.5
11.506	.853	.607E+00	.607E+00	.1
12.319	.773	.670E+00	.663E+00	1.0
13.071	.731	.709E+00	.715E+00	-.9
13.758	.644	.805E+00	.762E+00	5.3

THERMAL CONDUCTIVITY DATA FOR B-EPOXY(L1) 20MAY 75 1715 13

MEAN TEMPERATURE	TEMPERATURE DIFFERENCE	OBSERVED THERMAL CONDUCTIVITY	CALCULATED THERMAL CONDUCTIVITY	PERCENT DEVIATION
13.836	2.322	.750E+00	.771E+00	-2.7
15.994	1.893	.920E+00	.912E+00	.9
17.812	1.743	.999E+00	.103E+01	-2.9
19.443	1.520	.115E+01	.113E+01	1.5
20.904	1.401	.124E+01	.122E+01	2.2
22.276	1.344	.130E+01	.129E+01	.3
23.564	1.232	.141E+01	.136E+01	3.8

TABLE 2 (CONTINUED)

THERMAL CONDUCTIVITY DATA FOR B-EPOXY(L1) 20MAY 75 1740 14

MEAN TEMPERATURE	TEMPERATURE DIFFERENCE	OBSERVED THERMAL CONDUCTIVITY	CALCULATED THERMAL CONDUCTIVITY	PERCENT DEVIATION
22.996	4.390	.130E+01	.133E+01	-2.1
27.058	3.734	.153E+01	.153E+01	.4
30.714	3.578	.160E+01	.167E+01	-4.5
34.132	3.257	.176E+01	.178E+01	-1.2
37.304	3.088	.186E+01	.186E+01	-.2
40.374	3.051	.188E+01	.192E+01	-2.1
43.349	2.900	.198E+01	.196E+01	.8

THERMAL CONDUCTIVITY DATA FOR B-EPOXY(L1) 20MAY 75 1945 15

MEAN TEMPERATURE	TEMPERATURE DIFFERENCE	OBSERVED THERMAL CONDUCTIVITY	CALCULATED THERMAL CONDUCTIVITY	PERCENT DEVIATION
47.792	3.007	.202E+01	.200E+01	1.1
50.825	3.058	.199E+01	.202E+01	-1.5
53.739	2.771	.220E+01	.203E+01	7.6
56.667	3.085	.197E+01	.204E+01	-3.2
59.783	3.146	.193E+01	.204E+01	-5.3
62.793	2.873	.212E+01	.203E+01	4.0
65.688	2.918	.209E+01	.203E+01	2.7

THERMAL CONDUCTIVITY DATA FOR B-EPOXY(L1) 17 MAY 75 221 7

MEAN TEMPERATURE	TEMPERATURE DIFFERENCE	OBSERVED THERMAL CONDUCTIVITY	CALCULATED THERMAL CONDUCTIVITY	PERCENT DEVIATION
83.469	2.702	.193E+01	.199E+01	-2.9
86.118	2.595	.200E+01	.197E+01	1.5
88.785	2.739	.190E+01	.197E+01	-3.6
91.484	2.667	.195E+01	.196E+01	-.5
94.126	2.610	.199E+01	.195E+01	2.0
96.777	2.691	.193E+01	.195E+01	-.8
99.393	2.542	.205E+01	.194E+01	5.1

TABLE 2 (CONTINUED)

THERMAL CONDUCTIVITY DATA FOR B-EPOXY(L1) 20MAY 75 1040 10

MEAN TEMPERATURE	TEMPERATURE DIFFERENCE	OBSERVED THERMAL CONDUCTIVITY	CALCULATED THERMAL CONDUCTIVITY	PERCENT DEVIATION
147.398	8.133	.182E+01	.189E+01	-4.0
155.391	7.833	.189E+01	.189E+01	.1
163.386	8.176	.181E+01	.189E+01	-4.1
171.445	7.942	.186E+01	.188E+01	-.9
179.281	7.731	.192E+01	.188E+01	2.0
187.100	7.907	.187E+01	.187E+01	.0
194.710	7.313	.202E+01	.187E+01	7.8

THERMAL CONDUCTIVITY DATA FOR B-EPOXY(L1) 18 MAY 75 1155 8

MEAN TEMPERATURE	TEMPERATURE DIFFERENCE	OBSERVED THERMAL CONDUCTIVITY	CALCULATED THERMAL CONDUCTIVITY	PERCENT DEVIATION
97.938	6.300	.190E+01	.195E+01	-2.6
104.189	6.079	.196E+01	.193E+01	1.6
110.488	6.522	.183E+01	.192E+01	-5.0
116.885	6.272	.190E+01	.191E+01	-.6
123.030	6.139	.195E+01	.191E+01	1.9
129.324	6.330	.189E+01	.190E+01	-.9
135.464	5.950	.201E+01	.190E+01	5.4

THERMAL CONDUCTIVITY DATA FOR B-EPOXY(L1) 14 MAY 75 1345 3

MEAN TEMPERATURE	TEMPERATURE DIFFERENCE	OBSERVED THERMAL CONDUCTIVITY	CALCULATED THERMAL CONDUCTIVITY	PERCENT DEVIATION
200.766	3.208	.191E+01	.186E+01	-2.9
203.936	3.134	.185E+01	.186E+01	-.5
207.164	3.321	.175E+01	.186E+01	-6.4
210.412	3.175	.183E+01	.186E+01	-1.6
213.525	3.050	.190E+01	.186E+01	2.5
216.593	3.086	.188E+01	.185E+01	1.5
219.593	2.895	.201E+01	.185E+01	7.7

TABLE 2. (CONTINUED)

THERMAL CONDUCTIVITY DATA FOR B-EPOXY(L1) 15 MAY 75 2140 5

MEAN TEMPERATURE	TEMPERATURE DIFFERENCE	OBSERVED THERMAL CONDUCTIVITY	CALCULATED THERMAL CONDUCTIVITY	PERCENT DEVIATION
225.745	8.433	.182E+01	.185E+01	-1.8
234.104	8.285	.185E+01	.185E+01	.2
242.656	8.819	.174E+01	.184E+01	-6.2
251.275	8.418	.182E+01	.184E+01	-1.3
259.512	8.056	.190E+01	.185E+01	2.9
267.609	8.139	.188E+01	.185E+01	1.5
275.382	7.407	.207E+01	.186E+01	10.0

THERMAL CONDUCTIVITY DATA FOR B-EPOXY(L1) 7 MAY 75 835 1

MEAN TEMPERATURE	TEMPERATURE DIFFERENCE	OBSERVED THERMAL CONDUCTIVITY	CALCULATED THERMAL CONDUCTIVITY	PERCENT DEVIATION
276.882	2.414	.175E+01	.186E+01	-6.7
279.237	2.295	.184E+01	.187E+01	-1.6
281.612	2.455	.172E+01	.187E+01	-8.9
284.005	2.332	.181E+01	.188E+01	-3.7
286.287	2.232	.189E+01	.188E+01	.5
288.533	2.260	.187E+01	.189E+01	-1.0
290.687	2.049	.206E+01	.189E+01	8.1

TABLE 3. Parameters in equation 1 for a longitudinal boron-epoxy composite specimen

i	a_i
1	-17.065713
2	29.019209
3	-21.740071
4	9.1816220
5	- 2.3311507
6	0.35284329
7	- 0.029346836
8	0.001032607

TABLE 4. Thermal conductivity values of a longitudinal boron-epoxy composite specimen as calculated from equation 1

T (K)	λ ($W \cdot m^{-1} \cdot K^{-1}$)	T (K)	λ ($W \cdot m^{-1} \cdot K^{-1}$)
6	0.221	60	2.04
7	0.289	70	2.02
8	0.359	80	1.99
9	0.430	90	1.96
10	0.501	100	1.94
12	0.641	120	1.91
14	0.779	140	1.90
16	0.912	160	1.89
18	1.04	180	1.88
20	1.16	200	1.86
25	1.43	220	1.85
30	1.65	240	1.84
35	1.80	260	1.85
40	1.91	280	1.87
45	1.98		
50	2.02		

TABLE 5. Thermal conductivity values of a transverse and a longitudinal boron-epoxy composite specimen as measured using the fixed-point apparatus

T (K)	λ ($W \cdot m^{-1} \cdot K^{-1}$)	
7.83	0.178	Longitudinal Specimen
82.0	0.913	
196	1.11	
280	1.02	
14.7	0.174	Transverse Specimen
86.7	0.466	
200	0.553	
280	0.581	

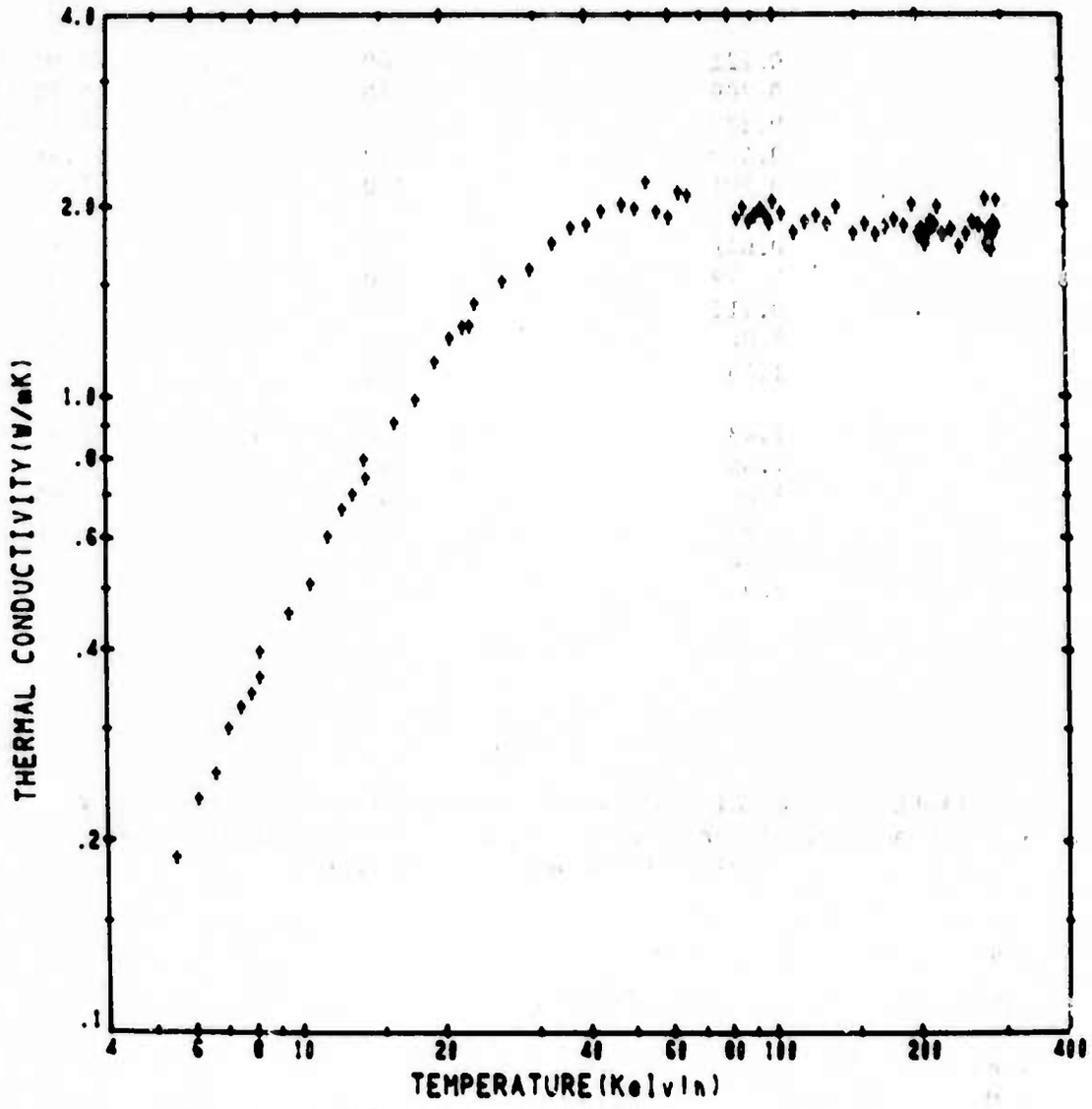

Figure 1 - Experimental data on longitudinal boron-epoxy composite specimen.

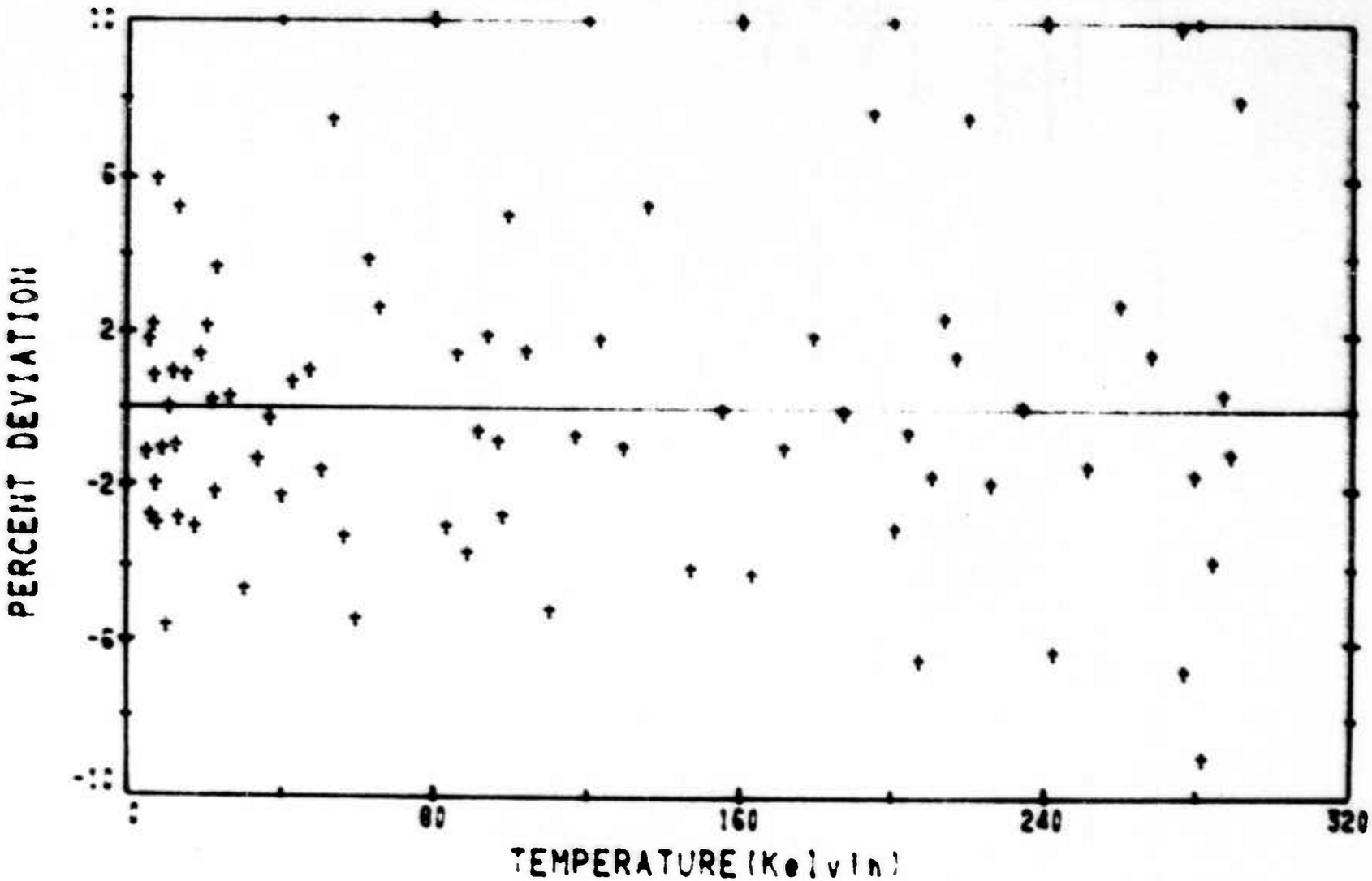

Figure 2 - Thermal conductivity deviations of experimental data from equation 1 for boron-epoxy composite.

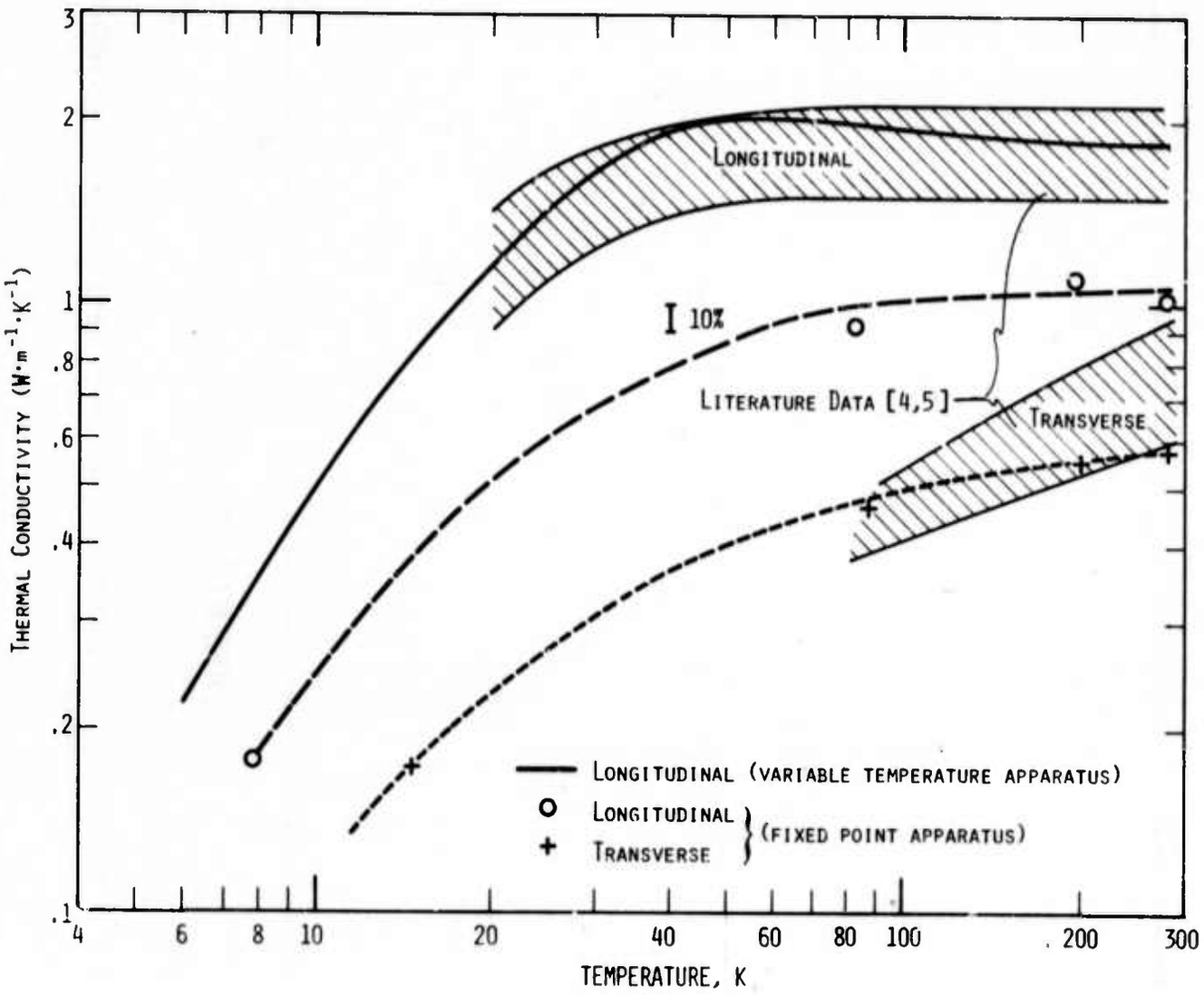

FIGURE 3 - Thermal conductivity of longitudinal and transverse boron-epoxy composite specimens.

This research was supported by the Advanced Research Projects Agency of the Department of Defense and was monitored by the Cryogenics Div., NBS, Boulder, CO under Contract No. CST-8304 Contract Amount $313K.

Sponsored by Advanced Research Projects Agency ARPA Order No. 2569, Program Code No. 4D10

TITLE: Structural Materials for Cryogenic Applications
(Fourth Semi-Annual Technical Report - October 10, 1975)

CONTRACTOR: Westinghouse Electric Corporation
Research and Development Center
Pittsburgh, Pennslyvania 15235

Westinghouse Program Manager: Dr. J. M. Wells (412) 256-3633

Westinghouse Principal Investigators:

Mr. W. A. Logsdon (412) 256-3652
Dr. R. Kossowsky (412) 256-3684
Dr. M. R. Daniel (412) 256-3289
Dr. J. M. Wells (412) 256-3633

FY 74 Contract Start Date: September 10, 1973

FY 74 Contract Expiration Date: September 9, 1974

FY 75 Contract Start Date: September 10, 1974

FY 75 Contract Expiration Date: September 9, 1975

TABLE OF CONTENTS

TABLE OF CONTENTS (CONTINUED)

LIST OF FIGURES

LIST OF FIGURES (CONTINUED)

LIST OF FIGURES (CONTINUED)

LIST OF FIGURES (CONTINUED)

LIST OF FIGURES (CONTINUED)

LIST OF FIGURES (CONTINUED)

LIST OF FIGURES (CONTINUED)

LIST OF FIGURES (CONTINUED)

LIST OF TABLES

LIST OF TABLES (CONTINUED)

1.0 ABSTRACT

A program description and progress to date are presented for the fourth semi-annual period (March to September 1975) on ARPA/NBS - Boulder Contract No. CST-8304. Further results are presented on Structural Materials of interest in first generation superconducting machinery prototypes. Task I involves characterization and evaluation of structural base metals, Task II involves processing effects and Task III - the evaluation of fabricated joints in structural materials. Processing effects have included supplier melting and primary working practice, powder metallurgical hot isostatic pressing (HIP), slow cooling rates (sensitization) and cold working with various recrystallization - grain growth schedules. Fabrication techniques have included soldering brazing and various fusion welding practices including vacuum electron beam, gas tungsten arc, gas metal arc, and shielded metal arc.

Evaluation procedure includes mechanical and fracture mechanics testing, metallography, fractography and magnetic and electrical resistivity measurements from room temperature to liquid helium (4.2 K). Emphasis in the focused direction of this effort is placed upon: (1) utilizing fracture mechanics technology to cryogenic temperatures to evaluate the K_{IC} (J_{IC}) fracture toughness and the fatigue crack growth rate (FCGR) of various sample conditions, (2) utilizing various selected materials/processing and fabrication (MPF) techniques to elucidate significant effects of MPF on the cryogenic behavior of these alloys, (3) employment of modern metallographic and fractographic analysis techniques to characterize the microstructures and the fracture surfaces of the tested materials, and (4) evaluating the general and specific cryogenic structural materails considerations required to establish failure-safe design materials selection and utilization criteria.

Initial materials considered in the first year's program (FY 74) included OFHC Copper, Inconel X750, AISI 310S and Kroamrc 58 Stainless Steel. Augmented results on first year's materials include the attribution of reduced ductility and toughness in MP-1 X750 to continuous grain boundary carbides, the characterization of aniostropic texture by automatic pole figures in K58 stainless, and improved fracture mechanics behavior of weldments in IN X750 but not in 310S and K58 stainless steels over their respective base metals. Additional materials evaluated in this second year program include Inconel 706, Inconel 718, INCO LEA and PD-135 Copper Alloy. Results indicate that previously selected materails can be significantly improved by proper integration of processing and fabrication techniques with improved materials selection and utilization design criteria.

2.0 INTRODUCTION

Work described in this report represents the most recent Westinghouse Research Laboratories contribution to the Advanced Research Project Agency Program entitled "Materials Research for Superconducting Machinery". This program is supported by DOD-ARPA under the direction of Dr. Edward C. vanReuth. Program management is administered by the Cryogenics Division of the National Bureau of Standards with Dr. Richard P. Reed as overall program manager and Dr. Alan F. Clark as contract monitor.

The present Westinghouse Research Laboratories (WRL) program has as its objectives:

(1) To select, characterize and evaluate candidate structural materials for suitability of use in advanced superconducting machinery.

(2) To investigate the influence of selected processing and fabrication/joining factors or techniques on the mechanical, fracture mechanics and physical (magnetic and electrical resistivity) properties of candidate structural materials.

(3) To develop engineering cryogenic mechanical and physical property data of direct usefulness to designers of prototype S.C. machinery.

(4) To help establish with designers of such systems, more specific criteria for selecting and improving the utilization of structural materials in S.C. machinery prototypes.

Three previous WRL semi-annual technical reports have been issued on this program as follows:

(a) WRL Report No. 74-9D4-CRYMT-R1, dated March 1, 1974

(b) WRL Report No. 74-9D4-CRYMT-R2, dated September 9, 1974

(c) WRL Report No. 75-9D4-CRYMT-R1, dated March 10, 1974

These Westinghouse reports along with those of all other participating laboratories are included in the three corresponding NBS-ARPA overall program semi-annual technical reports, entitled "Materials Research For Superconducting Machinery-I (dated March 1974), - II (dated October 1974)" and - III (dated March 1975), respectively. In addition, a "Handbook on Materials for Superconducting Machinery" has been published by the Metals and Ceramics Information Center at Battelle as MCIC-HB-04.

Three technical papers have been written by WRL staff members concerning work mainly accomplished during the Westinghouse FY 74 program and are included in the Appendix of this report. These papers were presented at the 1975 ICMC Conference at Kingston, Ontario and have been submitted for publicating in Vol. 22 of Advances in Cryogenic Engineering.

373

3.0 INTERPRETIVE SUMMARY

The purpose of this section is to provide for the casual as well as the involved reader both an overall summation of what information has been developed in the Westinghouse program and a perspective on the significance of such information relative to the design considerations of advanced cryogenic machinery.

3.1 Program Status

A testing and evaluation status summary for the FY 74 effort is shown in Table 3-1 and for the FY 75 effort in the Table 3-2. The remaining previously unreported test elements from the FY 74 program (i.e. the fracture toughness evaluation of the silver brazed OFHC copper and the copper brazed X750 alloy) are reported herein.

Testing of material/processing and fabrication conditions specified in Table 3-2 is completed with the exception of the following: (a) weldments in HIP Inconel X750, (b) weldments in INCO LEA, (c) grain size variations in Inconel 718 base metal and (d) fatigue crack growth rate tests for alloys 706, 718, LEA and PD-135 at RT, 77K, 4.2K. Weldments in both the HIP X750 and the LEA alloy have been made but have not been tested. Due to the reorientation of program priorities necessitated by the cut back in the funding level of the ARPA/NBS contract extensions, the testing of these two materials has been indefinately postponed. The grain size variations in Inconel 718 base metal and the remaining FCGR tests remain in the program and should be reported in the next report.

3.2 Alloy Selection and Utilization

The Westinghouse FY 74 program concentrated on four metal alloys which had seen prior cryogenic structural application, namely: OFHC

Copper, AISI 310S and Kromarc 58 Stainless Steels and Inconel X750 nickel base superalloy. The logic of evaluating structural materials already being utilized in croygenic structures was based upon:

- The need for establishing a reliable materials data base line, fully documented, to assess the validity of prior "best judgement" materials selection, processing and fabrication decisions associated with first generation prototype hardware.
- The need for improved characterization and evaluation of such materials to establish practical design utilization values and performance criteria which should be exceeded by alternative candidate materials.
- The need to investigate and demonstrate the appreciable variation in both mechanical and physical property levels of selected materials with certain processing and fabrication operations likely to be experienced in actual prototype hardware fabrication.

During the second program year (FY 75), four alternative cryogenic structural candidate materials were considered, namely: PD-135 (a precipitation hardenable Cd-Cr-Copper alloy), INCO LEA (an unnamed, precipitation hardenable, low expansion, nickel base alloy), Inconel 718 nickel-base superalloy and Inconel 706 (a less expensive but more machineable and formable nickel base superalloy than 718). The logic of selecting these alternative candidate materials was generally to achieve increased strength levels (e.g. PD-135 vs OFHC-Copper and 718 vs X750), improved fabrication ease (e.g. 706 vs X750 or 718) and reduced thermal expansion (INCO LEA) behavior. Since design requirements are many and varied with respect to the several structural components of superconducting machinery hardware, it also is necessary to have this expanded data base for greater design flexibility, fabrication ease, cost effectiveness and expediency by substituting for non-available materials.

Additional candidate materials have also been identified (see Table 5-1) which, on the basis of limited available data in the literature, appear to be worthy of at least initial screening tests for cryogenic structural applications. In addition to technological attributes, however, it appears that material procurement, processing and fabrication costs will become an increasingly significant materials selection criteria since prototype machinery sizes are rapidly escallating. For example, while earlier superconducting machinery prototypes[1-2] were rated at 5MVA, recent programs sponsored by EPRI[3-4] are considering 300 to 1200 MVA devices. The results to date of this entire ARPA/NBS program will, undoubtedly, be of direct usefulness to designers considering such large capacity prototypes.

3.3 Mechanical Properties

Mechanical property values of all candidate materials evaluated to date in this program are graphical summarized in Figs. 3-1 to 3-4. Fracture toughness values at 4 K are summarized in Fig. 3-5 and are coded to indicate base metal, processing effects and weldment or brazed conditions. As much of the data presented was summarized in Section 3 of the previous report, remarks following will pertain primarily to the additional data presented.

Figure 3-2 contains the recent data for the Kromarc 58 stainless base metal in the 30% cold worked condition and in the L-T orientation (Code 87XX), i.e. with the specimen loading direction parallel to the cold rolling direction. This data should be compared directly with that for the T-L oriented cold worked condition (Code 81XX). The most significant difference in mechanical property values between these two orientations is observed in the difference in reduction in area which is greater for the L-T orientation by a Δ% of 22% at RT, 12% at 77 K and 18% at 4 K over the corresponding values.

Figure 3-3 now includes the recent data for the Inconel 718 (VIM-VAR), Inconel 706 (VIM-EFR), and 706 (VIM-VAR) alloys in the STDA conditions only (Codes 64XX, 70XX and 71XX respectively). The yield

strength of the 718 alloy at all three temperatures is the highest of all the alloys shown. At 4 K for example, the yield strength of the 718 is about 62% greater than for the X750 (VIM-VAR) material (Code 31XX). The ductility of the 718 although not particularly large, is nevertheless equal to or greater, at all test temperatures, than that of the same X750 alloy in the STDA condition. At 4 K, both the reduction in area and the total elongation of the 718 is 10% (versus 6% for the X750), a difference of about 67%, both alloys being from the same supplier and from comparable size forging billet stock. Both of the 706 materials demonstrated slightly lower yield strengths, comparable ultimate tensile strengths and superior notched tensile strength levels as compared to the 718 material. The NTS/σ_{ys} ratio of both 706 materials was 1.8 versus the 1.5 to 1.4 ratio value for the 718. The ductility levels for the 706 proved far superior to the 718 material tested. Little difference is observed between the two 706 materials.

Figure 3-5 now includes the fracture toughness values at 4 K for the K 58 as 30% cold worked and L-T orientation, Inconel 718 as base metal, weldment fusion zone (FZ) and heat-affected zone (HAZ), Inconel 706 as base metal (VIM-EFR)and both base metal and weld fusion zone for the VIM-VAR material, INCO LEA base metal and the A-286 base metal. The fracture toughness of the 30% CW K-58 material was found to be slightly greater (by $\sim$ 8%) in the L-T orientation as opposed to the T-L plate orientation. The fracture toughness of the Inconel 718 STDA base metal (Code 64XX) was approximately 5% greater than that for the Inconel X750 STDA (Code 31XX). The weldment HAZ and FZ fracture toughness values in the 718 material with a full post weld STDA heat treatment were only 76% and 65% respectively of the 718 base metal values. The fracture toughness at 4 K for the two Inconel 706 alloys were appreciably greater than for the Inconel 718 alloy; the 706 VIM-EFR material (Code 70XX) being approximately 90% greater and the 706 VIM-VAR material (Code 71XX) being about 109% greater. The GTA weldment FZ fracture toughness value (Code 72XX - again with the full post weld STDA treatment) for the Inconel 706 material is drastically lower ($\sim$35%) than the 706 base metal value

and is only about 12% greater than the GTA weldment FZ in the 718 alloy. The 4 K fracture toughness of the INCO LEA STDA material (Code 73XX) was about 13% greater than that for the 718 STDA material, a surprising result considering the significantly lower 4 K ductility values of the LEA versus the 718 material. Finally, in Fig. 3-5 one observes the fracture toughness for the A-286 STQA heat treated stainless steel is greater than the Inconel 718, 706 or LEA alloys but is lower than either the 310S or the Kromarc 58 stainless steel alloys previously tested.

3.4 Effect of Processing

The effects of the various processing operations included in the Westinghouse program on the yield and tensile strength and the fracture toughness values evaluated to date is presented in Figs. 3-6 and 3-7, normalized to the respective base metal condition. The previous discussion of most of this data was included in the preceeding report and will not be repeated herein. However, the recent data plotted for the 30% CW Kromarc 58 for the (L-T)/(T-L) orientations is included and a small difference ($\sim$ 10%) is observed at room temperature for the yield strength ratio. Figure 3-7 now includes the normalized 4 K fracture toughness ratio for these two K-58 orientations and one again observes the L-T orientation is greater by about 8%. For the comparison of the 706 alloy produced by the VIM-VAR practice versus the VIM-VAR practice versus the VIM-ESR material, one finds the fracture toughness of the VAR material greater by about 10%.

3.5 Effects of Fabricated Joints

The effects of various metals joining processes including both brazements and fusion weldments on the yield strength and ultimate tensile strength ratio is presented in Figs. 3-8 and 3-9 and on the 4 K fracture toughness ratio is presented in Fig. 3-10. Again, comments were presented in the previous report[5] concerning much of the data

presented in these figures. However, pertaining to the recently added data, the following comments are made:

- A correction was made in Fig. 3-8 to reflect the fact that the fracture location in the 310S weldments were in the weld fusion zone and not in the base metal as previously indicated.
- The yield strength and the ultimate tensile strength ratios of the GTA weldments in the Inconel 718 alloy are only slightly below unity indicating a high strength efficiency ($\sim$ 90% or better). All fractures of these composite weld samples were in the weld fusion zone.
- The yield strength and the ultimate tensile strength ratios of the GTA weldments in the Inconel 706 (VIM-VAR) alloy are again of high strength efficiency ($\geq$ 83%). These weldments also fractured in the weld fusion zone.
- The fracture toughness ratio of the copper brazed X750 with respect to the ST X750 base metal (Codes 38XX/30XX) was about 0.68. This was the only joint condition with the MP-1 X750 material showing a ratio < 1.
- The 4 K fracture toughness ratio for the GTA weldment in the Inconel 718 alloy (Code 65XX/64XX) was about 0.65 and that for the GTA weldment in the Inconel 706 alloy (Code 72XX/71XX) was about 0.35. Thus the fracture toughness "efficiency" of these weldments was found to be considerably less than unity.

3.6 Metallurgical and Fractographic Analysis

The inclusion of metallurgical and fractographic analyses in this program has provided the means for both improved characterization of each specific material being tested and a means for better deciphering

and understanding the correlation between observed structure and mechanical behavior. The improved characterization is essential in order to adequately describe the basic features of the particular alloy being evaluated and to discriminate between differences in these features for the various processing and fabrication conditions. The improved correlation associated with the respective fracture structural aspects and the corresponding mechanical and fracture mechanics property values enables us to better understand the wide differences in such property values.

Some examples of such metallographic and fractographic analyses which have been reported in Section 7 of this report series are as follows:

- The wide difference in strength, ducility and fracture toughness values for the three different heats of Inconel X750 material are understandable in terms of the observed difference in grain size, dislocation substructure, grain boundary carbide form and distribution, morphology of precipitated phases, and fracture surface appearance.
- The improved mechanical properties of the MP-1 X750 hipped material over the heat treated original base metal was attributed to both the reduced grain size and the elimination of a continuous grain boundary MC carbide film in the hipped material.
- The improved mechanical behavior of the weldments in the X750 alloy over the original heat treated base metal was attributed to both a reduced microstructural grain size and again to the elimination of the continuous MC carbide film in the X750 weld metal.
- The nature and extent of impurities on the fracture surfaces of various specimens both base metal and weldments has indicated a potential improvement direction, i.e. to

better control the impurity levels in both as received base metal and in fusion welding operations.

- The identification of the fracture locations on welded samples assists in establishing the capability of the weldments to plastically deform and work harden, thereby increasing the structural reliability of such weldments with respect to the corresponding base metals.
- Examination of the copper brazed X750 material revealed nonuniform wetting, dissolution of the X750 material interface and grain boundary penetration by the copper-all leading to reduced strength, ductility and toughness levels and a transition zone fracture location.
- The relatively low ductility in the Inconel 718 base metal was attributed to either thin carbide films or an agglomeration of very small carbide particles along the grain boundaries, whereas in the higher ductility Udimet 718 base metal, the dominant phase at or near the grain boundary is γ'' (Ni_3Nb). Fracture in the Inconel 718 material tensile specimens is by intergranular cracking with little deformation associated with the above grain boundary carbides.
- The even lower ductility of the GTA weldments on the Inconel 718 alloy are associated with cellular carbide films which dominate the fracture surface.
- The relatively high ductility and toughness of the Inconel 706 material is associated with the absences of grain boundary carbide films. The drastic reduction in both ductility and toughness of the GTA weldments in the 706 alloy is once again associated with the appearance of carbide films in the weld fusion zone.

3.7 Physical Properties

Physical property determinations are being conducted on samples of the identical base metal and weldments conditions included in this Westinghouse program. Data on thermal conductivity, magneto-thermal conductivity and elastic constants are being developed by NBS[6] and data on thermal expansion and specific heats are being developed by Battelle-Columbus[7].

Specific magnetic behavior and electrical resistivity measurements are being conducted on these materials as an integral part of this Westinghouse program. To date, magnetic and electrical resistivity data have been reported on all sample conditions otherwise evaluated in this program. This data can be found in Section 8 of this and the previous reports. Significant results of this effort can be summarized as follows:

- AISI 310S stainless steel is found to be feebly ferromagnetic at 4 K with Bs $\approx$ 1000 Gauss. Kromarc 58 stainless was found to be antiferromagnetic at low field strengths with very small traces of ferromagnetic behavior at high field strength (> 50 KG).
- Inconel X750 and 718 alloys have been found to be weakly ferromagnetic at 4 K with Bs values of about 1500 and 1100 Gauss respectively. The Inconel 706 alloys demonstrate greater ferromagnetic behavior (Bs $\approx$ 3200 Gauss at 4 K), most probably due to the higher iron content (about twice that of the 718 alloy). Interestingly the saturation moment of the weldments in the 706 alloy is about half (i.e. Bs $\sim$ 1500 Gauss) that of the 706 base metal. This reduced magnetic behavior in the 706 weldments is attributed to the use of 718 filler wire which would yield an iron level in the as-deposited weld metal closer to the composition for 718.

- The INCO LEA alloy evidences strong ferromagnetic behavior (Bs ≈ 13,000 Gauss) and is attributed to the high iron content (∿ 55%) in this alloy.
- Processing and fabrication effects appear not to change the basic magnetic behavior except for situations as noted above where a significant composition change in the weldment from the base metal is occurring.

References (Section 3)

1. Fagan, T. J., Jr., Litz, D. C., Murphy, J. H., Patterson, A., Sterrett, C. C., Sonter, D. R. and Ulke, A., "Development of a 5 MVA Superconducting Generator, Mechanical and Cryogenic Design", Conference Paper C 73 255-7 presented at the IEEE Winter Power Meeting, New York, January 1973.
2. Blougher, R. D., Fagan, T. J., Parker, J. H., Jr., Wells, J. M. and McCabria, J. L., "A High Speed Superconducting Generator", Proc. ICEC-5, Kyoto, Japan (1974).
3. Sterrett, C. C., Towne, R. A., Baldwin, M. S. and Parker, J. H., Jr., "Superconducting Turbine Generators For the Electric Utilities - A Status Report", Conference Paper at ASME - IEEE Joint Power Conference, Portland, Oregon, September 1975.
4. Westinghouse Project "Superconducting Generator Design", EPRI Contract No. RP-429-1.
5. Wells, J. M., Kossowsky, R., Logsdon, W. A. and Daniel, M. R., "Structural Materials for Cryogenic Applications - Third Semi-Annual Technical Report", Westinghouse Research Report 75-9D4-CRYMT-R1, March 10, 1975.
6. Reed, R. P., Hust, J. G., Kasen, M. B., Ledbetter, H. M., Mikesell, R. P., Schramm, R. E., Sparks, L. L., Tooler, R. L. and Weston, W. F. NBS IR 75-810, Materials Research For Superconducting Machinery III, NBS/ARPA, April 1975.
7. Jelinek, F. J. and Collings, E. W., "Low Temperature Thermal Expansion and Specific Heat Properties of Structural Materials", ibid.

Curve 679865-B

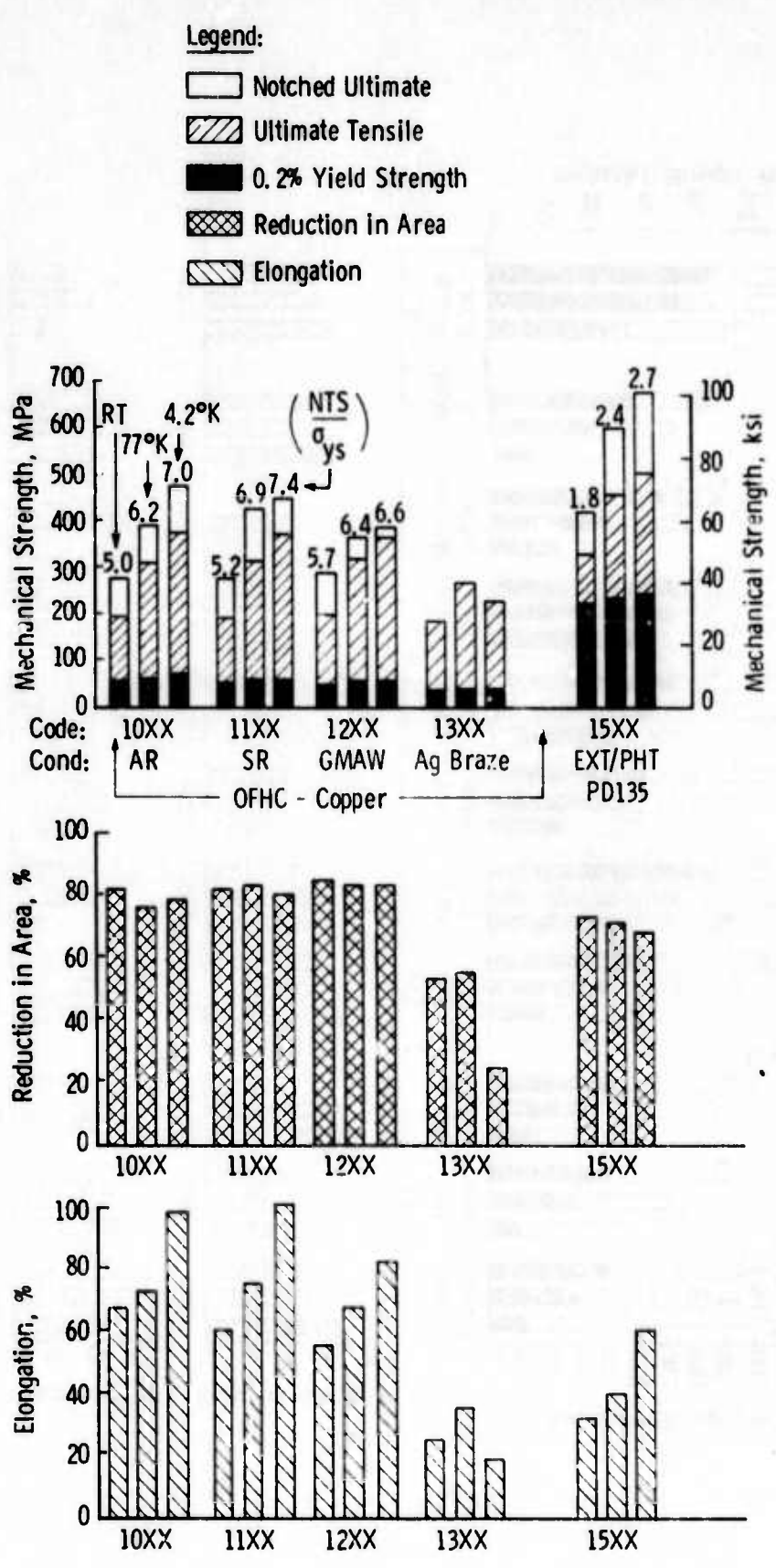

Fig. 3-1—Summary comparison of mechanical strength and ductility values for copper alloys including processing and fabricated joints at RT, 77K, and 4.2 K

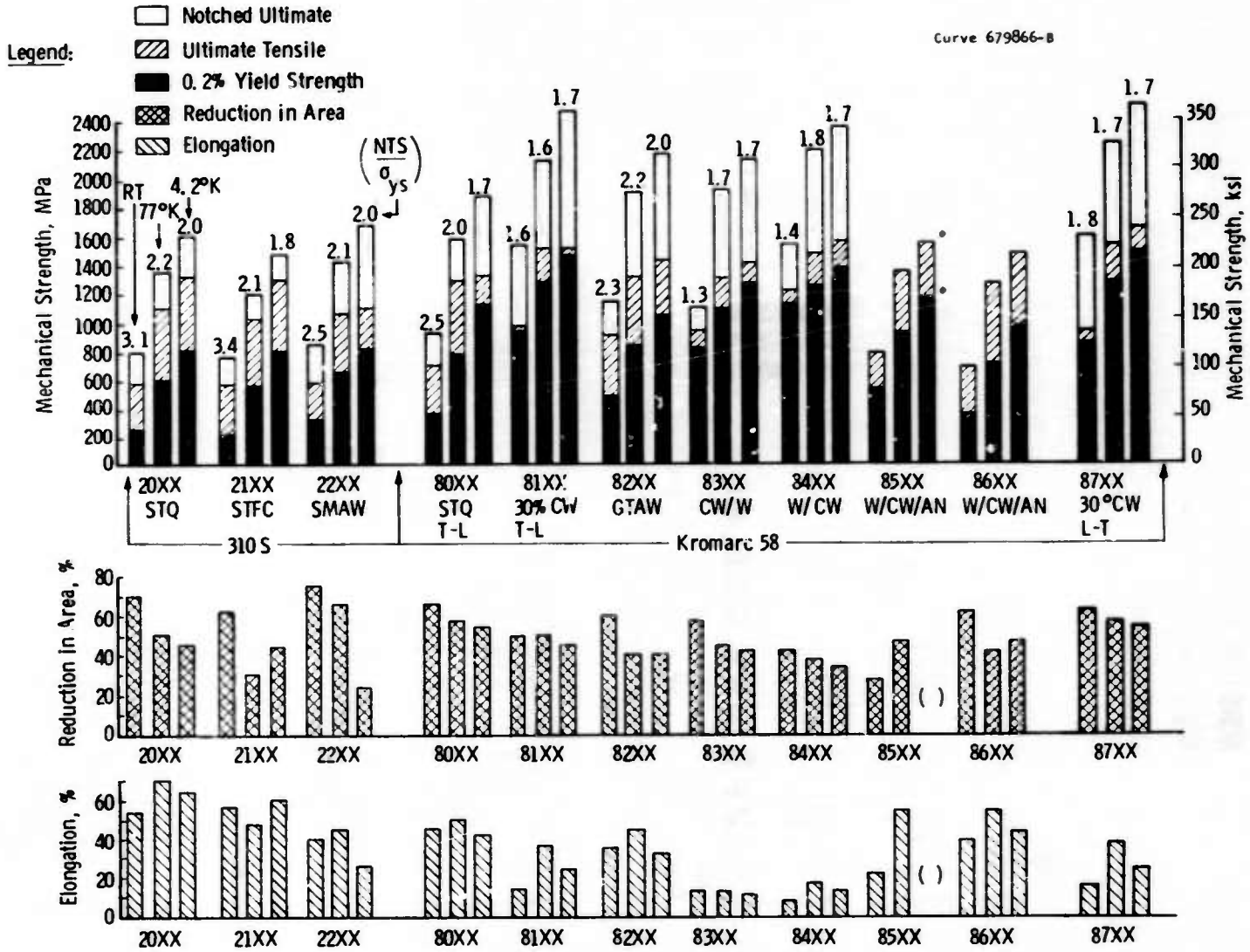

Fig 3-2— Summary comparison of mechanical strength and ductility values for AISI 310 S and Kromarc 58 stainless steels including processing and welded joints at RT, 77 K and 4.2 K

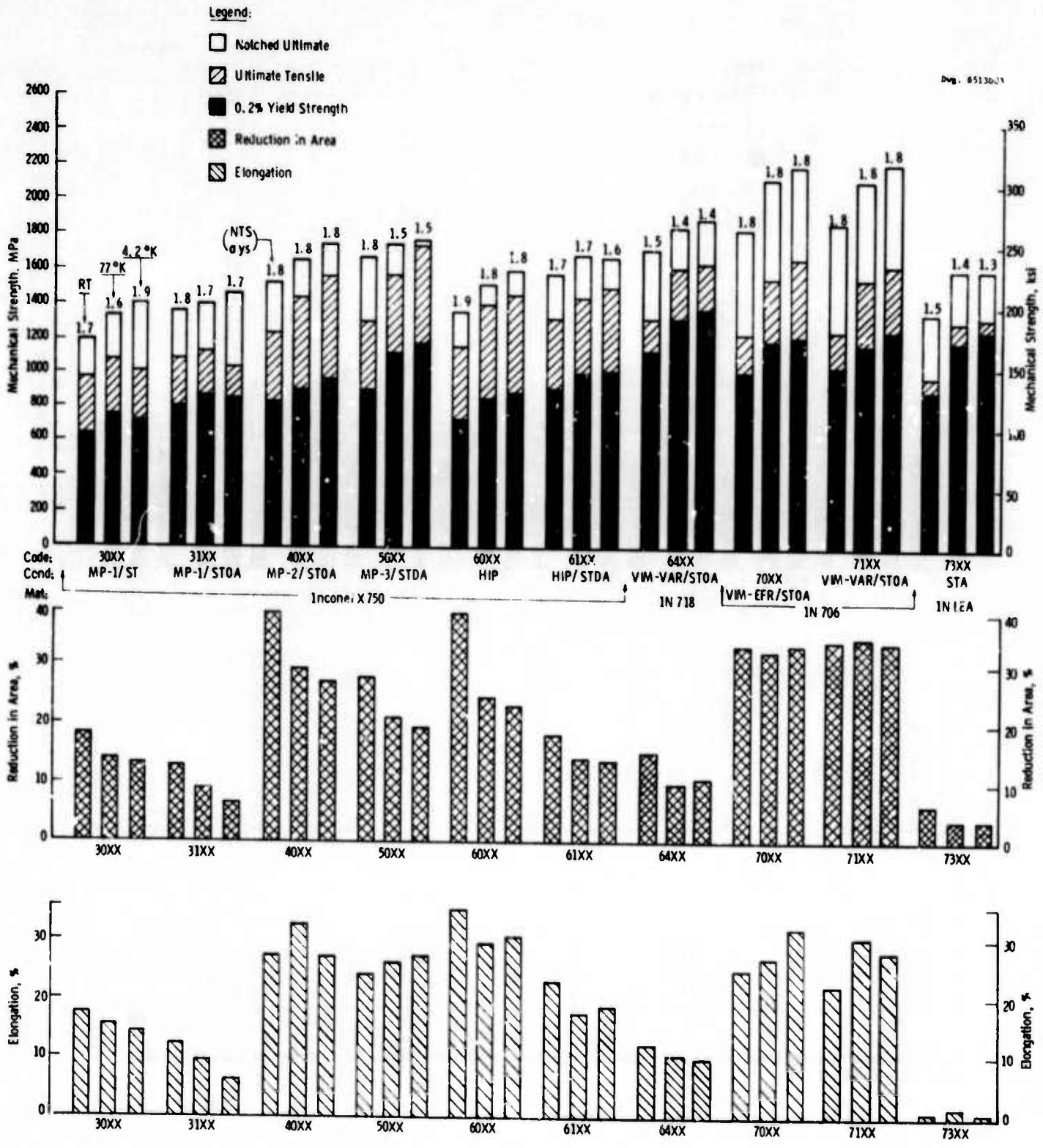

Fig. 3-3- Summary comparison of mechanical strength and ductility values for nickel based superalloys in various processed conditions at RT, 77 K, and 4.2K

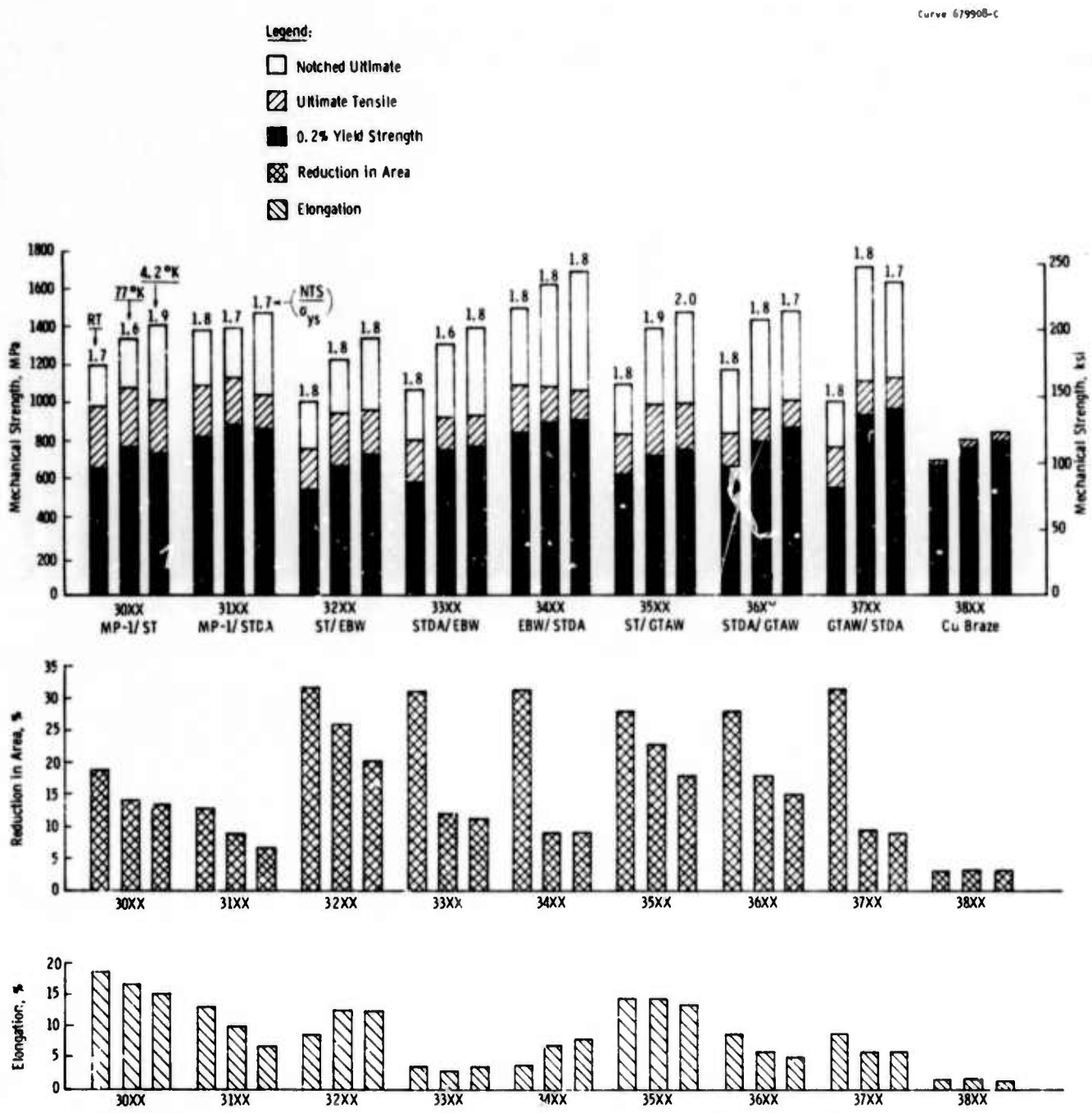

Fig. 3-4—Summary comparison of mechanical strength and ductility values for Inconel X 750 base metal, electron beam and GTA weldments and copper brazement at RT, 77 K and 4. 2K

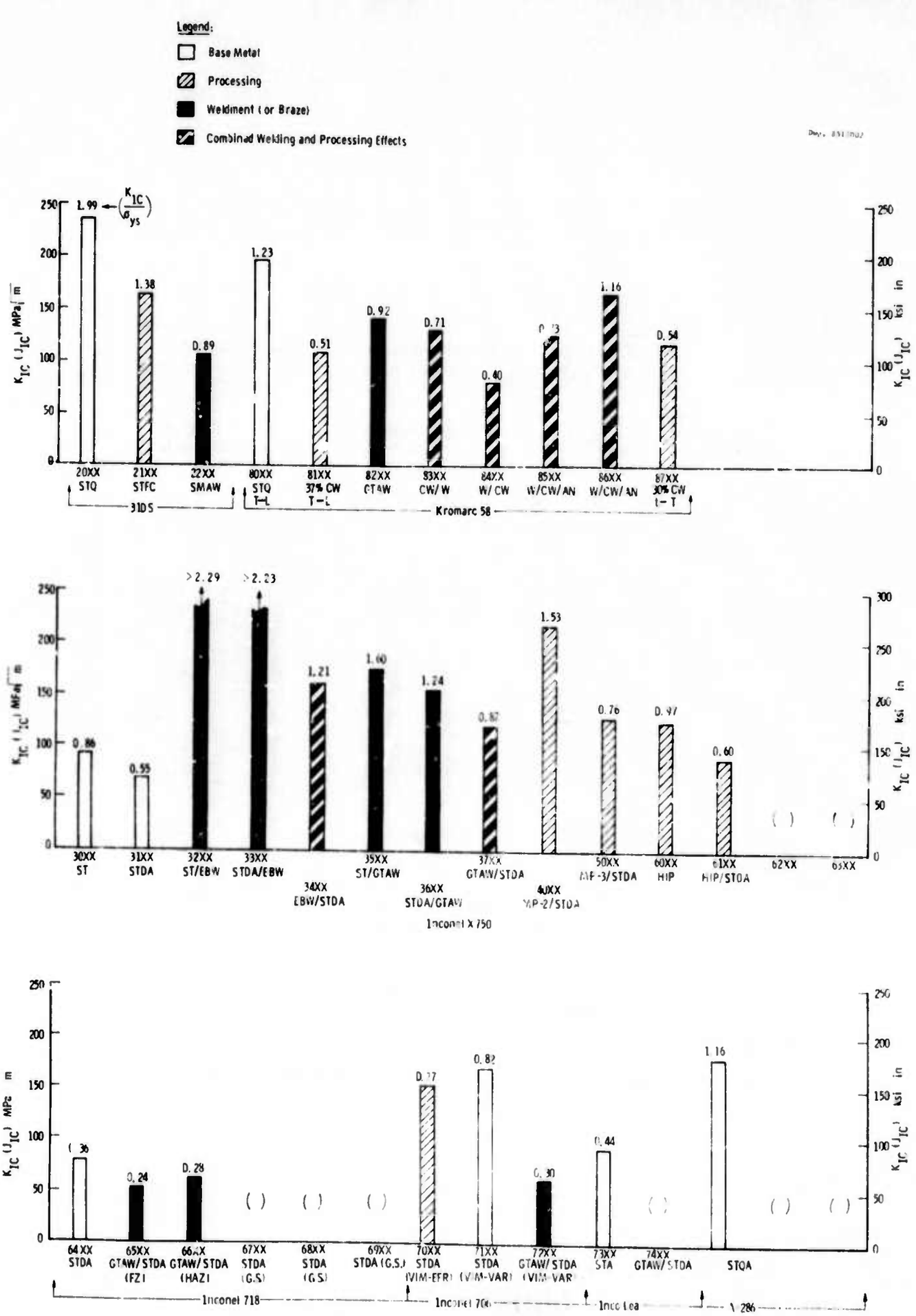

Fig. 3-5—Summary comparison of fracture toughness values at 4.2 K for 310S, Kromarc 58, Inconel X750, Inconel 718, Inconel 706, INCO LE[illegible], and A-286 materials including effects of processing and metals joining

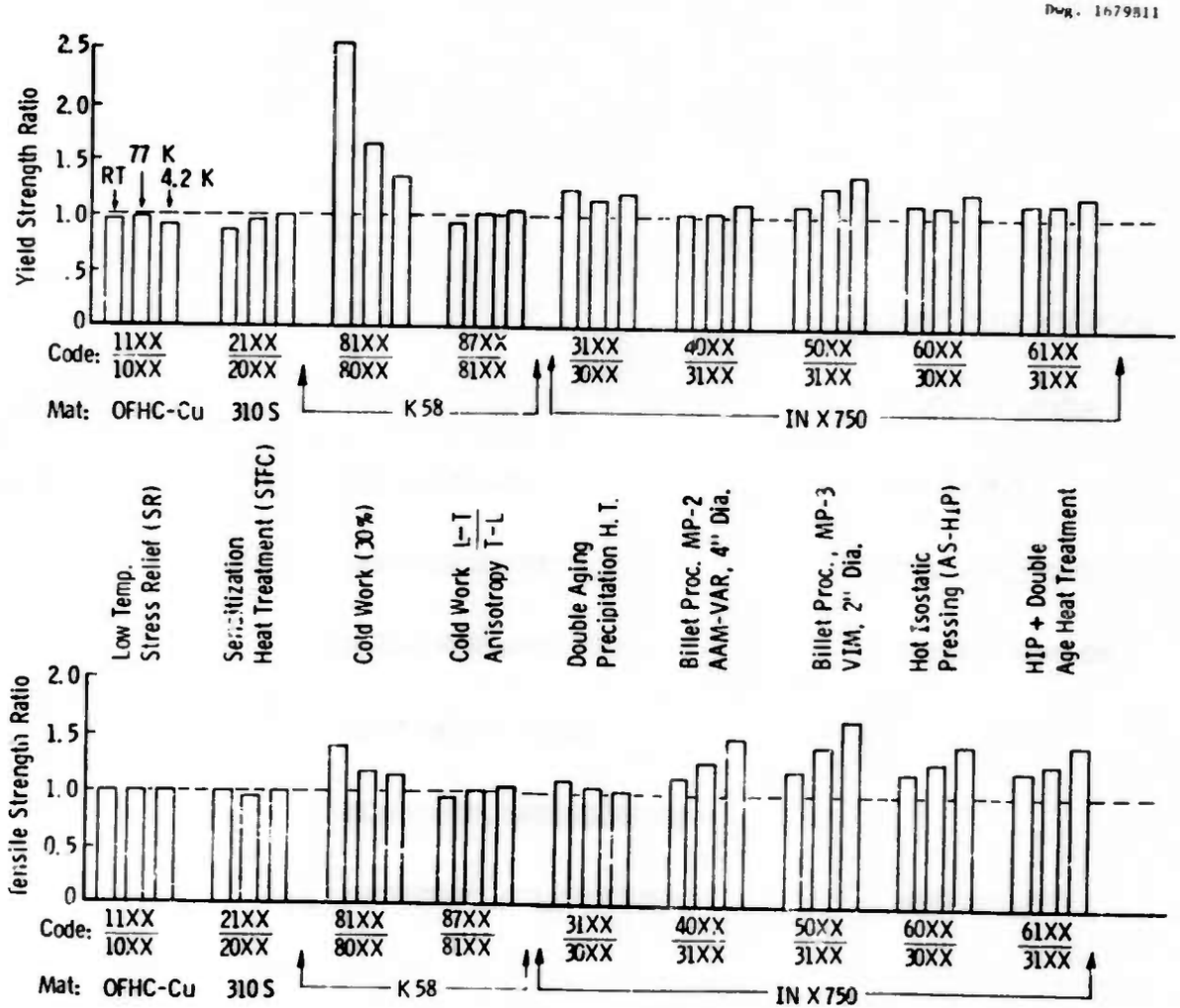

Fig. 3-6—Effect of processing conditions on yield strength and ultimate tensile strength ratios for OFHC Cu, 310 S, Kromarc 58 and IN X 750 at RT, 77 K and 4.2 K

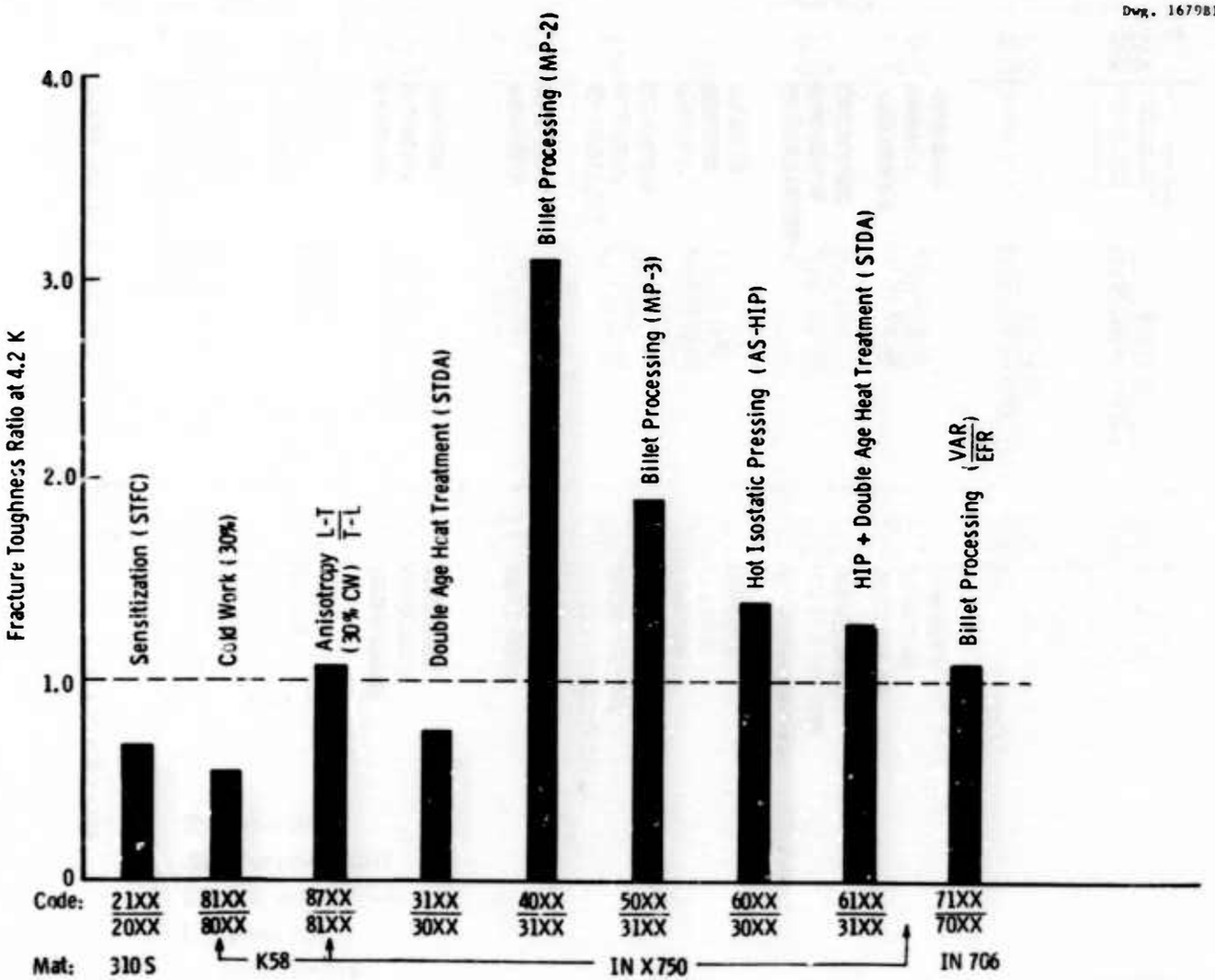

Fig. 3-7—Effect of processing conditions on fracture toughness ratio for 310 S, Kromarc 58, Inconel X750, and Inconel 706 at 4.2K

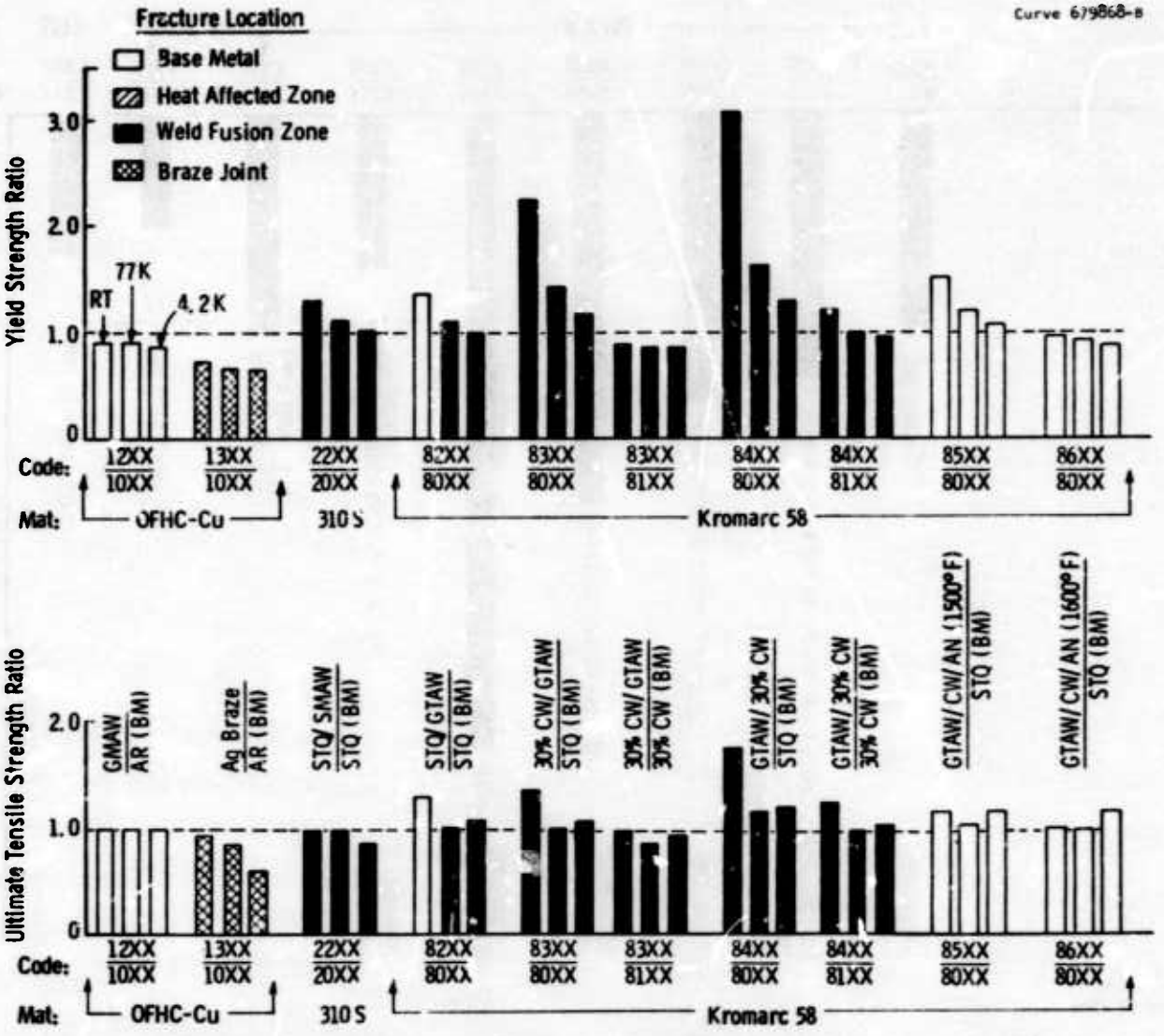

Fig. 3-8— Effect of metals joining conditions on yield strength and ultimate tensile strength ratios for OFHC copper, 310 S and K-58 stainless steel at RT, 77 K and 4.2 K

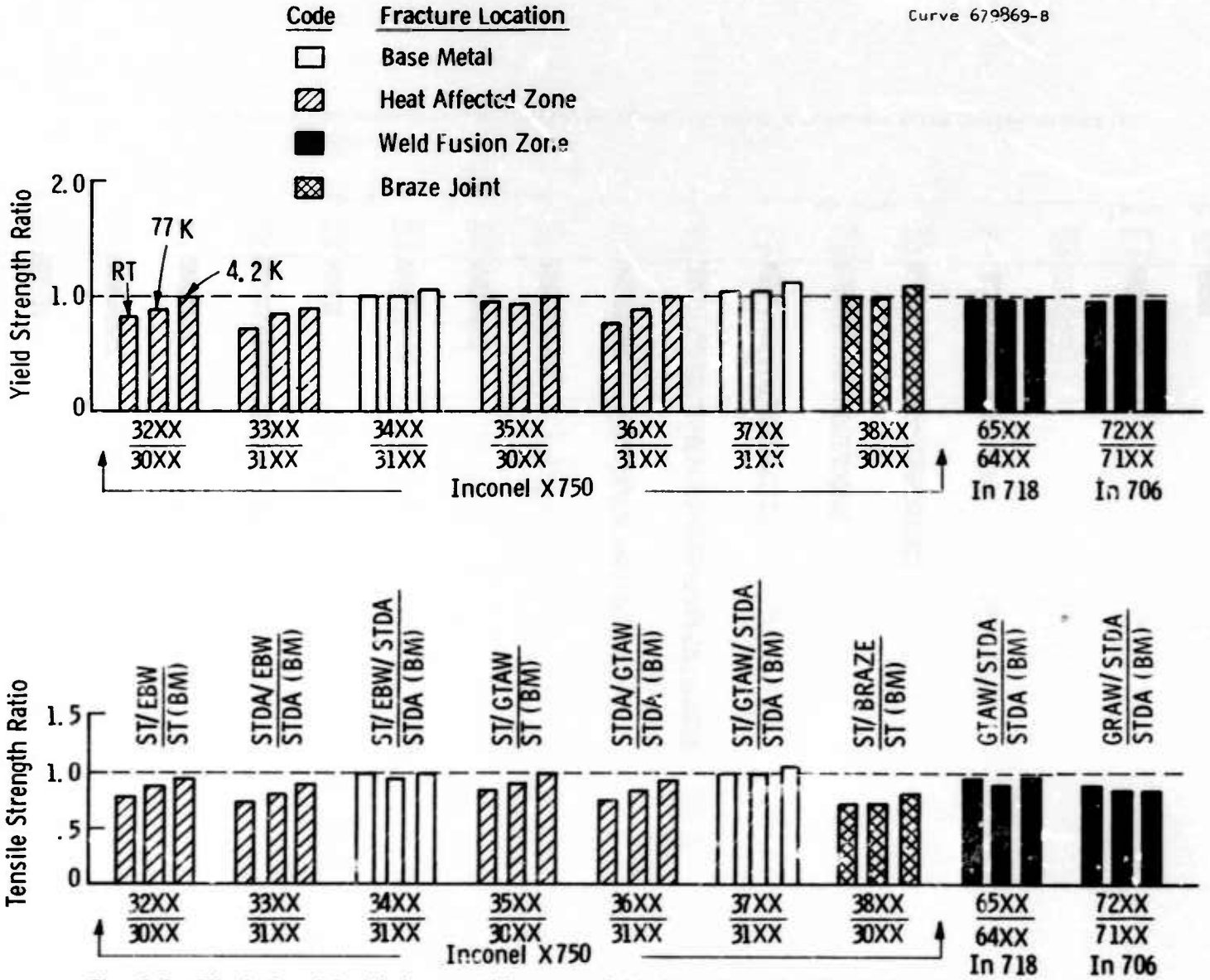

Fig. 3-9—Effect of metals joining conditions on yield strength and ultimate tensile strength ratios for Inconel X750, Inconel 718 and Inconel 706 at RT, 77K and 4.2K

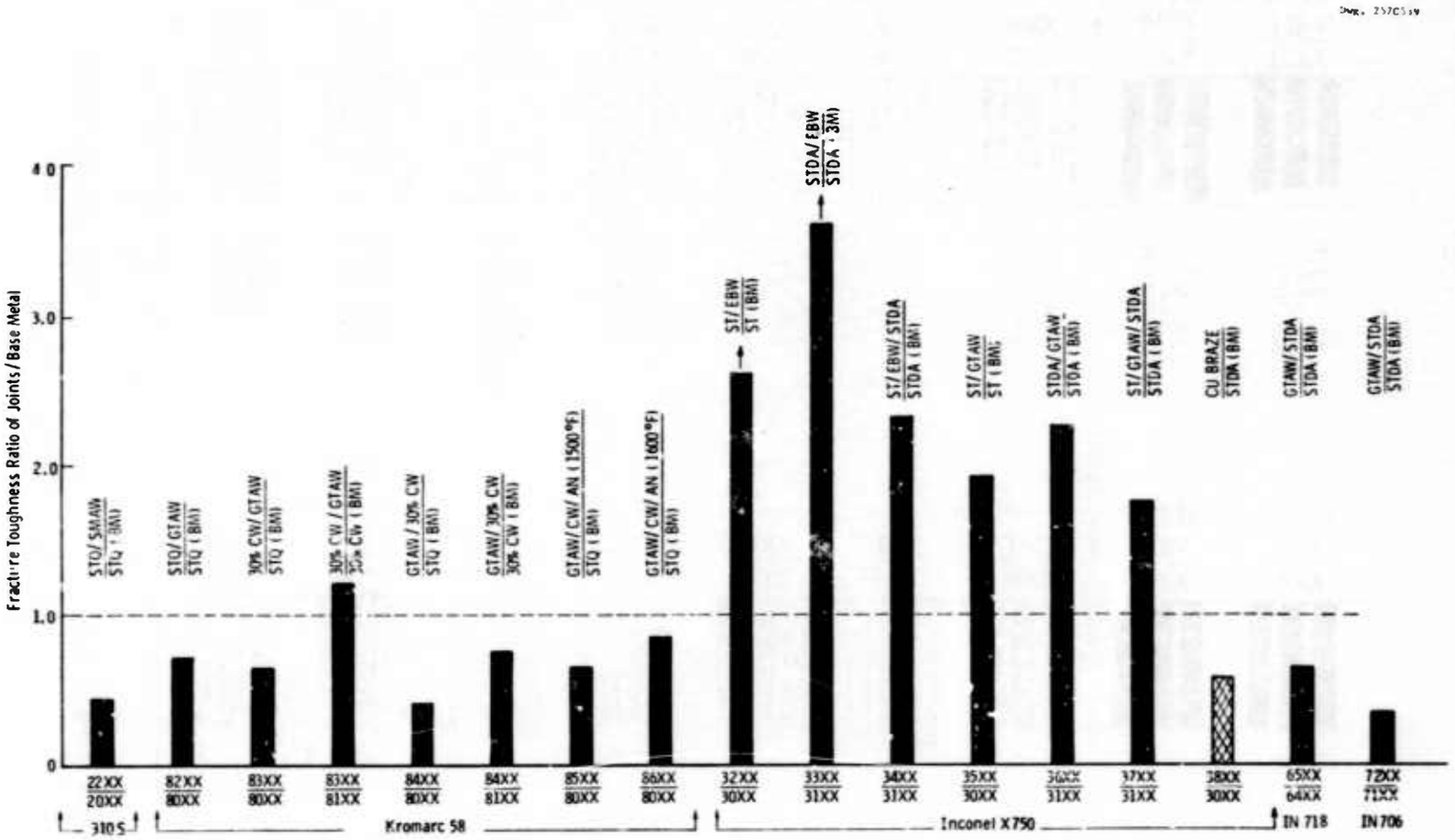

Fig. 3-10—Effect of metals joining conditions on fracture toughness ratio for 310S, Kromarc 58 stainless steel, INX750, IN718 and IN706 at 4.2 K

TABLE 3-1 STRUCTURAL MATERIALS FOR CRYOGENIC APPLICATIONS

FY74 Ⓡ Program Status As Of March 10, 1975

Material Code	Condition	Chem. Analy.	Metallography (1)	Metallography (2)	Physical Prop. Mag.	Physical Prop. Res.	Processing	Joining	Tensile R	Tensile N	Tensile H	Notched Tensile R	Notched Tensile N	Notched Tensile H	K1C R	K1C N	K1C H	J_{1C} (3) R	J_{1C} (3) H	FCGR R	FCGR N	FCGR H	Fractography (4) R	Fractography (4) N	Fractography (4) H
OFHC-Cu																									
10XX	AR	/1	2/1	1		1			1/1	1/1	1/1	1/1	1/1	1/1		1/2	1/2				/2	/3	1/1	3/3	3/3
11XX	SR		2/1	1			1/1		1/1	1/1	1/1	1/1	1/1	1/1		•/2	1/2				/2	/3			3/3
12XX	GMAW		3/2	1		1		3/2	2/2	2/2	2/2	2/1	2/2	2/2		•/2	→/2					/2	/1	/1	3/3
13XX	B		3/2	2				2/2	1/2	1/2	1/2	1/1	1/2	1/2		/2	→/2	4					/1	/1	2/2
14XX ◇	S		3/2	2				2/2	/2	/2	/2	/1	/2	/2		/2	/2						/1	/1	2/2
AISI 310S																									
20XX	STQ	□/1	2/2	1	2/1	2/1	1/1		1/1	3/2	4/2	1/1	1/2	1/2	•/1	2/2	2/3	4		●/1	1/2	4/3	1/2	1/3	3/3
21XX	STFC		1/1	1		1	1/1		1/1	1/2	2/2	1/1	1/2	1/2	•/1	2/2	2/3	5		●/1	2/2	2/3	1/2	1/3	3/3
22XX	SMW	□	2/2		1/1	1/1	2/2	2/2	2/1	2/2	2/2	2/1	2/2	2/2		•/2	→/	6			2/2	2/2	/1	/3	3/3
Inconel X750																									
30XX	ST	2/1	3/2	3	2/2	2/2	2/2		1/1	2/2	2/2	1/1	2/2	1/2	→/1	4/2	2/3	5	4	2/2	/2	2/3	2/2	2/3	4/4
31XX	STDA		3/2	3	2/1	2/1	2/2		1/1	2/2	2/2	1/1	2/2	2/2	•/1	4/2	2/3	5		2/2	/2	4/3	2/2	2/3	2/3
32XX	ST/EBW		2/3	1			3/3	3/3	1/1	1/2	1/2	1/1	1/2	1/2	•	/2	→/2	2			1/1	2/1	1/1	1/2	2/2
33XX	STDA/EBW		2/3	1			3/3	3/3	1/1	1/2	1/2	1/1	1/2	1/2	•	/2	→/2	2			1/1	1/1	1	1	2/2
34XX	EBW/STDA		2/3				3/3	3/3	1/1	1/2	1/2	1/1	1/2	1/2	•	/2	→/2	3			1/2	2/2	1	1	2/2
35XX	ST/GTW		3/3	1			3/3	4/3	1/1	1/2	1/2	1/1	1/2	1/2	•	/2	→/2	6			1/1	2/2	1	1	2/2
36XX	STDA/GTW		3/3	1			3/3	4/3	1/1	1/2	1/2	1/1	1/2	1/2	•	/2	→/2	5			1/1	2/2	1	1	2/2
37XX	GTW/STDA		3/3				3/3	3/3	1/1	1/2	1/2	1/1	1/2	1/2	•	/2	→/2	5			1/1	2/2	1	1	2/2
38XX	B		2/2	2			2/2	2/2	2/2	2/2	2/2	1/1	1/2	1/2	1	2/2	2/2						1	2/2	2/2
40XX	MP2/STDA	■/1	2/2	3			2/2		1/1	2/2	2/2	1/1	2/2	2/2	•	/2	→/2	6		1	1	1	1	1	2/2
50XX	MP3/STDA	■/1	2/2	3			2/2		1/1	2/2	2/2	1/1	2/2	2/2	•	/2	→/2	7		1	1	1	1	1	2/2
60XX	HIP	2/2	2/2	3			5/2		2/1	2/2	2/2	2/1	2/2	2/2	•	/2	→/2	7			2/2	2/2	1/1	2/2	2/2
61XX	HIP/STDA	1	2/2	3	1	1	3/2		2/1	2/2	2/2	2/1	2/2	2/2	•	/2	→/2	6			2/2	2/2	1	1	1/2
Kromarc 58																									
80XX	STQ	1/1	1/2	2	1/1	1/1	2/2		1/1	2/2	2/2	1/1	2/2	2/2	•	/2	→/3	5		1/2	1/2	2/3	1/2	1/3	2/3
81XX	CW		2/2	2	1/1	1/1	2/2		1/1	2/2	2/2	1/1	2/2	2/2	•	/2	→/3	5		1/2	1/2	2/3	1/2	1/3	2/3
82XX	GTW	1/1	4/2	2	1	1	2/2	2/2	1/1	2/2	2/2	2/1	2/2	2/2		/2	→/3	6			2/2	2/2	1/1	1/3	2/3
83XX	CW/GTW		1/2		1	1	1/1	1/1	2/1	2/2	2/2	2/1	2/2	2/2		/2	→/3	6					1	1	2/2
84XX	GTW/CW		1/2		1	1	1/1	1/1	2/1	2/2	2/2	2/1	2/2	2/2		/2	→/2	6							2/2
85XX	GTW/CW/AN		10/2				3/1	1/1	1/1	1/1	1/1	/1	/2	/2		/2	→/2	4							2/2
86XX	GTW/CW/AN						1	1/1	1/1	1/1	1/1							5							2/2

Notes: 1 Optical Microscopy

2 Replicate and Transmission Electron Microscopy, X-Ray Dispersive and Mic oprobe Analysis to be Incorporated as Required

3 Elastic-Plastic t J_{1C}) Testing and Analysis Techniques to be Incorporated Where Linear-Elastic t K_{1C}' Data is Non-Valid

4 Macro-and Microfractographic t SEM) Examination Sct.edute to be Adjusted in Response to Exhibition of Unusual Material Behavicr

• Available Specimen Size Invalid tor Meaningtui K_{1C} Interpretation - Test Eliminated

□ Certified Chemical Analysis from Supplier

■ Dilto-Additional Interstitial Analysis Comoleted at Ⓡ

→ J_{1C} Tests Substituted for K_{1C}

◇ Solder Joints Not Suitable for Mechanical Tests, Tests Eliminated

Dwg. 257C159

TABLE 3-2—STRUCTURAL MATERIALS FOR CRYOGENIC APPLICATIONS

FY75 Program Status as of September 10, 1975

Material Code	Condition	Chem. Analysis	Metallography (1)	Metallography (2)	Physical Mag.	Prop. Res. (3)	Processing Operations	Plates Joined	Tensile R	Tensile N	Tensile H	Notched Tensile R	Notched Tensile N	Notched Tensile H	K_{1C} (J_{1C}) R	K_{1C} (J_{1C}) N	K_{1C} (J_{1C}) H	FCGR R	FCGR N	FCGR H	Fractography R	Fractography N	Fractography H
PD135 Copper																							
15XX	EXT/PHT	■	2/2		1/1	2/2	2/2		2/2	2/2	2/2	2/2	2/2	2/2			6/6			/2	1/1	1/2	2/3
Inconel X750 HIP																							
62XX	GTAW/STDA(FZ)	□	2/2		1/1	1/1	2/2	2/2	/2	/2	/2	/2	/2	/2			/6			/2	/1	/1	/3
63XX	GTAW/STDA(HAZ)		2/2				2/2	2/2				/2	/2	/2			/6			/2	/1	/1	/3
Inconel 718																							
64XX	STDA	■	4/4	4	1/1	1/1	2/1		2/2	2/2	2/2	2/2	2/2	2/2	6	5/6				/2	1/1	2/2	3/3
65XX	ST/GTAW/STDA(FZ)		3/3	4	1/1	1/1	2/2	3/3	2/2	2/2	2/2	2/2	2/2	2/2		2 2/6				/2	1/1	1/1	3/3
66XX	ST/GTAW/STDA(HAZ)		3/3	4			2/2	3/3				2/2	2/2	2/2		2 2/6				/2	1/1	1/1	2/3
67XX	ST/CW/AN		2/3				2/3		/2	/2	/2	/2	/2	/2			/6						/2
68XX	ST/CW/AN		2/3				2/3		/2	/2	/2	/2	/2	/2			/6						/2
69XX	ST/CW/AN		2/3				2/3		/2	/2	/2	/2	/2	/2			/6						/2
Inconel 706																							
(EFR) 70XX	STDA	■	4/4	4	1/1	1/1	1/1		2/2	2/2	2/2	2/2	2/2	2/2			5/6			/2	1/1	1/1	2/3
(VAR)71XX	STDA	■	4/4	4	1/1	1/1	1/1		2/2	2/2	2/2	2/2	2/2	2/2	7	7/6				/2	1/1	1/1	3/3
(VAR) 72XX	ST/GTAW/STDA		3/3	4	1/1	1	2/2	3/3	2/2	2/2	2/2	2/2	2/2	2/2			4/6			/2	1/1	1/1	3/3
INCO LEA																							
73XX	STA	■	3/3	4	1/1	1/1	2/2		2/2	2/2	2/2	2/2	2/2	2/2	5	5/6				/2	1/1	1/1	2/3
74XX	ST/GTAW/STA		2/2	3	1/1	1	2/2	2/2	/2	/2	/2	/2	/2	/2			/6			/2	/1	/1	/3
Kromarc 58																							
87XX	STW/CW/θ*	□	1/1				2/2		2/2	2/2	2/2	2/2	2/2	2/2			6/6	1	1	1/2	1/1	1/1	1/3

Notes: (1) Standard optical microscopy
(2) Electron microscopy, microprobe & X-ray dispersive analysis incorporated as required
■ Certified chem. analysis from supplier, additional interstitial gas analysis by
□ Analysis conducted for this material in FY74 program
(3) Physical property determinations also conducted on five materials (Fe - 9% Ni, Fe - 68% Ni, Fe - 3% Si, AISI 416SS and ARMCO Fe) requested by NBS

4.0 WESTINGHOUSE PROGRAM DESCRIPTION

This program represents the active participation of the Research Laboratories of the Westinghouse Electric Corporation under Contract CST-8304 in a comprehensive overall program for cryogenic structural materials monitored by the Cryogenics Division of the National Bureau of Standards. The overall program is sponsored by the Advanced Research Projects Agency (ARPA) of the Department of Defense. The overall outline for the Westinghouse portion of the ARPA-NBS program is shown schematically in Fig. 4-1. The principal personnel involved are listed in Fig. 4-2 according to their respective functional project responsibility areas.

Several advanced cryogenic application areas are identified in which the subject matter of this program will be mutually beneficial. One such advanced application area for cryogenic structural materials requiring immediate attention is that of superconducting electrical machinery[2] as typified by two recent 5 MVA S.C. generator prototypes developed by Westinghouse[3-5]. Other important cryogenic application areas include electrical transmission lines, superconducting magnet support structures for Controlled Thermonuclear Reactor (CTR) devices, and structural materials for second generation rotating superconducting machinery designs.

4.1 FY 74 Program

The first year's programs (Sept. 73-Sept. 74) key off typical structural materials requirements for S.C. machinery prototypes. This project is subdivided into three tasks as follows:

Task I

Characterization of four materials currently being considered for superconducting machinery applications. These materials include OFHC Copper (CDA No. 102), AISI 310S Stainless Steel, Inconel X750 Superalloy and Kromarc-58 Stainless Steel. An operational flow chart of Task I is shown in Fig. 4-3.

Task II

Evaluation of selected processing effects on the structure and properties of two representative structural materials being considered for cryogenic applications. These processing considerations include three different commercial melting and primary working practices of Inconel X750, hot isostatically pressed (HIP) consolidation of Inconel X750 powder, slow cooling (sensitization) effect in AISI 310S stainless and the combined effects of cold working and welding in Kromarc 58 stainless steel alloy. An operational flow chart of Task II is shown as Fig. 4-4.

Task III

Evaluation of selective joint fabrication methods in four materials for cryogenic applications. Joining techniques include shielded metal arc (SMA), gas metal arc (GMA), gas tungsten arc (GTA), vacuum electron beam (EB) welding, brazing and soldering. An operational flow chart of Task III is shown as Fig. 4-5.

4.2 FY 75 Program

The FY 1975 continuation of the Westinghouse portion of this ARPA-NBS program is also divided into three similar task areas which are outlined schematically in Figs. 4-6 to 4-8.

The approach to this present continuation effort is similar to the FY 74 effort reported previously. All material has been procured and identified with respect to heat number, melting practice employed, chemical composition and microstructural analysis in the as-received condition. One judiciously selected thermal treatment was identified and performed on each of the three selected base materials.

Then, the previously employed functional test areas were used in characterizing these materials.

In addition to the characterization of weld fusion zones on composite weldment specimens of these additional materials, testing has also been conducted on the heat-affected-zone (HAZ) areas of selected weldments in Inconel 718. For this effort, specially prepared weldments using "K" shaped joint designs with their approximate planar (on one side) HAZ were employed.

The results of the FY 75 respective study elements are presented, analyzed and summarized in a quantitaitve as well as a qualitative manner. In addition, a relative interpretation of these results is continued with respect to the similar previously attained information on FY 74 materials and with respect to the relative overall applicability of these selected materials for general and specific cryogenic structural applications.

References (Section 4)

1. Bishop, J., Jr., "Study of the Markets for Large Rotating Electrical Machinery 1970-2000", A. D. Little, Inc. Report to U.S. Dept. of Commerce, NBS, Contract CST-8221, February 1973.

2. Baldwin, M. S. and Sterrett, C. C., "The Potential Impact of Superconducting Turbine Generators on the Electric Utility Industry", Proc. of the American Power Conference, V. 36, 1974.

3. Mole, C. J., Fagan, T. J., Haller, H. E. III, Litz, D. C. and Patterson, A., "Five MVA Superconducting Generator Development", Westinghouse Research Laboratories Paper 72-1J2-CRYAL-P3 (Unrestricted), September 22, 1972.

4. Blougher, R. D., Fagan, T. J., Parker, J. H., Jr., Wells, J. M. and McCabria, J. L., "A High Speed Superconducting Generator", Inter. Cryogenic Eng. Conf. held in Kyoto, Japan, May 1974 (Proceedings to be published.).

5. Blaugher, R. D., McCabria, J. L. and Parker, J. H., Jr., "Program For the Development of a Superconducting Generator", Technical Report AFAPL-TR-74-84, Part I (1974).

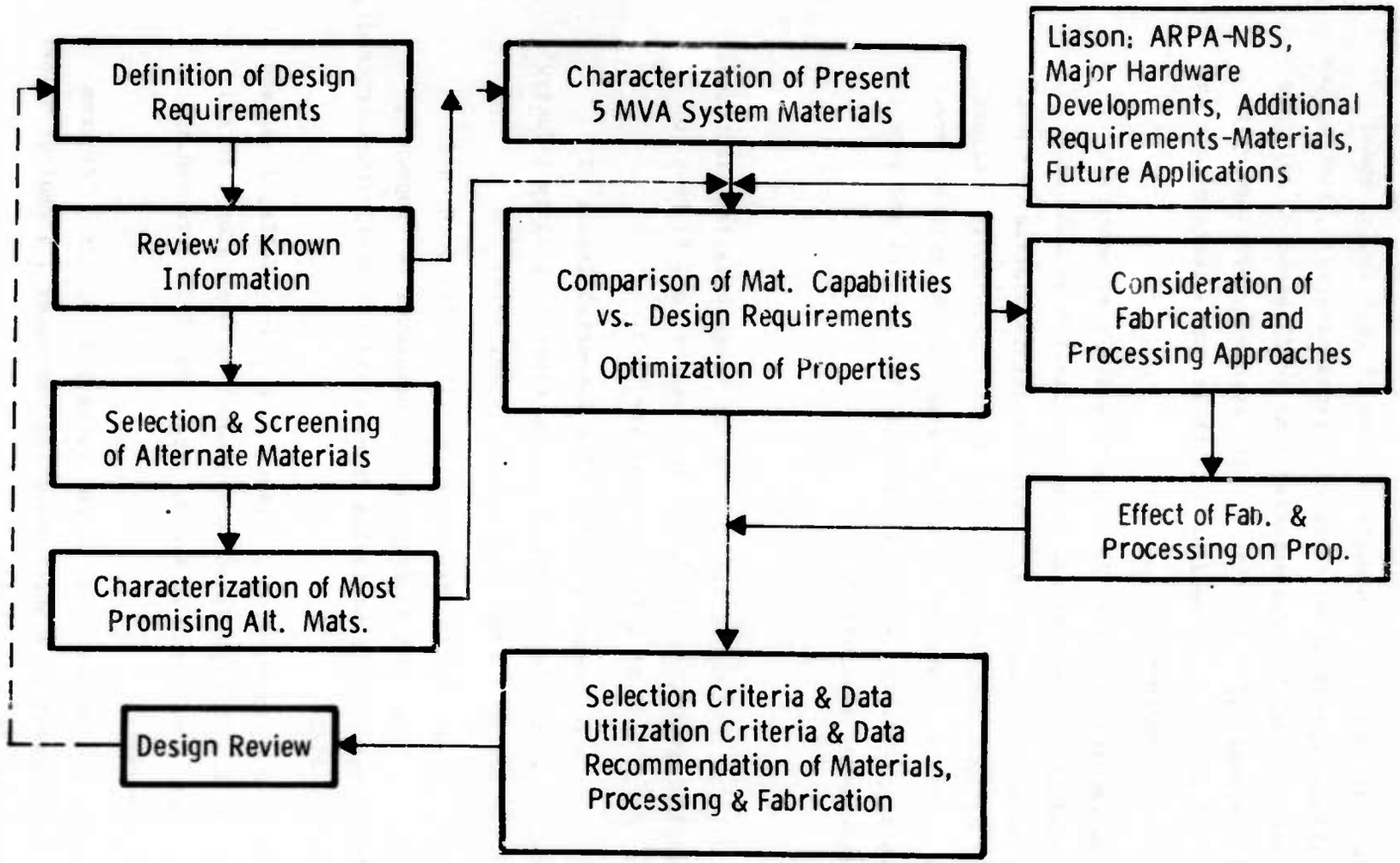

Fig. 4-1 Program Outline – Structural Materials for Cryogenic Applications

EVALUATION OF CRYOGENIC STRUCTURAL MATERIALS, NBS CONTRACT 8304

Functions	Task I Basic Characterization	Task II Processing Effects	Task III Joint Behavior
Metallurgy, Processing, Joining	•	•	•
Fracture Mechanics	•	•	•
Fractographic & Micro-Structural Analysis	•	•	•
Magnetic Properties	•	•	•

Westinghouse Program Organization

Management

Program Manager - J. M. Wells
Advisors - G. G. Lessmann
E. T. Wessel

Principal Investigators

Materials, Processing, Fabrication - J. M. Wells
Fracture Mechanics - W. A. Logsdon
Microstructural Analysis - R. Kossowsky
Magnetic Properties - M. R. Daniel

Fig. 4-2 Westinghouse Program Organization - FY75

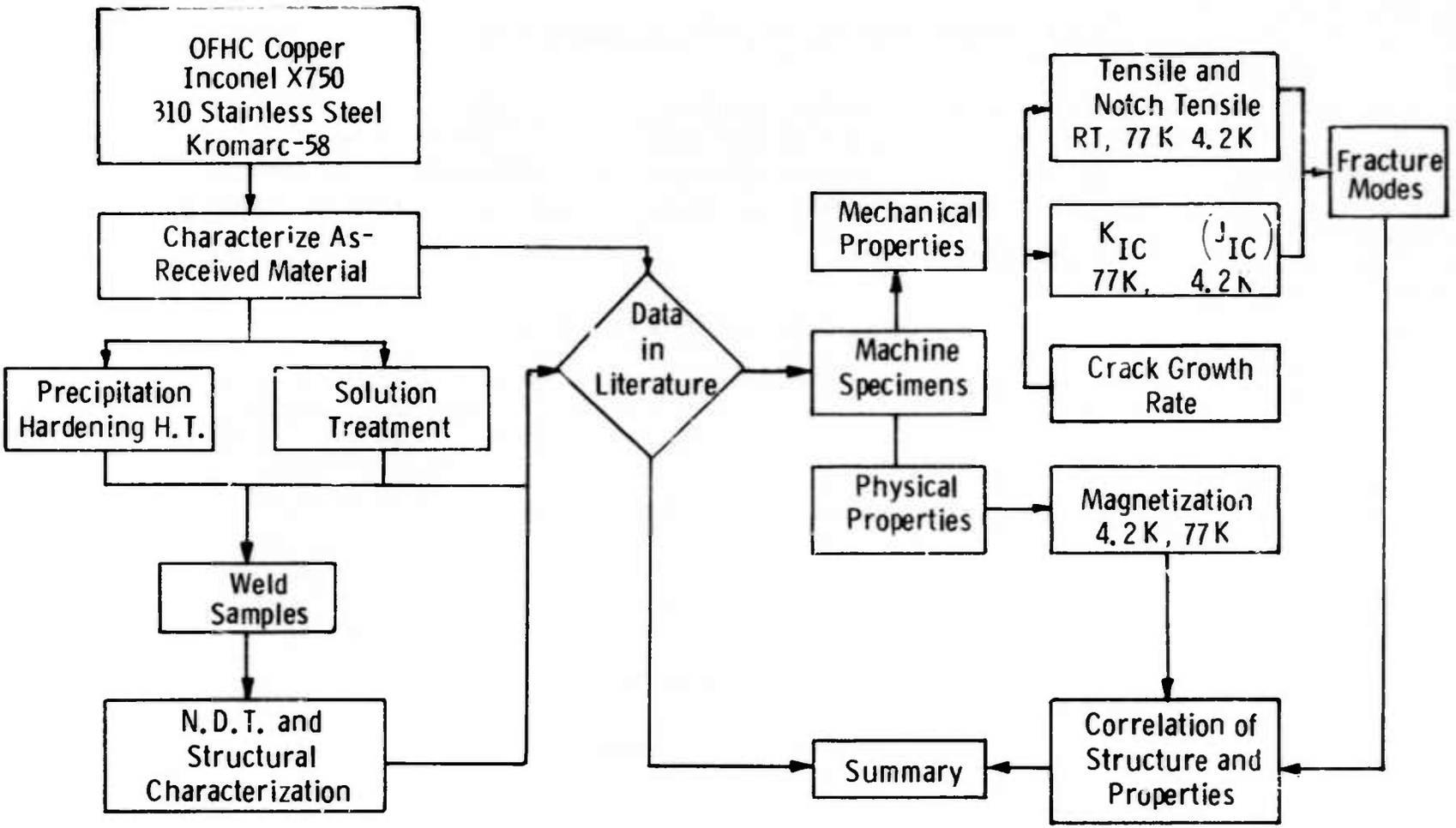

Fig. 4-3 TASK I – (Ⓨ FY74 Program) Characterization of Candidate cryogenic structural materials

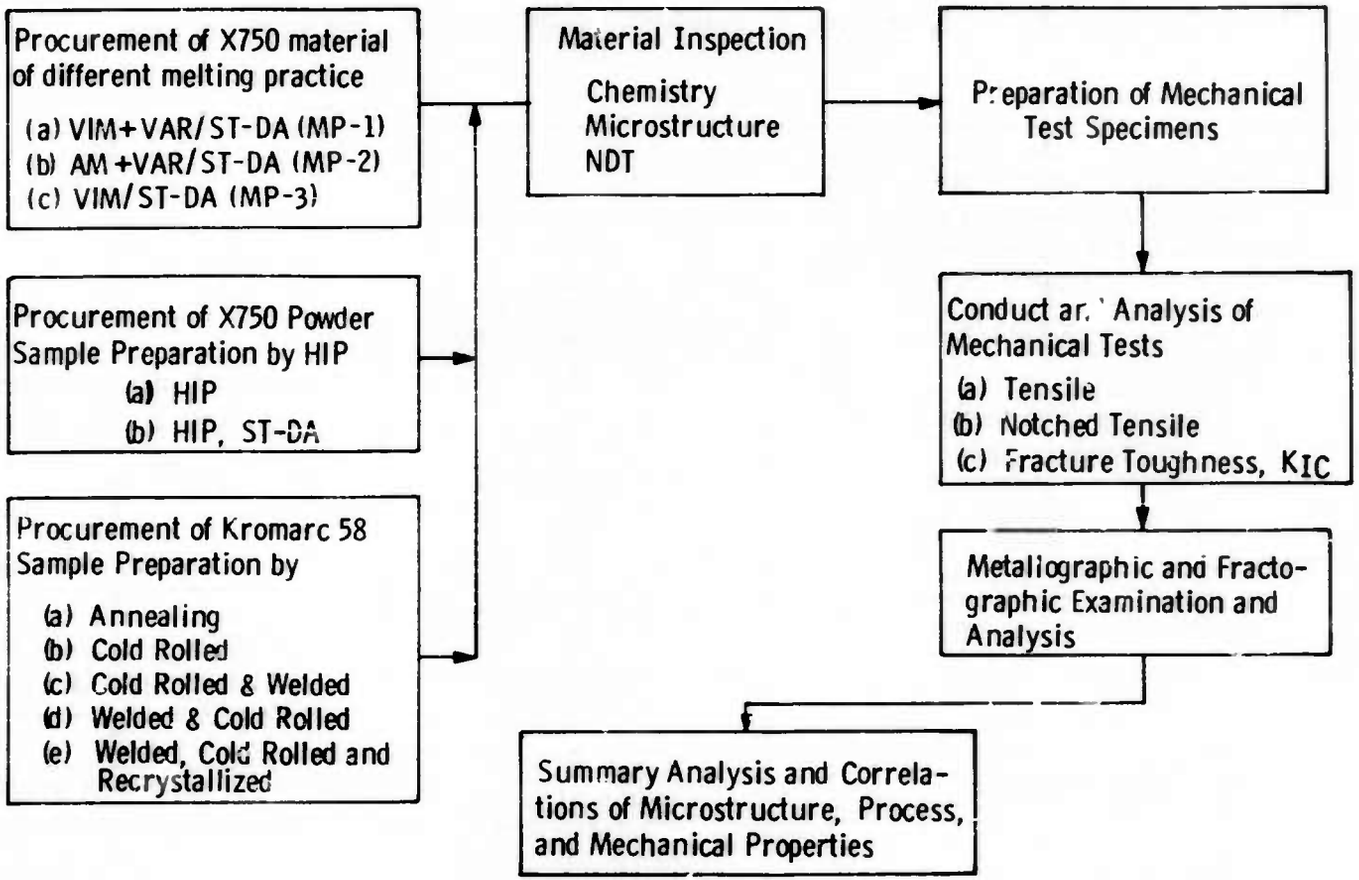

FIG. 4-4 TASK II-(Ⓦ FY74 Program) Processing Effects On Properties Of Structural Cryogenic Materials

Dwg. 7258081

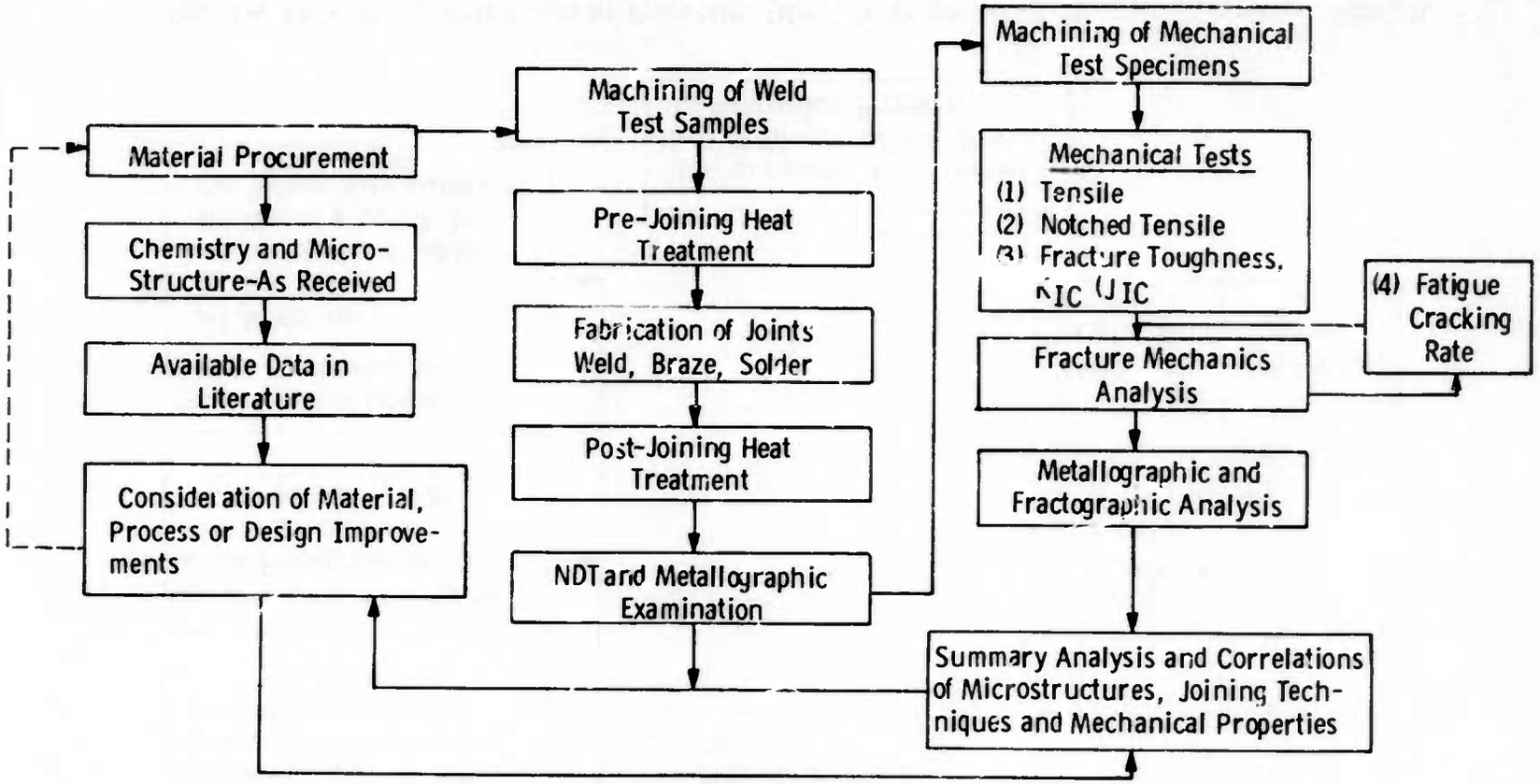

FIG. 4-5 TASK III–(FY74 Program) Evaluation Of Joints In Structural Cryogenic Materials

Dwg. 1670B63

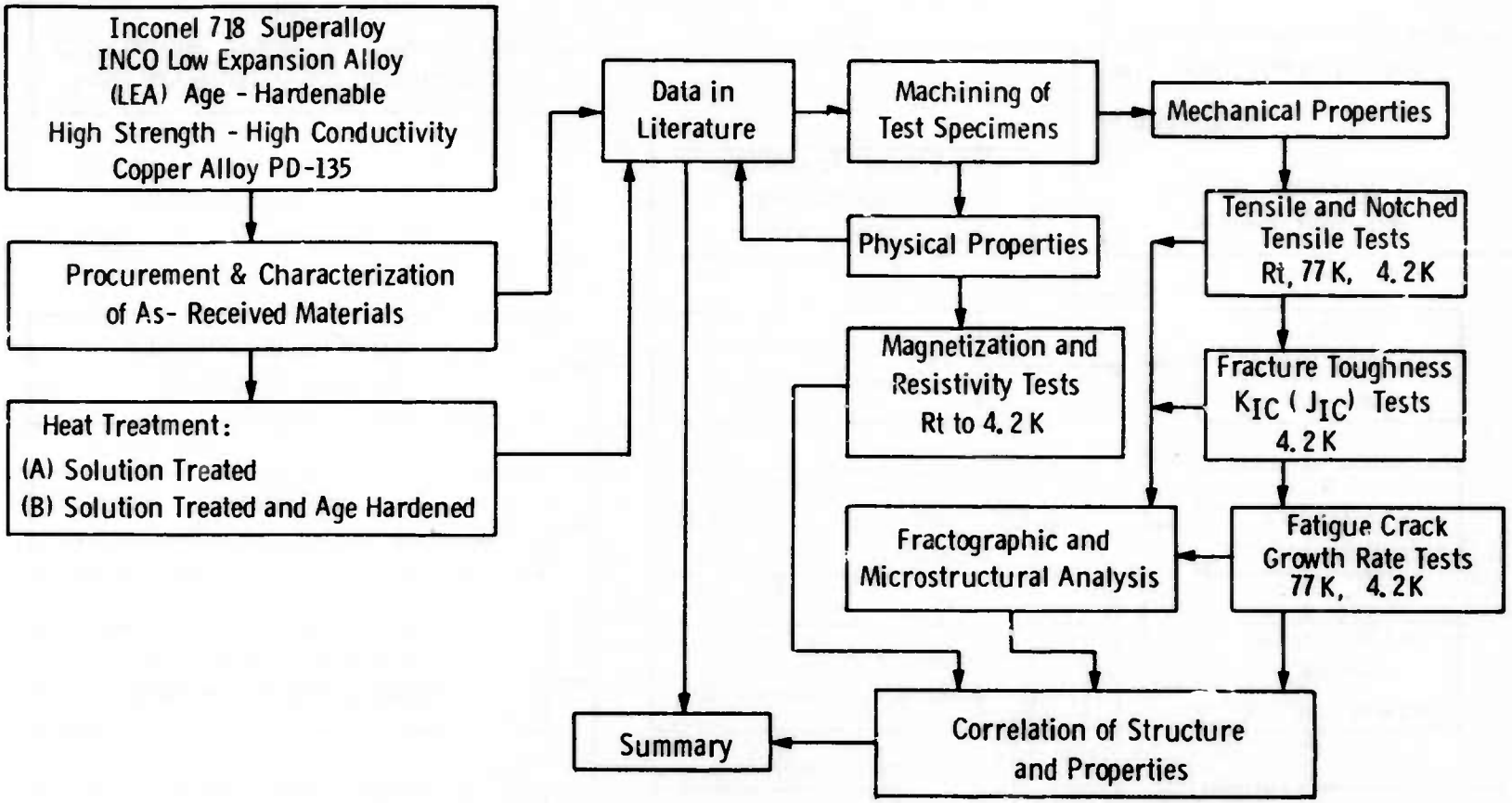

Fig. 4-6 — Task I (Ⓦ FY 75 Program) Characterization of Structural Base-Materials For Advanced Cryogenic Applications

Dwg. 6708B64

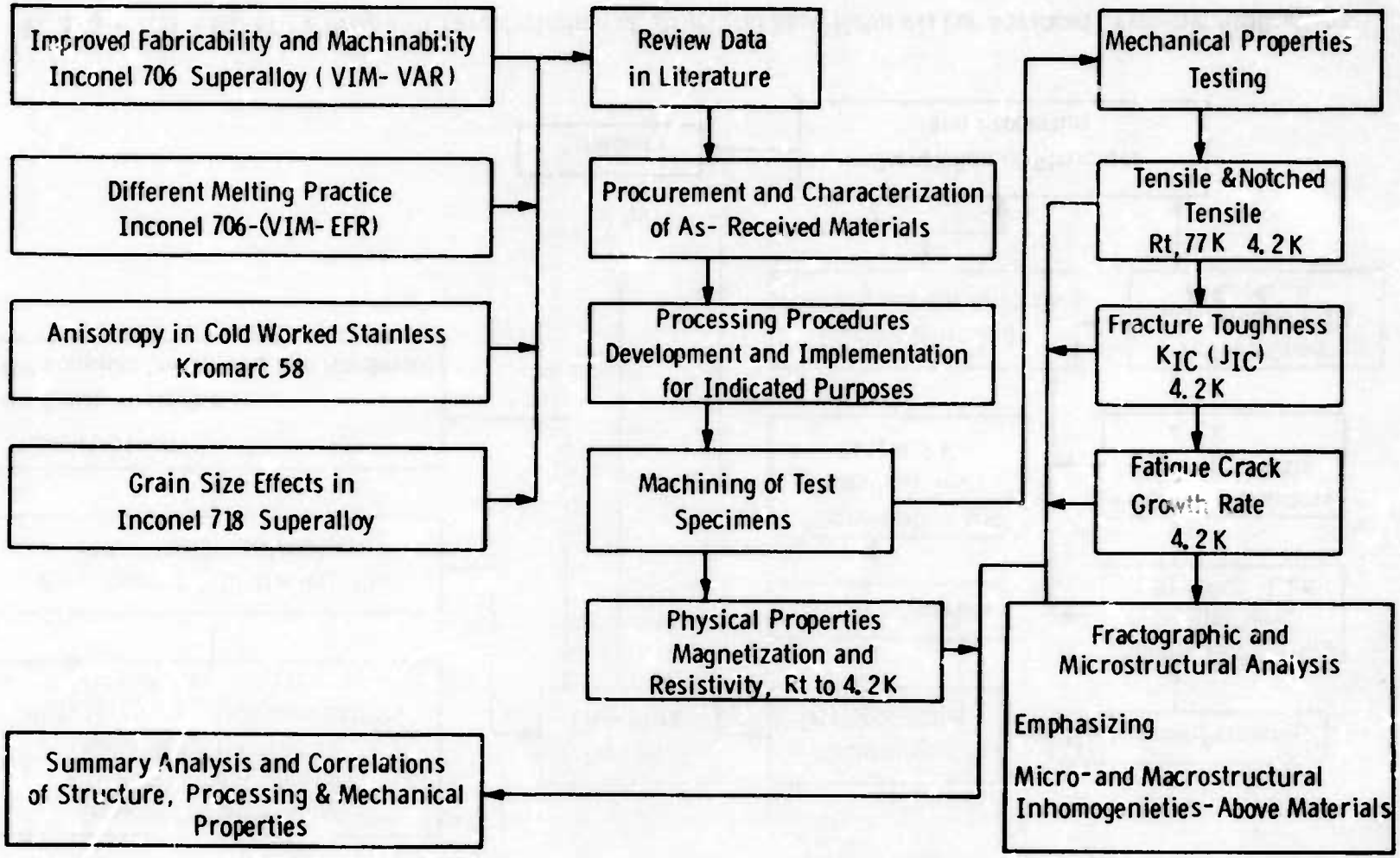

Fig. 4-7– Task II (Ⓦ FY75 Program) - Processing Effects On Cryogenic Structural Materials Properties

Dwg. 1670B65

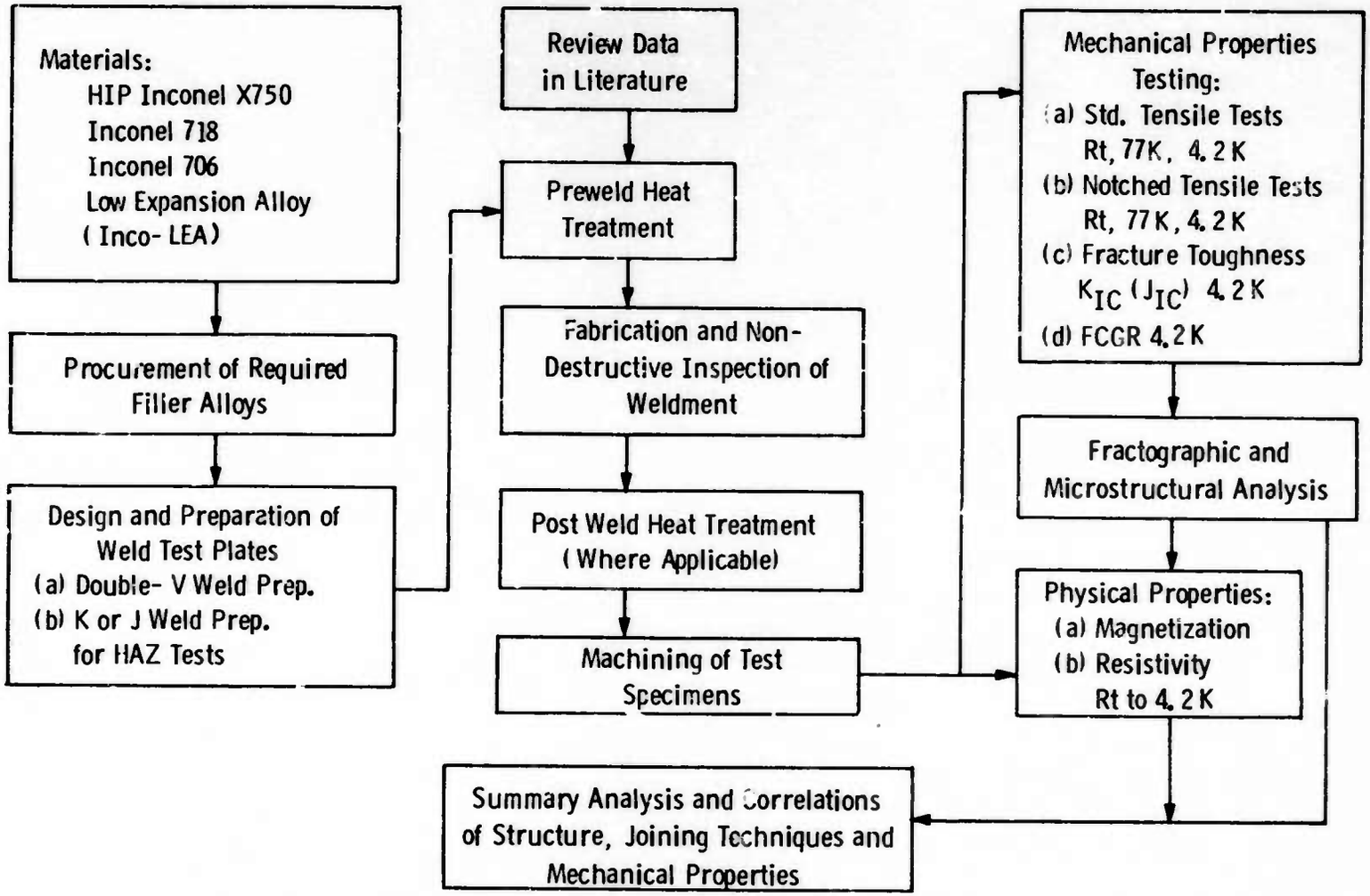

Fig. 4-8 -Task III (Ⓦ FY75 Program) - Fabricated Joints In Cryogenic Structural Materials

5.0 GENERAL CRYOGENIC STRUCTURAL MATERIALS/PROCESSING/ FABRICATION CONSIDERATIONS

Several aspects of structural materials considerations of general interest to both designers and materials specialists have been presented in Section 5 of the three previous Westinghouse Semi-Annual Technical reports[1-3]. While it is not practical to repeat such discussion here in this report, it does appear worthwhile to briefly mention the following topical areas which have been discussed to date in the preceeding reports:

- Primary catagories of cryogenic structural materials applications.
- Deficiencies of previously developed cryogenic materials data.
- Logic and objectives of establishing materials selection and utilization criteria.
- A listing of specific alloys, literature review and discussion of candidate materials for structural cryogenic applications.
- Review of materials processing and fabrication considerations including welding, brazing and soldering for cryogenic applications.
- Characterization as per the Materials Advisory Board (MAB) recommendations.
- Practical basis for materials selection, processing and fabrication data generation.
- Definition and discussion of "Advanced" cryogenic structural applications.

- Suggested designer/materials selection, processing and fabrication toward achieving a failure-safe design.
- Literature review of non-austenitic steels for cryogenic application.

The rationale for presenting such continuing discussions throughout this series of technical reports is to provide a written practical perspective on the selection and utilization of structural materials for extreme cryogenic application. As such, we find this perspective useful in establishing a basis of discussion and interaction with concerned design and administrative personnel rather than solely presenting the volumnious empirical test data also being generated.

5.1 Material Selection Considerations

5.1.1 Metal Alloy Designation Terminology

The Westinghouse portion of this ARPA/NBS program has mainly been concerned with the evaluation of various metal alloys as cryogenic structural materials. A listing of the more promising candidate structural metals for cryogenic superconducing machinery applications compiled by the present author is included as Table 5-1.

One decision area which arises in a materials evaluation program is in selection of terminology used to refer to such alloys so that designers, materials specialists, metals producers, and fabricators all understand exactly what materials are being characterized and evaluated. The cryogenic structural materials candidates in Table 5-1 are listed by common commercial trade designations, which is by no means to be construed as an endorsement of any particular alloy. Although generally recognized and understood these trade names can, admittedly, still lead to some confusion. For example, Inconel 718 is the commercial designation (trade name) which Huntington Alloys Division of the International Nickel Corporation uses to designate a particular nickel base superalloy. This alloy is also produced by Special Metals Corporation (as Udimet 718),

Universal-Cyclops Specialty Steel Division (as Unitemp 718) and by Carpenter Technology Corporation (as Pyromet 718) to name just a few alternative producers fo the same basic alloy composition. In addition, the various producers may employ different and even alternative melting and mill hot working schedules such that although the alloy compositions are all within a given specification range, the microstructure and hence the structure sensitive mechanical properties may be considerably different.

Other alternative ways of designating such alloys rather than by commercial trade designations are:

- Primarily metal producer sponsored organization specifications such as the Aluminum Association (AA), The Copper Development Association (CDA) and The American Iron and Steel Institute (AISI).
- Primarily metal user sponsored organization specifications such as the Society of Automotive Engineers (SAE), American Society of Mechanical Engineers (ASME) and Federal and Military Specifications (QQ and MIL Specs).
- Combined user and producer sponsored specifications such as American Society for Testing and Materials (ASTM), American National Standards Institute (ANSI), and the American Welding Society (AWS).

Using such "standard" specifications for the purpose of alternative alloy designation terminology is not without its own inadequacies, however. For example, a given alloy may be included in several different specifications originating from the same society (Oxygen Free Copper is covered by over 30 ASTM specifications depending on the product form and intended use). Furthermore, the alpha-numerical designation used in a particular specification often bears no resemblance to the commonly known alloy designation (trade name). For example, the

precipitation hardening stainless steel referred to in this work as A-286 is designated as Alloy 660 by AISI, A638 by ASTM, J 467 (A 286) by the SAE and is covered by approximately nine different Aerospace Materials Specifications (AMS).

A relatively recent and comprehensive metal alloy designation system has been advanced jointly by the Society of Automotive Engineers, Inc. (SAE) and the American Society for Testing and Materials (ASTM)[4]. This system, identified as the Unified Numbering System For Metals and Alloys, provides a systematic means of correlating the various alpha-numerical systems mentioned above and will hopefully avoid the confusion associated with more than one designation for the same material and having the same designation assigned to more than one material. This system does not replace nor serve as a product specification but rather serves only as a unified identification system for metals and alloys meeting a certain chemical composition range. A cross reference is included as Table 5-2 in this report which contains the commercial designation, the Unified Numbering System (UNS) designation and various society specification designations for those candidate cryogenic structural materials listed in Table 5-1.

It is the opinion of the present authors, that if one has reservations to referring to engineering metal alloys by the commercail trade designation, the UNS alloy designation system is a more meaningful and potentially useful alloy designation technique, in general, than the use of various association or society materials specifications, which are in our opinion, more useful for product form specifications. The UNS System does not, at present, include metal matrix composite materials or any non-metallic materials.

5.1.2 Variations in Reported Alloy Property Data

One of the general criteria for selection of structural materials for cryogenic temperature applications is, of course, mechanical behavior. While the designer would like to be able to go to a handbook, select an alloy and obtain a design reliable value for a given mechanical property,

unfortunately such is not now the case. Published mechanical property values for extreme cryogenic temperatures are specific (or averaged) measured values which may or may not be acceptable design values. The usefulness of such published property data (including that from the present work) to a designer of cryogenic structures is strongly dependent upon the familiarity of the designer with the associated material characterization (i.e. composition, form, processing and fabrication history and microstructure).

An examination of the variations in the mechanical properties of two alloys being evaluated in this overall ARPA/NBS program is quite useful in demonstrating the need for the designer wishing to employ such alloys to become familiar with the alloy characterization data as well as the mechanical property data. Table 5-3 presents a comparison of some available documentation data on two cryogenic structural alloys (A-286, a precipitation hardening austenitic stainless steel and X750, a nickel-base superalloy) which have been evaluated by three of the participating laboratories in the present program, namely: The Westinghouse Research Laboratories (WRL), The Cryogenics Division of the National Bureau of Standards (NBS) and the Denver Division of Martin-Marietta (M-M). Figures 5-1 and 5-2 present a graphical comparison of the tensile and fracture toughness property values respectively as determined by these laboratories.

For the A-286 alloy, one observes yield strength values reported at room temperature from about 90 to 120 ksi (Δ = 33%), and at 4K from 130 to 160 ksi (estimated), a difference of 23%. Ductility values can only be compared at room temperature from the data reported. Nevertheless, a difference of 34% in reduction in area and 17% in elongation values are observed. Fracture toughness values at room temperature differ by $\sim$ 17% and at 4K, the difference increases to $\sim$ 50% between the WRL and the NBS reported data. Such differences in mechanical properties in the same alloy are significant from a design reliability viewpoint. Some general clues as to the reason(s) for this spread in

reported property values for A-286 can be obtained from Table 5- 3 . Both the WRL and the NBS A-286 material was obtained from different size square forging billets whereas the M-M material was from thinner "plate" stock. Chemical composition differences, while within general specification limits, could nevertheless be significant (e.g. the manganese level in the M-M material is less than half that in the WRL and NBS tested material, while the Ni and Cr levels are higher). There is a difference in the time at solution treatment and both time and temperature at aging between the NBS and the WRL heat treatments. The details for the M-M heat treatment were not reported. Other differences in the A-286 materials tested could be with inclusion and grain size and uniformly, prior processing structural effects and orientation of test specimens.

For the X750 alloy, one observes similar significant variations in tensile properties (see Fig. 5- 1) and in fracture toughness behavior (see Fig. 5- 2). Differences in yield strength of 29% at room temperature to 36% at 4K and in ultimate tensile strength of 19% at RT to 65% at 4K are reported. Ductility values again are incomplete but still differ by 216% at RT to 333% at 4K for reduction in area and 116% at RT to 350% at 4K for total elongation. Fracture toughness value differences of 207% at 4K have also been observed. Once again, general clues to these property differences can be obtained from the data of Table 5- 3. There is a variation in the product form (round and square forging billet to plate), size (5 cm to 25 cm), chemical composition and perhaps most significantly in the mill processing and subsequent laboratory heat treatments employed. As shown, the aging heat treatments employed are appreciably different between the three laboratories. Microstructural differences most probably exist between these various lots of X750 alloy, but have only been characterized and reported for the WRL tested material.

Thus, a few summarizing comments can be made concerning the design relevancy of much of the cryogenic structural materials data presently available:

- Mechanical property data pertaining to a given metal alloy can vary significantly with a wide variety of factors, some of which are subtle and often unreported.
- Most alloys have been developed for high temperature applications where creep and stress rupture requirements predominate. The benefit of such minor alloying elements as cobalt, vanadium, boron and zirconium in many of these alloys being considered for cryogenic applications is questionable.
- Certain product forms such as large round stock (including forging billets) are provided with no guaranty on mechanical properties from the supplier. The actual microstructure and resulting mechanical properties can vary appreciably in a single alloy from supplier to supplier and even between different lots or heats of material from the same supplier.
- Handbook compilations of mechanical property data intended for design purposes should include all pertinent characterization data available for improved alloy discrimination.
- More detailed material characterization efforts are required to better ascertain the reasons for property variations in alloys being considered for extreme cryogenic applications. Through such efforts, means of controlling and hopefully improving the cryogenic behavior can be effected. Then, after a sound technical foundation exists, perhaps the establishment of cryogenic structural materials specifications can be initiated.

5.2 Materials Processing Considerations

An overall Westinghouse program test specimen identification system code is explained in Table 5-4. Chemical compositions of the Westinghouse FY 75 program materials are given in Table 5-5. Documentation data including supplier, heat no. and form received is listed in Table 5-6. The various processing and heat treatment schedules for these materials are summarized in Table 5-7. Hardness and ASTM Grain Size Measurements for these various FY 75 materials and conditions are presented in Table 5-8. Limited documentation on five materials added by NBS for magnetic measurements only is included in Table 5-9.

5.2.1 Inconel 706 Superalloy

The Inconel 706 Ni-Fe-Cr precipitation hardening superalloy[5,6] was obtained as both (1) 29 cm (11-3/8") diameter hot finished forging billet, vacuum induction melted - vacuum arc remelted (VIM-VAR) and as (2) 14 cm (5-1/2") diameter billet, vacuum induction melted - electroflux remelted (VIM-EFR). Microstructures of both these materials in the as-received, solution treated 982°C (1800°F) and solution treated (982°C) followed by double aging at 732°C (1350°F)/8 hrs furnace cooled to 621°C (1150°F)/8 hrs and air cooled, were presented in Figs. 5-1 and 5-2 and were discussed in Section 5.2.1 of the preceeding report[3]. Further discussion of the microstructure of these alloys is included in Section 7 of this report.

5.2.2 Inconel 718 Superalloy

The Inconel 718[7-11] Ni-Cr-Fe-Nb precipitation hardening superalloy evaluated in this Westinghouse FY 75 program was obtained as a 29 cm (11-3/8") diameter hot finished forging billet, vacuum induction melted - vacuum arc remelted (VIM-VAR). The microstructure of the as-received billet both at the stock center line and at the 13.3 cm (5-1/4") radius location, and at the 13.3 cm radius for the solution treated at 982°C (1800°F), and the ST (982°C) - double aged at 718°C (1325°F)/8 hrs furnace cooled to 621°C (1150°F)/8 hrs and air cooled conditions were shown in Fig. 5-3 and discussed in Section 5.2.2 of the previous report[3].

Briefly, it was found that in the as-received conditions, a pronounced contigous grain boundary network existed at the stock center line position, while at the 13.3 cm location such contiguous particles were not observed at the equiaxed matrix grain boundaries but rather at prior "ghost" grain boundaries. These contiguous particles, which were initially presumed to be carbides, have since been so verified (see Section 7.3 of this report).

As mentioned in the previous report, it was desired to examine the effect of a higher solution treating temperature alone and then followed by cold work with subsequent recrystallization heat treatment in reducing or removing this contiguous carbide grain boundary network as well as to modify the base metal grain size. The microstructure of the Inconel 718 alloy solution treated at 1066°C (1950°F) is shown in Fig. 5-3 along with the earlier material solution treated at 982°C (1800°F). The carbide network in the higher solution treated temperature 718 material was appreciably reduced at the matrix grain boundaries and the ghost boundary network was no longer observed. Grain size of the 1066°C ST material increased to approximately ASTM No. 2 from that of lower 982°C ST material of ASTM 4 to 5.

A subsequent unidirectional cold rolling processing operation was performed on the 1066°C Inconel 718 material providing a reduction in thickness from 1.169 to 0.729", or 38%. The series of reheat treatments were then conducted at temperatures from 900°C (1650°F) to 1066°C (1950°F) on small samples of this cold worked material. Hardness and ASTM grain size measurements and the respective microstructures of these various conditions are shown in Fig. 5-4. After the 900°C/30 minute treatment some recrystallization is observed but the average grain size is still quite large at ASTM No. 4. From 927°C/30 minutes through 1038°C/2 hours, the change in average grain size was measured as ASTM 8.5 to 7.4. The hardenss variation over this same heat treating range is likewise relatively small. A sharp increase in grain size again occurs for samples treated at 1066°C/30 minutes (ASTM No. 4) and 1066°C/2 hours (ASTM No. 3).

Interestingly, the grain size is smaller and the hardness appreciably less for the 1066°C recrystallized material than that of the original 1066°C solution treated material.

5.2.3 Comparison of Udimet 718 to Inconel 718 material

Further interesting observations concerning the 718 alloy can be made by comparing the microstructure of the present 29 cm diameter Inconel 718 billet material with that of a comparable size (26 cm diameter) Udimet 718 billet which has been procurred and is being utilized for a separate program. Figure 5-5 compares the microstructures at both the billet centerline and at the outer surface location for these two 718 materials, both in the as-received condition. No contiguous carbide chains are observed at grain boundaries for the Udimet 718 billet centerline location as are observed at the corresponding location in the Inconel 718 billet. Furthermore, no prior ghost boundaries similarly decorated with carbide chains or films are observed at the billet OD location for the Udimet 718 as they were for the Inconel 718.

The pertinent documentation data for the Udimet 718 material is shown in Table 5-10. By comparing the Udimet 718 data with the Inconel 718 data presented in Tables 5-5, 5-6, 5-7 and 5-8, we can make the following comments:

- Both billets are of comparable size and were produced by the same double vacuum melting process (VIM-VAR).
- These materials are of comparable but not exact chemical composition.
- The as-received hardness of the Udimet 718 (Rc 36 to 38) is significantly greater than the Inconel 718 (Rc 23).

- Hardness response to identical heat treatment schedules revealed the following results:

	Udimet 718	Inconel 718
ST - 1800°F	Rc 28 - 33	Rc 38
STDA - 1800°F/1325°F/1150°F	Rc 43	Rc 44
ST - 1950°F	R_B 83	Rc 25
STDA - 1950°F/1325°F/1150°F	Rc 43	--

- Grain sizes are generally comparable but are not uniform in either material.

A limited amount of mechanical test data is available for the two materials both in the ST (1800°F) DA condition and is presented below:

		Udimet 718	Inconel 718
UTS	RT	194 ksi	195 ksi
	77K	248 ksi	237 ksi
	4K	256 ksi	242 ksi
0.2% YS	RT	164 ksi	168 ksi
	77K	188 ksi	195 ksi
	4K	201 ksi	204 ksi
Total Elongation	RT	19.7%	12.0 %
	77K	22.8%	10.1 %
	4K	18.5%	9.4 %
Red. in Area	RT	27.1 %	14.8 %
	77K	18.2 %	9.1 %
	4K	18.6 %	10.0 %
K_{IC} (J_{IC})	RT	--	63.3 ksi $\sqrt{in.}$
	77K	88.1 ksi $\sqrt{in.}$	--
	4K	--	72.5 ksi $\sqrt{in.}$

Thus from the above available information, it appears that the higher ductility and toughness and basically the same strength levels obtained in the Udimet 718 over the Inconel 718 billet material are attributable to much reduced grain boundary carbide networks. Such microstructural

differences are apparent results of the particular mill thermomechanical reduction schedules which are not known in detail for either material.

5.3 Materials Fabrication Considerations

5.3.1 Current Program Weldments

Weldments evaluated in the Westinghouse FY 75 program were all by the manual gas tungsten arc welding (GTAW) process. The welding parameters and process details of these weldments are presented in Table 5-11. Weldments were fabricated in the Inconel 706 (VIM-VAR), Inconel 718 (VIM-VAR), Inconel X750 (Hipped) and the INCO LEA materials. All weldments were given a full post weld solution treatment followed by the respective aging heat treatment prior to mechanical and fracture mechanics testing. As mentioned earlier, the weldments in X750 Hipped and the LEA material have not been tested due to priority reorientations associated with the program funding situation.

Hardness traverses, macro and microstructures of these weldments were presented for the as-welded condition in Figs. 5-7 through 5-13 in the previous report[3]. Similar information (but for the full post weld heat treated condition) is presented in Figs. 5-6 through 5-10 in this report for the 706, 718 and X750 HIP weldments. If one compares these heat treated structures with the corresponding as-welded structures, one can detect significant microstructural differences in the weld fusion zones in particular. Also, the hardness level of the post weld heat treated weld metal is significantly higher than in the as-welded condition for each material.

5.3.2 Weldability Considerations

The present program is concerned with the evaluation of fabricated weldments in terms of mechanical, fracture mechanics, fractographic and magnetic behavior. In general, no particular problems were experienced in making any of the present test weldments except for some weld metal cracking experienced with the Inconel 706 material as mentioned in Section 5.3.1.4 of the previous Westinghouse report[3]. However, it

should be recognized that welding problems in fabrication of actual components for s.c. machinery could yet arise.

One basic difference between hardware fabrication and the present laboratory test weldments is that the former will, in general, be subjected to significant restraint levels whereas the laboratory butt weld test plate samples of this program were essentially unrestrained. One useful testing procedure which can augment the present program results without (or before) the actual fabrication of large component hardware is the Varestraint test[12-14]. This test provides the means for applying, under controlled conditions, a prespecified degree of strain to a gas tungsten arc autogeneous weldment as the molten weld zone is solidifying. By maintaining specimen size and welding conditions constant, one can assess the hot cracking susceptibility of different alloys or of different conditions of a given alloy with varying amounts of applied strain, usually in the range of 0 to 4%.

Some data is available concerning Varestraint testing on the nickel base superalloys X750, 718 and 706. Valdez and Steinman[15] have investigated heat affected zone (HAZ) hot cracking by Varestraint testing in 718 material and report that the sensitivity to hot cracking increases with:

(a) increasing sample thickness

(b) increasing annealing (solution treating) temperature

(c) differences in material provided from different suppliers with increased amounts of grain boundary segregation, particularly in areas of TiCb (C, N) particles interdispersed with some laves phase aligned in the direction of rolling.

Lingenfelter[16-17] has investigated fusion zone hot cracking susceptibility in several nickel base alloys including the 706, 718 and X750 alloys. The limited data available indicates that hot cracking in both the fusion zone and in the heat affected zone is likely for these alloys under restraint conditions where strain levels of from 0.6 to 2.6% occur.

The longitudinal Varestraint test has also been employed by Arata et al.[18] to investigate the solidification (hot) cracking susceptibility in weld metal of several austenitic stainless steel alloys. These authors found that: (1) fusion zone (FZ) hot cracking was usually more severe than that of the HAZ and that (2) the solidification crack susceptibility for the austenitic stainless steels is strongly dependent upon the amount of delta ferrite present in the austenitic phase. The FZ crack susceptibility increases with decreasing amounts of delta ferrite present. Wells and Hagadorn[19] have reported on Varestraint tests in high manganese stainless steel base metal (Nitronic 33). This material was found to contain no significant delta ferrite prior to the autogeneous GTA varestraint weld pass, and a measured ferrite number (FN) of 2.7 after Varestraint testing. Most importantly, this fully austenitic stainless steel revealed no indications of FZ or HAZ hot cracking susceptibility at augmented strain levels to 4%.

It thus appears that Varestraint tests on both base metals and prior deposited weld passes in the materials of interest to this program can be of significant usefulness to this program. Some limited testing of this nature has been started and results will be presented in the next report.

References (Section 5)

1. Lessmann, G. G., Logsdon, W. A., Kossowsky, R., Mathur, M. P. and Wells, J. M., "Structural Materials For Cryogenic Applications First Semi-Annual Technical Report", Westinghouse Research Report 74-9D4-CRYMT-R1, March 1, 1974.

2. Lessmann, G. G., Logsdon, W. A., Kossowsky, R., Mathur, M. P. and Wells, J. M., "Structural Materials For Cryogenic Applications, Second Semi-Annual Technical Report", Westinghouse Research Report 74-9D4-CRYMT-R2, September 9, 1974.

3. Wells, J. M., Kossowsky, R., Logsdon, W. A. and Daniel, M. P., "Structural Materials For Cryogenic Applications, Third Semi-Annual Technical Report", Westinghouse Research Report 75-9D4-CRYMT-R1, March 10, 1975.

4. Anon., Unified Numbering System for Metals and Alloys, ASTM DS-56, SAE J1086, published by Soc. of Automotive Engineers, Warrendale, PA, January 1975.

5. Anon., "Inconel Alloy 706", Huntington Alloy Product Division, INCO Technical Bulletin 9-70T-45, (1970).

6. Eiselstein, H. L., "Properties of a Fabricable, High Strength Superalloy", M.E.Q., V. 11, No. 4, November 1971.

7. Anon., "Inconel 718", Huntington Alloy Products Division, INCO, Technical Bulletin 2-68T-39, (1968).

8. Sessler, J. and Weiss, V. - Ed., "Materials Data Handbook - Inconel 718", NASA Contract NAS8-11347, September 1966.

9. Anon., "Unitemp 718 High Temperature Alloy", Universal-Cyclops Specialty Steel Division, Bulletin HT-3033 (1973).

10. Eiselstein, H. L., "Metallurgy of a Columbium-Hardened Nickel-Chromium-Iron Alloy", ASTM STP 369, (1965), pp. 62-79.

11. Muzyka, D. R. and Maniar, C. N., "Effects of Solution Treating Temperature and Microstructure on the Properties of Hot Rolled 718 Alloy", Metals Engrg. Quarterly, Vol. 9 (4), November 1969, pp. 23-37.

12. Savage, W. F. and Lundin, C. D., "The Varestraint Test", Welding Journal, V. 44, No. 10, Oct. 1965, pp. 433S-442S.

13. Savage, W. F. and Lundin, C. D., "Applicability of the Varestraint Technique to the Study of Weldability", Welding Journal, V. 45, No. 11, Nov. 1966, pp. 499S-503S.

14. Savage, W. F. and Lundin, C. D., "The Evaluation of the Weldability of Structural Alloys with the Varestraint Test", Report No. AFML-TR-68-48, January 1968.

15. Valdez, P. J. and Steinman, J. B., "Effect of Composition and Thermal Treatments on the Weldability of Nickel-Base 718 Alloy", WRC, Symposium on Effects of Minor Elements on Weldability of Hi-Nickel Alloys, July 1969, pp. 93-120.

16. Lingenfelter, A. C., "Varestraint Testing of Nickel Alloys", Welding Journal, Vol. 51, No. 9, September 1972, pp. 430S-436S.

17. Lingenfelter, A. C., Huntington Alloys Product Division, INCO private communication.

18. Arata, Y., Matsuda, F., and Saruwartri, S., "Varestraint Test For Solidification Crack Susceptibility in Weld Metal of Austenitic Stainless Steels", Welding Research Abroad, Vol. XXI, No. 1, January 1975, pp. 2-11.

19. Wells, J. M. and Hagadorn, M. W., "Evaluation of Nitronic 33 Stainless Steel for TFTR Device Applications", Westinghouse Research Report 75-8C3-WETWO-R1 (Unrestricted), September 1975.

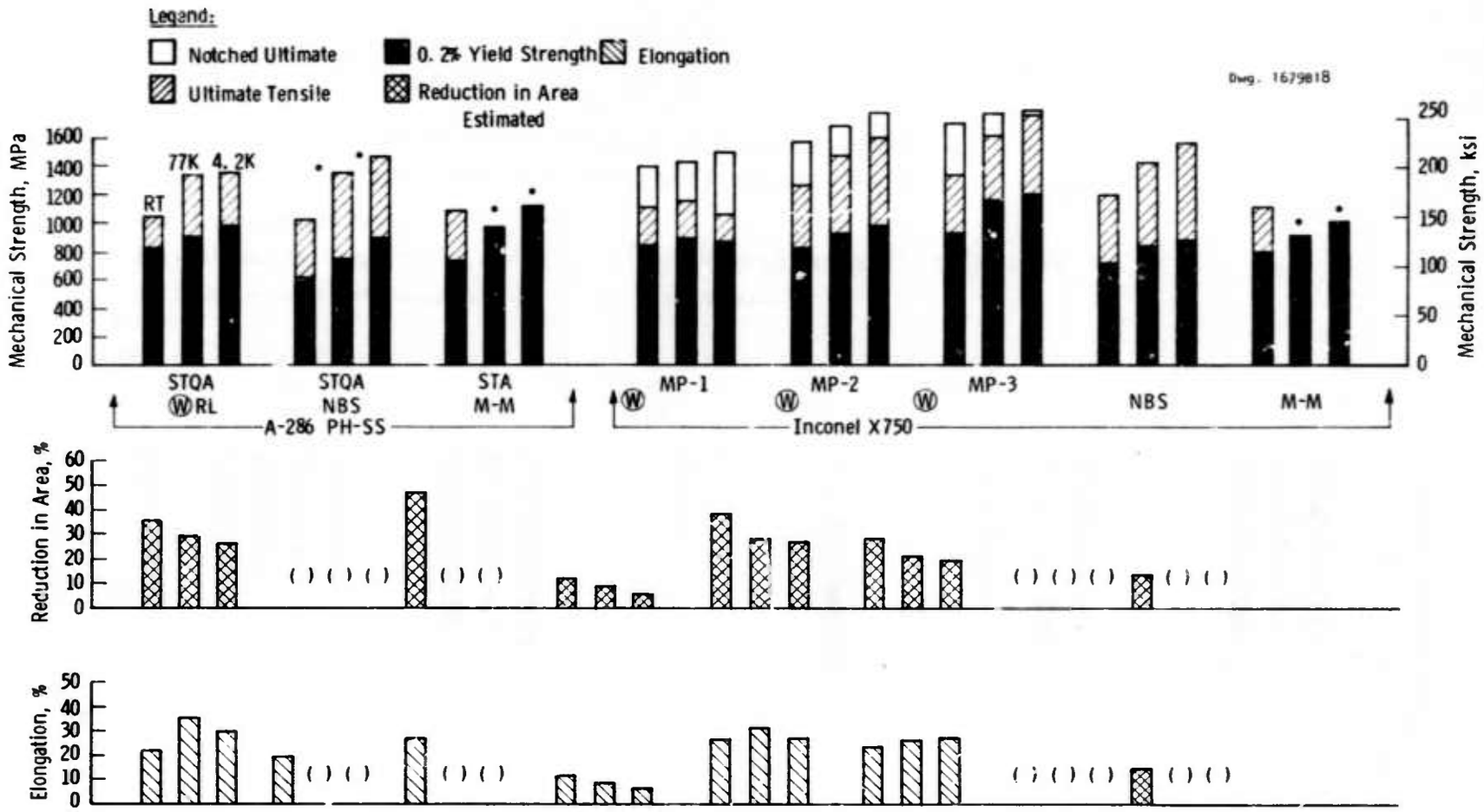

Fig. 5-1 — Summary comparison of cryogenic mechanical strength and ductility values for A-286 stainless steel and Inconel X750 superalloy obtained by various laboratories

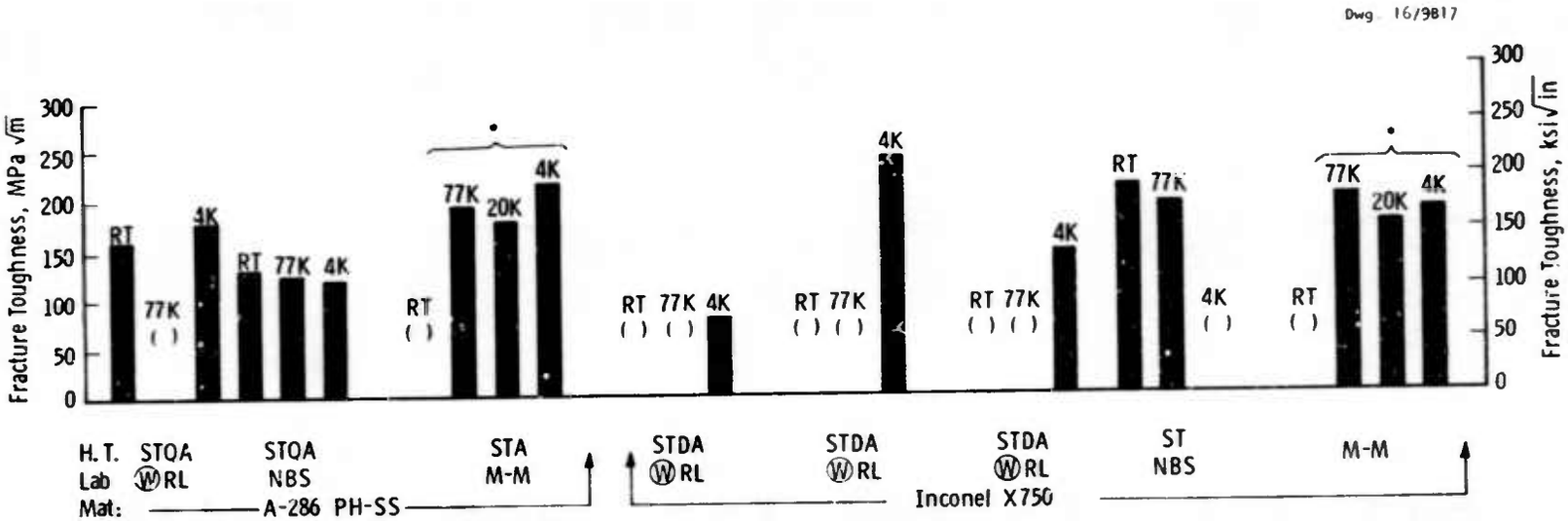

Notes:

W R L - Westinghouse Research Laboratories

NBS - Cryogenic Div., Nat. Bureau of Stds.

M-M - Martin-Marietta, Denver

( ) - Not Reported

*K_Q Values (Data did not meet K_{IC} Validity Criteria)

Fig. 5-2 — Comparison of cryogenic fracture toughness values (K_{IC}) for A-286 stainless steel and Inconel X750 superalloy obtained by various laboratories

(A) As- Received Condition

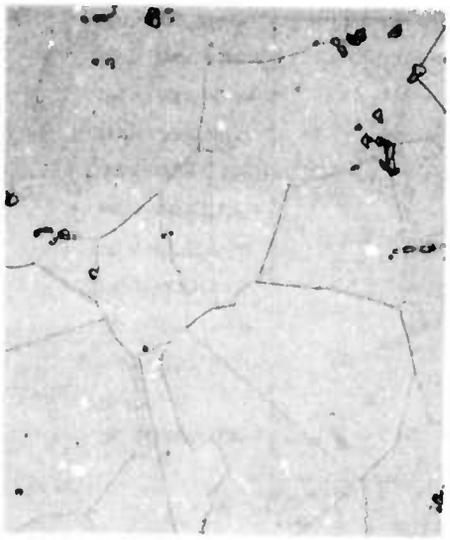

(B) ST—1066°C (1950°F)/1 hr

(C) ST—982°C (1800°F)/1 hr

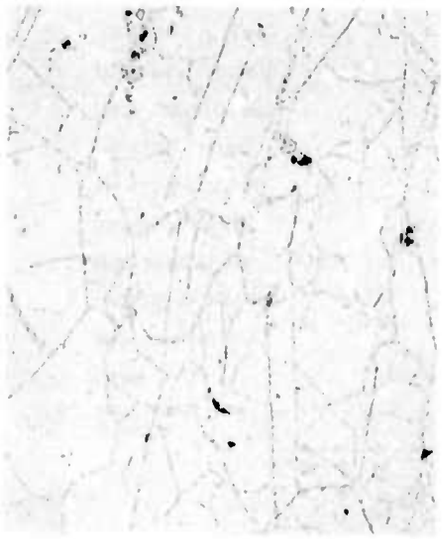

(D) ST (982°C) DA—718°C (13250°F) /8 hrs/FC to 621°C (1150°F) /8 hrs, AC

Fig. 5-3 — Photomicrographs of Inconel 718 Base Metal, As Received (A), ST at 1066°C (1950°F)/1 hr (B), ST at 982°C (1800°F)/1 hr (C) and ST (982°C) DA (D) (X225)

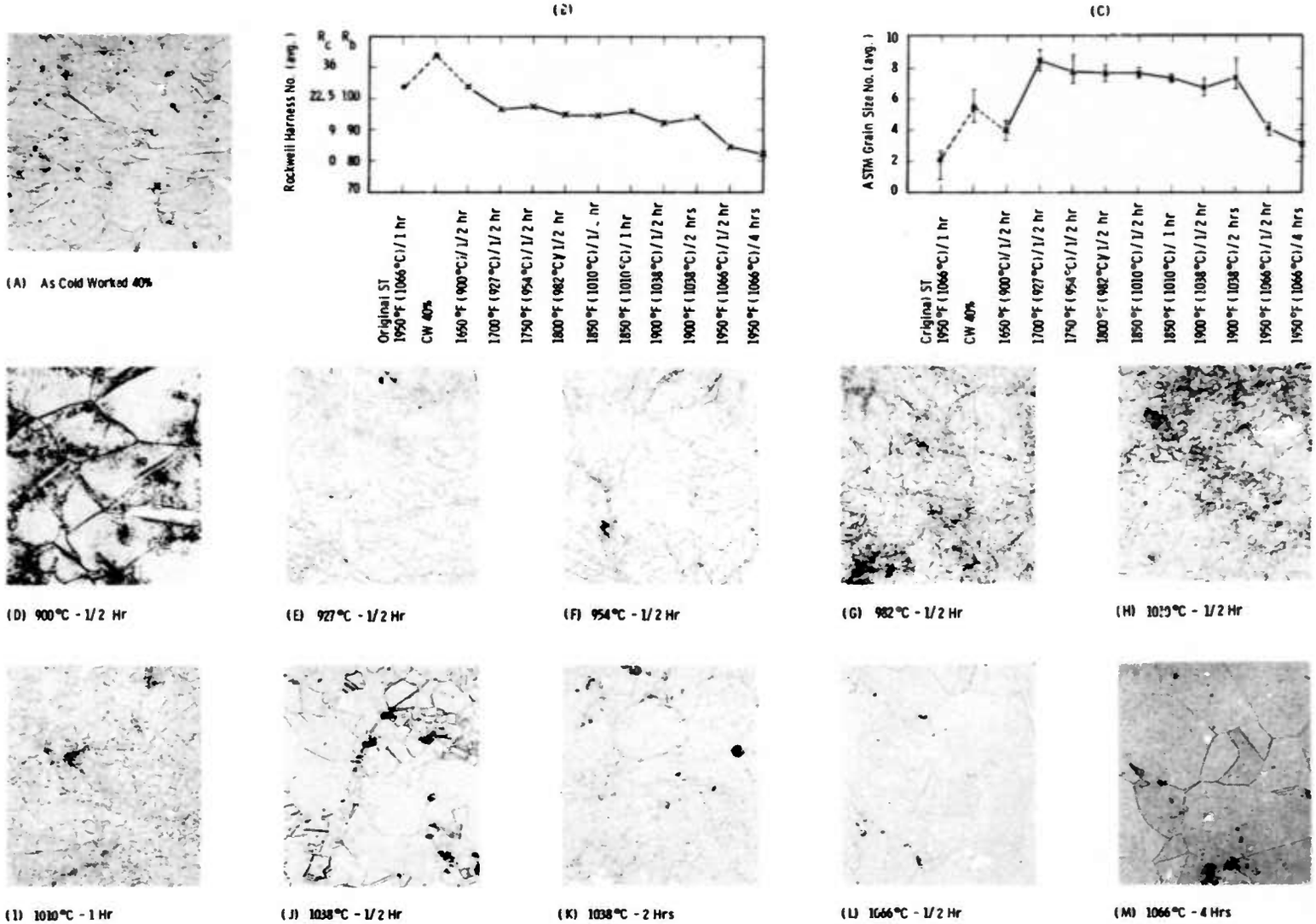

Fig. 5-4 — Photomicrographs, hardness and grain size measurements for Inconel 718 original solution treatment 1066°C (1950°F) / 1 Hr, cold worked 40% and then given final recrystallization heat treatment as shown (X225)

I - Inconel 718 Billet - 28.9 cm O. D.

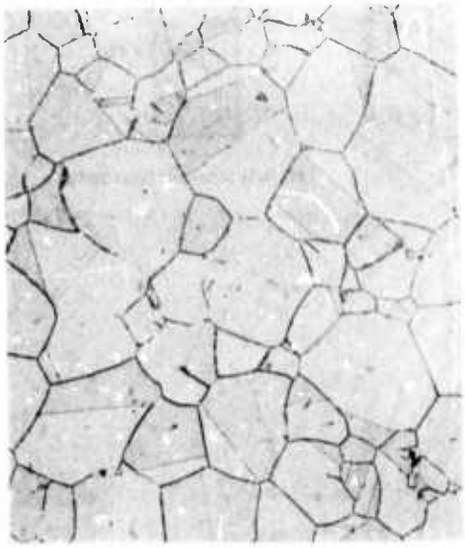

(A) Billet Centerline Location

(B) Billet O. D. Location

II-Udimet 718 Billet-26 cm O. D.

(A) Billet Centerline Location

(B) Billet O. D. Location

Fig. 5-5 – Photomicrographs of Inconel 718 Base Metal (I) and Udimet 718 (II) - as received at billet center line (A) and at Billet O. D. (X225)

706-C / As Welded

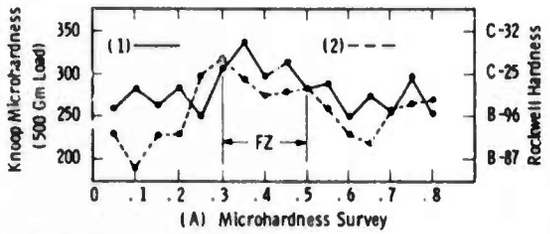

(A) Microhardness Survey

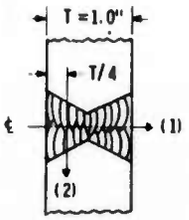

(B) Weld Schematic Cross Section

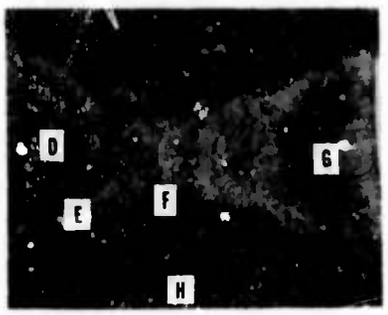

(C) Weld Macro-Section

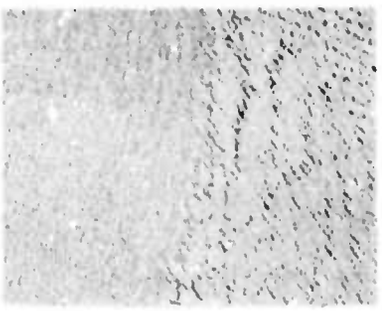

(D) Weld Fusion Zone

(E) FZ-HAZ Transition

(F) FZ-HAZ Transition

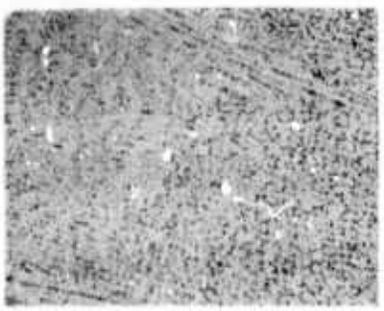

(G) Weld Fusion Zone

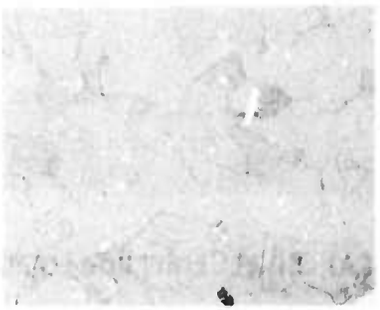

(H) Base Metal

Fig. 5-6 – Microhardness Survey (A & B), Macrostructure (C) (X4.5) and Microstructure of GTA welded Inconel 706 (weld plate no. C) as welded, (D) through (H) (X225)

706 - B/ STDA

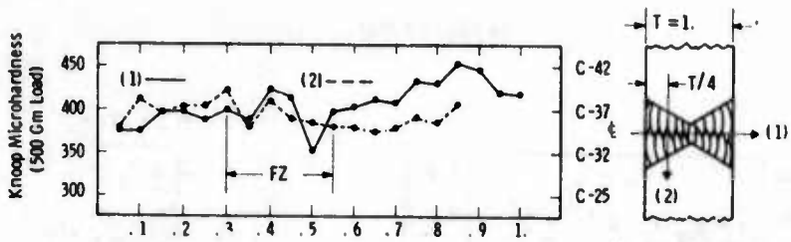

(A) Microhardness Survey

(B) Weld Schematic Cross Section

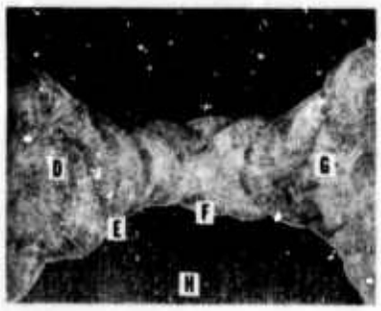

(C) Weld Macro-Section

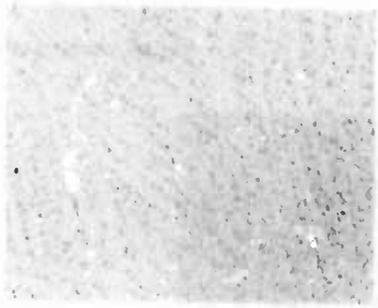

(D) Weld Fusion Zone

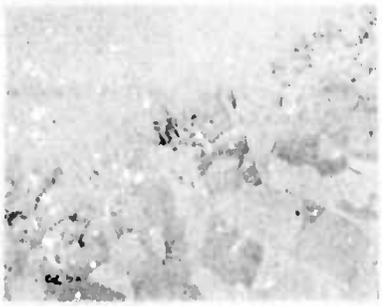

(E) FZ-HAZ Transition

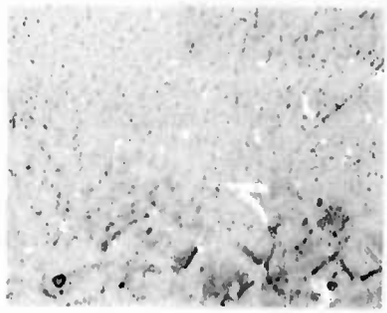

(F) FZ-HAZ Transition

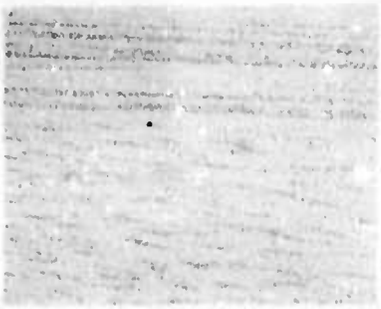

(G) Weld Fusion Zone

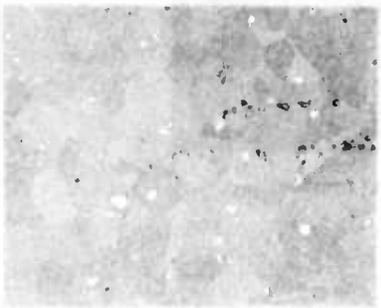

(H) Base Metal

Fig. 5-7 – Microhardness Survey (A & B), Macrostructure (C) (X4.5) and Microstructure of GTA Welded Inconel 706 (weld plate no. B1 (D) Through (H), Full STDA Post Weld H.T. (X225)

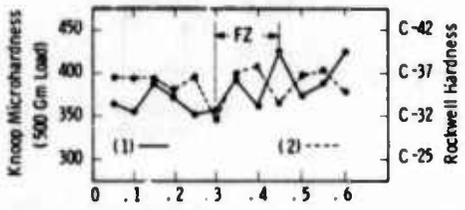

(A) Microhardness Survey

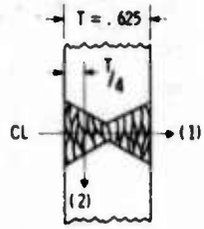

(B) Weld Schematic Cross Section

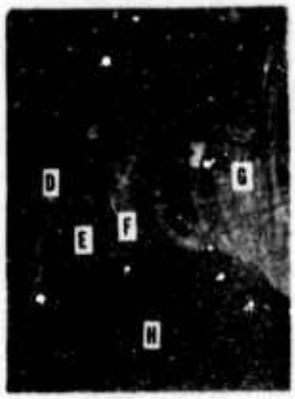

(C) Weld Macro-Section

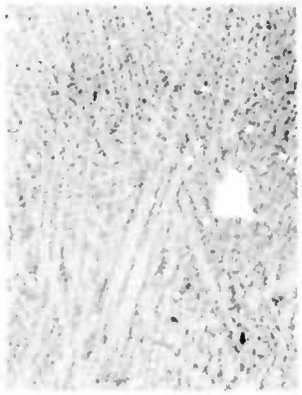

(D) Weld Fusion Zone

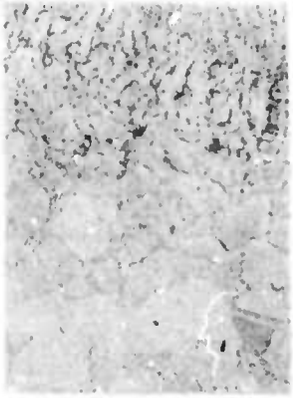

(E) FZ-HAZ Transition

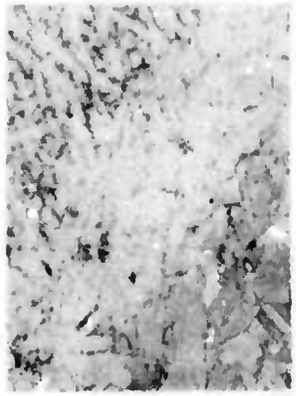

(F) FZ-HAZ Transition

(G) Weld Fusion Zone

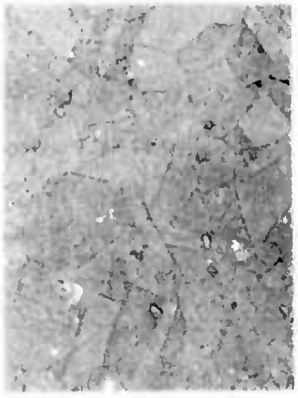

(H) Base Metal

Fig. 5-8 – Microhardness survey (A & B), macrostructure (C) (X5) and microstructure of GTA welded Inconel X718 (weld plate No. 1 C) (D) through (H), full STDA post-weld H. T. (X?.5)

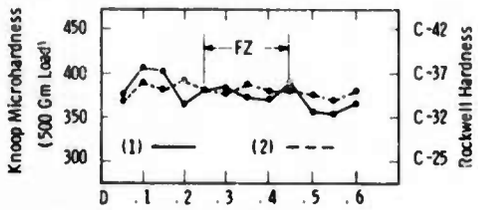

(A) Microhardness Survey

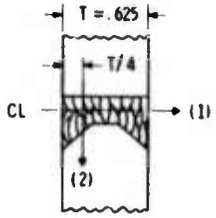

(B) Weld Schematic Cross Section

(C) Weld Macro-Section

(D) Weld Fusion Zone

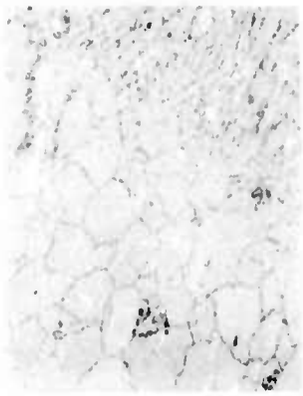

(E) FZ-HAZ Transition

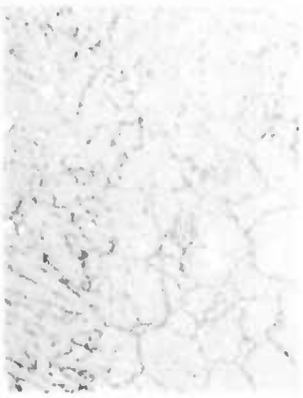

(F) FZ-HAZ Transition

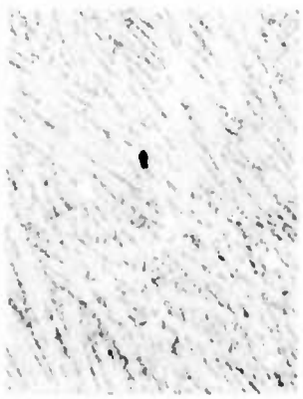

(G) Weld Fusion Zone

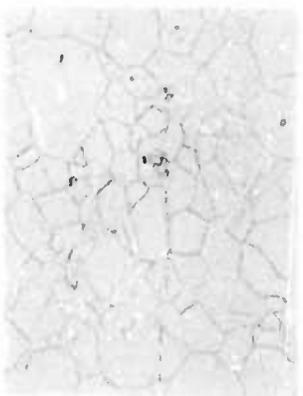

(H) Base Metal

Fig. 5-9 – Microhardness Survey (A & B), Macrostructure (C) (X5) and Microstructure of GTA welded Inconel 718 (weld plate No. 2A) (D) through (H), Full STDA post weld H. T. (X225)

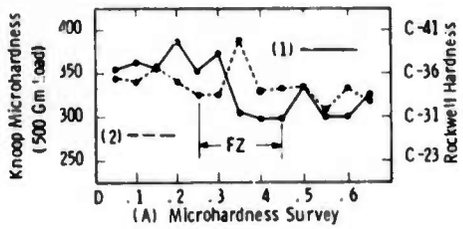

(A) Microhardness Survey

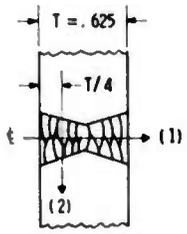

(B) Weld Schematic Cross Section

(C) Macro - Section (X5)

(D) Weld Fusion Zone

(E) FZ-HAZ Transition

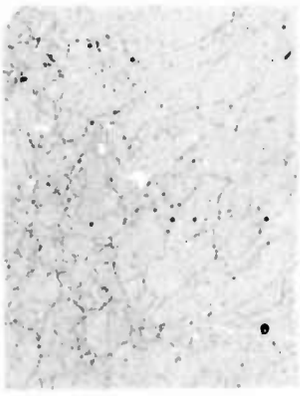

(F) FZ-HAZ Transition

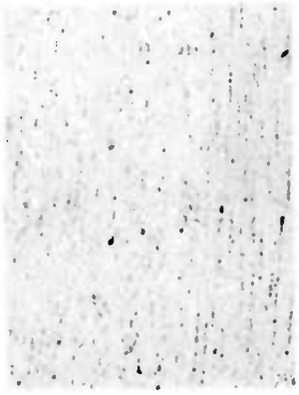

(G) Weld Fusion Zone

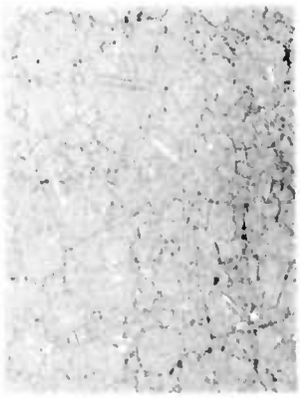

(H) Base Metal

Fig. 5-10 — Microhardness survey (A & B), macrostructure (C) and microstructures of GTA weldment in Inconel X750 (HIP), (D) through (H), with full STDA postweld H. T. (X225)

TABLE 5-1 -- CANDIDATE MATERIALS FOR STRUCTURAL CRYOGENIC APPLICATIONS

AUSTENITIC STAINLESS STEELS

* AISI 310S
* Kromarc 58
  Nitronic 33 (18-3Mn)
  Nitronic 40 (21-6-9)
  Nitronic 50 (22-13-5)
  Carpenter 20Cb-3

IRON BASE SUPERALLOYS

  A-286
  W-545
  Pyromet 860
  Discaloy

NICKEL BASE SUPERALLOYS

  Inconel 625
** Inconel 718
** Inconel 706
 * Inconel X750 (751)
  Hastelloy C-276
  Pyromet 680
  Pyromet 102

OTHER SUPERALLOYS

Haynes 188
Multiphase MP35N

LOW EXPANSION ALLOYS

  Incoloy 903
** INCO (Unnamed) LEA

TITANIUM ALLOYS

Ti-6Al-4V (ELI)
Ti-5Al--2.5Sn (ELI)

ALUMINUM ALLOYS

2014
2219
5083
X2048

COPPER AND COPPER ALLOYS

* OFHC-Cu
  Amzirc Cu (CW/HT)
  Glidcop (Al_2O_3-D.S.)
** PD-135 (Cu-Cr-Cd/PHT)

* Materials characterized in Westinghouse FY 1974 program. ARPA/NBS Contract CST-8034

** Materials included in Westinghouse FY 1975 Program.

TABLE 5- 2 Metal Alloy Designation Cross Reference Summation Table

Trade Name	UNS	AMS	ASTM	Other
AISI 310S	S31008	5521 5572 5577 5651	A167(310S) A240(310S) A276(310S) A314(310S) A473(310S) A479(310S) A580(310S)	AISI 310S SAE J405(30310S)
Kromarc 58	--	--	--	--
Nitronic 33 (18-3Mn)	S24000	--	A240(XM-29) A412(XM-29)	--
Nitronic 40 (21-6-9)	S21900	--	A276(XM-10) A580(XM-10)	--
Nitronic 40LC (21-6-9LC)	S21904	--	A276(XM-11) A580(XM-11)	AMS 5595 AMS 5656
Carpenter 20Cb3	N08020	--	B462-4 B468 B471-5	
A286	K66286	5525 5731 5732 5734 to 5737 5804 5805	A638(660)	SAE J467(A286)
W 545	K66545	5543 5741	--	AISI 665
Pyromet 860	--	--	--	--
Oiscaloy	K66220	5733	A638(662)	AISI 662 SAE J467(Oiscaloy)
Inconel 625	N06625	5599 5666 5837	B443 B444 B446	
Inconel 706	N09706	5605 5606 5701-3		
Inconel 718	N07718	5383 5589 5590 5596 5597 5662-4 5832	A637 A670	MIL-N-24469
Inconel X750	N07750	5542 5582 5598 5567-71 5698-9 5778-9	A637	AISI 688 MIL-N-7786 MIL-N-8550 MIL-N-24114 MIL-S-23192

Trade Name	UNS	AMS	ASTM	Other
Hastelloy C-276	N10276		B574 B575	
Pyromet 680	N06002	5536E 5587A 5588A 5598B	A567 B365 B435 B372	AISI 680
Pyromet 102	--	--	--	--
Haynes 188	R30188	5608 5772 5801		
Mulitphase MP35N	R30035	5844 5845 5758		
Incoloy 903	--	--	--	--
INCO LEA	--	--	--	--
Ti-6Al-4V(ELI)	--	--	--	--
Ti-5Al-2.5Sn(ELI)	--	--	--	--
2014	A92014	4014 4028-9 4121 4134-5 4153	B209/11(2014) B221(2014) B241(2014) B247(2014)	AA2014 MIL-A-25994 MIL-A-22771 MIL-A-12545
2219	A92219	4031 4143-4 4162	B209(2219) B211(2219 B221(2219) B241(2219)	AA2219 QQ-A-367 MIL-A-8920 MIL-A-46118
5083	A95083	4056 4057 4058 4059	B209/10(5083) B221(5083) B241(5083) B247(5083) B345(5083) B547(5083)	AA-5083 QQ-A-200 QQ-A-367 MIL-A-46027 MIL-A-46083 MIL-A-45225
X2048	--	--	--	--
OFHC-Cu	C10200	4500 4701	B1-3 B12(102) B13(102) B33 B42(102) (+ 26 others)	CDA 102 SAE J461(CA102) SAE J463(CA102) QQ-B-825 QQ-C-576 MIL-B-18907 MIL-R-19631
AMZIRC-Cu	C15000	--	--	COA 150 SAE J461(CA150) SAE J463(CA150)
Glidcop	--	--	--	--
PD-135	--	--	--	--

TABLE 5- 3 -- COMPARISON OF MATERIAL DOCUMENTATION DATA FROM VARIOUS LABORATORIES

I. MATERIAL: A-286 Precipitation Hardening Stainless Steel

- Form:

  (W) RL Forging billet, 14 cm x 14 cm x RL, Ht. No. 4X0836
  NBS Forging billet, 11.4 cm x 11.4 cm x RL, Ht. No. (Not Reported)
  M-M Forging plate, 5 cm x 12.7 cm x RL, Ht. No. 6870-6

- Composition:

	C	Mn	P	S	Si	Cr	Ni	Mo	Ti	Al	B	V
(W) RL	0.036	1.72	0.017	0.0025	0.57	14.9	25.8	1.31	2.35	0.15	--	0.31
NBS	0.05	1.52	0.016	0.007	0.54	13.96	24.97	1.30	2.23	0.19	0.004	0.30
M-M	0.05	0.74	--	--	0.45	15.30	26.66	1.36	2.16	--	--	0.31

- Condition:

  (W) RL STQA - ST at 900°C (1650°F) - 5 hours, oil quench; Age 718°C (1325°F) - 20 hours and air cool
  NBS STQA - St at 900°C (1650°F) - 2 hours, oil quench; Age 732°C (1350°F) - 16 hours and air cool
  M-M STA (details not reported)

II. MATERIAL: X750 Nickel Base Superalloy

- Form:

  (W) RL MP-1, Forging billet, 25.4 cm dia., Ht. No. HT56C1XY (VIM-VAR)
  MP-2, Forging billet, 10.2 cm dia., Ht. No. HT1250XV (AAM-VAR)
  MP-3, Hot finished round, 5 cm dia., Ht. No. HT57F8XS (VIM)
  NBS Forging, 10.8 xm x 10.8 xm x 4.4 cm, Ht. No. (Not Reported)
  M-M Forging, 5 cm x 12.7 cm, Ht. No. 31C6X8

- Composition:

		C	Mn	P	S	Si	Cr	Ni	(Nb + Ta)	Fe	Ti	Al	Cu	Co
(W) RL	MP-1	0.04	0.09	0.003	< 0.001	0.11	15.2	73.0	0.90	6.47	2.40	0.92	0.02	0.017
	MP-2	0.02	0.12	0.004	0.007	0.24	14.2	74.8	0.95	6.22	2.62	0.73	0.06	0.051
	MP-3	0.04	0.13	0.004	0.003	0.27	15.4	73.0	0.89	6.87	2.64	0.68	0.04	0.009
NBS		0.04	0.20	--	0.007	0.25	15.2	73.5	0.89	6.58	2.51	0.78	0.04	--
M-M		0.05	--	--	--	--	15.3	73.8	0.89	6.22	2.69	--	--	--

- Condition:

  (W) RL STDA - ST at 982°C (1800°F)-1 hr, A.C.; Age at 732°C (1350°F)-8 hrs-F.C. to 621°C (1150°F) 8 hrs, A.C.
  NBS STDA - ST at 982°C (1800°F)-1 hr, A.C.; Age at 871°C (1600°F)-24 hrs, A.C. and 704°C (1300°F) 20 hrs, A.C.
  M-M STA - ST (Temp. unspecified); Age at 704°C (1300°F)-20 hrs, A.C.

TABLE 5-4

TEST SPECIMEN IDENTIFICATION SYSTEM

Material	Condition	Code No.
OFHC Copper	As Received, AR	10XX-X
	Stress Relieved, SR	11XX-X
	GTAW	12XX-X
	Braze, B	13XX-X
	Solder, S	14XX-X
PD 135 Copper	EXT/PHT	15XX-X
AISI 310S	Sol'n Treated & Quenched, STQ	20XX-X
	Sensitized, STFC	21XX-X
	SMAW	22XX-X
Inconel X750 MP-1 (VIM-VAR)	Solution Treated, ST	30XX-X
	ST + Double Age, STDA	31XX-X
	ST/EBW	32XX-X
	STDA/EBW	33XX-X
	EBW/STDA	34XX-X
	ST/GTAW	35XX-X
	STDA/GTAW	36XX-X
	GTAW/STDA	37XX-X
	ST/Cu-Braze	38XX-X
X750, MP-2 (AAM-VAR)	STDA	40XX-X
X750, MP-3 (VIM)	STDA	50XX-X
X750, HIP	HIP	60XX-X
	HIP/STDA	61XX-X
	HIP/GTAW/STDA (FZ)	62XX-X
	HIP/GTAW/STDA (HAZ)	63XX-X

Specimen ID System

4 Digits + Dash No.

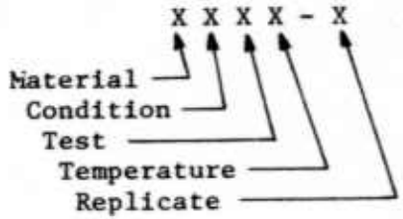

Test (3rd Digit)

Smooth Tensile	XX1X
Notched Tensile	XX2X
K_{IC}	XX3X
J_{IC}	XX4X
FCCR	XX5X

Temperature (4th Digit)

Room Temp. (293°K)	XXX1
LN_2 (77°K)	XXX2
LHe (4°K)	XXX3

TABLE 5- 4 (CONTINUED)

Material	Condition	Code No.
Inconel 718	STDA (VIM-VAR)	64XX-X
	ST/GTAW/STDA (FZ)	65XX-X
	ST/GTAW/STDA (HAZ)	66XX-X
	ST/CW/Recrystallized (Fine Grain Size)	67XX-X
	ST/CW/Recrystallized (Moderate Grain Size)	68XX-X
	ST/CW/Recrystallized (Coarse Grain Size)	69XX-X
Inconel 706	STDA (VIM-EFR)	70XX-X
	STDA (VIM-VAR)	71XX-X
	ST/GTAW/STDA	72XX-X
Inco LEA	STA	73XX-X
	ST/GTAW/STA	74XX-X
Kromarc 58	STQ	80XX-X
	CW	81XX-X
	STQ/GTAW	82XX-X
	CW/GTAW	83XX-X
	GTAW/CW	84XX-X
	GTAW/CW/(Partially Recrystallized)	85XX-X
	GTAW/CW/(Fully Recrystallized)	86XX-X
	STQ/CW (Anisotropy L-T)	87XX-X

TABLE 5-5

CHEMICAL COMPOSITION OF MATERIAL ADDED IN WESTINGHOUSE FY 75 PROGRAM

	Cd	Cr	Pb	Fe	Ni	Mn	Cu	O	N	H
PD 135 Copper										
t = 5/8"	.30	.43	<.01	<.01	<.01	<.01	Bal.	.0004/.0027	.0003	
t = 1"	.31	.33	<.01	<.01	<.01	<.01	Bal.			

	C	P	S	Si	Mn	Ni	Cr	Nb + Ta	Cu	Fe	Al	Ti	Co	Mo	O	N	H
IN 718 (VIM-VAR)	.06	.010	.004	.27	.15	52.67	18.30	5.29	.17	18.47	.58	.97	.03	3.04	.0003	.0085	
IN 718 Filler Metal (.045" diameter)	.04	.011	.007	.19	.04	54.58	17.91	(5.07+.01)	.05	17.60	.49	.99	.04	2.96			
IN 718 Filler Metal (.062" diameter)	.06		.007	.21	.07	53.49	17.99	5.12	.10	18.24	.59	1.00	.07	3.03			
IN 706 (VIM-EFM)	.03		.002	.10	.10	41.49	16.09	2.95	.02	37.27	.27	1.66			.0005	.0050	
IN 706 (VIM-VAR)	.04		.007	.07	.13	41.80	16.33	2.96	.02	36.64	.20	1.78			.0005	.0044	
INCO Low Expansion Alloy	.01		.007	.12	.22	39.56		2.90	.04	55.44	.22	1.46			.0016	.0031	

NOTE: Chemical composition of materials considered in Ⓦ FY 74 program are given in Table 5-3 of the preceeding report.

TABLE 5-6

DOCUMENTATION DATA FOR WESTINGHOUSE PROJECT MATERIALS (FY 75)

Material	Source	Heat No.	Form
PD 135	Phelps Dodge	NR	Flat extrusion 5/8" thick x 4" x 48" 1 " thick x 4-1/4" x 48"
IN 718	INCO Huntington Alloy Div.	HT 16G6EY	HFFQ Round 11-3/8" dia. x 12" ℓ (VIM-VAR)
	INCO Huntington Alloy Div.	HT 52BOE	.045" dia. x 25# spool filler wire
	INCO Huntington Alloy Div.	HT 73C4E	.062" dia. x 25# spool filler wire
IN 706	INCO Huntington Alloy Div.	HT 48C5HK	HFFQ Round 5-1/2" dia. (VIM-EFR)
	INCO Huntington Alloy Div.	HT 79COHY	HFFQ Round 11-3/8" dia. x 12" ℓ (VIM-VAR)
IN LEA	INCO Huntington Alloy Div.	HT Y8798	Plate HR 3" x 6.5" w x 14" ℓ
	INCO Huntington Alloy Div.	HT Y8798	Sheet CR .125" x 22" x 26" (Sheared into 1/8" x 1/8" x 26" ℓ filler metal)
K-58	Westinghouse R&D Stock	HT D8339	Plate 1" thick (same as Ⓦ FY 74 material)
IN X750 HIP Powder	Federal-Mogul Corp.	HT 56C1XY	-60 mwsh powder from IN X750 MP-1 material (same as Ⓦ FY 74 material)

TABLE 5-7

PROCESSING AND HEAT TREATMENT SCHEDULES*- WESTINGHOUSE FY 75 PROJECT MATERIALS

Material	Code	Condition	Remarks
PD 135 Copper	15XX	EXT/PHT	Extruded from 8" dia. x 16" ℓ billet at 1750°F followed by precipitation H.T., 1100°F for 1 hour
IN 718 (VIM-VAR)	64XX	STDA	Solution treated 1800°F - 1 hour - Air Cooled Double Aged 1325°F - 8 hours; F.C. to 1150°F, hold 8 hours and A.C.
	67XX	ST/CW/Recrystallized	ST (1950°F - 1 hr - A.C.), cold work and recrystallize to yield small (ASTM 9-11), moderate (ASTM (5-7) and coarse (ASTM 0-2) grain size range. (Exact procedural details being determined)
	68XX	ST/CW/Recrystallized	
	69XX	ST/CW/Recrystallized	
IN 706 (VIM-EFR)	70XX	STDA	ST - 1800°F - 1 hr - A.C. then double age 1350°F - 8 hrs, F.C. to 1150°F, hold 8 hrs then A.C.
(VIM-VAR)	71XX	STDA	
IN LEA (AM-VAR)	73XX	STA	ST - 1800°F - 1 hr - A.C., age at 1225°F for 8 hrs, A. C.
K 58	87XX	STQ/CW/(Anisotropy)	STQ - 1800°F - 1 hr - Water Quench, cold worked ∿ 37% reduction in thickness. Specimen orientation to be selected to accent pronounced anisotropy of CW texture.
IN X750 HIP	62XX	HIP/GTAW/STDA	HIP - Hot Isostatic Press 1200°C and 10,000 psi for 2 hrs, GTAW, ST - 1800°F - 1 hr - A.C., double age 1350°F - 8 hrs - F.C. to 1150°F, hold 8 hrs, A.C.
	63XX		

* FY 74 Materials reported in Table 5-5 of previous report

TABLE 5-8

MATERIAL HARDNESS AND ASTM GRAIN SIZE MEASUREMENTS - WESTINGHOUSE FY 75 PROJECT MATERIALS

Material	Code	Condition	Hardness	Grain Size (ASTM No.)
PD-135	15XX	EXT/PHT (t = 5/8")	60 R30-T	5
		(t = 1")	57.5 R30-T	5
IN X750 HIP		HIP/ST (HX-8)	32.5 Rc	
	62XX	HIP/ST/GTAW/STDA (FZ)	See Fig. 5-10A	
		HIP/ST (HX-9)	29 Rc	
	63XX	HIP/ST/GTAW/STDA (HAZ)		
IN 718 (VIM-VAR)		As Received	23 Rc	4-5
		ST	38 Rc	4-5
	64XX	STDA	44 Rc	4-5
	65XX	ST/GTAW/STDA (FZ)	See Fig. 5-8 A	
	66XX	ST/GTAW/STDA (HAZ)	See Fig. 5-9 A	
	67XX	ST/CW/Recrystallized		
	68XX	ST/CW/Recrystallized		
	69XX	ST/CW/Recrystallized		
IN 706 (VIM-EFR)		As Received	26 Rc	4-5
		ST	87 RB	5-7
	70XX	STDA	40 Rc	5-7
IN 706 (VIM-VAR)		As Received	88 RB	2-5
		ST	79 RB	4-5
	71XX	STDA	41 Rc	4-5
	72XX	ST/GTAW/STDA	See Fig. 5-7 A	
INCO LEA (AM-VAR)		As Received	93 RB	3-4
		ST	84 RB	4
	73XX	STA	36 Rc	4
	74XX	ST/GTAW/STA		

TABLE 5-9

ADDITIONAL MATERIALS (FY 75) ADDED FOR MAGNETIC MEASUREMENTS

Material	Source	Heat No.	Condition	Remarks
Fe - 9 Ni Steel (ASTM A533-70, Grade A)	Nippon Steel Corp. (via NBS)	D9521	Q&T	C - .06, Si - .27, Mn - .56, P - .007, S - .003, Ni - 9.25, Fe - Balance
Fe - 70 Ni	(via NBS)	Unidentified	Annealed	Received as 2-3/4" x 2-3/4" x 3/4" and rough cut section
AISI 416SS	(via NBS)	Unidentified	STQ & T	Received as 3/4" dia. x 4-1/2" ℓ rod
Armco Fe	Ⓦ Laboratory Stock	Unidentified	Unknown	
Fe - 3% Si (Transformer Steel)	Armco Steel Corp. (via WRL)	250424	Unknown	Received as 3/4" x 1.1" x 4" ℓ Rough cut bar

TABLE 5-10

DOCUMENTATION AND CHARACTERIZATION DATA FOR UDIMET 718 ALLOY

Alloy Designation: Udimet 718 Nickel-base Superalloy

Source: Special Metals Corp. (Subsidary of Allegheny Ludlum Industries)

Heat No.: 9-3688 (VIM-VAR)

Form: Forging Billet, 10-1/4" diameter, HFFQ

Chemical Composition:

C	P	S	Si	Mn	Ni	Cr	Nb+Ta	Cu	Fe	Al	Ti	Co	Mo	B
0.05	<0.01	0.002	<0.10	<0.10	54.1	18.0	5.35	<0.10	Bal.	0.51	1.00	<0.10	3.05	0.003

Condition	Hardness	ASTM Grain Size No.
As Received - OD	Rc 36-38	4-7
- CL		5-6
ST (1) 1800°F/1 hr/A.C.	Rc 28-33	5-6
ST (2) 1950°F/1 hr/A.C.	R_B 83	4-5
ST (1) + DA 1325°F/8 hrs/FC to 1150°F/8 hrs/A.C.	Rc 43	4-5
ST (2) + DA 1325°F/8 hrs/FC to 1150°F/8 hrs/A.C.	Rc 43	4-5

NOTE: An appreciable difference in the as-received grain size and distribution was noted for this material from one end of billet to the other, and from the billet center line to the outer diameter surface.

TABLE 5-11 – SUMMARY TABLE OF WELDING DATA (FY 75)

Code	62XX (HX-8A, B)	63XX (HX-9A, B)	74XX (L-1)
Base Metal	In X750 HIP	In X750 HIP	INCO LEA
Thickness	5/8 Inch	3/4 Inch	1 1/8 Inch
Weld Joint	Butt, Double-V, 60° Incl. Angle	Butt, K-Groove, 45° Incl. Angle	Butt, Double-V, 60° Incl. Angle
Process	GTAW-Manual	GTAW-Manual	GTAW-Manual
Filler Metal	F-69, 3/32" Dia., HT 21C8	F-69, 3/32" Dia., HT 21C8	IN LEA, 1/8" × 1/8" × 26"
Current	DCSP-180 Amps (#2, 5-12) (1)	DCSP-185-190 Amps (#4-13) (2)	DCSP-170 Amps (1, 2, 4-9), 185 Amps (#10-39) (6)
Voltage	17-18 Volts	16-17 Volts	14.5-15 Volts (1, 2, 4-9), 15-17 Volts (#10-39)
Electrode	EWTh-2, 3/32" Dia.	EWTh-2, 3/32" Dia.	EWTh-2, 3/32" Dia.
Welding Speed	~3 to 6 ipm	~3 to 6 ipm	~3 to 6 ipm
No. of Passes	12	13	39
Shielding Gas	50% Ar-50% He, 20 cfh	50% Ar-50% He, 20 cfh	100% Ar, 20 cfh
Root Backing Gas	100% He, 60 cfh	100% He, 60 cfh	100% Ar, 10 cfh
Root Gap	3/32" Approx.	3/32" Approx.	3/32" Approx.
Dye Chec, (DPT)*	Yes	Yes	Yes
Radiographs	R HX-8A R HX-8B	R HX-9A R HX-9B	RD 75131

(1) Root Pass (#1), 140 Amps, 14-15 Volts; Pass #3 & 4, 160 Amps, 15-16 Volts

(2) Root Pass (#1), 145 Amps, 14-14.5 Volts; Pass #2 & 3, 165 Amps, 15-17 Volts

Pass #3, 120 Amps, 12 Volts

Code	65XX (1A, B, C)	66XX (2A, B, C)	74XX (L-1)
Base Metal	In 718 (VIM-VAR)	In 718 (VIM-VAR)	INCO LEA
Thickness	11/16 Inch	5/8 Inch	1/2 Inch
Weld Joint	Butt, Double-V, 60° Incl. Angle	Butt, K-Groove, 45° Incl. Angle	Butt, Double-V, 60° Incl. Angle
Process	GTAW-Manual	GTAW-Manual	GTAW-Manual
Filler Metal	F-718, 1/16" Dia., HT 73C4	F718, 1/16" Dia., HT 73C4	IN LEA, 1/8" × 1/8" × 26"
Current	DCSP-165 Amps (#2-8), 140 Amps (#9-14)	DCSP-180 A (#4-9), 130 Amps (#10-17)	DCSP-165 Amps (#1, 2, 4, 7-10), 185 Amps (#5, 6) (7)
Voltage	15-16 Volts (#2-8), 14-15 Volts (#9-14) (3)	16-17 Volts (#4-9), 14-15 Volts (#10-17) (4)	15-16 Volts
Electrode	EWTh-2, 3/32" Dia.	EWTh-2, 3/32" Dia.	EWTh-2, 3/32" Dia.
Welding Speed	~3 to 6 ipm	~3 to 6 ipm	~3 to 6 ipm
No. of Passes	14	17	10
Shielding Gas	50% Ar-50% He, 20 cfh	50% Ar-50% He, 20 cfh	100% Ar, 20 cfh
Root Backing Gas	100% He, 60 cfh	100% He, 60 cfh	100% Ar, 10 cfh
Root Gap	3/32" Approx.	3/32" Approx.	3/32" Approx.
Dye Check (DPT)*	Yes	Yes	Yes
Radiographs			RD 75192

(3) Root Pass (#1) 145 Amps, 14-15 Volts

(4) Root Pass (#1) 145 Amps, 14-14.5 Volts; Pass 2 & 3, 165 Amps, 15-16 Volts

Pass (#3), 120 Amps, 12-12.5 Volts

Code	72XX (A, B)	72XX (C)
Base Metal	In 706 (VIM-VAR)	In 706 (VIM-VAR)
Thickness	1 1/16 Inch	1 1/16" Inch
Weld Joint	Butt, Double-V 60° Incl. Angle	Butt, Double-V 60° Incl. Angle
Process	GTAW-Manual	GTAW-Manual
Filler Metal	F-718, 1/16" Dia. HT 73C4	F-718 1/16" Dia. HT 73C4
Current	DCSP-180 Amps (2-4), 140 Amps (5-25)	DCSP-160-165 Amps (1-4), 140 Amps (5-10)
Voltage	14.5-17 Volts	14.5-16 Volts
Electrode	EWTh-2, 3/32" Dia.	EWTh-2, 3/32" Dia.
Welding Speed	~3 to 6 ipm	~2 to 4 ipm
No. of Passes	25	10
Shielding Gas	50% Ar-50% He 20 cfh	50% Ar-50% He 20 cfh
Root Backing Gas	100% He 60 cfh	100% He 60 cfh
Root Gap	3/32" Approx.	3/32" Approx.
Dye Check (DPT)*	Yes	Yes
Radiographs	RD 75256 RD 75257	RD 75339

*Note– Dye checked after root pass groundout, after second pass, and after last pass both sides

6.0 FRACTURE MECHANICS

Introduction

The development of increasingly more cryogenic or superconducting devices and the almost total lack of low temperature fracture mechanics material properties (especially relative to the austenitic materials so ideally suited for low temperature structural applications) has created a strong demand by designers for the material properties required to insure immunity from structural failure of these systems. Naturally, the cryogenic environment has placed severe restrictions on the development of these required material properties, especially those in the area of fracture mechanics technology. Recent advances in fracture mechanics technology, especially in the area of elastic plastic fracture, have now made it possible to determine the required fracture mechanics material properties (specifically fracture toughness and crack growth rate) necessary to permit the application of fracture mechanics technology to structures and components subjected to cryogenic environments, thus insuring their structural performance.

This section of the technical report presents and summarizes the material properties (tensile, notched tensile, fracture toughness and fatigue crack growth rate) generated throughout the Westinghouse FY 75 ARPA/NBS program.

6.1 Tensile Results

All tensile and notched tensile properties developed throughout the Westinghouse FY 75 program are summarized in Tables 6-1 through 6-3, although these same properties relative to Inconel 706 (VIM-EFR) and INCO LEA base metals were previously described in detail elsewhere[1].

Figures 6-1 and 6-2 illustrate the tensile properties of solution treated and double aged Inconel 706 (VIM-EFR) and (VIM-VAR), respectively. Note all the tensile properties (0.2 percent yield strength, ultimate tensile strength, reduction in area and elongation) of Inconel 706 are independent of manufacturing process. The yield strength of Inconel 706 increases slightly with decreasing temperature and exceeds the yield strengths of all manufacturing process/heat treatment combinations of Inconel X750 previously investigated[1,2] at each comparable test temperature. The ultimate tensile strength of Inconel 706 was surpassed at all three test temperatures only by the ultimate strength of vacuum induction melted (VIM) Inconel X750.[1,2] The ductility of Inconel 706 is comparable with that demonstrated by the more ductile manufacturing process/heat treatment combinations of Inconel X750.[1,2]

The tensile properties of Inconel 706 (VIM-VAR) gas tungsten arc (GTA) welds are illustrated in Figure 6-3. Note these Inconel 706 welds were post-weld heat treated (STDA), and that all tensile specimens fractured in the weld fusion zone. Three of the six tensile specimens (one per test temperature) exhibited visual gauge length porosity prior to testing. Specimens containing this porosity demonstrated significant degradation of ultimate tensile strength and ductility, especially at low temperatures, when compared with specimens which visually featured porosity free gauge lengths. The yield strengths displayed only moderate dependence on porosity. The Inconel 706 gas tungsten arc weld yield strengths are only slightly below those of Inconel 706 base metal. The ultimate tensile strengths, reduction in area and elongation of the welds, however, are significantly below the correspondingly STDA heat treated base metal properties.

Tensile properties of solution treated and double aged Inconel 718 (VIM-VAR), a nickel base superalloy similar to Inconel 706, are shown in Figure 6-4. The yield and ultimate tensile strengths of Inconel 718, like those of Inconel 706, increase slightly with decreasing temperature. The yield strength of Inconel 718 exceeds that

of Inconel 706 by approximately 12 percent at each temperature while their ultimate tensile strengths are quite similar, especially at cryogenic temperatures. In addition, the 75°F (297 K) and -320°F (77 K) Inconel 718 yield strength values are 8 to 9 ksi below those reported by Pettit on Inconel 718 sheet[3] whereas the room temperature yield and ultimate tensile strengths compare quite closely with values developed by Forman.[4] The ductility properties of Inconel 718 are substantially inferior to those of Inconel 706 at all test temperatures.

The tensile properties of Inconel 718 gas tungsten arc (GTA) welds are illustrated in Figure 6-5. Like the Inconel 706 GTA welds, the Inconel 718 welds were also post-weld heat treated (STDA) and each tensile specimen failed in the weld fusion zone. Compared with Inconel 718 base metal yield and ultimate tensile strengths, the corresponding GTA weld properties are moderately inferior. Pettit also discovered this same slight drop in yield strength on welded Inconel 718 sheet.[3] Forman investigated four types of Inconel 718 welds (electron beam, gas tungsten arc, pulse-current gas tungsten arc and plasma-arc root weld with gas tungsten arc fill passes).[4] Forman also noted a slight drop in room temperature yield strength for each of the welds investigated. Furthermore, in comparison with the room temperature ultimate tensile strength of Inconel 718 base metal, Forman found room temperature ultimate tensile strengths of the various GTA welds moderately inferior while a single electron beam weld's ultimate tensile strength actually proved superior. Although Forman developed -320°F (77 K) tensile data on the same four weld types, he reported no low temperature Inconel 718 base metal tensile test data, so direct comparisons between base and weld metal mechanical properties at low temperatures are impossible. Inconel 718 GTA weld ductility is extremely poor with elongations at 75°F (297 K) and -320°F (77 K) below 2 percent.

Figure 6-6 presents the tensile properties of a solution treated and aged unnamed low expansion iron-nickel alloy identified here as Inco LEA. The increase in yield strength with decreasing temperature demonstrated by Inco LEA is considerably greater than that

displayed by any manufacturing process/heat treatment combination of Inconel X750[1,2] or by Inconel 706 and 718. This large increase in yield strength versus decreasing temperature is probably largely due to the very high iron content of the low expansion alloy as compared with Inconel X750, 706 and 718. In other words, the yield strength behavior of Inco LEA is not unlike that of a ferritic as opposed to an austenitic type material. The room temperature yield strength of STA heat treated Inco LEA is less than that of STDA heat treated Inconel 706 and 718 and essentially equal to that of the various STDA heat treated Inconel X750's.[1,2] At cryogenic temperatures, the yield strengths of Inco LEA and Inconel 706 are equivalent. The ultimate tensile strength of Inco LEA is at most only 10 percent greater than its corresponding yield strength, indicating that Inco LEA experiences little deformation before failure. This fact is further substantiated by the very poor ductility properties (both reduction in area and elongation) exhibited by Inco LEA.

Figure 6-7 examines the influence of test specimen orientation on the mechanical properties of cold worked Kromarc 58 stainless steel. Two test specimen orientations, designated T-L and L-T in accordance with ASTM E399-74, were investigated. The T-L orientation specifies that the loading direction for both tensile as well as compact tension geometry fracture specimens is perpendicular (transverse) to the rolling direction whereas the L-T orientation specifies the loading direction parallel to the rolling direction. All previously reported Kromarc 58 mechanical, fracture toughness and crack growth rate data were generated with specimens machined in the T-L orientation.[1,5] The yield strengths of Kromarc 58 stainless steel were independent of orientation at cryogenic temperatures. At room temperature, however, specimens loaded perpendicular to the rolling direction (T-L orientation) resulted in a moderately higher yield strength. The ultimate tensile strength of Kromarc 58 was relatively insensitive to orientation except at -452°F (4 K), where loading parallel to the rolling direction (L-T orientation) produced a higher ultimate tensile strength. Concerning the ductility of Kromarc 58,

specimens loaded parallel to the rolling direction realized moderately superior reductions in area and slightly greater elongations at all test temperatures.

Overall, the yield and ultimate tensile strengths of cold worked Kromarc 58 are comparable with those of Inconel 706 and 718 plus Inco LEA. Compared with the various Inconel materials, the ductility of cold worked Kromarc 58 (especially reduction in area) is often superior.

The tensile properties of solution treated, quenched and aged A286 stainless steel are presented in Figure 6-8. Mechanical, fracture toughness and crack growth rate properties were developed on this precipitation hardenable, Fe-Ni-Cr superalloy often referred to as ASTM A453 or AISI 660 as part of an internal Westinghouse research program totally independent from the present ARPA-NBS program. The yield and ultimate tensile strengths of A286 are considerably below those of Inconel 706 and 718 while the yield strengths of A286 and Inconel X750 (AAM-VAR)[1,2] are surprisingly similar. The ductility of A286 stainless steel is above average and on a par with that of Inconel X750 (AAM-VAR)[1,2] and Inconel 706.

Reed, et al. observed the mechanical properties of an A286 stainless steel of almost identical chemical composition and heat treatment.[6] Although Reed's yield strength values were significantly below those reported here regardless of temperature, Reed's tensile and associated compact tension geometry fracture and crack growth specimens were machined in the T-S orientation with respect to the forging axis (per ASTM E399-74) while the Westinghouse specimens were oriented in the L-T direction. These two distinct specimen orientations could easily account for the large variation in mechanical properties.

The tensile properties of a high strength, high conductivity copper base alloy identified as PD 135 are summarized in Table 6-4. The yield and ultimate tensile strengths of PD 135 are approximately four times and 20 ksi greater than those of as received OFHC copper, respectively, regardless of test temperature.[1] In addition, as

demonstrated by OFHC copper, the yield strength of PD 135 remains essentially constant with temperature while the ultimate tensile strength increases slightly with decreasing temperature. The reduction in area experienced by PD 135 is at most 13.5 percent below that of as received OFHC copper whereas the elongation of PD 135 is significantly below that of as received OFHC copper regardless of test temperature.[1] The ductility properties demonstrated by PD 135 are quite good, however, especially when compared with those of Inconel X750, 706 and 718 plus Inco LEA.

6.2 Notched Tensile Results

The purpose of notched tensile tests is to screen the notch toughness in terms of the comparison parameter defined as the ratio of notched tensile fracture strength to the tensile yield strength of a particular material for a specific notch acuity. Increasing values of the ratio above 1.0 are considered to indicate increasing ability of the material for plastic deformation at the notch tip. Stated alternatively, increasing values of the ratio above 1.0 can be utilized as a measure of the material's resistance to catastrophic brittle fracture.

In all cases the root radius at the bottom of a particular test specimen's sharp V-notch was adjusted to yield a stress concentration factor (K_t) equivalent to 10. It should be pointed out that the notched tensile fracture strength was calculated by dividing the maximum load experienced by a test specimen, or in a few cases where the load dropped slightly before failure dividing the fracture load, by its original as opposed to final cross-sectional area. This was largely due to the great difficulty in accurately measuring the extremely small change in test section diameter (hence cross-sectional area) experienced by the test specimen.

As previously mentioned, all the notched tensile properties are summarized in Tables 6-1 through 6-3. The notched tensile strength to tensile yield strength ratios (NTS/σ_{ys}) for Inconel 706 compare with those previously developed on Inconel X750[1,2] and exceed

those of Inconel 718 and Inco LEA. Also, note the (NTS/σ_{ys}) ratios of both Inconel 706 and Inconel 718 gas tungsten arc welds are significantly below those of the corresponding base materials. Recall, all Inconel 706 and 718 GTA weld smooth bar tensile specimens failed in the weld fusion zone. On the other hand, the (NTS/σ_{ys}) ratios relative to Inconel X750 gas tungsten arc and electron beam welds are comparable to those of the Inconel X750 (VIM-VAR) base metal.[1] It is interesting to note that all Inconel X750 smooth bar weld tensile specimens which were heat treated following welding (as were the Inconel 706 and 718 welds) failed in the base metal. Obviously, from a mechanical properties standpoint, post-weld heat treated Inconel X750 welds are at least as strong as the corresponding base metal where post-weld heat treated Inconel 706 and 718 welds are not.

6.3 Fracture Toughness Results

The well documented linear elastic (K_{I_C}) fracture criterion with its inherent plane strain specimen size limitation cannot produce valid fracture toughness results (per the ASTM Test for Plane Strain Fracture Toughness of Metallic Materials, E399-74) on tough austenitic materials unless specimens of very large thickness are employed, which in turn are not representative of the cross-sectional thicknesses found in the majority of actual cryogenic structures. Furthermore, if a failure should occur, proper design of cryogenic structures or components would cause these structures or components to fail plastically (elastic plastic fracture) as opposed to catastrophically (linear elastic fracture). Therefore, where applicable, all our fracture toughness values were obtained via the elastic plastic (J_{I_C}) fracture criterion[7,8] and the associated resistance curve test technique for determining elastic plastic fracture toughness values.[9] This resistance curve test technique is described in detail in Reference 9 and in addition, the primary steps were outlined in a previous technical report[5] and as such will not be repeated here.

Tables 6-4 and 6-5 summarize all the fracture toughness values relative to the various materials covered in this report. For comparison purposes, the ratios $\frac{K_{I_C}}{\sigma_{ys}}$ and $(\frac{K_{I_C}}{\sigma_{ys}})^2$ are also included in Tables 6-4 and 6-5. Typically, the material with the highest $\frac{K_{I_C}}{\sigma_{ys}}$ ratio can be expected to be the most tough material for a given application.[10] The plane strain crack size factor $(\frac{K_{I_C}}{\sigma_{ys}})^2$ provides a measure of toughness that accounts in a single parameter for the interactions of K_{I_C} and strength on crack size tolerance.[11,12]* Stated alternatively, when conducting a parametric fracture mechanics analysis (that is, the applied stress is considered to be a fixed percentage of the particular material's yield strength) the critical defect size for failure in one cycle of loading will be proportional to the crack size factor.[10]

The J resistance curves relative to Inconel 706 (VIM-EFR) and (VIM-VAR) are illustrated in Figures 6-9 and 6-10, respectively. Some explanation is in order concerning the J resistance curve for Inconel 706 (VIM-VAR) at -452°F (4 K). Each of three specimens which sustained less than 0.010 in. crack extension had smooth load-deflection records from the initiation of loading until the unloading point was reached. The remaining four specimens, however, experienced audible "pop-ins" along with the associated gross amounts of crack extension. This partially accounts for the large amount of data scatter demonstrated by these specimens. The only feasible solution was to fit two straight lines to the J versus Δa data as shown in Figure 6-10 where, in effect, the straight line through points representing specimens which experienced "pop-ins" is ignored in determining J_{I_C}.

The -452°F (4 K) fracture toughness of this (VIM-VAR) Inconel 706 material exceeds that of (VIM-EFR) Inconel 706 by approximately 9 percent. Recall, the mechanical properties of these Inconel 706 materials

---

*The crack size factor is not related to critical crack size at a stress equal to the yield strength but only under small-scale yielding, that is, at applied stresses appreciably below the yield strength.[11,12]

were essentially independent of manufacturing process. The real surprise, however, is the room temperature fracture toughness of (VIM-VAR) Inconel 706, which is 27 percent below the -452°F (4 K) value. The difference in crack size factor was almost as large (24 percent).

As was suggested by notched tensile tests, the -452°F (4 K) fracture toughness of Inconel 706 (VIM-VAR) gas tungsten arc welds was substantially below that of the corresponding base material. In fact, fracture toughness of the Inconel 706 GTA welds was low enough that valid K_{IC} numbers were obtained utilizing 0.5 in. (1.3 cm) thick compact tension specimens and a J resistance curve was unnecessary.

J resistance curves for solution treated and double aged Inconel 718 (VIM-VAR) are presented in Figure 6-11. Like the -452°F (4 K) Inconel 706 J versus Δa data, a large amount of scatter is apparent, again due to some test specimens experiencing unstable "pop-in" crack extensions while others did not. The fracture toughness of this Inconel 718 (VIM-VAR) material is substantially below that of both Inconel 706 (VIM-EFR) and (VIM-VAR). Therefore, Inconel 718 pays a heavy penalty in terms of fracture toughness for its marginal strength advantage. Like Inconel 706 (VIM-VAR), the fracture toughness of Inconel 718 (VIM-VAR) is lower at room temperature than at liquid helium temperature.

The fracture toughness of Inconel 718 (VIM-VAR) gas tungsten arc welds and associated heat affected zones are revealed in Table 6-4. Again like the Inconel 706 gas tungsten arc (GTA) welds, the cryogenic fracture toughness of both Inconel 718 GTA welds and associated heat affected zones is well below that of the corresponding base material. In addition, valid K_{IC} values were obtained and resistance curves proved unnecessary. Although the difference in fracture toughness between Inconel 706 and 718 base materials is large, their GTA weld fracture toughnesses are quite similar. Also, note the Inconel 718 heat affected zone fracture toughness is greater than that of the associated GTA weld.

It should be mentioned that the previously developed fracture toughness of (VIM-VAR) Inconel X750 post-weld heat treated (STDA) gas tungsten arc and electron beam welds considerably exceeded that of the companion base material and as such would certainly not be a weak point in a structure or component manufactured from (VIM-VAR) Inconel X750.[1,5,13] Obviously, the same cannot be said of post-weld heat treated (STDA) Inconel 706 and 718 gas tungsten arc welds or the associated Inconel 718 heat affected zone material.

Figure 6-12 presents the J resistance curves for solution treated and aged Inco LEA. Although the fracture toughness of this low expansion alloy is well below that of Inconel 706 (VIM-EFR) and (VIM-VAR), its fracture toughness transcends that of Inconel 718 (VIM-VAR), especially at room temperature. Unlike Inconel 706 and 718, the room temperature fracture toughness of Inco LEA is 14 percent greater than the -452°F (4 K) value. The drop in fracture toughness with decreasing temperature experienced by this low expansion alloy may be a direct result of its high iron content. Recall, of the various austenitic materials we investigated, Inco LEA demonstrated the largest increase in yield strength with decreasing temperature. In other words, both the tensile and fracture behavior of this material approaches that of a ferritic material although, based on the degree of fracture toughness degradation with decreasing temperature, if Inco LEA experiences a ductile to brittle fracture transition, it occurs below -452°F (4 K).

J resistance curves for both solution treated and quenched plus cold worked (T-L and L-T ASTM E399-74 orientations) Kromarc 58 stainless steel are illustrated in Figure 6-13 while Table 6-5 summarizes the fracture properties. The influence of cold working on the strength and fracture properties of Kromarc 58 stainless steel is revealed in Table 6-5 and has been previously covered in detail for the T-L orientation (loading perpendicular to the rolling direction).[1,5] Our main purpose here is to note that at this level of cold work (30 percent) the Kromarc 58 does not produce an especially weak fracture plane. The -452°F (4 K) fracture toughness for the T-L and L-T orientations varies by only 8.7 ksi$\sqrt{in.}$ (9.6 MPa$\sqrt{m}$). The corresponding difference in yield strength equals just 2.4 ksi (16.5 MPa).

Figure 6-14 illustrates the J resistance curves for solution treated, quenched and aged A286 stainless steel. The fracture toughness of A286 is surpassed solely by that of solution treated and double aged Inconel X750 (AAM-VAR) plus solution treated and quenched Kromarc 58 and AISI 310 S stainless steels while its plane strain crack size factors, $(\frac{K_{Ic}}{\sigma_{ys}})^2$, are exceeded only by those relative to the same three materials and in addition to sensitized AISI 310 S stainless steel.[1] Also, like Inconel 706 and 718, the fracture toughness of A286 is less at room temperature than at liquid helium temperature. This trend toward decreasing fracture toughness with increasing temperature for A286 stainless steel was further exemplified by additional J tests at 400°F (477 K) and 800°F (700 K).[14]

Reed, et al.[6] obtained fracture toughness values ranging from 107 ksi$\sqrt{in.}$ (118 MPa$\sqrt{m}$) to 119 ksi$\sqrt{in.}$ (126 MPa$\sqrt{m}$) over the temperature range -452°F (4 K) to 75°F (297 K) on an A286 stainless steel of almost identical chemical composition and heat treatment. Although Reed's fracture toughness and yield strength values were significantly below ours regardless of temperature, as previously mentioned Reed's specimens were machined in the T-S orientation with respect to the forging axis (per ASTM E399-74) while our specimens were oriented in the L-T direction. These two distinct specimen orientations could easily account for the large variation in mechanical and fracture toughness properties.

The fracture toughness properties of copper brazed Inconel X750 (VIM-VAR) in the as brazed condition are also summarized in Table 6-4. Note that valid plane strain linear elastic fracture toughness results (per ASTM E399-74) were obtained on these copper brazements at all three test temperatures. In addition, the brazement fracture toughness decreased moderately with increasing temperature. Surprisingly, at -452°F (4 K), the fracture toughness of copper brazed Inconel X750 (VIM-VAR) is only 6.6 ksi$\sqrt{in.}$ (7.3 MPa$\sqrt{m}$) below that of GTA welded Inconel 718 (VIM-VAR).

Four elastic plastic (J) fracture tests were performed at -452°F (4 K) on silver brazed OFHC copper. As was the case with OFHC copper base metal and gas metal arc weld tests, the 0.5 in. (1.27 cm) thick silver brazed copper compact tension specimens supported tremendous amounts of plasticity without experiencing crack extension, thus valid elastic plastic J tests proved impossible. It is interesting to note, however, that each of the silver brazed copper specimens sustained between 430 lb (195 kg) and 480 lb (218 kg) of elastic loading before becoming plastic. Based on an elastic load of 430 lb (195 kg), these brazements could support a maximum elastic stress intensity equal to 9.8 ksi$\sqrt{in.}$ (10.8 MPa$\sqrt{m}$).

Finally, a few remarks are in order concerning PD135, a high strength, high conductivity copper base alloy whose mechanical properties are described in detail in Reference 1. All -452°F (4 K) elastic plastic fracture toughness tests on this copper alloy have been completed. Unlike OFHC copper, it was possible to obtain stable, measurable crack extension on PD135. Without the elastic properties of this material (specifically the modulus of elasticity and Poisson's ratio at both room and liquid helium temperatures), however, interpreting the J versus Δa data and calculating corresponding K_{I_C} values is impossible. Fortunately, the elastic properties of PD135 will soon be available through NBS.

6.4 Crack Growth Rate Results

The test procedures utilized in the development of our cryogenic fatigue crack growth rate data were spelled out in detail in a previcus technical report and as such will not be repeated here.[5] It is sufficient to state that all the raw log $\frac{da}{dN}$ versus log ΔK data we developed on each of the materials investigated demonstrated the nearly linear relationship typical of most fatigue crack growth rate data. Since this linear relationship existed, the crack growth rate data was expressed in terms of the generalized fatigue crack growth rate law developed by Paris.[15] This crack growth rate law is expressed as:

$$\frac{da}{dN} = Co\ \Delta K^n$$

where $\frac{da}{dN}$ is the rate of crack growth, Co is an intercept constant determined from the log $\frac{da}{dN}$ versus log ΔK plot, n is the slope of the log-log plot and ΔK is the stress intensity factor range.

The room temperature and cryogenic fatigue crack growth rate properties of Kromarc 58 (both the T-L and L-T orientations) are presented in Figure 6-15. The cryogenic fatigue crack growth rate properties for the T-L orientation were previously presented in Reference 1. Recall, these cryogenic Kromarc 58 fatigue crack growth rate properties were independent of whether the Kromarc 58 was solution treated and quenched or cold worked. As it turns out, both the room temperature and cryogenic fatigue crack growth rate properties of cold worked Kromarc 58 are also independent of test specimen orientation. Therefore, Kromarc 58 stainless steel can be cold worked without creating specially oriented planes with exceptionally low resistance to catastrophic fracture or fatigue crack propagation. In fact, although all cyrogenic Kromarc 58 fatigue crack growth rate properties are described by a single $\frac{da}{dN}$ versus ΔK relationship, at room temperature the growth rate of fatigue cracks in solution treated and quenched Kromarc 58 exceeds that in cold worked Kromarc 58. Furthermore, note the growth rate of fatigue cracks in Kromarc 58 at room temperature is substantially greater than at cryogenic temperatures independent of test specimen orientation or whether the Kromarc 58 was solution treated and quenched or cold worked. This same fatigue crack growth behavior was previously observed on Inconel X750 by Westinghouse[1,2] and on AISI 310 and A286 stainless steels as well as Inconel X750 by Tobler[16] and Reed.[6]

This behavior is further substantiated by the data of Figure 6-16, which reveals that the growth rate of fatigue cracks in solution treated, quenched and aged A286 stainless steel is directly proportional to temperature; that is, the higher the temperature the greater the fatigue crack propagation rate. Therefore, a general trend for stable austenitic

materials has been demonstrated whereby the growth rate of fatigue cracks at room temperature is at least equal to or in most cases substantially greater that at cryogenic temperatures.

Comparatively speaking, the cryogenic fatigue crack growth rate properties of A286 stainless steel fall midway between those of Kromarc 58 and Inconel X750 (AAM-VAR) (see Figure 6-16, Reference 1) and therefore are quite good. Above a stress intensity factor range of approximately 40 ksi$\sqrt{in.}$ (44.3 MPa$\sqrt{m}$) our A286 fatigue crack growth properties are mildly conservative when compared with those developed by Reed on a very similar A286 stainless steel.[6] Again, the moderate difference in fatigue crack growth rates may be attributed to test specimen orientation.

REFERENCES - SECTION 6

1. Wells, J. M., Logsdon, W. A., Kossowsky, R. and Daniel, M. R., "Structural Materials for Cryogenic Applications, Third Semi-annual Technical Report", Westinghouse Research Report 75-9D4-CRYMT-R1, March 1975.

2. Logsdon, W. A., "Cryogenic Fracture Mechanics Properties of Several Manufacturing Process/Heat Treatment Combinations of Inconel X750", presented at the International Cryogenic Materials Conference, Kingston, Ontario, July 1975.

3. Pettit, D. E., Feddersen, C. E. and Mindlin, H., "Flaw Growth Behavior of Inconel 718 at Room and Cryogenic Temperature", NASA Report CR-101942, Battelle-Columbus Laboratories, Columbus, Ohio, Contract NAS 9-7689, 1969.

4. Forman, R. G., "Crack-Growth Behavior in Thick Welded Plates of Inconel 718 at Room and Cryogenic Temperatures", NASA Technical Note TN D-7665, May 1974.

5. Lessmann, G. G., Logsdon, W. A., Kossowsky, R., Mathur, M. P. and Wells, J. M., "Structural Materials for Cryogenic Applications, Second Semi-annual Technical Report", Westinghouse Research Report 74-9D4-CRYMT-R2, September 1974.

6. Reed, R. P., Tobler, R. L. and Mikesell, R. P., "The Fracture Toughness and Fatigue Crack Growth Rate of an Fe-Ni-Cr Superalloy at 298, 76 and 4 K", presented at the International Cryogenic Materials Conference, Kingston, Ontario, July 1975.

7. Begley, J. A. and Landes, J. D., "The J Integral as a Fracture Criterion", Fracture Toughness, Proceedings of the 1971 National Symposium on Fracture Mechanics, Part II, ASTM STP 514, American Society for Testing and Materials, 1972, pp. 1-20.

8. Landes, J. D. and Begley, J. A., "The Effect of Specimen Geometry on J_{Ic}", Fracture Toughness, Proceedings of the 1971 National Symposium on Fracture Mechanics, Part II, ASTM STP 514, American Society for Testing and Materials, 1972, pp. 24-39.

9. Landes, J. D. and Begley, J. A., "Test Results from J-Integral Studies: An Attempt to Establish a J_{Ic} Testing Procedure", Fracture Analysis, ASTM STP 560, American Scoiety for Testing and Materials, 1974, pp. 170-186.

10. Wessel, E. T., Clark, W. G. and Wilson, W. K., "Engineering Methods for the Design and Selection of Materials Against Fracture", U.S. Army Tank-Automotive Center Report AD No. 801005, June 1966.

11. Brown, W. F., Jr. and Srawley, J. E., "Commentary on Present Practice", Review of Developments in Plane Strain Fracture Toughness Testing, ASTM STP 463, American Society of Testing and Materials, 1970, pp. 216-248.

12. Vishnevsky, C. and Steigerwald, E. A., "Plane Strain Fracture Toughness of Some Cryogenic Materials at Room and Subzero Temperatures",Fracture Toughness Testing at Cryogenic Temperatures, ASTM STP 496, American Society for Testing and Materials, 1971, pp. 3-26.

13. Wells, J. M., "Evaluation of Inconel X750 Weldments for Advanced Cryogenic Applications", presented at the International Cryogenic Materials Conference, Kingston, Ontario, July 1975.

14. Sheinker, A. A. and Logsdon, W. A., "Mechanical Properties and Fracture Toughness of Four Pressurized Water Reactor Structural Alloys", Unpublished Westinghouse Research data, 1975.

15. Paris, P. C., "The Fracture Mechanics Approach to Fatigue", Proc. Tenth Sagamore Army Materials Research Conference, August 1963, Syracuse University Press, 1964.

16. Tobler, R. L., Mikesell, R. P., Durcholz, R. L. and Reed, R. P., "Fatigue and Fracture Toughness Testing at Cryogenic Temperatures", in Semi-annual Report on Materials Research in Support of Superconducting Machinery, NBSIR 74-393, National Bureau of Standards, October 1974, pp. 57-121.

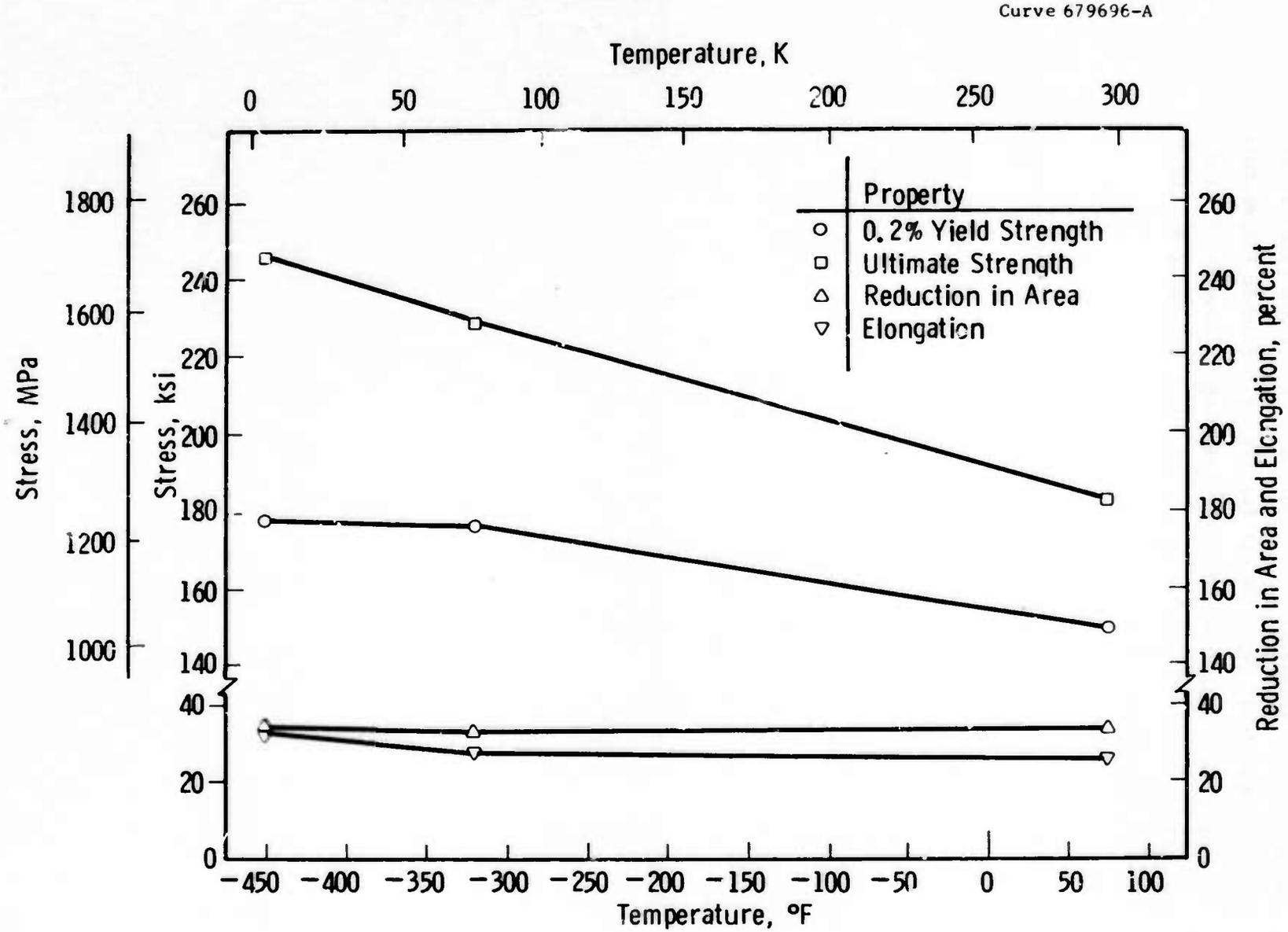

Fig. 6-1—Tensile properties of solution treated and double aged Inconel 706 (VIM-EFR)

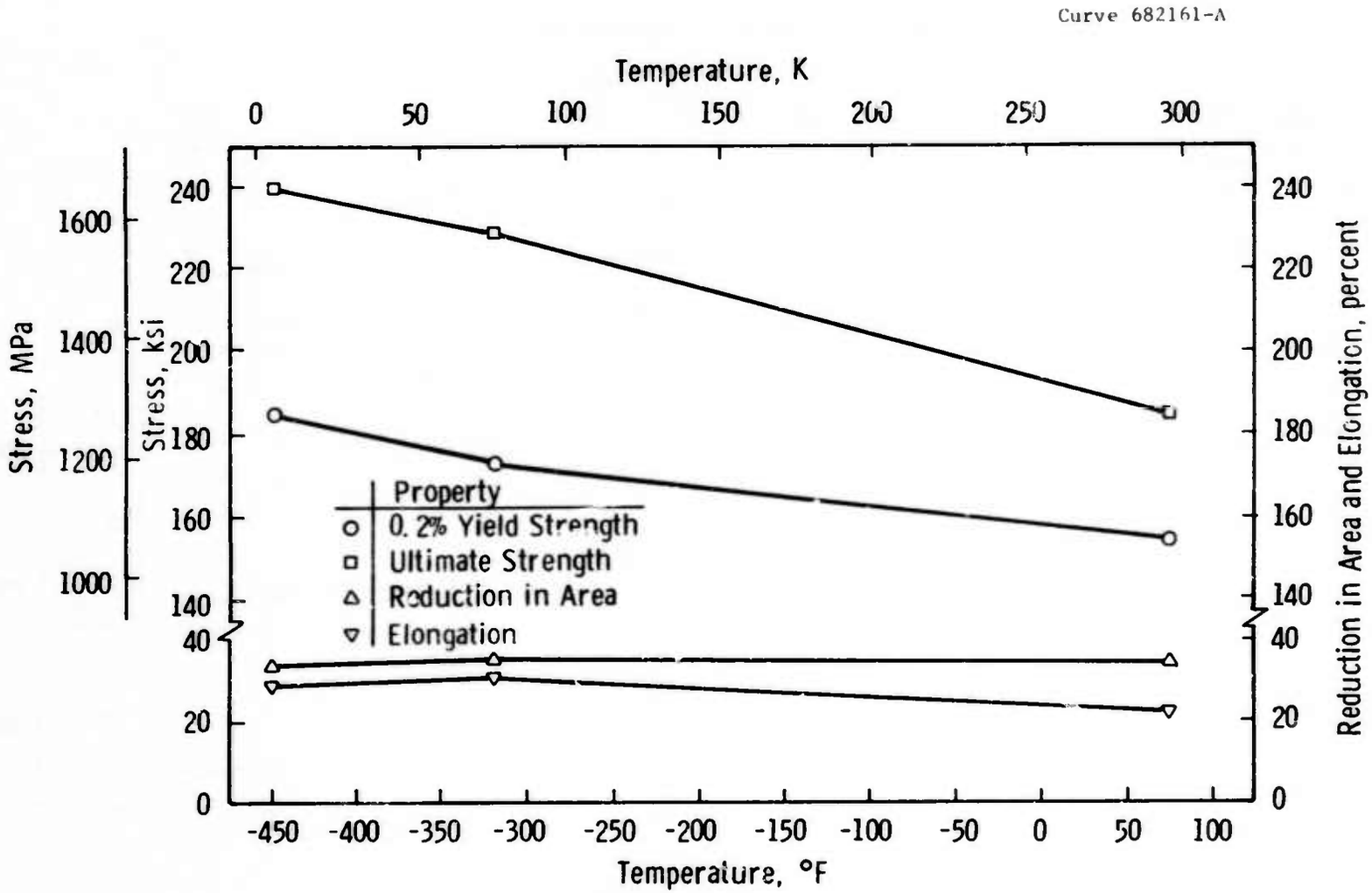

Fig.6-2—Tensile properties of solution treated and double aged Inconel 706 (VIM - VAR)

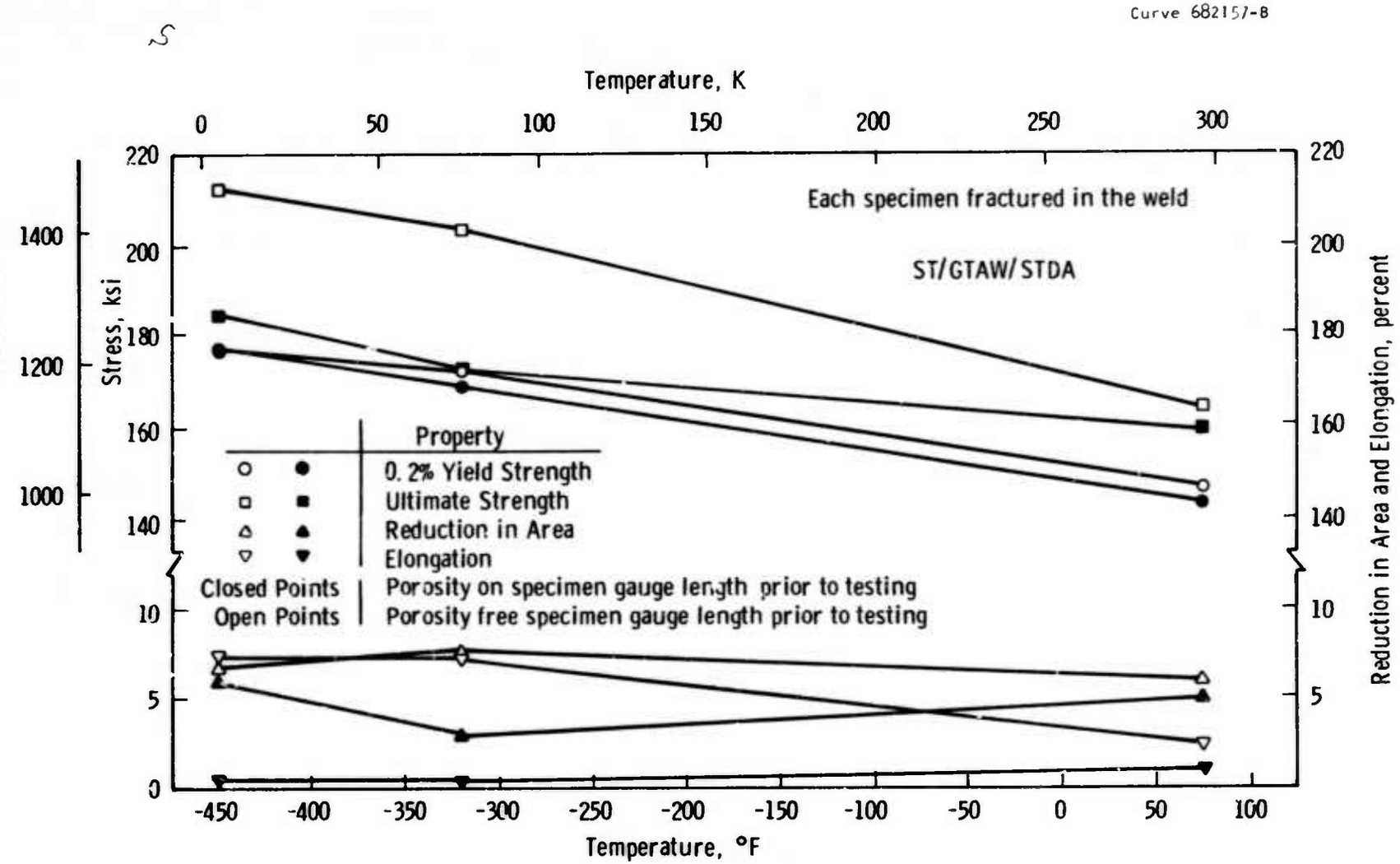

Fig.6-3— Tensile properties of Inconel 706 gas tungsten arc welds

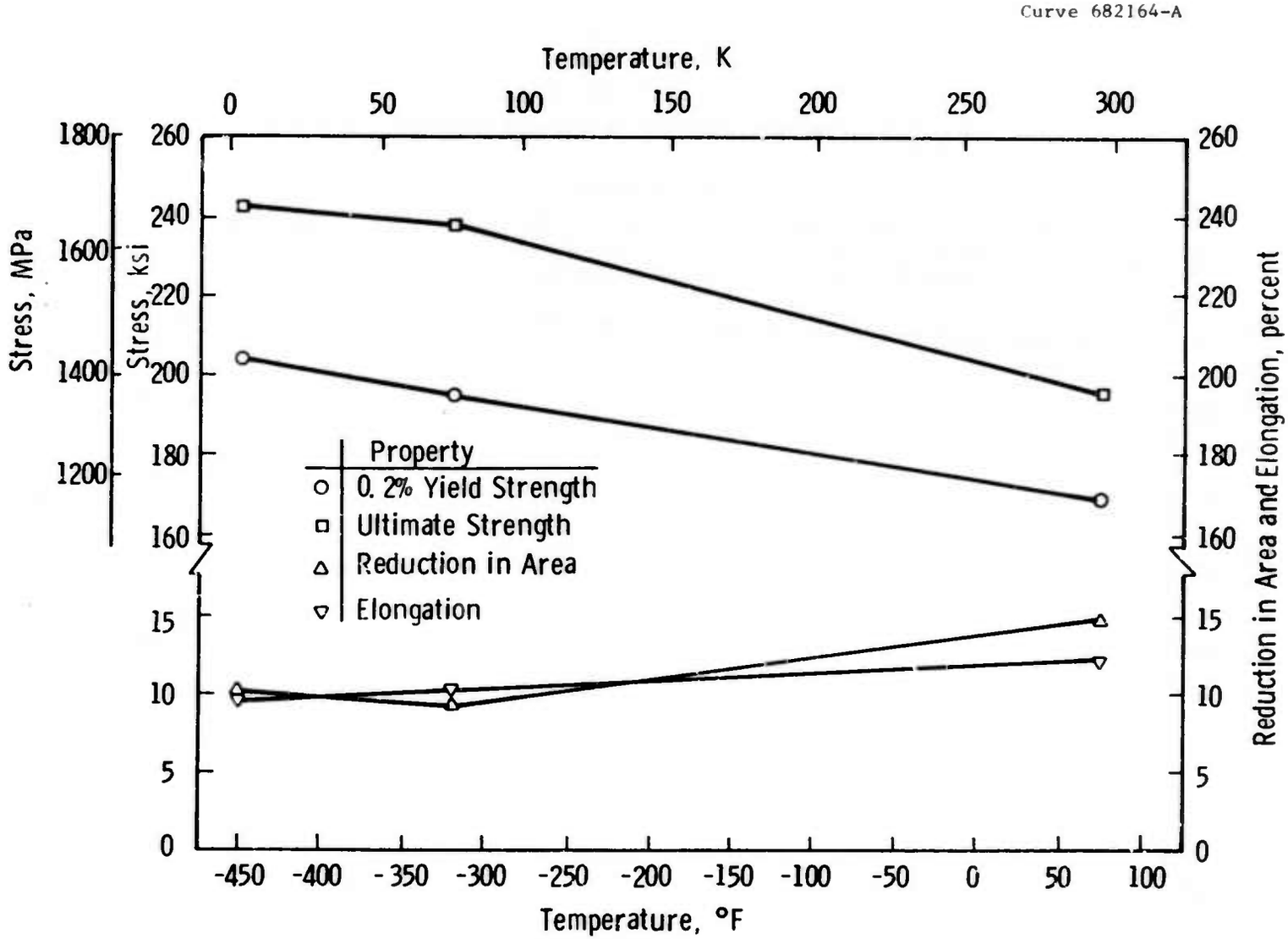

Fig.6-4—Tensile properties of solution treated and double aged Inconel 718 (VIM - VAR)

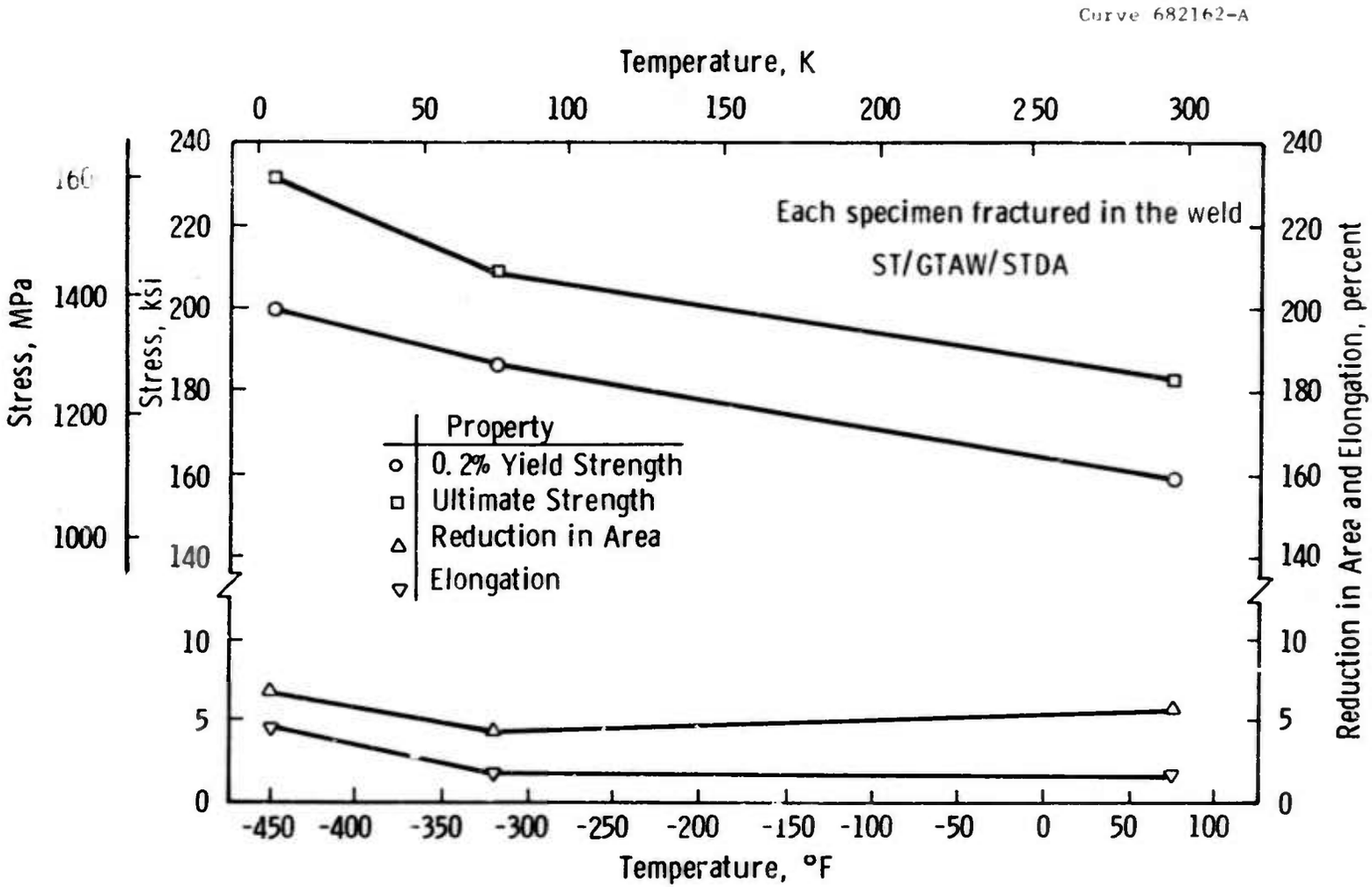

Fig. 6-5— Tensile properties of Inconel 718 gas tungsten arc welds

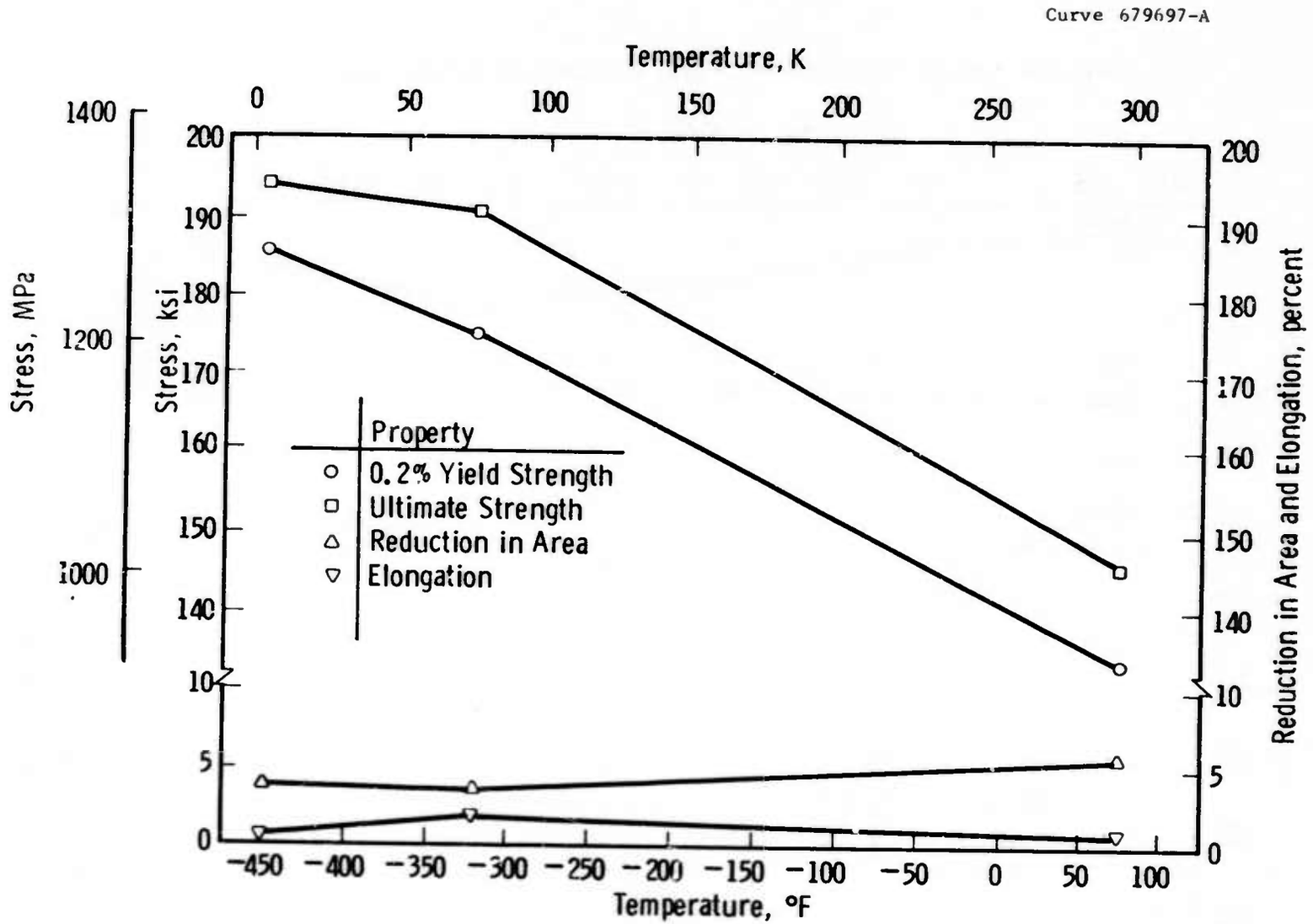

Fig. 6-6 – Tensile properties of solution treated and aged Inco L. E. A.

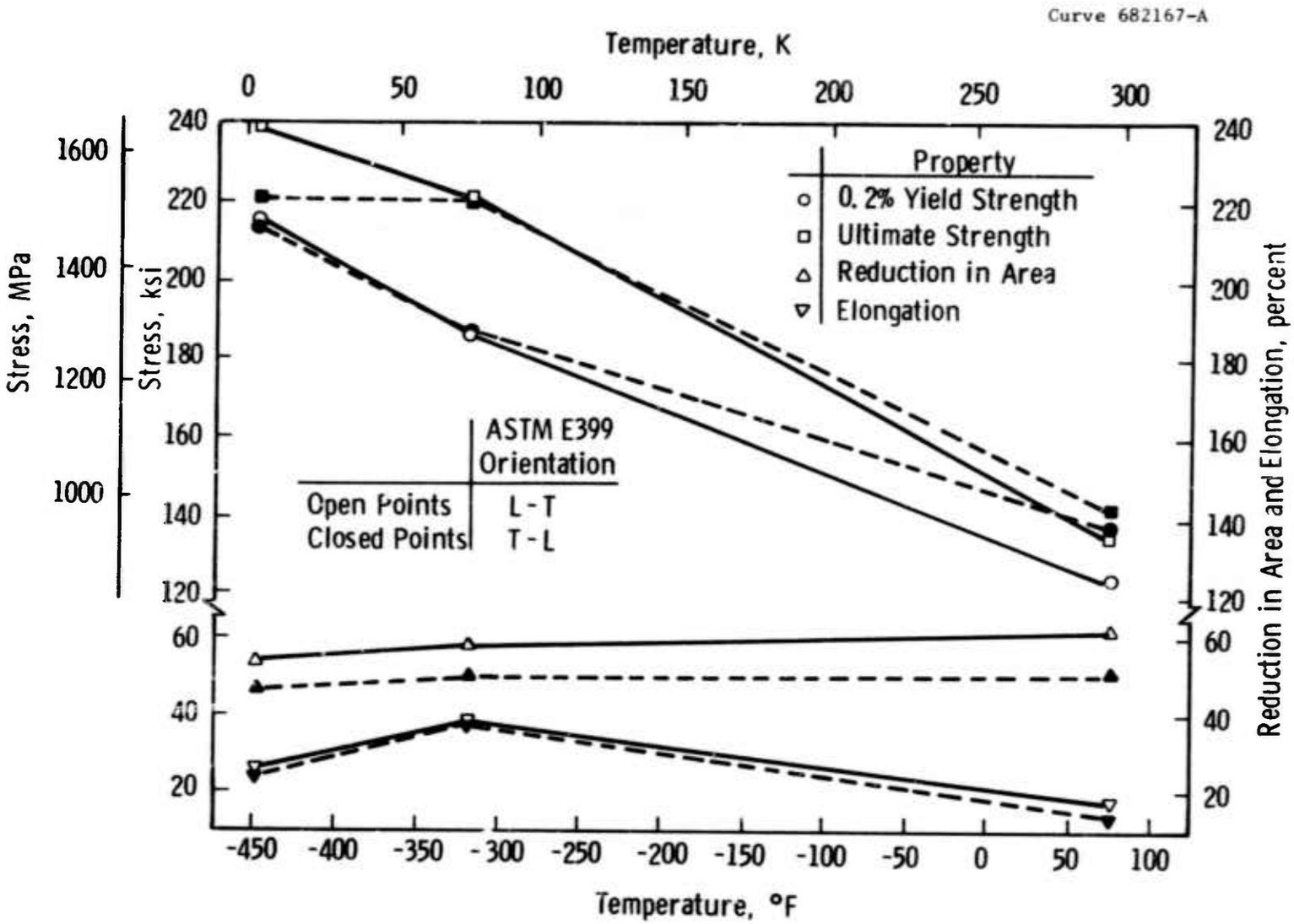

Fig.6-7—Tensile properties of cold worked Kromarc 58 stainless steel

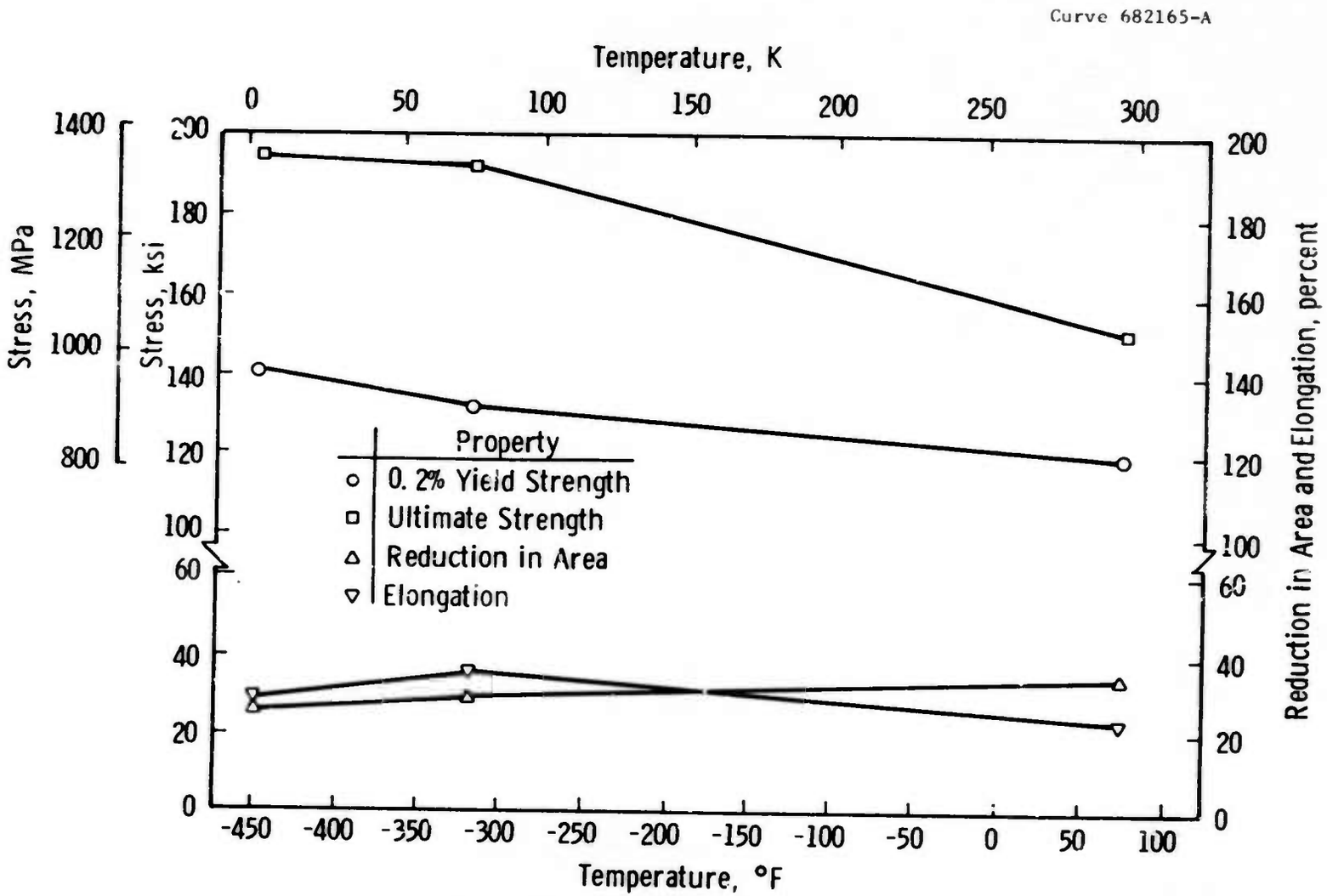

Fig.6-8 — Tensile properties of solution treated, quenched and aged A286 stainless steel

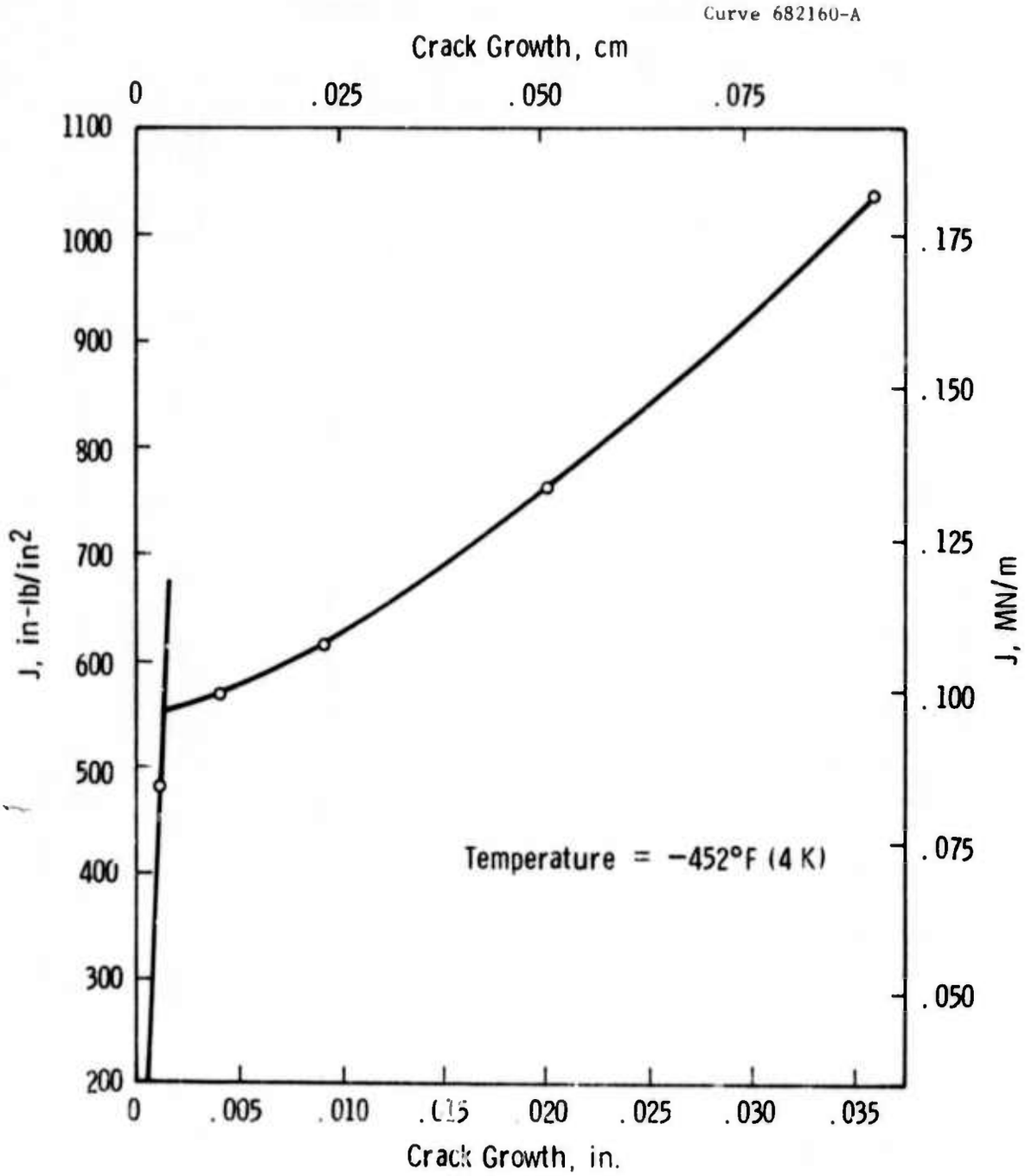

Fig.6-9 — J resistance curve for solution treated and double aged Inconel 706 (VIM - EFR)

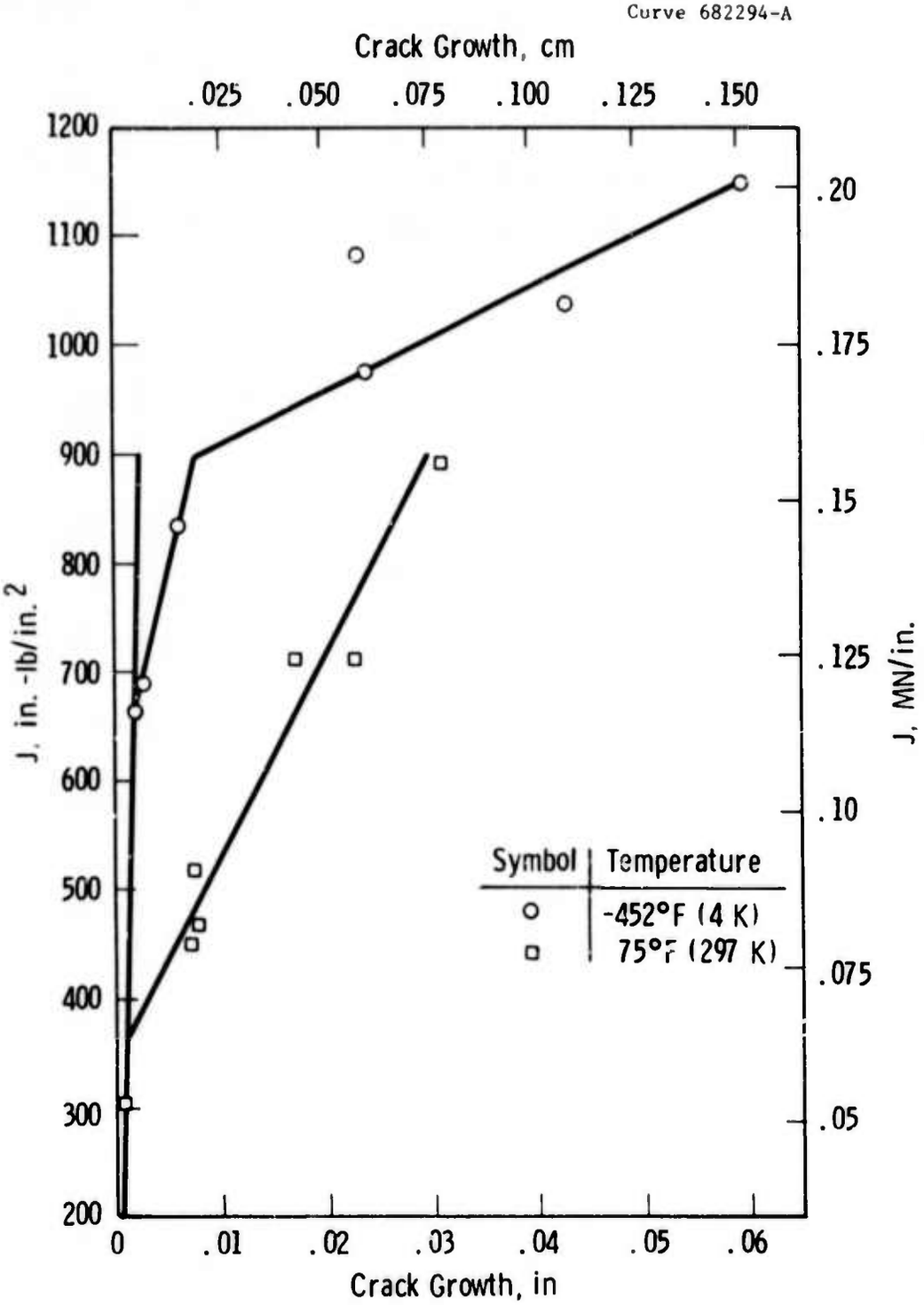

Fig.6-10— J resistance curves for solution treated and double aged Inconel 706 (VIM-VAR)

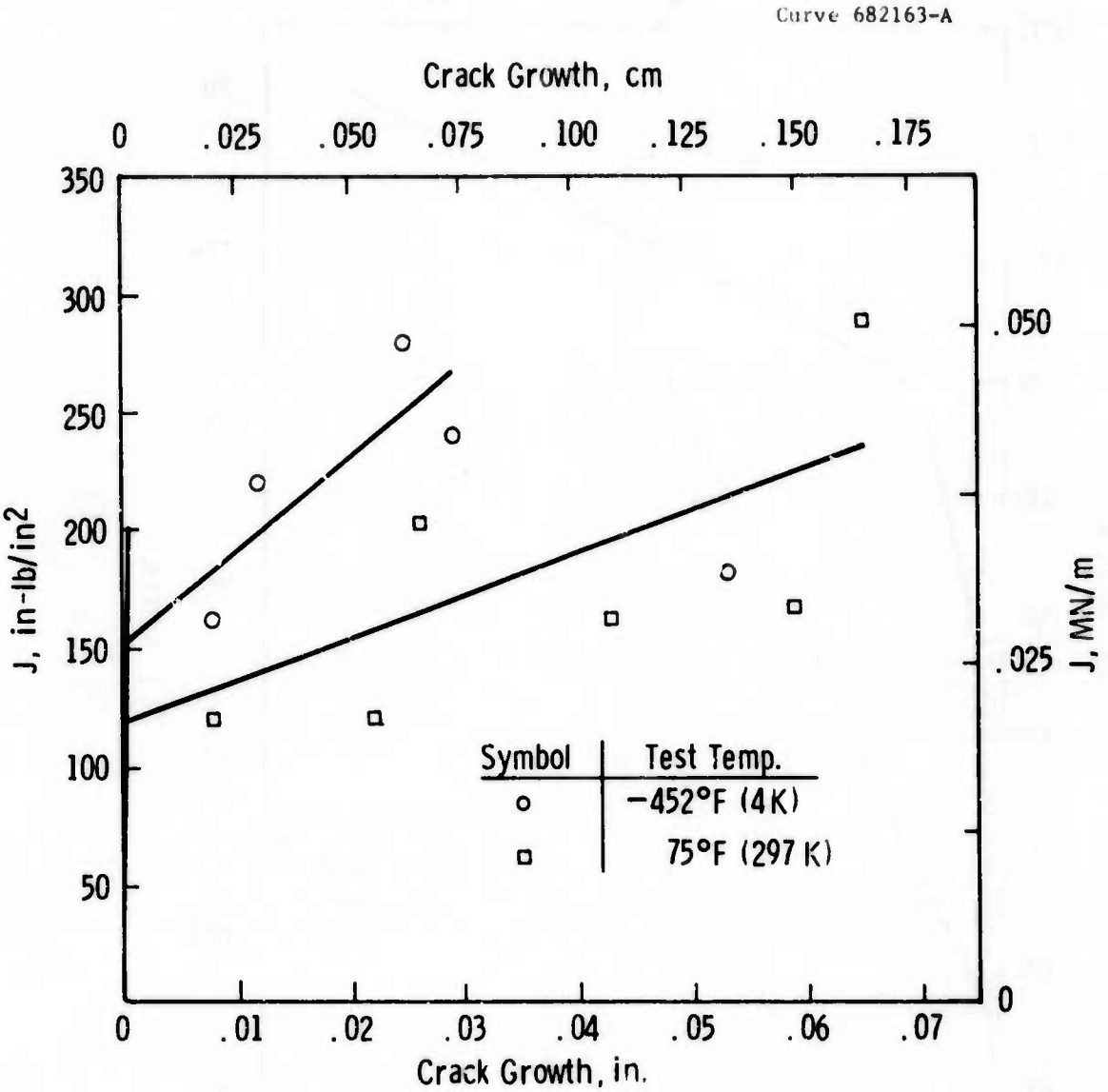

Fig.6-11 -J resistance curves for solution treated and double aged Inconel 718 (VIM - VAR)

Curve 682158-A

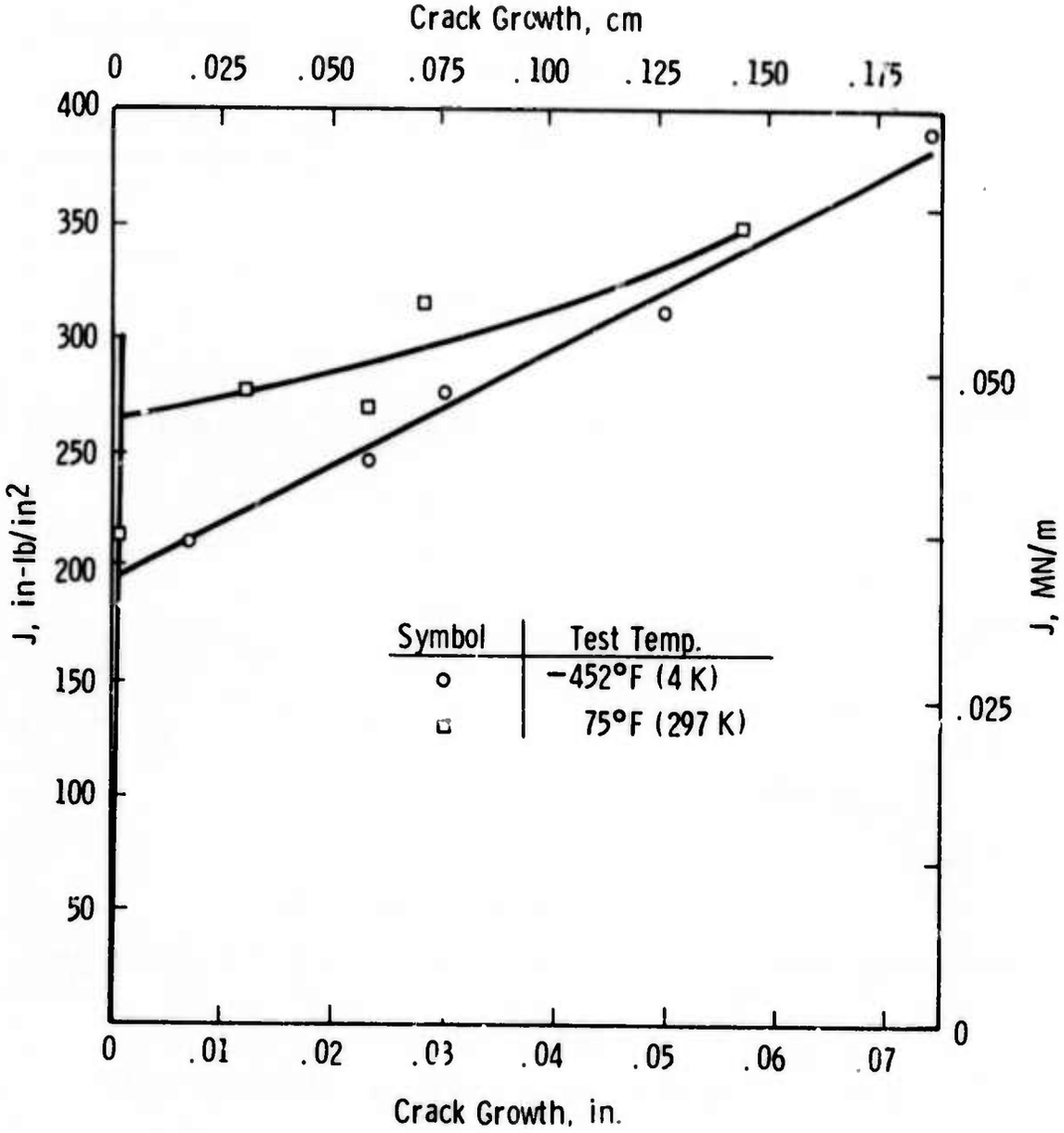

Fig. 6-12 — J resistance curves for solution treated and aged Inco L. E. A.

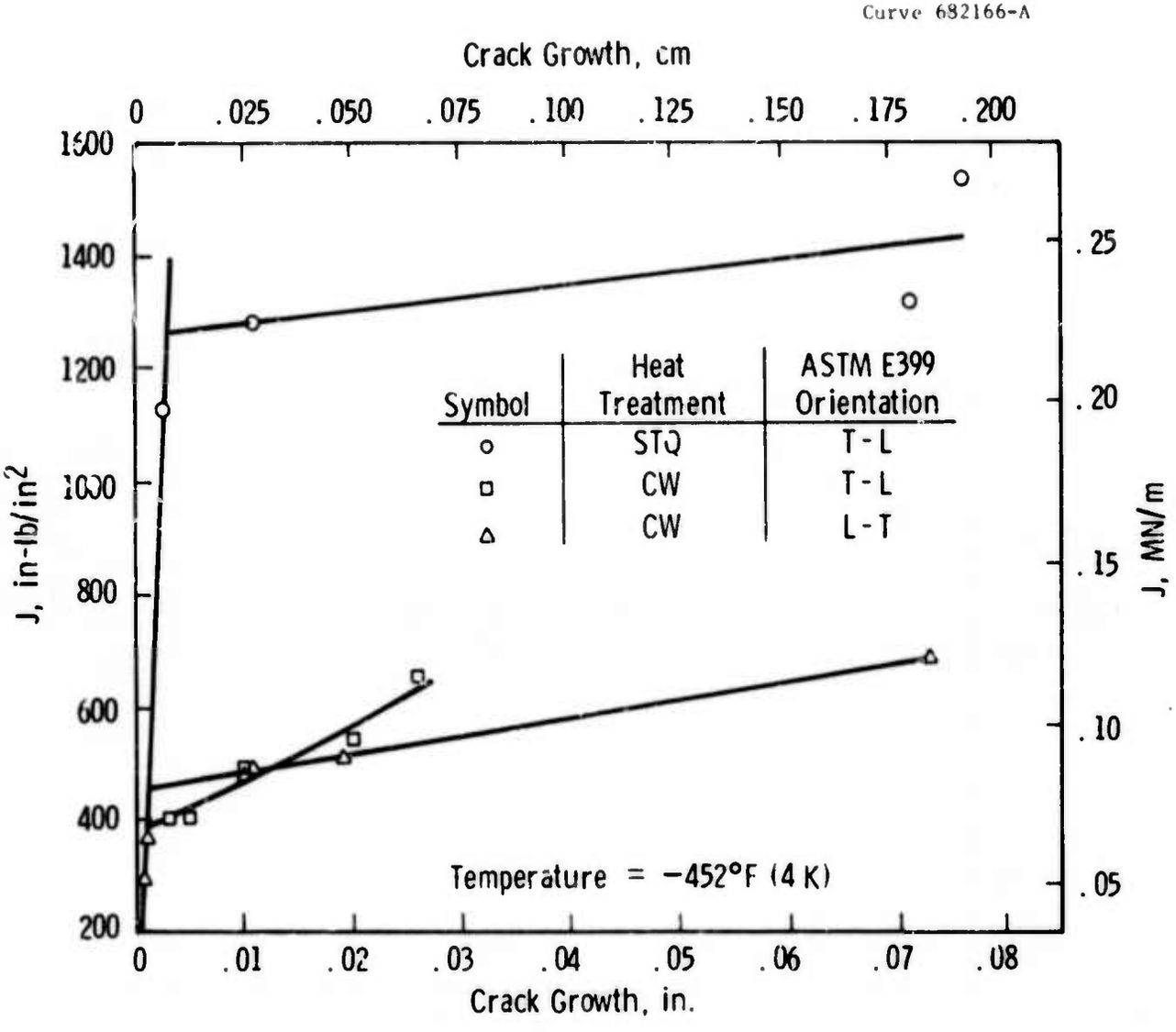

Fig. 6-13 −J resistance curves for Kromarc 58 stainless steel

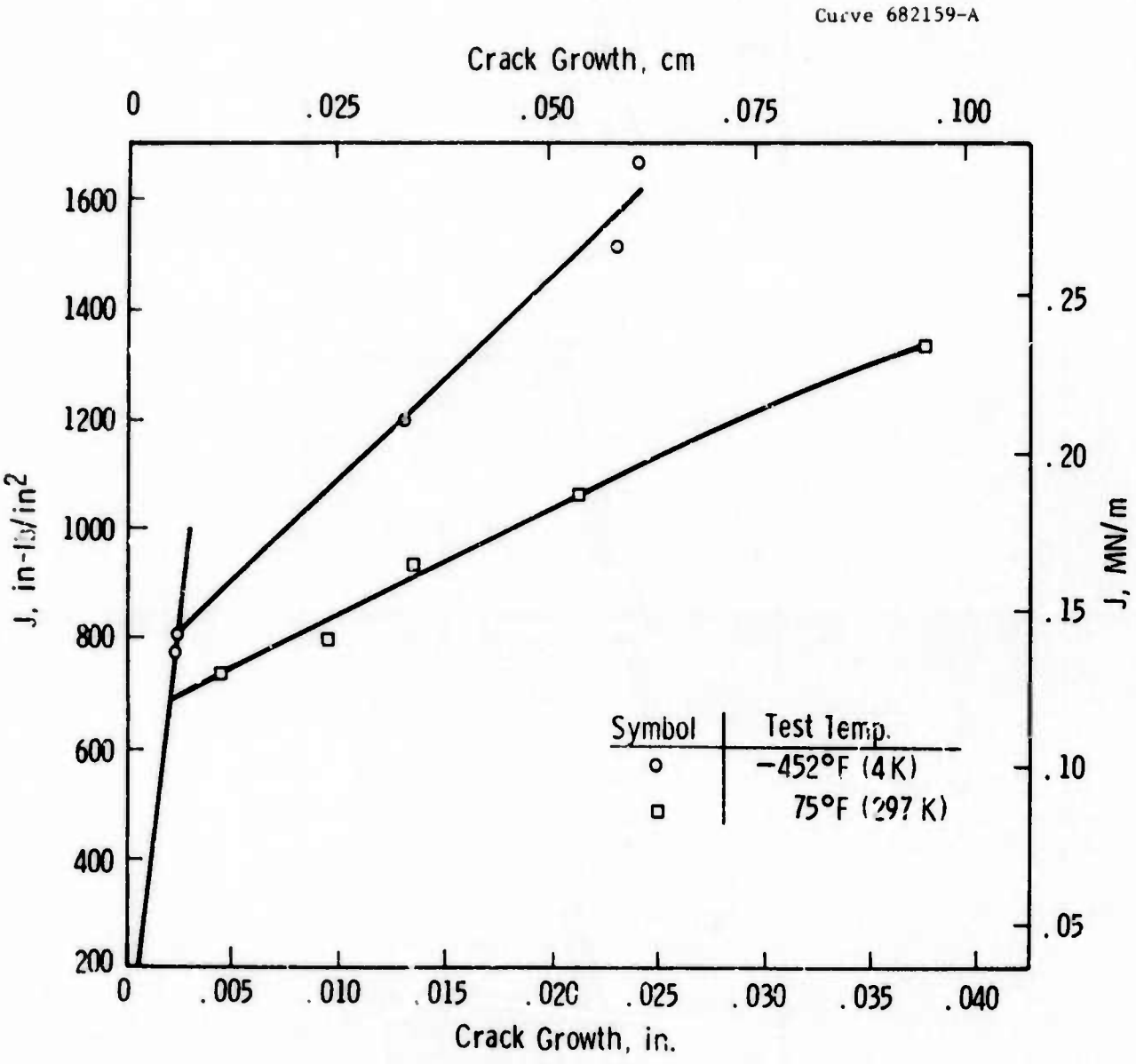

Fig. 6-14 – J resistance curves for solution treated, quenched and aged A286 stainless steel

Curve 682499-B

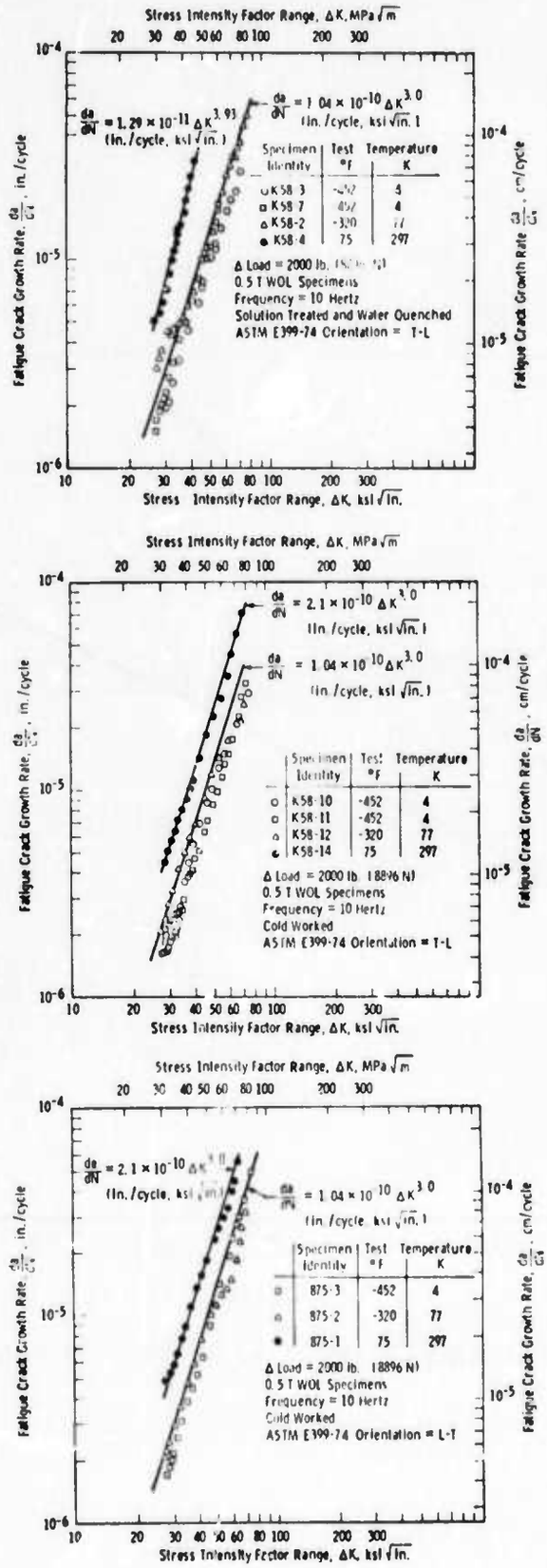

Fig. 6-15 — Fatigue crack growth rate properties of Kromarc 58 stainless steel

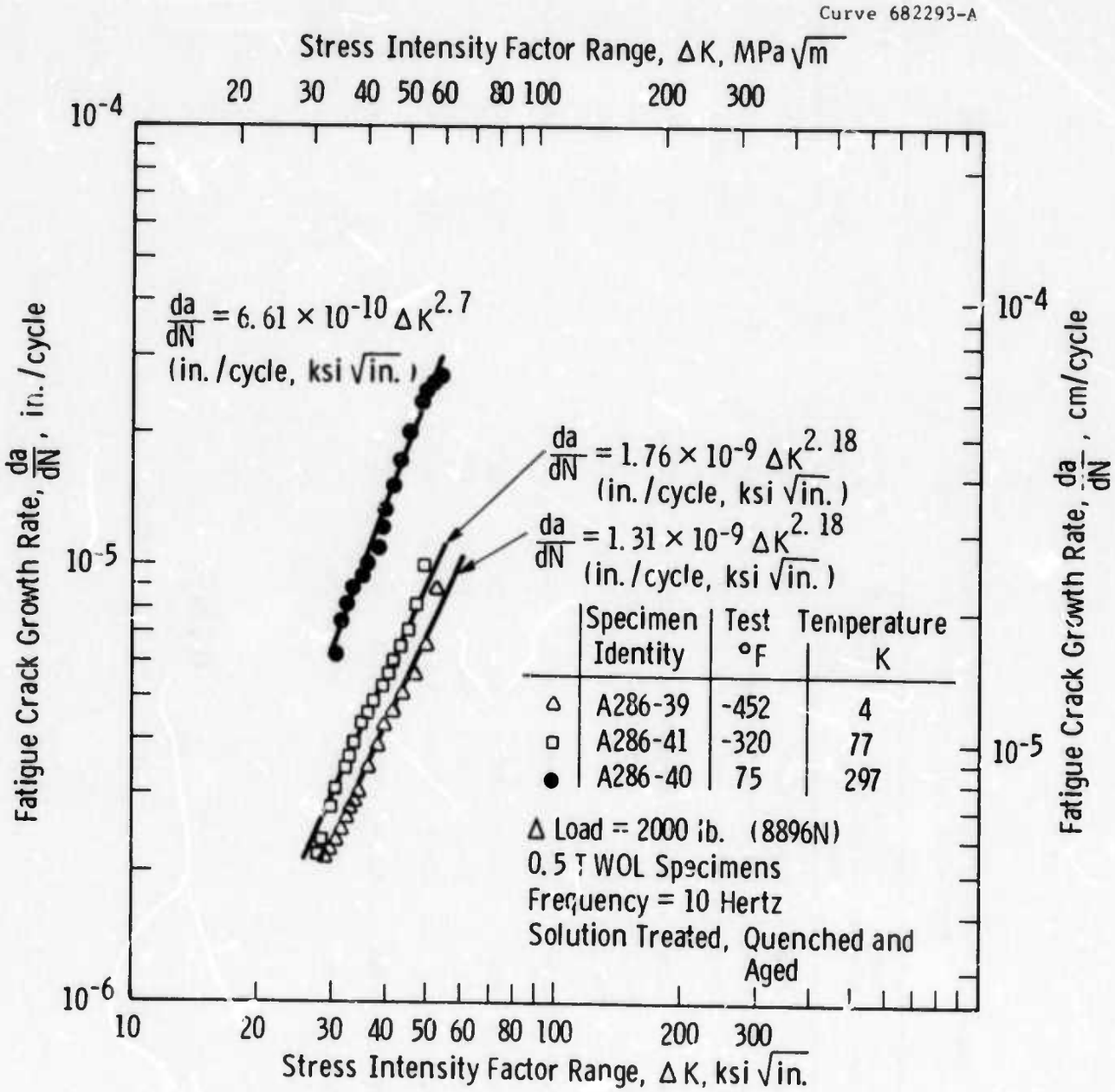

Fig. 6-16—Fatigue crack growth rate properties for A286 stainless steel

TABLE 6-1 - TENSILE AND NOTCHED TENSILE PROPERTIES OF INCONEL 706 AND 718 PLUS INCO LEA, KROMARC 58, PD135 AND A286 AT 75°F (297 K)

Material	Manu. Process	Material Condition	Heat Treatment	Yield Strength Ksi	Yield Strength MPa	Ultimate Strength Ksi	Ultimate Strength MPa	Reduction in Area %	Elongation %	NTS Ksi	NTS MPa	NTS/σ_{ys}	Comments
Inconel 706	VIM-EFR	BASE	STDA	149.0	1027.3	182.2	1256.2	32.9	25.2	268.4	1850.6	1.8	
Inconel 706	VIM-VAR	BASE	STDA	154.2	1063.2	184.2	1270.0	33.9	22.0	275.8	1901.6	1.8	
Inconel 706	VIM-VAR	GTAW	ST/W/STDA	145.0	999.7	161.2	1111.4	5.4	1.7	236.0	1627.2	1.6	
Inconel 718	VIM-VAR	BASE	STDA	168.8	1163.8	195.4	1347.2	14.8	12.0	253.6	1748.5	1.5	
Inconel 718	VIM-VAR	GTAW	ST/W/STDA	158.6	1093.5	182.6	1259.0	5.7	1.7	201.8	1391.4	1.3	
Inconel 718	VIM-VAR	HAZ	ST/W/STDA	--	--	--	--	--	--	232.4	1602.3	1.5	
Inco LEA	--	BASE	STA	133.2	918.4	145.6	1003.9	6.0	1.0	198.4	1367.9	1.5	
Kromarc 58	--	BASE	STQ	53.8	370.9	101.7	701.2	66.8	45.8	134.6	928.0	2.5	T-L Orientation
Kromarc 58	--	BASE	CW	137.3	946.6	142.2	980.4	50.4	13.9	223.5	1541.0	1.6	T-L Orientation
Kromarc 58	--	BASE	CW	124.4	857.7	135.6	934.9	61.8	17.0	230.2	1587.2	1.8	L-T Orientation
A286		BASE	STQA	119.3	822.5	151.2	1042.5	34.8	23.5	--	--	--	
PD135	--	BASE	--	35.3	243.4	50.8	350.3	73.4	32.0	63.3	436.4	1.8	

TABLE 6-2 - TENSILE AND NOTCHED TENSILE PROPERTIES OF INCONEL 706 AND 718 PLUS INCO LEA, KROMARC 58, PD135 AND A286 AT -320°F (77 K)

Material	Manu. Process	Material Condition	Heat Treatment	Yield Strength Ksi	Yield Strength MPa	Ultimate Strength Ksi	Ultimate Strength MPa	Reduction in Area %	Elongation %	NTS Ksi	NTS MPa	NTS/σ_{ys}	Comments
Inconel 706	VIM-ERP	BASE	STDA	176.2	1214.9	228.3	1574.1	32.1	27.0	316.0	2178.7	1.8	
Inconel 706	VIM-VAR	BASE	STDA	172.8	1191.4	228.2	1573.4	34.4	30.3	314.8	2170.5	1.8	
Inconel 706	VIM-VAR	GTAW	ST/W/STDA	170.3	1174.2	187.8	1294.8	4.4	3.8	254.8	1756.8	1.5	
Inconel 718	VIM-VAR	BASE	STDA	194.9	1343.8	237.8	1639.6	9.1	10.1	272.1	1876.1	1.4	
Inconel 718	VIM-VAR	GTAW	ST/W/STDA	185.8	1281.0	208.2	1435.5	4.3	1.8	213.2	1470.0	1.1	
Inconel 718	VIM-VAR	HAZ	ST/W/STDA	--	--	--	--	--	--	243.9	1681.4	1.3	
Inco LEA	--	BASE	STA	175.0	1206.6	191.0	1316.9	3.5	1.9	238.0	1641.0	1.4	
Kromarc 58	--	BASE	STQ	114.3	788.1	188.1	1296.9	58.2	49.8	228.9	1578.2	2.0	T-L Orientation
Kromarc 58	--	BASE	CW	186.8	1287.9	220.4	1519.6	49.7	37.0	308.4	2126.3	1.6	T-L Orientation
Kromarc 58	--	BASE	CW	186.3	1284.5	221.5	1527.2	57.3	38.0	324.5	2237.3	1.7	L-T Orientation
A286	--	BASE	STQA	131.4	906.4	191.6	1321.0	29.0	35.7	--	--	--	
PD135	--	BASE	--	38.1	262.7	69.3	477.8	71.2	40.2	90.2	621.9	2.4	

TABLE 6-3 - TENSILE AND NOTCHED TENSILE PROPERTIES OF INCONEL 706 AND 718 PLUS INCO LEA, KROMARC 58, PD135 AND A286 AT -452°F (4 K)

Material	Manu. Process	Material Condition	Heat Treatment	Yield Strength Ksi	Yield Strength MPa	Ultimate Strength Ksi	Ultimate Strength MPa	Reduction in Area %	Elongation %	NTS Ksi	NTS MPa	NTS/σ_{ys}	Comments
Inconel 706	VIM-EFR	BASE	STDA	178.0	1227.3	245.9	1695.4	33.1	32.1	321.6	2217.4	1.8	
Inconel 706	VIM-VAR	BASE	STDA	184.6	1272.8	239.4	1650.6	33.5	28.2	330.9	2281.5	1.8	
Inconel 706	VIM-VAR	GTAW	ST/W/STDA	177.2	1221.8	198.7	1370.0	5.7	4.0	273.2	1883.6	1.4	
Inconel 718	VIM-VAR	BASE	STDA	203.9	1405.8	242.2	1669.9	10.0	9.4	279.5	1927.1	1.4	
Inconel 718	VIM-VAR	GTAW	ST/W/STDA	199.2	1373.4	231.2	1594.1	6.7	4.7	220.5	1520.3	1.1	
Inconel 718	VIM-VAR	HAZ	ST/W/STDA	--	--	--	--	--	--	222.2	1532.0	1.1	
Inco LEA	--	BASE	STA	185.9	1281.7	194.2	1339.0	3.8	0.7	234.3	1615.4	1.3	
Kromarc 58	--	BASE	STQ	158.7	1094.2	192.2	1325.2	55.0	42.0	272.3	1877.4	1.7	T-L Orientation
Kromarc 58	--	BASE	CW	213.4	1471.3	220.7	1521.7	46.0	23.8	356.2	2455.9	1.7	T-L Orientation
Kromarc 58	--	BASE	CW	215.8	1487.9	238.5	1644.4	53.6	26.0	362.1	2496.6	1.7	L-T Orientation
A286	--	BASE	STQA	140.5	968.7	194.2	1339.0	26.0	29.7	--	--	--	
PD135	--	BASE	--	37.0	255.1	75.8	522.6	67.8	59.8	100.7	694.3	2.7	

TABLE 6-4 - FRACTURE TOUGHNESS PROPERTIES OF INCONEL 706, 718 AND X750 PLUS INCO LEA AND A286

Material	Manu. Process	Material Condition	Heat Treatment	Test Temperature °F	Test Temperature K	Yield Strength Ksi	Yield Strength MPa	J_{IC} in.-lb/in.^{2}	J_{IC} MN/m	K_{IC} Ksi$\sqrt{in.}$	K_{IC} MPa$\sqrt{m}$	K_{IC}/σ_{ys} $\sqrt{in.}$	$(K_{IC}/\sigma_{ys})^2$ in.
Inconel 706	VIM-EFR	BASE	STDA	-452	4	178.0	1227.3	550	.096	137.9	152.7	0.77	0.60
Inconel 706	VIM-VAR	BASE	STDA	-452	4	184.6	1272.8	664	.116	151.5	167.7	0.82	0.67
Inconel 706	VIM-VAR	BASE	STDA	75	297	154.2	1063.2	364	.064	110.2	122.0	0.71	0.51
Inconel 706	VIM-VAR	GTAW	ST/W/STDA	-452	4	177.2	1221.8	--	--	53.0	58.7	0.30	0.09
Inconel 718	VIM-VAR	BASE	STDA	-452	4	203.9	1405.8	152	.027	72.5	80.3	0.36	0.13
Inconel 718	VIM-VAR	BASE	STDA	75	297	168.8	1163.8	120	.021	63.3	70.1	0.38	0.14
Inconel 718	VIM-VAR	GTAW	ST/W/STDA	-452	4	199.2	1373.4	--	--	47.1	52.1	0.24	0.06
Inconel 718	VIM-VAR	GTAW	ST/W/STDA	-320	77	185.8	1281.0	--	--	46.5	51.5	0.25	0.06
Inconel 718	VIM-VAR	HAZ	ST/W/STDA	-452	4	199.2	1373.4	--	--	55.4	61.3	0.28	0.08
Inconel 718	VIM-VAR	HAZ	ST/W/STDA	-320	77	185.8	1281.0	--	--	60.2	66.6	0.32	0.10
Inconel X750	VIM-VAR	Cu BRAZE	ST/B	-452	4	115.1	793.6	--	--	40.5	44.8	0.35	0.12
Inconel X750	VIM-VAR	Cu BRAZE	ST/B	-320	77	108.4	747.4	--	--	35.3	39.1	0.33	0.11
Inconel X750	VIM-VAR	Cu BRAZE	ST/B	75	297	94.5	651.6	--	--	34.7	38.4	0.37	0.13
Inco LEA	--	BASE	STA	-452	4	185.9	1281.7	195	.034	82.1	90.9	0.44	0.20
Inco LEA	--	BASE	STA	75	297	133.2	918.4	263	.046	93.7	103.7	0.70	0.49
A286	--	BASE	STQA	-452	4	140.5	968.7	815	.143	162.8	180.2	1.16	1.34
A286	--	BASE	STQA	75	297	119.3	822.5	692	.121	145.6	161.2	1.22	1.49

TABLE 6-5 - COMPARISON OF THE -452°F (4 K) BASE METAL FRACTURE PROPERTIES OF KROMARC 58 STAINLESS STEEL

Orientation	Heat Treatment	Yield Strength		J_{IC}		K_{IC}		K_{IC}/σ_{ys}	$(K_{IC}/\sigma_{ys})^2$
		Ksi	MPa	in.-lb/in.^{2}	MN/m	Ksi$\sqrt{in.}$	MPa$\sqrt{m}$	$\sqrt{in.}$	in.
T-L	STQ	158.7	1094.2	1250	.219	195.4	216.3	1.23	1.52
T-L	CW	213.4	1471.3	388	.068	108.8	120.4	0.51	0.26
L-T	CW	215.8	1487.9	452	.079	117.5	130.1	0.54	0.30

7. MICROSTRUCTURAL ANALYSIS

The purpose of this phase of the work is two-fold: (a) examine the microstructures of tested specimens to determine the cause and mode of failure, (b) correlate the microstructural features with mechanical test data to establish failure mechanisms and effects of processing variables. With this knowledge at hand, one is able to identify critical areas in processing, material use, and performance realization. During this reporting period, solution treatment of X-750 discussed in previous reports[1] was investigated. Also examined were specimens of PD135 Cu and Inconel LEA (low expansion alloy). A detailed microstructural investigation of base metal and welds of Inconel 718 and 706 are presented. Alloy 718 is discussed with reference to two sources; namely, Inconel 718 (International Nickel) and Udimet-718 (Special Metals). Results are presented in terms of light microscopy, scanning electron microscopy with energy dispersive X-ray data, transmission electron microscopy, and Auger spectroscopy.

7.1 Alloy X-750

In previous reports[1,2] the effects of thermomechanical treatments on the resulting microstructures and their correlations with mechanical properties were discussed in detail. It was shown that the lower strength and ductility, coupled with low fracture toughness of the MP-1 material was related to continuous films of carbides in the grain boundaries. The marked improvements in MP-2 and MP-3 materials was shown to result from elimination of the carbide films, and the residual dislocation-γ' networks within the grain. This was related to thermal-mechanical treatments imparted during processing.

In this section we show briefly that improvements in MP-1 material cannot, apparently, be obtained by thermal treatment only. That is, solutioning of the alloy at higher temperatures than those employed during the standard solutioning and aging process do not eliminate grain boundary carbides. Figure 1 (light microscopy) and

Fig. 2 (SEM) demonstrate heavy carbides near and at grain boundaries. These carbides are mainly of the MC type ((Nb, Ti)C) which do not enter solution at temperatures below 2350°F.

7.2 PD135 Copper Alloy

This is a precipitation hardenable alloy where strengthening is imparted by precipitation of Cr and Cd. Specimens were prepared from the original extruded billets[1] after precipitation treatment at 1100°F for 1 hour. Longitudinal and cross sections of tensile specimens tested at 77 K and 42 K, and two examples from a notched tensile specimen are shown in the light micrographs, Figs. 7.3 to 7.5, respectively. All three figures indicate a substantial ductility prior to failure with isolated cavitation due to localized instabilities. Dimpled fracture surface, typical of cross-granular ductile mode of failure is shown by the scanning micrographs in Fig. 6. The scanning electron micrographs in Fig. 7 show a similar dimpled structure developed during fracture of notch-tensile specimens. A Cr-Cd rich particle is usually present at the bottom of the dimple. Occasionally observed inclusions, rich in S, Cl, K and Fe are shown in Fig. 7c.

7.2.1 Summary

1) Precipitation hardenable PD135 Cu deforms in a ductile manner showing a typical dimpled structure.

2) Occasional inclusions containing S, Cl, K and Fe are found on the fracture surface. There is no direct evidence that these inclusions cause degradation of strength in the tensile mode.

7.3 Alloy 718, Base Metal Characteristics

Microstructures of 718 alloys in the as-received conditions, and after various heat treatment, received from two sources are compared: (a) Udimet-718, produced by Special Metals and (b) Inconel 718 produced by the International Nickel (Huntington Alloy Product Div.). I-718 was obtained in the form of 11-3/8" dia. billets, U-718 was a 10-1/4" billet.

7.3.1 Udimet-718

Figures 8 and 9 show grain morphologies from top and bottom ends of the billet and the inner and outer portions of each end. Generally speaking, the outer diameter portion of the billet exhibits a higher degree of deformation as evidenced by the wavy structure and higher density of slip lines within the grain. (Compare Figs. 8, ab to cd, Fig. 9ab to cd). Typical scanning electron micrographs obtained from various sections of the billet are shown in Fig. 10. One should notice that in these micrographs the grain boundaries appear to be void of heavy precipitation. Occasional precipitation of (Nb, Ti)C carbides are seen in Fig. 10b.

The effects of heat treatment on the type and morphology of precipitates are shown in the transmission electron micrographs, Figs. 11-13. $Ni_3Cb(\gamma'')$ cellular precipitation develops after solution anneal at 1800°F (1255 K) and standard double/aging treatment. The platelets of γ'' are shown in Fig. 11a, and the identification by dark field is illustrated in Figs. 11b and 11c.

A few more examples of cellular precipitation of γ'' at the grain boundaries are shown in Figs. 12a and 12b. Heavy particle-dislocation networks within the grain are illustrated in Fig. 12c. The diffraction pattern in 12d shows that the fine precipitation includes both γ' (Ni_3Al) and γ'' (Ni_3Nb).[3,4] Also note that the grain boundaries do not show any heavy precipitation.

The absence of carbide film or other heavy grain boundary precipitates in U-718 is again shown in Fig. 13, which depicts typical structural features following solution-anneal at 1900°F (1311 K) and standard double aging. Figures 13a and 13b shows particle-($\gamma' + \gamma''$) dislocation networks within the grain and relatively, precipitation-free grain boundaries. The diffraction pattern in 13c shows streaking[5] -- typical of preferred-oriented precipitates. The dark field micrograph in 12d is from the (001) reflection of γ' (arrow in 12c).

7.3.2 Inconel 718

The general morphology of IN-718 in the as-received condition (11-3/8 inch diameter, hot finished billet[1]) is illustrated in Fig. 14. Note two families of precipitates, i.e., small particles dispersed within the grain boundaries network and coarser particles dispersed in a secondary network, not related directly to grain boundaries. The energy dispersive X-ray data, shown in Fig. 15 identify the large particles as (Nb, Ti)C carbides. The small, grain boundary precipitation is somewhat more complex and contains Si and Mo as well.

The series of micrographs in Figs. 16 through 22 demonstrate the effect of solutioning temperature and aging treatment on the development of precipitation in the alloy. The SEM micrographs, Fig. 16, show that most of the grain boundary precipitation is resolutioned after 2 hours at 2100°F (1422 K). Only the large MC carbides are still present. However, a more detailed examination by transmission electron microscopy, shows that thin films of carbides are still present in the grain boundaries (Fig. 17). The dark field micrograph, Fig. 17b, was taken from the spot at d = 1.72 Å, which can be assigned unambiguously to M_6C type carbide. Solutioning at 1950°F (1339 K) also dissolves most of the grain boundary carbides, as shown in Fig. 18. However, within the grain (Fig. 19) precipitation of Ni_3Al, Ti (γ') and Ni_3Nb (γ'') is detected. These precipitates are expected to go into solution[6] at 1950°F, and thus could have precipitated during cooling.[7] Solutioning at 1800°F (1255 K) does not dissolve any of the particles which are distributed in a network of "ghost" boundaries, Fig. 2a. The standard 1800°F solution anneal and double-aging results in additional fine precipitation of $\gamma' + \gamma''$ within the grain, and γ'', fine MC, and coarse M_6C carbides within the grain boundaries (Figs. 21).

Fracture characteristics of tensile specimens, IN-718 STDA are shown in Figs. 22 through 26. The light micrographs in Fig. 22 indicate an intergranular fracture at room temperatures as well as at 4.2 K when tested in tension. Note the bimodal grain size in the

cross sections. Most of the grains are in the range of 50 μm. The large grains are of the order of 150 μm. Notch-tensile specimens, Fig. 23, exhibit a mixture of intergranular fracture and cross granular cleavage (arrows). Both figures indicate small amount of deformation due to the lack of slip lines. This is in agreement with the test data (Table 6). Figures 24 and 25 show the morphology of the fracture surfaces of tensile specimens where intergranular fracture mode is clearly indicated. Note long chains of cleaved carbides in Fig. 25c and the dimpled structure within the grain that shows at high magnification, Figs. 24 and 25d. Small particles are clearly visible at the center of each dimple. These micrographs indicate small amounts of ductile deformation within the grain and failure associated with carbide particles of a variety of sizes and shapes. Figure 26 confirms the observations related to Fig. 23 in that in the notch-tensile mode, the fracture proceeds by a mixture of intergranular and cleavage modes. Cleaved grains are marked (c) in Fig. 26. Again note the many small particles at the bottom of each dimple on the grain face (Fig. 26d).

To test the hypothesis that fracture proceeds along grain boundary carbide chains, the material was examined by Auger spectroscopy, where fresh fractured surfaces were analyzed at 5×10^{-10} torr, excluding any external contamination. It should be noted that the fracturing device in the Auger spectrograph subjects a notched specimen to shear fracture. Since the notched-tensile mode introduces some cleavage, it is to be expected that only part of the surface fractured in the Auger spectrograph will reveal a true intergranular failure.

Auger spectra of a freshly fractured surface of IN-718-STDA (specimen code 64XX) is shown in Fig. 27. By comparing peak to peak heights of each of the elements to known standards, it can be shown that the amount of Nb and Ti in Fig. 27 is twice of that in the bulk alloy. Furthermore, the Nb + Ti can account for the total amount of C shown, if an MC combination is considered (where M is Nb + Ti). Figure 28a shows a carbon scan taken of the area covered by the spectra shown in Fig. 27. Note the large patches of carbon, which extend over 15-20 grain

lengths. (Compare to the SEM micrograph in Fig. 28b, which was taken from a fractured tensile specimen). The largest carbide particles observed were never more than a fraction of a grain diameter (see for example, Fig. 14). We, therefore, conclude that the bright patches in Fig. 28a indicate a continuous film or a chain of very fine carbides lying on grain surfaces. Figure 29 shows another area on the same fractured surface, at twice the magnification as Fig. 28. Note the direct correspondence among the C, Nb and Ti scans and the reverse correspondence with the Mo and Cr scans. This confirms again a carbide film or a dense agglomeration of small particles of the MC type carbides. Mo and Cr do not participate in these carbides.[8] Oxide formation can be ruled out as the Auger spectra, Fig. 27, do not show O (which should show at 505-510 ev).

Finally, it is interesting to note that we could not fracture in the Auger spectrograph a specimen prepared from Udimet-718 alloy in the STDA condition. The specimen simply bent on repeated impact. This should be compared with IN-718 that fractured on the first impact.

7.3.3 Summary

1) The microstructured characteristics of Udimet-718 vs Inconel-718, where specimens were prepared from large hot-worked billets (over 10" diameter), indicate a possible significant difference in their mechanical behavior.

2) Relatively low ductility in IN-718 alloy is attributed to thin carbide films or an agglomeration of very small carbide particles within the grain boundaries.

3) In U-718 the dominant phase near or in the grain boundary is γ'' (Ni_3Nb).

4) The matrix in 718 alloys is strengthened by a combination of $\gamma' + \gamma''$ precipitates which form networks of small cells with dislocations generated during hot rolling. These networks seem to be stable through the standard solutioning-aging treatments.

5) Ghost boundaries found in IN-718 are due to MC carbide and δ chains which precipitated in grain boundaries at the early stages of working. New boundaries formed by recrystallization during hot working caused the residual precipitates to appear as ghost boundaries. Most, but not all of these precipitates can be dissolved during solution annealing above 2000°F (probably δ only).

6) 718 alloys in the STDA condition fail in tension by intergranular cracking. Small amounts of deformation occurs within the grain, near the grain boundary, but is limited by carbide concentration.

7.4 Inconel-718 Weldments

Figure 30 is a representative light micrograph of a failed weld specimen. All tensile specimens but one, shown in Fig. 31, failed by fractures within the fusion zone. Specimen 6513, tested at 4.2 K failed in the base metal, exhibiting the characteristic intergranular mode of fracture (Fig. 31). The corresponding SEM micrograph of the fracture surfaces are shown in Figs. 32 and 33. Note again the intergranular character of the fracture within the base metal (Fig. 33) and the large number of carbides that cover the fracture surface (Fig. 33c), and in the boundaries, (arrows in Fig. 33b). The SEM micrographs of the fracture surface of the fusion zone (Fig. 32) reveal a morphology which may be interpreted as a dimpled structure. However, it is more likely that the cell walls, which appear brighter in the micrographs (large arrows, Fig. 32c) are actually a less conducting film which covers the entire fracture surface as seen in Fig. 32a. The cellular film appearance is more pronounced on the fracture surface of tensile-notched specimens where the notch was machined in the center of the fusion zone, Fig. 34 (arrows). The large particles, marked A, were identified as (Ti, Nb)C by energy dispersive X-ray analysis. Energy dispersive X-ray scan of the area shown in Fig. 34c reveals twice as much Nb (Fig. 35) as compared to the bulk composition (see Fig. 15c).

Auger spectra of a freshly fractured fusion zone is shown in Fig. 36 where carbon and oxygen appear strong. Figure 37 reveals the nature of the cellular structure referred to above. There is a direct correspondence between the C and O, which seem to cover a large portion of the surface scanned and appear to form a cellular structure, very much like that seen in Figs. 32 and 34.

The light micrographs in Figs. 38 and 39 confirm that fracture of HAZ-notch-tensile specimens (group 662X) has indeed occurred within the heat-affected-zone. As in the case of the base metal, the fracture mode is entirely intergranular. The scanning micrographs, Figs. 40 and 41 confirm the intergranular mode of fracture. However, the occurrence of occasional cleavage can be seen in Fig. 40d. Also note large, fractured carbides in Fig. 41d. A comparison of Figs. 40 and 41 with Figs. 26 and 27, which show the fractured surface of the base metal, indicate a more severe breakdown of granular interfaces. This is evidenced by the deep holes (pulled grains) in Figs. 40c and 41b (marked G) and the long deep crack in Fig. 40d.

7.4.1 Summary

1) GTA welded tensile specimens failed in the fusion zone (save for one specimen that failed in the base metal). The tensile data in Table 6 shows only minute decreases in the yield strength of welded specimens, as compared to base metal. This indicates no change in the basic strength of the material which is derived from $\gamma' + \gamma''$ precipitation hardening and Mo solution strengthening. However, the ultimate strength of the weld is lower by about 10%; and more significantly, elongation is reduced by 80% (1.8% for welded specimens as compared to 10.1% for base metal).

It is significant that the ductility of the weld is very low, but also of significance is the fact that the base metal IN-718 exhibits limited ductility as well.

We conclude that the microstructural data presented in Sections 7.3 and 7.4 show that the most probable source of the low ductility are the grain boundary carbides.

The situation is aggrevated more in the case of the welded specimens where cellular carbide films dominate the fracture surface.

It is conceivable that a thermo-mechanical working schedule of the welds can alleviate the problem by breaking down the continuous carbide chains. Lowering the carbon content of the alloy may also contribute to an increase in the ductility.

2) The heat affected zone strength lies between the base metal and the weld. Since all specimens were resolutioned and aged after welding, and for lack of electron transmission microscopy to examine γ' and γ'' distribution, we assume that the ductility of the heat affected zone is impared due to additional carbide conglomeration during welding. These carbides will not dissolve during the standard heat treatment.

3) The strength of the weld and the heat affected zone may be improved by a mechanical working schedule. However, since this may not be feasible in practical applications, higher solutioning temperature may be explored as a partial cure. One has to be aware that higher solutioning may result in adverse grain growth.

7.5 Inconel 706 Alloys

7.5.1 Base Metal

Two Inconel 706 materials were examined, i.e., vacuum induction melted + vacuum arc remelted (VIM-VAR) and VIM + electroflux remelt - VIM-EFR. As the discussion proceeds, it will be shown that there are no significant differences in the microstructural characteristics of the two materials. This is also born by the mechanical test data (Table 6) which show virtually identical results.

The effect of heat treatment on grain morphology is shown in Fig. 42. A 2100°F (1422 K) solution-anneal results in a relatively uniform, very large grain size of the order 2 mm. Solution anneal at 1800°F followed by standard double age results in a recrystallized structure, with grain size of the order of 60 μm for the VIM-EFR material, and somewhat larger grain size, of the order of 100 μm for

the VIM-VAR material. The scanning electron micrographs in Fig. 43 show a relatively "clean" microstructure with only occasional MC ((Nb, Ti)C) carbides.

Typical transmission electron microscopy data are summarized in Figs. 44 through 46. A few dislocation pile-ups, Figs. 44a and c, very clean grain boundaries, Figs. 44b, and a diffraction pattern showing only the f.c.c. structure, is typical of IN-706 material solutioned at 2100°F (1244 K). This is true for both VIM-EFR (Fig. 44) and VIM-VAR materials (Fig. 45). The standard heat treatment, which employs a lower (1800°F) solutioning temperature does not result in a complete annealing of dislocations, introduced during hot working. The micrographs in Fig. 46, which are typical of both VIM-VAR and VIM-EFR materials show dense networks of dislocations and γ' (Ni_3, Al, Ti) + γ'' (Ni_3Nb) (γ'' is also referred to as BCT-Ni_3Nb) and virtually precipitation free grain boundaries. Occasional discrete carbide particles have been seen in the boundaries (Fig. 46b).

The fracture characteristics of tensile specimens are illustrated in Figs. 47 through 51. Although final failure occurred by intergranular fracture, the cross sections of Fig. 47 show that a substantial amount of deformation has taken place prior to failure. The data in Table 6 indicate about 30% uniform elongation. The scanning electron micrographs in Fig. 48 show a dimpled structure (Fig. 48b, c) with cracking along grain boundaries containing concentrations of carbides (Fig. 48a, d). The same general features are depicted by the scanning electron micrographs of Fig. 49 which were taken on the fracture surface of notch-tensile specimens tested at 4.2 K. Figure 50 shows Auger scans of a fracture surface of IN-706, STDA (Specimen 71XX). Note that carbon covers a large portion of the surface. Some of the particles appear richer in Nb, other particles are richer in Ti. Neither of the Nb or Ti rich areas contain Cr, which is otherwise distributed over the entire surface.

7.5.2 Weld Specimens

Typical longitudinal sections of a welded IN-706 tensile specimens are shown in Fig. 51. All tensile specimens broke in the fusion zone (Fig. 51a) and in most specimens, both tensile and notch-tensile, cracks and voids such as shown in Fig. 51b were present in the fusion zone. The voids and cracks in the fusion zone are demonstrated further in the SEM micrographs of Fig. 52 (arrows) which were taken from a tensile notch specimen (7211) tested at room temperature.

Fracture mode of the fusion zone is illustrated in the SEM micrographs of Fig. 53. A small amount of ductility is associated with fracture surface as evidenced by the shallow dimples. One can also observe many particles and bright films associated with the crests of the dimples, Fig. 53c. The fracture proceeds by shear-cleavage steps seen in Fig. 53a, and at higher magnifications, Point B, Fig. 53c. Energy dispersive X-ray analyses of the inclusion in Fig. 53b and various points in Fig. 53c are shown in Fig. 54. The inclusion, only occasionally observed, is probably a low melting aluminum silicate. The particles, like A and C, Fig. 53c contain Nb, Ti and are either carbides or δ phase. It is interesting to note that the shear surface, spot B shows lower Fe/Ni ratios and higher Cr/Ni ratios that expected from the bulk composition (Table 3). The bulk composition calls for about equal amounts of Fe and Ni and a ratio of Cr/Ni of about 1/3. Similar results were obtained by Auger analysis of a fusion zone fracture, Fig. 55. The surface composition calculated from the values of peak-to-peak heights of each element with reference to standard yield, in atomic percent: Nb-5.7, C-8.7, Ti-3.2, Cr-23.1, Fe-20.8 and Ni-38.5. It is interesting to note that the total Nb + Ti can be associated with C by (Nb, Ti)C. This will indicate MC carbides as the dominant feature on the fracture surface.

7.5.3 Summary

1) Alloy 706 base metal has adequate ductility and toughness due to the lack of grain boundary carbide films.

2) Carbide films form in the weld fusion zone thus drastically reducing the ductility and toughness of the weld.

3) Welded tensile specimens failed in the fusion zone. Cracks and cavities were also found frequently in the fusion zone.

7.6 Inconel-LEA

During the period of this report, the investigation of the LEA material was confined to the examination of failed tensile, and notch-tensile specimens. Two typical longitudinal sections are shown in Fig. 56. The mode of failure is a mixture of intergranular and cross-granular fracture. Partial cracking along grain boundaries can be observed below the fracture surface. The horizontal lines in Fig. 56b are due to bend contours left over from the rolling operation (Section 3). The light micrographs do not reveal particular precipitates or foreign inclusions. Low magnification SEM micrographs, Figs. 57a and 57b confirm the combined mode of intergranular and cross-granular deformation mode. The grain surfaces are covered with dimples, indicating some ductility prior to failure. Higher magnification SEM micrographs, Fig. 57c and d show, however, that ductile deformation (elongation) was probably limited (shallow dimples). Furthermore, there is a high concentration of cleaved, plate-like particles in every dimple. These platelets, marked 1, have been analyzed by dispersive X-ray and are probably (Nb, Ti)C, MC type carbides. This is shown in Fig. 58a. The matrix, such as points 2 in Fig. 57, are analyzed in Fig. 58b and show the bulk composition of the alloy, i.e., Fe-Ni matrix with small amounts of Al, Nb and Ti.

The low ductility nature of the LEA material, Table 6 can thus be related directly to a high concentration of plate-like MC type carbides that confine the deformation within the interlacing matrix and fail by brittle cleavage.

7.7 Discussion - Alloys 718, 706, LEA

Alloys 718, 706 and LEA belong to the Class II nickel-iron Nb containing superalloys.[7] These materials derive their primary strengthening from a combination of γ' (f.c.c. (Ni_3Al, Ti)) and γ' (BCT Ni_3Nb) precipitation within the grain. In the case of alloy 718, additional strengthening is provided by solution hardening through the addition of Mo. Coherent γ' and γ'' precipitates have been identified in solution and aged INCO-718 and 706, see Figs. 19, 46. A significant feature shown in these micrographs are the particle-dislocation networks that account for a stable precipitation and high strength. We have previously shown[2] that such dislocation-γ' networks account for the increase strength in alloy X-750.

Other common phases in this class of alloys[7,8] are η(hcp Ni_3Ti) and δ (orthorombic Ni_3Nb). These phases usually appear after prolonged exposure to temperature and result from transformation, respectively, of γ' and γ''. The extensive data shown above do not indicate massive η or δ phases. However, a more rigorous X-ray diffraction analysis of non-soluble residues is planned to define all phases present. It is conceivable that the interlacing-chain structure observed in as-received INCO-718 (Fig. 14) may contain δ particles, which are known to form during processing.[7] The solvus temperature for δ in alloy 718 is slightly above 1800°F.[6] It is thus possible that the decrease in the volume of particles following the solution treatments above 1950°F (Figs. 16, 17) and the stability of the "ghost" structure after the standard heat treatment (SA at 1800°F) is related to the resolution of the δ particles.

The most prevalent phase, identified in all our specimens are MC carbides. The data show that the particles precipitating within the grain are Nb rich (Nb, Ti)C carbides, while the precipitation within the grain boundary may include Si as a substitution for Ti (for example, particle B, Fig. 14). The adverse effect of the MC carbides is aggrevated by the fact that their solvus temperature is near the melting point of the alloys. Thus, one cannot remove these carbides by heat treatment alone. This requires a carefully planned sequence of thermal mechanical working,

which will result in breaking up the carbides, particularly the continuous chains and films in the grain boundaries.

The adverse effect of the grain boundary carbides is demonstrated by the mechanical test results of alloy IN-718 and the fusion zone weld specimens of all three alloys. The existence of these chains and films is clearly demonstrated by the many micrographs shown above.

There are not too many variations in the yield strength among the three alloys. Generally, the STDA IN-718 shows yield strength of about 10% higher than the corresponding heat treated 706 and LEA. Our conclusion is, therefore, that the intrinsic strength is derived from $\gamma' + \gamma''$ precipitation hardening, with a small increment in strength added to IN-718 by solution hardening through Mo additions. The temperature dependence of strength reflects, also, the effect of γ'. Generally, the f.c.c. matrix does not display a strong temperature component. In all three alloys there is about 20,000 psi increase in yield strength from RT to 4.2 K which we attribute to the increased resistance of γ'-dislocation network to dislocation cutting.[9]

The differences among the three alloys are manifested in their ultimate strength, ductility and fracture toughness, which are all related properties. The low ductility and fracture toughness in IN-718 and the essential lack of elongation in the LEA material is attributed to grain boundary carbide chains and films. Conversely, the high ductility of the 706 alloy is attributed to the lack of carbides in the grain boundaries (see for example, Figs. 44-46). The effect of carbides is manifested clearly in the properties of the weld specimens. In both the IN-718 and IN-706 weldments, failure occurred in the fusion zone accompanied by a drastic reduction in ductility. This is contrasted by the fact that the yield strengths of all welded specimens were very close to the strengths of the corresponding base metals.

The standard heat treatment following welding resulted in precipitation hardened structures similar to the base metal. However,

uncontrolled carbide precipitation that occurred during cool down after welding resulted in a structure that cannot be modified by heat treatment alone, and is detrimental to the mechanical strength of the alloys.

There is, usually, a direct correlation between ductility (total elongation) and fracture toughness. The data in Table 6 show the highest K_{IC} for 706 alloy, and half of that for the 718 alloy. Also, K_{IC} for the welds deteriorates sharply. The temperature dependence of K_{IC} also parallels that of elongation, where both parameters show an increasing trend with lower temperature. This effect is related to increased work hardening of the matrix with lower temperature.

The improvement of K_{IC} with increased work hardening has been discussed by Laird[10] and has been shown to explain the improved properties of alloy X-750.[2] The increase in elongation is related to work hardening by delaying the setting of instability.

The sharp decrease in K_{IC} of the weld is also related to the microstructure. Continuous film of carbide provide an easy path for crack propagation, which also accounts for the relatively low K_{IC} of base metal IN-718.

Alloy LEA provides an interesting apparent anomaly. Whereas the elongation recorded is as low as welded IN-718 and IN-706, it shows higher fracture toughness than the welded specimens of alloy 718 and 706. The micrographs in Fig. 57 may provide the clue. Although the fracture surface shows many cleaved carbides, there is indication of deformation in the matrix surrounding them. The matrix is the continuous path across the specimen and thus interrupts the motion of crack through the carbides during K_{IC} testing. Elongation, however, is related to the total gauge length. Thus, though local deformation may be high, it is confined to the matrix surrounding the carbides and thus will be recorded as a low value on the overall gauge length.

In conclusion: we have shown that in both base metal and welded specimens adequate strength is derived from the aging cycle via the precipitation hardening effect. The most detrimental phase to these alloys

are the MC carbides which precipitate as grain boundary films in IN-718 and in all welded specimens. A thermo-mechanical schedule may improve materials properties. Conversely, limiting carbide formation by chemistry modifications, i.e., lowering the carbon content or the Nb level, or limiting carbide formation by controlled cooling during welding should be explored as means to optimize performance of these alloys.

7.8 References

1. Materials Research for Superconducting Machinery III, NBS-ARPA Semi-Annual Report, April 1975, Section V.
2. Ram Kossowsky, "Microstructure of Inconel X-750 Materials for Cryogenic Structural Applications", ICMC, Kingston, Canada, July 1975.
3. R. F. Decker, in Symposium, Steel Strengthening Mechanisms, Zurich, 1969.
4. P. S. Kotral, Trans. TMS-AIME, 242 (1968), p. 1764.
5. E. L. Raymons, Trans. TMS-AIME, 239 (1967), p. 1415.
6. D. R. Muzyka, Met. Eng. Q. 11 (1971), p. 12.
7. D. R. Muzyka, in "The Superalloys", Sims and Hagel, Edts., John Wiley & Sons, NY, 1972, p. 133.
8. R. F. Decker and C. T. Sims, Ibid, p. 52.
9. N. S. Stoloff, Ibid, p. 79.
10. C. Laird, in "Fatigue at Elevated Temperatures", STP 520, ASTM 1972.

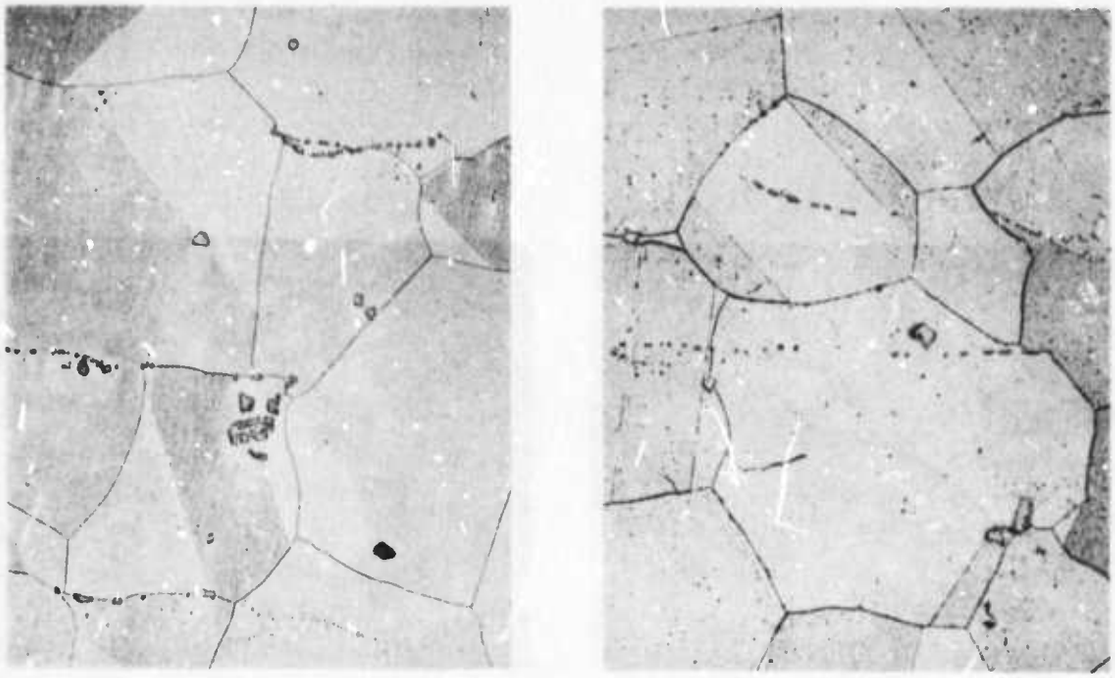

(a) (b)

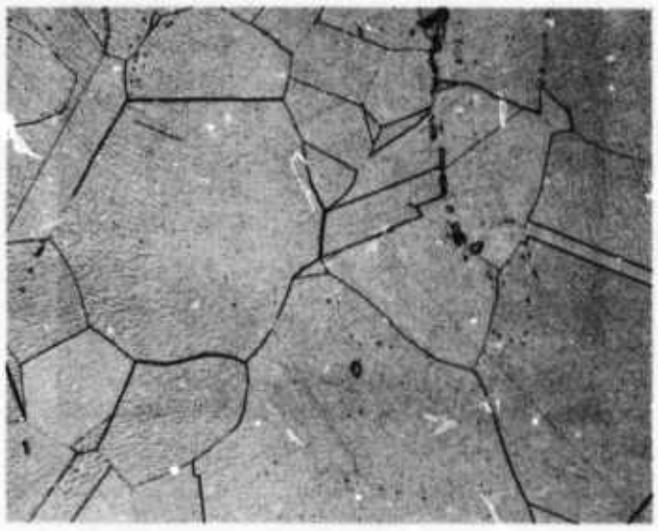

(c)

Fig. 1—Light micrographs of specimens from alloy X-750, MP-1 treated at various conditions (a) S. A at 2100°F (1422°K) followed by standard aging. (b) S. A at 2100°F (1422°K) followed by aging 2 hrs. at 1500°F (843°C) and 2 hrs. at 1300°F. (c) S. A at 2100°F, (1422°K) 2 hrs. 200X

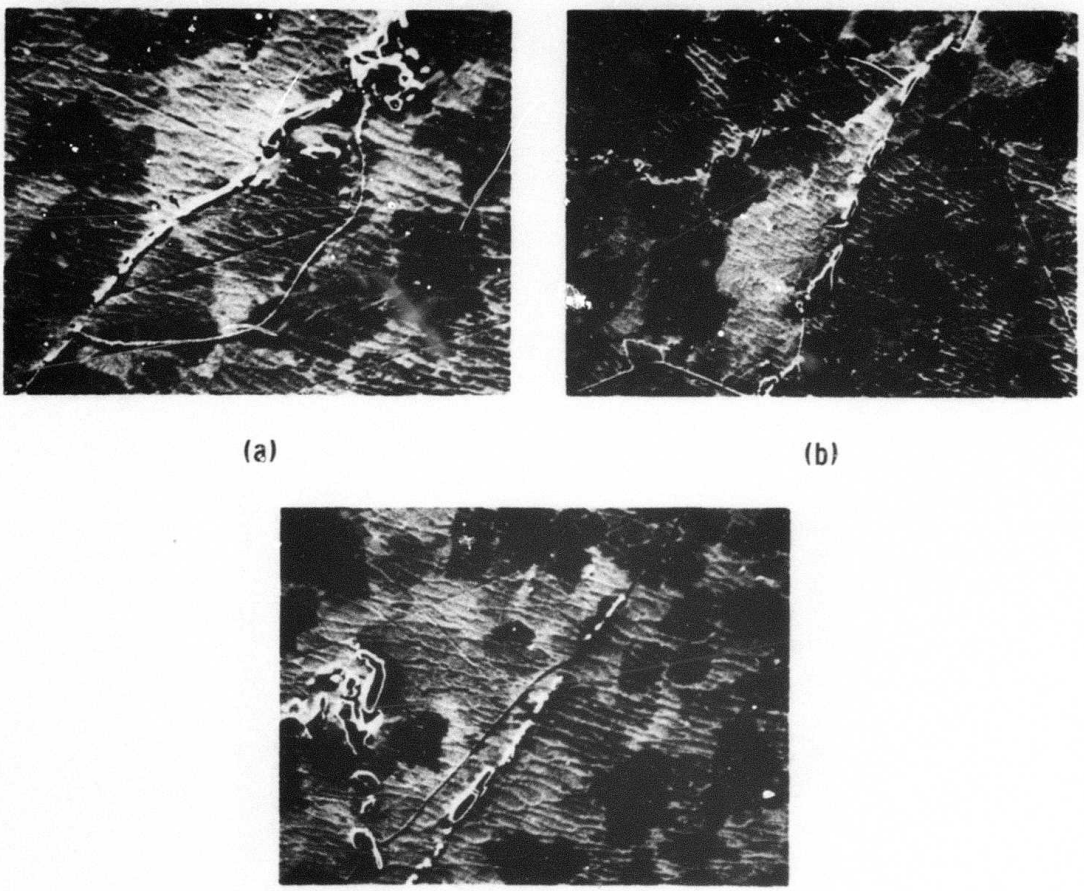

(a) (b)

(c)

Fig. 2—Scanning electron micrographs showing grain boundary carbides in X-750 S.A for 2 hrs. at 2100°F (1422°K) (a) 1225X (b) 650X (c) 600X

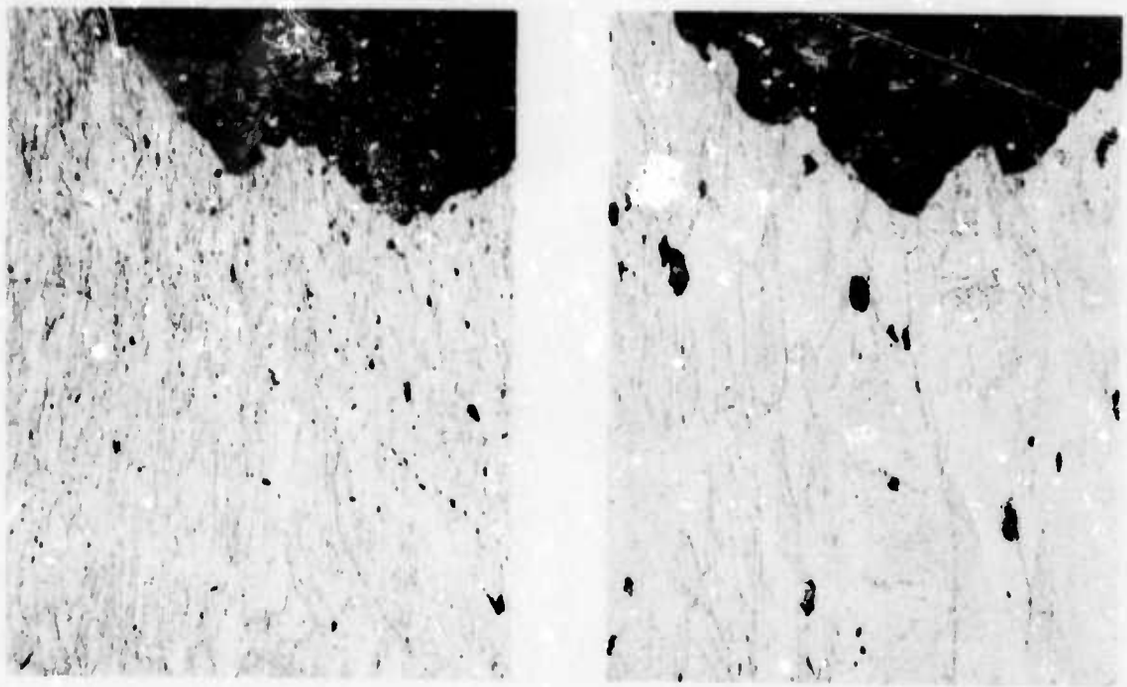

(a) (b)

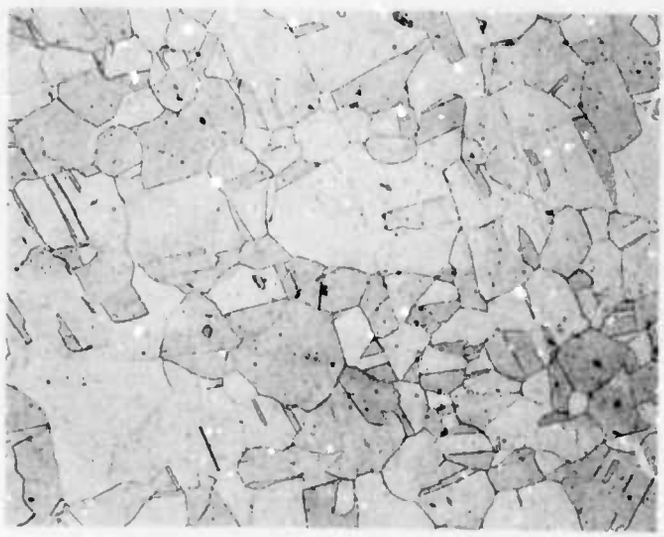

(c)

Fig. 3—PD-135 Cu tensils specimen 1512 tested at 77°K (a) longitudinal section 50X (b) same, 200x (c) cross section

(a)

(b)

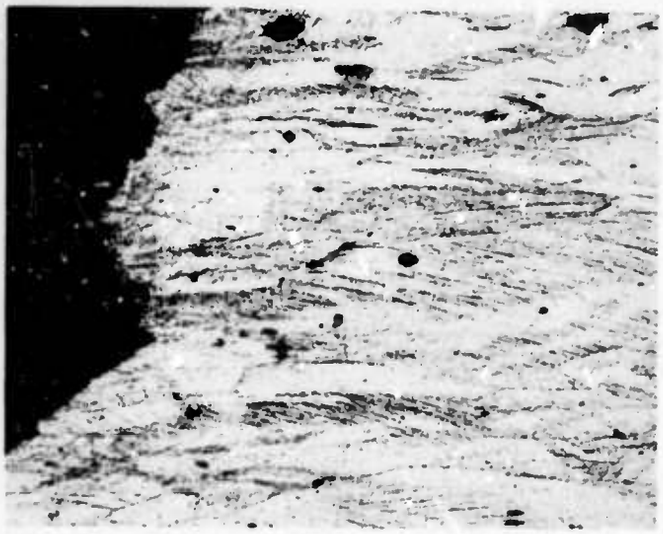

(c)

Fig. 4—PD-135 Cu tensile specimen 1513, tested at 4.2°K (a) longitudinal section in gauge section 1 cm from fracture 100X (b) cross section 100X (c) fracture end 200X

(a)

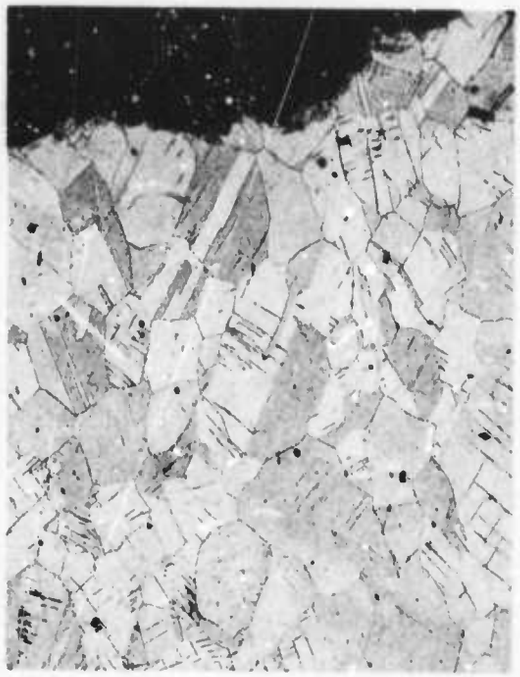

(b)

(c)

Fig. 5—PD-135 Cu longitudinal section of notched-tensile specimens (a) tested at 4.2°K, specimen 1523 50X (b) same 200X (c) tested at 77°K, specimen 1522, 200X

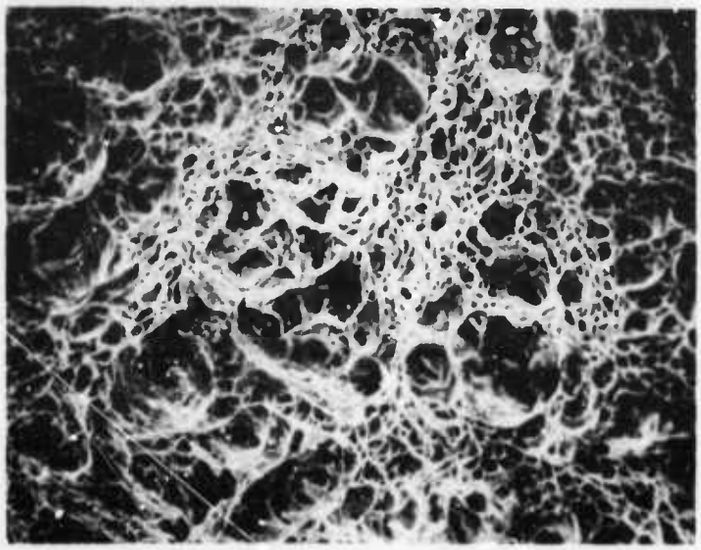

(a)

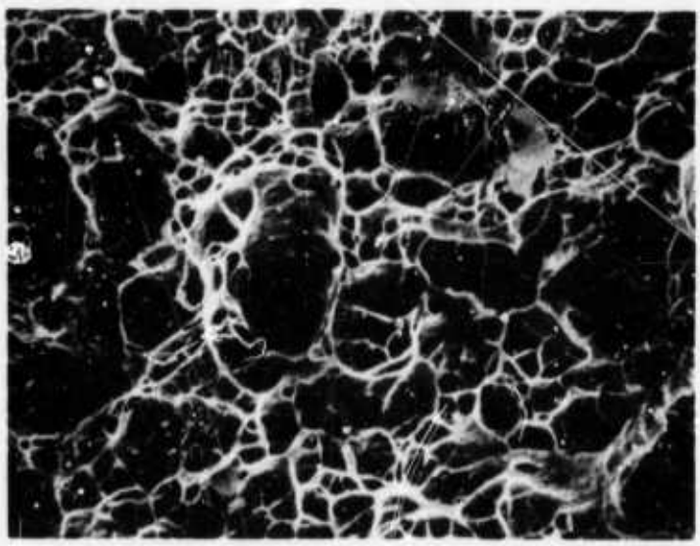

(b)

Fig. 6—SEM micrographs showing typical dimpled fracture surfaces. PD-135 cu, tested at 4.2°K, specimen 1523 (a) 700X (b) 1400X

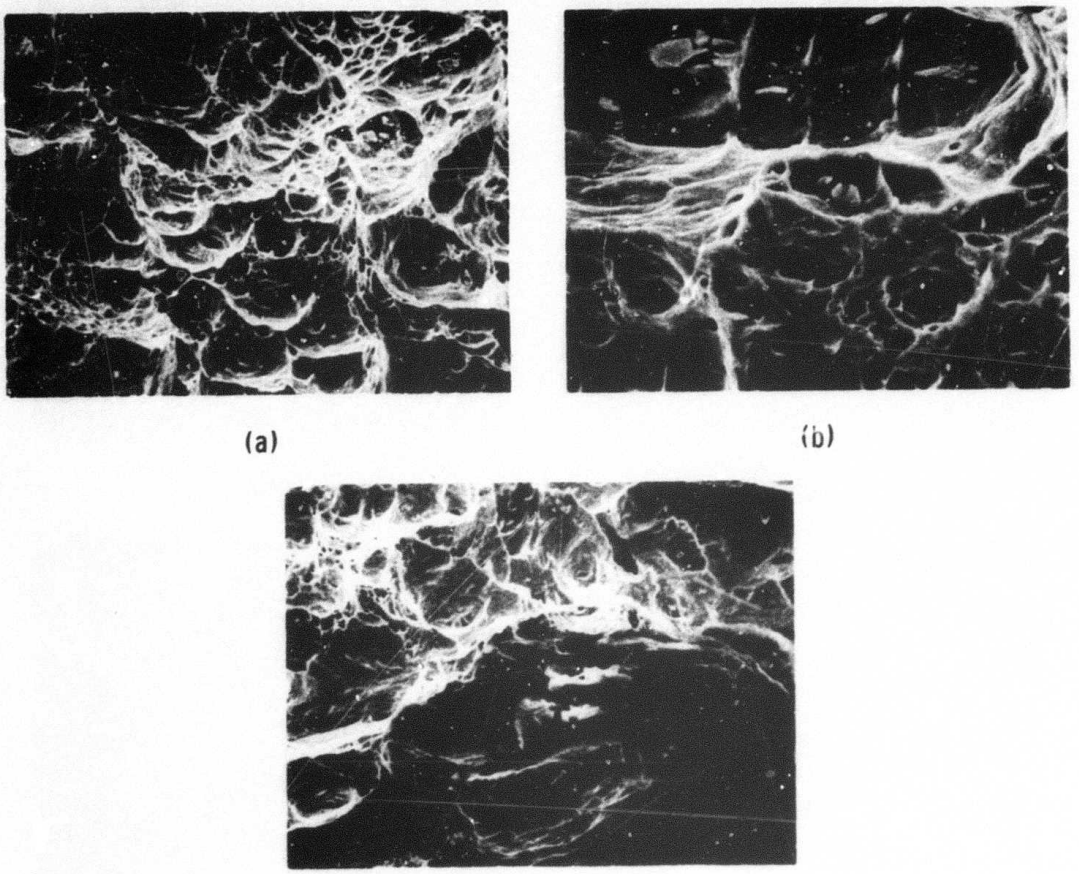

Fig. 7—SEM micrographs of fracture surfaces, notch tensile specimen (1522), PD-135 Cu (a) 675X (b) 2700X Cu-PD rich particle (P) at bottom of dimple (c) 650X Cl, K, S, Fe containing inclusion (I)

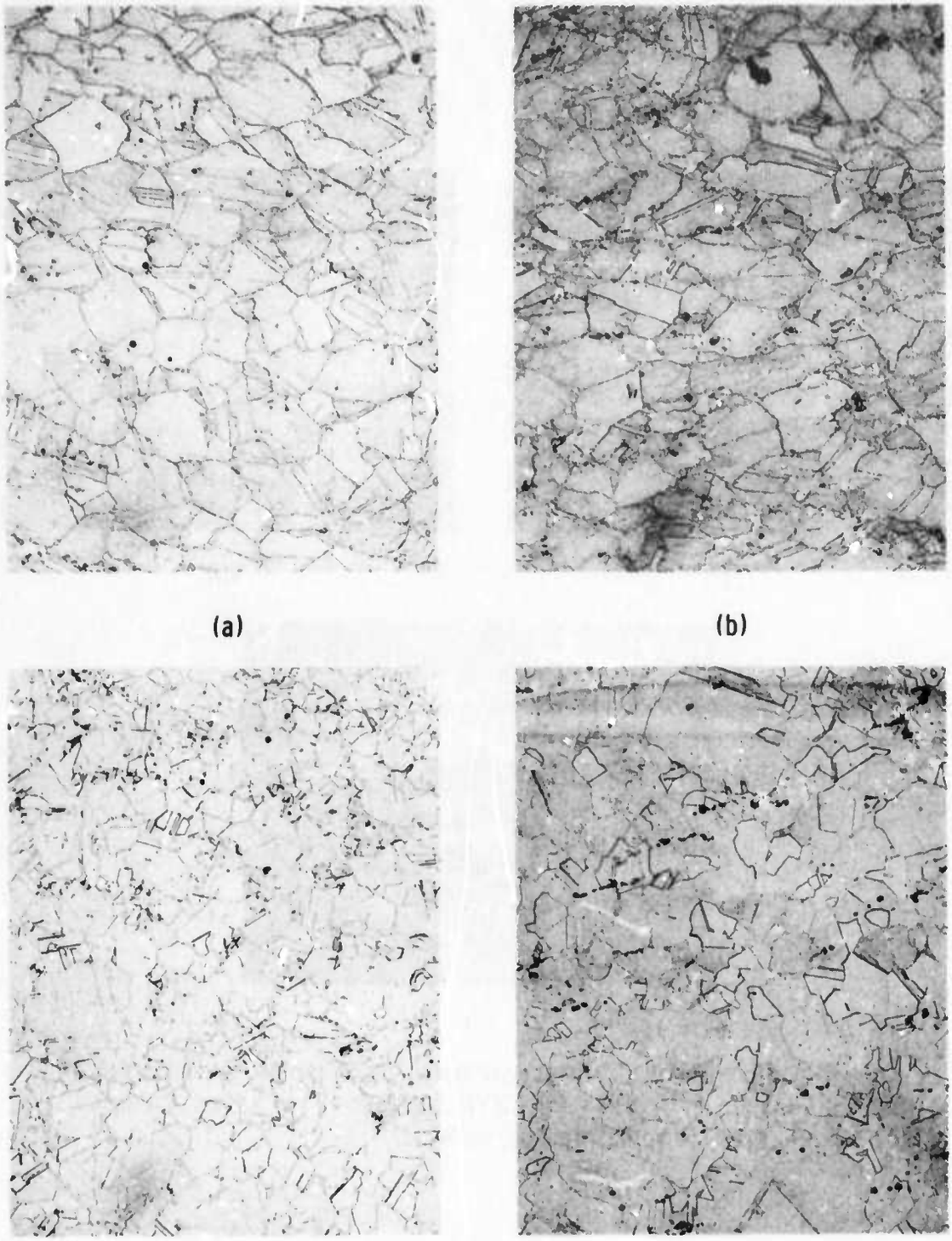

(a) (b)

(c) (d)

Fig. 8—U-718 light micrographs, 100X, top of billet (a) outer section (b) same, longitudinal cut (c) inner section (d) same, longitudinal cut

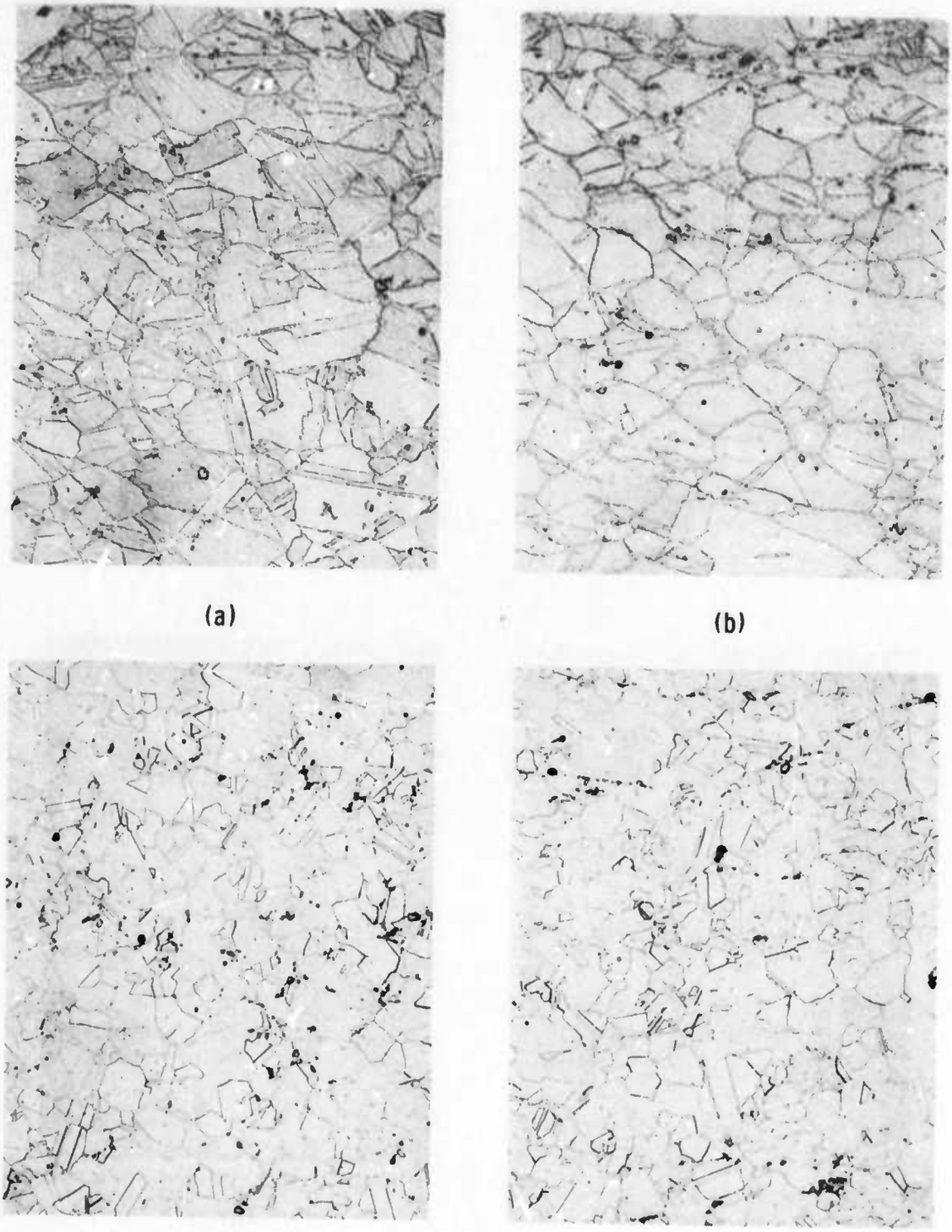

(a) (b)

(c) (d)

Fig. 9—U-718, light micrograph 100X, bottom of billet (a) outer section (b) same, longitudinal cut (c) inner section (d) same, longitudinal cut

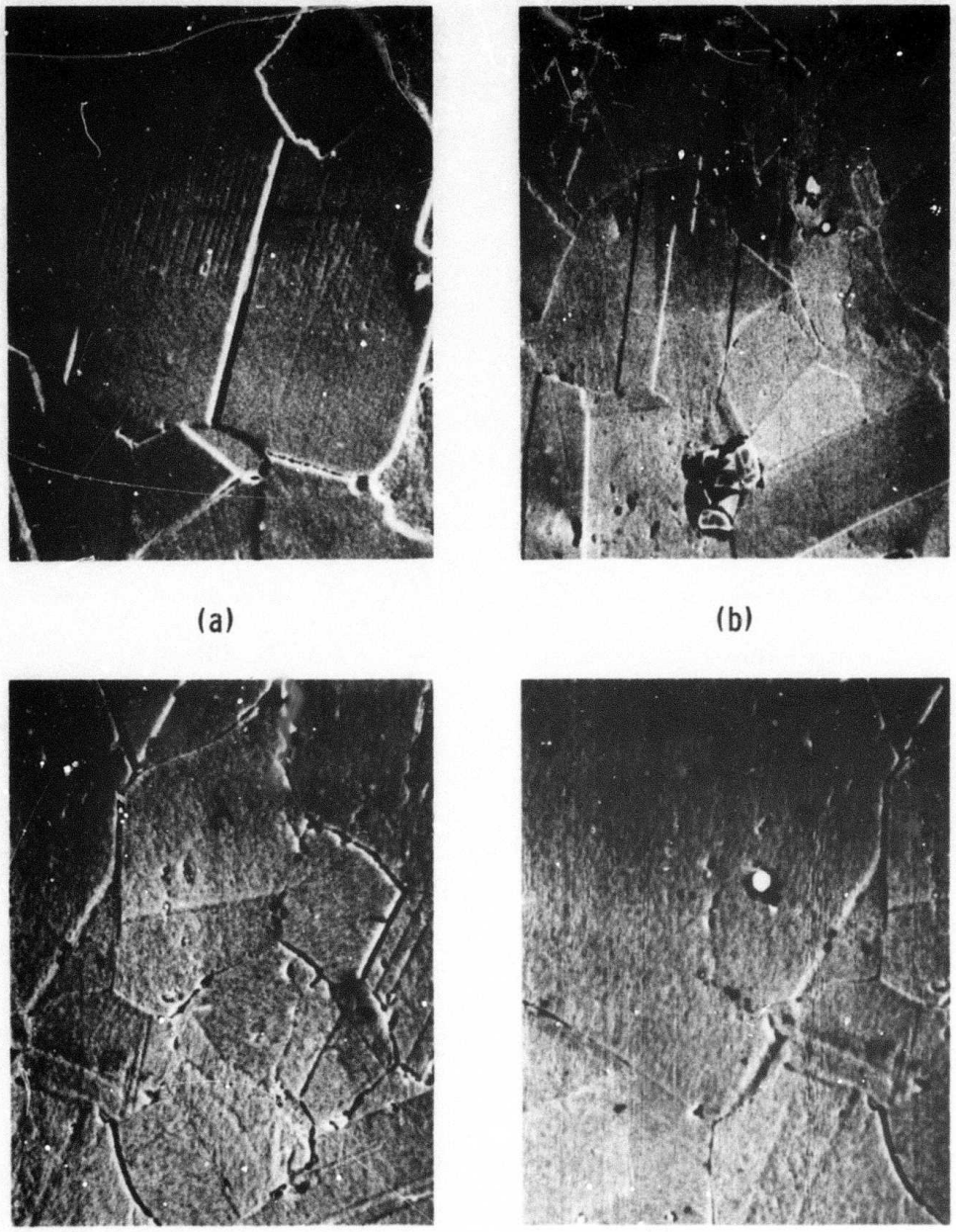

Fig. 10—U-718 SEM micrographs from various sections of the billet, as received (a) top inner section 1400X (b) bottom inner section 1200X (c) bottom outer section 2400X (d) top outer section 2400X

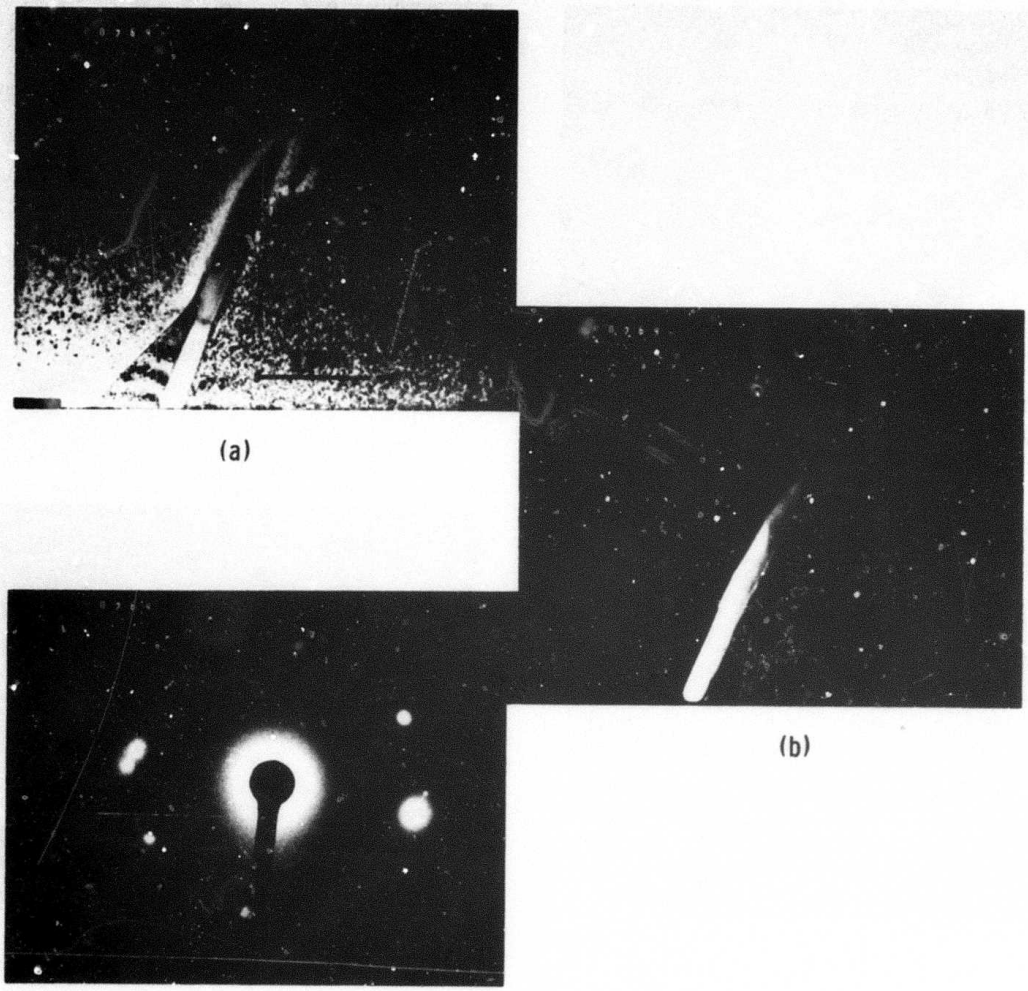

(a)

(b)

(c)

Fig. 11 – Cellular γ'' (Ni_3Nb) precipitation in U-718 S. A at 1800° F (1255° K) and double aged (a) bright field (b) dark field (c) diffraction pattern showing the dark field reflection

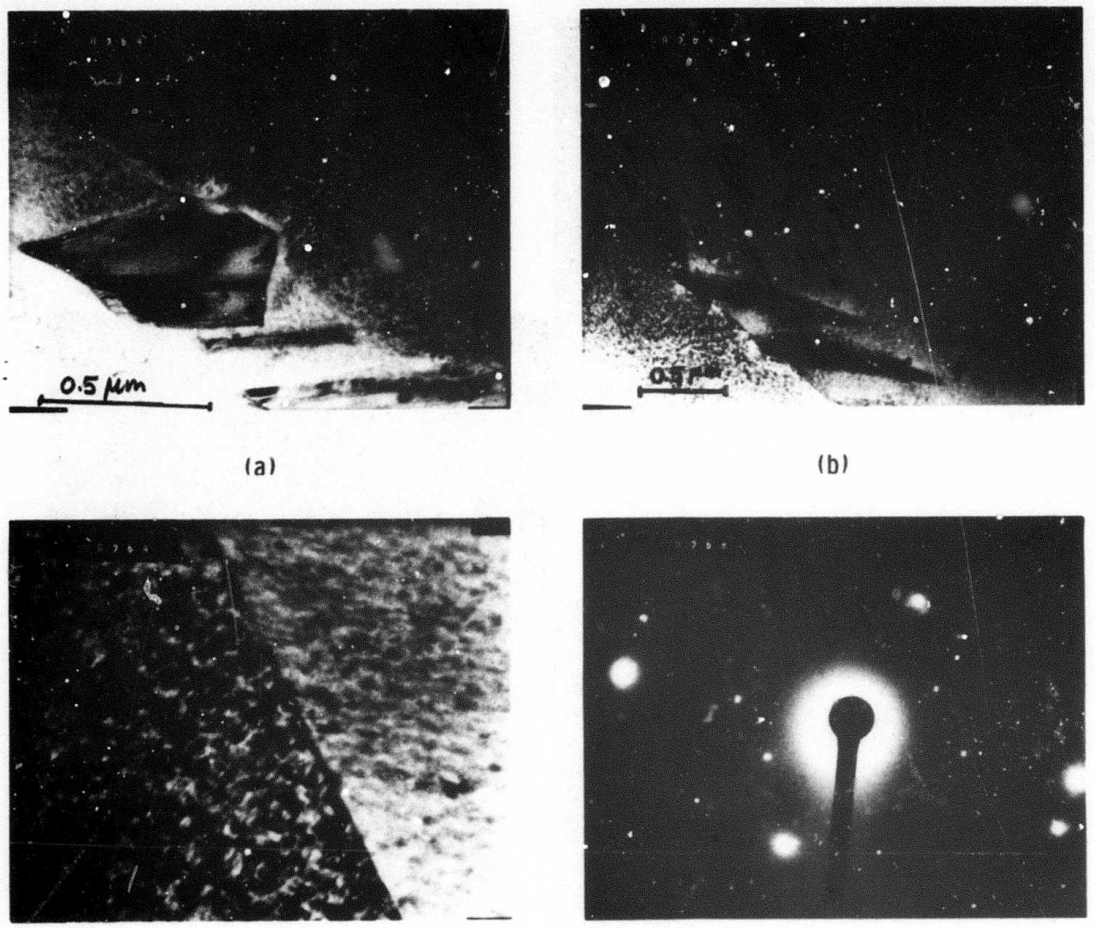

Fig. 12—U-718, STDA transmission electron micrographs (a,b) typical cellular growth of γ'' (Ni_3Nb) (c) $\gamma' + \gamma''$ precipitater in grain (d) diffraction pattern

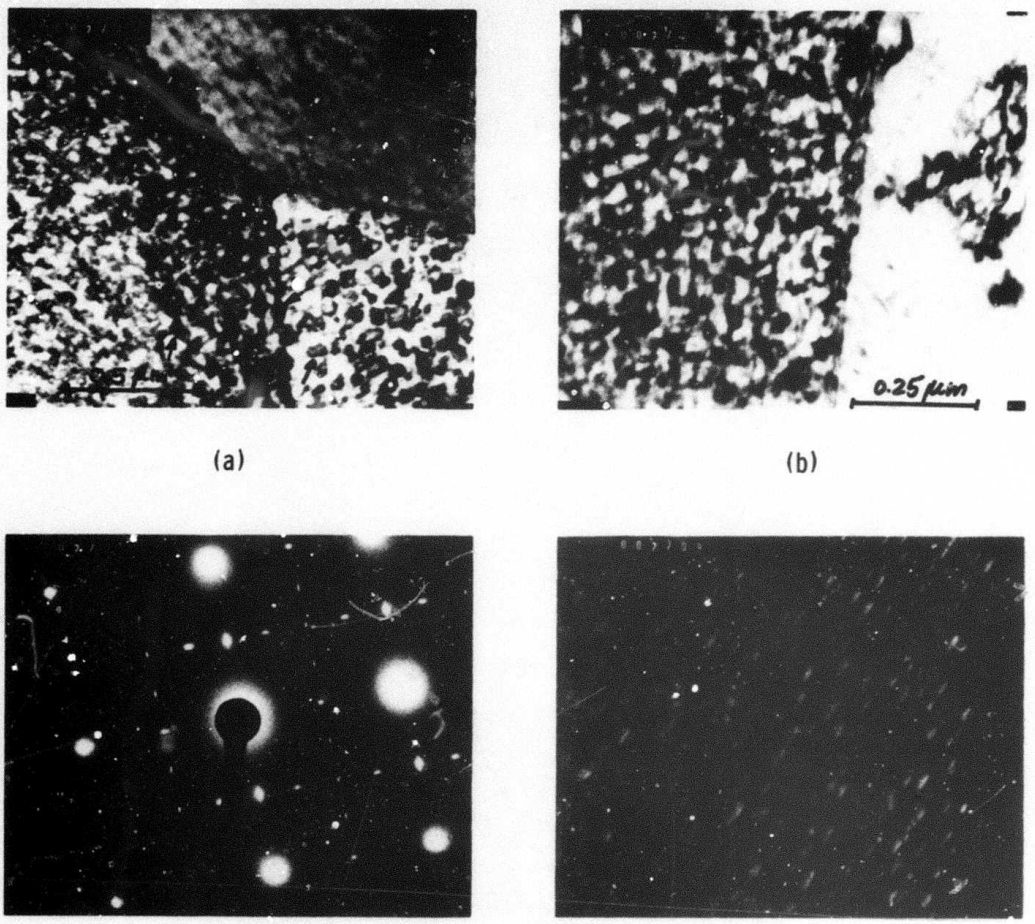

(a) (b)

(c) (d)

Fig. 13—U-718 STDA, transmission electron micrographs (a,b) particle-dislocation networks within the grain ($\gamma' + \gamma''$), grain boundaries relatively free of precipitation (c) diffraction pattern (d) dark field, (001) γ'

RM-64985

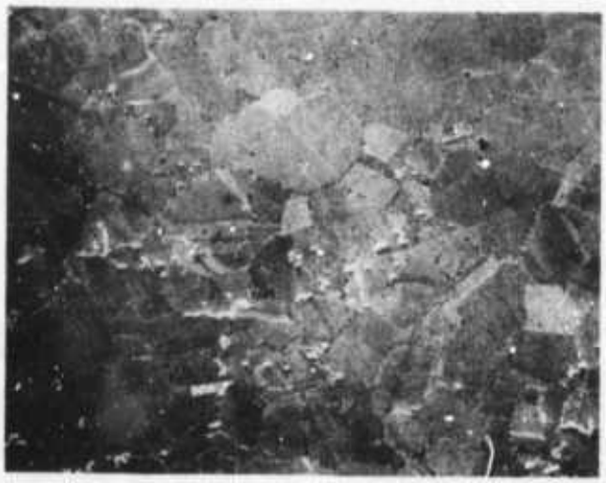

(a)

(b)

(c)

Fig. 14—I-718, as received. SEM micrographs (a) 150X (b) 300X c: 1500X. Energy dispersive X-ray analyses of points in (c) are shown in Figure 15

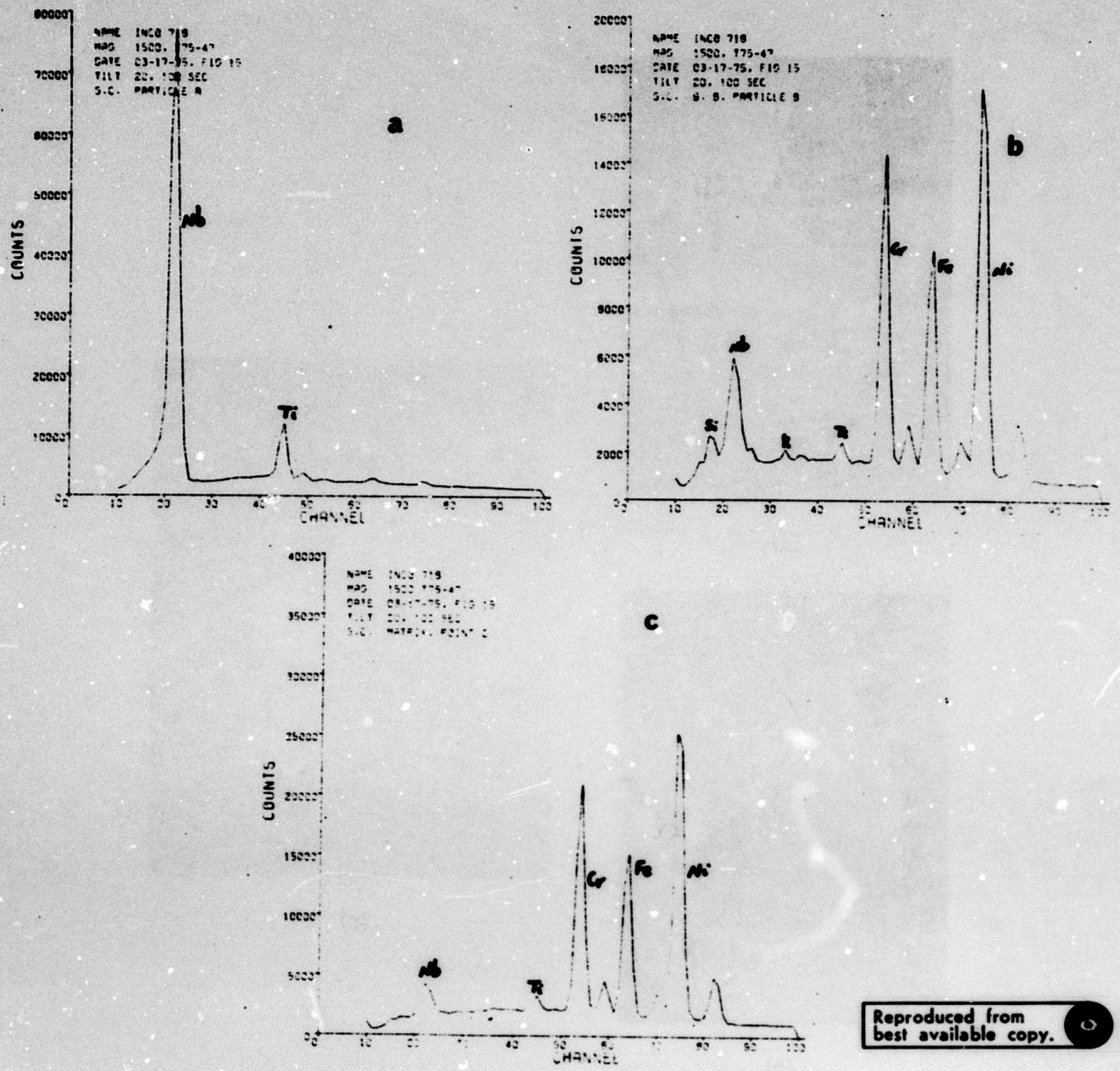

Reproduced from best available copy.

Fig. 15—Energy dispersive X-ray spectra (a) particle A, Figure 14 (b) particle B, Figure 14 (c) Matrix, point c, Figure 14

(a)

(b)

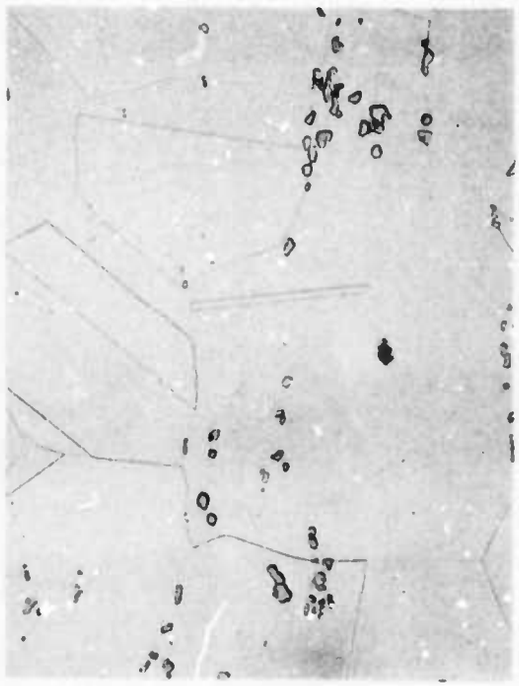

(c)

Fig. 16—Effect of solutioning at 2100° F (1422°K), I-718
(a) 250X (b) 650X (c) light micrograph, 200X

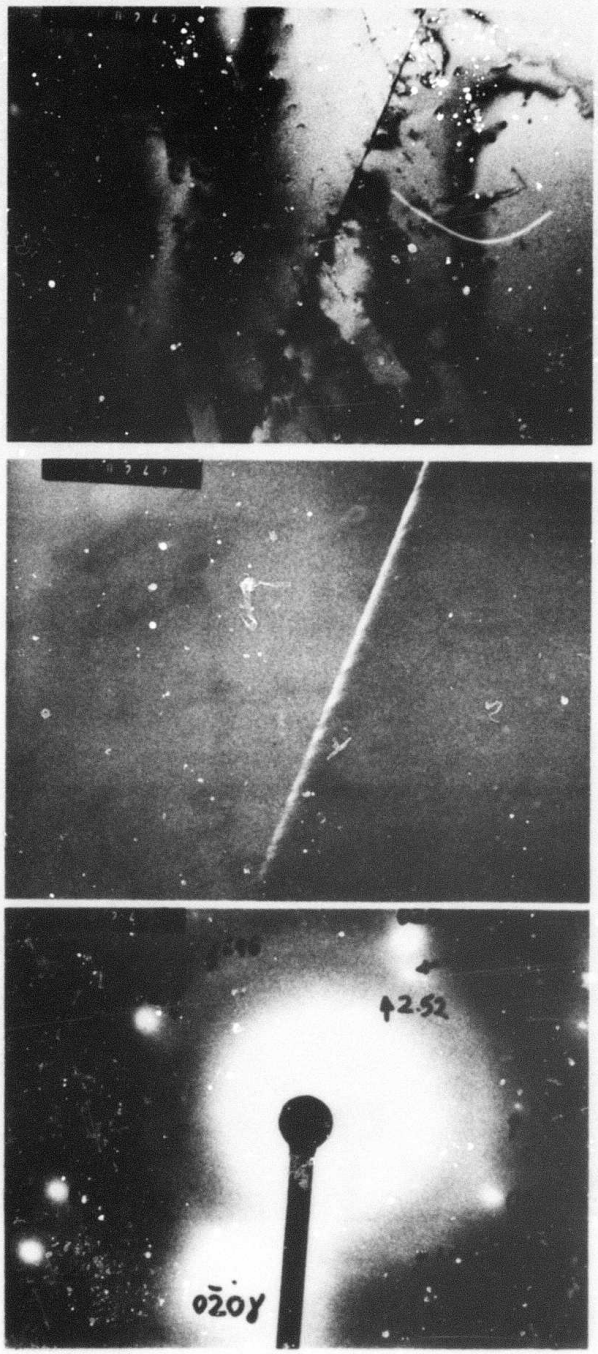

Fig. 17 – Transmission electron micrographs I-718, solution annealed at 2100°F (1422°K) showing M_6C carbide film in grain boundary

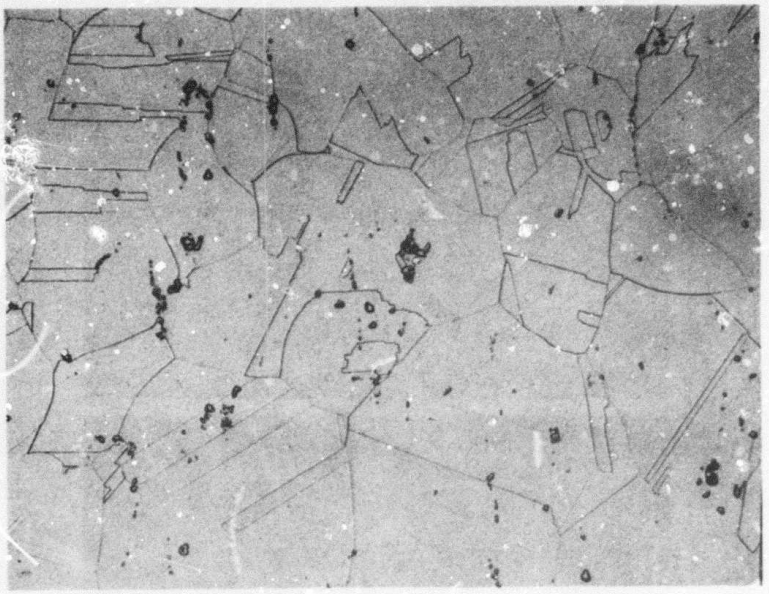

(a)

(b)

Fig. 18—Effect of solutioning at 1950°F (1339°K), I-718 (a) light micrograph 100X (b) SEM micrograph 265X

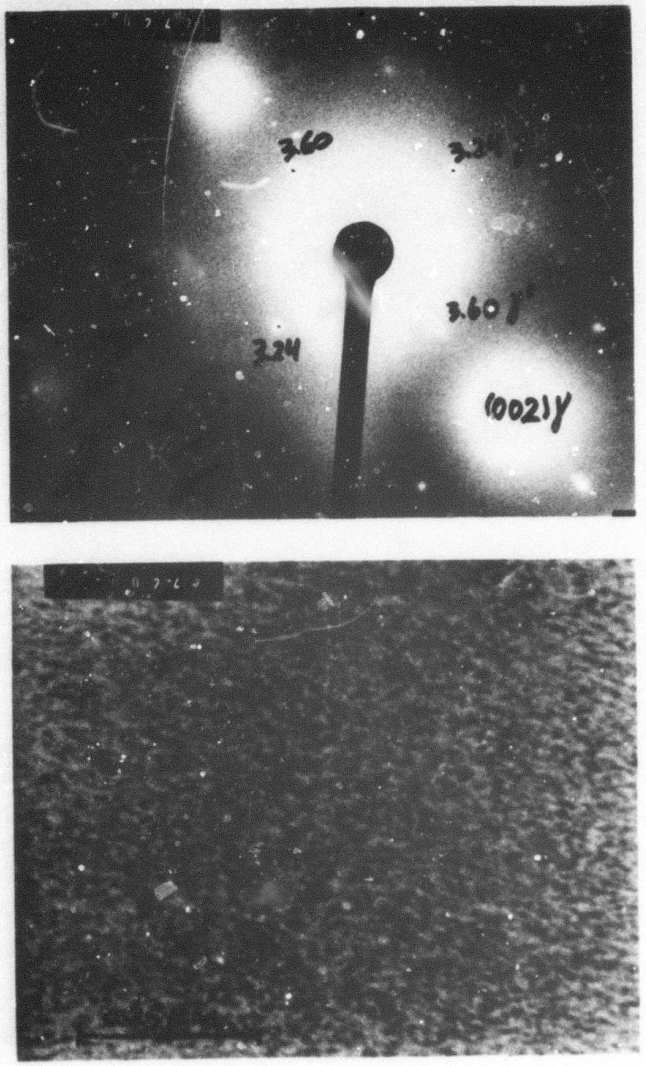

Fig. 19—Transmission electron micrograph, I-718, solution annealed at 1950°F (1339°K) Diffraction pattern identifier Ni_3; Al, Ti (γ') and Ni_3Nb (γ'')

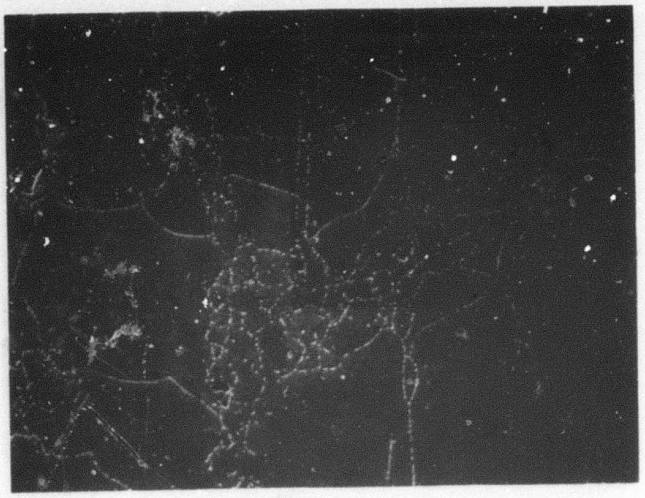

(a)

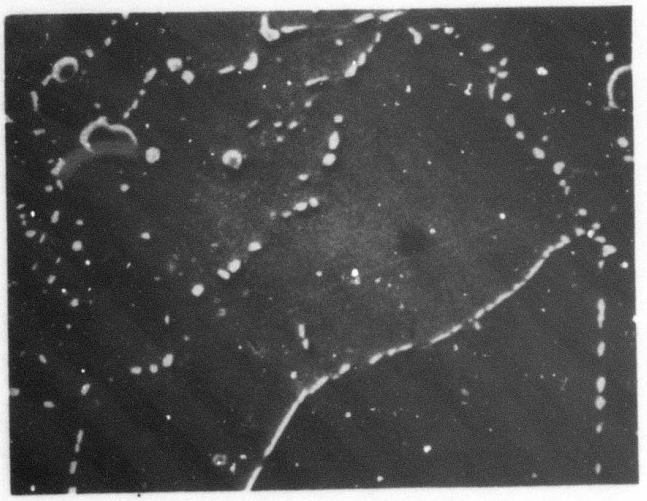

(b)

Fig. 20—"Ghost" boundaries composed of MC carbides in I-718 solution annealed at 1800°F (1255°K) (a) 315X (b) 1550X

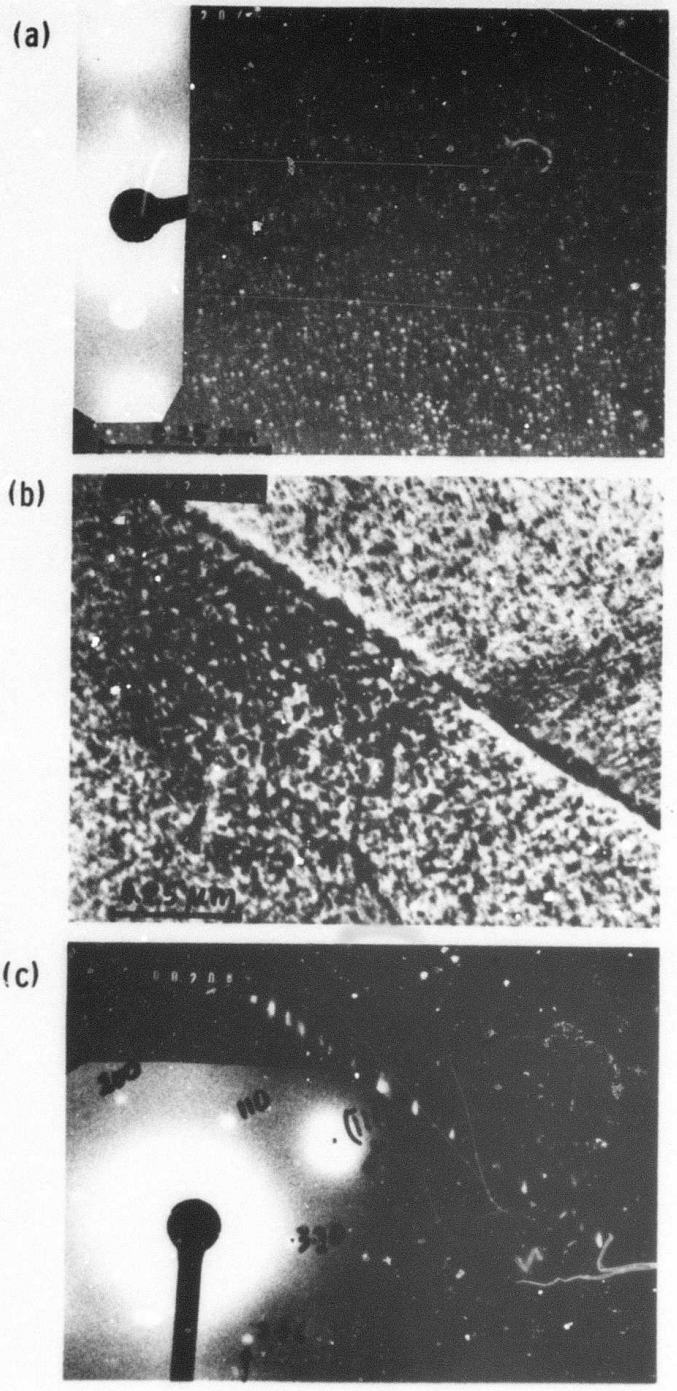

Fig. 21 — Transmission electron micrographs I-718 STDA (a) dark field (001) γ' (b) bright field (c) dark field, same as b, showing γ'' or MC carbides in grain boundaries and within the grain

(d)

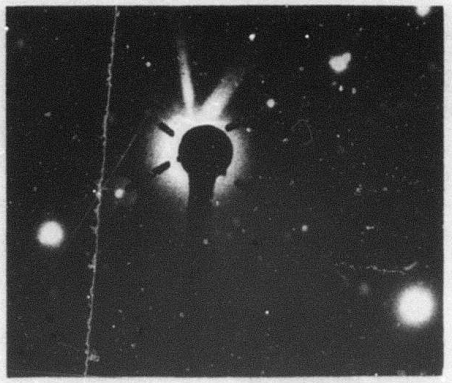

(e)

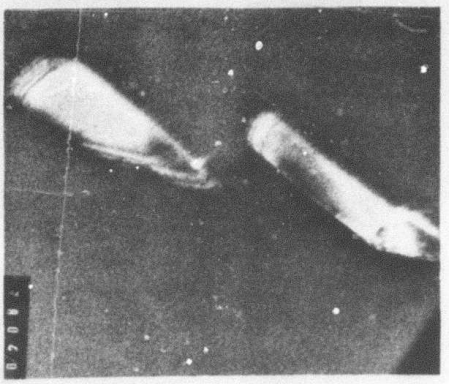

(f)

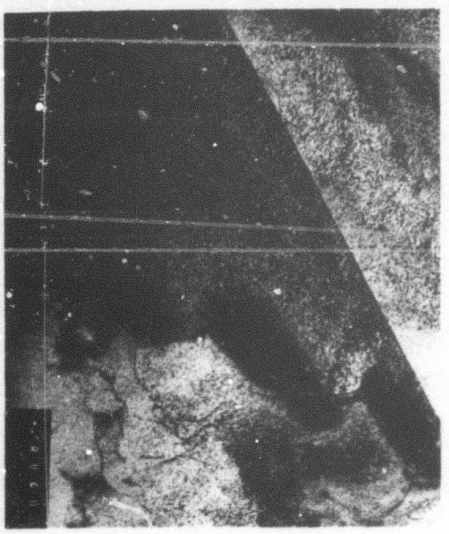

Fig. 21 – (d, e, f) diffraction pattern, dark field and bright field, showing M_6C precipitation in the grain boundary

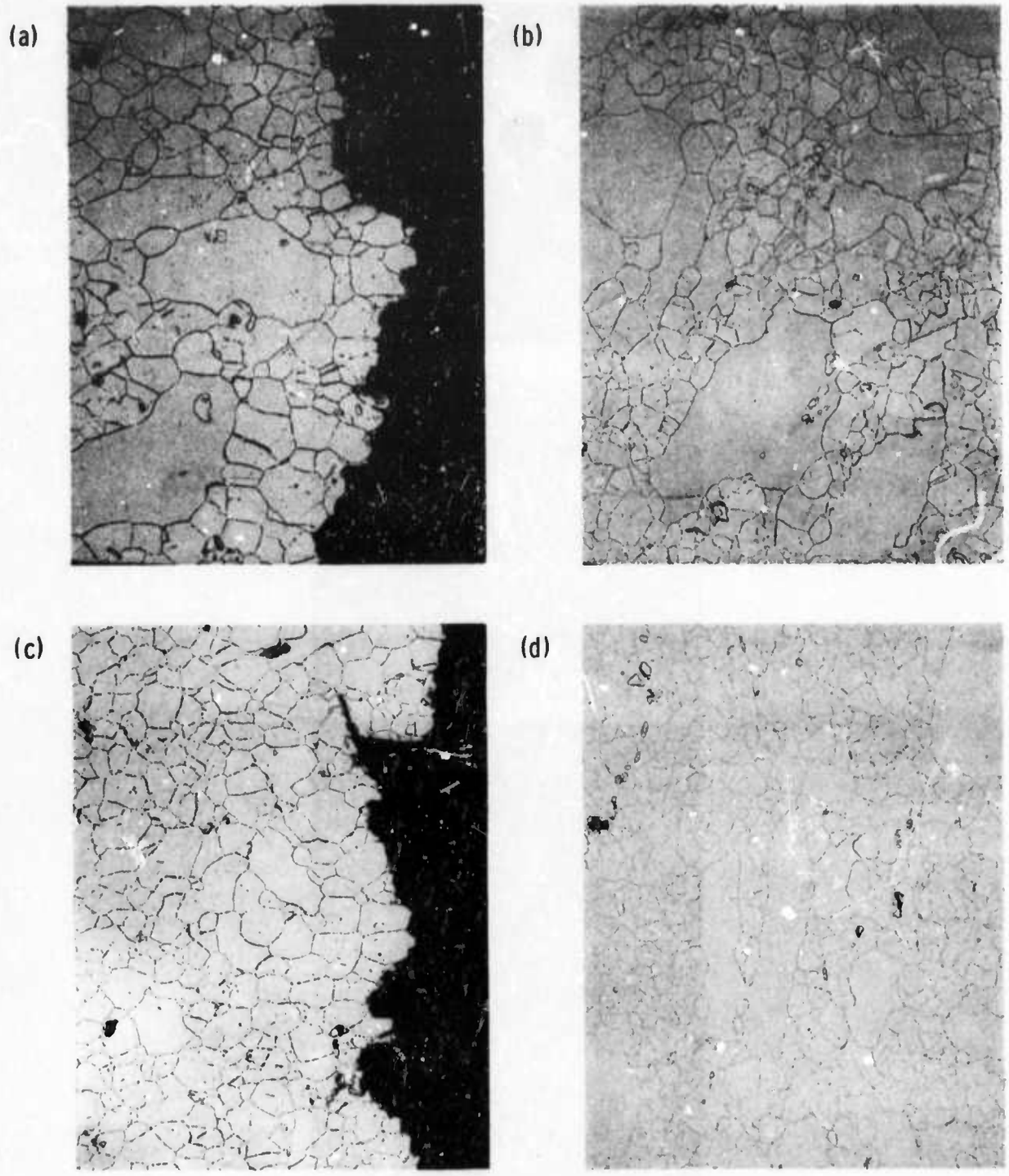

Fig. 22 – Light micrographs of fractured tensile specimen, I-718 STDA (a) longitudinal section specimen 6411 tested at RT (b) cross section, as on a (c) longitudinal section specimen 6413 tested at 4.2°K (d) cross section, as in c. 200X

(a)

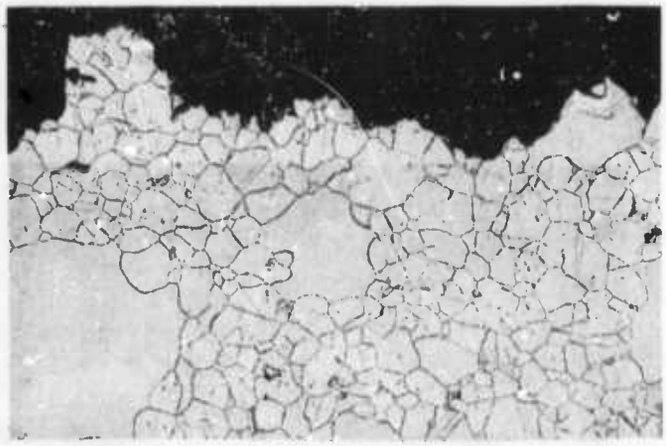

(b)

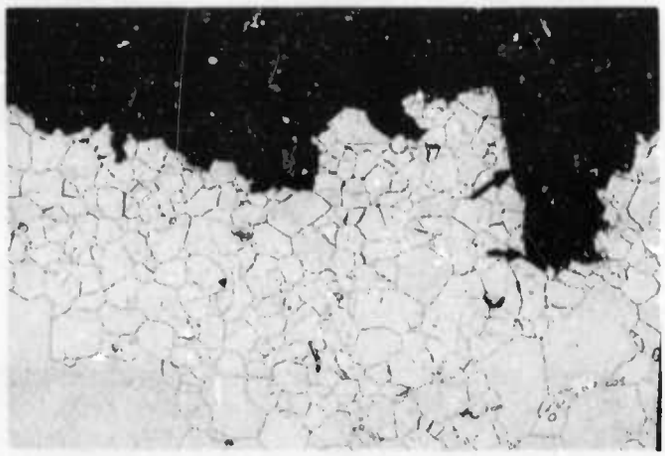

(c)

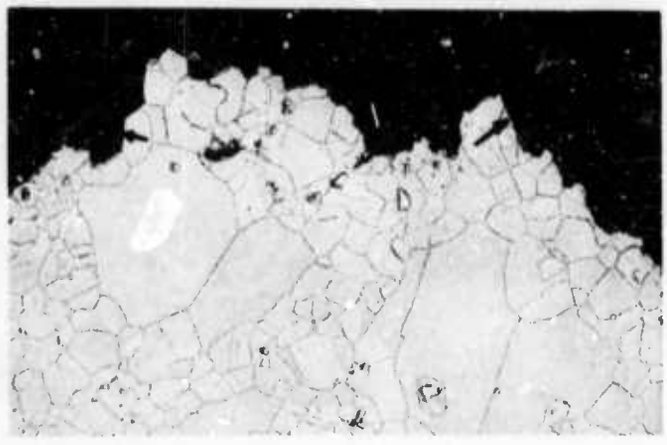

Fig. 23--Light micrographs longitudinal sections of notch-tensile specimens, I-718 STDA (a) tested at RT (6421) (b) tested at 77°K (6422) (c) tested at 4.2°K (6423) 200X arrows indicate cleavage otherwise intergranular fracture

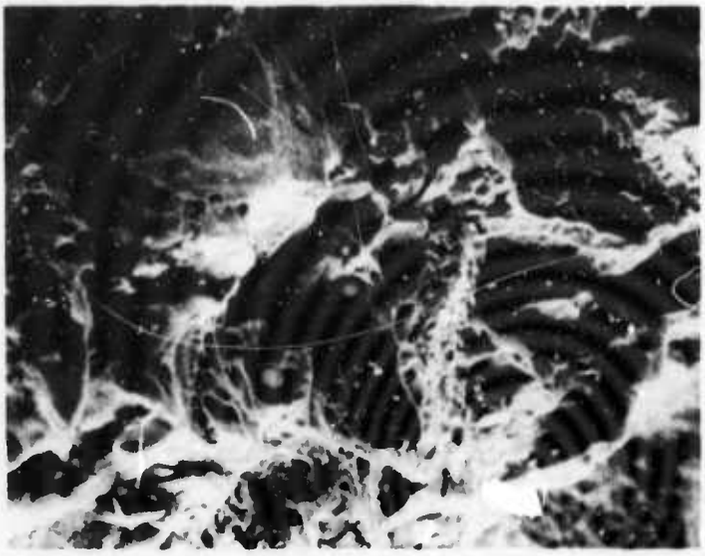

(a)

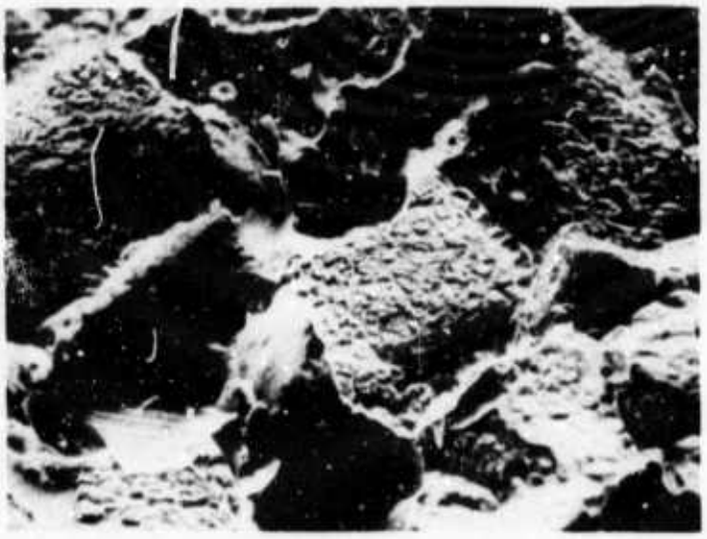

(b)

Fig. 24—SEM micrographs, fracture surfaces, I-718 STDA, tested at RT (6411), 1100X

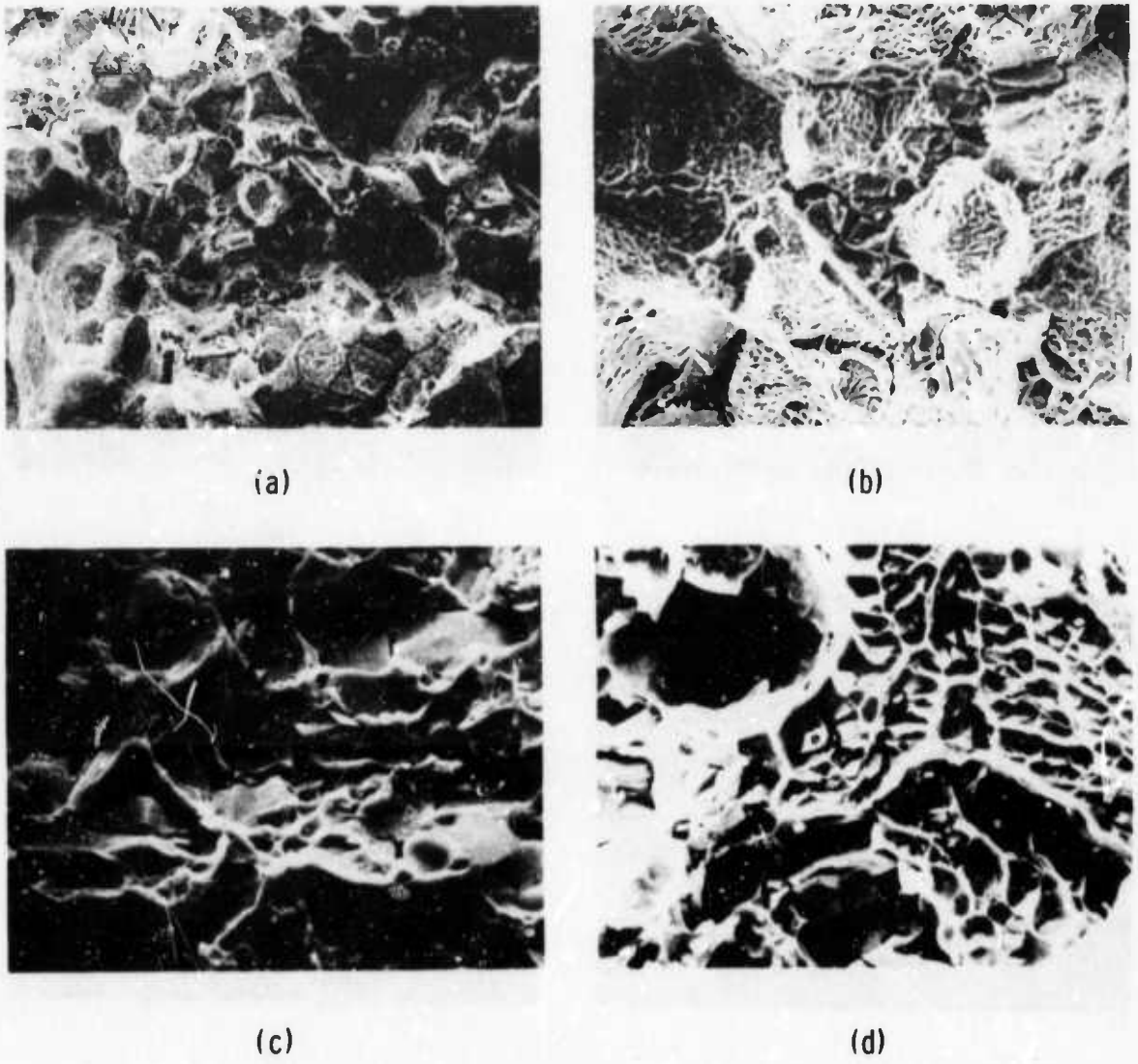

(a) (b)

(c) (d)

Fig. 25—SEM micrographs, fracture surfaces, I-718 STDA, tested at 4.2°K (6413)
(a) 300X (b) 750X (c) 2000X (d) 3000X. Surface covered with carbides

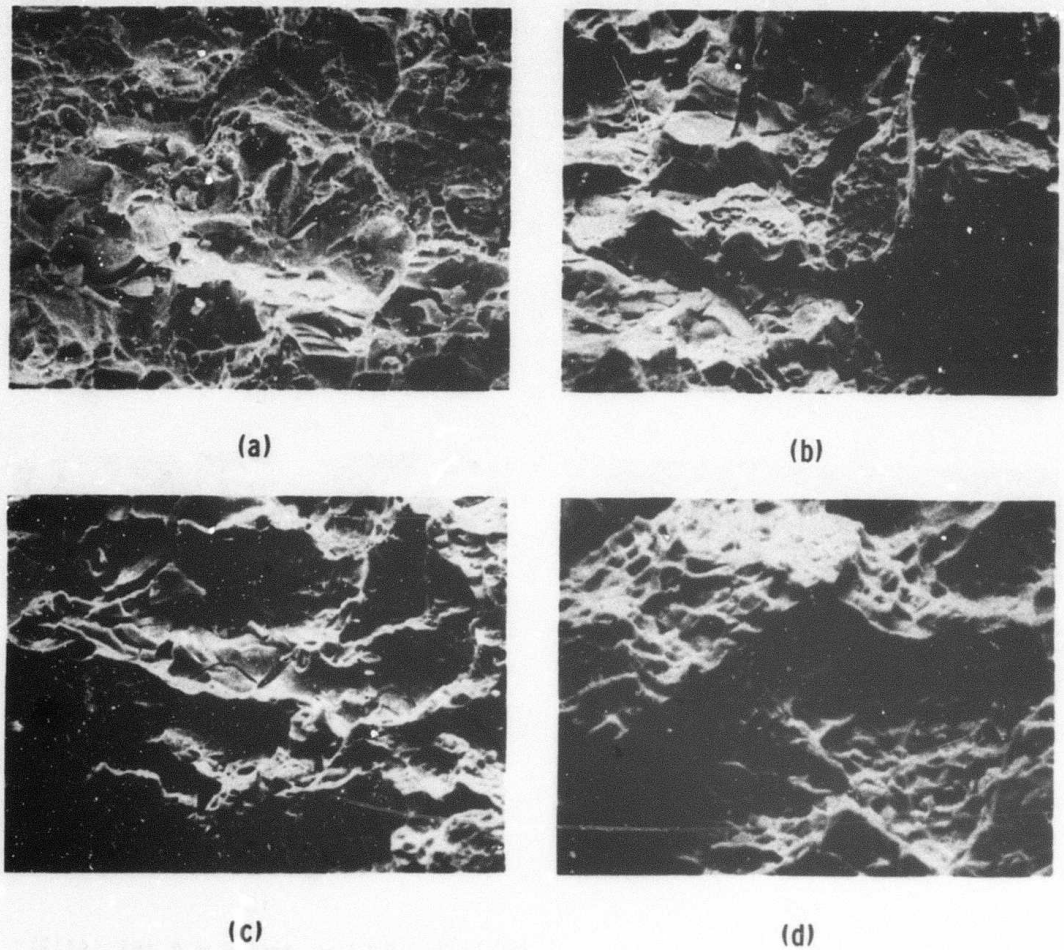

Fig. 26 — SEM micrographs, fracture surfaces, notch-tensile specimens (a, b) RT test (6421) 1100X (c) 4.2°K test (6423) 1100X (d) as in c, 2300X

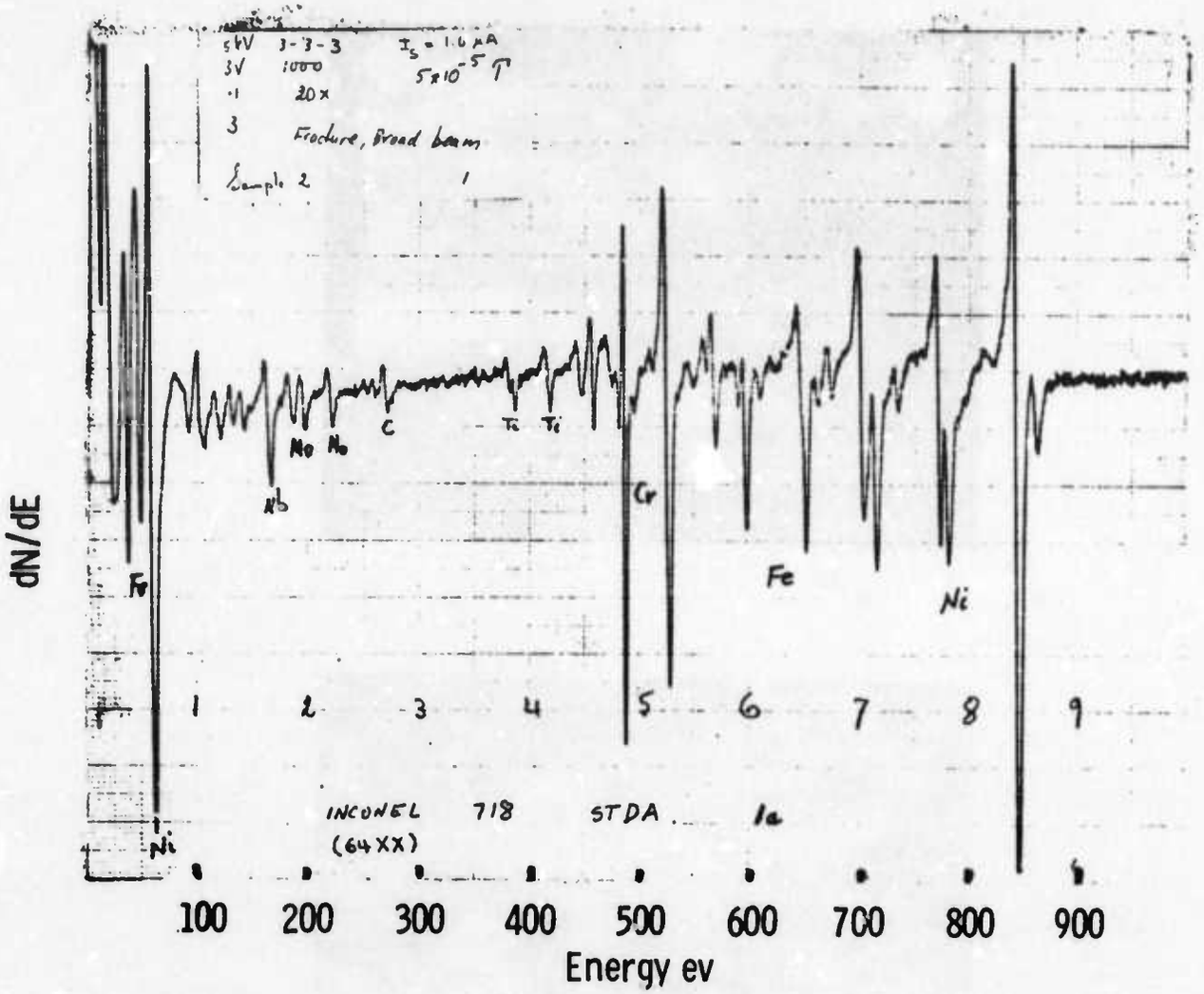

Fig. 27—Auger spectra, fresh fracture surface specimen 64XX I-718, STDA

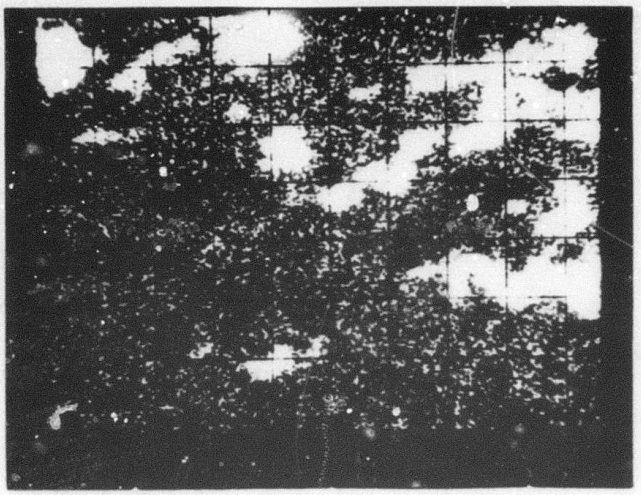

(a)

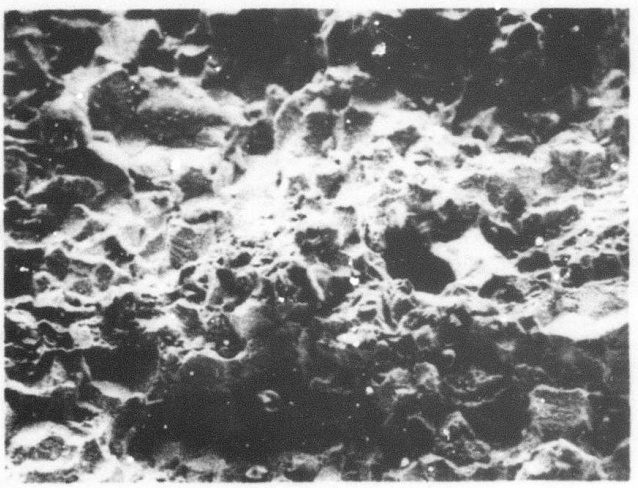

(b)

Fig. 28—I-718, STDA, fracture surfaces (a) scanning auger micrograph of carbon distribution 250X (b) SEM micrograph of typical fracture appearance 200X

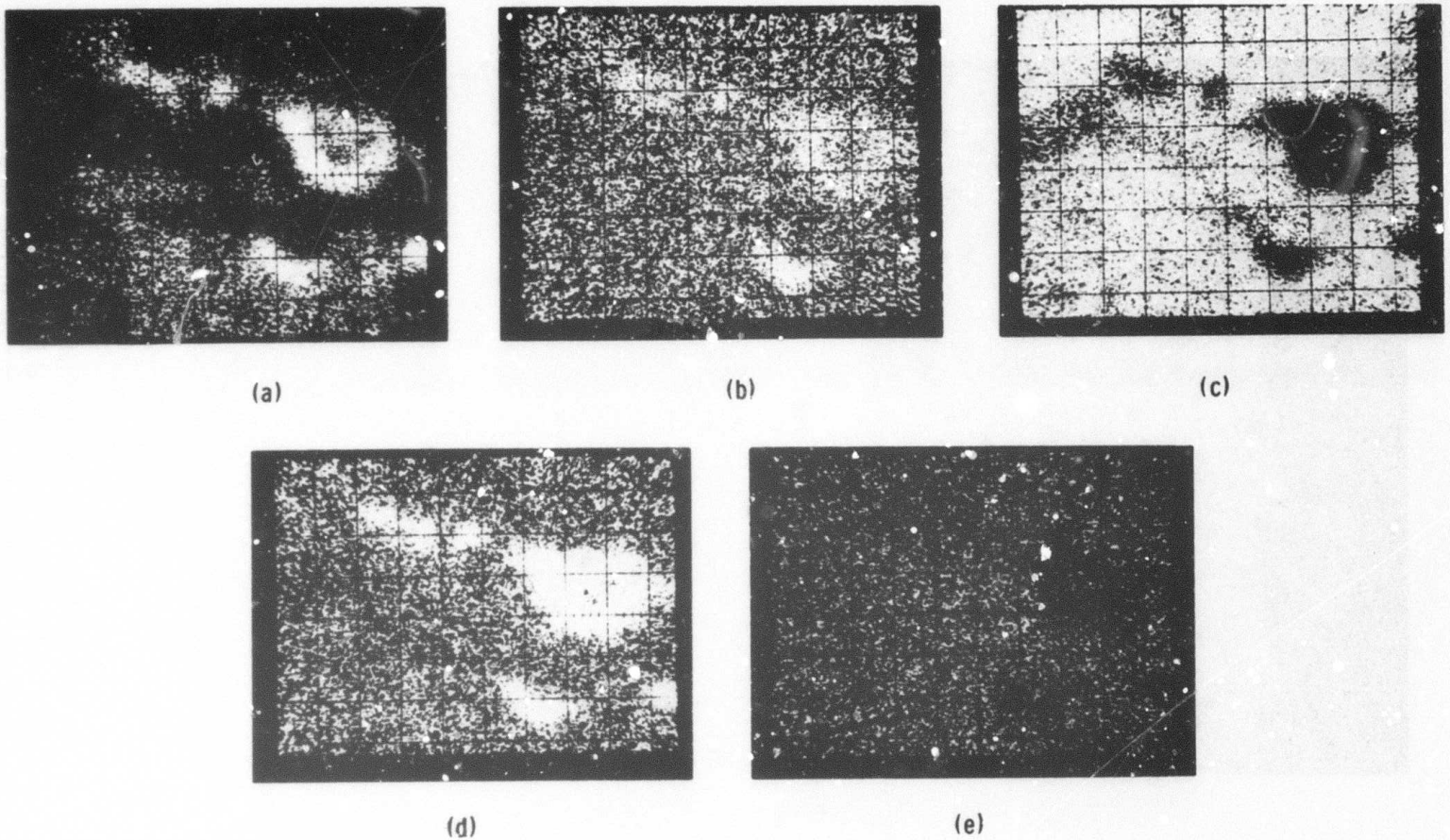

Fig. 29—I-718 STDA, scanning auger micrographs of a fresh fractured surface, 500 X
(a) C 272 ev (b) Ti 385 ev (c) Cr 489 ev (d) Nb 166 ev (e) Mo 222 ev

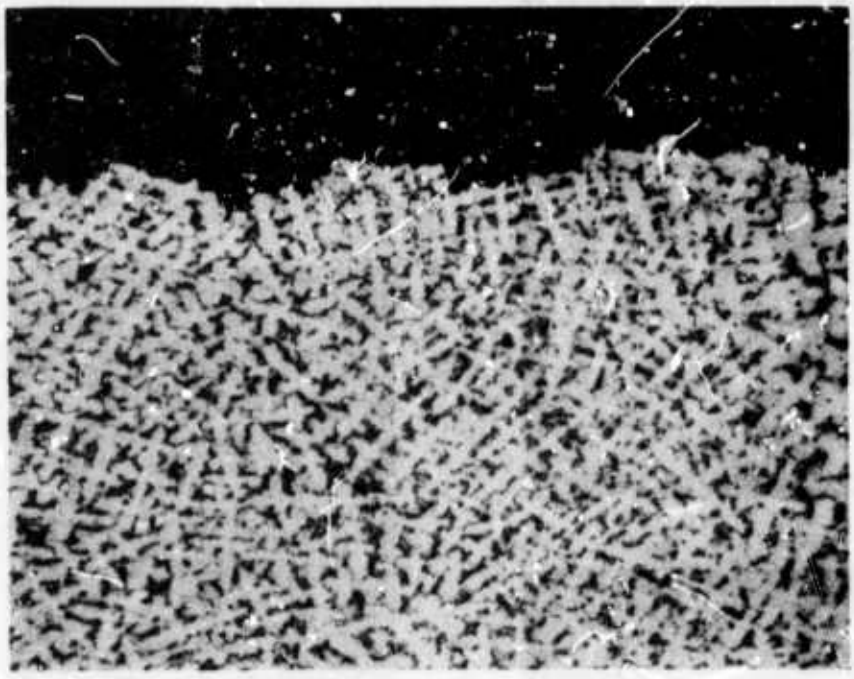

(a)

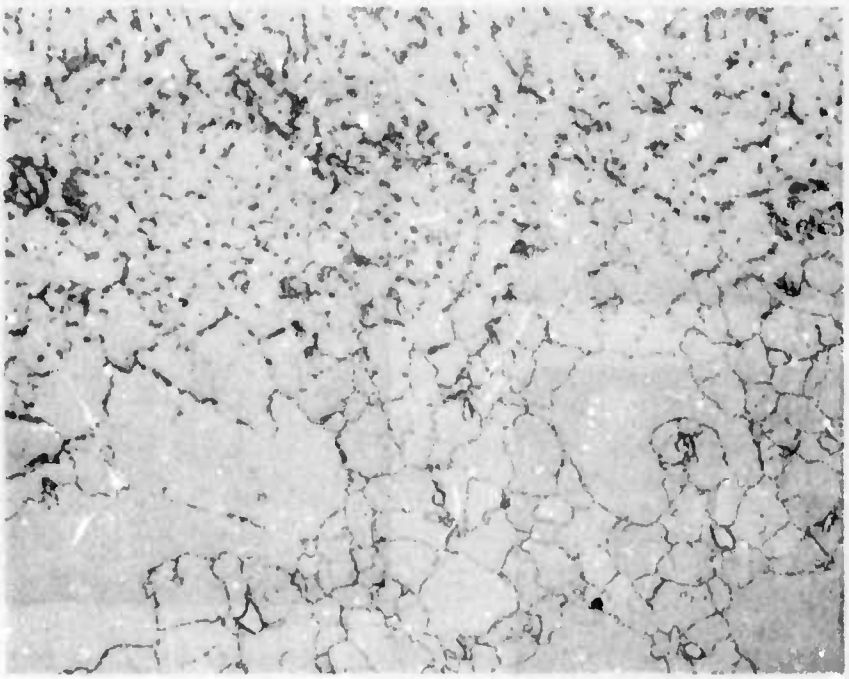

(b)

Fig. 30—Light micrographs weld tensile specimen 6511, I-718 weld + STDA tested at RT. 200X (a) longitudinal section at fracture (b) at heat affected zone

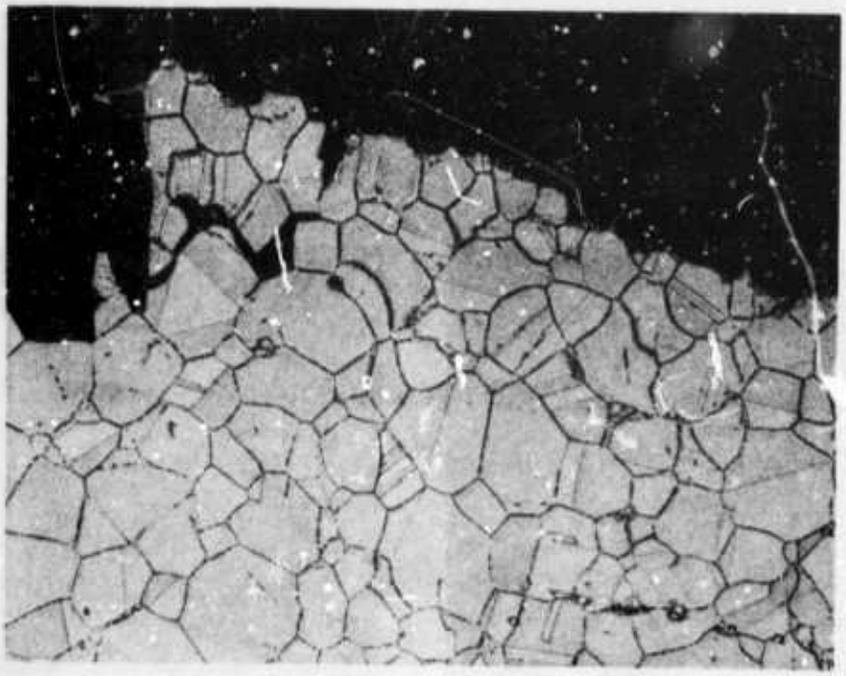

(a)

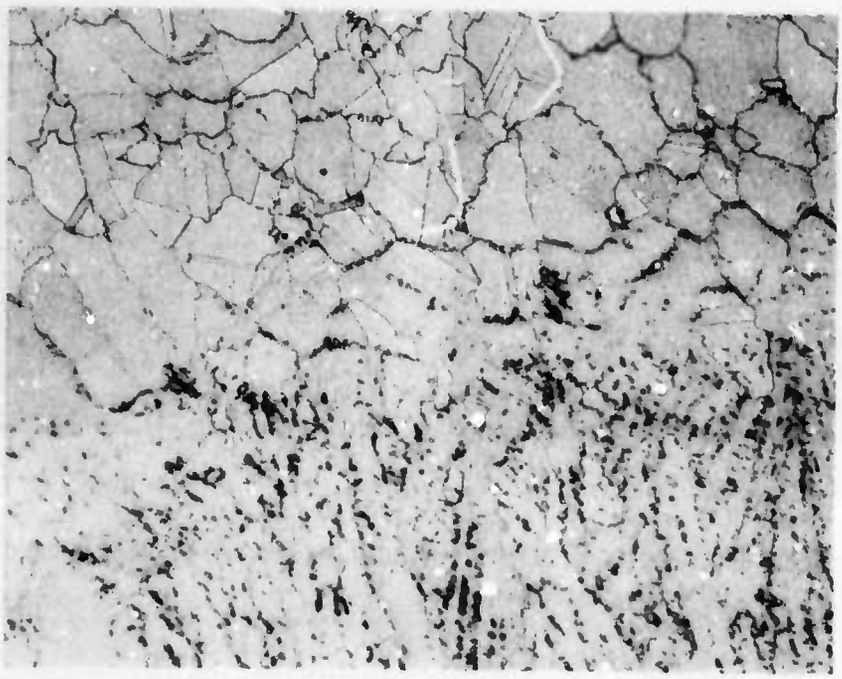

(b)

Fig. 31 — Light micrographs, longitudinal section, weld tensile specimen 6513, I-718 weld + STDA, tested at 4.2°K. 200X (a) at fracture (b) at HAZ

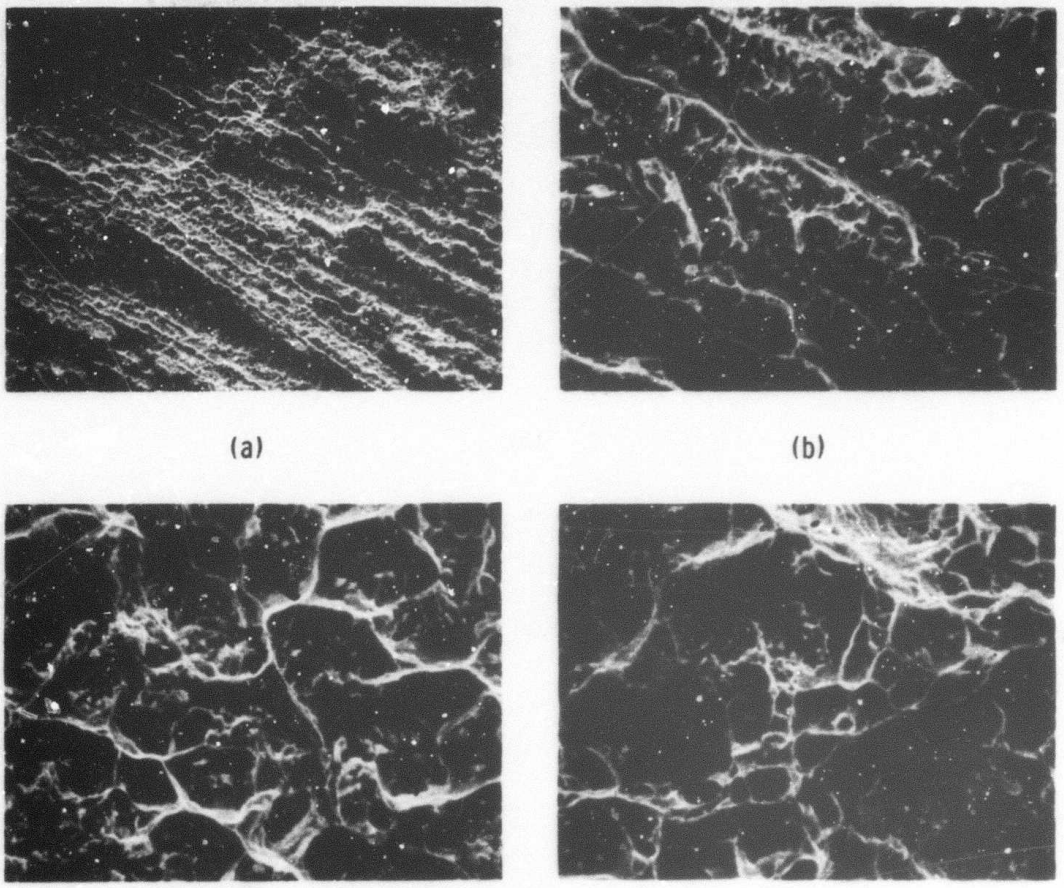

(a) (b)

(c) (d)

Fig. 32—SEM micrographs, fracture surface specimen 6511, I-718 weld + STDA tested at RT (a) 200X (b, c, d) 2000X

(a)

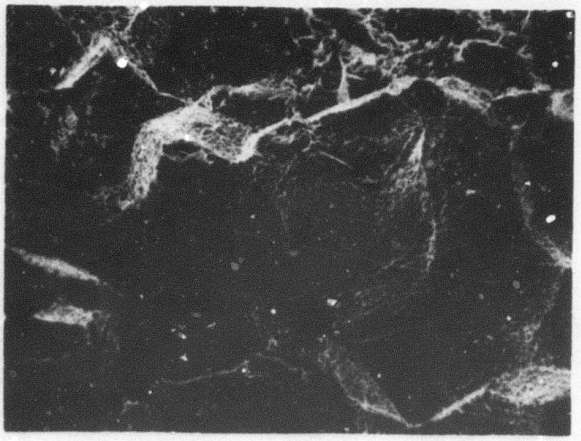

(b)

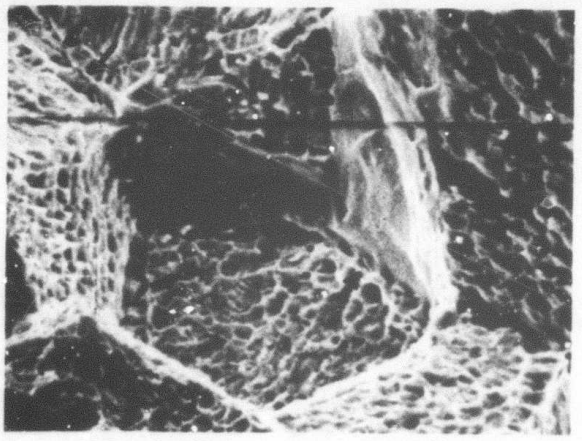

(c)

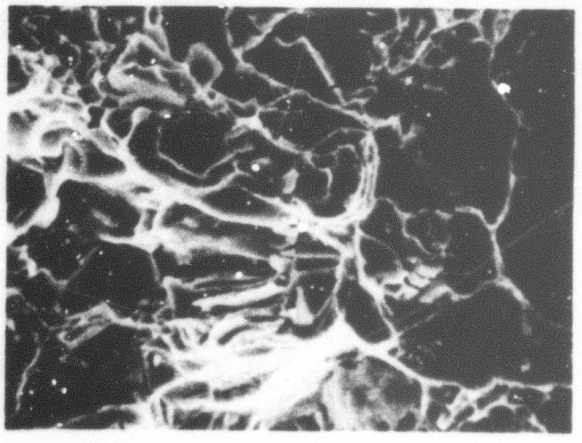

Fig. 33—SEM micrographs, fracture surface, specimen 6513, I-718 weld + STDA tested at 4.2°K (a) 500X (b, c) 2000X

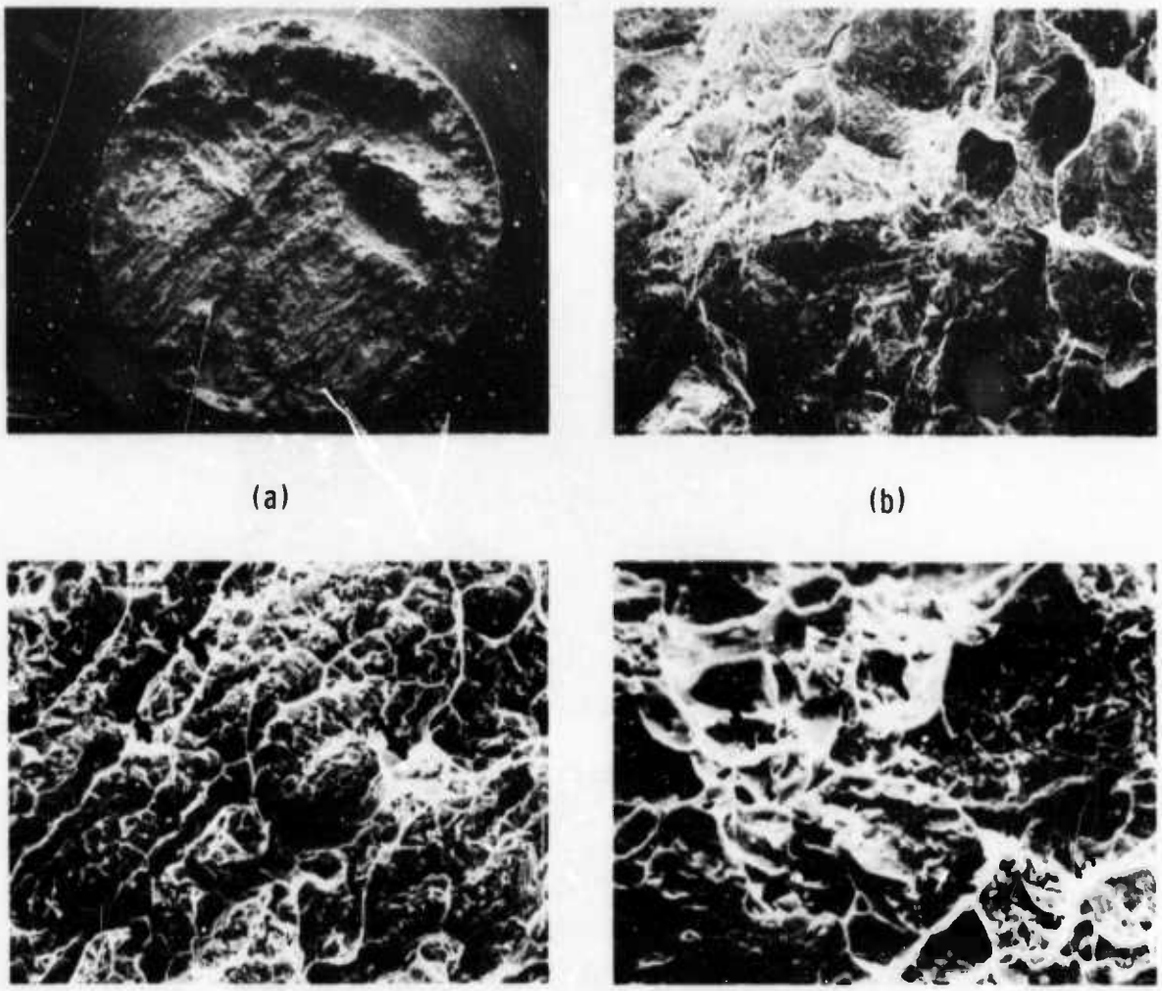

(a) (b)

(c) (d)

Fig. 34 – SEM micrographs, fracture surface specimen 6521, notch-tensile I-718, weld + STDA tested at RT (a) 20X (b) 200X fracture path moved to HAZ (c) 1000X (d) 2000X arrows indicate ridges of carbide film

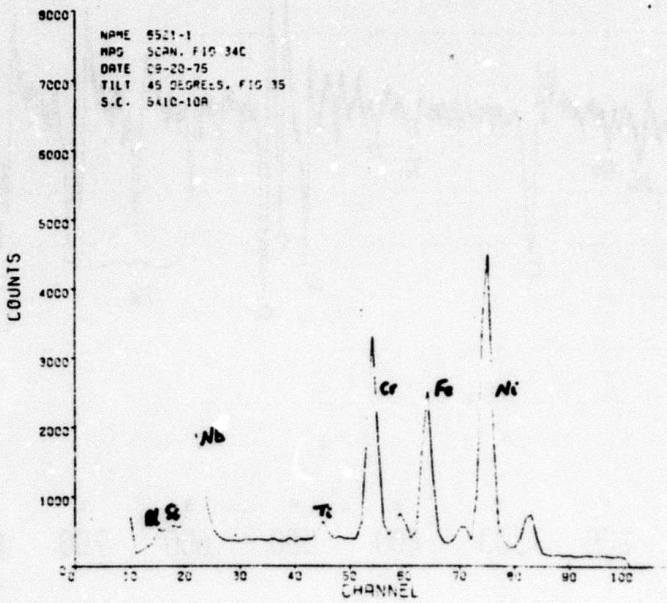

Fig. 35—Energy dispersive X-ray spectra, area scan of Figure 34C

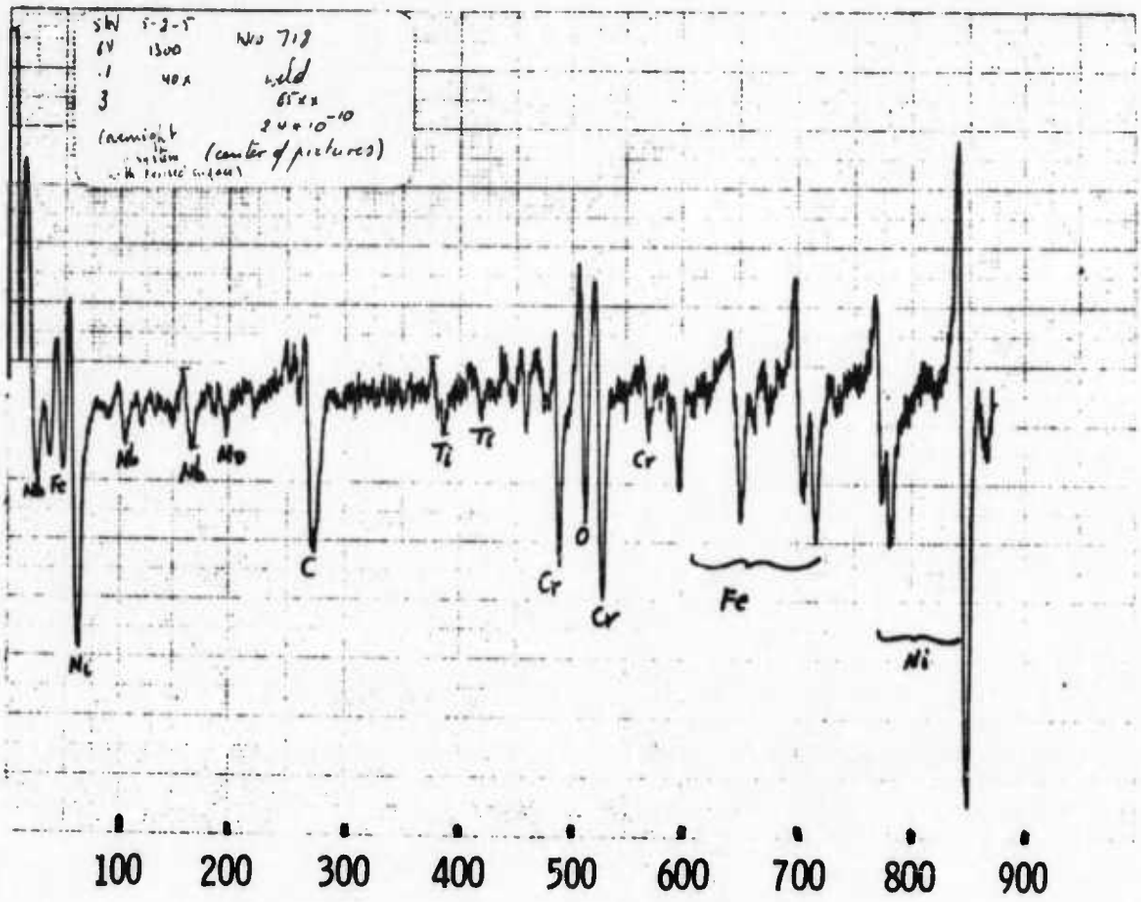

Fig. 36 — Auger spectra, fusion zone fresh fracture surface, specimen 65XX. I-718 weld + STDA,

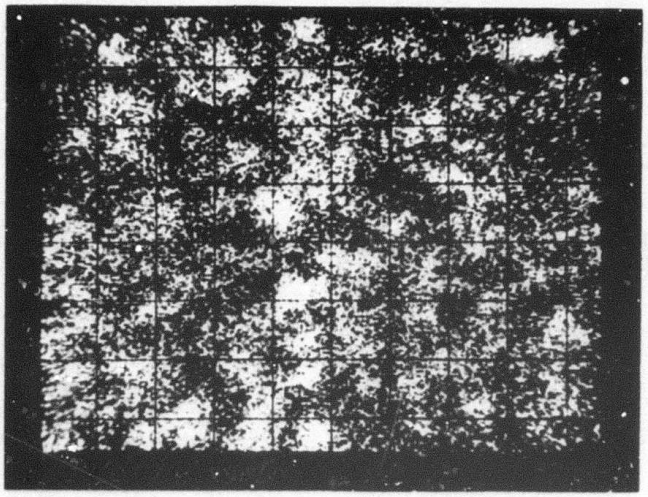

(a)

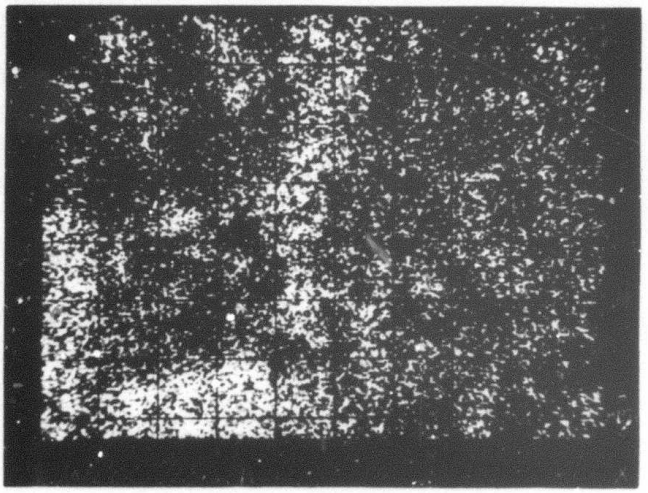

(b)

Fig. 37 - Scanning auger micrographs, fracture surface, I-718 weld + STDA (65XX). 500X
(a) carbon, 272 ev, distribution (b) oxygen 512 ev distribution

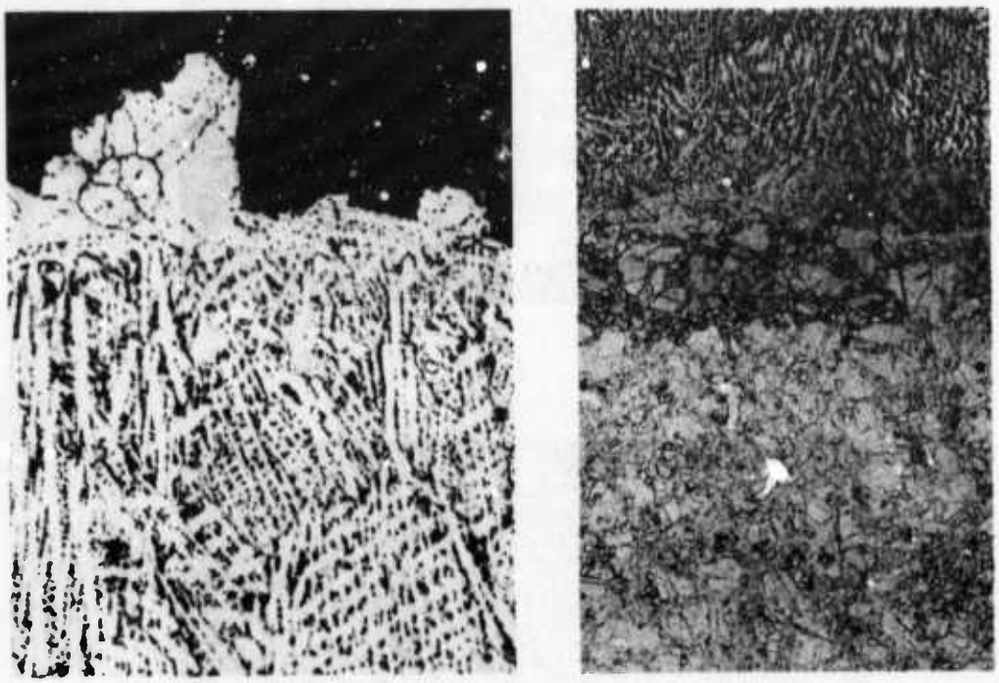

(a) (b)

Fig. 38—Light micrographs, longitudinal section HAZ notch-tensile specimen 6621, I-718 weld + STDA tested at RT (a) at fracture, 200X (b) HAZ on other end, 50X

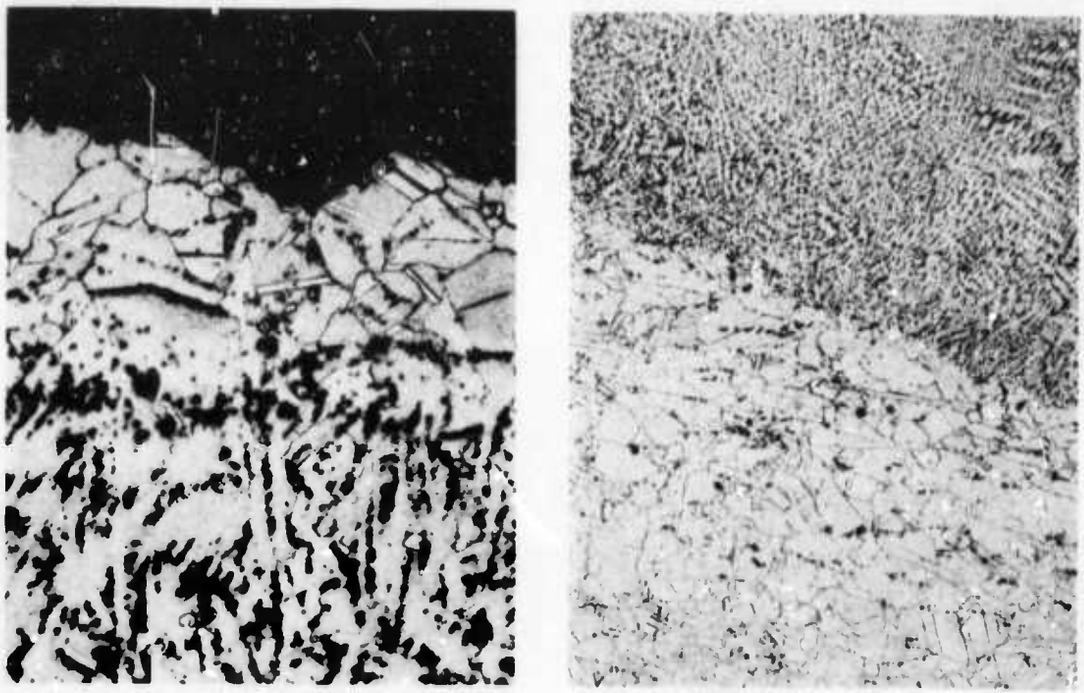

(a) (b)

Fig. 39—Light micrographs, longitudinal sections, HAZ notch-tensile specimen 6623, I-718 weld + STDA tested at 4.2°K (a) at fracture, 200X (b) HAZ on other end, 50 X

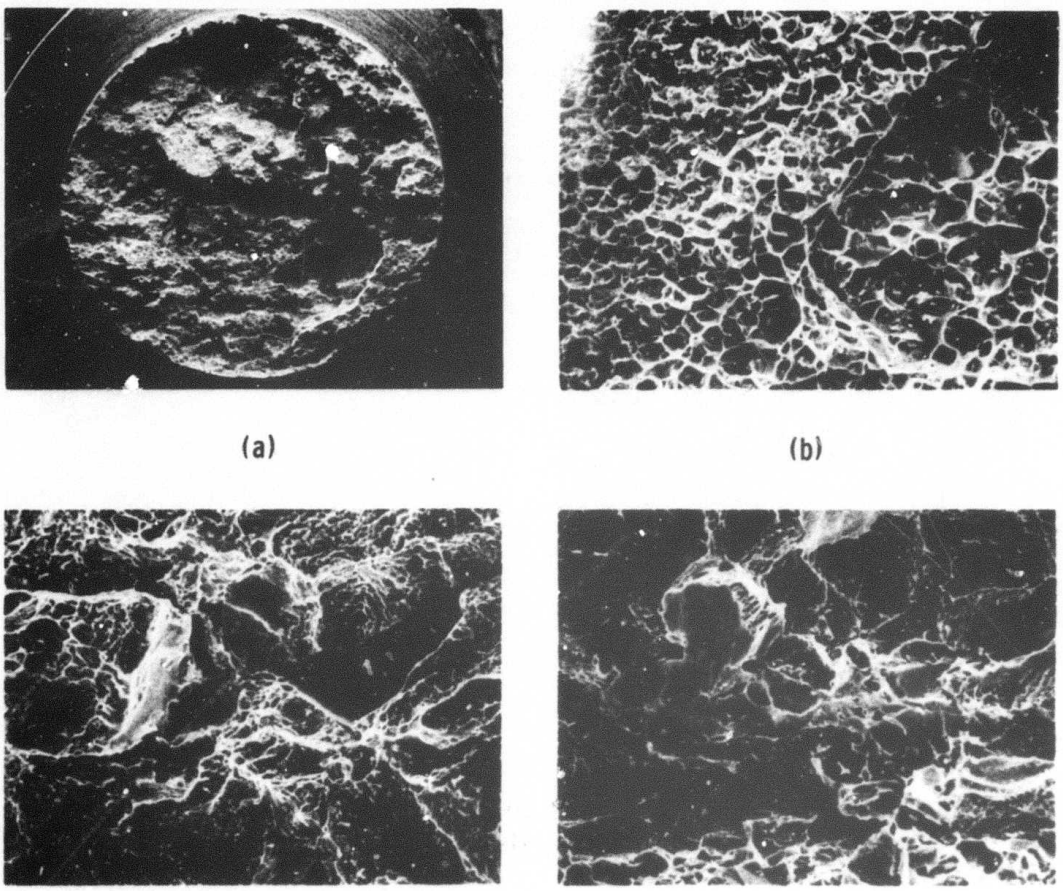

(a) (b)

(c) (d)

Fig. 40—SEM micrographs, fracture surfaces, HAZ notch-tensile specimen 6621, I-718 weld + STDA tested at RT (a) 20X (b) 2000X (c, d) 1000X

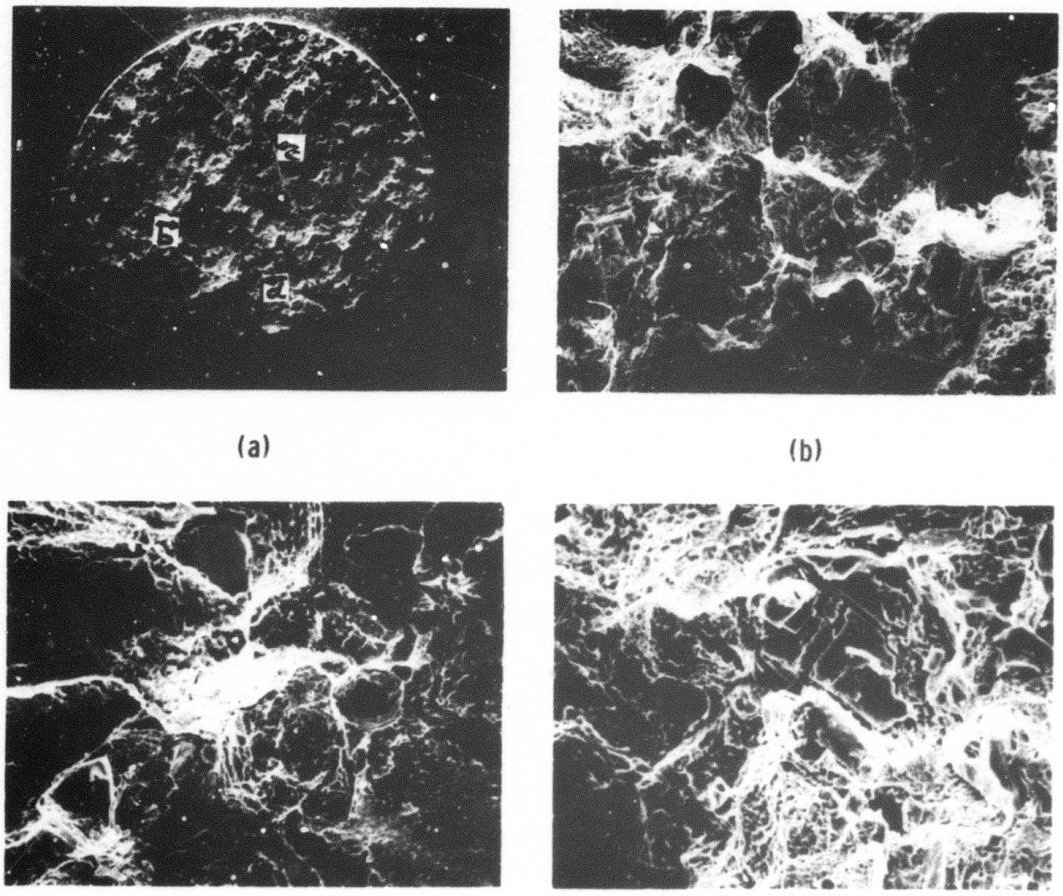

Fig. 41 – SEM micrographs, fracture surfaces HAZ notch-tensile specimen 6623, I-718 weld + STDA tested at 4.2°K (a) 20X (b) 200X (c,d) 2000X

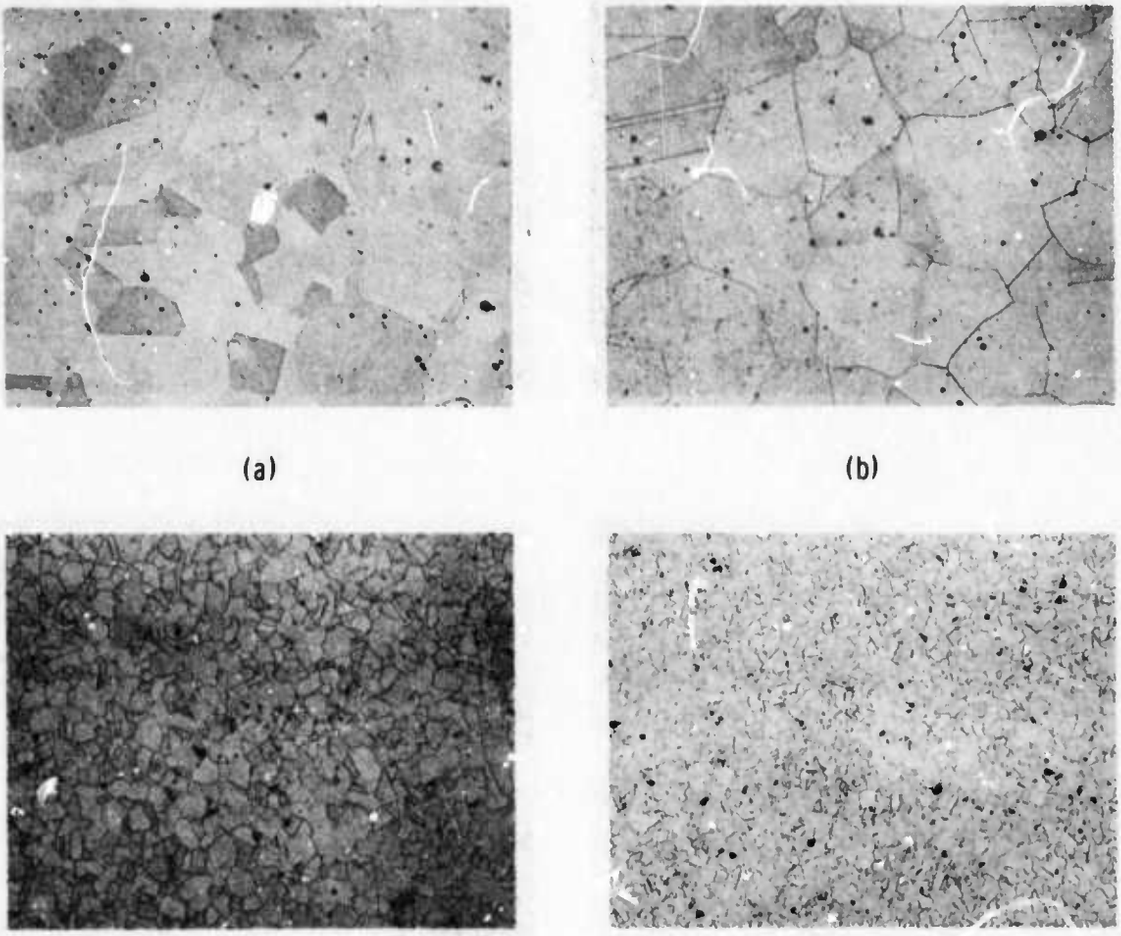

Fig. 42--Light micrographs Inconel 706 (a) VIM-VAR, solution annealed 2100°F (1422°K) 2 hr, 100X (b) VIM-EFR, solution annealed 2100°F (1422°K) 2 hr, 100X (c) VIM-VAR STDA (70XX) 50X (d) VIM-EFR STDA (70XX) 50X

(a)

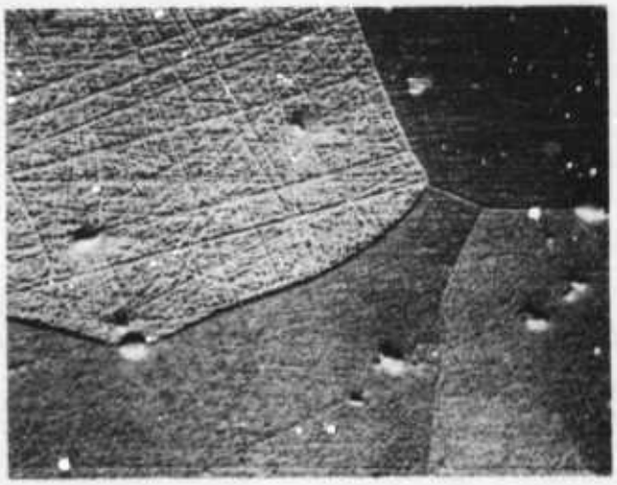

(b)

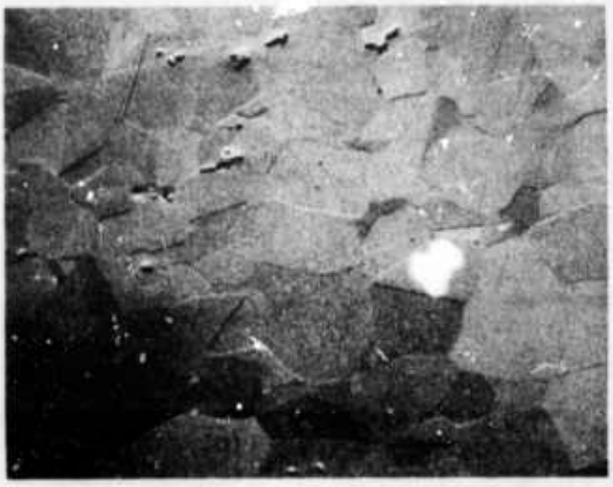

(c)

Fig. 43—SEM micrographs I-706 (a) VIM-VAR, S. A 2100°F (1422°K) 2 hr, 650X (b) VIM-VAR, STDA (71XX) 200X (c) VIM-EFR, STDA (70XX) 1250X

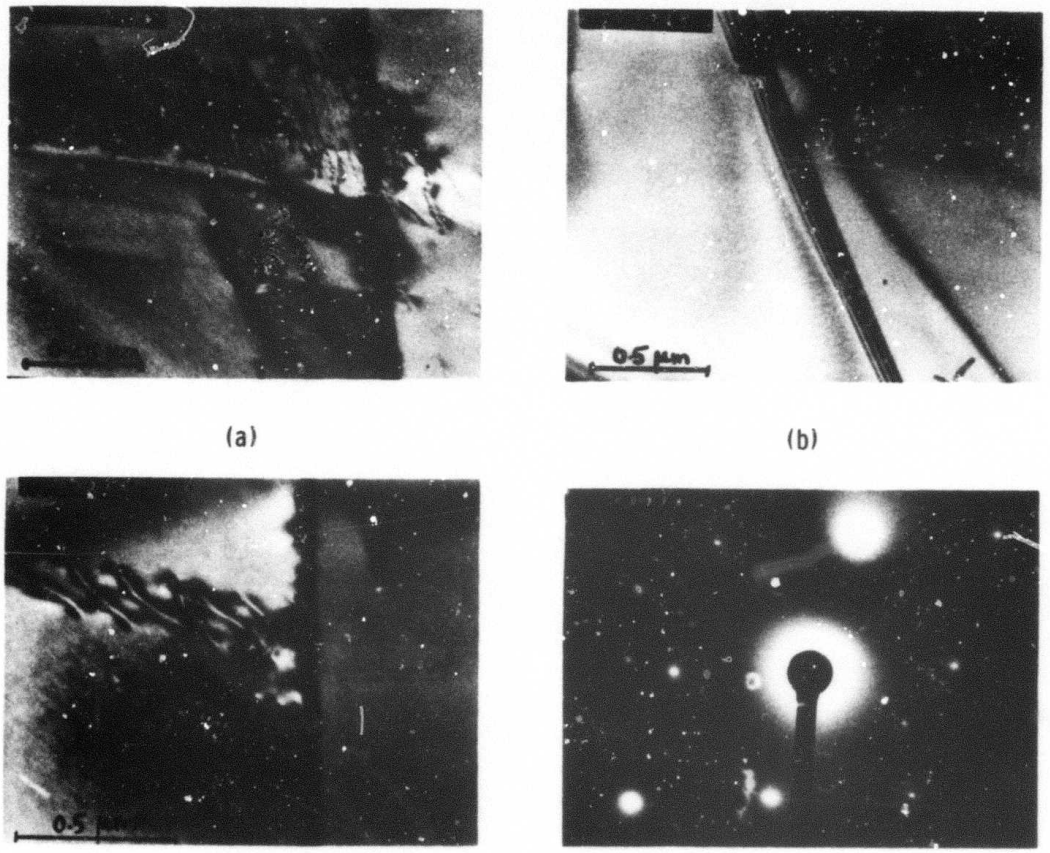

(a) (b)

(c) (d)

Fig. 44—Transmission electron micrographs, I-706 VIM-VAR, solution annealed 2000°F (1400°K). Note dislocation pile-ups and precipitation free boundaries

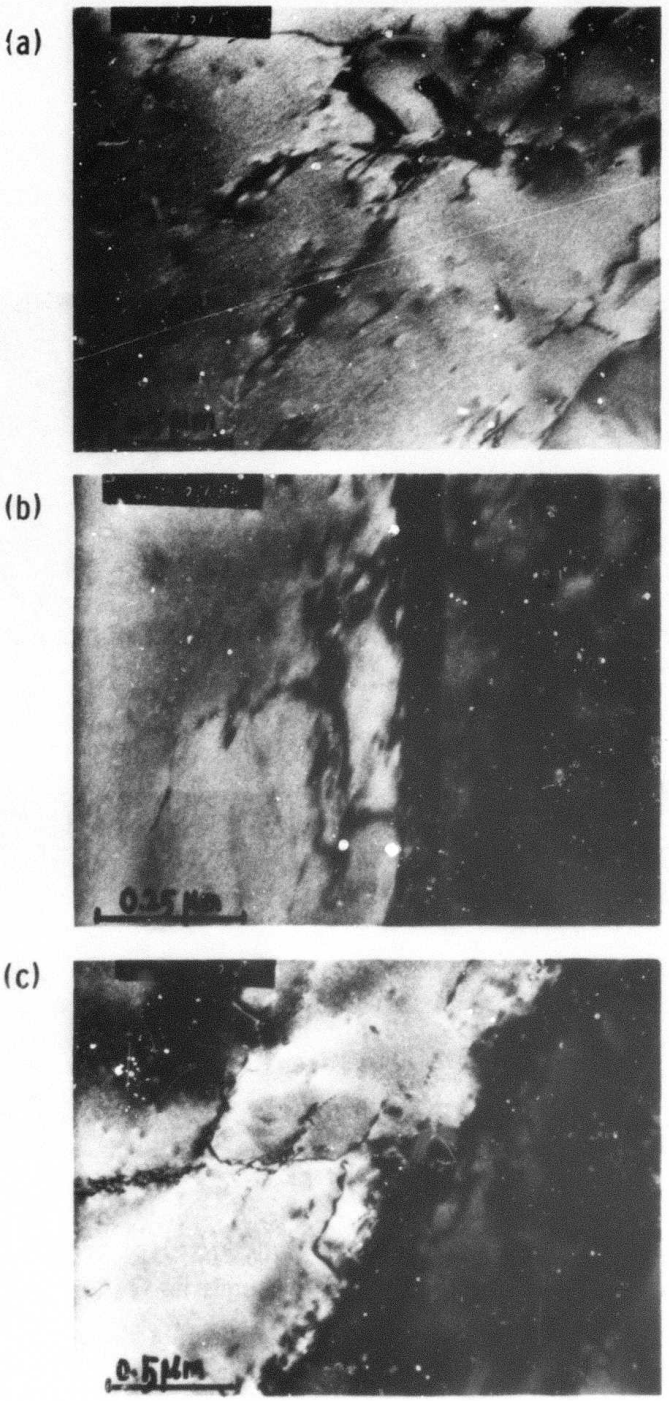

Fig. 45—Transmission electron micrographs I-706 VIM-EFR solution annealed 2100°F (1422°K). General features as in Figure 44

RM-64995

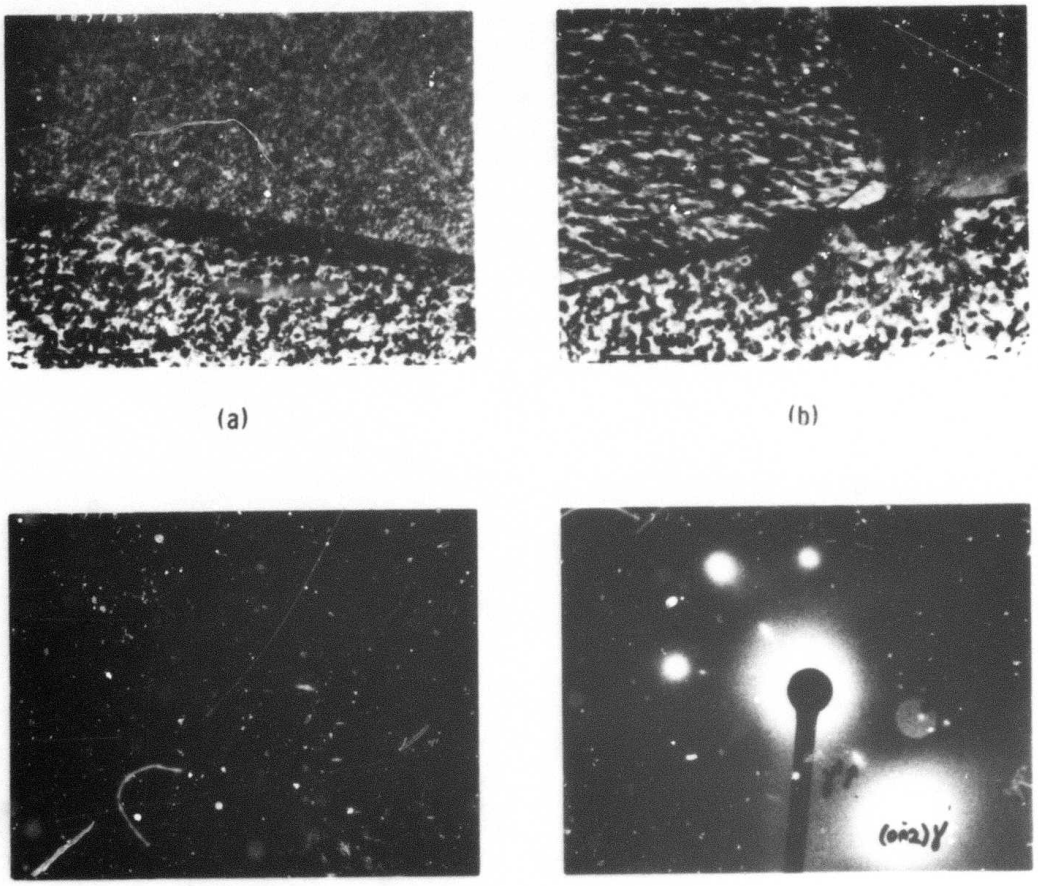

Fig. 46—Transmission electron micrographs I-706 VIM-VAR, STDA (71 XX). Note γ' + γ'' particle-dislocation networks, precipitation free boundaries (a,b), dark field showing plate like γ'' (c)

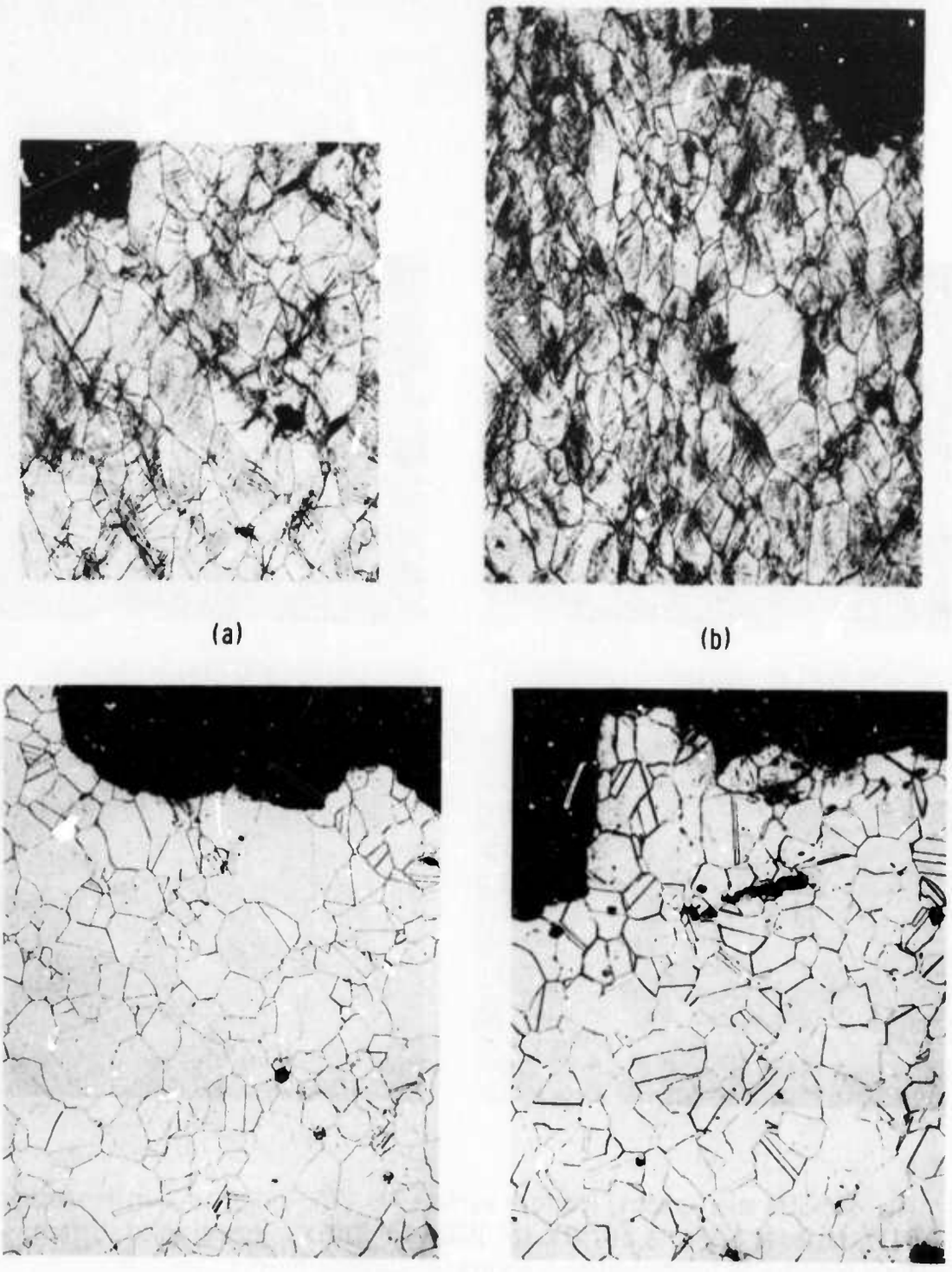

Fig. 47—Light micrographs, longitudinal sections I-706 tensile specimens 200X (a) 7011 (tested at RT) (b) 7013 (tested at 4.2°K) (c) 7021 (N.T, RT) (d) 7023 (N.T 4.2°K)

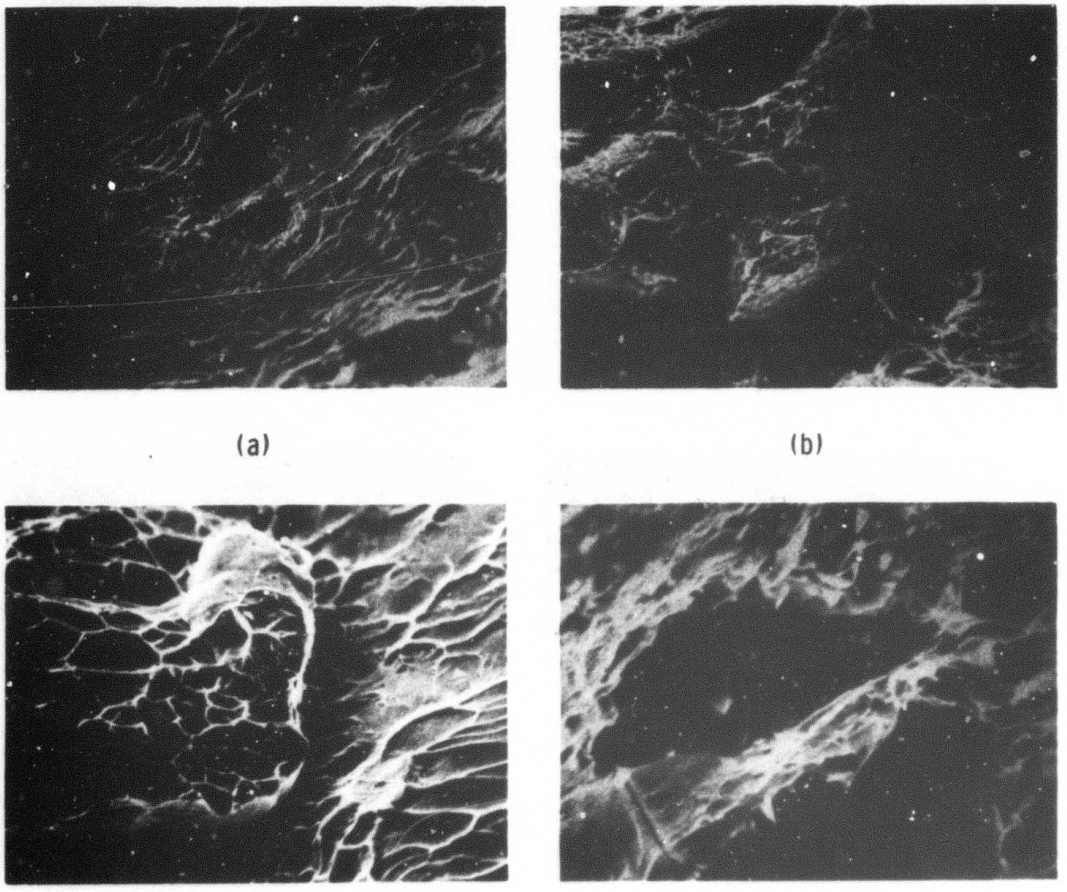

(a) (b)

(c) (d)

Fig. 48—SEM micrographs, fracture surface 706 VIM-VAR STDA tensile specimen 7113, tested at 4.2°K (a,b) 750X (c) 1500X (d) 3100X. Note dimpled surface, final fracture by intergranular cracking (b) carbides in (d)

(a)

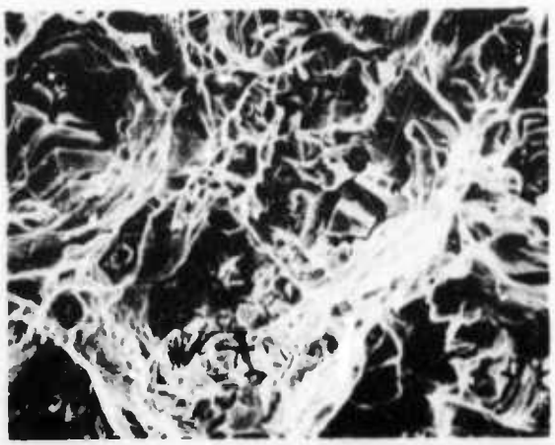

(b)

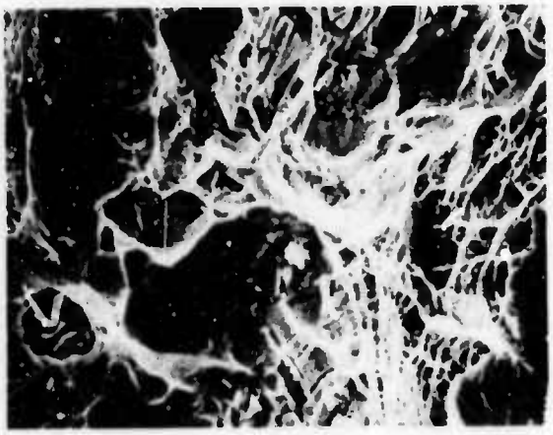

(c)

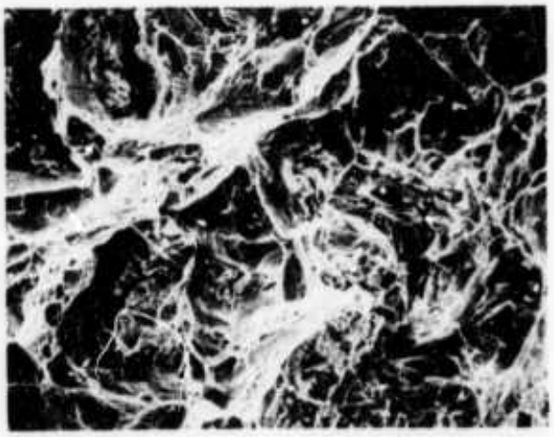

(d)

Fig. 49— SEM micrographs, fracture surface 706 notch-tensile specimens (a) 600X (b) 1200X VIM-EFR STDA specimen 7023. (c) 600X (d) 1200X VIM-VAR STDA specimen 7123

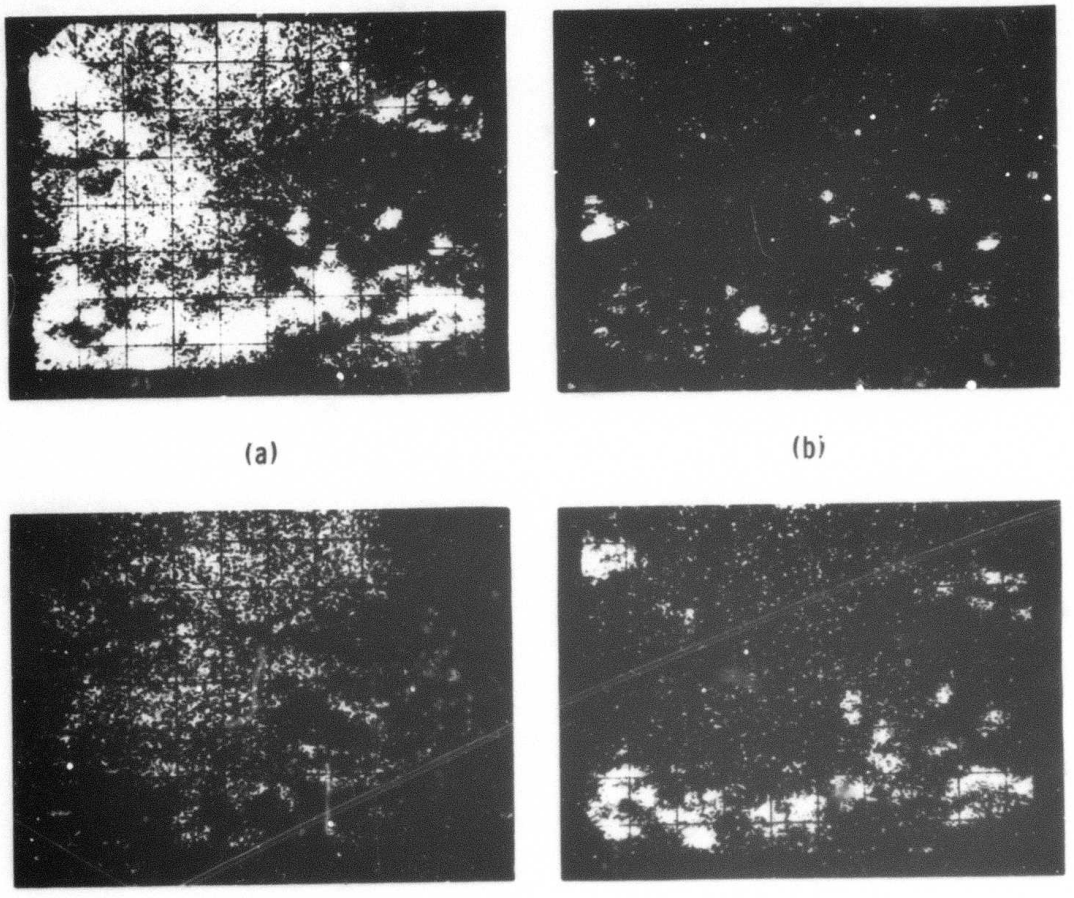

(a) (b)

(c) (d)

Fig. 50— Auger scanning micrographs fresh fracture I-706 STDA (71 XX)
(a) C-272 ev (b) Ti 385 ev (c) Cr 489 ev (d) Nb 168 ev 250 X

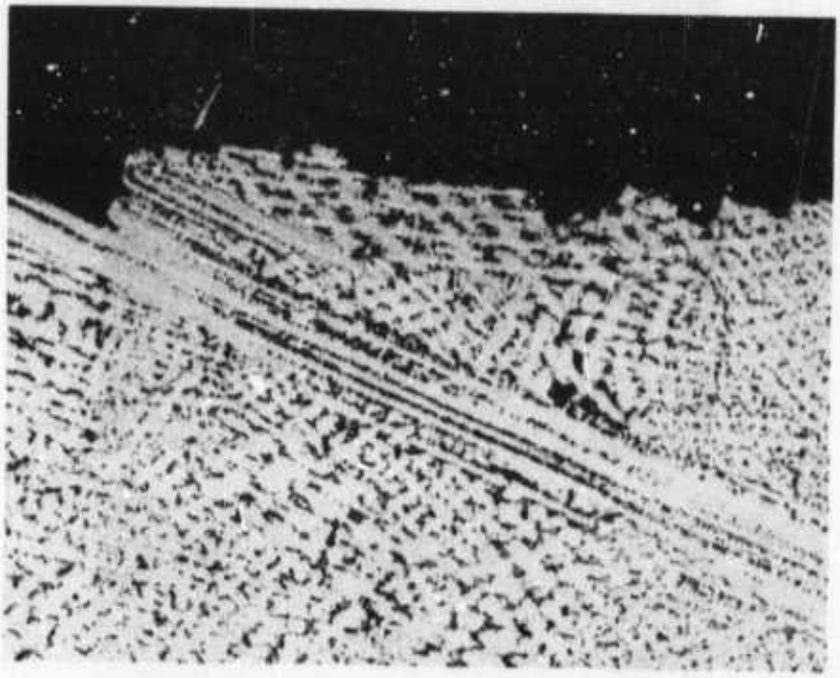

(a)

(b)

Fig. 51 – Light micrographs fusion zone fracture I-706 (a) specimen 7213 (b) specimen 7223 both tested at 4.2°K 200X

(a)

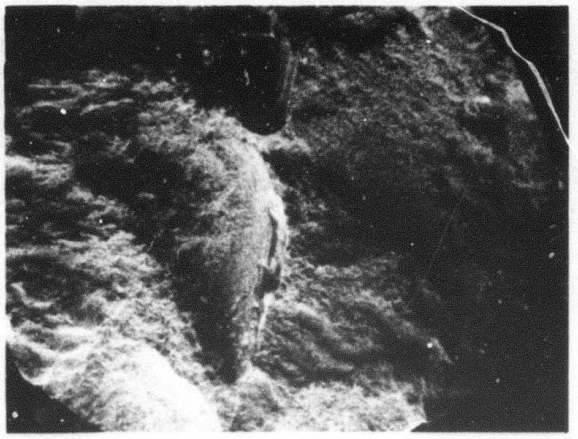

(b)

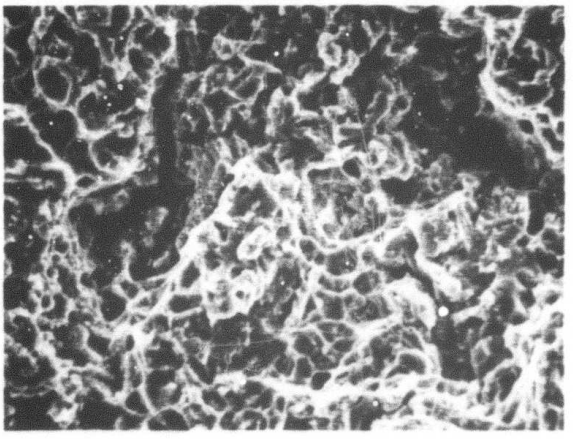

(c)

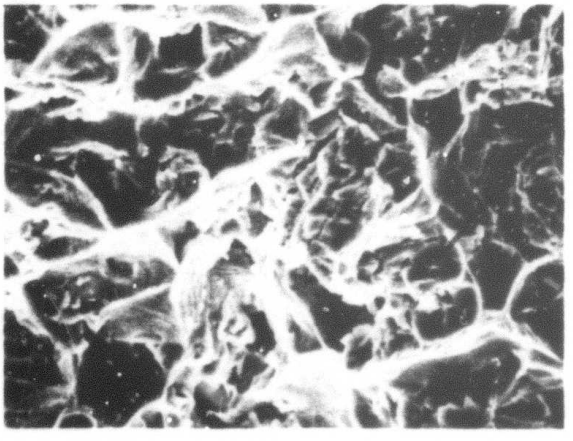

Fig. 52—SEM micrographs of fusion zone fracture I-706, tensile specimen 7211 tested at 4.2°K (a) 20X (b, c) 2000 X. Arrows indicate voids and cracks in weldment

RM-64994

(a)

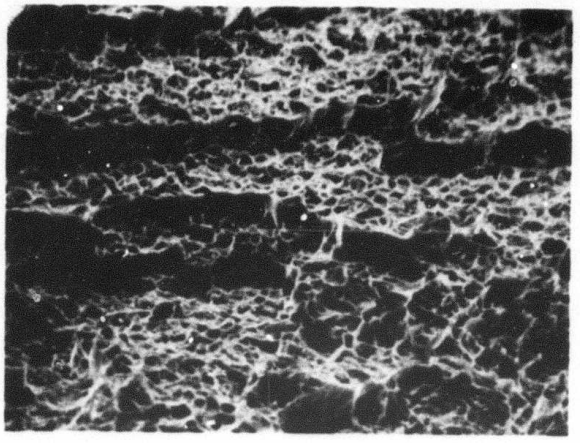

(b)

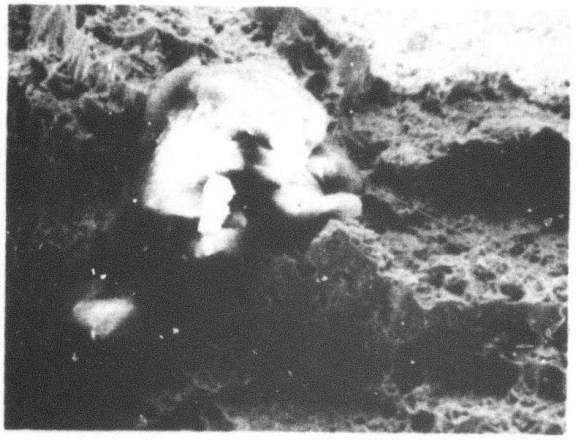

(c)

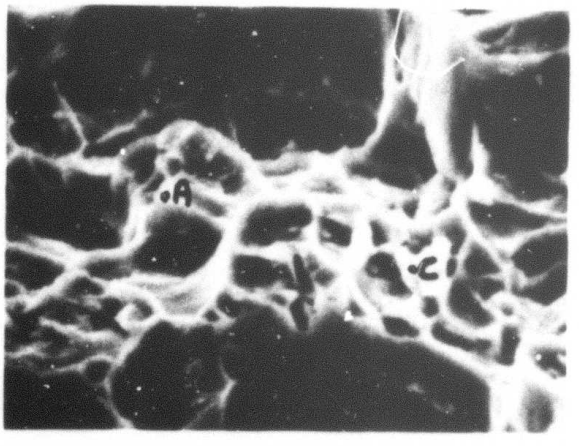

Fig. 53—SEM micrographs, fusion-zone fracture I-706, notch-tensile specimen 7213. (a) 820X (b) 4200X (c) 4200X. EDAX analysis shown in Figure 54

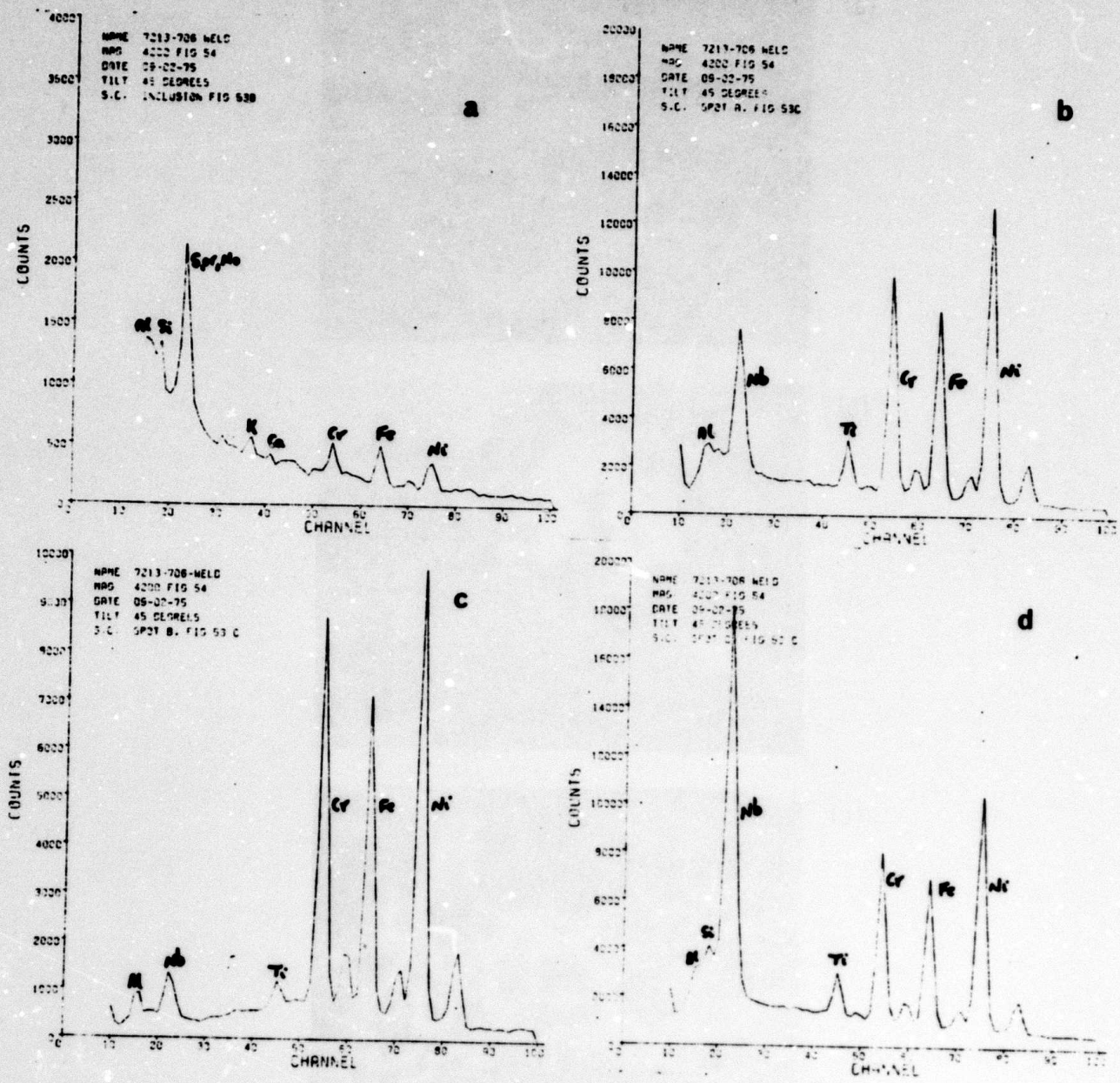

Fig. 54—Energy dispersive X-ray spectra (a) inclusion, Figure 53b (b) spot A, Figure 53c (c) spot B, Figure 53c (d) spot C, Figure 53c

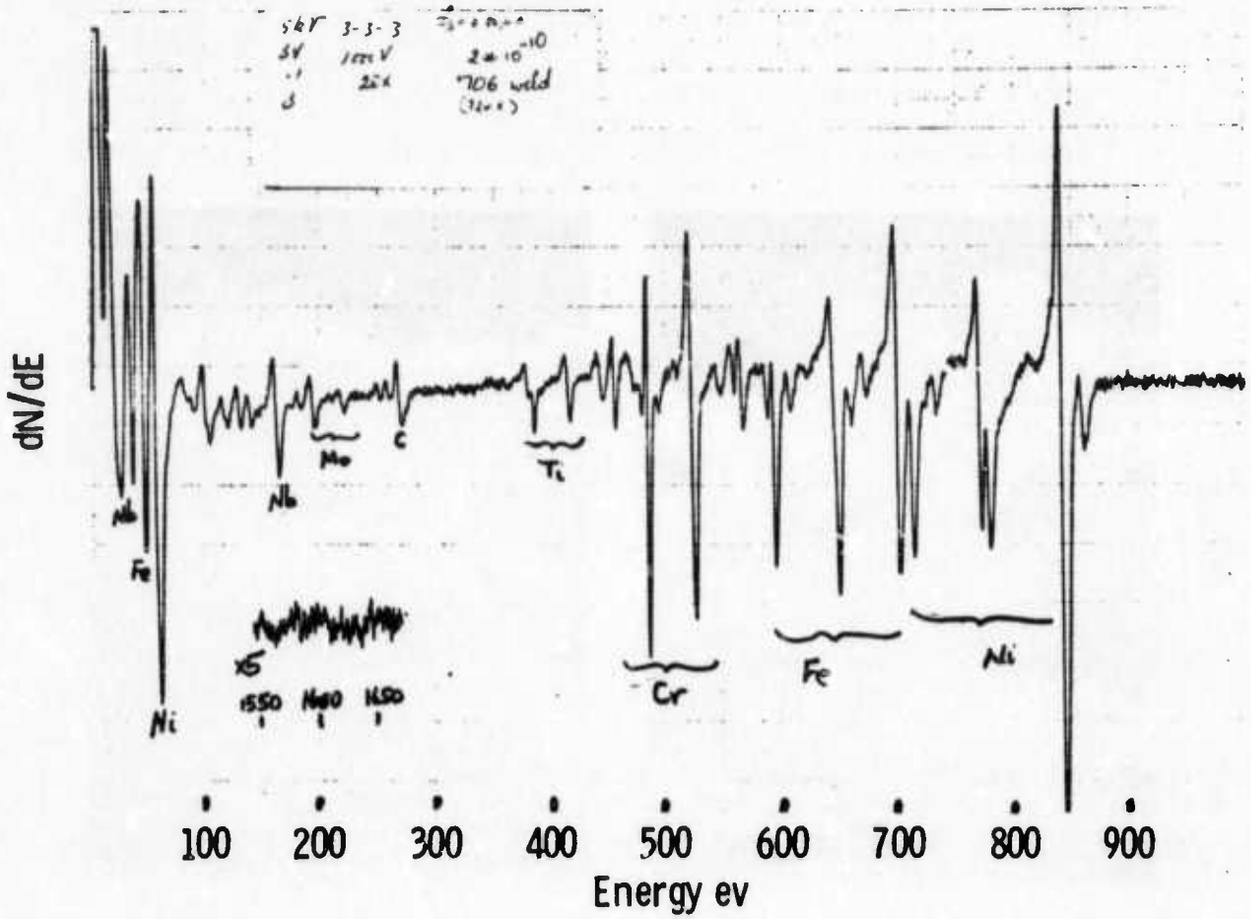

Fig. 55—Auger spectra, fresh fusion zone fracture surface specimen 72XX, I-706 weld + STDA

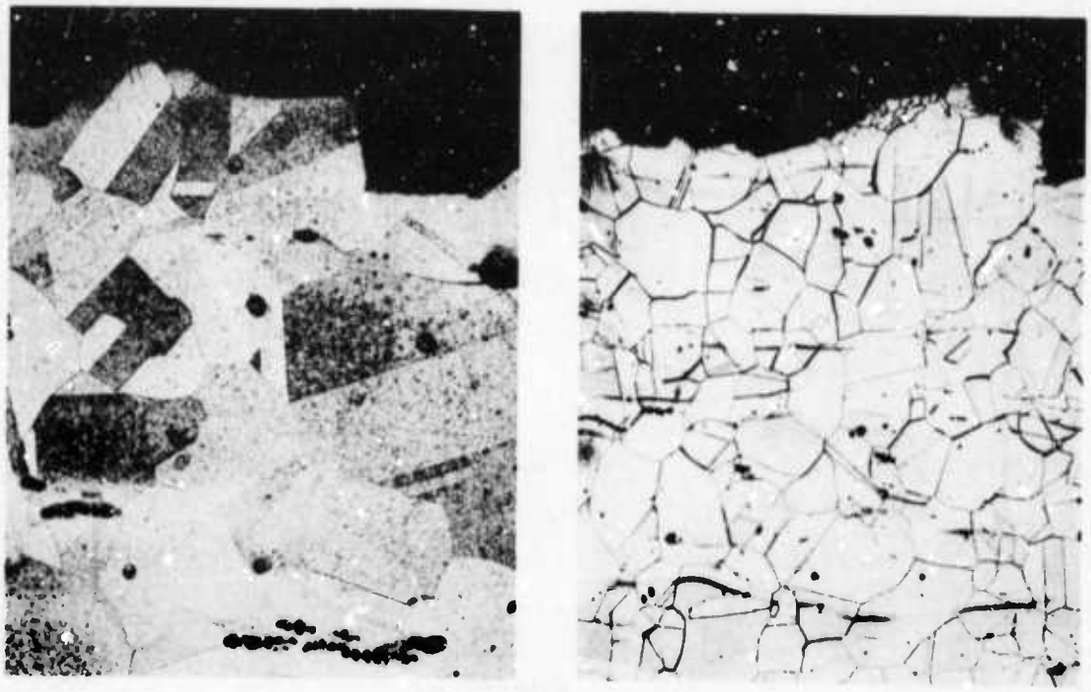

(a) (b)

Fig. 56—Light micrographs longitudinal sections LEA tensile specimens (a) 7313, tested at 4.2°K 200X (b) 2323, notch-tensile, tested at 4.5°K, 100X

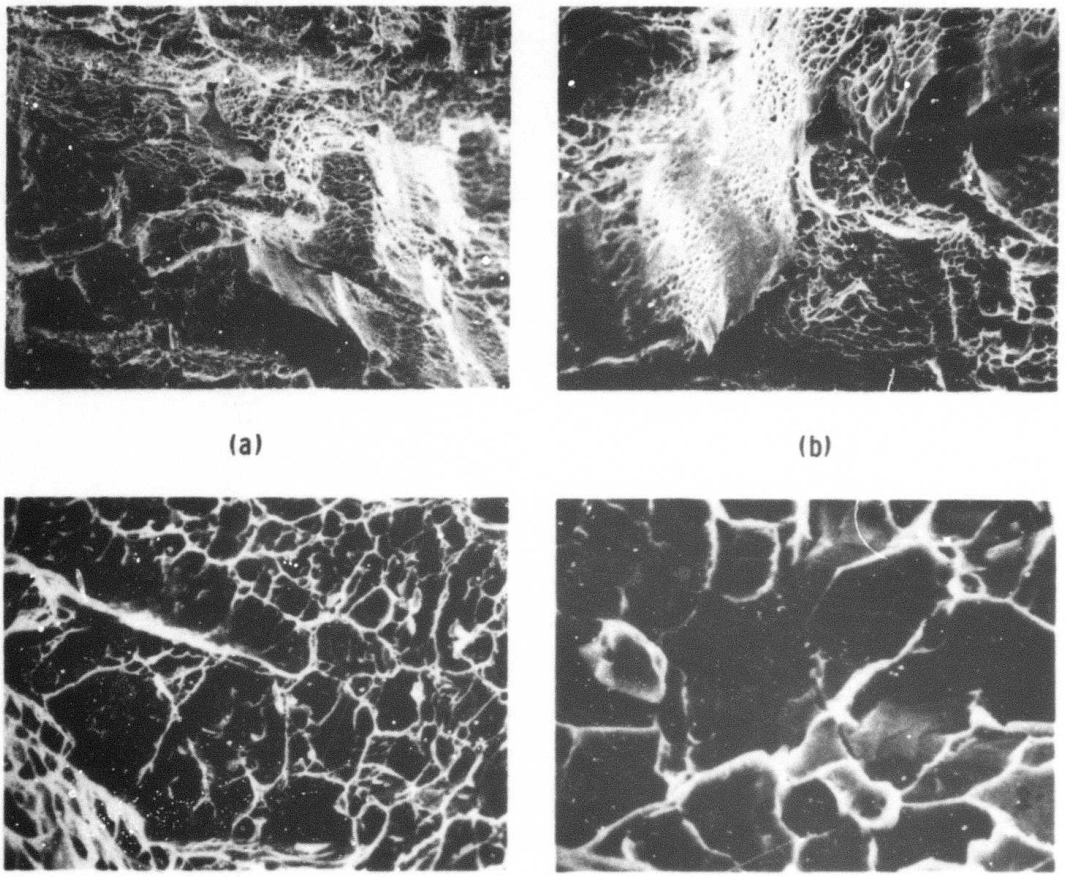

(a) (b)

(c) (d)

Fig. 57 – SEM micrographs, LEA. tensile fracture surfaces (a) 7313 150X (b) 7313 300X (c) 7313 1600X (d) 7323 (notch tensile) 4500X tested at 4.2°K. EDAX analysis shown in Figure 58

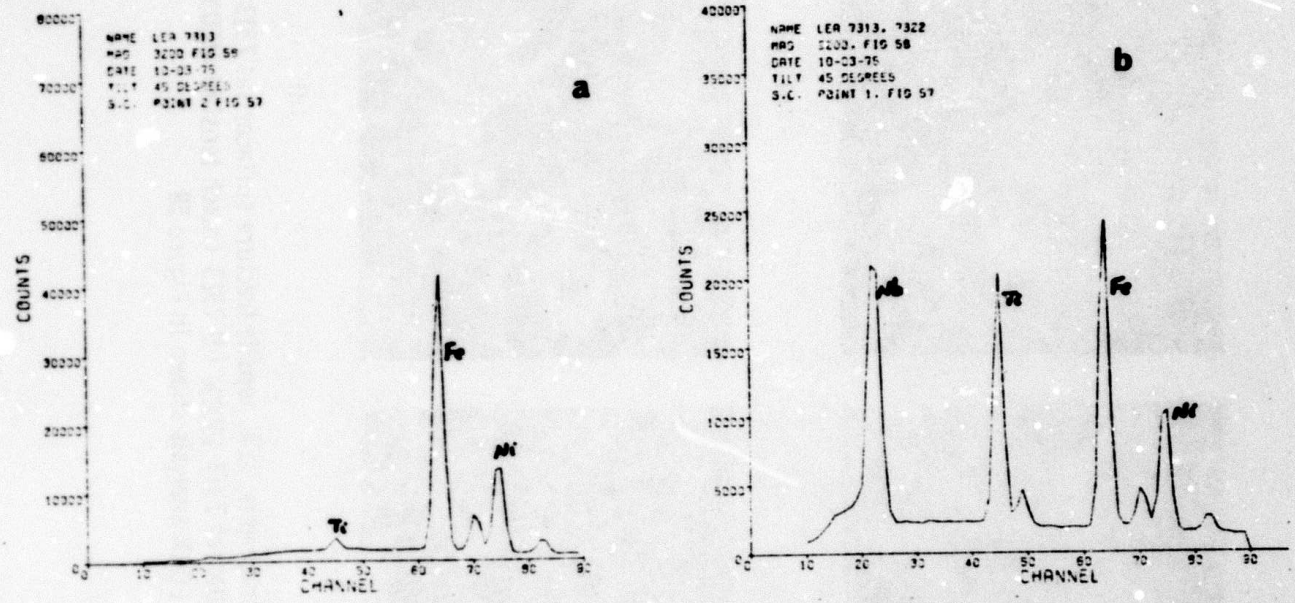

Fig. 58—Energy dispersive X-ray spectra of details, Figure 57 (a) Matrix, point 2 (b) plate-like particles, point 1

8.0 MAGNETIC AND ELECTRICAL MEASUREMENTS

Introduction

The magnetic and electrical resistivity measurements conducted in this portion of the Westinghouse FY 75 program are reported herein. The purpose of such measurements is to provide basic magnetic and electrical resistivity characterization from RT to 4K of those structural candidate materials in conditions being evaluated in the Westinghouse program. In addition, five materials submitted by NBS have also been included. The extent of this effort does not at present allow for more intensive investigation into further understanding of such behavior. However, their engineering potential for cryogenic applications renders a cataloging of their magnetic condition and electrical resistivity necessary. In fact, as will be discussed later, the results obtained to date under this contract enable an alloy composition to be given which should be nonmagnetic at 4.2K. Whether such a composition would have suitable mechanical properties also is another question.

As given in previous reports under this contract, the magnetic measurements were made on a Foner type magnetometer (PAR model 155). Samples were cut in the form of cylinders 3 mm diameter by 3 mm in length. The magnetometer can give magnetization as a continuous function applied magnetic field and this can be done as a function of temperature. In order to examine all the materials provided it was necessary to restrict measurements to three temperatures -- liquid helium (4.2 K), liquid hydrogen (20 K) and liquid nitrogen (78 K). These were obviously chosen for their cryogenic usefulness.

Figure 1 shows the basic behavior of ferromagnetic and antiferromagnetic materials in an applied magnetic field. A magnetic field of H oesteds induces a magnetization M per unit volume in a magnetic

material. The magnetization M produces a magnetic field of $4\pi M$ gauss which adds (vectorially) to the applied field H to give a total magnetic field or induction $B = H + 4\pi M$. Antiferromagnets exhibit a simple linear dependence of M on H whereas the ferromagnetics have a more complicated non-linear dependence. However, M for a ferromagnet increases with increasing H up to a maximum or saturation value M_s at a magnetic field value H_s. The magnetic field B_s which this saturation value produces is $4\pi M_s$ and is also called the saturation induction B_s. Two quantities of further interest are the permeability $\mu = \frac{dB}{dH}$ and the susceptibility $X = \frac{dM}{dH}$ which from the equation $B = H + 4\pi M$ are related by $\mu = 1 + 4\pi X$. Note that although H is measured in oesteds and B and M in gauss the distinction is only of historical significance. B, H and M are the same quantities dimensionally-field (or force) lines per unit area. Oesteds and gauss are used as interchangeable units for H unless a confusion between B and H needs to be avoided.

8.1 Magnetic Measurements

Table 8.1 sets out the materials and their magnetic condition together with the saturation induction value (B_S) at the above three temperatures. Except for the PD-135 copper, all were ferromagnetic to some degree. In this connection it is useful to draw up a scale of ferromagnetic strengths. Pure iron has a generally accepted B_S value of 22 kG (kilogauss) at 4.2 K. Based on this we catalogue a material according to its B_S value

- Values in the range 22 to 10 kG are strongly ferromagnetic.
- Values in the range 10 to 2 kG are ferromagnetic.
- Values in the range 2 to 0.5 kG are weakly ferromagnetic.
- Values in the range 0.5 to 0 kG are feebly ferromagnetic.

It was realized during the course of these measurements that for most ferromagnetic materials it was not possible to measure the initial permeability or susceptibility from the magnetization curves. The solenoid employed to develop the applied magnetic field was of the superconducting variety. Although well suited to providing fields in

the kilogauss range it is not useable in low fields (< 100 gauss). The leakage current from the solenoid power supply developed a high enough field to cause saturation in most of the ferromagnetic alloys.

Quantitatively useful measurements are possible on materials which are still far from saturation in fields of a few hundred gauss. This implies the permeability $\mu \sim 1$ and the susceptibility $\chi \gtrsim 10^{-2}$. Only feebly ferromagnetic materials fulfill these conditions (we ignore for the moment para-, dia- and antiferromagnetism).

8.2 Discussion

Before obtaining the results of Table 8.1 a literature survey was conducted of published results in magnetic properties of steels at cryogenic temperatures. The search yielded references 1 through 5 which testifies to the small amount of work performed in this field to date. Bearing in mind the reservations expressed at the beginning of this section we can make one conclusion regarding the ferromagnetic materials listed in Table 8.1. The basic magnetic condition is not changed by different heat treatments. The magnetization is determined primarily by the magnetic elements in the alloy. Differing heat treatments only change the size of the magnetization. Pure copper is diamagnetic, however, PD-135 copper contains 0.3% cadmium and 0.3% chromium. Both these are intrinsically paramagnetic in the atomic state and clearly dominate the diamagnetism of the copper. However, PD-135 copper is only weakly paramagnetic with $\chi \sim 10^{-6}$ and thus should present no problems in any cryogenic applications.

The use of magnetic structural materials in cryogenic machinery has a number of possible effects. Both ferromagnetic and antiferromagnetic materials can perturb a field generated by windings. This is because both generate a magnetic moment in the presence of the field. A small element dV of a structure acquiring a magnetic moment M in a field H experiences a couple $\underline{M} \times \underline{H}\ dV$ and a force $\frac{dM}{dH}\frac{dH}{dx}\ dV$ in a field gradient $\frac{dH}{dx}$. This couple and force integrated over the whole structure must be known when designing cryogenic machinery. If structural materials need to be non-magnetic, i.e. dia or paramagnetic or at least only very slight magnetic then this implies M and $\frac{dM}{dH} \approx 0$.

In the presence of alternating or transient fields ferromagnetic materials may exhibit a hysteresis loss with a consequent rise in their temperature. Thus, if magnetism cannot be eliminated entirely, structures should be at least antiferromagnetic to eliminate hysteresis heating. Table 8-2 sets out all the alloys studied to date under the present contract plus a few others for added interest. Examination of this table shows that ferromagnetism predominates over antiferromagnetism. The weight percent compositions are rounded off nominal values. Of more fundamental value would be the atomic percentages, however, since the atomic weights of Mn, Cr, Ni and Fe are respectively 55, 52, 59 and 56 the weight percentages are sufficiently close to the atomic percentages for the following comments to hold.

Mn seems to be an important element in determining whether an alloy is anti- or ferro-magnetic. Cr does not seem to have the same degree of influence for in Kromarc 58 and 310(S) the Mn + Cr percentage remains roughly constant yet Kromarc 58 with the higher Mn content is antiferromagnetic and 310(S) with the low Mn content is weakly ferromagnetic. The Mn percentages in Table 8-2 suggest that if a non-magnetic alloy is desired it would be worthwhile to examine a composition with Mn (5%), Cr (20%) and more Ni than Fe to keep the ferromagnetic contribution down. Note that the atomic moments of Mn, Cr, Ni and Fe are respectively 5, 4, 0.6 and 2.2 Bohr magnetons so that Ni tends to dilute the ferromagnetism of Fe. We have implicitly -- and very naively -- assumed so far that the antiferromagnetic components Mn and Cr dilute and ultimately swamp the ferromagnetic Ni and Fe. Carr[8] has studied the intrinsic magnetization of the iron transition group of metals in a much more systematic and proper way, but his considerations were only for binary alloys.

Nitronic 33 stainless steel was also characterized for magnetic behavior at 4K in the form of both base metal and as weldments made by three different welding processes. These results (shown in Table 8-3) indicate that the unstrained base metal is antiferromagnetic at 4K regardless of teh condition tested. All weldments made with Nitronic 35W

filler material (which produced from 2 to 5% delta ferrite in the weld fusion zone) were found to be feebly magnetic. However, weldments on Nitronic 33 made by the GTAW process using a special filler material (13-20 MnCb) which did not produce ferrite in the as deposited weld metal were found to be antiferromagnetic like the base metal. Figure 8.2 presents additional room temperature magnetic permeability comparisons of these various Nitronic 33 base metal and weldment conditions and is taken from Ref. 7. Additional RT permeability survey data on various austenitic stainless steels also taken from Ref. 7 is included in Fig. 8.3 and Table 8-4.

8.3 Electrical Measurements

Electrical resistivity measurements were limited to three temperatures -- room (295 K), liquid nitrogen (78 K) and liquid helium (4.2 K). Most alloys show so little resistance change below 78 K that measurements between 78 K and 4.2 K are unnecessary. Measurements were made as before with a standard four contact technique on bars of the materials measuring approximately 3 mm by 3 mm by 2.5 cm. Table 8.5 sets out the resistivity values.

A few general comments are appropriate. For the highly alloyed metals the resistivity is very roughly 100 μΩcm and reasonably temperature independent. This demonstrates that impurities, polycrystallites, multiple phases, etc. dominate the electron scattering over the lattice or phonon contributions. A particular alloy composition determines the resistivity with only very minor changes occurring for different heat treatments, a situation similar to and even more striking than the variation in magnetic properties with heat treatment. PD-135 copper shows a surprisingly small variation in resistivity which is believed to be accounted for by its relatively high "impurity" content of 0.3% Cd and 0.4% Cr. The 4.2 K value of 0.6 μΩcm is very much greater than the OHFC copper value of 0.016 μΩcm. While PD-135 may have more desirable structural properties over OHFC its use as say a damper shield at cryogenic temperatures would be very inferior. However, at room temperature the two materials are similar electrically and would function equally well when acting as screens by eddy current effects.

REFERENCES (Section 8)

1. L. Flansburg, "Magnetism in Austenitic Stainless Steels", thesis (1970), Univ. of Iowa, available from University Microfilms, Ann Arbor, Mich.

2. J.W. Ackermann, W.A. Klawitter and J.J. Drautman, "Magnetic Properties of Commercial Soft Magnetic Alloys at Cryogenic Temperatures", Adv. in Cryogenic Eng., 16, 46 (1971), Ed. by K. D. Timmerhaus, Plenum Press.

3. R. Kolhaus, A.R. Raible and W.D. Weiss, "Über das magnetische Verhalten einiger stabiler austenitischer Chrom-Nickel-Stähle in Bereich tiefer Temperaturen", Arch Eisenhütten, 41 #8, 769 (1970).

4. D.C. Larbalestier and H.W. King, "Austenitic Stainless Steels at Cryogenic Temperatures 1-Structural Stability and Magnetic Properties", Cryogenics, p. 160, March 1973.

5. W. Stutuis and J.R. Dillinger, "Magnetic and Thermal Properties of Some Austenitic Stainless Steels at Low Temperatures", J. Appl. Phys. 44, 2887 (1973).

6. W.J. Carr, Jr., "Intrinsic Magnetization in Alloys", Phys. Rev. 85, 590 (1952).

7. J.M. Wells and M.W. Hagadorn,"Evaluation of Nitronic 33 Stainless Steel for TFTR Device Applications", Westinghouse Research Report 75-8C3-WETWO-R1, September 1975.

Fig. 8.1 – Ferromagnetic and antiferromagnetic behavior in an applied magnetic field

Curve 681976-A

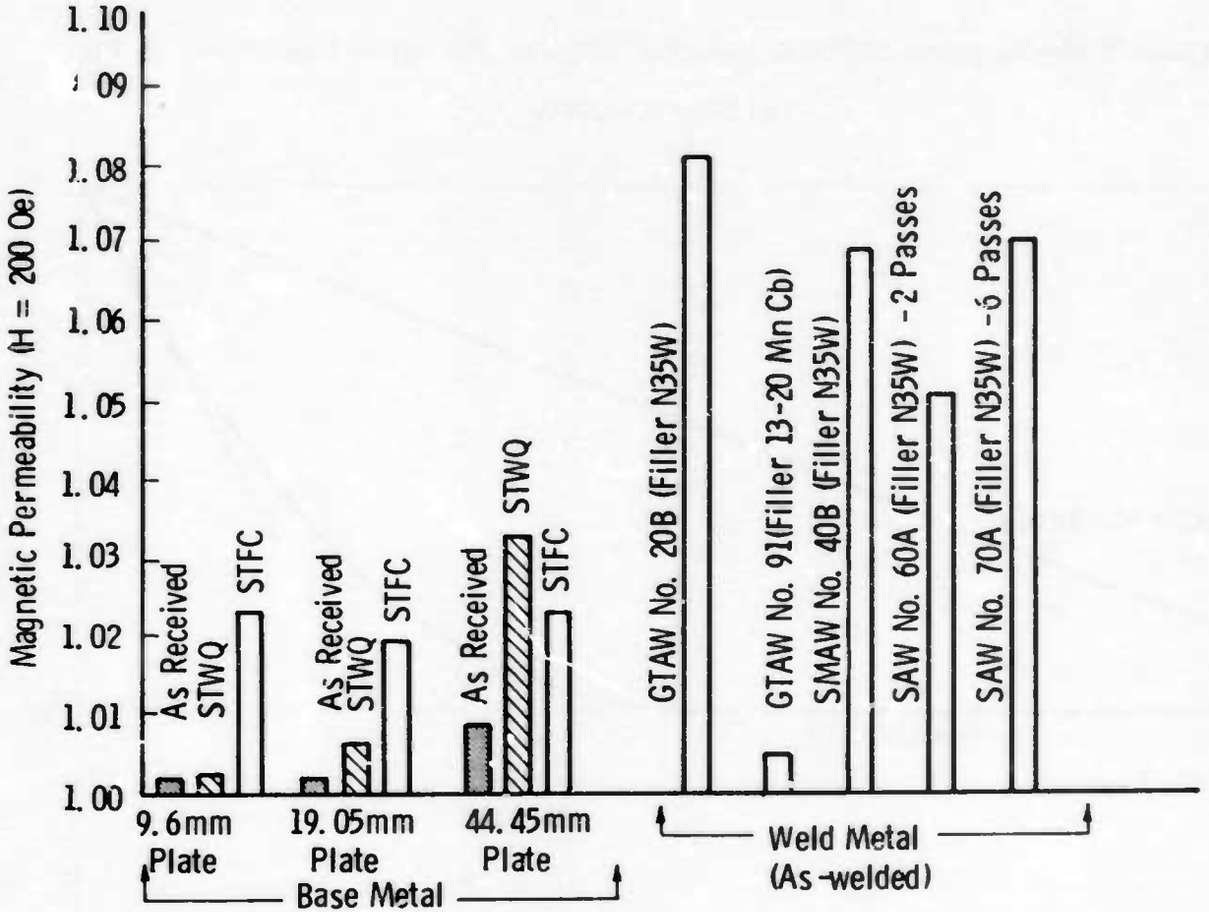

Fig. 8.2—Magnetic permeability measurements at a magnetizing force of 200 oersteds in Nitronic 33 stainless steel base metal and weld metal

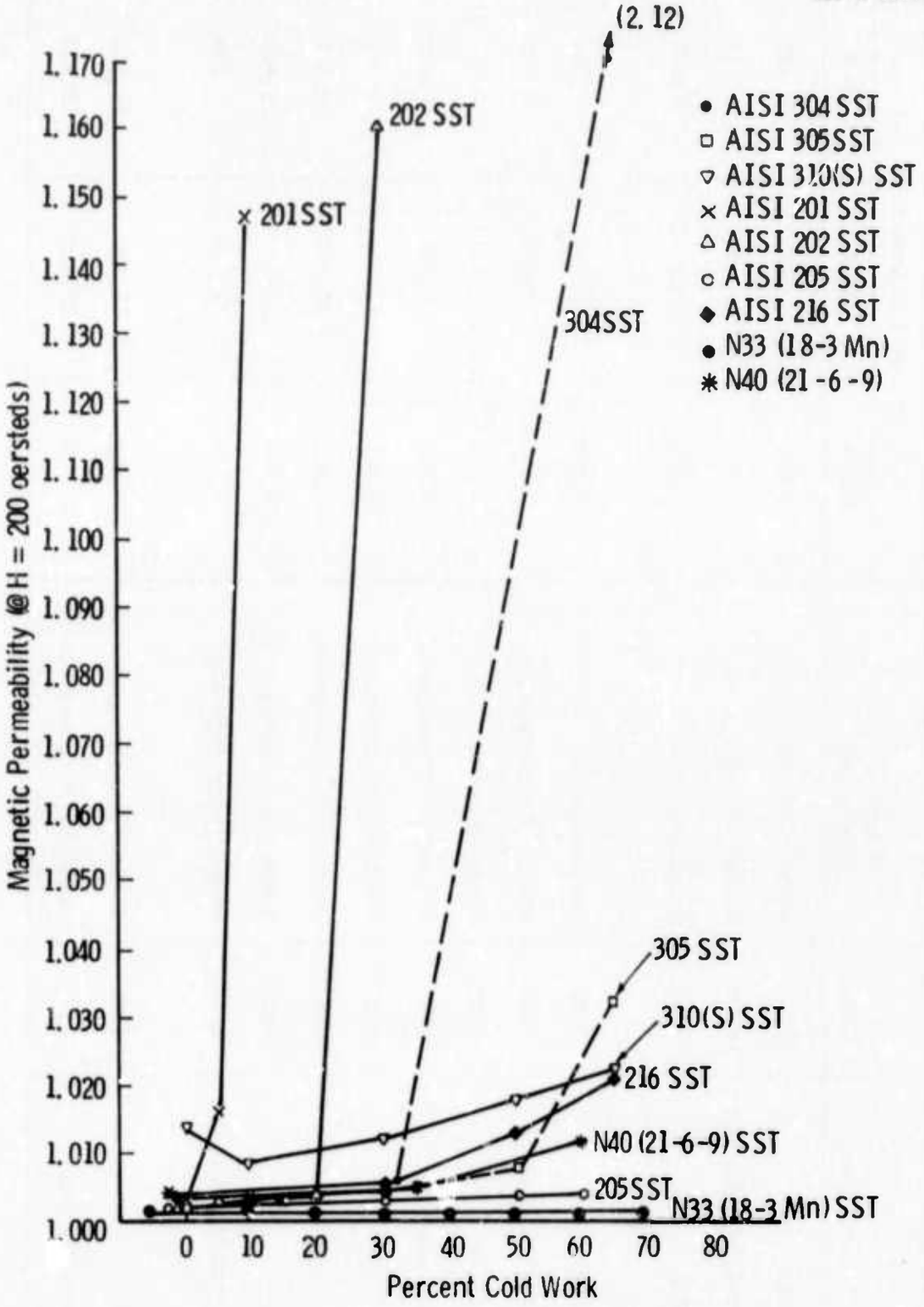

Fig. 8.3—Summary comparison of published magnetic permeability values of various austenitic stainless steels at room temperature

TABLE 8-1

MAGNETIC PROPERTIES OF MATERIALS

Material	Condition	Code	Magnetic Condition	Saturation Induction (G)		
				4.2 K	20 K	78 K
INCONEL 718 -	STDA	64XX	Weakly Ferromagnetic	1,090	996	495
(VIM-VAR)	ST/GTAW/STDA(FZ)	65XX	Weakly Ferromagnetic	1,140	1,060	622
INCONEL 706 -	STDA	70XX	Ferromagnetic	3,110	3,060	2,600
(VIM-EFR)						
INCONEL 706 -	STDA	71XX	Ferromagnetic	3,200	3,100	2,680
(VIM-VAR)	ST/GTAW/STDA	72XX	Weakly Ferromagnetic	1,540	1,430	965
Copper-PD-135	EXT/PHT	15XX	Paramagnetic	$\chi = 3 \times 10^{-6}$	$\chi = 1 \times 10^{-6}$	$\chi = 0.5 \times 10^{-6}$
Fe-68% Ni	Annealed	NBS	Strongly Ferromagnetic	10,700	10,600	10,600
AISI - 416 SS	STQ&T	NBS	Strongly Ferromagnetic	16,400	16,200	16,100
Fe-3% Si	--	NBS	Strongly Ferromagnetic	19,800	19,500	19,500
ARMCO-FE	--	NBS	Strongly Ferromagnetic	21,700	21,700	21,600
INCONEL X750 -	ST/GTAW/STDA	62XX	Weakly Ferromagnetic	1,200	1,100	594
(HIP)						
INCONEL LEA -	STA	73XX	Strongly Ferromagnetic	13,300	13,100	12,700
(AM-VAR)	ST/GTAW/STA	74XX	Strongly Ferromagnetic	12,900	12,800	12,400

TABLE 8-2

COMPARISON OF MAGNETIC PROPERTIES WITH COMPOSITION

Material	Nominal Composition (wt. %)				Magnetic Condition at 4.2 K	Induction at 4.2 K (G)
	Mn	Cr	Ni	Fe		
KROMARC 58†	10	15	22	49	Antiferromagnetic	--
310(S) SS	2	24	20	53	Weakly Ferromagnetic	500
NITRONIC 40	9	21	7	62	Antiferromagnetic	--
NITRONIC 33*	13	18	3	65	Antiferromagnetic	--
416 SS	1	13	--	85	Strongly Ferromagnetic	16,400
INCONEL X-750†	-	15	73	6	Weakly Ferromagnetic	1,200
INCONEL 706†	-	16	42	37	Ferromagnetic	3,200
INCONEL 718†	-	18	53	18	Weakly Ferromagnetic	1,100
INCONEL LEA†	-	--	40	55	Strongly Ferromagnetic	13,000
HASTELLOY B**	0.5	0.3	65	5	Weakly Ferromagnetic	500

*See Reference 7

** Contains also 0.4% Co

†Applies to all base metal and weldment conditions tested.

TABLE 8-3

MAGNETIC PROPERTIES OF THE ALLOY NITRONIC-33

	NITRONIC 33	
Condition*	Magnetic Condition	Induction at 4.2 K
SAW	Feebly Ferromagnetic	330
SMAW	Feebly Ferromagnetic	420
GTAW	Feebly Ferromagnetic	330
STQ	Antiferromagnetic	-
STFC	Antiferromagnetic	-
AR	Antiferromagnetic	-
GTA(13-20)	Antiferromagnetic	-

*Weldments: SAW - (filler N35W)
SMAW - (filler N35W)
GTAW - (filler N35W)
GTA(13-20) - (filler 13-20 MnCb)

*Base Metals: AR - as received
STQ - annealed (solution treated) at 1066°C for 1 hour and water quenched
STFC - annealed (solution treated) at 1066°C for 1 hour and slow furnace cooled.

TABLE 8-4 SUMMARY OF PUBLISHED MAGNETIC PERMEABILITY DATA FOR VARIOUS AUSTENITIC STAINLESS STEEL ALLOYS AT ROOM TEMPERATURE

Material	Heat No.	Annealing Temp.	Magnetizing Force H (Oersteds)	Percent Cold Work							Reference
				0%	5%	10%	20%	30%	50%	65%	
Type 301	317674	1950°F-A.C.	H = 200	1.029	NR	1.630	NR	17.85	37.89	40.77	A-L Data Sheet 145-51860-X
	91904	1950°F-A.C.	H = 200	1.001	NR	1.015	NR	1.698	5.721	12.29	A-L Data Sheet 145-51860-X
	97606	1950°F-A.C.	H = 200	1.036	NR	1.717	NR	16.05	37.16	45.11	A-L Data Sheet 145-51860-X
Type 302	62794	1950°F-A.C.	H = 200	1.004	NR	1.039	NR	1.414	3.214	7.205	A-L Data Sheet 145-51860-X
	11058	1950°F-A.C.	H = 200	1.005	NR	1.079	NR	1.144	5.520	11.77	A-L Data Sheet 145-51860-X
Type 304	328067	1950°F-A.C.	H = 200	1.015	NR	1.064	NR	3.235	8.480	14.41	A-L Data Sheet 145-51860-X
	62880	1950°F-A.C.	H = 200	1.083	NR	1.638	NR	4.762	10.01	19.35	A-L Data Sheet 145-51860-X
	NR	NR	H = 200	1.0040	NR	NR	NR	1.0060	NR	2.12	Alloy Digest (SS-254) May 1971
Type 305	333854	1950°F-A.C.	H = 200	1.002	NR	1.003	NR	1.004	1.008	1.032	A-L Data Sheet 145-51860-X
	NR	NR	H = 200	NR	NR	NR	NR	NR	NR	1.068	Alloy Digest (SS-154) April 1964
Type 310 (S)	45016	2100°F-A.C.	H = 200	1.014	NR	1.009	NR	1.012	1.018	1.022	A-L Data Sheet 145-51860-X
Type 316	52548	1950°F-A.C.	H = 200	1.010	NR	1.003	NR	1.003	1.004	1.006	A-L Data Sheet 145-51860-X
Type 321	11067	1950°F-A.C.	H = 200	1.006	NR	1.008	NR	1.033	1.380	2.493	A-L Data Sheet 145-51860-X
Type 347	35849	1950°F-A.C.	H = 200	1.006	NR	1.017	NR	1.300	3.040	5.243	A-L Data Sheet 145-51860-X
Type 384	FD-93-5	1950°F-A.C.	H = 200	1.004	NR	1.006	NR	1.005	1.006	1.007	A-L Data Sheet 145-51860-X
	FB-74-3	1950°F-A.C.	H = 200	1.004	NR	NR	NR	1.004	1.005	1.005	A-L Data Sheet 145-51860-X
	FB-76-3	1950°F-A.C.	H = 200	1.005	NR	1.006	NR	1.007	1.006	1.006	A-L Data Sheet 145-51860-X
Type 201	345614	1950°F-A.C.	H = 200	1.035	NR	1.501	NR	16.76	27.44	29.78	A-L Data Sheet 145-51860-X
	336316	1950°F-A.C.	H = 200	1.005	NR	1.047	NR	5.886	11.72	19.20	A-L Data Sheet 145-51860-X
	NR	NR	H = 200	1.003	1.016	1.147	2.738	7.006	15.395	NR	Alloy Digest (SS-174) November 1965
Type 202	62886	1950°F-A.C.	H = 200	1.002	NR	1.002	NR	1.021	1.226	1.707	A-L Data Sheet 145-51860-X
	345585	1950°F-A.C.	H = 200	1.020	NR	1.037	NR	1.132	5.493	3.404	A-L Data Sheet 145-51860-X
	NR	NR	H = 200	1.002	1.003	1.004	1.0035	1.16	1.42	NR	Alloy Digest (SS-159) August 1964
Type 205	17172	1950°F-A.C.	H = 200	1.002	NR	1.002	NR	1.003	1.003	1.004	A-L Data Sheet 145-51860-X
	NR	NR	H = 200	1.002	NR	NR	NR	NR	NR	1.004	P. Bonanos, AEC R&D Report TM-227, December 1966
Type 216	NR	NR	H = 200	1.003	NR	NR	NR	1.006	1.013	1.021	Alloy Digest (SS-243) September 1970
Nitronic 33 (Type 18-3MN)	NR	1950°F-A.C.	H = 500	1.0014	NR	1.0013	1.0015	1.0010	1.0011	1.0012	Alloy Digest (SS-286)
			H = 1000	1.0013	NR	1.0012	1.0011	1.0013	1.0012	1.0012	February 1973 also Armco Bulletin No. LA-3173 (April 1973)
Nitronic 40 (Type 21-6-9)	NR	1950°F-A.C.	H = 200	1.004	NR	1.003(15%)	NR	1.005(35%)	NR	1.012	Armco Bulletin LA-7673 November 1973

NR - Not Reported

TABLE 8-5

ELECTRICAL RESISTIVITY OF MATERIALS

Material	Condition	Code	Resistivity in μΩ cm		
			4.2 K	78 K	295 K
INCONEL 718 -	STDA	64XX	111	112	118
(VIM-VAR)	ST/GTAW/STDA(FZ)	65XX	113	113	121
INCONEL 706 -	STDA	70XX	95	96	108
(VIM-EFR)					
INCONEL 706 -	STDA	71XX	96	98	109
(VIM-VAR)	ST/GTAW/STDA	72XX	94	96	114
Copper-PD-135	EXT/PHT	15XX	0.60	0.78	2.3
Fe-68% Ni	Annealed	NBS	12	13	24
AISI - 416 SS	STQ & T	NBS	55	56	71
Fe-3% Si	--	NBS	39	40	49
ARMCO-Fe	--	NBS	3.2	4.1	14
INCONEL X750 -	ST/GTAW/STDA	62XX	117	118	139
(HIP)					
INCONEL LEA -	STA	73XX	71	76	98
(AM-VAR)	ST/GTAW/STA	74XX	72	76	99

ACKNOWLEDGEMENT

The authors wish to gratefully acknowledge the following Westinghouse personnel for their respective advice, contributions, and cooperation and encouragement in the conduct of this work:

Dr. J. H. Parker, Jr.
Dr. D. W. Deis
J. L. McCabria
D. C. Litz
G. G. Lessmann
W. T. Reynolds
R. M. Slepian
J. E. Smith
B. F. Yonkovitz
W. R. Kuba
E. T. Wessel
W. A. Pryle
D. R. Young
R. R. Hovan
A. R. Petrush
W. H. Halligan
R. C. Brown
M. J. Airgood
M. A. Braithwaite

In addition, special acknowledgement is extended to (1) The Huntington Alloys Product Division of the International Nickel Company, for providing The Low Expansion Alloy and (2) to the Phelps Dodge Copper Products Company for providing the PD-135 Copper Alloy at no charge to the program.

APPENDIX I

Scientific Paper 75-1E7-CRYMT-P1 May 7, 1975
Proprietary Class: Unrestricted

CRYOGENIC FRACTURE MECHANICS PROPERTIES OF SEVERAL MANUFACTURING PROCESS/HEAT TREATMENT COMBINATIONS OF INCONEL X750

W. A. Logsdon
Mechanics Department
Westinghouse Research Laboratories
Pittsburgh, Pennsylvania 15235

INTRODUCTION

Inconel X750, an austenitic nickel base superalloy, has been extensively utilized in the torque tube, damper shield, outer rotor shell and stub shafts of a Westinghouse prototype 5 MVA superconducting generator.[1,2] To aid in evaluating the fail-safe performance of this superconducting generator, the fracture mechanics as well as mechanical properties of several manufacturing process/heat treatment combinations of Inconel X750 were determined in cryogenic environments. These included three commercial melting practices plus hot isostatic pressed Inconel X750. The two heat treatments explored included a solution treat (ST) and a solution treat and double age (STDA).

The -452°F (4.2 K) yield strengths of the various manufacturing process/heat treatment combinations of Inconel X750, each with essentially the same chemical composition, ranged from 106.8 ksi (736 MPa) to 173.2 ksi (1194 MPa) while the fracture toughness at this same temperature ranged from 92.2 ksi$\sqrt{in.}$ (102 MPa$\sqrt{m}$) to 216.0 ksi$\sqrt{in.}$

(239 MPa$\sqrt{m}$). In addition, the fracture toughness of Inconel X750 decreased only slightly with decreasing temperature over the temperature range 75°F (297 K) to -452°F (4.2 K). Finally, a general trend for austenitic materials may have been demonstrated by Inconel X750 whereby the growth rate of fatigue cracks at room temperature was at least equal to or in most cases substantially greater than at -452°F (4.2 K).

MATERIALS

Four forms of Inconel X750 materials including three commercial melting practices plus hot isostatic pressed Inconel X750, each essentially of the same chemical composition, were examined. The chemical compositions and heat treatments relative to these materials are presented in Table I. Hardness and grain size measurements are included in Table II.

The three commercial melting practices relative to Inconel X750 included:

VIM-VAR - Vacuum induction melted followed by vacuum arc remelt

AAM-VAR - Air arc melted followed by vacuum arc remelt

VIM - Vacuum induction melted

The (VIM-VAR) Inconel X750 was purchased as a ten inch (25.4 cm) diameter, hot finished forging quality (HFFQ) round. The (AAM-VAR) Inconel X750 was obtained as a four inch (10.2 cm) diameter HFFQ round while the (VIM) Inconel X750 was obtained as a two inch (5.1 cm) diameter hot finished (HF) round.

The largest grain size is associated with (VIM-VAR) Inconel X750 and the smallest with (VIM) Inconel X750, while significant grain size differences between adjacent grains within a particular microstructure exist in both (VIM-VAR) and (AAM-VAR) Inconel X750.

The starting material for hot isostatic pressed Inconel X750 was (VIM-VAR) Inconel X750 billet stock which was reduced to powder through the inert gas atomizing process by Federal-Mogul. All test specimens were manufactured according to the following HIP process:

HIP at 2190°F (1473 K) and 10,000 psi (69 MPa) (Argon)

An examination of this material both as HIPed and HIP/STDA conducted with a scanning electron microscope revealed a few infrequent small pores at interparticle boundaries, although full consolidation was achieved. Hardness of the HIPed Inconel X750 (both as HIPed and HIP/STDA) was approximately 15 percent higher than the corresponding (VIM-VAR) Inconel X750 (note Table II).

EXPERIMENTAL PROCEDURES

Fracture Toughness

The well documented linear elastic (K_{Ic}) fracture criterion with its inherent plane strain specimen size limitation cannot produce valid fracture toughness results (per the ASTM Test for Plane Strain Fracture Toughness of Metallic Materials, E399-74) on tough austenitic materials such as Inconel X750 unless specimens of very large thickness are employed, which in turn are not representative of the cross-sectional thicknesses found in actual cryogenic structures. Furthermore, if a failure should occur, proper design of cryogenic structures or components would cause these structures or components to fail plastically (elastic plastic fracture) as opposed to catastrophically (linear elastic fracture). Therefore, the fracture toughness of Inconel X750 was obtained via the elastic plastic (J_{Ic}) fracture criterion[3,4] and the associated resistance curve test technique for determining elastic plastic fracture toughness values.[5]

All fracture toughness tests were conducted on one-half inch (1.27 cm) thick compact tension specimens. The tests were performed on a servo-hydraulic test machine using stroke control at a ram rate of 0.0005 in./sec. (0.127 m/sec.). All fracture toughness specimens were precracked at room temperature at loads considerably less than those anticipated in the subsequent fracture toughness tests. Displacement

during these fracture toughness tests was measured via a linear variable differential transformer (LVDT) attached to the specimen front face. All specimens removed from round stock (VIM-VAR, AAM-VAR and VIM) were oriented so their cracks would propagate in a radial direction. The specimens machined from plate stock (HIP) were oriented so the crack starter notch was parallel to the principal longitudinal direction. According to the Crack Plane Orientation Identification Code per the ASTM Test for Plane Strain Fracture Toughness of Metallic Materials (E399-74), these orientations are referred to as the C-R and T-L orientations, respectively.

Crack Growth Rate

All fatigue crack growth rate tests were conducted on half inch (1.27 cm) thick wedge open loading (WOL) geometry compact tension specimens except for the room temperature, air environment fatigue crack growth rate tests on (VIM-VAR) Inconel X750, where one inch (2.54 cm) thick WOL specimens were utilized. Test specimen orientation was identical with that of the corresponding fracture toughness test specimens. All WOL specimens were precracked at room temperature at loads considerably less than those employed in the subsequent fatigue crack growth rate test. Since crack growth rates can be influenced by abrupt temperature changes, the crack growth rate was allowed to stabilize before data were accepted as valid.

Fatigue crack growth rate testing was conducted on a universal hydraulic fatigue machine under sinsoidal tension loading. The maximum

alternating load (ΔP) was maintained constant throughout each individual test. Test frequency equalled 10 Hertz.

Instanteous crack length in the cryogenic and room temperature environment one half inch thick WOL specimen tests was determined by first measuring test specimen crack opening displacement by utilizing a linear variable differential transformer (LVDT) attached to the specimen front face and finally transforming this crack opening displacement value via specimen compliance into crack length. Test specimen compliance was determined by utilizing a test procedure originally developed by Novak and Rolfe.[6]

The extent of fatigue crack growth encountered during room temperature, air environment cyclic loading (1TWOL test specimens) was measured and recorded with an ultrasonic nondestructive testing crack growth monitor.[7]

RESULTS

Tensile Tests

Smooth-bar uniaxial tensile tests were conducted to determine the 0.2 percent offset yield strength, ultimate strength, reduction in area and percent elongation of Inconel X750. Tensile specimen geometry was 0.20 in. (0.51 cm) diameter with a 1.00 in. (2.54 cm) gauge length. The fracture plane orientation of the tensile specimens was equivalent to that of the corresponding fracture toughness and crack growth rate specimens.

The tensile properties of six manufacturing process/heat treatment combinations of Inconel X750 are presented graphically in Figures 1 and 2. For the most part, each data point is the average of two tensile tests. Note the (VIM) Inconel X750 produced the maximum 0.2 percent yield strength level compared with all other manufacturing process/heat treatment combinations of Inconel X750 throughout the majority of the test temperature range. In addition, (VIM) Inconel X750 experienced the largest increase in yield strength with decreasing temperature. Also, note the 0.2 percent yield strength of (AAM-VAR) Inconel X750 exceeds that of solution treated and double aged (VIM-VAR) Inconel X750 throughout the entire test temperature range. In other words, a major processing constraint demonstrated for Inconel X750 is inferred as the requirement for adequate thermal-mechanical working. Recall (VIM-VAR) Inconel X750 was the largest as received billet and (VIM) Inconel X750 the smallest.

In this case, the most heavily worked structures produced the higher yield strengths. Strength levels were inverse to as received billet size. As expected, strength appears to be an inverse function of grain size. From a ductility standpoint, this shows up as improved ductility in Fig. 2 for (AAM-VAR) and (VIM) Inconel X750 versus (VIM-VAR) Inconel X750.

Further conformation of grain size effects is obtained in the powder processed (HIP) Inconel X750. Recall, the starting material before hot isostatic pressing was (VIM-VAR) Inconel X750. Note, hot isostatic pressing the Inconel X750 resulted in a modest strength increase and improved ductility.

A final grain size effect can be observed in the decrease in yield strength with decreasing temperature (between -320°F and -452°F) demonstrated by (VIM-VAR) Inconel X750. This apparent decrease in yield strength at -452°F (4.2 K) may be explained by the fact that all tensile specimens tested at -452°F (4.2 K) had a grain size about twice as large as those tested at higher temperatures.[8]

Solution treating and double aging the Inconel X750 (both VIM-VAR and HIP) resulted in a 15 to 25 percent increase in yield strength and a significant decrease in ductility.

Notched Tensile Tests

The purpose of notched tensile tests is to screen the notch toughness in terms of the comparison parameter defined as the ratio of notched tensile fracture strength to the tensile yield strength of a particular material for a specific notch acuity. Increasing values of

the ratio above 1.0 are considered to indicate increasing ability of the material for plastic deformation at the notch tip. Stated alternatively, increasing values of the ratio above 1.0 can be utilized as a measure of the material's resistance to catastropic brittle fracture.

In all cases, the root radius at the bottom of a particular test specimen's sharp V-notch was adjusted to yield a stress concentration factor (K_t) equivalent to 10. It should be pointed out that the notched tensile fracture strength was calculated by dividing the maximum load experienced by a test specimen, or in a few cases where the load dropped slightly before failure dividing the fracture load, by its original as opposed to final cross-sectional area. This was largely due to the great difficulty in accurately measuring the extremely small change in test section diameter (hence cross-sectional area) experienced by the test specimen.

The notched tensile properties of Inconel X750 are summarized in Table II. Note for Inconel X750 regardless of manufacturing process, heat treatment or test temperature, the ratio of notched tensile fracture strength to tensile yield strength is always greater than one, the minimum value equaling 1.5.

Fracture Toughness Tests

The elastic plastic (J_{Ic}) fracture toughness values of Inconel X750 are summarized in Table III while the associated J resistance curves are illustrated in Fig. 3. For comparison purposes, the ratios K_{Ic}/σ_{ys} and $(K_{Ic}/\sigma_{ys})^2$ are also included in Table III. Typically, the material with the highest K_{Ic}/σ_{ys} ratio can be expected to be the most

tough material for a given application.[9] The plane strain crack size factor, $(K_{Ic}/\sigma_{ys})^2$, provides a measure of toughness that accounts in a single parameter for the interactions of K_{Ic} and strength on crack size tolerance.[10,11]* Stated alternatively, when conducting a parametric fracture mechanics analysis (that is, the applied stress is considered to be a fixed percentage of the particular material's yield strength), the critical defect size for failure in one cycle of loading will be proportional to the crack size factor.[9]

Returning to Table III, note the fracture toughness of solution treated (VIM-VAR) Inconel X750 was determined at both room temperature as well as -452°F (4.2 K). The fracture toughness of solution treated (VIM-VAR) Inconel X750 decreases by only 11 percent in going from 75°F (297 K) to -452°F (4.2 K). This behavior is typical for austenitic materials, where the fracture toughness essentially remains constant with temperature from room temperature down to as low as -452°F (4.2 K). Further conformation of this behavior has been presented by Tobler, et al, who observed an 8 percent decrease in fracture toughness of solution treated and double aged Inconel X750 over the temperature range 75°F (297 K) to -320°F (77 K).[12] In addition, Pettit, et al, observed this same moderate insensitivity of fracture toughness to temperature on Inconel 718 sheet and welds.[13]

---

*The crack size factor is not related to critical crack size at a stress equal to the yield strength but only under small-scale yield, that is, at applied stresses appreciably below the yield strength.[10,11]

Clearly, the highest fracture toughness and crack size factor results from (AAM-VAR) Inconel X750. Note also the fracture toughness of (VIM) and unheat treated (HIP) Inconel X750 are quite adequate. The fracture toughness demonstrated by (VIM-VAR) and (HIP/STDA) Inconel X750, however, are considerably below those of the other manufacturing process/heat treatment combinations of Inconel X750. According to Kossowsky, the low fracture toughness of the (VIM-VAR) Inconel X750 can be attributed in part to the continuous precipi ation of carbides in the grain boundaries.[14] These carbides provide easy crack initiation sites and a continuous path for crack propagation. Thus, cracking initiates at lower stress levels and crack propagation through the boundaries encounters little resistance. Recall, the starting material before hot isostatic pressing was (VIM-VAR) Inconel X750. On the other hand, neither the (AAM-VAR) or (VIM) Inconel X750 exhibited continuous chains of grain boundary carbides, which accounts in part for their high ductility and fracture toughness.[14]

It is interesting to note that the -452°F (4.2 K) fracture toughness values of the various manufacturing process/heat treatment combinations of Inconel X750, each with essentially the same chemical composition, ranged from 92.2 ksi$\sqrt{in.}$ (102 MPa$\sqrt{m}$) to 216.0 ksi$\sqrt{in.}$ (239 MPa$\sqrt{m}$) while the yield strength at this same temperature ranged from 106.8 ksi (736 MPa) to 173.2 ksi (1194 MPa). Obviously, a designer must select not only the best material for a particular application but also the best manufacturing process/heat treatment combination relative to that material.

Crack Growth Rate Tests

The fatigue crack growth rate data generated on the various manufacturing process/heat treatment combinations of Inconel X750 are summarized in Fig. 4. The raw log $\frac{da}{dN}$ versus log ΔK data demonstrated the nearly linear relationship typical of most fatigue crack growth rate data. Since this linear relationship existed, the crack growth rate data was expressed in terms of the generalized fatigue crack growth rate law developed by Paris.[15] This crack growth rate law is expressed as:

$$\frac{da}{dN} = C_o \Delta K^n \qquad (1)$$

where $\frac{da}{dN}$ is the rate of crack growth, C_o is an intercept constant determined from the log $\frac{da}{dN}$ versus log ΔK plot, n is the slope of the log-log plot and ΔK is the stress intensity factor range.

Returning to Fig. 4 perhaps the most obvious conclusion is that, for two of the three cases where both room temperature and -452°F (4.2 K) fatigue crack growth rate tests were conducted (Inconel X750 VIM-VAR and AAM-VAR), the growth rate of fatigue cracks is significantly faster at room temperature than at -452°F (4.2 K). For (VIM) Inconel X750, the growth rate of fatigue cracks was identical for each of the three temperatures investigated. Therefore, a general trend for austenitic materials may have been demonstrated by Inconel X750 whereby the growth rate of fatigue cracks at room temperature is at least equal to or in most cases substantially greater than at -452°F (4.2 K). Further clarification of this trend has been reported by Tobler, et al, who found

the fatigue crack growth rates lower at cryogenic temperatures than at room temperature for AISI 310 stainless steel and A-286 as well as Inconel X750.[12] If this trend toward faster crack growth rates at room temperature versus -452°F (4.2 K) is substantiated by future tests on several additional austenitic materials, conservative room temperature fatigue crack growth rate properties could be utilized when performing a fracture mechanics analysis on an austenitic material structure or component subjected to a liquid helium environment and expensive cryogenic environment fatigue crack growth rate tests could be eliminated.

Clearly, among the various manufacturing process/heat treatment combinations of Inconel X750 investigated, the (AAM-VAR) Inconel X750 has the most conservative fatigue crack growth rate properties. Recall, (AAM-VAR) Inconel X750 also yielded, by a significant margin, the highest fracture toughness of all the manufacturing process/heat treatment combinations of Inconel X750 and as such looks extremely attractive for cryogenic structural applications. Actually, in those cases where the various Inconel X750's were solution treated and double aged, above a stress intensity range of approximately 40 ksi$\sqrt{in.}$ (44 MPa$\sqrt{m}$) the fracture toughness and fatigue crack growth rate properties paralleled each other; that is, the greater the fracture toughness the slower the fatigue crack growth rate. This behavior is expected based on the work done by Kossowsky, who, as previously mentioned, found continuous chains of grain boundary carbides in (VIM-VAR) Inconel X750 but none in (AAM-VAR) or (VIM) Inconel X750.[14] Since these carbides provide easy crack initiation sites and a continuous path for crack propagation,

cracking initiates at lower stress levels and crack propagation through the boundaries encounters little resistance. Therefore, not only is the fracture toughness lowered but the growth rate of fatigue cracks is increased.

CONCLUSIONS

Several general conclusions can be drawn relative to the cryogenic fracture mechanics and mechanical properties of Inconel X750. First, a major processing constraint demonstrated for Inconel X750 is inferred as the requirement for adequate secondary working in breaking down cast ingot structures into wrought structures. Strength levels were inverse to as received billet size as well as grain size.

In addition, the fracture toughness of solution treated vacuum induction melted/vacuum arc remelted Inconel X750 decreased only slightly with decreasing temperature (over the temperature range 75°F (297 K) to -452°F (4.2 K)). This behavior is typical of austenitic materials, where the fracture toughness essentially remains constant with decreasing temperature.

Finally, a general trend for austenitic materials may have been demonstrated by Inconel X750 whereby the growth rate of fatigue cracks at room temperature is at least equal to or in most cases significantly greater than at -452°F (4.2 K). If this trend toward faster crack growth rates at room temperature versus -452°F (4.2 K) is substantiated by future tests on several additional austenitic materials, conservative room temperature fatigue crack growth rate properties could be utilized when performing a fracture mechanics analysis on an austenitic material structure or component subjected to a liquid helium environment and expensive cryogenic environment fatigue crack growth rate tests could be minimized or possibly eliminated.

ACKNOWLEDGMENTS

The author gratefully acknowledges Drs. J. M. Wells and R. Kossowsky of the Westinghouse Research Laboratories for their advice, contributions and cooperation in the conduct of this work and to Messrs. W. H. Pryle, D. R. Young, R. R. Hovan, A. R. Petrush, W. H. Halligan and R. C. Brown for their contributions to the experimental phases of this work. Special acknowledgment is extended to the Huntington Alloy Product Division of the International Nickel Company, Inc., for providing the Inconel X750 (AAM-VAR and VIM) material and for their helpful comments regarding commercial melting and refining practices for this alloy.

This work was supported in part by National Bureau of Standards (NBS) Contract CST-8304. The views and conclusions contained in this document are those of the author and should not be interpreted as necessarily representing the official policies, either expressed or implied, of the Advanced Research Projects Agency or the United States Government.

REFERENCES

1. Blaugher, R. D., Fagan, T. J., Parker, J. H., Jr., Wells, J. M. and McCabria, J. L., "A High Speed Superconducting Generator," Proc. Intl. Cryogenic Engineering Conference, 1974, Kyoto, Japan (to be published).
2. Parker, J. H., Jr., Blaugher, R. D., Patterson, A., Vecchio, P. D. and McCabria, J. L., "A High Speed Superconducting Rotor," Westinghouse Scientific Paper 74-8J2-SCGEN-P2, October 1974.
3. Begley, J. A. and Landes, J. D., "The J Integral as a Fracture Criterion," Fracture Toughness, Proceedings of the 1971 National Symposium on Fracture Mechanics, Part II, ASTM STP 514, American Society for Testing and Materials, 1972, pp. 1-20.
4. Landes, J. D. and Begley, J. A., "The Effect of Specimen Geometry on J_{Ic}," Fracture Toughness, Proceedings of the 1971 National Symposium on Fracture Mechanics, Part II, ASTM STP 514, American Society for Testing and Materials, 1972, pp. 24-39.
5. Landes, J. D. and Begley, J. A., "Test Results from J-Integral Studies: An Attempt to Establish a J_{Ic} Testing Procedure," Fracture Analysis, ASTM STP 560, American Society for Testing and Materials, 1974, pp. 170-186.

6. Novak, S. R. and Rolfe, S. T., "Modified WOL Specimen for K_{ISCC} Environmental Testing," Journal of Materials, JMLSA, Vol. 4, No. 3, September 1969, pp. 701-728.

7. Clark, W. G., Jr. and Ceschini, L. J., "An Ultrasonic Crack Growth Monitor," Materials Evaluation, August 1969, p. 180.

8. Lessmann, G. G., Logsdon, W. A., Kossowsky, R., Mathur, M. P. and Wells, J. M., "Structural Materials for Cryogenic Applications, First Semi-annual Progress Report," Westinghouse Research Report 74-9D4-CRYMT-R1, March 1974.

9. Wessel, E. T., Clark, W. G. and Wilson, W. K., "Engineering Methods for the Design and Selection of Materials Against Fracture," U.S. Army Tank-Automotive Center Report AD No. 801005, June 1966.

10. Brown, W. F., Jr. and Srawley, J. E., "Commentary on Present Practice," Review of Developments in Plane Strain Fracture Toughness Testing, ASTM STP 463, American Society of Testing and Materials, 1970, pp. 216-248.

11. Vishnevsky, C. and Steigerwald, E. A., "Plane Strain Fracture Toughness of Some Cryogenic Materials at Room and Subzero Temperatures," Fracture Toughness Testing at Cryogenic Temperatures, ASTM STP 496, American Society for Testing and Materials, 1971, pp. 3-26.

12. Tobler, R. L., Mikesell, R. P., Durcholz, R. L. and Reed, R. P., "Fatigue and Fracture Toughness Testing at Cryogenic Temperatures," in Semi-annual Report on Materials Research in Support of Superconducting Machinery, NBSIR 74-393, National Bureau of Standards, Oct. 1974, pp. 57-121.

13. Pettit, D. E., Feddersen, C. E. and Mindlin, H., "Flaw Growth Behavior of Inconel 718 at Room and Cryogenic Temperature," NASA Report CR-101942, Battelle-Columbus Laboratories, Columbus, Ohio, Contract NAS 9-7689, 1969.

14. Kossowsky, R., "Microstructures of Inconel X750 Materials for Cryogenic Structural Applications," to be presented at the International Cryogenic Materials Conference, Queen's University, Kingston, Ontario, Canada, July 22-25, 1975.

15. Paris, P. C., "The Fracture Mechanics Approach to Fatigue," Proc. Tenth Sagamore Army Materials Research Conference, August 1963, Syracuse University Press, 1964.

Table I

Chemical Compositions and Heat Treatments of Inconel X750

Chemical Compositions, Wt. Percent

Manu. Process	C	P	S	Si	Mn	Ni	Cr	Nb +Ta	Cu	Fe	Al	Ti	Co	O	N	H	Ar
VIM-VAR	.04	.003	<.001	.11	.089	73.0	15.2	.90	.022	6.47	.92	2.40	.017	.0016	.004	.00012	
AAM-VAR	.02	.004	.007	.24	.12	74.82	14.19	.95	.06	6.22	.73	2.62	.051	.0006	.004	.00007	
VIM	.04	.004	.003	.27	.13	73.02	15.40	.89	.04	6.87	.68	2.64	.009	.0006	.007	.00010	
HIP	.04	.003	<.001	.11	.089	73.0	15.2	.90	.022	6.47	.92	2.40	.017	.0099	.0056	.000004	<.0001
HIP/STDA	.04	.003	<.001	.11	.089	73.0	15.2	.90	.022	6.47	.92	2.40	.017	.013	.0060	.000022	<.0001

Heat Treatments

Solution Treat	ST	1800°F (1255 K) - 1 hr - Air Cool
Solution Treat and Double Age	STDA	ST, then age at 1350°F (1005 K) - 8 hours- Furnace Cool to 1150°F (894 K), hold 8 hrs and Air Cool

Table II

Hardness, Grain Size and Notched Tensile Properties of Inconel X750

Manu. Process	Heat Treatment	Hardness	Grain Size (ASTM No.)	Temperature 75°F (297 K) σ_{ys}	NTS	NTS/σ_{ys}	-320°F (77 K) σ_{ys}	NTS	NTS/σ_{ys}	-452°F (4.2 K) σ_{ys}	NTS	NTS/σ_{ys}
VIM-VAR	ST	29.5 R_c	3.5	96.2	174.2	1.7	111.6	194.7	1.6	106.8	204.6	1.9
VIM-VAR	STDA	35.7 R_c	3.5	119.5	200.5	1.8	129.4	204.2	1.7	125.7	214.7	1.7
AAM-VAR	STDA	36.0 R_c	6.5	123.0	223.8	1.8	133.3	241.9	1.8	141.3	256.1	1.8
VIM	STDA	38.5 R_c	9	133.1	244.8	1.8	164.8	254.2	1.5	173.2	257.2	1.5
HIP	--	35.0 R_c	8	107.8	200.0	1.9	124.1	222.4	1.8	130.1	233.6	1.8
HIP	STDA	41.0 R_c	8	134.9	232.3	1.7	147.3	246.3	1.7	150.5	246.2	1.6

1 ksi = 6.89 MPa

Table III

Fracture Toughness and Fatigue Crack Growth Rate Properties of Inconel X750

Manu. Process	Heat Treatment	Test Temp. (°F)	Yield Strength (ksi)	J_{Ic} (lb/in)	K_{Ic} ksi $\sqrt{in.}$	$\frac{K_{Ic}}{\sigma_{ys}}$	$(\frac{K_{Ic}}{\sigma_{ys}})^2$	n	Co
VIM-VAR	ST	-452	106.8	245	92.2	0.86	0.75	8.0	2.04×10^{-18}
VIM-VAR	ST	75	96.2	320	103.6	1.08	1.16	7.0	4.83×10^{-16}
VIM-VAR	STDA	-452	125.7	138	69.2	0.55	0.30	8.0	2.04×10^{-18}
AAM-VAR	STDA	-452	141.3	1350	216.0	1.53	2.34	3.45	8.26×10^{-12}
VIM	STDA	-452	173.2	500	131.5	0.76	0.58	4.4	1.57×10^{-12}
HIP	--	-452	130.1	465	126.8	0.97	0.95	3.9	6.72×10^{-12}
HIP	STDA	-452	150.5	233	89.7	0.60	0.36	4.85	2.62×10^{-13}

1 ksi = 6.89 MPa

$1 \frac{lb}{in.} = 175.1 \frac{N}{m}$

1 ksi$\sqrt{in.}$ = 1.107 MPa$\sqrt{m}$

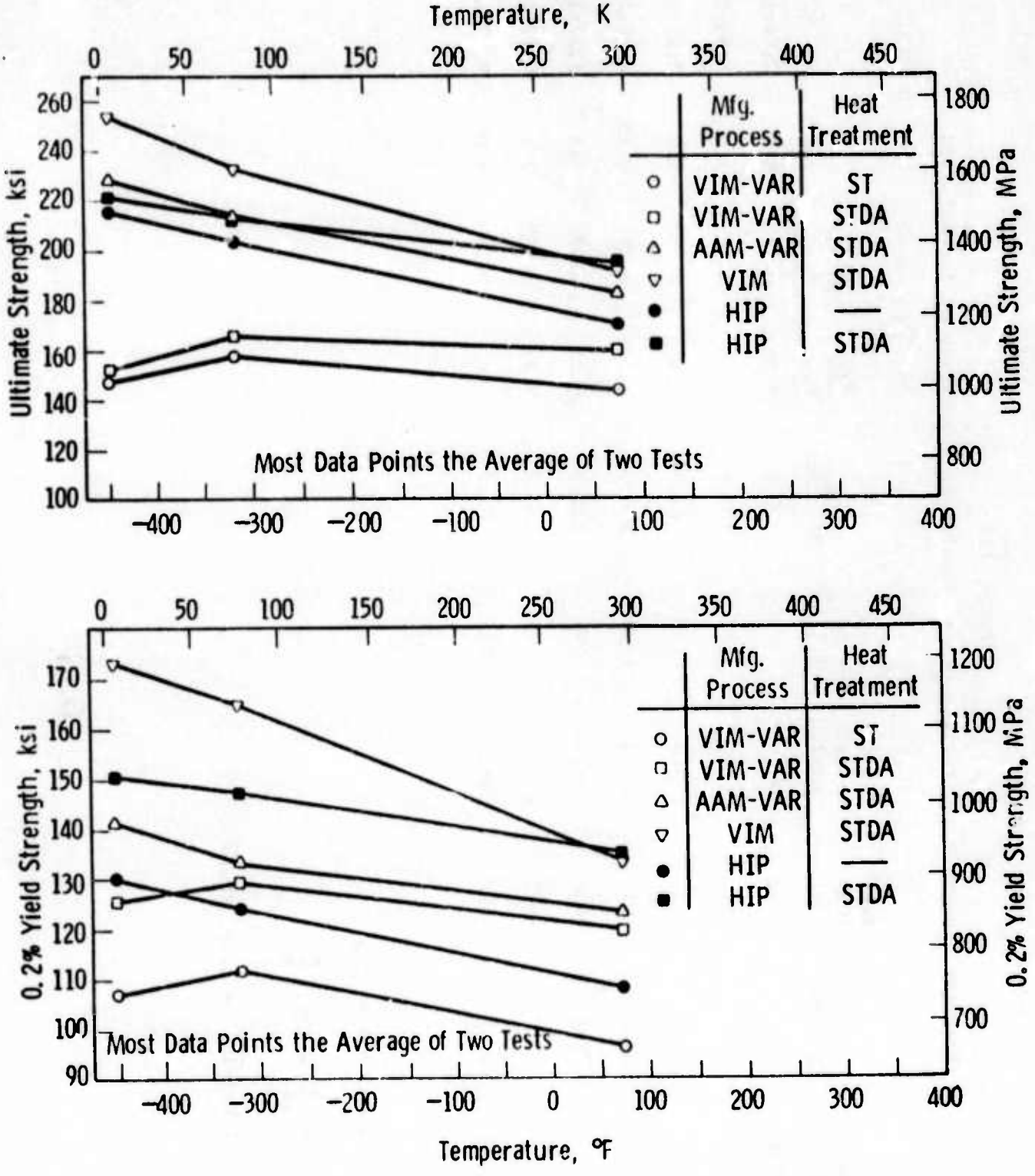

Fig 1 – Yield strengths and ultimate strengths of Inconel X750, various manufacturing process/ heat treatment combinations

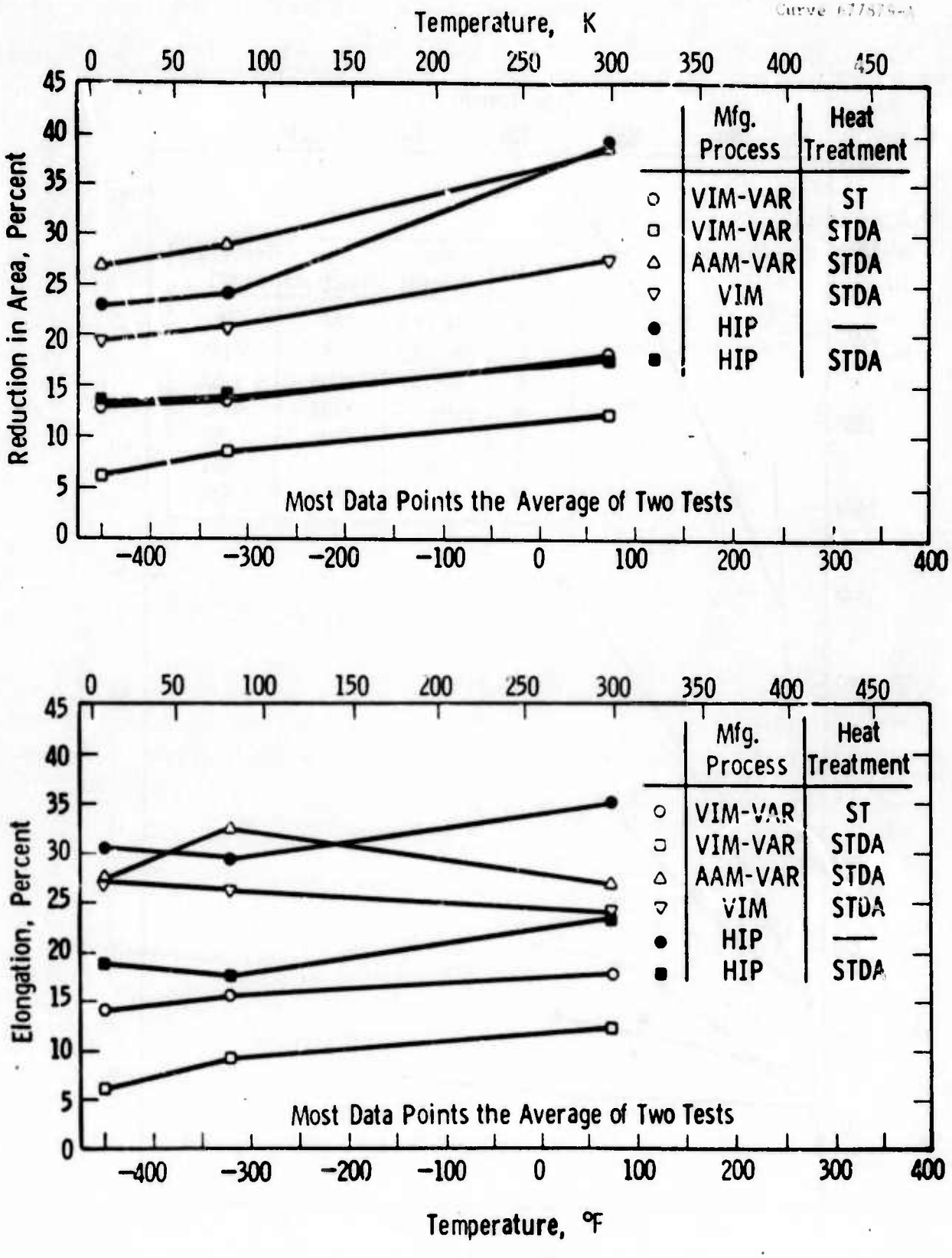

Fig. 2 —Reduction in area and elongation of Inconel X750, various manufacturing process/heat treatment combinations

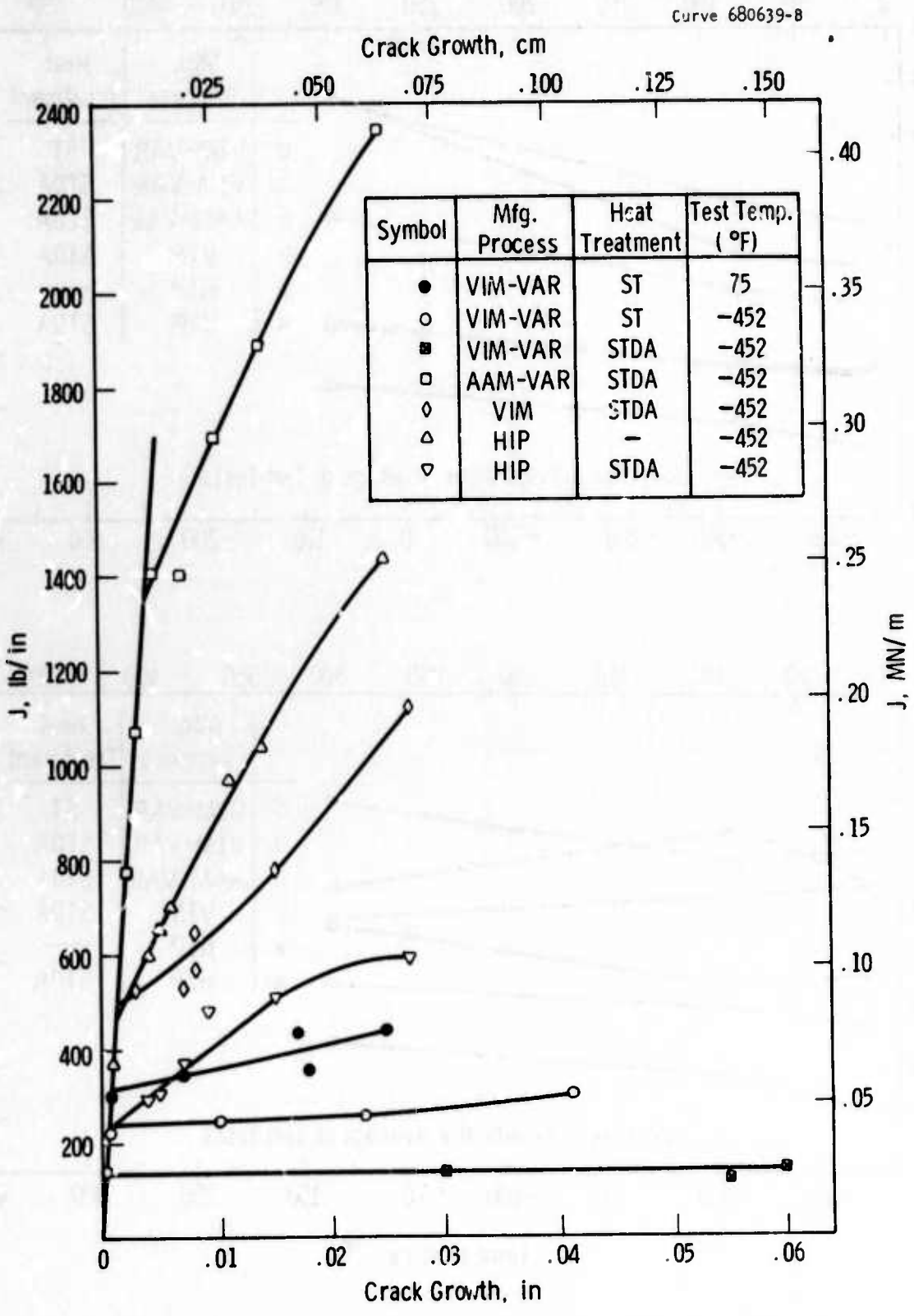

Fig. 3—J resistance curves for various manufacturing process/ heat treatment combinations of Inconel X750

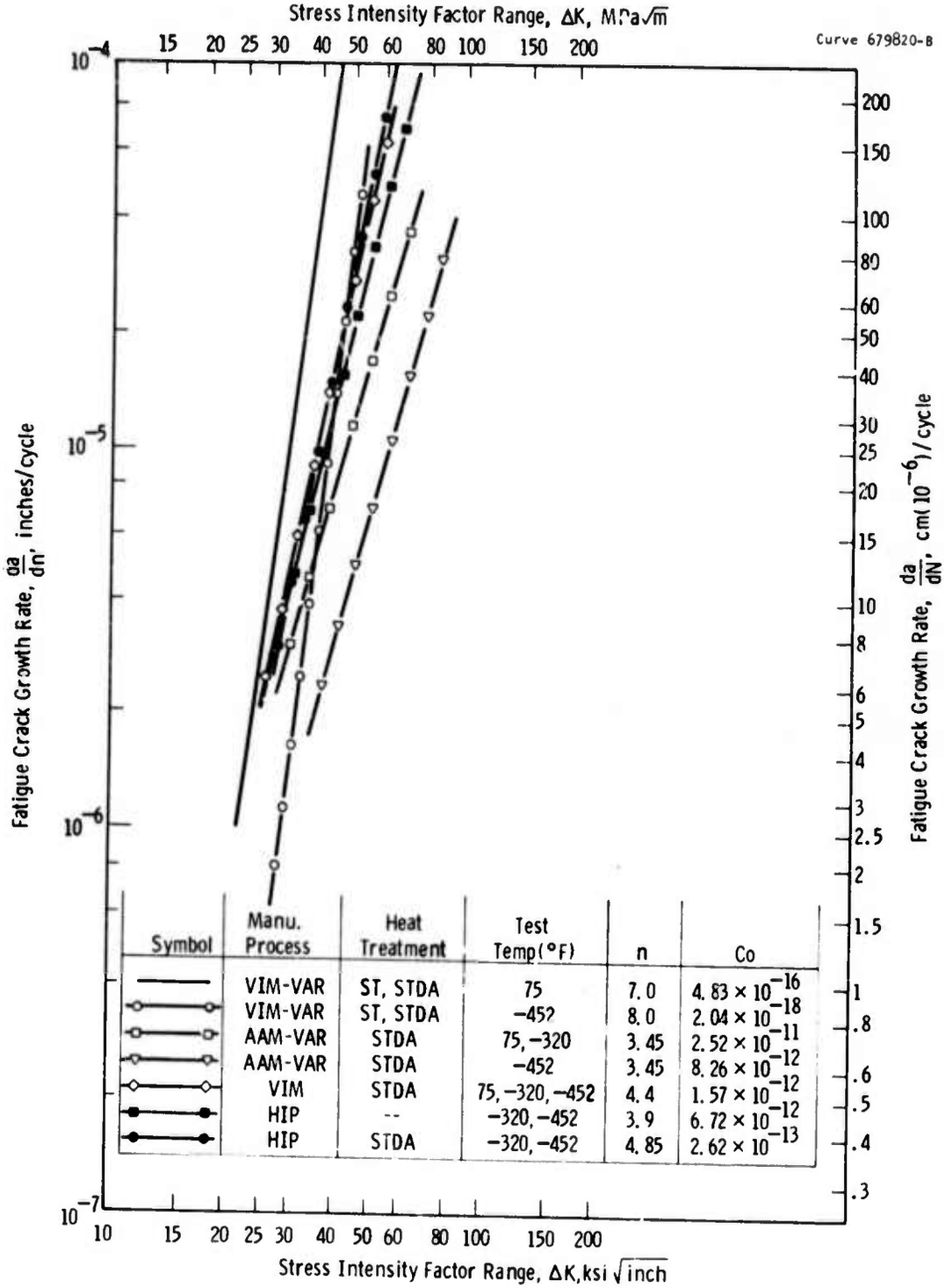

Fig. 4 —Comparison of the fatigue crack growth rate properties generated for Inconel X 750

APPENDIX II

Scientific Paper 75-9D4-CRYMT-P1
Proprietary Class 2

January 20, 1975

MICROSTRUCTURE OF INCONEL X-750 MATERIALS FOR CRYOGENIC STRUCTURAL APPLICATIONS

Ram Kossowsky
Materials Science Section
METALLURGY AND METALS PROCESSING DEPARTMENT
Westinghouse Research Laboratories
Pittsburgh, Pennsylvania 15235

ABSTRACT

Microstructural characteristic and fracture modes of four X-750 materials were examined using X-ray diffraction, light microscopy, and scanning electron transmission microscopy. The four materials were of the same nominal composition, but varied in the processing procedure; three were subjected to thermal-mechanical treatment following casting while the fourth was produced by Hot Isostatic Pressing (HIP) consolidation. The microstructural and fracture characteristics are used to rationalize the observations of strength, toughness and crack growth properties. Recommendations for optimization of properties for cryogenic applications are advanced.

1. INTRODUCTION

An application area for cryogenic structural materials requiring immediate attention is superconducting electrical machinery such as the two 5 MVA S.C. prototype generators recently developed by

Westinghouse. One of the major candidate structural materials is X-750 which is being utilized for the torque tube, damper shield, outer rotor shell, and stub shafts. The study described in this paper was aimed at: (a) defining the microstructural characteristics of X-750 and determining the effects of processing on microstructural variables; (b) defining the failure modes of specimens tested at cryogenic temperatures; and (c) establishing a correlation between the observed mechanical properties at cryogenic temperatures and microstructural details.

2. MATERIALS AND EXPERIMENTAL APPROACH

Four forms of Inconel X-750 materials all of the same nominal composition, Table 1, were examined. Processing conditions and stock sizes are summarized in Table 2. The MP designated materials were obtained from INCO-Huntington Alloy Products Division. The HIP materials were pressed from powders produced by inert-gas-atomization by Federal-Mogul Company. The starting stock for the powder preparation was the MP-1 material. The MP designated materials were studied following two thermal treatment conditions: (a) solution treated for 1 hour at 1000°C followed by air cooling (ST); and (b) solution treated, then aged at 740°C for 8 hours, furnace cooled to 630°C, held for 8 hours, then air cooled (STDA). The HIP material was examined in the as-pressed condition, and in the STDA condition, as in (2) above.

TABLE 1. COMPOSITION OF X-750 MATERIALS IN WT %

	C	P	Si	Mn	Ni	Cr	Nb+Ta	Cu	Fe	Al	Ti
MP-1	.04	.003	.11	.09	73.0	15.2	.90	.02	6.5	.92	2.40
MP-2	.02	.004	.24	.12	74.8	14.2	.95	.06	6.2	.73	2.62
MP-3	.04	.004	.27	.13	73.2	15.4	.89	.04	6.9	.68	2.64

HIP powder was produced from MP-1

TABLE 2. PROCESSING OF X-750 MATERIALS

Designation	Melting Method	Original Billet Size	Reduction Method	Final Stock Size
MP-1	VIM + VAR	50 cm	hot-rolled, 1150-1200°C	25 cm
MP-2	AM + VAR	50 cm	press forged to 37 x 42 cm; hot-rolled	10 cm
MP-3	VIM	50 x 50	hot-rolled	5 cm
HIP	Isostatic hot-pressed	15 x 10 x 1 cm	---	15 x 10 x 1 cm

VIM = Vacuum Induction Melt

VAR = Vacuum Arc Remelt

AM = Air Melt

Microstructural characterization and fracture mode determinations were carried out by microscopical examination of polished and etched surfaces, X-ray analysis, and by transmission electron microscopy of thin foils. Fracture modes were determined by scanning electron microscopy of fractured surfaces obtained from tensile and fracture toughness specimens tested at 4.2°K.

3. RESULTS

The phases present in the materials are shown in Table 3. The diffraction patterns were obtained from non-soluble residues and, therefore, do not show γ(Ni) or γ'(Ni_3; AlTi). It is to be noted that $M_{23}C_6$ carbides are not present. This is in agreement with data obtained for a large variety of nickel-based superalloys,[2] where the dominant carbides precipitate during aging below 760°C are the MC types. The $M_{23}C_6$ carbides start to evolve at about 825°C. One should also note the oxides in the HIP material. These may have resulted from oxidation during the powder atomization process.

TABLE 3. X-RAY ANALYSIS OF NON-SOLUBLE RESIDUES

	Phases	
Material/Condition	Major	Minor
MP-1 STDA	(Ti, 35 Nb) C	(Ti, 20 Nb) C Al_2SiO_4
MP-2 STDA	(Ti, 35 Nb) C	TiN
MP-3 STDA	(Ti, 35 Nb) C	TiN
HIP, as-pressed	(Ti, 35 Nb) C TiC	
HIP, STDA	(Ti, 35 Nb) C TiC	Al_2O_3 Fe_3O_4

Grain morphologies are shown in Fig. 1 and grain size distributions are plotted in Fig. 2. The average grain size of the MP-1 material is about an order of magnitude larger than MP-2 and MP-3. In the HIP material, grain size was determined through prior-particle

boundaries, although, as seen in Fig. 1 there is a substructure associated with each particle.

Figures 3 and 4 show typical microstructural features revealed by thin foil transmission microscopy. Continuous sheets of carbides in the grain boundaries are typical of the MP-1 material (Fig. 3-a), while in the MP-2 and MP-3 materials the carbide precipitation is discontinuous and is confined mainly to narrow bands around high angle boundaries. There are also differences in the dislocation configurations and γ' morphologies. The γ' in the MP-1 material (Fig. 4-a) are 200-300 Å in diameter and there is no significant dislocation structure associated with the particles. The γ' particles in the MP-3 material are of about the same size but there are well defined networks of dislocations associated with them. The γ' in the MP-2 material appears as wide, shapeless spreads (Fig. 4-b). The change in the HIP material following the thermal treatment is evident by comparing Figs. 3-d to 3-e and Figs. 4-d to 4-e. The isostatic pressing induces a high degree of deformation. During aging most of these dislocations are annealed out (Fig. 3-d). It should be noted that the MP materials shown in Figs. 3 and 4 are also in the aged condition. Nevertheless, the dislocation networks built in during the thermal-mechanical processing are not annealed out completely.

Longitudinal sections of tensile specimens tested to fracture at 4.2°K are shown in Fig. 5. The fractures of the last three specimens are along the maximum shear stress, i.e., at 45° to the tensile axis, while the MP-1 material fractures in non-defined directions. Furthermore, it is apparent from Fig. 5 that the fracture in MP-1 is predominantly

intergranular, while the other three specimens exhibit mixed modes of intergranular and cross-granular fractures.

Fractured surfaces are shown in the scanning electron micrographs of Fig. 6. The intergranular mode of failure in MP-1 is evident (Fig. 6-a). Also note the long, deep grooves in the boundaries which are attributed to pulled out carbide chains. This is in agreement with the transmission micrograph of Fig. 3-a. Although Fig. 6-b indicates some intergranular fracture in MP-2, there is ample evidence for a dimpled, ductile deformation within the grains. The dimpled structure is less evident in MP-3 (Fig. 6-e), and there is an indication of cross-granular tearing. The HIP material shows features similar to MP-1 and MP-3. There is a combination of cross-granular tearing, intergranular cracking and a limited amount of dimpled appearance within the grains. The small particles seen in all the micrographs of Fig. 6 have been identified by energy-dispersive X-ray analysis as (Ti, Nb) C carbides.

The mechanical properties of the X-750 materials are summarized in Table 4.[1] More detailed data can be found elsewhere.[3] The data were chosen to represent the significant effects of microstructural variations.

4. DISCUSSION

The data presented in the above section indicate substantial variations in the mechanical response, in the fracture characteristics, and in the microstructural features among the four X-750 materials. In this section we will show that the mechanical behavior can be related to key microstructural features.

TABLE 4. SUMMARY OF MECHANICAL TEST RESULTS AT 4.2°K, (AFTER LOGSDON)

Material	Yield Strength σ_{ys}, MN/m^2	Elongation %	K_{IC} $MN/m^{-3/2}$	$(\frac{K_{IC}}{\sigma_{ys}})^2$
MP-1 ST	73.5	14.1	102.1	1.93
MP-1 STDA	86.5	6.2	75.6	0.76
MP-2 STDA	97.2	26.8	236.2	5.89
MP-3 STDA	119.1	19.4	147.9	1.52
HIP as-pressed	90.0	22.9	138.2	2.36
HIP STDA	103.3	13.3	98.2	0.91

The hardening effect of a fine dispersion of a second phase, such as γ', has been the key factor in the development of strong superalloys. The increase in strength after aging, for example, MP-1 and HIP materials, can be, therefore, related directly to the precipitation of γ'. There is also a small increase in yield strength of the aged MP-2 and MP-3 as compared to the aged MP-1. This is attributed to the smaller grain size in the former two materials. The degree of grain size dependence of strength, expressed in terms of the well known Hall-Petch relation, i.e., $\sigma = \sigma_o + Kd^{-1/2}$, depends on the slope K. It has been shown in numerous cases that the value of K is quite low for face-centered-cubic structures as compared to body-centered-cubic structures. For example, a factor of 5 decreases in grain size of Cu (K = 0.36) results in less than 10% increase in strength, while in Fe (K = 2.39) the same decrease in grain size results in more than 50% increase in strength. Since X-750 has the f.c.c. structure of Ni, one would anticipate the 20% increase in strength of the MP-2 and MP-3 over MP-1 with an order of magnitude decrease in grain size.

However, there are substantial increases in both ductility and fracture toughness of the MP-2 and MP-3 materials as compared to MP-1, with MP-2 showing the highest toughness in the group. The low toughness of the MP-1 material can be attributed to the continuous precipitation of carbides in the grain boundaries (Figs. 3-a and 6-a). These carbides provide easy crack nucleation sites and a continuous path for crack propagation. Thus, cracking initiates at lower stress levels and crack propagation through the boundaries encounters little resistance. MP-1 thus fails with low overall strain and low fracture toughness. The HIP materials exhibit an appreciable reduction in ductility and fracture toughness upon aging. As in the case of MP-1, long chains of grain boundary carbides (Fig. 6-d) can account for the deterioration in properties. Contrary to that, both MP-2 and MP-3 do not exhibit continuous chains of grain boundary carbides, which results in high ductility and fracture toughness.

The general appearance of the MP-2 material is that of a heavily worked structure. Even after aging, a substantial residual density of dislocation is present (Fig. 3-b). Figure 4-b shows that MP-2 has also a different morphology of γ', which appears in the form of ragged, widely spread particles, rather than the spherical particles typical of the other material. The indication is, therefore, that in the case of MP-2, γ' precipitation has lost coherency. One of the known effects of the semi-coherent, spherical γ', is to cause planar motion of dislocations during deformation. This implies a rather low rate of work hardening. On the other hand, the non-coherent γ' in MP-2, will not promote planar slip. Cross slip will become more prevalent leading to an increase in the rate of work hardening. One of the prevailing theories on the effect

of structure on crack propagation[4] equates the degree of work hardening with a decrease in the rate of crack propagation by invoking a blunting mechanism at the crack tip.

We, therefore, propose that the existing dislocation structure in the MP-2 material coupled with the non-spherical γ' precipitates promotes a high degree of work hardening which results in a substantial improvement in the fracture toughness of this material.

Additional support to the above argument is provided by comparing (a) MP-1 in the ST condition to HIP as-pressed (Table 4) and (b) the two HIP materials. In case (a) the detrimental effect of grain boundary carbides can be discounted. Figure 3-e shows a high residual dislocation density that resulted from the deformation during the pressing process. This is the major difference between MP-1 and the HIP material prior to aging and it accounts for the 30% increase in fracture toughness in the latter. In case (b) the residual dislocation density in the HIP material is completely annealed out after aging (Fig. 3-d). Although aging, which results in a 10% increase in strength due to γ' precipitation, canalso account for the 30% reduction in fracture toughness.

5. CONCLUSIONS

(1) Grain size has a small effect on the strength of X-750 at low temperatures.

(2) Residual dislocation density and γ' morphology accounts for an increase in fracture toughness.

(3) Carbide chains in the grain boundaries are detrimental to low temperature strength.

(4) A controlled microstructure, resulting from lowering carbide contents, and a built-in dislocation structure resulting from an optimized thermal-mechanical-treatment are recommended to improve strength and ductility of X-750 at low temperatures.

ACKNOWLEDGMENTS

The technical support of T. J. Mullen is acknowledged. Discussions with J. M. Wells and W. A. Logsden are appreciated. This work was supported by Contract NBS-CST-8304.

REFERENCES

1. W. A. Logsden, Westinghouse Research Labs, private communication.
2. "The Superalloys", C. T. Sims and W. C. Hagel, Edts., John Wiley and Sons, New York, 1972.
3. W. A. Logsden, in "Structural Materials for Cryogenic Applications", Westinghouse Report 74-9D4-CRYMT-R2, September 1974. Also a paper in this publication.
4. C. Laird, in "Fatigue at Elevated Temperatures", STP 520, ASTM 1972.

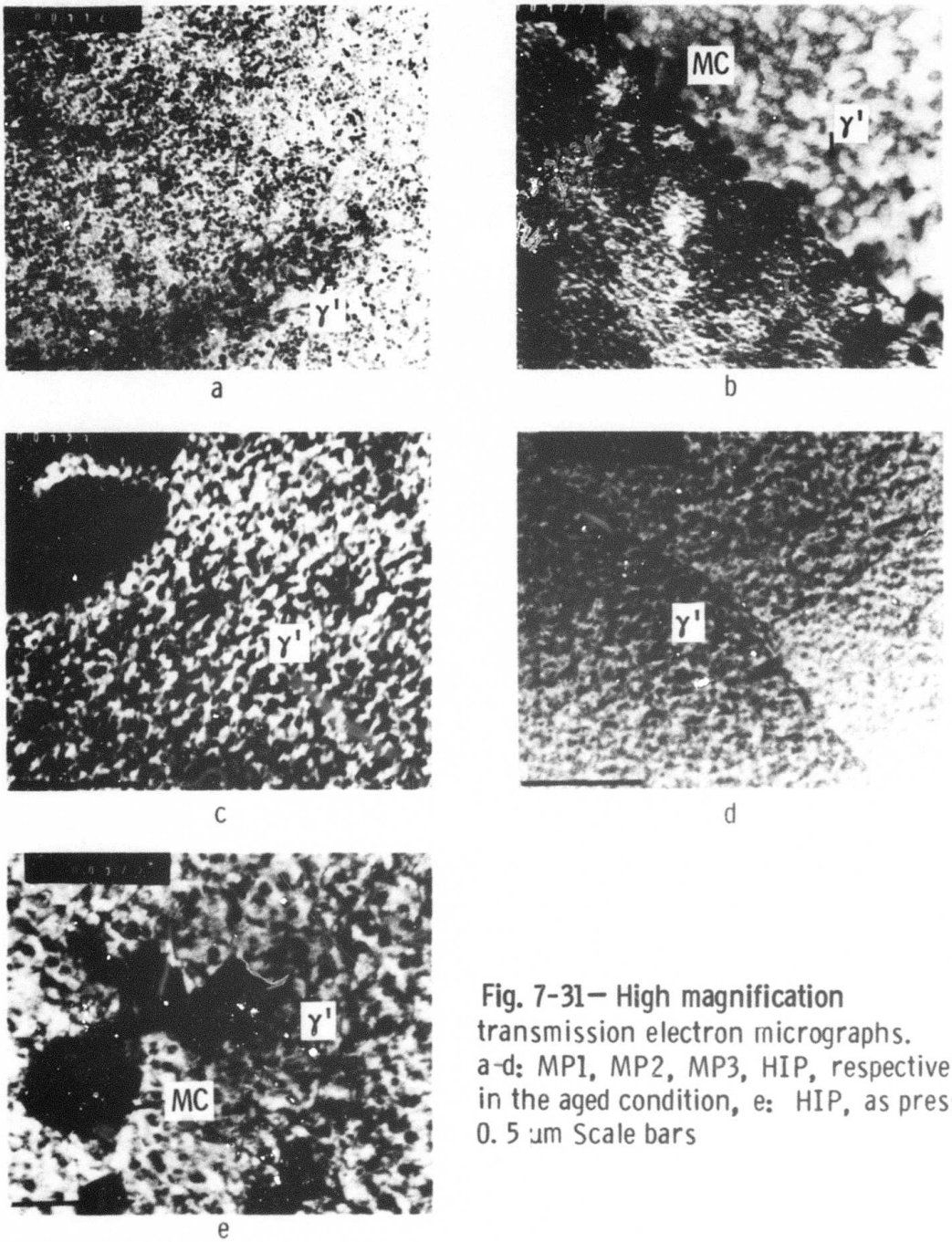

Fig. 7-31— High magnification transmission electron micrographs. a-d: MP1, MP2, MP3, HIP, respectively, in the aged condition, e: HIP, as pressed. 0.5 μm Scale bars

APPENDIX III

Scientific Paper 75-9D4-CRYMT-P2 May 27, 1975
Proprietary Class Unrestricted

EVALUATION OF INCONEL X750 WELDMENTS FOR CRYOGENIC APPLICATIONS

J. M. Wells
Westinghouse Research Laboratories
Pittsburgh, Pennsylvania 15235

1. INTRODUCTION

Advanced cryogenic machinery such as present generation 5MVA superconducting generator prototypes (1,2) contain welded rotor components which experience high rotational stresses at extreme cryogenic temperatures to 4.2 K. To ensure achievement of a reliable failure-safe design of such components, adequate characterization of weldments in specific materials of processed and fabricated conditions representative of those considered for employment in final fabricated hardware must be accomplished.

This paper, therefore, reviews the results of an evaluation of several weldments in Inconel X750 nickel-base superalloy, one prime candidate structural material for such cryogenic machinery applications. Gas Tungsten Arc (GTA) and Vacuum Electron Beam (VEB) weldments were evaluated in X750 material in three processed conditions, namely: (1) solution treated (ST) prior to welding, (2) solution treated and double aged (STDA) prior to welding and (3) solution treated and double aged following welding. Radiographic, metallographic and fractographic examinations of all weldments were conducted. Mechanical and fracture

mechanical tests were conducted on transverse weldment samples from room temperature to 4.2 K.

2. MATERIAL, PROCESSING AND WELDING APPROACH

All material was obtained from a single commercially procured 25.4 cm hot finished forging quality (HFFQ) billet, produced by vacuum induction melting-vacuum arc remelting (VIM-VAR). Transverse full cross sectional slices approximately 1.6 cm (5/8 inch) thick were cut from the original billet to provide round "plate" stock from which samples to be welded were machined. Chemical analysis of the X750 material used is given in Table I.

Samples were machined from each cross section slice to allow three weld test samples of approximately 25cm(10 in.) in length for each weldment/heat treatment condition. Weldments were made by both vacuum electron beam welding without filler wire addition and by manual gas tungsten arc welding with INCO F69 filler wire. For each of these two welding processes, a series of three pre-and/or post-weld heat treatment schedules were employed, namely (a) solution treat before welding and tested as welded, (b) solution treat and double age before welding and tested as welded, and (c) solution treat before welding with a full solution treat and double age after welding and before testing. The details of these heat treating schedules are given in Table II. Also listed in Table II are the basic welding conditions for both processes employed.

3. MECHANICAL TESTING - APPROACH AND RESULTS

Mechanical tests consisted of standard smooth bar uniaxial tensile tests on transverse composite base metal-heat affected zone - weldment samples to determine the 0.2 percent offset yield strength, (σ_{ys}), ultimate tensile strength, (σ_{UTS}), reduction in area,(R.A.), and percentage elongation, (Elong.). Smooth tensile specimen geometry was 0.51 cm (0.20 in.) diameter with a 2.54 cm (1.00 in.) gauge length centered on the weld fusion zone. Notched tensile strength (NTS) values were also determined on transverse composite weldment samples with a notch acuity (stress concentration factor) of K_t = 10 located in the approximate center of the weld fusion zone. Results of these mechanical tests at 297 K, 77 K and 4.2 K are given in Table III for both these weldments and the corresponding base material (unwelded).

Fracture mechanics tests were conducted to determine the fracture toughness parameter, K_{IC} (J_{IC}) and the fatigue crack growth rate, FCGR. Fracture toughness specimens consisted of 1.27 cm (0.500 in.) thick compact tension (1/2 TCT) specimens, while FCGR specimens consisted of 1.27 cm (0.500 in.) thick wedge open loading (WOL) geometry compact tension specimens. All samples were notched in the approximate center of the weld fusion zone, with precracking achieved at room temperature and at loads appreciably less than that achieved in the subsequent testing. The fracture toughness values K_{IC} (J_{IC}) were determined via the elastic-plastic (J_{IC}) fracture criterion and the associated resistance curve test technique for determining elastic-plastic fracture toughness values in the identical manner as employed with corresponding

IN X750 base metal as described elsewhere by Logsdon (3). Resulting values of K_{IC} (J_{IC}) and FCGR parameters for these weldments and the corresponding base metal material (unwelded) are listed in Table IV. The FCGR data is expressed in terms of a generalized fatigue crack growth rate law:

$$\frac{da}{dn} = C_o \Delta K^n \qquad (1)$$

where $\frac{da}{dn}$ is the rate of crack growth, C_o is an intercept constant determined from a log $\frac{da}{dn}$ versus log ΔK plot, n is the slope of the log-log plot and ΔK is the stress intensity factor range. Values of the exponent n and the coefficient C_o are listed in Table IV for the various conditions.

4. RADIOGRAPHIC, METALLOGRAPHIC AND FRACTOGRAPHIC RESULTS

Radiographs of all weldments were obtained and examined for possible defects. Photographs of these radiographs have been published elsewhere (4). In the VEB weldments, intermittent linear weld centerline indications were observed and were avoided in laying out mechanical and fracture mechanics tests specimens from these weld plates. In the GTA weldments, no linear defect indications were found, although some small scattered porosity was observed primarily along the center of the weld fusion zone.

Transverse sections were cut from all weld plates and specimens prepared for macro and microstructural examination. Photographs of typical macro and microstructural features of the weld fusion zone-heat affected zone and base metal were also presented in a previous report (5). With the exception of some microfissuring (see Fig. 1)

along grain boundaries in the VEB weld heat affected zone immediately adjacent to weld fusion line, no anomalies were noted.

A more detailed microstructural analysis of the base metal (unwelded) employing x-ray diffraction, light microscopy and scanning electron transmission microscopy is reported elsewhere by Kossowsky (6,7). One highly significant finding on this base material (MP-1), was the observance via thin foil transmission microscopy of a continuous sheet or film of (Ti, 35Nb)C Carbide along the matrix grain boundaries. Such carbide films are, therefore, present in the starting material used for the present weldments.

A series of microprobe trances was conducted on weldment samples by scanning across the weld heat affected zone (HAZ) into the weld fusion zone (FZ) and monitoring composition concentrations for Ti, Nb, Cr and Al. Photomicrographs of these microprobe areas are shown in Figs. 2A and 3A for the VEB and the GTA weldments respectively. The corresponding microprobe trace results for Ti and Nb are shown in Figs. 2B and 3B. Traces for Cr and Al in these weldments were not considered of sufficient significance for inclusion here. It is observed that localized concentration increases in both Ti and Nb occur at grain boundary (and twin locations) in both the HAZ and FZ. In addition, a localized concentration decrease in both Ti and Nb occurs at the HAZ-FZ interface. The general background level for these two elements in the weld FZ appears generally higher and experiences greater fluctuations than in the HAZ. While high Ti and Nb concentrations exist in the grain boundaries of the FZ as well, it is felt unlikely that continuous films of MC Carbide would persist following welding, but rather that discontinuous MC Carbide precipitation would occur.

5. DISCUSSION

The yield strength and the ultimate tensile strength of the IN X750 base material did not exhibit a pronounced temperature dependence in either the ST or the STDA heat treatment condition. A systematic decrease in both the reduction in area and percentage elongation with decreasing temperature was observed, however. Also, the notched tensile strength increased with decreasing temperature.

The general strength levels of both the VEB and the GTA weldments are comparable to the correspondingly heat treated base metal. Weldments without a post weld heat treatment had approximately 75% or more of the yield and tensile strength of the base metal (unweided) at 297 K, and their strength efficiencies increased to about 90% or greater at 4.2 K. With a full post weld STDA treatment, both the VEB and the GTA weldments demonstrated a strength efficiency of 95 to 110% of the corresponding STDA heat treated base metal through the temperature range of 297 to 4.2 K. Fracture locations of the smooth tensile specimens occurred in the weld HAZ for those weldments without a post weld heat treatment and in the base metal far removed from the weld in weldments with a post weld heat treatment. Thus, the weakest region in any of these specimens was found to be the HAZ in the as-welded condition.

Fracture toughness levels of all weld fusion zone samples were found to be well in excess of those of the base metal in either heat treatment. The VEB welded samples demonstrated the highest levels of fracture toughness; in fact, VEB weldments without a post weld heat treatment proved to have a K_{IC} (J_{IC}) value beyond the measuring capacity

of these tests which employed the 1/2 TCT specimens. The toughness levels of the GTA weldments were found to be somewhat less than that of the VEB weldments but still considerably above that of the unwelded base metal.

Such high fracture toughness values of these weldments were not predicted a priori on the basis of the simple mechanical property data given in Table III. On the contrary, past experience with fully austenitic AISI 310S and Kromarc 58 stainless steel weldments (4,5,7) had shown markedly reduced levels of fracture toughness in weldments as compared to those unwelded base metals. Of course, those austenitic stainless steels were non-hardenable and of significantly different chemical composition so as not to be directly comparable with the present IN X750 material. Nevertheless, the high K_{IC} (J_{IC}) values of these weldments in IN X750 is a more favorable situation indicative of larger defect size tolerance in the weld fusion zone than in the base material.

The results shown here may not be representative of weldments in all IN X750 material, since it was shown (6,7) that a continuous grain boundary carbide film existed in the specific lot of material used for these weldments. It has also been shown (3,7) that base metal fracture toughness levels of IN X750 material without such continuous grain boundary carbide films are significantly higher than that experienced with the present base material. Although no weldments were actually made in these other base metal X750 materials, it is the author's opinion that the difference in fracture toughness levels between such weldments and such alternative X750 base materials would not have been of such magnitude as the present results.

The fatigue crack growth rates measured for all X750 weldment conditions were identical to that of the base metal in either the ST or STDA heat treatment at 4.2 K. No temperature dependence of the FCGR of these weldments was detected from 77 K to 4.2 K. At present, it is not clear to the author why the FCGR for both the VEB and the GTA weldments should be identical to that of the unwelded base metal, since obvious microstructural differences exist.

It appears worthwhile to further examine the present weldment microstructures. An improved characterization of such weld fusion zone structures may lead to a better understanding of why weld structures in IN X750 possess such high fracture toughness levels and perhaps lead to processing technique modifications whereby fracture toughness of both base metals and weldments can be optimized.

6. CONCLUSIONS

1. Mechanical strength efficiencies (σ_{ys} and σ_{uts}) achieved by both VEB and GTA weldments in Inconel X750 without a post weld STDA heat treatment were around 75 to 90% of the unwelded base metal. Following a post weld STDA heat treatment, weldment efficiencies were 95 to 110% of the unwelded base metal. Notch tensile tests did not indicate a notch sensitivity of any weldment condition investigated.
2. Tensile fracture locations for weldments without a post weld heat treatment were in the weld HAZ area adjacent to the weld, whereas following a full STDA post weld heat treatment the tensile fracture location shifted to the base metal well away from the weld location.

3. Fracture toughness values K_{IC} (J_{IC}) of all IN X750 weldments at 4.2 K were appreciably greater than for the unwelded base metal, with the VEB weldments without a post weld heat treatment having the highest K_{IC} (J_{IC}) values. The STDA post weld heat treatment reduces the K_{IC} (J_{IC}) values of both VEB and GTA weldments.

4. No significant difference was observed in the fatigue crack growth rate of any weld condition investigated from that of the unwelded base metal at 4.2 K. Also, there appears to be no temperature dependence of the FCGR for these weldments from 77 K to 4.2 K.

5. The larger K_{IC} (J_{IC}) values for all weldments is partially attributed to the dissolution in the weld fusion zone of a continuous MC Carbide film present in the parent base metal. Moreover, it is felt that additional as yet unspecified microstructural characteristics of the weld fusion zone also contribute to the high fracture toughness levels obtained.

ACKNOWLEDGMENTS

The author gratefully acknowledges Dr. R. Kossowsky and Mr. W. A. Logsdon of the Westinghouse Research Laboratory for their advice, contributions and cooperation in the conduct of this work and to Messrs. W. R. Kuba and J. E. Smith for their contributions in the experimental conduct of this effort.

This work was supported in part by the Advanced Research Projects Agency of the Department of Defense and was monitored by the Cryogenics Division of the National Bureau of Standards, Boulder, CO under contract CST-8304. The views and conclusions contained in this paper are those of the author and should not be interpreted as necessarily representing official policies, expressed or implied, of the Advanced Research Projects Agency or of the U. S. Government.

REFERENCES

1. R. D. Blougher, T. J. Fagan, J. H. Parker, Jr., J. M. Wells and J. L. McCabria, "A High Speed Superconducting Generator", Proc. of International Cryogenic Engineering Conference, Kyoto, Japan, May 1974.
2. C. J. Mole, T. J. Fagan, H. E. Haller, III, D. C. Litz and A. Patterson, "Five MVA Superconducting Generator Development", Westinghouse Research Report 72-1J2-CRYAL-P3 (Unrestricted), September 22, 1972.
3. W. A. Logsdon, "Cryogenic Fracture Mechanics Properties of Several Manufacturing Process/Heat Treatment Combinations of Inconel X750", paper F-4 presented this conference.
4. G. G. Lessmann, W. A. Logsdon, R. Kossowsky, M. P. Mathur, and J. M. Wells, "Structural Materials for Cryogenic Applications -- Second Semi-Annual Technical Report", Westinghouse Research Report 74-9D4-CRYMT-R2, September 9, 1974.
5. G. G. Lessmann, W. A. Logsdon, R. Kossowsky, M. P. Mathur and J. M. Wells, "Structural Materials for Cryogenic Applications -- First Semi-Annual Technical Report", Westinghouse Research Report 74-9D4-CRYMT-R1, March 1, 1974.
6. R. Kossowsky, "Microstructure of Inconel X750 Materials for Cryogenic Structural Applications", paper F-5 presented this conference.
7. J. M. Wells, R. Kossowsky, W. A. Logsdon, and M. R. Daniel, "Structural Materials for Cryogenic Applications -- Third Semi-Annual Technical Report", Westinghouse Research Report 74-9D4-CRYMT-R1, March 10, 1975.

TABLE I - Material Documentation Data

MATERIAL	Inconel X750 (AISI 688, ASTM A637, Grade 688)
SOURCE	Huntington Alloys Division of INCO
HEAT NO.	HT56CIXY (VIM-VAR)
FORM	25.4 cm (10 in.) diameter HFFQ round stock

CHEMISTRY	C	P	S	Si	Mn	Ni	Cr	(Nb+Ta)	Cu	Fe	Al	Ti	Co	O	N	H
Supplier Analysis	.04	--	.007	.13	.10	73.72	15.21	.91	.02	6.49	.93	2.42	--	--	--	--
Ⓦ Analysis	.04	.003	<.001	.11	.089	73.0	15.2	.90	.022	6.47	.92	2.40	.017	.0016	.004	.00012

TABLE II - Weld Specimen Documentation Data

	Pre-Weld Condition	Weld Process	Postweld Treatment	Thickness
Plate No. 1	ST	VEB	(as-welded)	1.6 cm (5/8 in.)
Plate No. 2	STDA	VEB	(as-welded)	1.6 cm (5/8 in.)
Plate No. 3	ST	VEB	STDA	1.6 cm (5/8 in.)
Plate No. 5	ST	GTA	(as-welded)	1.6 cm (5/8 in.)
Plate No. 6	STDA	GTA	(as-welded)	1.6 cm (5/8 in.)
Plate No. 7	ST	GTA	STDA	1.6 cm (5/8 in.)

Heat Treatment

ST - Solution treat at 982°C (1800°F) for 1 hour, air cool (R_C 29.5).

STDA - ST + double age 732°C (1350°F) for 8 hours, furnace cool to 621°C (1150°F), hold 8 hours and air cool (R_C 35.7).

Welding Conditions

GTA - Butt joint, double V, 60° include angle, GTAW-manual, filler wire F69-0.24 cm (3/32") dia., Direct Current Straight Polarity - 180 amps, 14-15 volts, shield gas 50% Ar-50% He @ 20 cfh, weld speed ∿ 0.24 cm/sec (5 ipm), root gap ∿ .24 cm (3/32"), total 12 passes.

VEB - Butt joint, flat, vacuum electron beam, no filler, 150 kV, 42 ma, weld speed 0.85 cm/sec (20 ipm) single pass, full penetration.

TABLE III - Mechanical Test Results for IN X750 Weldments

Mat. Condition	Test Temp K	σ_{ys}, MPa (ksi)	σ_{UTS}, MPa (ksi)	R.A., %	Elong., %	NTS*, MPa (ksi)	NTS / σ_{ys}
ST (Base Metal)	297	663 (96.2)	987 (143.2)	18.2	17.6	1,201 (174.2)	1.7
	77	769 (111.6)	1,086 (157.5)	13.8	15.6	1,342 (194.7)	1.6
	4.2	736 (106.8)	1,018 (147.7)	12.9	14.1	1,411 (204.6)	1.9
STDA (Base Metal)	297	824 (119.5)	1,098 (159.2)	12.4	12.2	1,382 (200.5)	1.8
	77	892 (129.4)	1,140 (165.4)	8.6	9.2	1,408 (204.2)	1.7
	4.2	867 (125.7)	1,051 (152.5)	6.2	6.1	1,480 (214.7)	1.7
ST/VEBW	297	552 (80.0)	772 (112.0)	30.8	8.0	1,009 (146.3)	1.8
	77	677 (98.2)	948 (137.5)	25.0	11.8	1,227 (178.0)	1.8
	4.2	731 (106.0)	966 (140.1)	19.6	11.6	1,337 (193.9)	1.8
STDA/VEBW	297	594 (86.2)	807 (117.0)	30.3	3.2	1,070 (155.2)	1.8
	77	752 (109.0)	920 (133.5)	11.4	2.6	1,320 (191.5)	1.6
	4.2	771 (111.8)	936 (135.8)	10.3	3.0	1,403 (203.5)	1.8
ST/VEBW/STDA	297	842 (122.1)	1,089 (157.9)	10.3	10.0	1,496 (217.0)	1.8
	77	903 (131.0)	1,082 (156.9)	8.7	6.4	1,633 (236.9)	1.8
	4.2	914 (132.5)	1,063 (154.1)	8.7	7.1	1,683 (244.2)	1.8
ST/GTAW	297	627 (91.0)	838 (121.6)	27.0	13.3	1,098 (159.2)	1.8
	77	717 (104.0)	987 (143.2)	22.0	13.6	1,393 (202.0)	1.9
	4.2	750 (108.0)	1,003 (145.5)	17.1	12.7	1,475 (214.0)	2.0
STDA/GTAW	297	649 (94.1)	840 (121.9)	27.0	8.2	1,172 (170.0)	1.8
	77	800 (116.1)	969 (140.5)	17.0	5.5	1,434 (208.0)	1.8
	4.2	862 (125.0)	993 (144.0)	14.5	4.8	1,485 (215.4)	1.7
ST/GTAW/STDA	297	855 (124.2)	1,096 (159.0)	11.9	9.0	1,571 (277.8)	1.8
	77	931 (135.0)	1,109 (160.8)	9.2	5.6	1,710 (248.0)	1.8
	4.2	958 (139.0)	1,124 (163.0)	8.7	5.3	1,629 (236.2)	1.7

* K_t = 10 for NTS

1 ksi = 6.895 MPa

624<

TABLE IV - Fracture Mechanics Test Results for IN X750 Weldments

Mat. Condition	Test Temp. K	J_{IC} N/m (lb/in)	K_{IC} $MP_a\sqrt{m}$ (ksi$\sqrt{in}$)	$\frac{K_{IC}}{\sigma_{ys}}$	n	FCGR Co
ST (Base Material)	4.2	4.29×10^4 (245)	101 (92.2)	0.86	8.00	2.04×10^{-18}
STDA (Base Material)	4.2	2.42×10^4 (138)	76.1 (69.2)	0.55	8.00	2.04×10^{-18}
ST/VEBW	4.2	$>2.97 \times 10^5$ (>1696)*	>267 (>242.7)*	>2.29	8.00	2.04×10^{-18}
STDA/VEBW	4.2	$>3.13 \times 10^5$ (>1789)*	>274 (>249.2)*	>2.23	8.00	2.04×10^{-18}
ST/VEBW/STDA	4.2	1.29×10^5 (738)	176 (160.1)	1.21	8.00	2.04×10^{-18}
ST/GTAW	4.2	1.53×10^5 (875)	192 (174.3)	1.60	8.00	2.04×10^{-18}
STDA/GTAW	4.2	1.21×10^5 (690)	171 (154.8)	1.24	8.00	2.04×10^{-18}
ST/GTAW/STDA	4.2	7.44×10^4 (425)	134 (121.5)	0.87	8.00	2.04×10^{-18}

* Toughness exceeds the measurement capacity of 1/2 TCT specimens; i.e., the dimensional parameters of the 1/2 TCT specimens did not meet the size requirement for a valid J test:

$$a, B, b > 25 \left(\frac{J}{\sigma_{ys}}\right)$$

$1 \frac{lb}{in} = 175.1 \frac{N}{m}$

1 ksi$\sqrt{in}$ = 1.10 $MP_a\sqrt{m}$

Figure 1 - Typical microfissure observed along grain boundaries in HAZ immediately adjacent to the weld fusion line in vacuum EB welded IN X750, (X200).

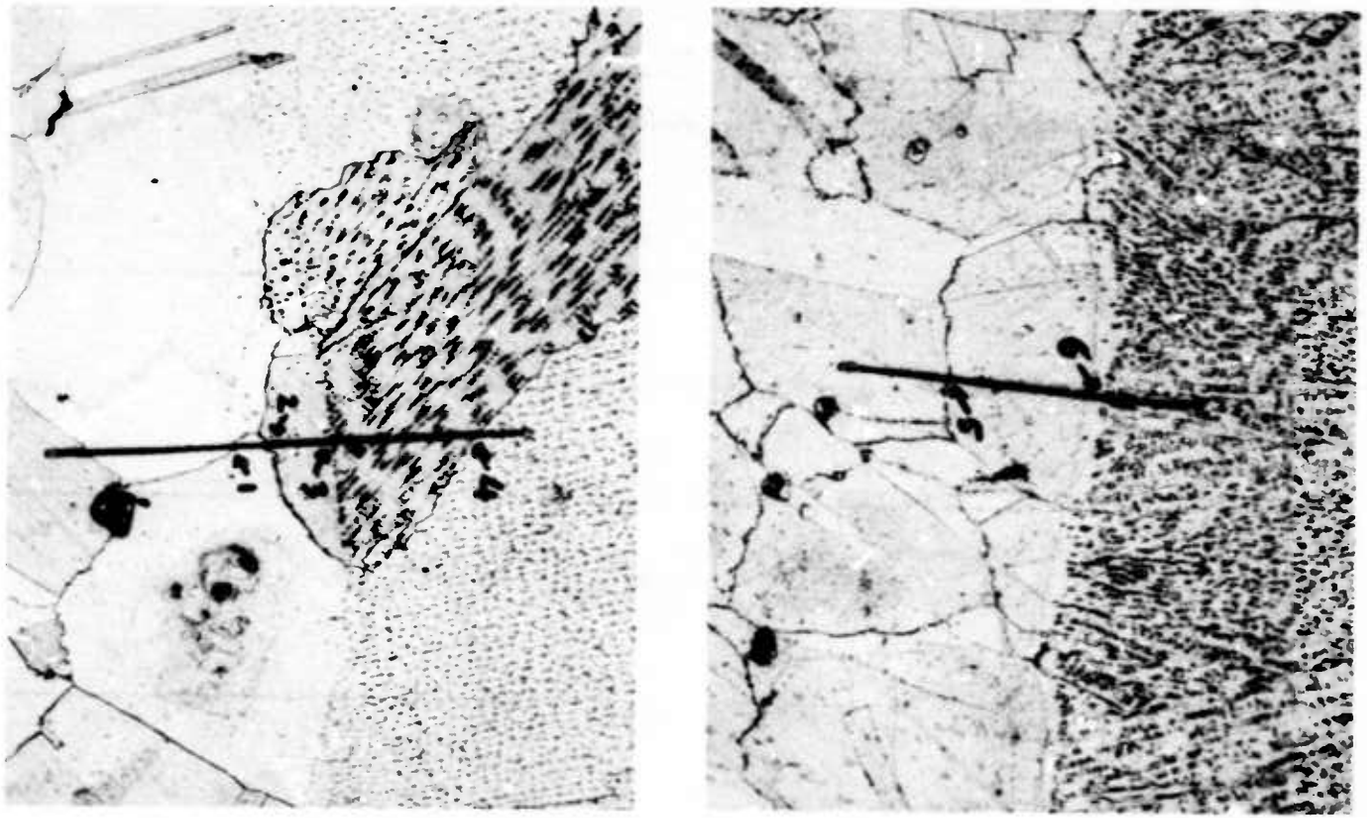

TRACE A

TRACE B

Figure 2A - Photomicrographs of microprobe trace areas across weld HAZ to FZ (left to right), trace A for ST/VEB/STDA and trace B for STDA/VEB weldments (X200).

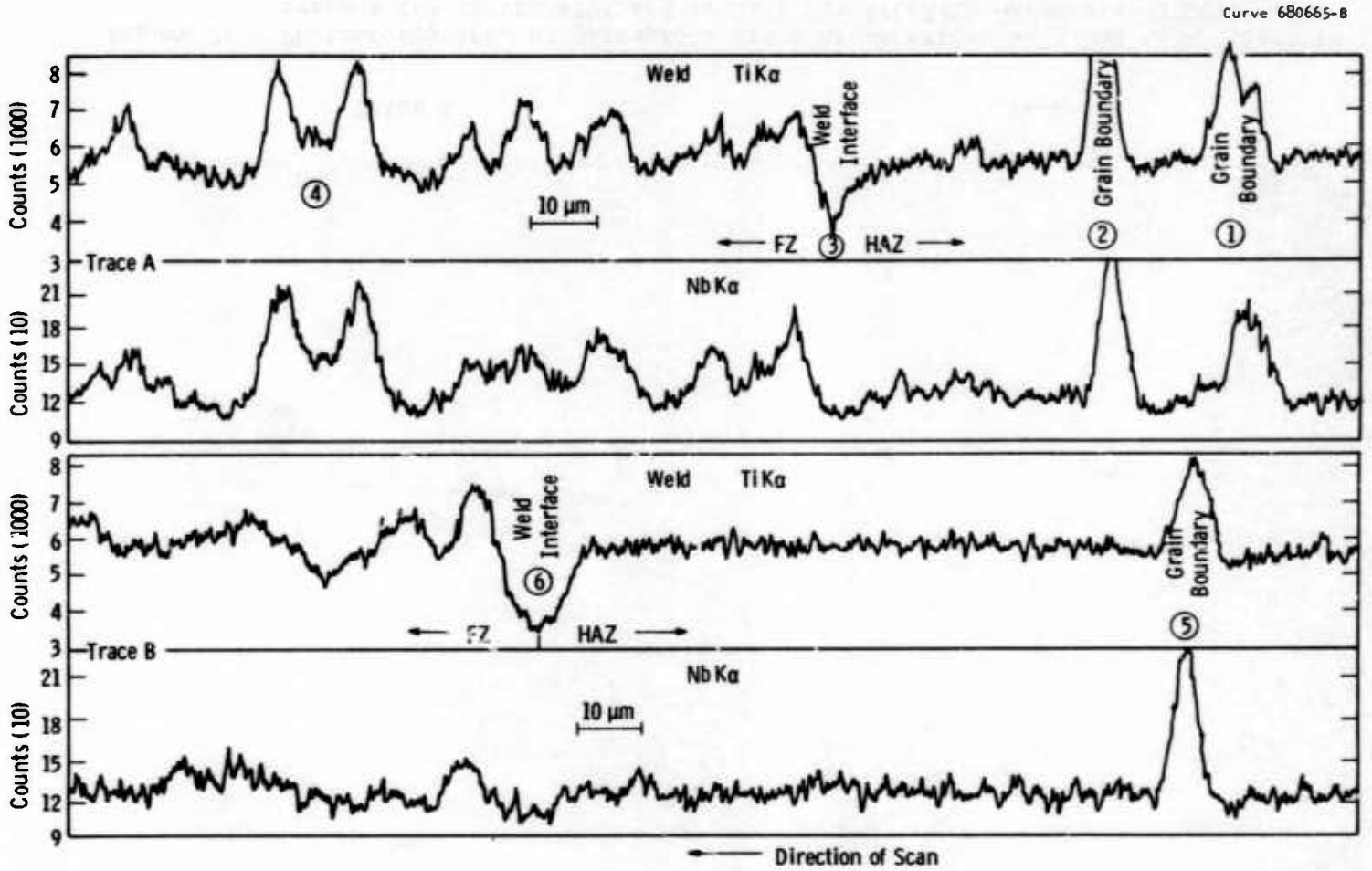

Fig. 2B—Microprobe traces of Ti and Nb across weld HAZ to FZ (right to left), trace A for ST/VEB/STDA and trace B for STDA/VEB weldments

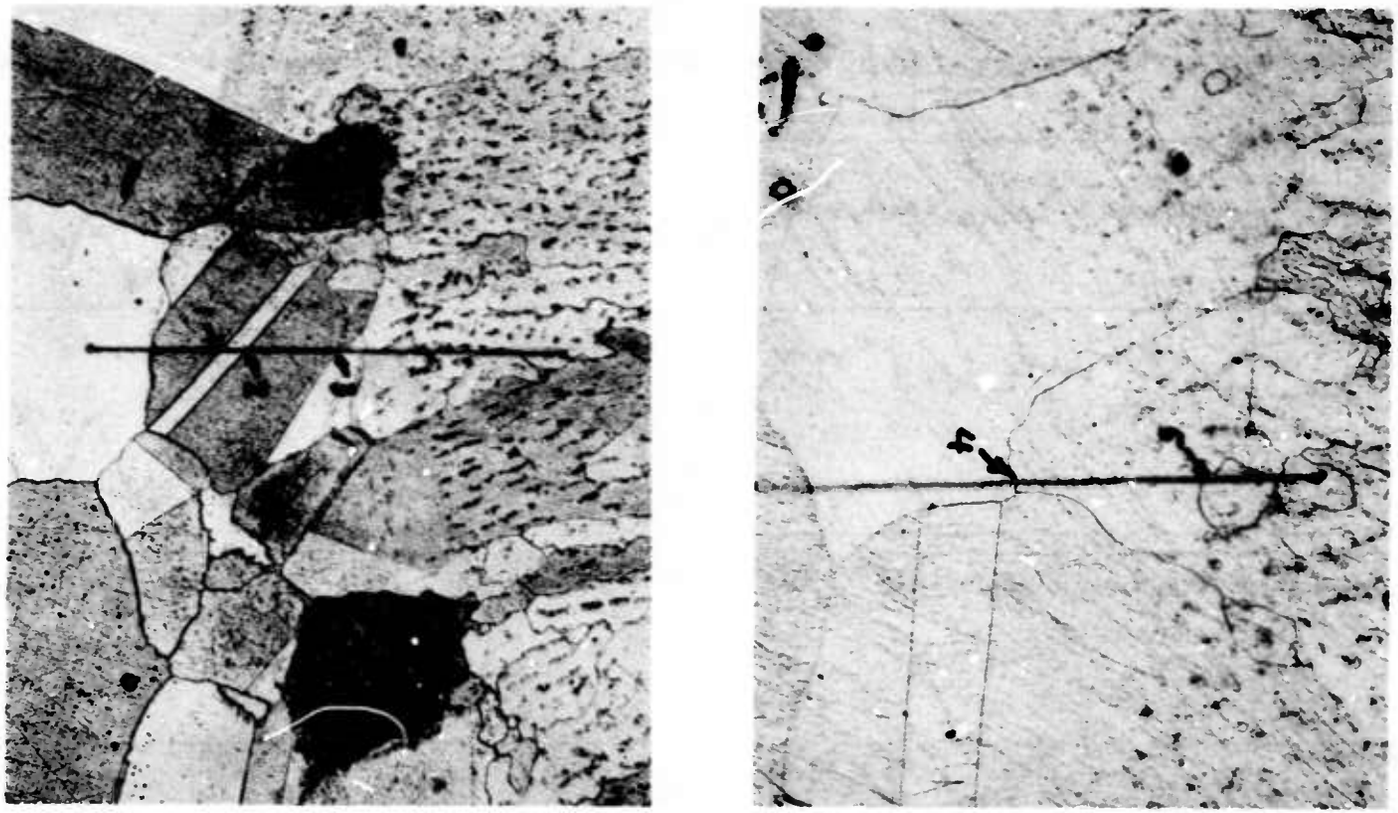

TRACE A

TRACE B

Figure 3A - Photomicrographs of microprobe trace areas across weld HAZ and FZ (left to right), trace A for ST/GTA/STDA and trace B for STDA/GTA weldments (X200).

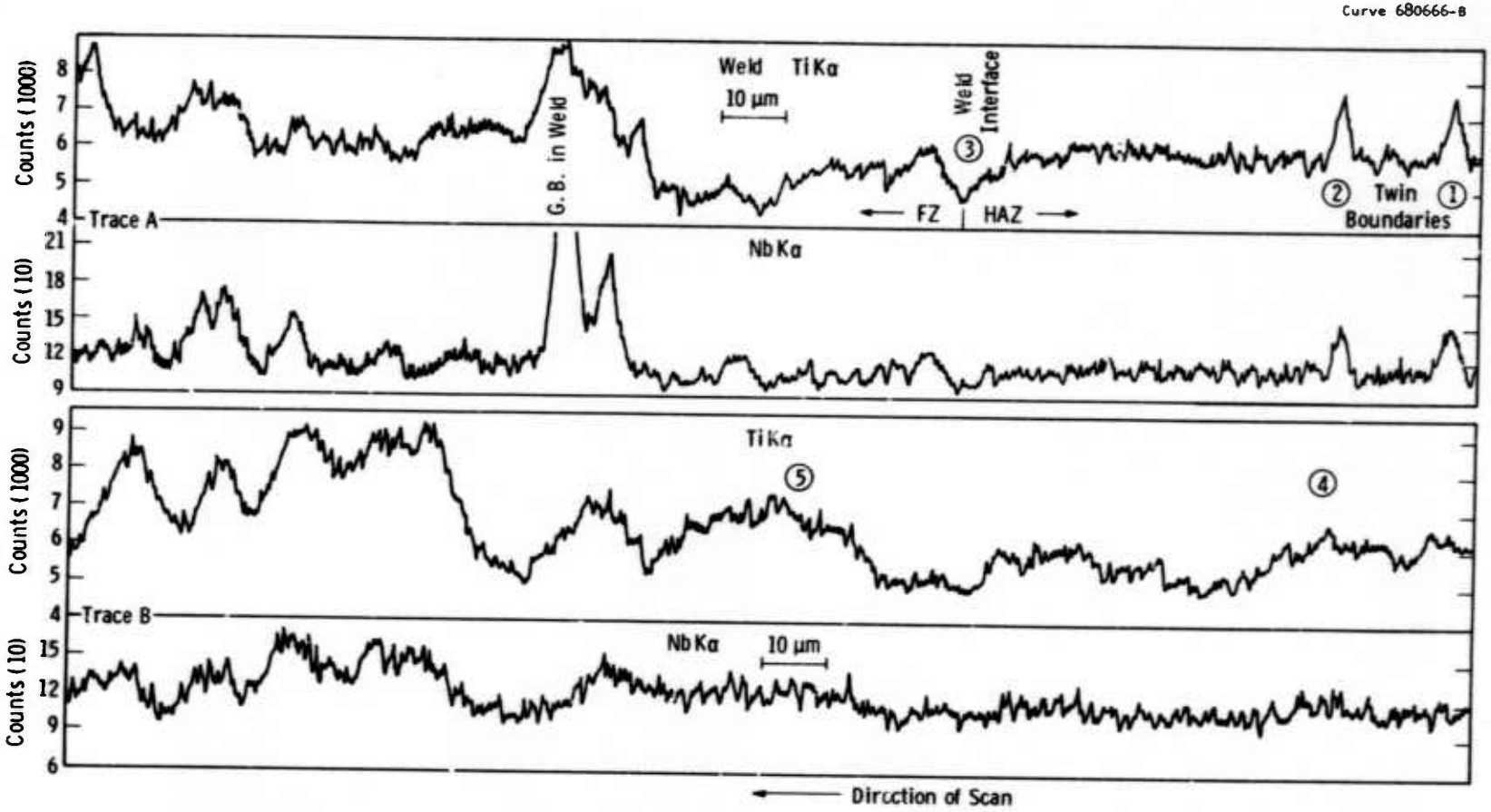

Fig. 38—Microprobe traces of Ti and Nb across weld HAZ to FZ (right to left) trace A for ST/GTA/STDA and trace B for STDA/GTA weldments